



**HAL**  
open science

# High resolution mass spectrometry for molecular characterization of bio-oils produced by pyrolysis of lignocellulosic biomass

Jasmine Hertzog

► **To cite this version:**

Jasmine Hertzog. High resolution mass spectrometry for molecular characterization of bio-oils produced by pyrolysis of lignocellulosic biomass. Chemical engineering. Université de Lorraine, 2017. English. NNT : 2017LORR0180 . tel-01905674

**HAL Id: tel-01905674**

**<https://hal.univ-lorraine.fr/tel-01905674v1>**

Submitted on 14 Jan 2020

**HAL** is a multi-disciplinary open access archive for the deposit and dissemination of scientific research documents, whether they are published or not. The documents may come from teaching and research institutions in France or abroad, or from public or private research centers.

L'archive ouverte pluridisciplinaire **HAL**, est destinée au dépôt et à la diffusion de documents scientifiques de niveau recherche, publiés ou non, émanant des établissements d'enseignement et de recherche français ou étrangers, des laboratoires publics ou privés.



## AVERTISSEMENT

Ce document est le fruit d'un long travail approuvé par le jury de soutenance et mis à disposition de l'ensemble de la communauté universitaire élargie.

Il est soumis à la propriété intellectuelle de l'auteur. Ceci implique une obligation de citation et de référencement lors de l'utilisation de ce document.

D'autre part, toute contrefaçon, plagiat, reproduction illicite encourt une poursuite pénale.

Contact : [ddoc-theses-contact@univ-lorraine.fr](mailto:ddoc-theses-contact@univ-lorraine.fr)

## LIENS

Code de la Propriété Intellectuelle. articles L 122. 4

Code de la Propriété Intellectuelle. articles L 335.2- L 335.10

[http://www.cfcopies.com/V2/leg/leg\\_droi.php](http://www.cfcopies.com/V2/leg/leg_droi.php)

<http://www.culture.gouv.fr/culture/infos-pratiques/droits/protection.htm>

High resolution mass spectrometry for molecular  
characterization of bio-oils produced by pyrolysis of  
lignocellulosic biomass

A DISSERTATION

Submitted in partial fulfillment of the requirement for the degree of

DOCTOR OF CHEMISTRY OF THE UNIVERSITY OF LORRAINE

by

**Jasmine Hertzog**

Pr. Laurence Charles	Université d'Aix-Marseille	Rapporteur
Pr. Dr. Wolfgang Schrader	University Duisburg-Essen, Germany	Rapporteur
Dr. Emmanuelle Leize-Wagner	Université de Strasbourg	Examiner
Dr. Marie Hubert-Roux	Université de Rouen	Examiner
Dr. Ondřej Mašek	University of Edinburgh, United-Kingdom	Examiner
Dr. Anthony Dufour	Université de Lorraine	Examiner
Dr. Vincent Carré	Université de Lorraine	Co-director
Pr. Frédéric Aubriet	Université de Lorraine	Co-director



## Préambule/Preamble

Les travaux de recherche effectués dans le cadre de cette thèse ont été financés par une bourse du Ministère de l'Enseignement Supérieur et de la Recherche, allouée par l'École Doctorale SESAMES. Ces travaux ont été réalisés au Laboratoire de Chimie et Physique – Approche Multi-échelles des Milieux Complexes (LCP-A2MC) à Metz, en collaboration avec l'équipe GRENNER du Laboratoire Réactions et Génie des Procédés (LRGP) de Nancy.

Dans un premier temps, je souhaiterais adresser mes vifs remerciements et exprimer toute ma gratitude à Frédéric Aubriet et Vincent Carré, porteurs de ce projet, pour leur disponibilité durant ces 3 années, pendant lesquelles ils m'ont transmis leurs connaissances scientifiques et techniques et leurs compétences. Mais également pour la confiance qu'ils ont su me témoigner, en de nombreuses occasions, en me laissant présenter ou effectuer des travaux de recherche en dehors du laboratoire.

Je remercie les membres de l'équipe GREENER pour m'avoir fourni les échantillons qui ont constitué mon corpus d'étude et avec qui j'ai partagé d'agréables moments. Je tiens plus particulièrement à remercier Anthony Dufour pour l'intérêt qu'il a porté à mes travaux de thèse, la confiance qu'il m'a témoignée en me proposant de participer à des événements scientifiques de qualité et enfin d'avoir accepté d'être examinateur de ma thèse.

Je prie le Dr Marie Hubert-Roux, le Dr Emmanuelle Leize-Wagner et le Pr Laurence Charles d'accepter mes remerciements pour l'honneur qu'elles me font en ayant accepté d'évaluer mes travaux de thèse en qualité d'examinatrice ou de rapporteur.

*I would like to thank Pr-Dr Wolfgang Schrader for the great honor I have been given by accepting to be rapporteur of my PhD thesis.*

*Many thanks to Dr Ondřej Mašek for the honour that has been bestowed upon me by accepting to be a member of my jury. But also, for having given me the opportunity to come to the University of Edinburgh, thanks to the European grant COST "Lignoal", for making some research works and to develop a fruitful collaboration between our labs. I also would like to thank Dr Logan Mackay for his kindness and help during the two months I spent in Edinburgh in the mass spec lab.*

*I sincerely thank Pr Peter O'Connor for his guidance and teaching.*

Mes remerciements vont également à Lionel Vernex-Loset et Gabriel Krier pour leur soutien technique et administratif et nos discussions animées. De même que Sandrine Rup pour son apport scientifique et technique en RMN. Je remercie particulièrement Patrick Chaimbault pour ses conseils scientifiques et professionnels ainsi que pour ses encouragements et son soutien. Merci également à Olivier Delhomme pour son soutien.

Je remercie les membres de l'IUT de Saint-Avold où j'ai pris un grand plaisir à superviser les travaux pratiques de chimie, et plus particulièrement, Marianne Cochez, Philippe Lavalette et Franck Le Douarin. J'adresse aussi mes remerciements aux personnes avec lesquelles j'ai

été engagée dans des projets extérieurs à ma thèse, Valérie Waechter-Chudy (projet CD21) et Bernard Bau (Trophée mc6).

Je témoigne aussi de toute ma reconnaissance aux étudiants, doctorants, post-doctorants et permanents de l'UFR SciFA et de l'ICPM que j'ai eu plaisir de côtoyer, et avec certains de partager des moments musicaux : Marie Bégin, Marie-Claude, Nelly, Jean-François, Jean-Jacques, Jill, Laurent, Loïc, Eric, Nathalie, Cristina, Loïc Becker, Nadège, Nawal, Céline, Clarisse, Anne-Marie...

Je remercie mes amis «lorrains ;)», Typhaine, Jo, Matthieu, Guillaume, Vincent et Clément, pour nos soirées nancéennes et messines. Je suis reconnaissante à mes amis de plus longue date, notamment Ouidad, pour leur patience et leur soutien. Je ne saurais oublier ma famille (ma sœur, mon frère, ma mère et mon père) de toujours croire en moi (plus que moi-même) et pour leur soutien moral. Merci aussi Cyril à qui je ne saurais témoigner ma reconnaissance pour ses encouragements et son soutien sans faille, depuis le début de notre belle aventure, sur le plan professionnel et personnel.

Enfin, j'ai une pensée émue pour ELISE sans qui je n'aurais peut-être pas eu le courage ni la force nécessaire d'arriver à ce niveau et à qui je souhaiterais dédier cette thèse.

## Nomenclature

2,4-DNPH	2,4-dinitrophenylhydrazine
2,5-DHB	2,5-Dihydroxybenzoic acid
2D	Bi-dimensional or two dimensional
2D FT MS	Two dimensional Fourier transform mass spectrometry
2D NMR	Two dimensional nuclear magnetic resonance
2DGC	Two dimensional gas chromatography
2DLC	Two dimensional liquid chromatography
ACN	Acetonitrile
AD	Adsorption chromatography
ADC	Analog-to-digital converter
amu	atomic mass unit
APCI	Atmospheric pressure chemical ionization
API	Atmospheric pressure ionization
APPI	Atmospheric pressure photoionization
BSA	Bovine serum albumin
BSTFA	<i>N,O</i> -bis(trimethylsilyl)-trifluoroacetamide
BTL	Biomass-to-liquids
CFP	Catalyst fast pyrolysis
CID	Collision-induced dissociation
CRM	Charge residue model
Da	Dalton
DAD	Diode array detector
DBE	Double bound equivalent
DEPT	Distortionless Enhancement Polarization Transfer
DMAN	1,8-Bis(dimethyl-amino)naphthalene
DMF	Dimethyl-formamide
EA	Electron affinity
EI	Electron ionization
ESI	Electrospray ionization
ETBE	Ethyl <i>tert</i> -butyl ether
FAME	Fatty acid methyl ester
FCC	Fluid catalytic cracking
FD	Field desorption
FFA	Free fatty acid
FFT	Fast Fourier transform
FID	Free induction decay <i>or</i> Flame ionization detector
F-T	Fischer-Tropsch
FT-ICR MS	Fourier transform ion cyclotron resonance mass spectrometry
FT-IR	Fourier transform infrared
GC	Gas chromatography
GC-FID	Gas chromatography coupled to flame ionization detector
GC-MS	Gas chromatography coupled to mass spectrometry
GCxGC	Comprehensive gas chromatography

GPC	Gel permeation chromatography
GTL	Gas-to-liquids
HDN	Hydrodenitrogenation
HDO	Hydrodeoxygenation
HDS	Hydrodesulfurization
HESI	Heated electrospray ionization
HHV	Higher heating value
HPTLC	High performance thin layer chromatography
HRMS	High resolution mass spectrometer
HSQC	Heteronuclear single quantum coherence/correlation
HTL	Hydrothermal liquefaction
HZSM-5	Acid (protonated) Zeolite Socony Mobil-5
IEM	Ion evaporation model
IR	Infrared
IUPAC	International Union of Pure and Applied Chemistry
KM	Kendrick mass
KMD	Kendrick mass defect
LC	Liquid chromatography
LC-MS	Liquid chromatography coupled to mass spectrometry
LDI	Laser desorption ionization
LIT	Linear ion trap
LLE	Liquid-liquid extraction
MALDI	Matrix assisted laser desorption ionization
MD	Molecular distillation
MS	Mass spectrometry
NMR	Nuclear magnetic resonance
PA	Proton affinity
PCA	Principal component analysis
PDA	Photodiode array
PFBHA	<i>o</i> -(2,3,4,5,6-pentafluorobenzyl)hydroxylamine hydrochloride
Py-GC	Pyrolysis gas chromatography
Py-SPME	Pyrolysis solid phase microextraction
Q-TOF	Quadrupole Time of flight
R.A.	Relative abundance
RDA	Retro Diels-Alder
RF	Radiofrequencies
RI	Refractive index
RMS	Root mean square
RP-HPLC	Reverse phase - high performance liquid chromatography
SD	Sample derivatization
SEC	Size exclusion chromatography
SFE	Supercritical fluid extraction
SPE	Solid phase extraction
SPI	Single photoionization
SPME	Solid phase microextraction
SWIFT	Stored waveform inverse Fourier transform



TAN	Total acid number
TFA	Trifluoroacetic acid
TG	Triglyceride
THF	Tetrahydrofuran
TIC	Total ion current
TMAH	Tetramethylammonium hydroxide
TMDP	2-chloro-4,4,5,5-tetramethyl-1,3,2-dioxaphospholane
TOF	Time of flight
UV	Ultraviolet
VUV	Vacuum ultraviolet
ZSM-5	Zeolite Socony Mobil-5

1 Torr = 1 mmHg

760 mmHg = 1 atm

1 atm =  $1.01325 \cdot 10^5$  Pa



# Table of Contents

<b>Préambule/Preamble</b> .....	<b>I</b>
<b>Nomenclature</b> .....	<b>III</b>
<b>General introduction</b> .....	<b>1</b>
<b>Chapter I - <i>State of the art</i></b> .....	<b>7</b>
I. Introduction .....	7
II. The biomass .....	7
II.A. Interest of the biomass .....	7
II.B. Biomass composition .....	8
III. First and third generation biofuels .....	11
III.A. First generation bio-fuels .....	11
III.B. Third generation bio-fuels .....	16
IV. Second generation bio-fuels .....	17
IV.A. Advantages of the feedstock .....	17
IV.B. Conversion processes .....	17
IV.C. Sustainability and bio-oil applications .....	24
V. Properties and upgrading of bio-oils .....	25
V.A. Physicochemical properties .....	25
V.B. Upgrading treatments .....	27
V.C. General conclusion .....	32
VI. Analytical methods for bio-oil characterization .....	32
VI.A. Introduction .....	32
VI.B. Sample preparation .....	32
VI.C. Targeted analytical methods .....	36
VII. Petroleomic non-targeted approach .....	50
VII.A. Introduction .....	50
VII.B. Analyses of bio-oils by ESI-HRMS .....	52
VII.C. Analyses of bio-oils by APPI, APCI, and LDI-HRMS as a complement to ESI-HRMS analyses .....	68
VII.D. Conclusion on the HRMS analyses .....	75
VIII. Conclusion .....	76
IX. References .....	77
<b>Chapter II – <i>Materials &amp; Methods</i></b> .....	<b>97</b>
I. Introduction .....	97
II. Production of the pyrolysis bio-oils .....	98
II.A. Fast pyrolysis experiments .....	98
II.B. Catalytic deoxygenation .....	100
III. Characterization of the pyrolysis bio-oils by petroleomic approach .....	101
III.A. Introduction .....	101
III.B. Ionization sources .....	102
III.C. Fourier Transform Ion Cyclotron Resonance Mass Spectrometry .....	119
IV. Other studies in mass spectrometry .....	139
IV.A. Introduction .....	139
IV.B. ESI-Linear ion trap (LTQ Velos Pro-Thermo Scientific) .....	139
V. Conclusion .....	141
VI. References .....	142

**Chapter III – *Development of a methodology by ESI FT-ICR MS for the characterization of bio-oils* ..147**

I.	Introduction .....	147
II.	Influence of the temperature and the solvent on the bio-oil ESI FT-ICR MS signature .....	147
	II.A. Introduction.....	147
	II.B. Experimental procedure.....	148
	II.C. Global description of obtained features in respect with the used ESI parameters.....	148
	II.D. Effect of the capillary temperature on the obtained distributions of C <sub>x</sub> H <sub>y</sub> O <sub>z</sub> compounds .....	150
	II.E. Influence of the solvent .....	152
III.	Influence of dopants on the bio-oil composition description.....	155
	III.A. Introduction.....	155
	III.B. Experimental procedure .....	155
	III.C. Bio-oil composition descriptions achieved by ESI FT-ICR MS analysis.....	156
	III.D. Complementarity of the detection modes.....	171
	III.E. Conclusion .....	172
IV.	Evidence of carbonyl compounds in complex mixtures with primary amines by petroleomic approach .....	173
	IV.A. Introduction .....	173
	IV.B. Materials and methods .....	174
	IV.C. Study of standard carbonyl compounds by ESI LIT MS .....	177
	IV.D. Complementary NMR analyses.....	200
	IV.E. Conclusion .....	205
	IV.F. (+) ESI-FT-ICR-MS analysis of bio-oil doped with 3-chloroaniline.....	205
	IV.G. Conclusion.....	211
V.	Conclusion.....	211
VI.	References .....	213

**Chapter IV – *Development of complementary methodologies by LDI and APPI FT-ICR MS for the characterization of bio-oils* ..... 219**

I.	Introduction .....	219
II.	Development of a LDI FT-ICR MS method to characterize bio-oils in positive and negative detection modes .....	219
	II.A. Introduction.....	219
	II.B. Experimental procedure.....	220
	II.C. Global bio-oil composition descriptions obtained by LDI and MALDI FT-ICR MS.....	220
	II.D. Influence of the laser fluence on the bio-oil composition description .....	222
	II.E. Comparison of MALDI and LDI for the investigation of bio-oils .....	225
	II.F. Comparison of the data obtained by LDI FT-ICR MS in positive and negative ion detection modes .....	230
	III.G. Conclusion .....	231
III.	Development of a APPI FT-ICR MS method to characterize bio-oils in positive and negative detection modes .....	231
	III.A. Introduction.....	231
	III.B. Experimental procedure .....	231
	III.C. Effect of the dopant on the APPI mass spectrum of bio-oil .....	232
	III.D. Bio-oil composition descriptions obtained by APPI FT-ICR MS .....	236
	III.E. Conclusion .....	240
IV.	Complementarity of the ESI, APPI, and LDI FT-ICR MS for the extensive characterization of bio-oils ..	240
	III.A. Introduction.....	240
	III.B. Experimental procedure .....	240
	III.C. Global composition descriptions of the bio-oil in respect the analytical conditions .....	242
	III.D. Complementarity of the different ionization sources .....	248
	III.E. Conclusion .....	252
V.	Conclusion.....	252
VI.	References .....	254

<b>Chapter V – <i>Application of the developed approach to assess the efficiency of the deoxygenation/cracking treatment by zeolites</i></b> .....	<b>257</b>
I. Introduction .....	257
II. Experimental procedure .....	257
III. Results and discussion .....	258
III.A. Effect of the nature of the catalyst on the bio-oil composition description .....	258
IV. Monitor of the catalyst lifetime .....	273
V. Conclusion.....	280
VI. References .....	281
<b>General conclusion</b> .....	<b>283</b>
<b>Table of figures and tables</b> .....	<b>287</b>
<b>Annexes</b> .....	<b>295</b>
<b>Résumé français de la thèse/French summary of the PhD thesis</b> .....	<b>299</b>



---

## *General introduction*

---





The reserves of the fossil resources (petroleum, gas, and charcoal) are decreasing while the global population and its energy demand are increasing. These energy sources are also responsible of ecological, economical, and geopolitical problems. Therefore, sustainable and greener alternatives have to be developed. Among the renewable existing energies such as solar and wind, biomass offers a great potential. The biomass refers to the organic material from the vegetal and animal kingdoms that can be converted to produce energy and represents the first source of renewable energy on the Earth. Its production is estimated at  $10^{11}$  tons per year but only 3 % are used for food and other applications.<sup>1</sup>

The biomass can be upgraded into biofuels and added-value chemicals by means of different pathways.<sup>2</sup> Different kinds of biofuels may be distinguished according to the used feedstock and process.<sup>2</sup> The first generation biofuels are the most commonly used.<sup>3,4</sup> They concern the biodiesel and the bioethanol. The former one is produced by esterification of the triglycerides contained in the vegetable oils such as rapeseed, sunflower, and palm.<sup>5</sup> The second one is obtained by fermentation of the glucose contained in crops like beetroot and sugar cane.<sup>6</sup> If their production processes are relatively easy, these biofuels present serious ethical problems as they involve foodstuffs.<sup>7</sup> Therefore, other biofuels are developed and produced from resources that do not directly interfere with the human food and the animal feed. These so-called second generation biofuels are generated from agricultural and forest residues or dedicated crops.<sup>8-10</sup> These raw materials are called "lignocellulosic biomass" because of the main components of the biomass which are the cellulose, the hemicellulose, and the lignin.<sup>11</sup> The conversion of the lignocellulosic biomass into liquid biofuels is performed through different approaches.<sup>12</sup> The first one is the biochemical route based on the catalytic hydrolysis and the fermentation of specific biomass components.<sup>13</sup> The second one, the so-called thermochemical process, includes the pyrolysis and the liquefaction of all the biomass components.<sup>14,15</sup> In these processes, the biomass is heated at high temperature and its thermal degradation leads to the formation of incondensable gas, biochar, and bio-oil. The latter is a liquid material that can be upgraded into biofuel. More recently, third generation biofuels have been developed which are produced from algae.<sup>16</sup> The processes that convert this feedstock into liquid fuel are similar to those employed for the production of the first and second generation biofuels. Bio-oils obtained from the biomass conversion by the thermochemical processes are highly oxygenated which is not suitable for motor engines.<sup>17</sup> Besides, this high amount of ox-

xygen is responsible of corrosiveness and storage issues.<sup>18</sup> The main strategy is to develop catalytic treatments aimed at reducing the oxygen content of the bio-oils and increasing their energy density in order to obtain “green petroleum” that can be refined into biofuels. Some of these upgrading processes are already present in petroleum refinery such as hydrodeoxygenation (HDO), deoxygenation and/or catalytic cracking.<sup>2</sup>

For the optimization of the production process (pyrolysis, liquefaction, catalysis...), the as extensive as possible bio-oil description has to be achieved before and after catalytic treatment. Several studies have been carried out in that way, in which different analytical techniques are used to characterize raw and upgraded bio-oils.<sup>19</sup> Unfortunately, there is no universal method that is able alone to fully characterize the bio-oils. A combination of several of them are required. Two different approaches have to be considered.<sup>19</sup>

The first one consists of targeted analyses and is related to all the techniques used to characterize known species. It involves the infrared spectroscopy and the nuclear magnetic resonance spectroscopy which are focused on given chemical functions of the bio-oil components.<sup>20,21</sup> Quantitative information may be obtained. Liquid and gas chromatography may also be employed and their coupling with mass spectrometry technique allows structural information to be obtained.<sup>22,23</sup> The chromatographic methods have also the advantage to quantify the targeted bio-oil components. Typically, only the low-mass compounds are investigated by these techniques, which represents a small portion of the bio-oil components.<sup>24</sup> The second approach has the capability to evidence thousands of compounds on a broader mass range. It is known as non-targeted approach and was firstly used for the analysis of petroleum derived oils.<sup>25</sup> Therefore, it is also called petroleomic approach. Contrary to the targeted methods, this method ensures to detect and assign thousands of compounds of a complex mixture such as bio-oils.<sup>26</sup> Typically, no chromatographic separation is used and the sample is directly introduced in the ionization source of the mass spectrometer. Due to the complexity of the sample, a high resolution mass spectrometer, such as Fourier transform ion cyclotron resonance (FT-ICR MS) or Orbitrap, is required. Indeed, the high resolute power provided by these instruments allows to distinguish all the different features.<sup>27</sup> Moreover, the high mass measurement accuracy of these mass spectrometers is necessary to unambiguously assign all the peaks of the mass spectrum with a unique molecular formula ( $C_cH_hN_nO_oS_s$ ). Different ionization sources may be used that ensure to ionize bio-oil compounds in respect with

their polarity.<sup>19</sup> The non-targeted approach does not allow to obtain quantitative or structural information. Moreover, the isomeric compounds are not separated.

This PhD thesis focuses on the development of effective, sensitive, and robust petroleomic methods by FT-ICR MS to reach the extensive composition description of raw and upgraded bio-oils.

In the first chapter, the interests and the composition of the biomass will be described as well as the different kinds of biofuels that can be produced. The focus will be put on the production processes and the sustainability of the second generation biofuels. More specifically, the properties and the used upgrading treatments of the bio-oils generated by liquefaction and pyrolysis of the lignocellulosic biomass will be detailed. The second part of this chapter is dedicated to the various analytical methods that may be used for the bio-oil characterization. An overview of the different studies performed on the bio-oils by petroleomic approach will be detailed.

The second chapter is dedicated to the description of the bio-oil production by pyrolysis and of the catalysts used for its upgrading. The different ionization sources used in this study will be described. The principle of both petroleomic approach and FT-ICR MS will be given.

In the chapter III, the development of bio-oil analysis by electrospray ionization (ESI) coupled to FT-ICR MS will be presented. Throughout this chapter, the influence of different important parameters on the ESI process will be investigated. The last part of this chapter is dedicated to the importance and the influence of primary amines, used as dopants, for the ESI bio-oil analyses.

In the fourth chapter, additional petroleomic analyses developed by laser desorption/ionization (LDI) and atmospheric pressure photoionisation (APPI) coupled to FT-ICR MS will be presented. The obtained results will be compared with the ESI FT-ICR MS ones to assess the complementarity of the proposed methodologies.

The chapter V is dedicated to the characterization of upgraded bio-oils by the developed petroleomic methods. In this study, the upgraded bio-oils produced by catalytic process on two different zeolites to undertake deoxygenation and cracking treatment will be studied. The efficiency of each catalyst will be assessed and compared according to the achieved bio-oil description.

## References

1. Sheldon, R. A. Green and sustainable manufacture of chemicals from biomass: state of the art. *Green Chem.* **16**, 950–963 (2014).
2. Huber, G. W., Iborra, S. & Corma, A. Synthesis of Transportation Fuels from Biomass: Chemistry, Catalysts, and Engineering. *Chem. Rev.* **106**, 4044–4098 (2006).
3. Industry Statistics. *Renewable Fuels Association* (2015).
4. Bozbas, K. Biodiesel as an alternative motor fuel: Production and policies in the European Union. *Renew. Sustain. Energy Rev.* **12**, 542–552 (2008).
5. Demirbas, A. Biodiesel production from vegetable oils via catalytic and non-catalytic supercritical methanol transesterification methods. *Prog. Energy Combust. Sci.* **31**, 466–487 (2005).
6. Sanchez, O. J. & Cardona, C. A. Trends in biotechnological production of fuel ethanol from different feedstocks. *Bioresour. Technol.* **99**, 5270–5295 (2008).
7. Mohr, A. & Raman, S. Lessons from first generation biofuels and implications for the sustainability appraisal of second generation biofuels. *Energy Policy* **63**, 114–122 (2013).
8. Cambero, C., Sowlati, T., Marinescu, M. & Roeser, D. Strategic optimization of forest residues to bioenergy and biofuel supply chain. *Int. J. Energy Res.* **39**, 439–452 (2015).
9. Chandra, R., Takeuchi, H. & Hasegawa, T. Methane production from lignocellulosic agricultural crop wastes: A review in context to second generation of biofuel production. *Renew. Sustain. Energy Rev.* **16**, 1462–1476 (2012).
10. Brosse, N., Dufour, A., Meng, X., Sun, Q. & Ragauskas, A. Miscanthus: a fast-growing crop for biofuels and chemicals production. *Biofuels Bioprod. Biorefining-Biofpr* **6**, 580–598 (2012).
11. Demirbas, A. Calculation of higher heating values of biomass fuels. *Fuel* **76**, 431–434 (1997).
12. Serrano-Ruiz, J. C. & Dumesic, J. A. Catalytic routes for the conversion of biomass into liquid hydrocarbon transportation fuels. *Energy Environ. Sci.* **4**, 83–99 (2010).
13. Zhu, J. Y. & Pan, X. J. Woody biomass pretreatment for cellulosic ethanol production: Technology and energy consumption evaluation. *Bioresour. Technol.* **101**, 4992–5002 (2010).
14. Demirbas, A. Pyrolysis of ground beech wood in irregular heating rate conditions. *J. Anal. Appl. Pyrolysis* **73**, 39–43 (2005).
15. Jindal, M. K. & Jha, M. K. Hydrothermal liquefaction of wood: a critical review. *Rev. Chem. Eng.* **32**, 459–488 (2016).
16. Chen, W.-H., Lin, B.-J., Huang, M.-Y. & Chang, J.-S. Thermochemical conversion of microalgal biomass into biofuels: A review. *Bioresour. Technol.* **184**, 314–327 (2015).
17. Elliott, D. C. & Schiefelbein, G. F. Liquid hydrocarbon fuels from biomass. *Am. Chem. Soc. Div. Fuel Chem. Annu. Meet. Prepr.* 1160–1166 (1989).
18. Oasmaa, A., Korhonen, J. & Kuoppala, E. An Approach for Stability Measurement of Wood-Based Fast Pyrolysis Bio-Oils. *Energy Fuels* **25**, 3307–3313 (2011).
19. Stas, M., Kubicka, D., Chudoba, J. & Pospisil, M. Overview of Analytical Methods Used for Chemical Characterization of Pyrolysis Bio-oil. *Energy Fuels* **28**, 385–402 (2014).

20. Hao, N., Ben, H., Yoo, C. G., Adhikari, S. & Ragauskas, A. J. Review of NMR Characterization of Pyrolysis Oils. *Energy Fuels* **30**, 6863–6880 (2016).
21. Qiang, L., Xu-lai, Y. & Xi-feng, Z. Analysis on chemical and physical properties of bio-oil pyrolyzed from rice husk. *J. Anal. Appl. Pyrolysis* **82**, 191–198 (2008).
22. Marsman, J. H., Wildschut, J., Mahfud, F. & Heeres, H. J. Identification of components in fast pyrolysis oil and upgraded products by comprehensive two-dimensional gas chromatography and flame ionisation detection. *J. Chromatogr. A* **1150**, 21–27 (2007).
23. Tomasini, D., Cacciola, F., Rigano, F., Sciarrone, D., Donato, P., Beccaria, M., Caramao, E. B., Dugo, P. & Mondello, L. Complementary Analytical Liquid Chromatography Methods for the Characterization of Aqueous Phase from Pyrolysis of Lignocellulosic Biomasses. *Anal. Chem.* **86**, 11255–11262 (2014).
24. Mohan, D., Pittman, Charles U. & Steele, P. H. Pyrolysis of Wood/Biomass for Bio-oil: A Critical Review. *Energy Fuels* **20**, 848–889 (2006).
25. Marshall, A. G. & Rodgers, R. P. Petroleomics: The Next Grand Challenge for Chemical Analysis. *Acc. Chem. Res.* **37**, 53–59 (2004).
26. Michailof, C. M., Kalogiannis, K. G., Sfetsas, T., Patiaka, D. T. & Lappas, A. A. Advanced analytical techniques for bio-oil characterization. *Wiley Interdiscip. Rev.-Energy Environ.* **5**, 614–639 (2016).
27. Marshall, A. G. & Hendrickson, C. L. High-Resolution Mass Spectrometers. *Annu. Rev. Anal. Chem.* **1**, 579–599 (2008).



---

## *Chapter I*

---

*State of the art*





## Table of Contents

I.	Introduction.....	7
II.	The biomass.....	7
II.A.	Interest of the biomass .....	7
II.B.	Biomass composition .....	8
II.B.1.	Cellulose .....	8
II.B.2.	Hemicellulose .....	9
II.B.3.	Lignin .....	10
II.B.4.	Minor components.....	10
III.	First and third generation biofuels.....	11
III.A.	First generation bio-fuels .....	11
III.A.1.	Bioethanol .....	11
III.A.2.	Biodiesel .....	13
III.A.3.	Sustainability .....	16
III.B.	Third generation bio-fuels.....	16
IV.	Second generation bio-fuels .....	17
IV.A.	Advantages of the feedstock.....	17
IV.B.	Conversion processes.....	17
IV.B.1.	Biochemical route.....	18
IV.B.2.	Gasification.....	19
IV.B.3.	Pyrolysis.....	19
IV.B.4.	Liquefaction .....	23
IV.C.	Sustainability and bio-oil applications .....	24
V.	Properties and upgrading of bio-oils.....	25
V.A.	Physicochemical properties .....	25
V.A.1.	Pyrolysis bio-oil.....	26
V.A.2.	Liquefaction bio-oil.....	26
V.B.	Upgrading treatments.....	27
V.B.1.	Hydropyrolysis and catalytic fast pyrolysis.....	27
V.B.2.	Zeolite upgrading.....	28
V.B.3.	Hydrotreatment.....	29
V.B.4.	Condensation.....	30
V.B.5.	Fractionation and aqueous phase processing.....	30
V.B.6.	Conclusion .....	31
V.C.	General conclusion.....	32
VI.	Analytical methods for bio-oil characterization .....	32
VI.A.	Introduction .....	32
VI.B.	Sample preparation.....	32
VI.B.1.	Wet methods.....	33
VI.B.2.	Solvent-free methods.....	35
VI.C.	Targeted analytical methods.....	36
VI.C.1.	Fourier transform infrared spectroscopy .....	36
VI.C.2.	Nuclear magnetic resonance spectroscopy.....	38
VI.C.3.	Gas chromatography .....	42
VI.C.4.	Liquid chromatography .....	47

VI.C.5.	General conclusion on chromatographic methods .....	49
VI.C.6.	Other analytical techniques .....	50
VII.	Petroleomic non-targeted approach.....	50
VII.A.	Introduction .....	50
VII.B.	Analyses of bio-oils by ESI-HRMS .....	52
VII.B.1.	Influence of the nature of the mass spectrometer and of the pH of the solution on the ESI mass spectrum of the bio-oil.....	58
VII.B.2.	Influence of the feedstock on the bio-oil composition obtained by ESI HRMS ....	58
VII.B.3.	Influence of the fractionation treatment on the bio-oil composition obtained by ESI HRMS .....	61
VII.B.5.	Effect of the processing conditions on the bio-oil composition obtained by ESI HRMS .....	64
VII.B.6.	Influence of dopants in the ESI HRMS analyses .....	67
VII.B.7.	Conclusion .....	68
VII.C.	Analyses of bio-oils by APPI, APCI, and LDI-HRMS as a complement to ESI-HRMS analyses .....	68
VII.D.	Conclusion on the HRMS analyses .....	75
VIII.	Conclusion .....	76
IX.	References.....	77

## I. Introduction

In this chapter, we will describe how the biomass may be considered as a promising resource to produce biofuels and added-value chemicals. The biomass composition will be firstly detailed in order to understand its potential. Then, the different kinds of biofuels will be presented as well as the various processes implemented for their production. The focus will be mainly put on the second generation biofuels produced from lignocellulosic biomass such as agricultural or forest residues. The processes, including the upgrading treatments, which have the ability to yield such a biofuel, will be extensively discussed. Among them, pyrolysis and liquefaction are the most commonly used pathways to convert biomass into a liquid, the so-called bio-oil. The bio-oil composition does not allow its direct use as a biofuel but requires upgrading treatments that provide, to the bio-oil, properties similar to petroleum. Both production and upgrading processes will be presented in this chapter. The last part will be dedicated to the different analytical methods that have been developed to describe the bio-oil composition. Indeed, a deep understanding of this material is required in order to assess and improve the conversion of the biomass and the upgrading of the bio-oil. A particular attention will be given to the exhaustive description of the studies performed by the petroleomic approach.

## II. The biomass

### *II.A. Interest of the biomass*

The biomass is the organic matter from the plant and animal kingdoms which may be used to produce energy. In this study, the focus will be only done on the plant derived biomass. It is generally considered as the most promising resource to the issues of the fossil energies (petroleum, gas, and coal).<sup>1</sup> The biomass may be converted into biofuels<sup>2-5</sup> and added-value molecules which can be used in the chemistry industry to produce, for example, polymers.<sup>6-8</sup> Global biomass production is evaluated at  $10^{11}$  tons per year. Only 3 % of this resource are used for food and other applications. This suggests the great outcomes of the biomass to replace a part of the fossil resource which is dramatically decreasing.<sup>9</sup>

The biomass uses the atmospheric CO<sub>2</sub> for its growing. Consequently, the biofuel combustion has a lower carbon impact on the climate than the petroleum based fuels (**Figure I-1**).

Therefore, biomass can be regarded as a sustainable resource because it is renewable and present in large amounts. Nevertheless, biofuel production must be improved to be more sustainable because its production processes is not fully carbon neutral.<sup>10,11</sup> At this time, different biofuels have been developed and may be distinguished according to the used raw material.

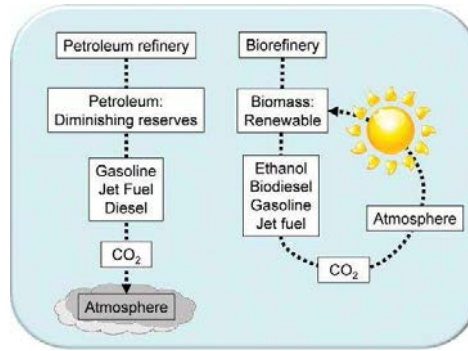


Figure I-1. Cycle of the CO<sub>2</sub> for the petroleum and biomass based fuels<sup>12</sup>

## II.B. Biomass composition

The biomass valorization is based on its primary components: cellulose (41 wt. %), hemicellulose (30 wt. %), lignin (25 wt. %), triglycerides, proteins, and terpenes.<sup>9,13</sup> Cellulose, hemicellulose, and lignin compose the cell membrane, as illustrated on the **Figure I-2**, and are the most abundant compounds of the biomass. But their amounts differ according to the nature of the considered biomass.<sup>13</sup> After a detailed presentation of each kind of compound, the different processes ensuring biofuel production will be discussed.

### II.B.1. Cellulose

The cellulose is the most important organic homopolymer on the Earth and represents 40 to 80 % of the biomass.<sup>14</sup> It is a linear polysaccharide of D-glucopyranose monomers linked with  $\beta$ -1,4 linkages (**Figure I-2**). The glucose unit that can be considered as the cellulose monomer is present in starch based plants such as corn and wheat. At the difference of the cellulose, the starch is an amorphous structure due to the  $\alpha$ -1,4 and  $\alpha$ -1,6 linkages. After treatment processes that ensure to convert cellulose or starch into glucose, bioethanol may be produced.<sup>15</sup>

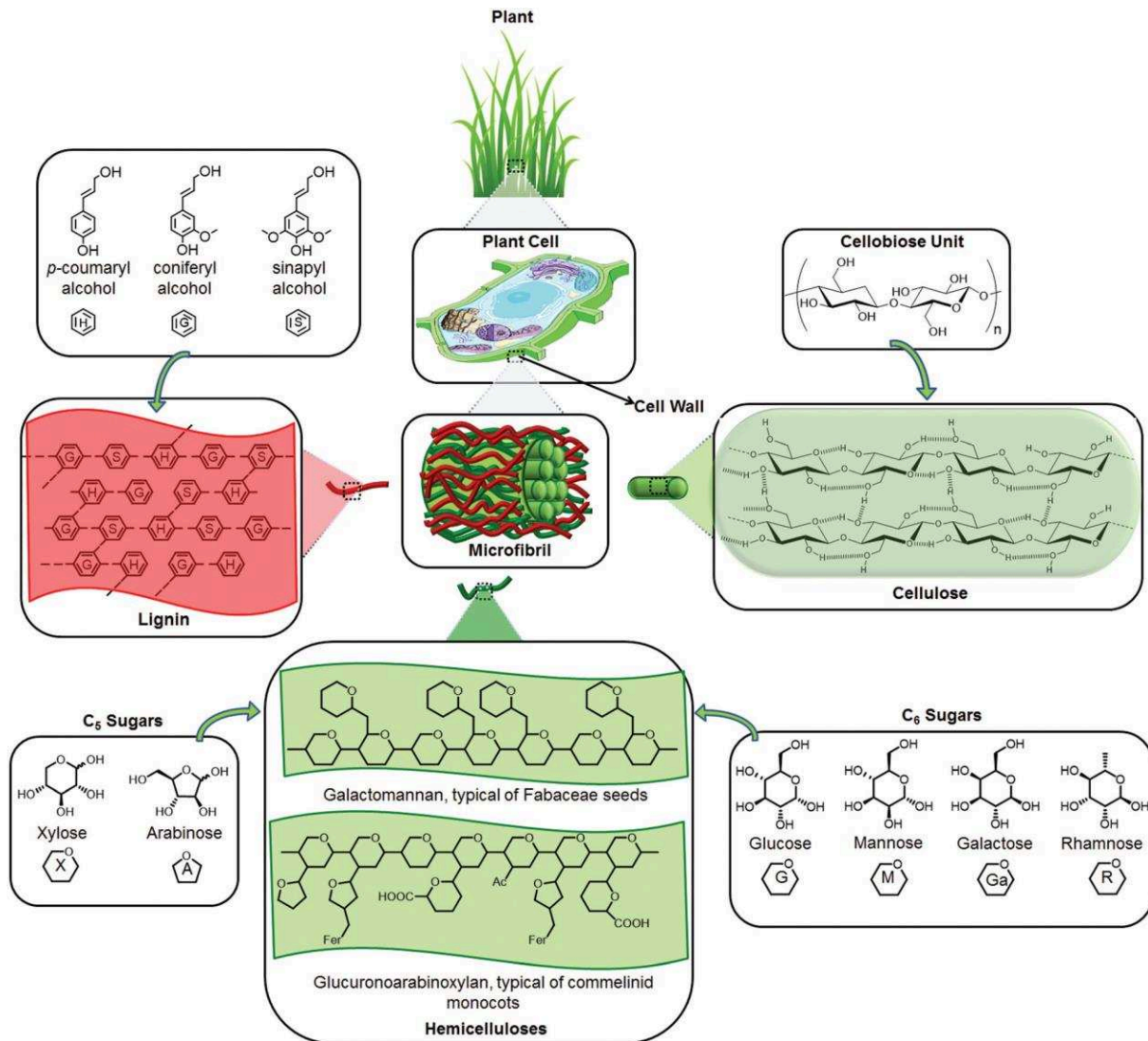


Figure I-2. Hierarchical and structural compositions of biomass from the cell membrane to the molecular level. The main components are cellulose, hemicellulose, and lignin.<sup>16</sup>

### II.B.2. Hemicellulose

This polymer is the second one in terms of abundance (15-30 %) and its structure is more complex than cellulose. Indeed different pentoses and hexoses compose this polysaccharide. Among them, there are C<sub>6</sub>-sugars (glucose, galactose, and mannose) and C<sub>5</sub>-sugars (xylose and arabinose).<sup>17</sup> The depolymerization of the hemicellulose by thermochemical processes ensures to obtain the different sugarc units. Then, C<sub>5</sub>- and C<sub>6</sub>-sugars may be involved in various upgrading treatments and used in polymer chemistry or converted into gasoline or jet fuel.<sup>9,16,18</sup>

### II.B.3. Lignin

Between 10 and 25 % of the biomass is relative to lignin.<sup>19</sup> It is a three-dimensional polyphenolic polymer which confers rigidity to the plant biomass, especially in woody species. Mainly three phenylpropanol units (*p*-coumaryl, coniferyl, and sinapyl alcohols) polymerize to form lignin.<sup>20</sup> The yielded corresponding phenylpropanoid moieties, evidenced in the lignin, are *p*-hydroxyphenyl (H), guaiacyl (G), and syringyl (S), respectively.<sup>21</sup> Depending on the ratio of the different aromatic subunits (S and G), the structure and the denomination of the lignin are different. Softwood lignins, such as spruce or pine, are mainly made of guaiacyl moieties from coniferyl units. While hardwood species such as oak, poplar, and eucalyptus, are based on an equivalent ratio of coniferyl (G) and sinapyl (S) monomers. Finally, grass plants contain similar amounts of guaiacyl and syringyl units with small amounts of *p*-hydroxyphenyl.<sup>22</sup>

Lignin is a side-product obtained in large quantity in the pulp and paper industries and it is used as a low-grade fuel. It represents an under-exploited resource that may be upgraded. Because of its significant aromatic content, it can be converted into fuels and added-value chemicals by means of thermochemical or biological treatments.<sup>23</sup>

### II.B.4. Minor components

#### II.B.4.a. Triglycerides

Some plants are specifically cultivated for their high amount of triglycerides. In soybean, they represent up to 20 wt. %.<sup>24</sup> Other triglyceride-producing plants (sunflower, cottonseed, oil palm fruit, and corn) are also grown up for their capabilities to produce vegetable oils from which fatty acids and glycerol may be extracted. Saturated C<sub>6</sub> to C<sub>20</sub>, monounsaturated C<sub>10,16,18</sub>, and polyunsaturated (18:2, 18:3 and 20:4) acids are commonly obtained.<sup>2,25</sup> The huge production and the higher heating values of vegetable oils offer a great potential for biodiesel production.<sup>2</sup> The glycerol co-product represents a promising feedstock that can be upgraded by various ways.<sup>26–29</sup>

#### II.B.4.b. Terpenes

The terpenes represent a tiny part of the biomass. For some plant species, the carbohydrates are converted into terpenes that may be regarded as polymer of isoprene C<sub>5</sub>H<sub>8</sub> units.

The most famous natural isoprene-based compounds is the latex which is a rubber produced by the hevea tree.<sup>30,31</sup>

#### *II.B.4.c. Proteins*

In plant, the amount of proteins is generally low. Nevertheless, the by-products of biomass derived biofuels may contain a significant amount of proteins.<sup>32,33</sup> Usually, they are used to feed animals. But this feedstock, and more particularly the amino acids present in these wastes, can be upgraded into value-added chemicals.<sup>34,35</sup>

#### *II.B.4.d. Inorganic materials*

Biomass contains very small amounts (< 1 wt. %) of inorganic compounds. Typically, it is mineral components such as calcium, potassium, phosphorus, magnesium, and sodium.<sup>36</sup>

### III. First and third generation biofuels

Different kinds of biofuels can be distinguished depending on the used feedstock and are so-called first, second, and third generation biofuels. In this study, the focus is on the second generation ones obtained from the lignocellulosic biomass pyrolysis. Therefore, the production processes and the sustainability of the first and third biofuels will be firstly discussed. Then, a specific section will be dedicated to the second generation biofuels in which their processing routes and their sustainability will be detailed.

#### *III.A. First generation bio-fuels*

First generation biofuels are fuels produced from edible feedstocks. Bioethanol and biodiesel are the most common first generation biofuels. They are obtained from specific biomass components that are converted by different processes.

##### *III.A.1. Bioethanol*

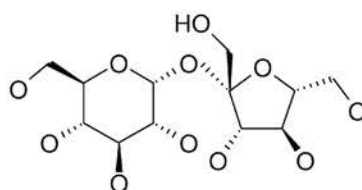
At the present time, the bioethanol production is the most developed biofuel technology. In 2016, the Renewable Fuels Association estimated the annual production of bioethanol at 10<sup>10</sup> L.<sup>37</sup> Ethanol is produced by the fermentation of the carbohydrates contained in specific crops.<sup>38</sup> These feedstocks can be classified into two categories<sup>39</sup>:

(a) Sugar-containing species: sugarcane, beetroot...

(b) Starch-containing species: seeds such as wheat, rice, corn...

### III.A.1.a. Ethanol from sugar-containing crops

Sugaric crops are grown up for bioethanol production due to their significant sucrose content (30 wt. % for the sugarcane).<sup>40,41</sup> The sucrose is a  $\alpha$ -D-glucopyranosyl-(1 $\rightarrow$ 2)- $\beta$ -D-fructofuranosyl disaccharide (**Figure I-3**). The first step is to grind the crop, which enables to extract the juice containing the sucrose from the insoluble lignocellulosic fraction.



**Sucrose**

$\alpha$ -D-glucopyranosyl  $\beta$ -D-fructofuranoside  
Glc( $\alpha$ 1 $\rightarrow$ 2 $\beta$ )Fri

Figure I-3. Sucrose molecule

Then, the water-soluble sugars are fermented to produce ethanol according to **Equation I-1**. This process is achieved in presence of microorganism such as yeast (*Saccharomyces cerevisiae*) or bacteria (*Zymomonas mobilis*) due to their capability to hydrolyze sucrose into glucose and fructose.<sup>42</sup>



The lignocellulosic insoluble portion such as bagasse is commonly burned to provide heat to the process but it may also be upgraded into second generation biofuels.<sup>43</sup>

### III.A.1.b. Ethanol from starch-containing crops

Unlike the sucrose, the starch polymer from the corn and wheat seeds cannot be directly fermented into ethanol. Some pretreatments are required in order to hydrolyze starch into glucose and maltose. Two kinds of processes are developed whose principle is illustrated on the **Figure I-4**.

The first process is the so-called wet-milling.<sup>44,45</sup> The grains are grinded in order to rupture the hull walls. Then, they are mixed with water to produce a mash containing 15-20 % of starch. Then, the mash is heated at high temperature (90-100 °C) and two different enzymes are consecutively added. The first one ( $\alpha$ -amylase) hydrolyzes, in acidic medium, the starch



molecules into short chains of glucose (dextran). The second one (glucoamylase) converts the dextrans into glucose and maltose.

The second process is called dry grinding and does not require water addition before hydrolysis by the different amylases.<sup>46,47</sup>

The resulting glucose and maltose are finally fermented with *Saccharomyces cerevisiae*.<sup>42</sup>

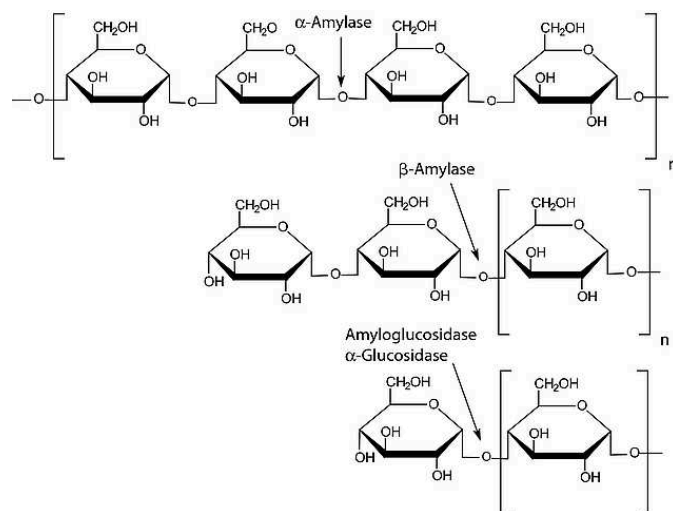


Figure I-4. Principle of the enzymatic hydrolysis of starch (Sigma-Aldrich source)

### III.A.1.c. Uses of bioethanol

The ethanol obtained from the biomass can be converted with isobutene into ethyl *tert*-butyl ether (ETBE).<sup>48</sup> The bioethanol and ETBE are added to the gasoline at a concentration of 5 and 15 %, respectively, which ensures to reduce the carbon footprint of these fuels.<sup>49</sup>

### III.A.2. Biodiesel

In 2003, 10<sup>6</sup> tons of biodiesel have been produced in the European Union, which represented 82 % of the biofuel production.<sup>50</sup> The biodiesel is dedicated to partially substitute diesel fuel and does not require to be mixed with petroleum based diesel. Actually, up to 20 vol. % of biodiesel can be blended with traditional diesel fuel without any engine modifications. Biodiesel is mainly obtained by transesterification of the triglycerides (TG) from vegetable oils into alkyl-fatty esters. Therefore, biodiesel is also called bio-ester. The most commonly used oleaginous plants are corn, rapeseed, soybean, and sunflower.<sup>2</sup> Different transesterification pathways may be used but only the main ones will be discussed.<sup>51</sup>

## III.A.2.a. Homogeneous catalysis

In this process, TG reacts with alcohol to produce alkyl esters, typically in presence of alkaline or acid catalysts (**Figure I-5**).

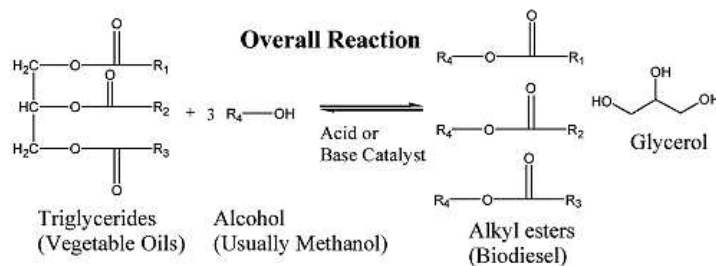


Figure I-5. Overall transesterification reaction from triglyceride and alcohol to produce alkyl-fatty esters (biodiesel) and glycerol<sup>1</sup>

Consecutive reactions are carried out to produce alkyl-fatty esters.<sup>52,53</sup> The triglyceride is converted stepwise to diglyceride, monoglyceride, and finally glycerol. At each step, an ester is formed. These reactions are reversible and characterized by kinetic constants.

The molar alcohol/TG ratio is a critical point influencing the reaction yield. Studies have been undertaken to assess the best ratio.<sup>54,55</sup> A complete transesterification requires to use large amounts of alcohol (typically 50-200 %). Methanol is commonly used, due to its low cost, and fatty acid methyl esters (FAME) are obtained. Ethanol and 1-butanol can also be used.<sup>2</sup>

Similarly, the addition of an acid or alkaline catalyst ensures to improve the transesterification reaction. They have to be introduced with a specific ratio. Alkaline catalysts were evidenced to be 4000 times more active than acid ones. These alkaline catalysts have also the advantage to reduce the corrosion issues.<sup>1,55</sup> Among the different alkali-catalysts, sodium methoxide and sodium hydroxide are the most commonly employed due to their efficiency and their low cost.<sup>55-57</sup> For acid catalysis, sulfuric, phosphoric, and hydrochloric acids can be used.<sup>55,57</sup> Acid-catalyzed transesterification is more suitable with fats containing a significant amount of free fatty acids (FFA). Indeed, the FFA undergo saponification reaction in alkaline conditions.<sup>56</sup> These FFA are mainly contained in waste vegetable oils (frying oil, for example) and their conversion into bio-esters requires modifications of the process.<sup>58</sup>

Another critical parameter to handle the transesterification process is the amount of water. Indeed, the water may react with the different esters (mono/di/triglycerides and alkyl esters) to form FFA. Therefore, it is crucial to use oils with poor water content.<sup>55,56,58,59</sup>

Some other parameters influence the efficiency of the transesterification process. Thus, the addition of solvent such as tetrahydrofuran increases the reaction rate.<sup>1</sup> Furthermore, the increase of the reaction time<sup>55,56</sup> and the temperature<sup>55,60</sup> leads to a higher reaction yield.

Homogeneous catalysis is undertaken at low temperatures (20-60 °C) and is very efficient. However, this process requires significant downstream steps to separate acid or alkaline catalyst from the resulting products and involves significant amount of alcohol. Therefore, heterogeneous catalysis has to be preferred to overcome this hurdle.

### III.A.2.b. Heterogeneous catalysis

Solid catalysts are promising alternatives to replace homogeneous catalysis. Even if they need higher reaction temperatures and pressures, they can be easily removed from the products and recycled. Different acid and alkaline solid catalysts have been developed. They are supported on alumina, zirconia or activated carbon surfaces.<sup>61–63</sup> The alkali-catalyzed transesterification in presence of FFA leads to the formation of soap which poisons the catalyst. Therefore, FFA have to be removed prior heterogeneous alkaline catalysis.<sup>64</sup> The acid catalysts are more convenient with oils containing high FFA amounts. Actually, some solid acid catalysts, such as the 12-tungstophosphoric acid based ones, are able to perform simultaneous esterification and transesterification of FFA and TG, respectively (**Figure I-6**), with a 77 % yield.<sup>65</sup>

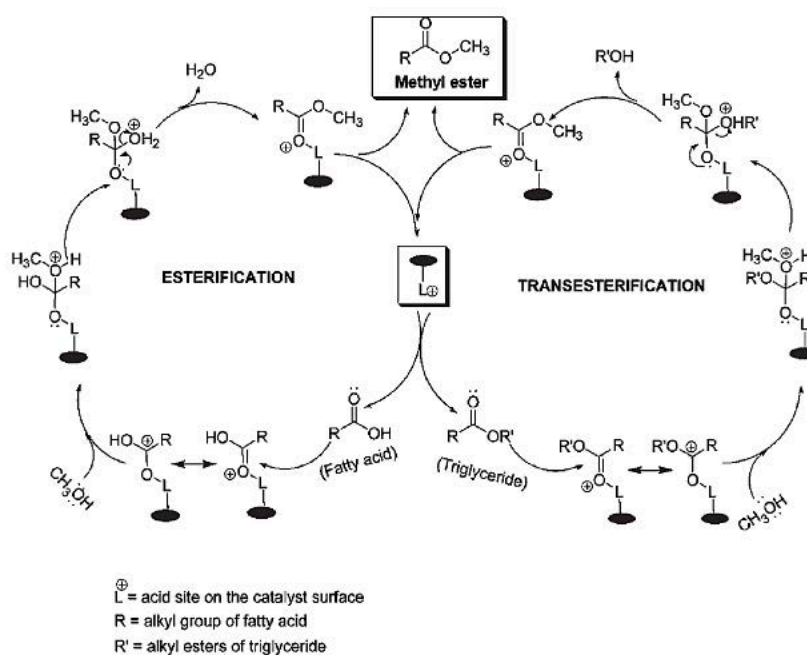


Figure I-6. Reactional scheme of the simultaneous solid acid catalyzed esterification and transesterification<sup>65</sup>

### *III.A.3. Sustainability*

Although the first generation biofuels have a low carbon footprint, their sustainability is compromised. As a matter of fact, several aspects dealing with their production are in disagreement with their sustainable development.<sup>66</sup>

Some ethical and ecological issues arise as they are produced from edible crops. Using food resources and agricultural areas to produce such biofuels cannot be considered while some populations are suffering from famine. Furthermore, the acquisition of large scale lands to grow dedicated crops can have harmful impacts on the environment. It can disturb ecosystems, uses significant amount of water, fertilizers, and phytosanitary products.<sup>67</sup>

Therefore, new sustainable resources that are not linked to animal feed and human food have to be used. The conversion of such raw materials produces biofuels called second and third generation biofuels. The processes and advantages of the latter will be discussed in the section **IV**.

### *III.B. Third generation bio-fuels*

The third generation biofuels are the most recent ones and are still in development.<sup>68</sup> They are obtained from macro and microalgae, which presents several advantages. First, they do not compete with animal and human feedstocks. Their growing is fast and they can survive and reproduce in constraining environments such as high saline water. Moreover, due to their high CO<sub>2</sub> fixation capabilities, they can trap the gas emitted by power plants and industries, which may also reduce the carbon footprint of the human activities.<sup>69</sup> The algae are composed of significant amounts of TG and cellulose which may be converted into biodiesel and bioethanol, respectively.<sup>70-73</sup>

For the ethanol production, the cellulose has firstly to undergo acid and enzymatic hydrolysis to obtain sugars.<sup>74-76</sup> The released sugaric monomers are converted into bioethanol by fermentation.<sup>77</sup>

After their extraction from algae, TG may be converted in biodiesel by transesterification reaction.

Furthermore, various thermochemical treatments may be used to obtain biofuels. In some of these processes, a bio-oil is obtained as an intermediate product which can be upgraded

into biofuels or added-value chemicals. The upgrading processes are similar to those applied to lignocellulosic bio-oils which will be detailed in the section **V.B.**<sup>68</sup>

## IV. Second generation bio-fuels

### IV.A. *Advantages of the feedstock*

Second generation biofuels are obtained from non-edible feedstocks. This represents a significant advantage.

As previously written, the total biomass production is huge ( $10^{11}$  tones) and only a tiny fraction of it is dedicated to human food and animal feed. The main part of the biomass is recycled or unused, which assesses its outstanding availability for biofuel production.<sup>9</sup>

The agricultural or forest residues, and the dedicated non-edible crops can be used for second generation bio-fuel production. Thus, agricultural by-products such as cereal straw, corn and rapeseed stalk are typically used.<sup>78–80</sup> Similarly, the wood shavings can also provide liquid biofuels.<sup>81,82</sup> Some specific plants are used due to their rapid growth. Among them, short rotation forestry crops (eucalyptus, poplar or willow) and perennial grasses (Miscanthus or grass) may be used.<sup>83–85</sup> Miscanthus presents some advantages as it can be cultivated on industrial wastelands and so, it does not compete with agricultural fields.<sup>86</sup> Moreover, it can help for the remediation of the soils polluted by hydrocarbons or heavy metals such as cadmium.<sup>87,88</sup>

These feedstocks do not present ethic issues as they are not in competition with food and animal feed. Moreover, they are environmentally friendlier than first generation biofuels. Neither fertilizer nor phytosanitary treatments are required. On an economic point of view, they are cheap materials. It may consequently be considered that this kind of biofuels are more sustainable than the first generation ones.<sup>39,66</sup>

The plant biomass involved in the production of the second generation biofuels are called lignocellulosic materials due to the high content of cellulose, hemicellulose, and lignin. Various processes enable to obtain these biofuels and will be discussed in the following paragraphs.

### IV.B. *Conversion processes*

The conversion of the lignocellulosic biomass into liquid biofuels is mainly performed through two different approaches (**Figure I-7**). The first one is the biochemical processing that

is based on catalytic hydrolysis and fermentation of specific biomass components. In the second process (thermochemical route), the biomass is heated and converted into a large range of products. Different thermochemical pathways can be distinguished depending on the heating temperature, the pressure, the residence time, the nature of the medium, and the oxygen concentration. Among them, gasification, pyrolysis, and liquefaction (not represented on the **Figure I-7**) are typically used. They present the main advantage to convert all the organic biomass components.

Different types of biofuels can be obtained. Some are refined such as bioethanol and biodiesel. The other are unrefined and are mainly represented by the production of bio-oils from the pyrolysis and the liquefaction of the biomass. The various conversion processes will be detailed in the following paragraphs with a specific focus on the Biomass-to-Liquids (BTL) processes.

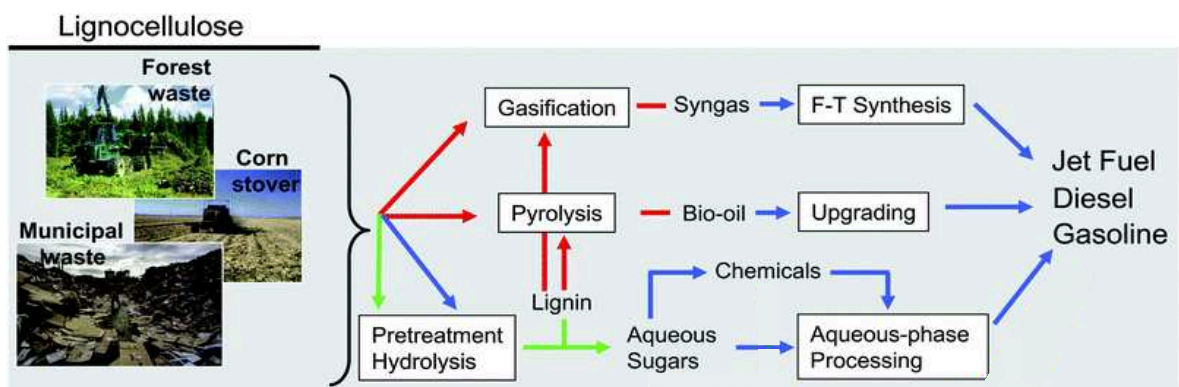


Figure I-7. Conversion processes of lignocellulosic biomass into liquid biofuels (green arrows refer to biochemical routes, red arrows to thermochemical routes, and blue arrows to catalytic routes) <sup>89</sup>

#### IV.B.1. Biochemical route

The biochemical processes are mainly focused on the conversion of the polysaccharides into second generation bioethanol. The principle is identical to the production of first generation bioethanol, but somewhat more complex. A pretreatment of the lignocellulosic biomass is required to separate cellulose from hemicellulose and lignin. Steam explosion is an efficient way to proceed.<sup>90</sup> The xylose from hemicellulose is obtained whereas cellulose is still under crystalline form. Therefore, enzymatic hydrolysis is carried out to convert cellulose into glucose. The enzymatic hydrolysis treatment is similar to what it is used for the first generation bioethanol. The yielded alcohol (ethanol) is blended with gasoline.<sup>91,92</sup>

### IV.B.2. Gasification

The gasification belongs to the Gas-to-Liquids (GTL) processes and is undertaken at high temperatures, between 850 and 1000 °C. The biomass reacts with the different components of the air or with steam water to yield a gaseous mixture. This latter, the so-called syngas, contains CO, H<sub>2</sub>, CO<sub>2</sub>, CH<sub>4</sub>, and N<sub>2</sub>. CO and H<sub>2</sub> can be converted into hydrocarbons by Fischer-Tropsch (F-T) synthesis for diesel and gasoline engines.<sup>93–95</sup> The advantage of this process is to not depend on the nature of the feedstock. The sensitivity of the gasification steps to the water contained in the biomass and to the impurities present in the produced biogas are the main drawbacks of this method.<sup>96</sup>

### IV.B.3. Pyrolysis

In pyrolysis process, the biomass is converted by thermal treatment in the absence of oxygen, at a pressure ranging from 1 to 5 atm. Depending on the operating parameters, different amounts of bio-oil, biochar (or charcoal), and gas (particularly syngas) are generated. The biomass pyrolysis generates vapors containing thousands of compounds that are condensed by cooling and give the so-called bio-oil. Depending on the reaction conditions, three kinds of pyrolysis have to be distinguished (**Table I-1**).<sup>97,98</sup>

Name	Particle size	Residence time	Heating rate	Temp. (° C)	Major products
<b>Slow</b>	Massive	5-30 min	Low	500 °C	<u>Charcoal</u> , bio-oil, gas
<b>Fast</b>	Fine (< 1 mm)	0.5-5 s	High	400 - 650 °C	<u>Bio-oil</u> , charcoal, gas
<b>Flash</b>	Very fine (< 0.2 mm)	< 1 s	Very high	650 - 1000 °C	<u>Bio-oil</u> , <u>gas</u> , charcoal

Table I-1. Pyrolysis methods and their key features<sup>99,100</sup>

#### IV.B.3.a. Slow pyrolysis

In this process, also called conventional pyrolysis, the biomass is heated at 500 °C with a slow heating rate (10 °C/s) and a long residence time (5-30 min). As the generated vapors do not rapidly escape from the reactor, the compounds can react with each other to yield carbonized compounds responsible of a significant amount of charcoal (30-50 wt. %). The bio-oil and the gas represent 35-50 wt. % and 10-30 wt. %, respectively.<sup>101</sup>

#### IV.B.3.b. Fast pyrolysis

Fast pyrolysis is typically performed at 500 °C with a residence time ranging from 0.5 to 5 s. It ensures to generate a high amount of bio-oil (60-75 wt. %). The amounts of charcoal (15-25 wt. %) and incondensable gas (10-20 wt. %) are lower than what it is typically observed in slow pyrolysis.

#### IV.B.3.c. Flash pyrolysis

Flash pyrolysis can be achieved with temperature ranging from 650 to 1000 °C with residence time lower than 1 s. Depending on the temperature, the percentage of the produced compounds varies<sup>102</sup> as demonstrated by Demirbas with four different nut shells.<sup>103</sup> When the temperature increases, the biochar percentage decreases whereas gas amount increases. The optimal temperature to obtain the largest amount of bio-oil is around 475 °C. The bio-oil yield decreases with the increase of the pyrolysis temperature. At the optimal conditions, up to 70 wt. % of the biomass is converted into bio-oil.

#### IV.B.3.d. Critical parameters of the biomass pyrolysis

The mechanism of pyrolysis is highly complex.<sup>104</sup> Indeed, each biomass component has its own degradation pathway, which is characterized by different kinetic constants. Different consecutive and competitive reactions occur. A significant number of works have been done to try to understand them.<sup>105,106</sup> Moreover, the kinetic factors involved in the pyrolysis process also depend on the operating parameters. Thus, the type of reactor, the temperature, the heating rate, the pressure, and the morphology of the raw material influence the pyrolysis process. Nevertheless, the reactions occurring during pyrolysis are very simple and correspond to dehydration, isomerization, dehydrogenation, aromatization, coking, cracking, and condensation.<sup>105,106</sup>

The amounts of the different pyrolysis products are highly dependent on the nature of the feedstock as well as the reactor temperature.<sup>107,108</sup> This was demonstrated by Chiodo *et al.* who performed several pyrolysis experiments at 400, 500, and 600 °C with three different raw materials.<sup>109</sup> The yields of the pyrolysis products in respect with the experimental conditions are given in the **Table I-2**. It is shown that an increase of the temperature is responsible of an increase of the gas amount and simultaneously a decrease of the biochar content. For the bio-oil, its yield is optimal at 500 °C.



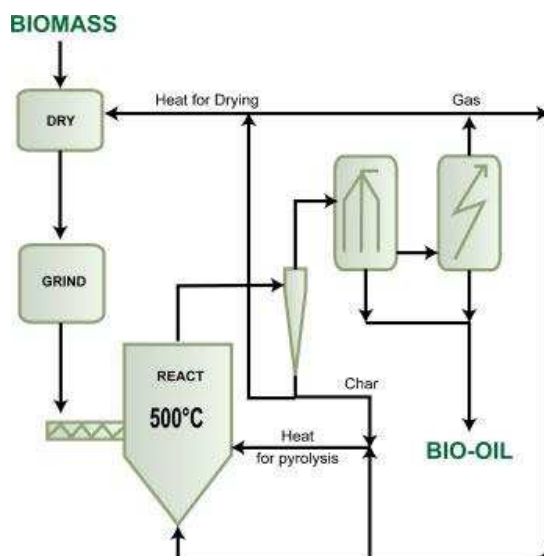
Materials	Temperature (°C)	Yield bio-char (wt%)	Yield bio-oil (wt%)	Yield gas (wt%)
White-Pine	400	26.4	46.1	27.5
	500	22.4	47.2	30.4
	600	20.4	41.4	38.2
Posidonia Oceanica	400	32.0	45.7	22.3
	500	22.8	52.4	24.8
	600	21.6	50.7	27.7
Lacustrine alga	400	48.3	33.7	18.0
	500	42.0	37.7	20.3
	600	41.3	36.2	22.5

Table I-2. Pyrolysis product yields in respect with the used feedstock and temperature<sup>109</sup>

The yield of the biomass conversion is also influenced by its residence-time in the reactor. It increases from 4 to 30 min. Lu *et al.*<sup>110</sup> demonstrated that the biochar amount decreases with the residence time while the production of gas increases and the water and bio-oil amounts remain constant. This behavior was also demonstrated by Salehi *et al.* for flash pyrolysis (residence-time ranging from 0.76 to 1.57 s).<sup>111</sup>

The bio-oil composition is also affected by the morphology and, more especially, by the size of the raw material.<sup>112,113</sup> Shen *et al.* evidenced that the use of small size of biomass particles (< 1 mm) favors the formation of the heaviest bio-oil components.<sup>112</sup> Heo *et al.* demonstrated that larger particles (> 0.7 mm) are responsible of a decrease of the bio-oil yield. For large size particles, a more important time is required to heat and to induce the pyrolysis. This behavior also explains the high amount of biochar when slow heating rates are used.<sup>113</sup>

The size of the biomass particles is also dependent on the type of the pyrolysis reactor. For rotating cone reactor, fluidized bed, and circulating bed, the size of the biomass particles is usually about 0.2, 2, and 6 mm, respectively.<sup>1,114</sup> Among all these pyrolysis systems, the fluidized bed (**Figure I-8**) is the most commonly used due to its advantages (**Table I-3**). Indeed, it provides a good temperature control and an efficient transfer of the heat. This is possible by the small size of the biomass particle (2-3 mm). The control of the flow rate of the fluidizing gas ensures to obtain a short residence-time of the vapors. The production of bio-oils with this system is simple and reliable. These properties make feasible the scaling from laboratory to pilot. In this setup, the char is rapidly removed. Thus, its concentration is very low (10-15 wt. %) and the bio-oil is obtained with a 75 wt. % yield.<sup>115,116</sup>

Figure I-8. Scheme of a fluidized bed pyrolysis system<sup>115</sup>

Property	Status #	Bio-oil (wt%)	Complexity	Feed size	Inert gas need	Specific size	Scale up
Fluid bed	Demo	75	Medium	Small	High	Medium	Easy
CFB	Pilot	75	High	Medium	High	Large	Easy
Entained		65	High	Small	High	Large	Easy
Rotating cone	Pilot	65	High	Very small	Low	Small	Hard
Ablative	Lab	75	High	Large	Low	Small	Hard
Vacuum	Demo	60	High	Large	Low	Large	Hard

Grey cells show undesirable characteristics

# Demo = demonstration (200–2000 kg h<sup>-1</sup>)

# Pilot = pilot plant (20–200 kg h<sup>-1</sup>)

# Lab = laboratory (1–20 kg h<sup>-1</sup>)

Table I-3. Characteristics of different pyrolysis units<sup>115</sup>

Several important parameters have to be considered to reach the optimal bio-oil production by pyrolysis. First, the feedstock has to be dry (< 10 % moisture) in order to minimize the amount of water in the final product. The biomass has to be grinded into small particles (1-3 mm). The optimum temperature is ~500 °C. A short residence time (< 2 s) and a rapid cooling of the pyrolysis vapors are also important features to limit side reactions.<sup>116</sup>

Typically, the pyrolysis of woody biomass at 500 °C yields liquid bio-oil (75 wt. %), char (12 wt. %) and gas (13 wt. %).<sup>116</sup>

The gas is mainly made of syngas that can be upgraded into F-T biofuels. The composition of the biochar varies in respect with the used temperature. It involves ashes (inorganics) and unconverted or not fully converted biomass materials. Moreover, the thermal degradation of the lignin produces solid carbonaceous residues. It can be upgraded as a fertilizer for the agriculture, used to produced energy, and for carbon storage.<sup>117</sup>

The pyrolysis bio-oil is a complex mixture with water (15-35 wt. %) and organics (65-85 wt. %). Among these chemicals, there is a broad range of compounds with different functional groups. Their molecular weight ranges from 30 to 1000 g.mol<sup>-1</sup>. There are acids, alcohols, aldehydes, ketones, phenols, aromatics, and nitrogen species.<sup>118</sup>

#### IV.B.4. Liquefaction

The liquefaction of the biomass occurs at a lower temperature than pyrolysis (200-500 °C) but at a higher pressure (5-30 MPa) with a reaction time ranging from 30 to 240 min.<sup>119,120</sup> The highly pressurized system is responsible of the important cost of the liquefaction process. Depending on the composition of the medium, three kinds of liquefaction process have to be distinguished.

- Hydropyrolysis consists of the heat of the lignocellulosic material at high pressure (H<sub>2</sub>) with a solid catalyst.<sup>121</sup>
- Hydrothermal liquefaction (HTL) is performed by mixing the biomass with a solvent.<sup>122</sup> Water is the most commonly used due to its low cost. In contrast to pyrolysis, this process does not require a drying step of the biomass.
- In solvolysis, a reactive solvent such as ethanol or acetone is added to the lignocellulosic raw material.<sup>123,124</sup>

The biomass liquefaction may be considered as a stepwise process. Each biomass component has specific reaction kinetics that have to be considered. First, the biomass is depolymerized into monomers by hydrolysis (dehydration, bound cleavage, and decarboxylation). Highly reactive products may recombine or depolymerize to form the different components of the bio-oil.<sup>125,126</sup>

The biomass liquefaction yields bio-oil (75 wt. %) including a small amount of water, gas (10-20 wt. %), and biochar (10-20 wt. %). All these products can be upgraded as shown in **Figure I-9**.<sup>127-129</sup>

The efficiency of the liquefaction process depends on different parameters.<sup>127,130,131</sup> Above 250-350 °C, the formation of gas and char is promoted. The residence-time is also a key feature to handle. It was demonstrated that a long retention time is favorable to high amounts of gas and char. As previously reported for fast pyrolysis, the heating rate and the nature of the feedstock are critical parameters. Other features have also to be considered such as the

solvent properties and the operating pressure. Reducing gases ( $H_2$  and  $CO$ ) are used to stabilize the liquefaction products and to increase the bio-oil yield. Catalysts are also used. Homogeneous catalysis (alkali salts such as sodium or potassium carbonate) increases the yield of the cellulose and hemicellulose hydrolysis.<sup>131,132</sup> Heterogeneous catalysts (metal supported) are used for hydrogenation of the bio-oil.<sup>127</sup>

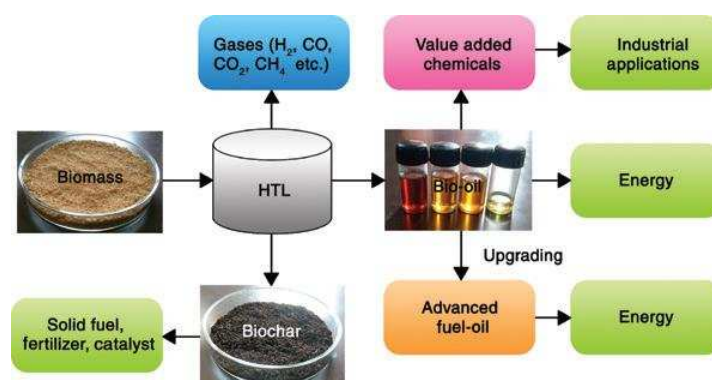


Figure I-9. Yielded products by biomass hydrothermal liquefaction and possible applications<sup>127</sup>

#### IV.C. Sustainability and bio-oil applications

It is established that the second generation bio-fuels present several advantages regarding its feedstock and its economic and ecological impacts.<sup>66,133</sup>

Different processes enable to generate biofuels from lignocellulosic biomass. Among them, the thermochemical ones present some assets. In contrast to the biochemical process, they do not require extraction pretreatment. This reduces the cost of the bio-oil production. Whatever the used feedstock, gasification, pyrolysis or liquefaction may be applied for bio-fuel production. Nevertheless, it was established that fast pyrolysis route is the cheapest.<sup>134</sup>

Bio-oil has a great potential due to its composition. Indeed, it can be upgraded by various pathways to obtain value-added chemicals, biofuels or to produce energy (**Figure I-10**).

The fractionation of the bio-oil, according to its water solubility, enables to access to specific compounds. Some aldehydes and phenolic compounds, from the aqueous fraction, are used in food industry for their organoleptic properties.<sup>135</sup> In the water-insoluble fraction, different lignin derivatives may be used in polymer chemistry for the production of resin.<sup>136</sup> Other liquid-liquid fractionation procedures ensure to isolate some targeted compounds. For

instance, the levoglucosan, a thermal degradation product of the cellulose, can be upgraded into pharmaceuticals, polymers, and surfactants.<sup>137</sup>

The physicochemical properties of the bio-oil enable to use it as boiler fuel for heat production. However, some sophisticated downstream processes are needed to upgrade the bio-oil to ensure its use as transportation fuel.

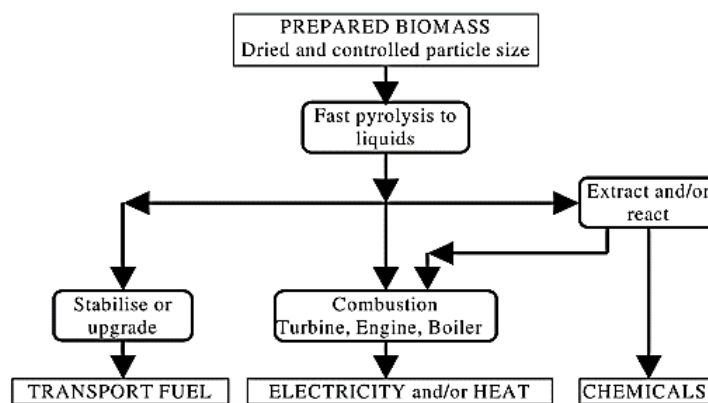


Figure I-10. Pyrolysis bio-oil applications<sup>116</sup>

## V. Properties and upgrading of bio-oils

### V.A. Physicochemical properties

Depending on the used process, the physicochemical properties of the bio-oil may be significantly different to the petroleum derived oil (**Table I-4**).

Properties	Pyrolysis oil	Liquefaction oil	Heavy fuel oil
Moisture, wt. %	15-30	5.1	0.1
pH	2.5	-	-
Elemental composition, wt. %			
C	54-58	72.6	85
H	5.5-7.0	8.0	11
O	35-40	16.3	1.0
N	0-0.2	-	0.3
S	0.00-0.02	0.00-0.03	1.0-1.8
Ash	0-0.2	-	0.1
Higher heating value, MJ.kg <sup>-1</sup>	16-19	34	40
Viscosity, cP	40-100 (at 50 °C)	15000 (at 61 °C)	180
Solids, wt. %	0.2-1	-	1
Distillation residue, wt. %	up to 50	-	1

Table I-4. Typical physicochemical properties of pyrolysis, liquefaction, and heavy fuel oil<sup>138,139</sup>

### V.A.1. Pyrolysis bio-oil

The following statements concern fast pyrolysis bio-oil at 500 °C. Indeed, this process was established to be the most appropriate to obtain the greatest amounts of bio-oil.

The composition of a pyrolysis bio-oil in terms of compound classes is given in the **Table I-5**. The major part of the bio-oil components presents at least one oxygenated chemical function. These oxygenated organic compounds extend on a wide range of molecular weight and abundance.

The large amount of carboxylic acids leads to a low pH of the bio-oil which is responsible of corrosiveness issues and consequently, storage problems. The acidity of the bio-oil may be evaluated by the total acid number (TAN). It is determined by acid-base titration and expressed as mg KOH/g of sample. It was estimated by Oasmaa *et al.* at 10.2 mg of KOH/g.<sup>140</sup>

Major components	Abundance wt. %
Aldehydes	10-20
Alcohols	2-5
Carboxylic acids	4-15
Furans	1-4
Ketones	1-5
Phenolic monomers	2-5
Phenolic oligomers	15-30
Sugars	20-35
Water	20-30

Table I-5. Typical abundances of major classes of bio-oil components<sup>118,141</sup>

A bio-oil is not thermodynamically stable. Indeed, its high reactive components may react with each other.<sup>142</sup> The efficiency of these reactions increases with the time and the temperature. During aging, the bio-oil properties are modified at the exception of the pH.<sup>143</sup> It was demonstrated that the viscosity increases due to the formation of water by the condensation mechanisms.<sup>143</sup> Polymerization reactions also occur, especially with aldehyde. This is responsible of a shift of the average molecular weight to higher values.<sup>142</sup>

### V.A.2. Liquefaction bio-oil

The liquefaction bio-oils have a higher energy density (HHV), a lower oxygen content, and a lower moisture (**Table I-4**) than the pyrolysis bio-oils. Nevertheless, they have a lower HHV

and a higher oxygen content than conventional fuel oils. They are water-insoluble liquids composed of phenols, carboxylic acids, aldehydes, ketones, alcohols, and nitrogen compounds.<sup>144,145</sup> This kind of bio-oil is also subjected to aging process.<sup>146,147</sup> Similarly to pyrolysis bio-oil, some upgrading processes involving heterogeneous catalysis are necessary to remove oxygen, reduce the viscosity and the TAN, and increase the HHV.

### V.B. Upgrading treatments

Different pathways have been developed to upgrade bio-oil into transportation fuels and value-added chemicals (**Figure I-11**). The focus will be mainly put on the various upgrading processes of pyrolysis bio-oil. But many of them are also applicable to liquefaction bio-oil.<sup>148–150</sup> Different upgrading treatments including heterogeneous catalysis, hydrotreatment, condensation or fractionation may be used after the production of the bio-oil. Nevertheless, some treatments may be conducted during the bio-oil production itself as the hydrolysis and the catalytic fast pyrolysis.

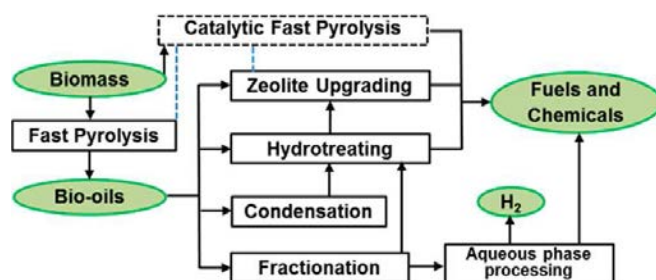


Figure I-11. Upgrading pathways for the conversion of the biomass and pyrolysis bio-oil into biofuels and chemicals<sup>151</sup>

#### V.B.1. Hydrolysis and catalytic fast pyrolysis

Fast pyrolysis performed in presence of reducing gas such as H<sub>2</sub> is called hydrolysis. It increases the amount of hydrocarbons.<sup>152,153</sup>

The catalytic fast pyrolysis ensures the *in situ* upgrading process. Some acid or alkaline catalysts such as carbonates (Na<sub>2</sub>CO<sub>3</sub>) and hydroxides (NaOH) are used to stabilize the bio-oil.<sup>154</sup> Typically, the alkaline compounds favor the formation of acetol and furfural, from cellulose degradation. Heterogeneous acid-catalysts, such as sulfate supported on SnO<sub>2</sub>, TiO<sub>2</sub>, ZrO<sub>2</sub> or Fe, favor the formation of furfural and furan.<sup>155,156</sup> These approaches are well suited to increase the yield of targeted products and high value-added chemicals.

The zeolite-based catalyst used in fast pyrolysis bed enables the deoxygenation of the bio-oil. Thus, it is possible to obtain a high-octane pyrolysis bio-oil and to increase the yield of aromatic compounds.<sup>157–159</sup>

Both hydrolysis and catalytic fast pyrolysis processes yield bio-oils with higher HHV. Nevertheless, these processes are not efficient enough to use the obtained liquid product for transportation fuel. Moreover, these techniques suffer from high operational complexity. An additional upgrading process is required for a more efficient oxygen removal and to obtain bio-oil with properties close to those of the petroleum.

### V.B.2. Zeolite upgrading

The zeolites are crystalline porous structures and are thermally stable. These silica-based materials have a high adsorption capacity and present an important specific surface. The pores present acidic active sites whose amount is related to the Si/Al ratio. In respect with the zeolite type, the pores are well-defined with diameter in the 5-12 Å range. This ensures to use the most suited zeolite according to the molecule to convert or to produce.<sup>160</sup>

Among the different kinds of zeolite<sup>161–163</sup>, ZSM-5 (Zeolite Socony Mobil-5) is characterized by an important stability and 5.5 Å pores (**Figure I-12**).<sup>164</sup> After specific treatments (calcination at 500 °C and then immersion in a HCl bath), acidic activities may be obtained to yield the HZSM-5.<sup>157,158</sup> The acidic zeolites are used for the bio-oil deoxygenation and cracking at temperature between 350 and 500 °C, under atmospheric pressure.<sup>157</sup> This process is most commonly named Fluid Catalytic Cracking (FCC).<sup>165,166</sup> It is widely used in petroleum refining and ensures to convert heavy crude oil fractions into gasoline. HZSM-5 demonstrated its capabilities to upgrade bio-oil into gasoline fuel with a high yield and low formation of coke.<sup>167–170</sup>

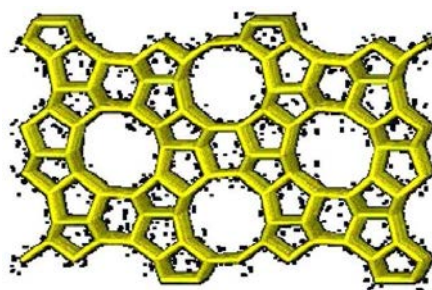


Figure I-12. Representation of the structure of the ZSM-5 catalyst<sup>164</sup>



Different chemical reactions are catalyzed by HZSM-5 (**Figure I-13**). Indeed, deoxygenation of alcohols, aldehydes, and ketones is carried out as well as dehydration, decarboxylation, and decarbonylation. The cracking process leads to the formation of alkenes, which may generate aromatics by cyclization, and ultimately, deposition of coke at the surface of the zeolite. The aromatic hydrocarbons resulting from the alcohol conversion represent up to 40 wt. % of the final product. The alkyl aromatics and the alkanes undergo cracking reaction to form ethylene, propylene, and butene.<sup>171–175</sup>

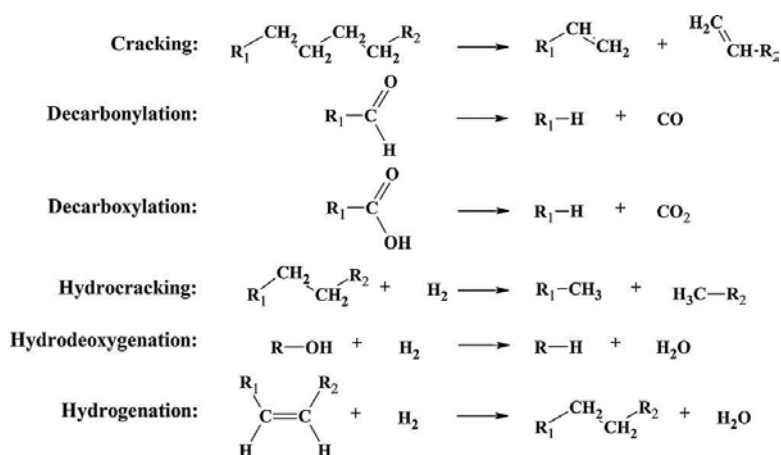


Figure I-13. Representative reactions associated with catalytic bio-oil upgrading.<sup>171,176</sup>

### V.B.3. Hydrotreatment

This hydrogenolysis process occurs at high temperature (125–500 °C) and under high pressure of hydrogen on a heterogeneous catalysis. This treatment can selectively remove oxygen, nitrogen, or sulfur and are called hydrodeoxygenation (HDO), hydrodenitrogenation (HDN), and hydrodesulfurization (HDS), respectively. The HDN and HDS processes are commonly used in petroleum refining.<sup>150,177</sup> For bio-oil, the HDO treatment is of significant interest due to the high amount of oxygen. For HDO, the bio-oil vapors interact with the catalyst and stepwise reactions occur which are responsible of oxygen removal. First, the C=O bonds are reduced to obtain C-O and finally C-H bonds. Reduction processes also occur for aromatic hydrocarbons which are responsible of a decrease of the energy density.<sup>178</sup> Therefore, simple deoxygenation will be preferred to not affect the HHV and to minimize the H<sub>2</sub> consumption.

Different HDO catalysts may be used: sulfide-based catalysts (CoMoS<sub>2</sub>- NiMoS<sub>2</sub>/Al<sub>2</sub>O<sub>3</sub>), bare metals (Ni and Cu), and noble metals (Pd, Ru, Pt, etc.).<sup>156,176</sup>

The resulting HDO upgraded bio-oil presents properties close to those of heavy fuel but with a lower viscosity.<sup>138</sup>

#### *V.B.4. Condensation*

This chemical treatment enables to reduce the value of the TAN. Low-cost alcohols are added to the bio-oil and react with the acid functions to yield esters.<sup>179</sup> This also induces a decrease of the boiling point of the bio-oils. This process may also occur with carbonyl compounds which easily lead to the formation of acetal. The water co-product has to be removed. Due to the no reduction of the oxygen amount and in spite of the decrease of the TAN, corrosion issue still remains. Moreover, it is not possible to refine this upgraded bio-oil with conventional petroleum refinery treatments. Therefore, deoxygenation or HDO has to be conducted.<sup>179,180</sup>

#### *V.B.5. Fractionation and aqueous phase processing*

The fractionation of bio-oil is mainly performed by the addition of water to form a biphasic solution. The oily phase, which is also the denser one, is viscous and contains organics, especially, phenolic compounds from the lignin pyrolysis. These species may be used as chemicals (production of resin) or converted into aromatic hydrocarbons and ethers which may supplement gasoline. The aqueous phase contains polar compounds such as acids, esters, and carbohydrate derived compounds. These sugarc compounds may be converted into alcohol by fermentation. Both phases may be upgraded by HDO.<sup>12</sup>

Another downstream process is the aqueous phase reforming (**Figure I-14**). It is mainly focused on the upgrading of the oxygenated carbohydrates into liquid fuels. The different involved reactions generate light alkanes, syngas (CO<sub>2</sub> and H<sub>2</sub>), and monofunctional compounds. Solid bare metal catalysts (Pt, Pd, Ni, Ru, and Rh) are used for C-C, C-O, and O-H bound cleavage.<sup>12,181,182</sup> Moreover, the water-soluble fraction can be processed by steam reforming to produce hydrogen.<sup>183,184</sup>

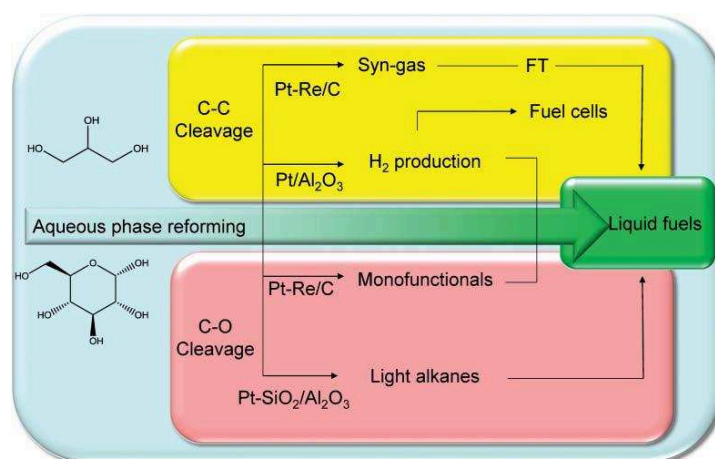


Figure I-14. Upgrading pathways involved in the aqueous phase reforming process<sup>12</sup>

### V.B.6. Conclusion

The most efficient upgrading treatments of bio-oil (heterogeneous catalysis) are still used for petroleum refinery. Therefore, the development of biomass derived fuels only requires a limited-cost development.<sup>185</sup>

Unfortunately, the deactivation of the used catalysts is significant and is mainly due to coke deposition. The coke formation is more important with zeolite based catalysts. The coke formation may be the result of the deposition of particles produced by the upgrading process or due to the polymerization of phenolic compounds. In that latter case, catalytic coke is formed in the micropores of the zeolite, over the catalytic sites, and is mainly associated with cyclization, oligomerization, aromatization, and condensation of the oxygenated compounds.<sup>186–188</sup> The water contained in the bio-oil vapors is also responsible of dealumination phenomenon which also induces the catalyst deactivation.<sup>189</sup>

For HDO catalysis, coke is also deposited on the surface of the catalysts, which poisons the active sites and deactivates the catalyst. The amount of the carbonaceous deposit increases with the acidity of the catalyst. It was also demonstrated that alkenes, aromatics, and oxygenated compounds, which have the highest affinity towards the catalyst, are the main contributor of the carbon formation.<sup>190</sup> Water and nitrogen species are also responsible of catalyst poisoning, as well as the alkali salts.<sup>190</sup>

Moreover, in pyrolysis process, the generated coke also plugs the reactor.<sup>150</sup> A proposed solution is to convert the coke into syngas by CO<sub>2</sub> steam reforming.<sup>191</sup> Therefore, fluidized bed are more suitable than fixed catalytic bed as coke formation is less favored.

### V.C. *General conclusion*

The biomass derived biofuels are promising sources of energy. More specifically, second generation biofuels are more sustainable. The production of liquid fuel from such feedstocks requires thermochemical processes such as liquefaction and pyrolysis. However, the physico-chemical properties of the bio-oil initially obtained do not enable its direct use as transportation fuels. Therefore, some upgrading strategies have been developed. Among them, HDO and catalysis on zeolite demonstrated the highest capabilities. These catalytic treatments generate liquid whose properties are close to the petroleum ones. Nevertheless, these upgrading treatments suffer from low yield and poor selectivity.

To improve the bio-oil yield and the catalyst efficiency, an extensive description of the bio-oil is necessary before and after upgrading treatment. This may be performed by employing an important analytical workflow. The different possible approaches will be described in the last section of this chapter.

## VI. Analytical methods for bio-oil characterization

### VI.A. *Introduction*

The chemical composition of the bio-oil is highly complex but a detailed knowledge of the thousands components is required. It ensures to improve the processes involved in the production, the upgrading, and the valorization of this resource. The thousands species that compose this material extend on a broad range of polarity and molecular weight. Hence, different analytical methods are applied depending on the class of investigated compounds. On the one hand, some techniques are dedicated to identify the chemical functions involved in the different bio-oil components. On the other hand, some approaches are developed to try to identify individual compound at the molecular level. These complementary approaches will be discussed in the following paragraphs.

### VI.B. *Sample preparation*

Prior the bio-oil analysis, pretreatments are often achieved in order to obtain a more detailed information. Adsorption chromatography (AD), liquid-liquid extraction (LLE), supercritical fluid extraction (SFE), gel permeation chromatography (GPC), sample derivatization (SD), solid phase extraction (SPE), and high performance thin layer chromatography (HPTLC) may

be used. Some solvent-free methods including solid phase microextraction (SPME) and molecular distillation (MD) are also employed.<sup>118,192</sup>

### VI.B.1. Wet methods

#### VI.B.1.a. Adsorption chromatography or liquid-solid chromatography

The bio-oil is fractionated on a silica chromatographic column with a sequence of increasing polarity solvents. The aliphatic, aromatic, ester, and polar components are eluted with *n*-pentane, toluene, ether, and methanol, respectively. These fractions are typically analyzed by gas chromatography coupled to mass spectrometry (GC-MS) or, in a lesser extent, by Fourier transform infrared (FT-IR) spectroscopy and nuclear magnetic resonance (NMR) spectroscopy.<sup>193–196</sup>

#### VI.B.1.b. Liquid-liquid extraction

In LLE, the bio-oil sample is divided into several fractions in respect with the used solvents. The most commonly used method is described in the **Figure I-15**. The sample is splitted into water-soluble and water-insoluble fractions. Typically, the former one is referred as the light fraction and the second one as the heavy fraction.<sup>197–199</sup> Subsequent diethyl ether and dichloromethane extractions are conducted on the aqueous fraction. The ether-soluble fraction mainly contains aldehydes, ketones, and lignin monomers. The ether-insoluble one is associated with sugars and short aliphatic hydroxy acids. The heavy fraction is separated with dichloromethane into CH<sub>2</sub>Cl<sub>2</sub> solubles (low-molecular mass lignin compounds) and CH<sub>2</sub>Cl<sub>2</sub> insolubles (high-molecular mass components).<sup>197–199</sup>

Alternatively, some fractionation methods may involve, prior the use of water, an extraction with an apolar solvent such as hexane or toluene.<sup>198,200</sup>

The obtained fractions are then analyzed by different analytical methods (GPC<sup>198,200</sup>, GC-MS<sup>197–200</sup>, FT-IR<sup>144,201</sup>, and NMR<sup>144,201</sup>).

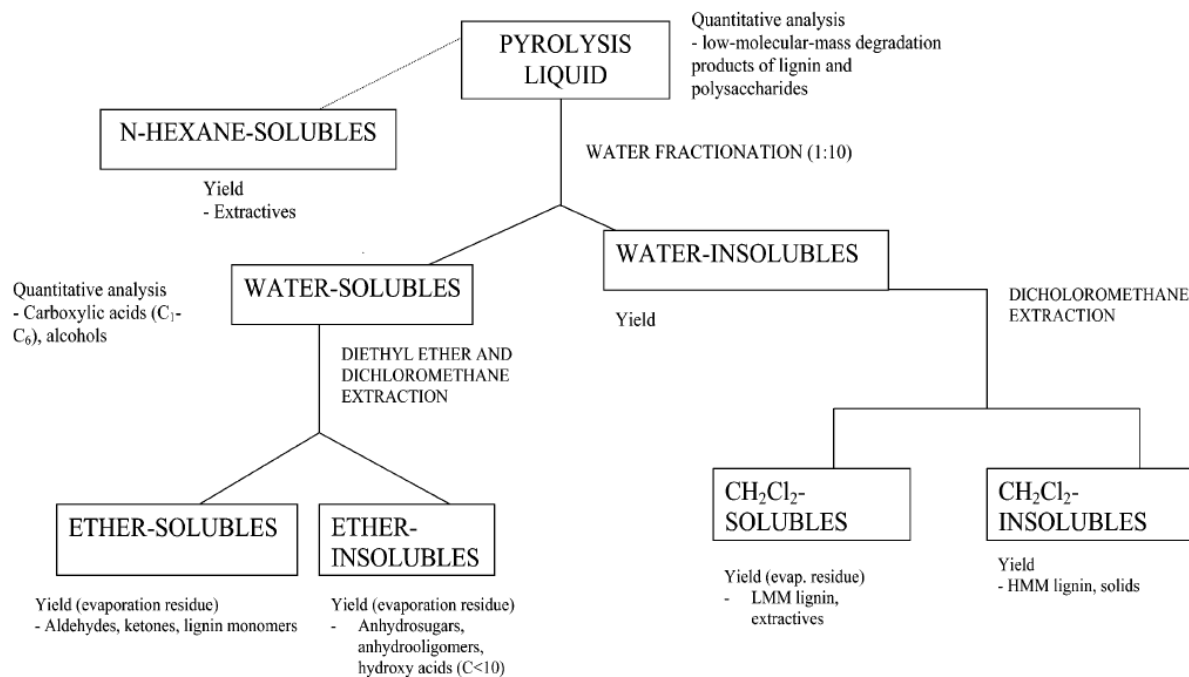


Figure I-15. Fractionation scheme with water-based LLE of bio-oil<sup>198</sup>

#### VI.B.1.c. Supercritical fluid extraction

In SFE, the solvents are held close to the pressure and the temperature of their critical point. Commonly, the carbon dioxide ( $P_{\text{critical}} = 73.8 \text{ atm}$  and  $T_{\text{critical}} = 31.1 \text{ }^\circ\text{C}$ ) is used. It presents the advantage to be nonflammable, nontoxic, cheap, and easily available. SFE with  $\text{CO}_2$  enables to selectively extract low-polar compounds such as aldehydes, ketones, and phenols. The other components (acids and water) are not extracted. The obtained fractions are then analyzed by GC-MS, nuclear magnetic resonance (NMR) or other analytical methods.<sup>202,203</sup>

#### VI.B.1.d. Gel permeation chromatography

This method can also be used as pretreatment in order to separate bio-oil compounds in respect with their size before to be analyzed by different methods.<sup>204,205</sup>

#### VI.B.1.e. Derivatization

The derivatization of some chemical functions can be applied prior the gas and liquid chromatography (GC and LC) analyses or, in specific cases, for NMR measurements. For NMR, the used derivatization reactions will be detailed in the **VI.C.2.b** following section.

The derivatization of targeted analytes in a complex mixture is generally performed for different purposes: (i) ensure their sensitive detection, (ii) modify the polarity of the analytes

to allow their separation by GC, (iii) increase the volatility of the analyte for GC analyses, and (iv) specifically evidence some chemical functions.<sup>206,207</sup> It mainly concerns polar compounds (alcohols, amines, acids, etc.). Thus, phenols and anhydrosugars may undergo acetylation with acetic anhydride<sup>208,209</sup> and trimethylsilylation with *N,O*-bis(trimethylsilyl)-trifluoroacetamide (BSTFA)<sup>210,211</sup>. The aldehydes are also derivatized with *o*-(2,3,4,5,6-pentafluorobenzyl)hydroxylamine hydrochloride (PFBHA).<sup>212</sup> For LC, 2,4-dinitrophenylhydrazine (2,4-DNPH) is used to derivatize the carbonyl compounds (aldehydes and ketones) to ensure their easier detection at the 365 nm wavelength.<sup>212,213</sup>

#### *VI.B.1.f. High performance thin layer chromatography*

Tessini *et al.* used HPTLC as a preparative tool to evidence some sugarc components in pyrolysis bio-oil. Some pyrolysis experiments were performed with different raw materials. The obtained bio-oils were either extracted with *n*-butanol and water or dispersed in cold water to achieve the precipitation of the pyrolytic lignin. Sugarc standard compounds (levoglucosan, xylose, arabinose, cellobiosan, and cellobiose) and the different bio-oil samples were deposited on HPTLC silica-gel plate and an anhydrous dipotassium phosphate/methanol solution was used as eluent.<sup>214</sup>

#### *VI.B.2. Solvent-free methods*

##### *VI.B.2.a. Solid phase extraction and microextraction*

For bio-oil analysis, C18 SPE may be used for the sample clean up<sup>215</sup> or to extract nonpolar compounds from aqueous fraction.<sup>209</sup> The SPME pretreatment ensures the adsorption of volatile low polar and low molecular-weight compounds when the stationary phase is exposed to the investigated bio-oil. The fibers of the SPME device are then introduced in a thermodesorber in front of a gas chromatograph instrument.<sup>209,216,217</sup> SPME can also be combined with derivatization and headspace extraction for a selective characterization of volatile aldehydes.<sup>212</sup>

##### *VI.B.2.b. Molecular distillation*

This process is widely used, more particularly, in petroleum industry, to separate and purify mixtures and chemicals. Some studies have been performed on bio-oils. The molecular distillation was carried out either by increasing the temperature<sup>213,218</sup> or the pressure.<sup>219</sup> The

bio-oil was separated into, at least, one distilled fraction and a residual one, depending on the operating conditions.<sup>219</sup> Thus, among the distilled fractions, there are the light, middle, and heavy ones<sup>218,220</sup> or the lights, naphta, jet, and gas oil related components.<sup>213</sup> The resulting fractions are generally analyzed by GC-MS.<sup>213,218–220</sup>

### VI.C. Targeted analytical methods

The targeted analyses refer to methods able to specifically characterize a given number of known compounds or species presenting a given chemical function. For example, FT-ICR or NMR ensures to give information on bio-oil compounds with specific functionality. The liquid or gas chromatography coupled to mass spectrometry is able to give quantitative information on known pre-selected components in respect with the retention time and the obtained mass spectrum in MS or MS<sup>n</sup>.

#### VI.C.1. Fourier transform infrared spectroscopy

The Fourier transform infrared spectroscopy (FT-IR) is used to highlight different functional groups of the molecules. The observed absorption signals in the mid-IR wavelength range (2.5 – 25  $\mu\text{m}$ ) are relative to transition between vibrational levels. The absorption properties of the molecules in IR are consequently associated to the vibrations linked to the motion of the atoms or group of atoms in the molecule. Thus, the FT-IR spectroscopy allows to characterize the compounds presenting in their structure a given chemical function (**Table I-6**). Moreover, some qualitative or at least semi-quantitative information may be obtained.<sup>221</sup>

The bio-oils from mallee constituents (wood, bark, and leaves) were characterized by FT-IR.<sup>222</sup> Lievens *et al.* also evidenced that the three investigated bio-oils presented various amounts of carbonyl compounds, which also appears to be specifically linked to the origin of the raw material. Indeed, the different ratio of lignin, cellulose, and hemicellulose in wood, bark, and leaves are responsible of the generation of different carbonyl compounds in the produced bio-oils. The authors also upgraded a raw bio-oil by esterification with methanol. The upgraded bio-oil was then distilled under vacuum to obtain a distilled fraction and a residual heavy fraction. Both acids and aldehydes/ketones were converted during the catalytic esterification.<sup>221</sup>



Wavenumber (cm <sup>-1</sup> )	Type of vibration	Compound class
3600-3200	O-H, N-H stretching	Phenols, alcohols, water, carboxylic acids, amides, amines
3100-3000	C-H stretching	Aromatic
2980-2870	C-H stretching	Alkanes
2350-2000	C≡C stretching	Alkynes, cyanides
1850-1650	C=O stretching	Aldehydes, ketones, carboxylic acids, esters
1650-1580	C=C stretching	Alkenes
1550-1490	NO <sub>2</sub> stretching, N-H bending, aromatic C=C stretching	Nitrogenous compounds, aromatics
1470-1350	C-H bending	Alkanes
1300-950	C-O stretching, O-H bending	Alcohols, ethers
915-650	C-H in-plane bending	Aromatics

Table I-6. Typical functional groups observed by FT-IR in bio-oil<sup>118,221</sup>

Due to their “chemical instability”, the carbonyl compounds have been used to monitor the aging of the bio-oil. Thus, they are good markers of bio-oil alteration. Scholze *et al.* demonstrated that the change of the oxygen amount in bio-oils is relative to the degradation of carbonyls. The alkoxy and hydroxy groups are less affected by aging.<sup>223</sup> This is confirmed by the Hilten *et al.* work which demonstrated that the relative abundance of the C-O stretching band increased over the time. Indeed, the esters are poorly sensitive to aging and the addition of methanol generally stabilizes bio-oils.<sup>224</sup>

Xu *et al.* used FT-IR to monitor the thermal degradation of bio-oil from rice husk pyrolysis by considering the deformation vibration of the C-H bond of the terminal olefins at 880 cm<sup>-1</sup>. They demonstrated that the appearance of this signal is related to the beginning of the aging process.<sup>225</sup>

Tripathi *et al.* developed a reliable method to predict the water content in bio-oil by using the near infrared spectroscopy and, consequently, to monitor the bio-oil quality during its production.<sup>226</sup>

In spite of some advantages (simple, fast, and cheap method), FT-IR presents some limitations. It is not sensitive enough to investigate all classes of compounds in the bio-oil, especially for compounds at a too low concentration and when the vibration modes are poorly active in IR. Moreover, FT-IR is only a semi-quantitative method related to the study of a given class of compounds and not to a specific bio-oil component. For an extensive bio-oil characterization, other analytical methods such as NMR, GC, and FT-ICR MS have to be used.<sup>227,228</sup>

### VI.C.2. Nuclear magnetic resonance spectroscopy

The nuclear magnetic resonance spectroscopy exploits the magnetic properties of specific atomic nuclei. This technique is widely used for the structural characterization and the compositional analysis of petroleum. The  $^1\text{H}$  and  $^{13}\text{C}$  NMR measurements may be performed to distinguish and quantify aromatics and aliphatics. Both one-dimensional (1D) and two-dimensional (2D) NMR experiments can be performed to characterize bio-oil.<sup>229</sup> In addition to  $^1\text{H}$  and  $^{13}\text{C}$  NMR, other active nuclei such as  $^{31}\text{P}$  and  $^{19}\text{F}$  may be used.<sup>229</sup>

#### VI.C.2.a. $^1\text{H}$ and $^{13}\text{C}$ NMR (1D and 2D)

The main advantage of  $^1\text{H}$  NMR analysis is the abundance of this nucleus, which allows a sensitive and rapid detection with a high signal-to-noise ratio. According to the chemical shift observed, it is possible to obtain structural information. In the study of bio-oil, the high complexity of the sample is responsible of overlappings which were evidenced by Joseph *et al.*<sup>230</sup> Correction factors and chemical-shift ranges for the assignments of the  $^1\text{H}$  NMR data have been proposed by these authors. The same methodology was conducted on  $^{13}\text{C}$  NMR data. Nevertheless, the range of the chemical shift is broader for  $^{13}\text{C}$  NMR which considerably decreases the overlapping issues. In that case, the main limitation is the poor natural abundance of  $^{13}\text{C}$  which is responsible of a lower sensitivity compared with the  $^1\text{H}$  one. Consequently, the acquisition time for  $^{13}\text{C}$  NMR measurement is more significant in order to obtain a S/N ratio ensuring the quantification.

The assignment is performed according to the chemical shifts which are well referenced.<sup>229,230</sup>

Different 1D and 2D  $^1\text{H}/^{13}\text{C}$  NMR studies have been performed to quantify the different functional groups of the bio-oil components. These works deal with bio-oils from slow or fast pyrolysis of different feedstocks. Both raw and fractionated bio-oils have been analyzed. Some experiments were also performed on catalytically upgraded bio-oils. A significant part of these studies have been reported by Hao *et al.*<sup>229</sup>

The  $^1\text{H}$  and  $^{13}\text{C}$  NMR were used to characterize and quantify oxygenated compounds in bio-oil. These information are useful to compare bio-oils from different processes. In some studies, 1D NMR analyses are associated with other analytical methods such as GC and FT-ICR MS.<sup>227,228,231</sup>

Even if 1D NMR method is valuable for qualitative and quantitative analyses of functional groups, it has some limitations. The overlapping phenomenon and long relaxation time make the interpretation more complicated. An attractive method to compensate these issues is the 2D NMR. In that case, the signal is “divided into two dimensions” which reduces the overlapping. The most used technique is the HSQC (Heteronuclear Single Quantum Coherence or Correlation) and the DEPT (Distortionless Enhancement Polarization Transfer) with  $^1\text{H}$  and  $^{13}\text{C}$ .<sup>229</sup>

Characterization of bio-oils by HSQC-NMR allows to distinguish methoxy groups, guaiacyl units, and pyrolytic sugars from whole or fractionated bio-oil.<sup>232,233</sup> This technique was also used to assess the bio-oil aging<sup>234</sup> and the efficiency of the hydrotreatment on HTL bio-oil.<sup>235</sup>

Mullen *et al.* used  $^1\text{H}$ ,  $^{13}\text{C}$ , and  $^{13}\text{C}$  DEPT NMR techniques to characterize pyrolysis bio-oils from six different feedstocks. The different classes of carbon and hydrogen atoms were quantified. The DEPT spectrum was used to classify and quantify carbon atoms in the bio-oils in respect with their branching degree ( $\text{CH}$ ,  $\text{CH}_2$ , and  $\text{CH}_3$ ). Significant differences were observed for the six investigated bio-oils. Moreover, these authors were also able to estimate the chain length of the alkyl substitutes of aromatics. They evidenced that the aliphatics from the corn stover bio-oil were highly substituted with very short branches (methyl groups). Conversely, the aliphatics of the switchgrass bio-oils are more straight.<sup>236</sup>

Similar approach was used by Strahan *et al.* for the characterization of fifteen bio-oils from different feedstocks and two fossil fuels were characterized by  $^{13}\text{C}$  and DEPT NMR. The determination and the quantification of various functional groups were performed. Complementary principal component analysis (PCA) was achieved. Thus, the combination of NMR measurements with PCA data demonstrated its capability to classify the different oils according to their energy density and their origin.<sup>237</sup>

The efficiency of the HDO process on a pyrolysis bio-oil was assessed by  $^1\text{H}$  NMR, among others, by Bi *et al.*<sup>238</sup> They demonstrated that the upgraded bio-oil contained less aldehydes but more aromatics. Moreover, signals related to methoxy and phenolic protons dropped whereas those from aliphatics increased. All these observations demonstrate the efficiency of the catalytic treatment. The effect of the temperature on the catalytic efficiency was also evidenced.

VI.C.2.b.  $^{31}\text{P}$  and  $^{19}\text{F}$  NMR (1D)

The  $^{31}\text{P}$  NMR analysis is performed after bio-oil derivatization. Hydroxyl functional groups undergo phosphorylation with 2-chloro-4,4,5,5-tetramethyl-1,3,2-dioxaphospholane (TMDP) (**Figure I-16**). These functional groups are then quantified in various bio-oils or fractions.

Naik *et al.* used TMDP to derivatize and quantify the hydroxyl groups of a raw and HDO bio-oils by  $^{31}\text{P}$  NMR. The authors have observed the suppression of the  $^{31}\text{P}$  NMR signals linked to the hydroxyl and mono lignol groups in the upgraded bio-oil, which assesses the efficiency of the HDO treatment.<sup>239</sup>

Ben *et al.* demonstrated, after phosphorylation with TMDP, that the aliphatic alcohols, the carboxylic acids, and the water contents are not stable after 2 hours. Moreover, these authors have evidenced that the acetic and formic acids were less stable than the aromatic carboxylic acids.<sup>240</sup>

Other derivatization agents can be used to quantify hydroxyl and carboxyl groups by  $^{31}\text{P}$  NMR. Balakshin *et al.* compared the accuracy of two phosphorylation reagents on the analysis of lignin hydroxyl and carboxyl groups. The 1,3,2-dioxaphospholane and the 2-chloro-4,4,5,5-tetramethyl-1,3,2-dioxaphospholane were used. The authors evidenced that the second one shown a good correlation with the results obtained in  $^{13}\text{C}$  NMR.<sup>241</sup>

Other studies have been performed by  $^{31}\text{P}$  NMR to quantitatively characterize the hydroxyl and carboxylic groups involved in the lignin constituents (guaiacyl, syringyl, catechol...) in bio-oils, after TMDP derivatization.<sup>242</sup> Stankovikj *et al.* have extensively characterized the water-soluble fraction of a bio-oil. The authors combined  $^{31}\text{P}$  NMR, GC-MS, Fourier transform ion cyclotron resonance mass spectrometry, and  $^{13}\text{C}$  and  $^1\text{H}$  NMR analyses. The  $^{31}\text{P}$  NMR analysis was aimed at quantifying the OH functional groups. They mainly evidenced aliphatic OH groups that were associated with anhydrosugars.<sup>243</sup>

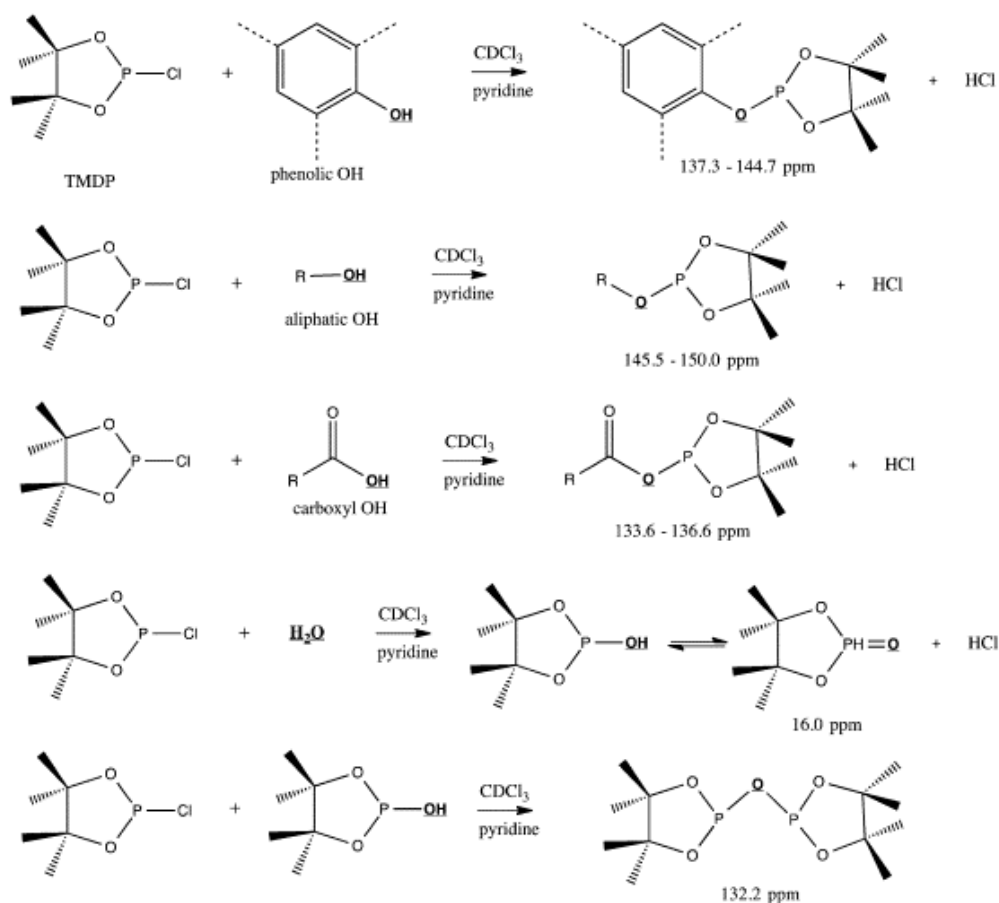


Figure I-16. Derivatization reactions of various hydroxyl functional groups with TMDP. Chemical shifts and assignments of the products in  $^{31}\text{P}$  NMR<sup>244</sup>

Similar to  $^{31}\text{P}$  NMR,  $^{19}\text{F}$  NMR analysis is an efficient method to characterize carbonyl functional groups. These chemical functions are derivatized with 4-(trifluoromethyl)phenylhydrazine (**Figure I-17**) before to be quantified. The aldehydes and, in a lesser extent, the ketones have been reported to be responsible of corrosion and aging issues. Their quantitation ensures to assess the efficiency of the different upgrading treatments of the bio-oils. Huang *et al.* used  $^{19}\text{F}$  NMR to quantify the amount of the carbonyl compounds in bio-oil. They obtained comparable results to the oxidation method. Moreover,  $^{19}\text{F}$  NMR gives an insight of the different kinds of carboxyl groups present in the bio-oil such as aldehydes, ketones, and quinone.<sup>245</sup>

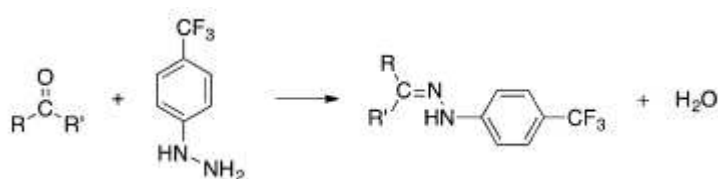


Figure I-17. Derivatization reaction of carbonyl group with 4-(trifluoromethyl)phenylhydrazine<sup>245</sup>

The NMR techniques, and more specifically 2D-NMR, are simple and informative methods in terms of functional group identification. Moreover, it is possible to do absolute quantitation of different classes of compounds. However, it provides only a partial and averaged information on the structure and no indication on the molecular weight of the bio-oil components.

### VI.C.3. Gas chromatography

The gas chromatography (GC) is widely used for the compositional characterization of the bio-oil. Typically, GC is coupled to a mass spectrometer (MS) or a flame ionization detector (FID). The GC-MS is well-suited for the identification of the unknown compounds. FID is more universal and presents a high sensitivity over a wide range of components with a broad linear dynamic range. Both couplings can be used to perform qualitative and quantitative analyses. However, GC-MS is preferred for the identification of bio-oil components whereas GC-FID is more reliable for quantitation.<sup>246,247</sup> Several studies performed to characterize raw and upgraded bio-oils from liquefaction and pyrolysis of biomass will be described in the following sections.

#### VI.C.3.a. GC-FID and GC-MS analyses

Murwanashyaka *et al.* performed one-step and stepwise pyrolysis of biomass at temperatures between 25 and 550 °C. The resulting bio-oils were analyzed in respect with the pyrolysis temperatures by GC-FID in order to monitor the thermal degradation of the biomass. In particular, the authors studied the evolution of the phenolic compounds depending on the pyrolysis temperature. They evidenced that phenols mainly decomposed between 275 and 350 °C.<sup>208</sup>

The GC-MS/FID technique was used by Doassans-Carrère *et al.* to respectively identify and quantify the major compounds of two different bio-oils. A gas chromatograph equipped with two columns (HAYSEP Q and molecular sieves 5A), which are used alternatively in series and bypass, was employed. After separation in the first column, the flow is splitted and directed to both detectors. These authors were able to compare the composition of bio-oils from fast pyrolysis and direct liquefaction. They demonstrated that the carbohydrates are prominent in pyrolysis oil while they were not detected when the bio-oil is produced by liquefaction. Inversely, etheric species and levulinic acid were specifically identified in the liquefaction bio-oil.<sup>231</sup>

The same method was used by Choi *et al.* to characterize a pyrolysis bio-oil. The detectable compounds were mainly (80 %) carbohydrate derived compounds. Some aldehydes and lignin derivatives were also evidenced.<sup>248</sup>

Tessini *et al.* have quantified the main part of the low-mass aliphatic aldehydes in a pyrolysis bio-oil by GC-MS. Prior analysis, these targeted compounds were derivatized by PFBHA.<sup>212</sup>

GC-MS also allows to highlight the influence of the feedstock on the chemical composition of bio-oil for low-mass components.<sup>249</sup>

#### VI.C.3.b. Pyrolysis GC-MS

Pyrolysis GC-MS (Py-GC-MS) is an interesting method to study the process of the biomass pyrolysis. It is possible to perform online and offline Py-GC-MS measurements. However, the off-line one appears to be easier to be implemented. Indeed, neither column deterioration nor memory effects are observed and high-mass compounds may be analyzed.<sup>216,250</sup>

Typically, pyrolysis products are collected by SPME (Py-SPME) and analyzed by GC-MS after thermal or liquid desorption.<sup>216</sup> Thus, experiments have been conducted by Py-GC-MS in order to assess the efficiency of different heterogeneous catalysts on the bio-oil properties.<sup>251,252</sup>

However, GC-MS and GC-FID present some limitations for the bio-oil characterization. Due to the significant number of bio-oil compounds, the one-dimensional GC does not present a sufficient separation capability. Therefore, qualitative and quantitative analyses are difficult to undertake.<sup>118</sup> To overcome this problem, two-dimensional gas chromatography measurements may be conducted.

#### VI.C.3.c. Two-dimensional gas chromatography

Two-dimensional or comprehensive gas chromatography (GCxGC or 2DGC) was introduced to overcome limitations of the one-dimension GC. In this technique, two capillary columns with different separation capabilities are used and are connected with a modulator. Typically, the first column is nonpolar and the second one, which is shorter, present a more polar stationary phase. The modulator ensures to focus the bio-oil eluents at the end of the first column, during a given time, before to be injected into the second column. This configuration provides to the GCxGC technique a superior peak capacity and a higher resolution than 1D-GC. Thus, more important number of compounds is detected.<sup>253,254</sup> Typically, GCxGC are

coupled to FID or MS detector. Both quantitative and qualitative analyses of bio-oil have been performed with comprehensive GC.

Fullana *et al.* carried out GC-Time Of Flight-MS (TOF-MS) and GCxGC-TOF-MS analyses of pyrolysis bio-oil. They demonstrated that 2DGC can identify 70 % of the peaks whereas only 47 % of the features are annotated with conventional GC (**Figure I-18**).<sup>253</sup>

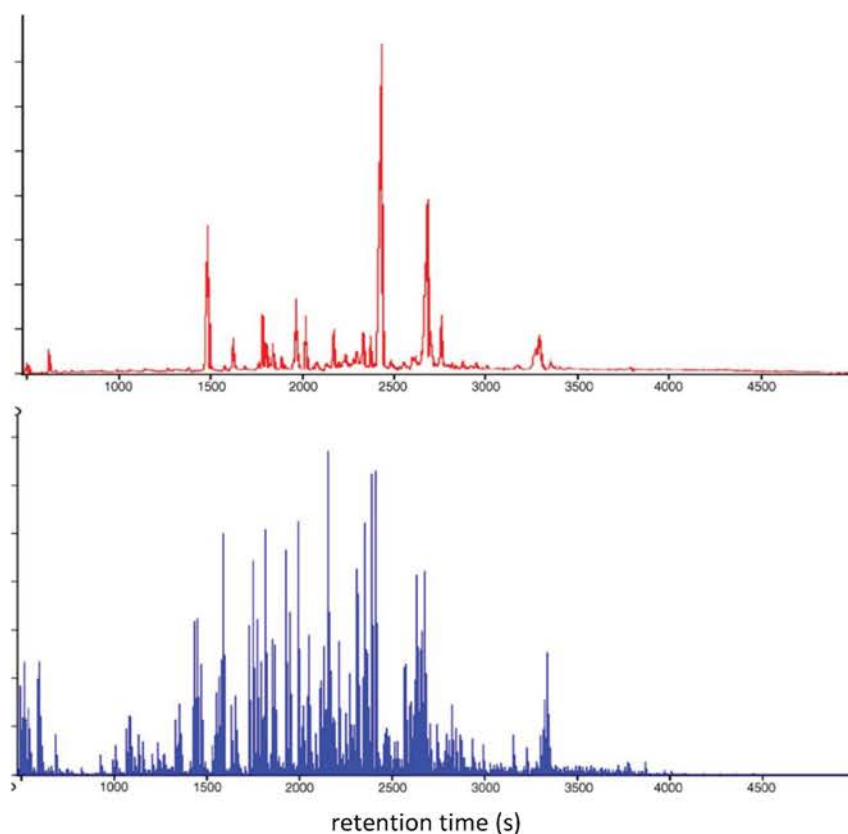


Figure I-18. Chromatograms achieved in GC (top) and 2DGC (bottom)<sup>253</sup>

Similar study was achieved by Marsman *et al.* who analyzed bio-oils by GC-MS and GCxGC-FID. They identified and quantified the main components of some raw and HDO pyrolysis bio-oils. The highlighted differences in terms of chemical composition ensured them to assess the efficiency of the upgrading process.<sup>254</sup> They used the same approach on raw and HDO fast pyrolysis oils after extraction with hexane.<sup>255</sup> The hexane-soluble and hexane-non soluble fractions were analyzed. The GCxGC-TOF-MS measurements ensured to detect 2000 and 100 compounds in the crude and upgraded bio-oils, respectively. It was also demonstrated that GCxGC-FID is more sensitive for the quantitation.

In the study of Sfetsas *et al.*, three different pyrolysis bio-oils were extracted with water to obtain aqueous phase. The compounds contained in the aqueous fractions were identified and quantified by GC-FID and by GCxGC-TOF-MS. Comprehensive GC allowed to identify



300 compounds which were classified into seven chemical families (acids and esters; aldehydes and ketones; furans; hydrocarbons; aromatic hydrocarbons; phenolics; and sugars). This enables to quantify and qualify the bio-oil components by means of an efficient mapping. However, GC-FID analysis provides reliable results, which allows a rapid screening of the sample.<sup>256</sup>

Michailof *et al.* have developed a suitable method by GCxGC-TOF-MS for the quantification and the qualification of the bio-oil components. The studied bio-oils were obtained by pyrolysis of cellulose, xylan, lignin, and a mixture of these three components. Upgraded bio-oils, which have been produced with the same raw material in a pyrolytic bed fitted with ZSM-5 catalyst, were also characterized. The raw hemicellulose bio-oil contains acetic acid, carbonyl compounds, and phenolic compounds. In the raw cellulose bio-oil, levoglucosan and, in a lesser extent, furanoic compounds are evidenced whereas phenolics, guaiacol, and its derivatives are identified in the raw lignin bio-oil. The deoxygenation effect related to the ZSM-5 catalyst was assessed by a pronounced decrease of the concentration of the methoxy-phenols and methoxy-benzenes and the respective increases of the alkyl-phenols and alkyl-benzenes.<sup>257</sup>

Olcese *et al.* used GCxGC (heart-cutting) /MS-FID-FID configuration (**Figure I-19**) to identify and quantify bio-oil components.<sup>258,259</sup> This technique enabled to quantify hundreds of species contained in raw and upgraded bio-oils. Moreover, differences in chemical compositions confirmed the HDO treatment efficiency. These results were compared with FT-ICR MS measurements (details will be given in the next section).

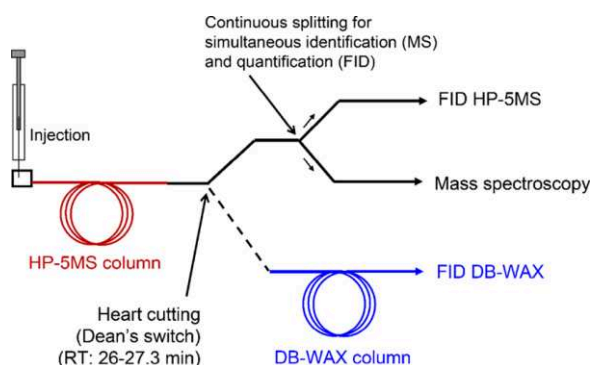


Figure I-19. Scheme of the GCxGC (heart-cutting)/MS-FID-FID device<sup>258</sup>

### VI.C.3.d. Conclusion

Conventional and comprehensive gas chromatography enabled the detailed characterization of bio-oil samples to be achieved. The typically detected compounds have been reviewed by Staš *et al.* (**Table I-7**).<sup>118</sup>

The use of derivatization pretreatments and 2DGC ensure to detect a more extensive range of compounds. However, these methods are restricted to volatiles and semi-volatiles. They correspond to a small portion of the bio-oil composition (**Figure I-20**).<sup>97</sup> Therefore, complementary techniques are required to attain an as extensive as possible bio-oil composition description and more specifically, to access the polar and/or high-mass compounds. Liquid chromatography<sup>212,248,249,260</sup> or Fourier transform mass spectrometry<sup>209,227,238,258,261–264</sup> that will be detailed in the following sections are, in that case, the techniques of choice.

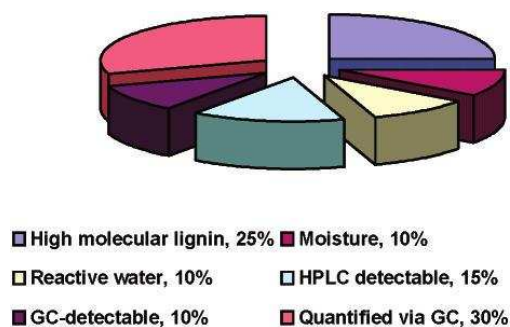
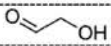
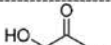
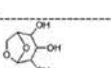

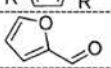


Figure I-20. Pie chart representing the typical portions of the bio-oil fractions<sup>97</sup>

Catalog	Typical Compounds	Structure <sup>b</sup>
Water	Water	H <sub>2</sub> O
Simple oxygenates	Acids	acetic acid, formic acid, propanoic acid, methyl-propanoic acid, butanoic acid, methyl butanoic acid, pentanoic acid, glycolic acid, etc.
	Esters	methyl acetate, methyl formate, methyl propionate, butyrolactone, dimethyl pentanedioate; etc.
	Alcohols	butane-2,3-diol, methanol, ethanol, 2-propene-1-ol, isobutanol; ethylene glycol etc.
	Ketones	acetone, 2-butanone, 2,3-butanedione; cyclopentanone; Methylcyclopentanone, 2-pentanone, cyclohexanone; 3-hexanone, methylcyclohexanone, cyclopentanedione; etc.
	Aldehydes	2-butenal, glyoxal, formaldehyde; acetaldehyde; 2-propenal; 2-methyl-2-butenal, pentanal, benzaldehyde; etc.
Miscellaneous oxygenates	glycolaldehyde	
	1-hydroxyl-2-propanone	
	methyl 2-oxopropanoate; 1-hydroxy-2-butanone; etc.	
Sugars	Levoglucosan	
	glucose, fructose, D-xylose, D-arabinose, etc.	
Furans	furan; methylfuran; dimethyl-furan;	
	furfural	
	2-furanone, 4-methyl-2-furanone, furfuryl alcohol, 2-acetyl furan; 5-methyl furfural; etc.	
Hydro-carbons	Alkene	hexane, methyl-propene, alkylated cyclohexene, etc.
	Aromatics	toluene; xylene, ethylbenzene, naphthalene, etc.
	Phenols	phenol, methylphenol, dimethylphenol
Phenolics	Anisoles	anisole
		methyl-anisole, ethyl-anisole, etc.
	Catechols	Catechol
		methyl-catechol, ethyl-catechol, methoxycatechol, etc.
	Guaiacols	guaiacol
		methyl-guaiacol, ethyl-guaiacol, eugenol, etc.
	Syringols	syringol, methyl-syringol, ethyl-syringol, propyl-syringol, 4-propenylsyringol, etc.
Others	vanillin, vanillic acid, sinapaldehyde, syringaldehyde, acetosyringone, etc.	
High-molecular-weight species	Dimmer, trimmer, and oligomer of cellulose, hemicellulose, and lignin pyrolysis products.	

<sup>b</sup> R, R' = H or CH<sub>3</sub>

Table I-7. Major compounds observed in typical bio-oils from biomass pyrolysis<sup>151</sup>

#### VI.C.4. Liquid chromatography

Liquid chromatography (LC) experiments are performed to detect both volatile and non-volatile compounds. Moreover, it is well adapted for the analysis of compounds having poor thermal stability and high polarity. The most commonly used LC methods are gel permeation

chromatography (GPC), also known as size exclusion chromatography (SEC), and reverse phase high performance liquid chromatography (RP-HPLC).

#### VI.C.4.a. Gel permeation chromatography

The GPC ensures the separation of the molecules according to their size. It is well-suited to define the molecular weight distribution of the bio-oil components. The typically used detectors are UV, refractive index (RI), and diode array detector (DAD). The mobile phase is generally tetrahydrofuran (THF) but dimethyl-formamide (DMF) can be added to help the solubilization of heavy polar species, polysugars, and high-molecular weight lignin. Measurements have been conducted on entire<sup>204,210,248,265</sup> or fractionated<sup>200,204</sup> bio-oils.

#### VI.C.4.b. High performance liquid chromatography

Choi *et al.* characterized oak pyrolysis bio-oil by HPLC-RI. They identified mono and disaccharides which were not detected by GC-MS. These compounds represent 15 wt. % of the bio-oil.<sup>248</sup>

Tessini *et al.*<sup>212</sup> and Christensen *et al.*<sup>213</sup> were focused on the identification and quantitation of the aldehyde and carbonyl compounds. In both studies, the targeted species were derivatized with 2,4-DNPH and detected by UV.

Some two-dimensional LC (LCxLC or 2DLC) analyses have been performed on bio-oils. The two columns present different stationary phases (non-silica-based x non-silica-based or non-silica-based x silica-based). Among the non-silica-based, there are the porous graphitic, the carbon-coated zirconia, and the polystyrene/divinylbenzene columns. The silica-based involved pentafluorophenyl-, C18-, and cynopropyl columns. The principle and the configurations are similar to what it is described for 2DGC, apart from the connection between the two columns, in that case a high pressure switching valve is used.

Le Masle *et al.* developed a suitable on-line 2DLC-UV method. They used different kinds of column and solvent gradient at different temperatures. The best operating condition given in **Table I-8** ensured to detect 2000 peaks and was applied for the analysis of the aqueous fraction of a wood bio-oil.<sup>266</sup>

	D1	D2
Stationary phase	Hypercarb	Acquity CSH Phenyl Hexyl
Column geometry	100 mm × 1 mm; 5 μm	50 mm × 2.1 mm; 1.7 μm
Mobile phase	A: H <sub>2</sub> O + 0.1% formic acid B: ACN + 0.1% formic acid	A: H <sub>2</sub> O + 0.1% formic acid B: MeOH + 0.1% formic acid
Gradient conditions	1%–99%B in 285 min	1%–81%B in 44s
Normalized gradient slope	1.6%	8.0%
Temperature	60 °C	80 °C
Flow-rate	10 μL/min	1400 μL/min
Injected volume	1 μL	11 μL
Run number	1	240
Sampling rate (6σ)	3.6	
Average peak width (4σ)	2.7 min	0.85s
Dilution factor <sup>a</sup>	17	1.1
Effective practical peak capacity	81 <sup>b</sup>	24 <sup>c</sup>
$n^*_{2D}$ <sup>d</sup>	1940	

1.15 min as sampling time.

Table I-8. Experimental conditions and results of the separation by RPLCxRPLC of the aqueous phase of a bio-oil<sup>266</sup>

Tomasini *et al.* also investigated the aqueous fractions of bio-oils from pyrolysis of different feedstocks by nanoLC-MS with electron ionization (NanoLC-EI-MS), LCxLC coupled to photodiode array (LCxLC-PDA), and atmospheric pressure chemical ionization-mass spectrometry (LCxLC-APCI-MS). The obtained features led to complementarity information. The 2DLC, which did not present overlapping peaks, enables the authors to detect more compounds which are mainly ketones, phenols, and furans.<sup>267</sup>

#### VI.C.5. General conclusion on chromatographic methods

Both GC and LC techniques ensure to carry out qualitative and quantitative analyses of bio-oils. But the compounds identified by these approaches represent only a portion of the bio-oil components. Moreover, the molecular weights of the detected compounds are generally low (< 370 amu). A global bio-oil description is necessary in order to improve the operating conditions of both its production and its upgrading processes. Consequently, other approaches have to be applied to identify compounds on a broader molecular weight range. High resolution mass spectrometry techniques with different ionization methods has this capability. These methods enable to detect and to assign thousands of compounds (at the exception of isomers) regardless of their functional groups or classes and are widely used for the analysis of petroleum crude oils. This non-targeted approach is named petroleomic approach and will be detailed in the last section of this chapter.<sup>118,268</sup>

### VI.C.6. Other analytical techniques

Other poor employed techniques are also used for the characterization of bio-oils. Laser desorption ionization-time of flight-mass spectrometry without and assisted by matrix (LDI-TOF-MS and MALDI-TOF-MS, respectively) may be applied. For low  $m/z$  range MALDI-TOF-MS is limited by the matrix signals that superimposed to the features of the bio-oils.<sup>204</sup>

Single photon ionization-time of flight-mass spectrometry (SPI-TOF-MS) is a soft technique that can analyze, in real-time, products generated during the biomass pyrolysis. Moreover, due to the relative high resolution of this instrument, compounds may be identified with a reasonable confidence.<sup>269,270</sup> Furthermore, SPI-TOF-MS allows to distinguish bio-oils in respect with the used feedstock and the employed pyrolysis regimes.<sup>270</sup>

## VII. Petroleomic non-targeted approach

### VII.A. Introduction

Marshall *et al.* were the first to introduce the petroleomic approach.<sup>271</sup> This method refers to the non-targeted analysis used to characterize petroleum crude oils. Typically, the sample is directly introduced in the ion source of the mass spectrometer to obtain a mass spectrum. Due to the complexity of the sample (thousands of compounds), a high resolution mass spectrometer (HRMS) is required to distinguish the different features with an ultrahigh mass resolving power (> 400 000). Moreover, the high mass measurement accuracy achieved by these instruments is needed to unambiguously assign a unique molecular formula ( $C_cH_hN_nO_oS_s$ ) to the different signals.

Mass spectrometer	Resolving power*	Mass accuracy	Mass range	Linear dynamic range
TOF	Up to 40 000	5 ppm	> 100 000	$10^6$
Orbitrap	Up to 150 000	1-5 ppm	6 000	$10^3$ - $10^4$
FT-ICR	Up to 1 000 000	<1 ppm	> 10 000	$10^3$ - $10^4$

\*equal to  $m/\Delta m_{50}$  with  $m$ , molecular mass and  $\Delta m_{50}$  mass spectral peak width at half-maximum peak height

Table I-9. Analytical capabilities of the common high resolution mass spectrometers<sup>118</sup>

The **Table I-9** reports the resolving power and the mass accuracy achieved by the TOF, Orbitrap, and FT-ICR instruments. The FT-ICR MS is the only technique that simultaneously ensures a resolving power better than one million and a mass accuracy lower than 1 ppm. It

is possible with this technique to assign more than 30 000 features in a petroleum crude oil mass spectrum.<sup>272</sup>

The critical parameter to obtain an extensive description of an oil is the efficiency of the ionization. Unfortunately, no universal technique is capable of ionizing all the components of an oil whatever its polarity and/or its molecular weight. The combination of the results obtained by complementary ionization sources has to be employed in order to achieve the as extensive as possible sample description.<sup>273</sup> Among the different available ionization techniques electrospray ionization (ESI), laser desorption ionization (LDI), and atmospheric pressure photoionization (APPI) are the most commonly used for petroleomic analyses. ESI allows medium to high polarity compounds to be ionized. The LDI enables the ionization of nonvolatile species that significantly absorb the laser light and have low to medium polarity. APPI is applicable for nonpolar to low polar compounds. Atmospheric pressure chemical ionization (APCI) is also suited for low polar to polar compounds, but the investigated species have to be thermally stable and volatile or semivolatile.

Due to the huge amount of collected data, their interpretation and comparison are not simple. Different graphical representations are generally used to facilitate the data treatment. The van Krevelen diagram is one of them. It represents the different  $C_xH_yO_z$  compound assignments by dots whose x and y coordinates are O/C and H/C ratios, respectively. Specific area of the diagram gathers lipids, cellulose and hemicellulose (sugaric) derivatives, or lignin derivatives (**Figure I-21**). For compounds involving nitrogen and/or sulfur, N/C and S/C ratios may also be used to draw similar diagrams.<sup>274–276</sup>

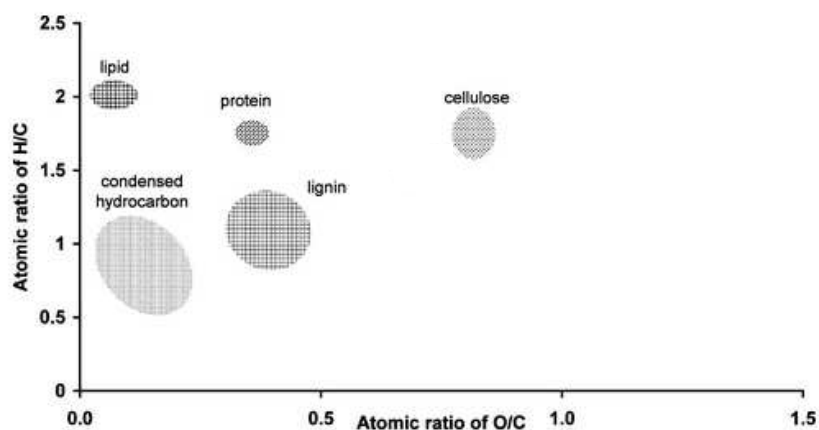


Figure I-21. Van Krevelen diagram with some major biomolecular component areas<sup>277</sup>

The double bound equivalent (DBE) represents the degree of unsaturation and aromaticity of a molecule and is given by the **Equation I-2**.<sup>274–276</sup>

$$\text{(Eq. I-2)} \quad \text{DBE} = C - \frac{H}{2} + \frac{N}{2} + 1$$

Kendrick Mass (KM) may be used to change the mass scale by taking, for example, CH<sub>2</sub> as the new mass scale reference and is calculated according to the **Equation I-3.1**. It enables to simplify and to facilitate the interpretation of the achieved data. Thus, formulae of the compounds having the same Kendrick Mass Defect (KMD), which is the difference between the nominal mass and the KM (**Equation I-3-2**), value differ only by the number of CH<sub>2</sub> unit.

$$\text{(Eq. I-3.1)} \quad \text{KM (CH}_2\text{)} = \text{IUPAC mass}_{\text{measured}} \times \left[ \frac{\text{Nominal mass CH}_2}{\text{IUPAC mass CH}_2} \right] =$$

$$\text{IUPAC mass}_{\text{measured}} \times \left[ \frac{14.00000}{14.01565} \right]$$

$$\text{(Eq. I-3.2)} \quad \text{KMD (CH}_2\text{)} = \text{nominal mass}_{\text{measured}} - \text{nominal KM (CH}_2\text{)}$$

Some graphical representations report the KMD vs.  $m/z$  or the DBE vs. the carbon number.<sup>274–276</sup> Details for the data treatment and the generation of the different graphical representations are given in the Chapter II.

### VII.B. Analyses of bio-oils by ESI-HRMS

Several studies have been performed to characterize bio-oils by ESI-HRMS, they will be detailed in the next paragraphs. Different factors influencing the bio-oil composition have been assessed such as the nature of the feedstock, the operating conditions or the bio-oil fractionation. An as exhaustive as possible review of the different published works is detailed in the **Table I-10**. The focus has been put on the implied process, the feedstock, the solvent, and the dopant used for the production and/or the analysis of these bio-oils.



Table I-10. Overview of the publications dealing with analysis of bio-oils by ESI-HRMS

Reference	Process – Feedstock	Ion source	Solvent - Dopant	Fractionation step	Oxygen range (Max)	Highlights
<b>Influence of the mass spectrometer and pH solution on the bio-oil mass spectrum</b>						
Smith <i>et al.</i> <sup>278</sup>	Fast pyrolysis Red oak	(-) ESI	MeOH:H <sub>2</sub> O (1:1)	-	O <sub>2</sub> -O <sub>12</sub> (O <sub>4</sub> -O <sub>6</sub> )	C <sub>x</sub> H <sub>y</sub> O <sub>z</sub> species with DBE < 5 are sugarc compounds C <sub>x</sub> H <sub>y</sub> O <sub>z</sub> species with DBE > 5 are phenolics
<b>Influence of the feedstock on the bio-oil composition</b>						
Jarvis <i>et al.</i> <sup>279</sup>	Fast pyrolysis ▪ Mixed conifer - normal - fire salvage - beetle kill salvage ▪ White Oak ▪ Scotch broom	(-) ESI	MeOH NH <sub>4</sub> OH (1 % v/v)	-	O <sub>1</sub> -O <sub>7</sub> (O <sub>2</sub> ,O <sub>4</sub> ) O <sub>2</sub> -O <sub>13</sub> (O <sub>7</sub> ,O <sub>10</sub> ) O <sub>2</sub> -O <sub>13</sub> (O <sub>7</sub> ) O <sub>2</sub> -O <sub>7</sub> (O <sub>2</sub> ,O <sub>4</sub> ) O <sub>1</sub> -O <sub>7</sub> (O <sub>2</sub> ,O <sub>4</sub> )	C <sub>10-50</sub> - DBE=0-15 - B <sub>1</sub> O <sub>5</sub> C <sub>10-45</sub> - DBE=0-20 - B <sub>1</sub> O <sub>4-12</sub> (B <sub>1</sub> O <sub>6</sub> ) - N <sub>1</sub> O <sub>6-10</sub> (N <sub>1</sub> O <sub>8</sub> ) C <sub>10-45</sub> - DBE=0-20 - B <sub>1</sub> O <sub>4-12</sub> (B <sub>1</sub> O <sub>7</sub> ) - N <sub>1</sub> O <sub>6-10</sub> (N <sub>1</sub> O <sub>8</sub> ) C <sub>10-40</sub> - DBE=0-25 - B <sub>1</sub> O <sub>4-6</sub> C <sub>10-50</sub> - DBE=0-30 - B <sub>1</sub> O <sub>4-6</sub>
Tessarolo <i>et al.</i> <sup>261</sup>	Flash pyrolysis ▪ Empty palm fruit ▪ Pine wood chips	(-) ESI	MeOH	-	O <sub>2</sub> -O <sub>14</sub> (O <sub>5</sub> ) O <sub>3</sub> -O <sub>13</sub> (O <sub>5</sub> )	C <sub>5-30</sub> - DBE=0-15 - N <sub>1</sub> O <sub>5-9</sub> C <sub>5-30</sub> - DBE=0-15
Abdelnur <i>et al.</i> <sup>280</sup>	Fast pyrolysis ▪ Eucalyptus ▪ Eucalyptus bark ▪ Cellulosic mud ▪ Water hyacinth ▪ Pine	(-) ESI	MeOH NH <sub>4</sub> OH (0.2 % v/v)	-	O <sub>2</sub> -O <sub>12</sub> (O <sub>7</sub> ) O <sub>2</sub> -O <sub>12</sub> (O <sub>5</sub> ) O <sub>2</sub> -O <sub>11</sub> (O <sub>5</sub> ) O <sub>2</sub> -O <sub>8</sub> (O <sub>2</sub> ) O <sub>2</sub> -O <sub>10</sub> (O <sub>5</sub> )	Lignin, sugarc derivatives, and lipids. Lignin, sugarc derivatives, and lipids. Lignin and lipids. Lipids, condensed aromatics, and lignin. Lignin, sugarc derivatives, and lipids.
Santos <i>et al.</i> <sup>281</sup>	Fast pyrolysis Three invasive aquatic plants	(-) ESI (+) ESI	MeOH:Toluene (1:1) NH <sub>4</sub> OH (0.2 % v/v) HCOOH (0.2 % v/v)	-		(+) ESI: N <sub>2</sub> O <sub>0-2</sub> and N <sub>3</sub> classes (-) ESI: O <sub>2-4</sub> and NO <sub>3</sub> , and N <sub>3</sub> O <sub>2</sub> classes O <sub>z</sub> species with DBE=1-17 (7 max)
Hartman <i>et al.</i> <sup>282</sup>	HTL Two plant cuticles	(-) ESI	MeOH:THF (1:1)	-	O <sub>1</sub> -O <sub>14</sub>	C <sub>10-51</sub> H <sub>y</sub> O <sub>1-14</sub> (90 %), C <sub>13-45</sub> H <sub>y</sub> NO <sub>2-7</sub> (5 %), and C <sub>x</sub> H <sub>y</sub> SO <sub>z</sub> (5 %) assigned classes.

Composition of fractionated bio-oils						
Miettinen <i>et al.</i> <sup>283</sup>	Slow pyrolysis Pine	(-) ESI	MeOH	Spontaneous bio-oil separation into aqueous <sup>1</sup> and oily <sup>2</sup> phases	O <sub>2</sub> -O <sub>14</sub> (O <sub>7</sub> ) <sup>1</sup> O <sub>2</sub> -O <sub>8</sub> (O <sub>2</sub> ) <sup>2</sup>	<sup>1</sup> Sugarc derivatives, pyrolytic lignin, and lipids. C <sub>8-25</sub> - DBE=0-15 <sup>2</sup> Lipids and pyrolytic lignin. C <sub>12-30</sub> - DBE=0-15
Jarvis <i>et al.</i> <sup>284</sup>	Fast pyrolysis ▪ Pine ▪ Peanut hull	(-) ESI	MeOH	Spontaneous bio-oil separation into aqueous <sup>1</sup> and oily <sup>2</sup> phases	Pine O <sub>2</sub> -O <sub>14</sub> (O <sub>10</sub> ) <sup>1</sup> O <sub>2</sub> -O <sub>11</sub> (O <sub>4</sub> ) <sup>2</sup> Peanut O <sub>2</sub> -O <sub>10</sub> (O <sub>7</sub> ) <sup>1</sup> O <sub>2</sub> -O <sub>8</sub> (O <sub>2</sub> ) <sup>2</sup>	C <sub>5-30</sub> - DBE=0-15 C <sub>5-40</sub> - DBE=0-20 C <sub>5-30</sub> - DBE=0-15 - N <sub>1-2</sub> O <sub>3-10</sub> - N <sub>3</sub> O <sub>4-9</sub> C <sub>5-35</sub> - DBE=0-20 - N <sub>1</sub> O <sub>3-8</sub> - N <sub>2</sub> O <sub>3-7</sub>
Stankovikj <i>et al.</i> <sup>243</sup>	Fast pyrolysis with 2 different technologies Pine	(-) ESI	MeOH	Bio-oils (BO) were injected into ice cold water, the water-insoluble fraction precipitate and the remaining solution formed the water-soluble fraction (WS). Bio-oil and WS were characterized.	Tech. 1 WS: O <sub>2</sub> -O <sub>18</sub> (O <sub>8</sub> ) BO: O <sub>2</sub> -O <sub>17</sub> (O <sub>7</sub> ) Tech. 2 WS: O <sub>2</sub> -O <sub>17</sub> (O <sub>10</sub> ) BO: O <sub>2</sub> -O <sub>16</sub> (O <sub>10</sub> )	C <sub>6-30</sub> - DBE=1-15 - M <sub>w</sub> =418 g/mol - C <sub>6-30</sub> - DBE=1-14 - M <sub>w</sub> =383 g/mol C <sub>6-27</sub> - DBE=1-12 - M <sub>w</sub> =410 g/mol C <sub>5-27</sub> - DBE=1-12 - M <sub>w</sub> =378 g/mol  ≈ 450 peaks assigned in the BO. ≈ 700 peaks assigned in the WS.
Sudasinghe <i>et al.</i> <sup>285</sup>	HTL Microalga	(-) ESI (+) ESI	CHCl <sub>3</sub> :MeOH:2-propanol (1:2:4) NH <sub>4</sub> OH (0.1 % v/v) HCOOH (0.1 % v/v)	Lighter oil (BO) and heavier aqueous fraction (AF) were spontaneously formed. The last one was diluted 200-fold and 1000-fold for (+) and (-) modes, respectively.	(-) ESI BO: O <sub>2</sub> -O <sub>8</sub> (O <sub>2</sub> ) AF: O <sub>2</sub> -O <sub>10</sub> (O <sub>2</sub> ) (+) ESI BO: / AF: /	Other compound classes were identified. N <sub>1</sub> O <sub>1-5</sub> - N <sub>2</sub> O <sub>1-6</sub> . ≈ 2770 identified peaks. N <sub>1</sub> O <sub>1-9</sub> - N <sub>2</sub> O <sub>1-6</sub> . ≈ 1740 identified peaks. N <sub>1</sub> O <sub>0-2</sub> - N <sub>2-3</sub> O <sub>0-3</sub> - N <sub>4</sub> O <sub>0-1</sub> . ≈ 4600 identified peaks. N <sub>1</sub> O <sub>0-2</sub> - N <sub>2-3</sub> O <sub>0-3</sub> - N <sub>4</sub> O <sub>0-1</sub> . ≈ 3370 identified peaks.

Cheng <i>et al.</i> <sup>227</sup>	Fast pyrolysis Red pine	(-) ESI	MeOH	Three fractions were obtained by a three-step CO <sub>2</sub> supercritical fluid extraction by increasing the pressure and the methanol ratio.	Raw BO O <sub>2</sub> -O <sub>16</sub> (O <sub>10</sub> ) E1 O <sub>2</sub> -O <sub>13</sub> (O <sub>8</sub> ) E2 O <sub>2</sub> -O <sub>17</sub> (O <sub>10</sub> ) E3 O <sub>4</sub> -O <sub>18</sub> (O <sub>12</sub> )	Lipids, condensed aromatics, sugarc and lignin derivatives. Lipids and lignin derivatives. Lipids, condensed aromatics, sugarc and lignin derivatives. Condensed aromatics, sugarc and lignin derivatives.
Liu <i>et al.</i> <sup>263</sup>	Fast pyrolysis Red pine	(-) ESI	MeOH	Liquid-liquid extraction were performed to obtain the hexane-soluble (HS), the ether-soluble (ES), ether-insoluble (EIS), dichloromethane-soluble (DS), and the methanol-soluble (MeS) fractions.	Raw BO O <sub>2</sub> -O <sub>16</sub> (O <sub>7</sub> ) HS O <sub>2</sub> -O <sub>13</sub> (O <sub>6</sub> ) ES O <sub>3</sub> -O <sub>14</sub> (O <sub>8</sub> ) EIS O <sub>2</sub> -O <sub>17</sub> (O <sub>10</sub> ) DS O <sub>2</sub> -O <sub>15</sub> (O <sub>7</sub> ) MeS O <sub>3</sub> -O <sub>16</sub> (O <sub>8</sub> )	C <sub>4-39</sub> - DBE=1-22 Acids, alcohols, and lignin monomers. Soluble polar compounds (acids, ketones, furans, phenols, alcohols, nitrides...) Polysaccharides prominent. Lignin dimers prominent. Lignin dimers and trimers prominent
<b>Effect of the production process and operating conditions on the bio-oil composition</b>						
Yan <i>et al.</i> <sup>286</sup>	Methanolysis*/ Ethanolysis** Sweet sorghum stalk	(-) ESI (+) ESI	MeOH:Toluene (1:3)	-	(-) ESI *: O <sub>1</sub> -O <sub>10</sub> (O <sub>4</sub> ) **: O <sub>1</sub> -O <sub>10</sub> (O <sub>3</sub> ) (+) ESI *: O <sub>1</sub> -O <sub>2</sub> **: O <sub>1</sub> -O <sub>2</sub>	C <sub>5-35</sub> - DBE=1-14 - N <sub>1</sub> O <sub>0-10</sub> (N <sub>1</sub> O <sub>3</sub> ) C <sub>5-35</sub> - DBE=1-14 - N <sub>1</sub> O <sub>0-10</sub> (N <sub>1</sub> O <sub>3</sub> ) DBE=1 - N <sub>1</sub> O <sub>0-3</sub> - N <sub>2</sub> O <sub>0-6</sub> (N <sub>2</sub> O <sub>3</sub> ) DBE=1-2 - N <sub>1</sub> O <sub>0-3</sub> - N <sub>2</sub> O <sub>0-6</sub> (N <sub>2</sub> O <sub>3</sub> )

Yan <i>et al.</i> <sup>287</sup>	Methanolysis Cornstalk	(-) ESI	MeOH:Toluene (1:3)	Sequential extraction of the bio-oil were performed according to the procedure from the <b>Figure 27</b> .	SP <sub>1</sub> O <sub>1</sub> -O <sub>10</sub> (O <sub>3</sub> ) SP <sub>2</sub> O <sub>1</sub> -O <sub>8</sub> (O <sub>3</sub> ) SP <sub>5</sub> O <sub>1</sub> -O <sub>10</sub> (O <sub>8</sub> )	1800 assigned formula. $M_w=334$ g/mol C <sub>5-35</sub> - DBE=1-14 - N <sub>1</sub> O <sub>2-8</sub> (N <sub>1</sub> O <sub>4</sub> ) 1800 assigned formula. $M_w=324$ g/mol C <sub>5-35</sub> - DBE=1-14 - N <sub>1</sub> O <sub>2-8</sub> (N <sub>1</sub> O <sub>4</sub> ) 1000 assigned formula. $M_w=286$ g/mol C <sub>5-35</sub> - DBE=1-14 - N <sub>1</sub> O <sub>1-8</sub> (N <sub>1</sub> O <sub>5</sub> )
Kekäläinen <i>et al.</i> <sup>288</sup>	Pyrolysis at 300* and 380** °C Silver birch	(-) ESI	MeOH NH <sub>4</sub> OH (1 % v/v)	-	* O <sub>2</sub> -O <sub>14</sub> (O <sub>7</sub> ) ** O <sub>2</sub> -O <sub>12</sub> (O <sub>6</sub> )	O <sub>x</sub> (90 % of the TIC), N <sub>n</sub> O <sub>x</sub> (5 %), S <sub>s</sub> O <sub>x</sub> (3 %), Na <sub>m</sub> O <sub>x</sub> (3 %) C <sub>10-24</sub> - DBE=0-14 - N <sub>1</sub> O <sub>4-10</sub> (N <sub>1</sub> O <sub>7</sub> ) C <sub>8-23</sub> - DBE=0-14 - N <sub>1</sub> O <sub>4-9</sub> (N <sub>1</sub> O <sub>7</sub> )
Sudasinghe <i>et al.</i> <sup>235</sup>	HTL*/Fast pyrolysis**/ Hydrotreatment with HTL*** Pine	(-) ESI (+) ESI	CHCl <sub>3</sub> :MeOH (1:1) NH <sub>4</sub> OH (0.1 % v/v) HCOOH (0.1 % v/v)	-	(-) ESI *: O <sub>1</sub> -O <sub>10</sub> (O <sub>4</sub> ) **: O <sub>1</sub> -O <sub>15</sub> (O <sub>6</sub> ) ***: O <sub>1</sub> -O <sub>3</sub> (O <sub>1</sub> ) (+) ESI *: / **: / ***: /	C <sub>8-45</sub> - DBE=5-28 C <sub>5-40</sub> - DBE=2-25 N <sub>1</sub> O <sub>0-5</sub> (N <sub>1</sub> O <sub>1</sub> ) - N <sub>2</sub> O <sub>0-3</sub> - N <sub>3</sub> N <sub>1</sub> O <sub>2-12</sub> (N <sub>1</sub> O <sub>8</sub> ) - N <sub>2</sub> O <sub>0-6</sub> - N <sub>3</sub> O <sub>0-1</sub> N <sub>1</sub> O <sub>0-3</sub> (N <sub>1</sub> ) - N <sub>2</sub> O <sub>0-2</sub>
Tessarolo <i>et al.</i> <sup>289</sup>	Fast pyrolysis at 450*, 500**, and 550*** °C without and with cata- lyst (Z) ▪ Pine ▪ Sugarcane bagasse	(-) ESI	MeOH	-	Pine *: O <sub>2</sub> -O <sub>12</sub> (O <sub>4</sub> ) **: O <sub>2</sub> -O <sub>11</sub> (O <sub>4</sub> ) ***: O <sub>2</sub> -O <sub>11</sub> (O <sub>4</sub> ) Pine+Z *: / **: O <sub>2</sub> -O <sub>9</sub> (O <sub>4</sub> ) ***: O <sub>2</sub> -O <sub>9</sub> (O <sub>4</sub> )	Among the O <sub>2</sub> species, - fatty acids (DBE=1) - aromatics (DBE > 5)  Some O <sub>4</sub> species related to lignin derivatives.
Koike <i>et al.</i> <sup>264</sup>	Fast pyrolysis without and with catalyst Cedar	(-) ESI	Ethanol (1 μL/mL)	-	Without catal. O <sub>1</sub> -O <sub>16</sub> (O <sub>7</sub> ) Ni <sub>2</sub> P/SiO <sub>2</sub> O <sub>1</sub> -O <sub>9</sub> (O <sub>2</sub> ) Ni/SiO <sub>2</sub> O <sub>1</sub> -O <sub>17</sub> (O <sub>3</sub> )	Results obtained with Ni <sub>2</sub> P/SiO <sub>2</sub> • At 300 °C: 10, 20, and 30 g of catalyst yield bio-oils with 21.9, 21.0, and 20.6 wt. % of oxygen. • At 350 °C: 5, 10, and 20 g of catalysts yield bio-oils with 25.8, 22.3, and 17.9 wt. % of oxygen.

Bi <i>et al.</i> <sup>238</sup>	Fast pyrolysis Forestry residues HDO treatment at 150 <sup>1</sup> , 210 <sup>2</sup> , 300 <sup>3</sup> , and 360 <sup>4</sup> °C.	(-) ESI	MeOH	-	Raw BO	
					O <sub>2</sub> -O <sub>16</sub> (O <sub>7</sub> )	DBE=1-21 (10)
					UBO <sup>1</sup>	
					O <sub>2</sub> -O <sub>14</sub> (O <sub>7</sub> )	DBE=1-20 (9)
					UBO <sup>2</sup>	
					O <sub>2</sub> -O <sub>13</sub> (O <sub>6</sub> )	DBE=1-21 (9)
UBO <sup>3</sup>						
O <sub>1</sub> -O <sub>11</sub> (O <sub>5</sub> )	DBE=1-21 (9)					
UBO <sup>4</sup>						
O <sub>1</sub> -O <sub>10</sub> (O <sub>4</sub> )	DBE=1-21 (9)					
<b>Influence of the dopant on the bio-oil mass spectrum</b>						
Alsbou <i>et al.</i> <sup>290</sup>	Fast pyrolysis ▪ Forest residue ▪ Cellulose ▪ Lignin	(-) ESI (+) ESI	MeOH:H <sub>2</sub> O (1:1)	Fractionation of the forest residue BO 1. Into ice cold wa- ter, the water-in- soluble fraction precipitate and the remaining so- lution formed the water-soluble fraction (WS). 2. Water-soluble fraction was re- covered after a C18-SPE.	-	NH <sub>4</sub> Cl ensures to distinguish sugarc derivatives. NaOH and NaCl produced the highest peak intensities in both positive and negative ion modes;
			(-) ESI			
			1 mg/mL NaOH			
			0.5 mg/mL NH <sub>4</sub> Cl			
			(+) ESI			
			0.1 mg/mL HCOOH			
0.5 mg/mL NH <sub>4</sub> Cl						
0.5 mg/mL NaCl						

### VII.B.1. Influence of the nature of the mass spectrometer and of the pH of the solution on the ESI mass spectrum of the bio-oil

Smith *et al.* characterized a bio-oil with different high resolution mass spectrometers (FT-ICR, Orbitrap, and Quadrupole Time of Flight Q-TOF) by (-) ESI.<sup>278</sup> They achieved similar results whatever the instrument. FT-ICR MS provides the best mass resolution but presents a significant low-mass discrimination. Similar observations was made by Abdelnur *et al.* who characterized bio-oil by FT-ICR and Q-TOF mass spectrometry.<sup>280</sup> The developed method by Smith *et al.* enabled to assign over 800 features, mainly  $C_xH_yO_{2-12}$  compounds related to sugarc derivatives and phenolics. Furthermore, the authors also evidenced the effect of the pH of the bio-oil solution on the ionization efficiency of the bio-oil components. To adjust the pH, acetic acid and ammonium hydroxide were added to obtain solutions with a pH value of 3.5, 5, 7, and 9. Variations of the ion signals was associated with the pKa of the bio-oil components. At high pH value, the signals for  $O_4-O_5$  sugarc compounds are suppressed while at pH 5, the best ion signal was obtained for this compound class. At low pH, acetate ions abstract protons from sugarc species, which ensures their detection. Regarding the phenolic derivatives, some of them are efficiently detected at low pH value while other are more intensely observed at neutral or alkaline pH. Nevertheless, ion suppression phenomenon is observed at high pH value.<sup>278</sup>

### VII.B.2. Influence of the feedstock on the bio-oil composition obtained by ESI HRMS

The bio-oils from three different woody species have been characterized by (-) ESI FT-ICR MS.<sup>279</sup> Jarvis *et al.* evidenced  $C_xH_yO_z$  and  $C_xH_yBO_z$  compound classes whose distributions are similar whatever the feedstock. In the oak and scotch broom bio-oils, the  $O_2$  species, with  $C_{12-30}$  and DBE=1, are related to fatty acids. While in the mixed conifer bio-oil, the  $O_2$  species possess 20 carbon atoms and DBE=6-7 and correspond to resin acids (abietic acid, dihydroabietic acid). For species with more than two oxygen atoms, the representation of the carbon number vs. DBE demonstrates a multimodal distribution with the similar behavior. The presence of boron in some bio-oil components was confirmed by  $^{11}B$  NMR analyses which demonstrated that boron atoms are involved in polysaccharide complexes. The presence of boron is not senseless as it was determined to be essential to the plant development.<sup>291</sup> The bio-oils

from mixed conifer after beetle kill salvage and fire salvage have similar compositions but differ from those of the oak, scotch broom, and mixed conifer bio-oils. Indeed, a broader distribution in respect with the oxygen atom count is obtained for the  $C_xH_yO_z$  and  $C_xH_yBO_z$  compound classes. The  $C_xH_yBO_z$  class is more abundant in the mixed conifer beetle kill salvage bio-oil. Moreover, some nitrogen species were assigned which are more intensely detected in the mixed conifer fire salvage bio-oil. For this bio-oil, the carbon number vs. DBE plots is different to the other investigated bio-oils. It did not present a bimodal distribution. The presence of boron and nitrogen in the bio-oil can be problematic in terms of upgrading process as these compounds may poison the catalyst.

Tessarolo *et al.* performed (-) ESI FT-ICR MS analyses in addition to GCxGC-TOF-MS on bio-oils from empty palm fruit and pine wood chips.<sup>261</sup> In both samples,  $C_xH_yO_z$  compound class was identified and the observed distributions in respect with the oxygen atom count are similar ( $O_5$  species are prominent and are mainly related to sugarc derivatives). The  $O_2$  compounds, only observed in the empty palm fruit bio-oil, correspond to fatty acids, such as palmitic and stearic acids. Nitrogen compounds which are specific of the palm fruit bio-oil are thought to be sugar derived components coupled with some nitrogen-contained secondary pyrolysis products of the biomass. The phenolics were evidenced in both samples. Thus, this technique ensured to assign 836 and 564 peaks of the mass spectra for the empty palm fruit and pine wood chip bio-oil, respectively. The authors also demonstrated the complementarity of the two techniques for the comprehensive bio-oil description.

The bio-oils from eucalyptus, eucalyptus bark, cellulosic mud, water hyacinth, and pine were characterized by Abdelnur *et al.* by (-) ESI coupled to a FT-ICR and a Q-TOF instrument.<sup>280</sup> Oxygen-containing compounds were detected and their distribution in respect with the oxygen atom count is dependent of the raw material (**Figure I-22**).

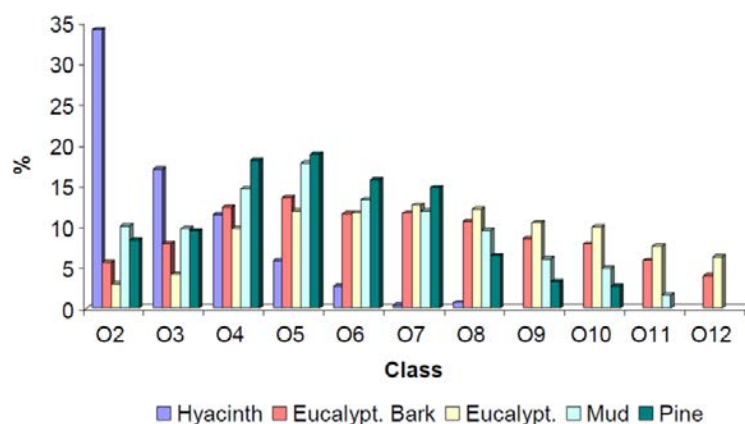


Figure I-22. Oxygen class distribution for each bio-oil analyzed by (-) ESI FT-ICR MS<sup>280</sup>

The van Krevelen diagrams were also drawn for these samples, which ensured the different biomass constituents to be highlighted. These diagrams may explain the differences observed in terms of heteroatom class distributions. Indeed, the O<sub>2</sub> compounds that are prominent in the water hyacinth bio-oil are related to lipids and more especially to fatty acids. In both eucalyptus and eucalyptus bark bio-oils, levoglucosan (C<sub>6</sub>H<sub>10</sub>O<sub>5</sub>) was intensely detected. The light bio-oil fraction of each sample was collected at different steps of the pyrolysis process, as shown on the **Figure I-23**. The yielded bio-oil composition is highly dependent of the location on the reactor of the bio-oil collection. For both eucalyptus based bio-oils, the oxygen class distributions extend on the same range but are less abundant in the light fraction. Concerning the water hyacinth bio-oils, the light fraction contains more oxygen-rich (O<sub>4</sub>-O<sub>11</sub>) compounds than the regular bio-oil which is mainly composed of O<sub>2</sub> and O<sub>3</sub> species. Indeed, on the van Krevelen diagram of the light fraction, sugarc derivatives (levoglucosan) are mainly evidenced and, in a lesser extent, aromatics. Lipids, condensed aromatics, and lignin are also identified in the regular bio-oil. Thus, these authors demonstrated that the bio-oil composition may be affected by the used biomass but also by the vapor residence time.

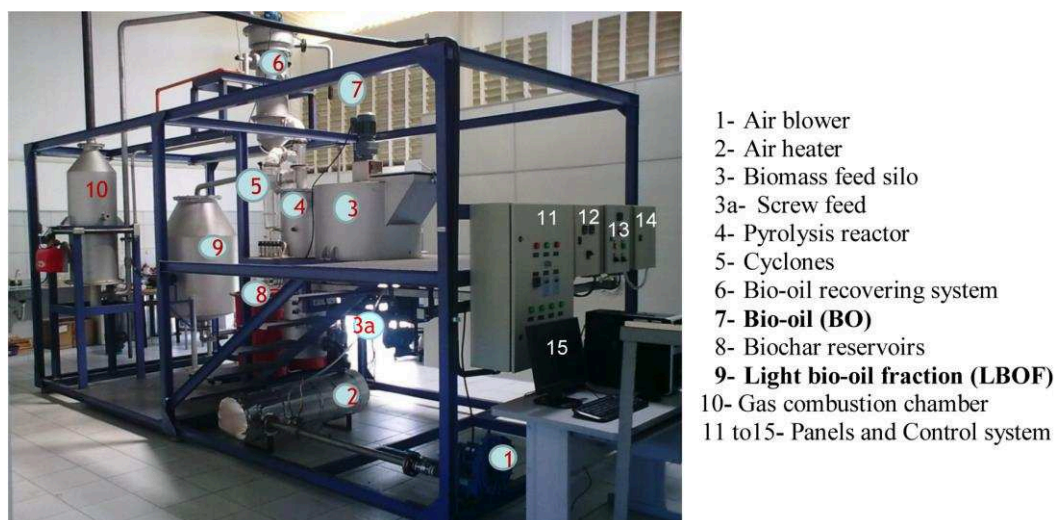


Figure I-23. Biomass fast pyrolysis pilot for bio-oil (7) and light fraction bio-oil (9) reservoirs

Santos *et al.* characterized bio-oils from three different freshwater plants in positive and negative ion ESI FT-ICR MS.<sup>281</sup> In positive ion detection mode, more than 1000 formulae were assigned whatever the studied sample and N<sub>2</sub>O<sub>0-2</sub> compounds were the main detected species. These compounds are related to pyridine, imidazole, and pyrazine derivatives. In negative ion detection mode, between 718 and 944 features were assigned. Oxygen-containing



species and, in a lesser extent, nitrogen compounds were identified. In the former class of compounds, phenols and carboxylic acids were identified. For the O<sub>2</sub> species, fatty acids are the major detected species. Thus, these authors demonstrated the contribution of the main acidic and basic components of bio-oils by using negative and positive detection modes, respectively.

The HTL bio-oils from two plant cuticles were characterized by (-) ESI FT-ICR MS in the work of Hartman *et al.*<sup>282</sup> Similar bio-oil compositions were obtained with close to 90 % of the signal related to C<sub>x</sub>H<sub>y</sub>O<sub>z</sub> species. For the agave cuticle bio-oil mass spectrum, 861 peaks were assigned whereas 1683 ones were attributed in the study of *Capsicum* cuticle bio-oil. Close to 650 of the obtained features are common to both bio-oils. The van Krevelen diagrams of both samples evidenced that the main part of the compounds were relative to lipids. These authors demonstrated that the achieved bio-oils have a HHV of 40 MJ.kg<sup>-1</sup>.

### VII.B.3. Influence of the fractionation treatment on the bio-oil composition obtained by ESI HRMS

#### VII.B.3.a. Water-soluble and water-insoluble fractions

In the study of Miettinen *et al.*, the slow pyrolysis bio-oil of pine spontaneously separated into aqueous and oily phases which were successively analyzed by (-) ESI FT-ICR MS.<sup>283</sup> In both fractions, C<sub>x</sub>H<sub>y</sub>O<sub>z</sub> compounds were identified whereas some C<sub>x</sub>H<sub>y</sub>Na<sub>m</sub>O<sub>z</sub> species were specifically evidenced in the aqueous phase. Both classes of compounds contribute to more than 95 % of the signal. In the oily phase, the distribution of the C<sub>x</sub>H<sub>y</sub>O<sub>z</sub> class in respect with the oxygen atom count is narrower than in the aqueous phase (**Figure I-24**). The obtained van Krevelen diagrams demonstrated that lipids (fatty and resin acids) and phenolic compounds from lignin pyrolysis are the major components of the oily phase. Even if these components are also evidenced in the aqueous phase, this fraction mainly contains sugarc compounds from cellulose and hemicellulose pyrolysis (**Figure I-25**). The oxygen amount of these sugarc derivatives is higher than those of the pyrolytic lignin and lipid components, which explains the observed differences.

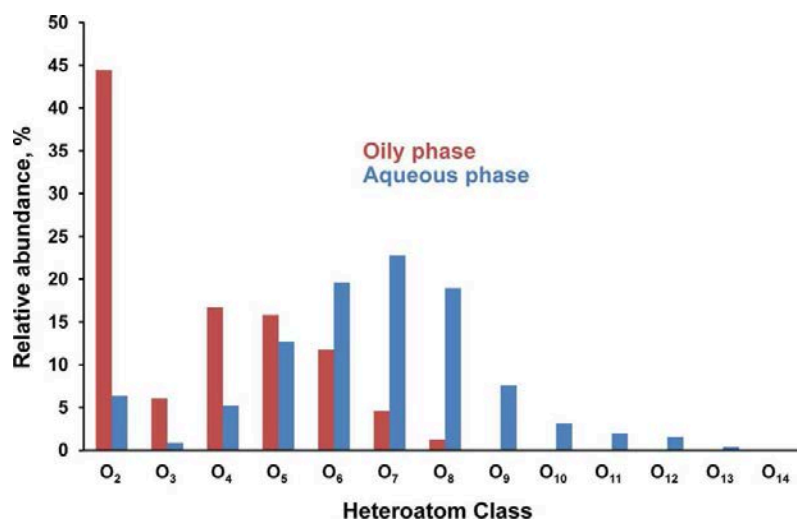


Figure I-24. Distribution of  $C_xH_yO_z$  compounds in respect with oxygen atom count from the oily and aqueous phases analyzed by (-) ESI FT-ICR MS<sup>283</sup>

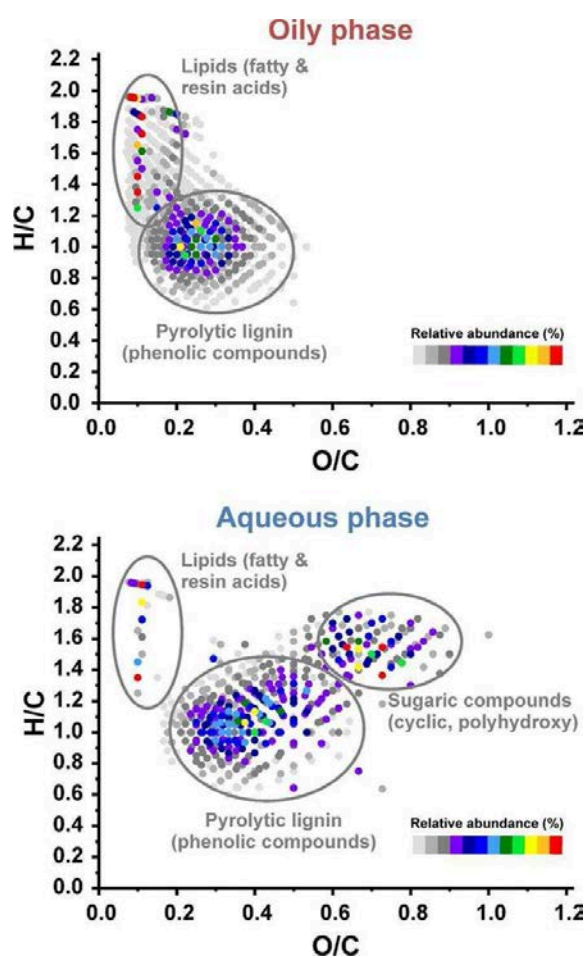


Figure I-25. Color-mapped van Krevelen diagrams of  $C_xH_yO_z$  compounds in the oily and aqueous phases analyzed by (-) ESI FT-ICR MS<sup>283</sup>

Similar experiments were performed by Jarvis *et al.*<sup>284</sup> on aqueous and oily phases from bio-oils from pine and peanut hull. Both bio-oils spontaneously splitted into two phases which were analyzed by (-) ESI FT-ICR MS. The authors observed a broader distribution of the oxygen class in the aqueous fraction than in the oily phase, whatever the used feedstock. The O<sub>2</sub> species, more intensely detected in the oily phases, were attributed to fatty and resins acids. The other compounds are relative to aromatics. Some nitrogen species were assigned for the peanut hull bio-oil, in the aqueous phase and, in lesser extent, in the oily one. This is in agreement with the bulk analyses performed on the used feedstock. This study demonstrates the capability of the petroleomic approach to distinguish bio-oil regarding the nature of the feedstock and the analyzed fraction.

Stankovikj *et al.* characterized bio-oils from pine wood obtained by two different pyrolysis technologies. After fractionation into water-soluble and water-insoluble phases, different analytical methods have been used (GC-MS, ion chromatography, UV spectroscopy, NMR, and ESI-MS) which allowed to quantify more than 90 wt. % of the water-soluble fraction and the raw bio-oils.<sup>243</sup>

The light bio-oil and the aqueous fraction of a microalga HTL bio-oil were analyzed in both positive and negative ion ESI FT-ICR MS by Sudasinghe *et al.*<sup>285</sup> In (-) ESI, C<sub>x</sub>H<sub>y</sub>O<sub>z</sub> and C<sub>x</sub>H<sub>y</sub>N<sub>1-2</sub>O<sub>z</sub> compounds were evidenced for all samples. In (+) ESI, the bio-oil compositions were similar and contained only basic C<sub>x</sub>H<sub>y</sub>N<sub>1-4</sub>O<sub>z</sub> species. The predominant species observed in both samples are related to aromatic nitrogen compounds and free fatty acids.

#### VII.B.4. Other fractionation process

Cheng *et al.* carried out supercritical CO<sub>2</sub> extraction on bio-oil to obtain three subfractions.<sup>227</sup> The four samples were analyzed by (-) ESI FT-ICR MS, combined to other analytical methods (<sup>1</sup>H NMR, FT-IR, and GC-MS). The C<sub>x</sub>H<sub>y</sub>O<sub>z</sub> and C<sub>x</sub>H<sub>y</sub>N<sub>1</sub>O<sub>3-16</sub> compounds were evidenced. However, the van Krevelen diagrams of the C<sub>x</sub>H<sub>y</sub>O<sub>z</sub> compound class achieved for the four bio-oil samples were different, which demonstrates that bio-oil fractionation by supercritical extraction facilitates the characterization of the bio-oil composition and gives insights at the molecular level.<sup>227</sup>

Liu *et al.* performed solvent fractionation according to the schematic diagram of the **Figure I-26**. Hexane-soluble (HS), ether-soluble (ES), ether-insoluble (EIS), dichloromethane-soluble (DS), and methanol-soluble (MeS) fractions were obtained. The bio-oil and its five subfractions

were characterized by (-) ESI FT-ICR MS and GC-MS.  $C_xH_yO_z$  and  $C_xH_yN_1O_{3-14}$  compounds were evidenced in all investigated samples. GC-MS ensures to observe the most volatile and/or the lightest components whereas ESI FT-ICR MS is more suited to the analysis of the less volatile and/or the heaviest compounds. Specific classes of compounds have been identified by both mass spectrometry approaches combined with solvent fractionation.<sup>263</sup>

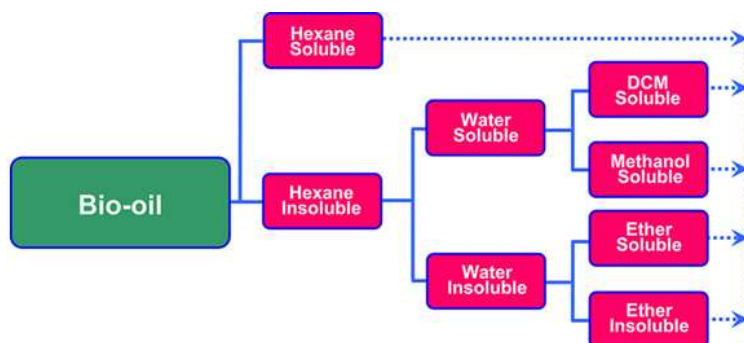


Figure I-26. Solvent fractionation process<sup>263</sup>

#### VII.B.5. Effect of the processing conditions on the bio-oil composition obtained by ESI HRMS

Yan *et al.* compared the chemical composition of two bio-oils obtained by the methanolysis and the ethanolysis of sweet sorghum stalk by ESI FT-ICR MS in negative and positive ion detection modes.<sup>286</sup> In negative ion mode,  $C_{5-35}H_yO_{1-10}$  and  $C_{7-35}H_yN_1O_{0-10}$  compounds were identified in both samples. The  $O_1-O_3$  species were more intensely detected in the bio-oil from ethanolysis than in the methanolysis one. The van Krevelen diagrams of the oxygenated compounds demonstrate that lipids (fatty acids), sugarc compounds, and lignin derivatives were detected in both bio-oils. The authors evidenced that lignin derived compounds were the main acidic species. In positive ion mode, basic nitrogen compounds were the main contributor to the mass spectrum. The  $C_{10-40}H_yN_2O_{1-6}$  compounds are predominant. These species were relative to amine, pyridine, and quinolone.

The same research group performed the methanolysis of cornstalk with different NaOH amounts, at different temperatures.<sup>287</sup> The solvent fractionation, according to the procedure described on the **Figure I-27**, was applied. Five fractions (SP<sub>1</sub>-SP<sub>5</sub>) and an inextractable portion (IEP) were obtained. The authors demonstrated that whatever the operating conditions (temperature and NaOH amount), the highest liquid amounts were obtained for the SP<sub>1</sub> and SP<sub>5</sub> fractions. Increasing the NaOH/cornstalk ratio and the temperature led to a significant

increase of the SP<sub>1</sub> amount. The same behavior was observed for the SP<sub>2</sub>, SP<sub>3</sub>, and SP<sub>4</sub> fractions, but in a lesser extent. The yield of the SP<sub>5</sub> fraction decreases with raising temperature but increases with increasing the NaOH/cornstalk ratio. Overall, the total yield increases with the increase of the temperature and the NaOH/cornstalk ratio. These 6 samples were analyzed by GC-MS whereas the chemical composition of SP<sub>1</sub>, SP<sub>2</sub>, and SP<sub>5</sub> fractions were assessed by (-) ESI FT-ICR MS. The results achieved by petroleomic approach ensured to identify C<sub>5-35</sub>H<sub>y</sub>O<sub>1-10</sub> and C<sub>10-30</sub>H<sub>y</sub>N<sub>1</sub>O<sub>0-8</sub> compounds in the three fractions. Some differences in terms of mass range and oxygen distribution were evidenced in respect with the investigated fraction.

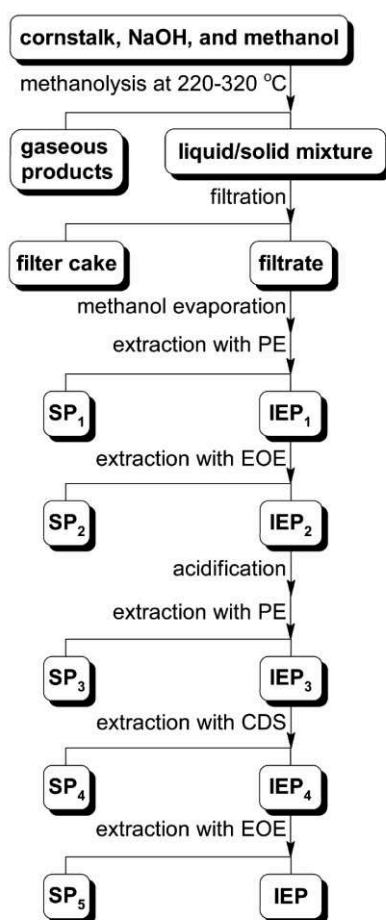


Figure I-27. Solvent fractionation procedure for cornstalk bio-oil obtained by methanolysis. PE=Petroleum ether, EOE=ethoxyethane, and CDS=carbon disulphide.

Kekäläinen *et al.* studied the influence of the pyrolysis temperature on birch wood bio-oils obtained at 300 °C and 380 °C. The O<sub>2</sub>-O<sub>4</sub> species were attributed to lipids (resin and fatty acids) whereas the O<sub>5</sub>-O<sub>7</sub> ones were relative to lignin-derived compounds. The most oxygen-

ated species were associated with cellulose and hemicellulose derivatives. However, the compounds obtained at 300 °C were more abundant and more oxygenated than at 380 °C. Sulfur hydrocarbons were also observed and assigned to sulfonic acids.<sup>288</sup>

#### VII.B.5.a. Studies performed on upgraded bio-oils

The bio-oils from the same feedstock produced by HTL, pyrolysis, and hydrotreated HTL were characterized by ESI FT-ICR MS in both detection modes in the work of Sudasinghe *et al.*<sup>235</sup> The pyrolysis process yielded more bio-oil than the HTL one. Moreover, the pyrolysis bio-oil contained a broader range of oxygenated and nitrogen compounds than the HTL one. For a given oxygen compound family, the bio-oil components are more unsaturated for the HTL oil than for the pyrolysis one. A Co/Mo catalyst was used to upgrade the HTL bio-oil. The resulting compounds contain lower oxygen and nitrogen amounts, which demonstrates the efficiency of this upgrading treatment.

Tessarolo *et al.* characterized pyrolysis bio-oils from pine wood and sugarcane bagasse by (-) ESI FT-ICR MS, <sup>1</sup>H NMR, and GCxGC-TOF-MS.<sup>289</sup> These authors investigated the effects of the pyrolysis temperature and the use of a catalyst (ZSM-5) on the produced bio-oil composition. They demonstrated that an increase of the temperature was responsible of a higher degradation rate of the biomass with poorly oxygenated detected compounds. The efficiency of the deoxygenation treatment was assessed by the removal of the highest oxygenated compounds and the increase of the less oxygenated ones. However, the temperature did not influence the effectiveness of the catalytic treatment. The authors also evidenced that ZSM-5 catalyst provided an increase of the phenolics due to the lignin decomposition.

The same analytical technics were used by Koike *et al.* who studied the efficiency of different deoxygenation catalysts (Ni<sub>2</sub>P/SiO<sub>2</sub>, Ni/SiO<sub>2</sub>, Pd/C, and ZSM-5) on the upgrading of a pyrolysis bio-oil at 300 and 350 °C. They observed that the activity of Ni<sub>2</sub>P/SiO<sub>2</sub> was superior to the other ones. Moreover, the lowest oxygen content in the bio-oil was obtained when the highest amount of catalyst was used at 350 °C.<sup>264</sup>

A similar study was performed by Bi *et al.* who assessed in what extent the applied temperature during HDO treatment may affect the chemical composition of bio-oils.<sup>238</sup> Thus, the chemical composition of the raw bio-oil was compared with those obtained after HDO treatment performed at five different temperatures. Oxygenated compounds were assigned in all samples and their distribution in respect with the oxygen atom count was narrower and

shifted to lower values when the temperature was increased. However, the distribution of the DBE values was not influenced by the reactor temperature. The van Krevelen diagrams obtained for this class of compounds evidenced some reactions occurring during the HDO treatment (**Figure I-28**). The authors demonstrated that HDO at 150 °C promotes the breakdown of the ether linkages. Between 210 and 300 °C, dehydration and hydrodeoxygenation occur. Other reactions such as decarboxylation and decarbonylation require a temperature higher than 360 °C.

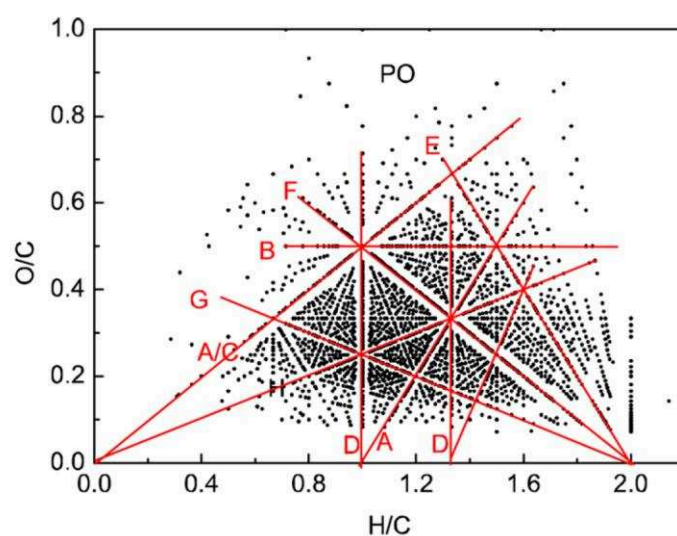


Figure I-28. van Krevelen diagram of  $C_xH_yO_z$  compounds assigned by (-) ESI FT-ICR MS analysis of the raw pyrolysis bio-oil. Red lines represent chemical reactions: methoxylation/demethoxylation (A), hydrogenation/dehydrogenation (B), hydration/dehydration (A/C), hydrodeoxygenation (D), decarboxylation (E), decarbonylation (F), and de-ethoxylation (G)<sup>238</sup>

#### VII.B.6. Influence of dopants in the ESI HRMS analyses

As it can be seen in the **Table I-10**, formic acid and ammonium hydroxide can be used to increase protonation and deprotonation for positive and negative ion ESI analyses, respectively.

Other dopants may be used to promote the ionization. Alsbou *et al.* used NaCl, NH<sub>4</sub>Cl, and formic acid to investigate bio-oils by (+) ESI-Ion-Trap-MS and NaOH and NH<sub>4</sub>Cl, for (-) ESI analysis. In respect with the sample preparation, the bio-oil components were detected as [M+H]<sup>+</sup>, [M+Na]<sup>+</sup> or [M+NH<sub>4</sub>]<sup>+</sup> and [M-H]<sup>-</sup> or [M+Cl]<sup>-</sup> pseudo-molecular ion in positive and negative detection modes, respectively.<sup>290</sup>

### VII.B.7. Conclusion

ESI is an effective and commonly used technique to characterize bio-oils. However it only ionizes the mid-polar to polar bio-oil components. To detect the less polar and apolar compounds, other ionization sources have to be employed. Typically, laser desorption ionization (LDI), atmospheric pressure photoionization (APPI), and atmospheric pressure chemical ionization (APCI) source are less sensitive to compound polarity than ESI. Moreover, these ionization techniques are well-suited to follow up the upgrading treatment by the efficient ionization of the less oxygenated and, consequently, the less polar compounds.

### VII.C. *Analyses of bio-oils by APPI, APCI, and LDI-HRMS as a complement to ESI-HRMS analyses*

**Table I-11.** gathers and compares the different still published works dealing with the analysis of bio-oil by LDI, APPI, and APCI.



Table I-11. Overview of the publications dealing with the analysis of bio-oils by APPI, APCI, and LDI-HRMS as complement to ESI-HRMS analyses

Reference	Process – Feedstock	Ion source	Solvent - Dopant	Chemical composition
<b>Analyses involving APPI-HRMS</b>				
Jarvis <i>et al.</i> <sup>292</sup>	HTL ▪ Pine ▪ Microalgae ▪ Sewage sludge	(-) ESI (+) ESI (+) APPI	MeOH TMAH (0.25 % v/v) HCCOH (1 % v/v) MeOH:Toluene (9:1)	<ul style="list-style-type: none"> <li>• More than 85 % of the assigned formula from the (+) ESI mass spectra are exclusive to HTL bio-oils against more than 43 % in negative ion mode.</li> <li>• On average, APPI ensured to assign more peaks (<math>\approx 10923</math>), than (+) ESI (<math>\approx 9906</math>) and (-) ESI (<math>\approx 1645</math>) in the HTL bio-oils. While, for the shale and crude oils, <math>\approx 3142</math>, <math>\approx 2366</math>, and <math>\approx 4225</math> peaks were assigned with (+) APPI, (+) ESI, and (-) ESI, respectively.</li> <li>• The oxygen-containing species range from 1 to 8 in the pine bio-oil, from 1 to 4 in the microalgae one, and from 1 to 5 in the sewage sludge bio-oil.</li> </ul>
Cole <i>et al.</i> <sup>293</sup>	Fast pyrolysis Switchgrass	(-) ESI (+) ESI (+) APPI	MeOH:H <sub>2</sub> O (1:1) MeOH:Toluene (85:15)	<ul style="list-style-type: none"> <li>• (-) ESI: C<sub>x</sub>H<sub>y</sub>O<sub>z</sub> compounds mainly (sugarc derivatives and acidic species) observed.</li> <li>• (+) ESI: C<sub>x</sub>H<sub>y</sub>NO<sub>z</sub> (95 %) and C<sub>x</sub>H<sub>y</sub>O<sub>z</sub> (5 %) compounds observed. N<sub>1</sub>O<sub>0-6</sub> (N<sub>1</sub>O<sub>1</sub>) - N<sub>2</sub>O<sub>0-3</sub> (N<sub>2</sub>) - N<sub>3</sub>O<sub>0-1</sub> - O<sub>1-6</sub> (O<sub>2-3</sub>) - NaO<sub>1-7</sub> (O<sub>3-4</sub>)</li> <li>• (+) APPI: C<sub>x</sub>H<sub>y</sub>O<sub>z</sub> (76 %) and C<sub>x</sub>H<sub>y</sub>NO<sub>z</sub> (24%) compounds observed. N<sub>1</sub>O<sub>0-3</sub> (N<sub>1</sub>O<sub>2</sub>) - N<sub>2</sub>O<sub>0-2</sub> (N<sub>2</sub>)</li> </ul>
Leonardis <i>et al.</i> <sup>294</sup>	HTL Organic solid wastes	(+) APPI	MeOH:Toluene (1:1)	<ul style="list-style-type: none"> <li>• 2091 assigned formulas.</li> <li>• In the N<sub>1-2</sub>, N<sub>1</sub>O<sub>1-2</sub>, and N<sub>2</sub>O<sub>1</sub> classes about 45 % of the carbon atoms are aliphatic and 55 % are aromatic. Inversed values were observed for the N<sub>2</sub>O<sub>2</sub> class.</li> </ul>
Croce <i>et al.</i> <sup>262</sup>	HTL ▪ Glucose ▪ Cellulose	(-) ESI (+) APPI	MeOH MeOH:Toluene (1:1)	The resulting bio-oil is composed by two different phases: an aqueous phase analyzed in (-) ESI and an organic one analyzed in (+) APPI.
Croce <i>et al.</i> <sup>295</sup>	HTL ▪ Cellulose ▪ BSA ▪ Tripalmitin	(+) APPI	MeOH MeOH:Toluene (1:1)	The resulting bio-oil is composed by an aqueous phase and an organic phase, both analyzed in (+) APPI.

Analyses involving APCI-HRMS					
Chiaberge <i>et al.</i> <sup>296</sup>	HTL	(+) ESI	MeOH		(+) ESI: N <sub>1-3</sub> (N <sub>2</sub> ) - N <sub>1-4</sub> O <sub>1</sub> (N <sub>1</sub> O <sub>1</sub> ) - N <sub>1-3</sub> O <sub>2</sub> (N <sub>2</sub> O <sub>2</sub> ) - N <sub>1-3</sub> O <sub>3</sub>
	Organic solid wastes	(+) APPI	MeOH:Toluene (1:1)	-	(+) APPI: CH, O <sub>1-2</sub> (O <sub>2</sub> ) - N <sub>1-3</sub> (N <sub>2</sub> ) - N <sub>1-4</sub> O <sub>1</sub> (N <sub>1</sub> O <sub>1</sub> ) - N <sub>1-3</sub> O <sub>2</sub> (N <sub>2</sub> O <sub>2</sub> ) - N <sub>1-3</sub> O <sub>3</sub>
		(+) APCI	MeOH		(+) APCI: CH, O <sub>1-2</sub> (O <sub>2</sub> ) - N <sub>1-3</sub> (N <sub>2</sub> ) - N <sub>1-4</sub> O <sub>1</sub> (N <sub>1</sub> O <sub>1</sub> ) - N <sub>1-3</sub> O <sub>2</sub> (N <sub>2</sub> O <sub>2</sub> ) - N <sub>1-3</sub> O <sub>3</sub>
Staš <i>et al.</i> <sup>297</sup>	Fast pyrolysis	(-) ESI	MeOH	-	Similar oxygen class distributions were obtained whatever the mass spectrometer and the ionization source. O <sub>1-12</sub> (O <sub>4</sub> )
	Wood	(-) APCI			
Sanguineti <i>et al.</i> <sup>298</sup>	HTL Microalgae	(+) APCI	Heptane	-	HHV of the HTL bio-oils average between 35 and 39 MJ/kg which makes them heavy crude-like bio-oil.
Analyses involving LDI-HRMS					
Smith <i>et al.</i> <sup>299</sup>	Fast pyrolysis	(-) LDI (337.7 nm)	Sample dissolved in methanol, 2-propanol, and ACN	-	O <sub>3-8</sub> (O <sub>4</sub> ) O <sub>3-7</sub> (O <sub>4</sub> ) – 136 assigned chemical formulas. Lignin derivatives.
	<ul style="list-style-type: none"> <li>▪ Hydrolytic lignin</li> <li>▪ Pine</li> </ul>				
Olcese <i>et al.</i> <sup>258</sup>	Fast pyrolysis Lignin	(-) ESI (-) LDI 355 nm	MeOH	-	(-) ESI O <sub>2-8</sub> (O <sub>4</sub> ) (-) LDI Raw BO: O <sub>2-8</sub> (O <sub>4</sub> ) With 2 g of catalyst: O <sub>1-6</sub> (O <sub>3</sub> ) With 4 g of catalyst: O <sub>1-5</sub> (O <sub>3</sub> )

The HTL bio-oils from three different feedstocks were characterized by (+/-) ESI and (+) APPI FT-ICR MS. The results were combined and compared to what it was obtained in the study of crude petroleum and shale oils.<sup>292</sup> The heteroatom class distributions obtained by Jarvis *et al.* are reported in **Figure I-29**. They evidenced that HTL bio-oils were compositionally more similar to the shale oil than to the petroleum crude oil. Nevertheless, the HTL bio-oil mainly contains oxygenated compounds whereas crude and shale oils are essentially mixtures of hydrocarbons and nitrogen species.<sup>292</sup>

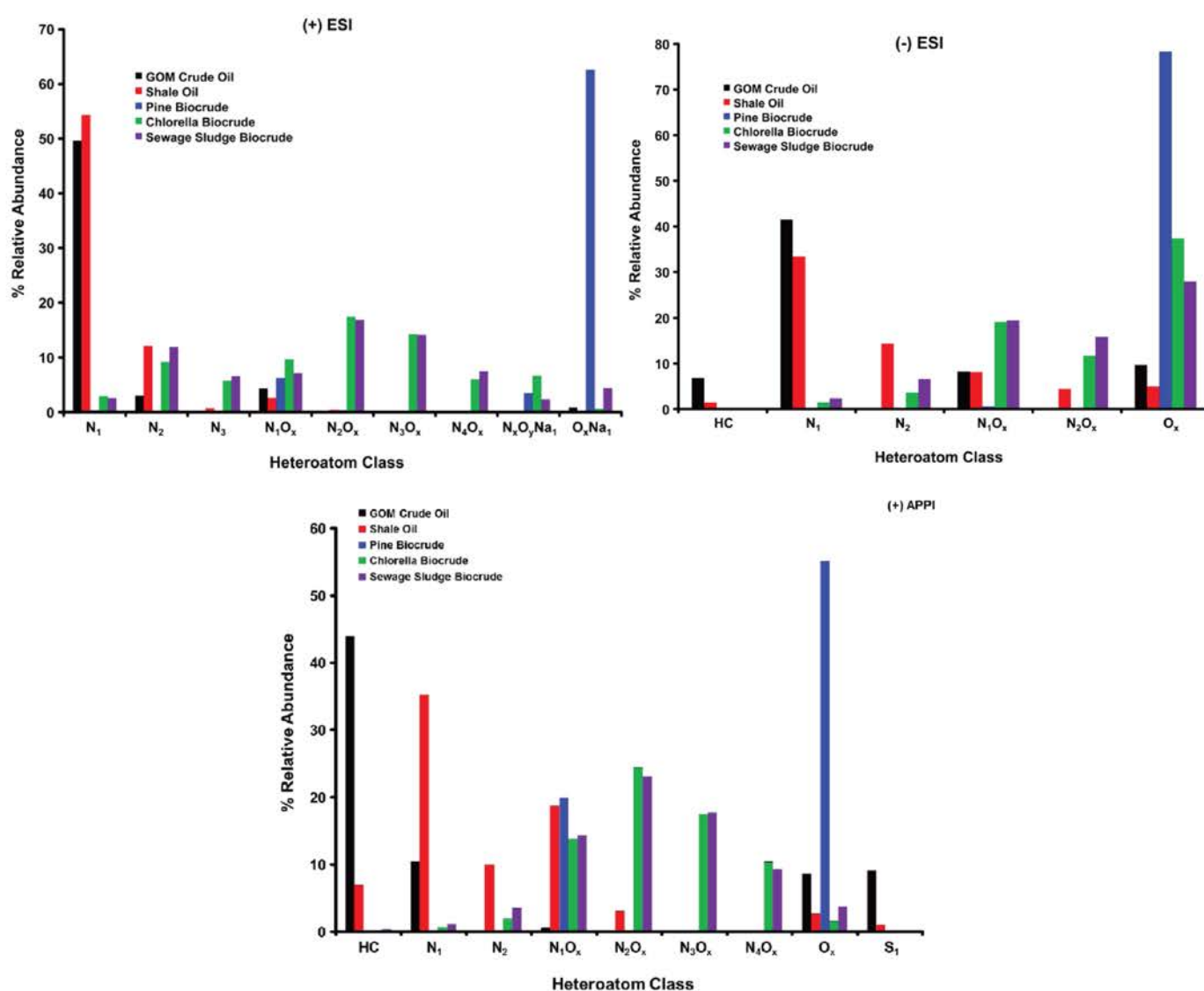


Figure I-29. Heteroatom class distributions derived from the (+) ESI (top left), (-) ESI (top right), and (+) APPI (bottom) mass spectra in respect with the different samples<sup>292</sup>

Cole *et al.* characterized the pyrolysis bio-oils of switchgrass harvested on June, July, August, and November 2010, and April 2011.<sup>293</sup> The bio-oils were analyzed in positive and negative ion modes by ESI Orbitrap-MS and in positive ion mode by APPI Orbitrap-MS. In (+) ESI, a broad variety of nitrogen compounds have been observed whose amount is in agreement with the elemental composition of the used feedstock. The  $C_xH_yN_z$  compounds were efficiently protonated according to their basicity and represent 95 % of the TIC. The remaining contribution was due to oxygenated compounds detected as proton and sodium adduct ions. From June to April, the relative abundance of all nitrogen compounds decreased whereas those of the oxygenated species increased. In (+) APPI, the nitrogen species only represent 24 % of the TIC. Finally, this study demonstrates the compositional change, concerning the abundances of the nitrogen and oxygenated species in respect with the harvest time.

Leonardis *et al.* characterized a HTL bio-oil from organic wastes. Such a bio-oil was investigated by FT-ICR MS,  $^1H$  and  $^{13}C$  NMR, and GC-MS to develop a quantitation method of the different heteroatom bio-oil class of compounds. The measurement performed by (+) APPI FT-ICR MS ensured to “quantify” pure hydrocarbons,  $N_{1-3}$ ,  $N_{0-4}O_1$ ,  $N_{0-3}O_2$ , and  $N_{1-3}O_3$  classes, as shown in the **Figure I-30**.<sup>294</sup>

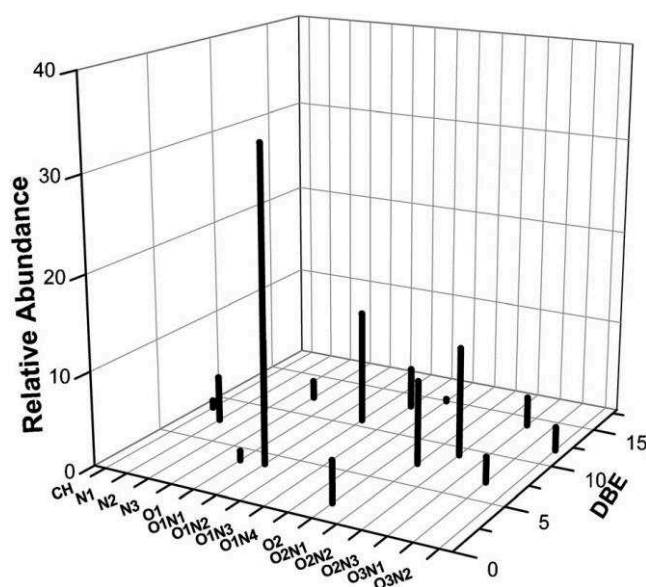


Figure I-30. Relative abundances in respect with the DBE value of the compound classes identified in bio-oil by (+) APPI FT-ICR MS<sup>294</sup>

Croce *et al.* used a similar approach to study and model the HTL process of cellulose and glucose. More specifically, the authors investigated the decomposition of these carbohydrates under HTL. They demonstrated that polymerization, dehydration, and decarboxylation

reactions occurred.<sup>262</sup> They recently extended this model to other compounds of bio-oil produced by HTL of organic wastes.<sup>295</sup> Proteins (with bovine serum albumin *BSA*), lipids (with tri-palmitin), and cellulose were used as model compounds. The achieved molecular composition is very similar to the HTL bio-oil one obtained by Leonardis *et al.* with solid organic wastes.<sup>294</sup>

Chiaberge *et al.* investigated a bio-oil produced by HTL of organic solid wastes by ESI, APPI, and APCI FT-ICR MS, in positive ion mode.<sup>296</sup> The results obtained in APCI and APPI were found to be very similar. Indeed, among the 2356 and 2247 formulae assigned in APCI and APPI, respectively, 598 are common to both analyses. More than 2000 features were observed in ESI, only a tiny fraction of them were also observed by APPI (41) or APCI (210). ESI was found to be more sensitive to the most polar components of the bio-oil which are characterized by a higher N/C ratio.

A bio-oil from wood pyrolysis was characterized by ESI and APCI-Orbitrap-MS in negative ion detection mode in the work of Staš *et al.*<sup>297</sup> The capabilities of different generations of Orbitrap mass spectrometers were evaluated in this study. Whatever the ionization source and the instrument, O<sub>1</sub> to O<sub>12</sub> species were observed. The maximum of their distributions in respect with the oxygen atom count was always the O<sub>4</sub> compounds. However, some differences have been highlighted according to the resolution power of the different instruments and the used ionization source. In ESI, O<sub>2</sub> and O<sub>3</sub> compounds are more intensely detected with the most powerful instrument (R 240 000 and 480 000). In contrast, the relative abundance of the oxygen-rich assignment is more important with the less powerful device (R 30 000 and 100 000). A similar trend is observed with the DBE distribution in ESI. With low mass resolution instrument, the relative abundance of the low unsaturated compounds is more important than with the high mass resolution device. In APPI, the different distributions did not reveal significant differences whatever the mass spectrometer. Furthermore, for both ionization sources, an increasing number of assigned molecular formulae was reached with the increase of the mass resolution. This demonstrates the necessity of the most powerful mass spectrometer.

Sanguinetti *et al.* performed (+) APCI FT-ICR MS analyses of HTL bio-oils from algae to evaluate the influence of the temperature (250 °C or 300 °C) and the nature of the medium (distilled water or saltwater) on the composition of the produced bio-oil.<sup>298</sup> Among the thousand identified compounds, N<sub>1</sub>O<sub>1</sub>, CH, and O<sub>2</sub> classes represented the most abundant com-

pounds whatever the used process conditions. The authors demonstrated that a higher temperature was responsible of a greater number of conversion compounds. In contrast, a lower number of compounds was obtained when saltwater was added. At 300 °C with saltwater, the abundance of the N<sub>1</sub>O<sub>1</sub> class was definitely lower than with other operation conditions.

LDI may also be used to study bio-oil. For example, Smith *et al.* used LDI to characterize hydrolytic lignin and a bio-oil from pine pyrolysis by Orbitrap-MS.<sup>299</sup> The authors investigated the influence of several matrixes for MALDI analysis. A slight improvement of the signal was achieved when colloidal graphite was used but graphite significantly contributed to the background. For the other evaluated matrixes, no significant differences were observed in comparison with LDI experiments. A same behavior was observed for oxygenated compounds. The DBE distribution in respect with the oxygen atom count demonstrates that the O<sub>4</sub> compounds are less unsaturated than the O<sub>6</sub> species. In fact, they assessed that these O<sub>4</sub> and O<sub>6</sub> compounds correspond to dimer and trimer units of lignin depolymerization, respectively. This study demonstrated that LDI is well-suited for the characterization of non-volatile aromatic compounds.

The combination of negative ion ESI and LDI FT-ICR MS analyses was done by Olcese *et al.* to monitor the effectiveness of a catalytic hydrotreatment on a bio-oil produced by lignin pyrolysis.<sup>258</sup> Indeed, the polarity of bio-oil decreases after upgrading, which makes ESI less adapted to characterize the treated bio-oil. In contrast, LDI is less sensitive to the compound polarity. When experiments were performed on the raw bio-oil, the distributions of the oxygenated compounds in respect with the oxygen atom count were similar for both ionization sources (**Figure I-31**). Significant differences were observed for the distributions of these oxygenated compounds in respect with the DBE value (**Figure I-31**). LDI enables to detect more unsaturated compounds than ESI. The van Krevelen diagrams confirmed these observations with compounds of lower O/C and H/C ratios, more intensely detected by LDI. Compounds with a lower amount of oxygen were observed after bio-oil upgrading treatment, especially by LDI FT-ICR MS. Consequently, LDI was used to more specifically investigate the influence of the catalytic treatment. The abundances of the poor-oxygen compounds were more important when larger amount of catalyst was used. The authors also demonstrated the limitations of the catalytic treatment and the occurrence of some oxygenated compounds that were catalysis refractory.

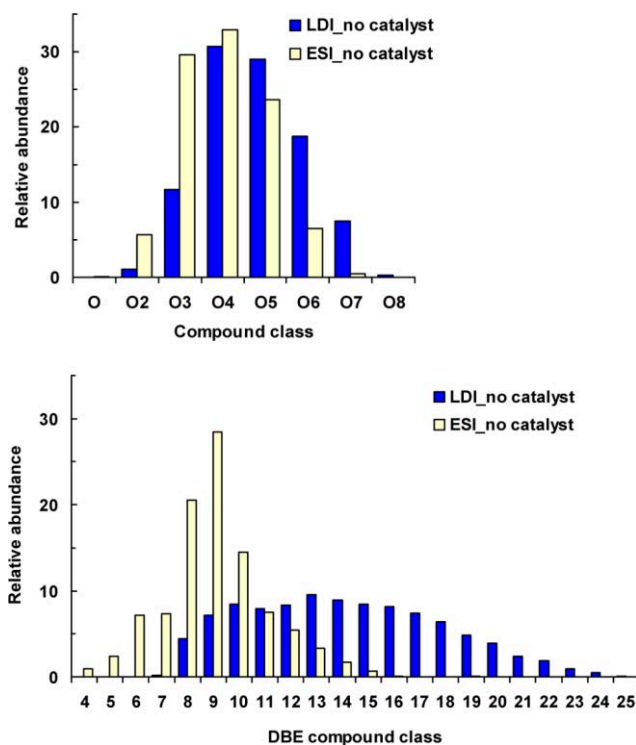


Figure I-31. Oxygen (top) and DBE (bottom) distributions for the  $C_xH_yO_z$  compounds of the raw lignin pyrolysis bio-oil analyzed in ESI and LDI FT-ICR MS in negative ion mode <sup>258</sup>

#### VII.D. Conclusion on the HRMS analyses

Regarding the different studies performed by HRMS on bio-oils, most of the experiments were conducted by ESI, and more specifically in negative ion mode (**Table I-10** and **Table I-11**).<sup>268</sup> In fact, the bio-oil components have the ability to intensely yield negative ions. For this reason, (-) ESI appears to be more efficient and sensitive than (+) ESI.<sup>263,278,284</sup> Typically, the bio-oils are characterized without pretreatment, apart from dilution in appropriate solvents. The addition of deprotonation and protonation agents can also be carried out to improve ionization. It is well known that ESI is more sensitive to polar compounds which represent only a part of the bio-oil components. Therefore, ionization sources that are less sensitive to the compound polarity such as APPI, LDI, and APCI have to be employed to achieve an extensive description of bio-oils.

The petroleomic approach is suitable to obtain the chemical signature and the global composition of the bio-oil by assignment of thousands of compounds. Such analyses ensure to observe compositional changes depending on the feedstock and the parameters of the thermochemical process (nature of the medium, temperature...). It is also a very useful tool for

monitoring the efficiency of an upgrading treatment such as the catalytic cracking and the deoxygenation.

Even if HRMS analyses enable to detect and assign thousands of species, they have some limitations. Indeed, volatile and low-mass compounds are not analyzed and no structural information is achieved. Moreover, quantitation of the different species or classes of compounds cannot be achieved. The isomers are not distinguished by this method.

## VIII. Conclusion

The valorization of the biomass into second generation biofuels and value-added chemicals can be performed by means of different thermochemical processes. First, the conversion of the solid biomass into a liquid bio-oil can be achieved by liquefaction or pyrolysis. Due to its composition, the bio-oil has to be upgraded by various pathways to obtain fuels or chemicals. Some of the valorization routes are already integrated to petroleum refineries which will require a smaller financial investment for the biofuel development.

However, the proper exploitation of a bio-oil needs its exhaustive composition to be known. The high complexity of this material makes its detailed description still impossible as no universal characterization technique exists. Indeed, each used analytical method has its own specificity. FT-IR and NMR techniques are dedicated to the quantitation and qualification of different functional groups. The chromatographic methods are used to quantify and identify some classes of compounds according to their polarity or volatility. Additionally, structural information can be obtained with these techniques when they are coupled to MS<sup>n</sup>. HRMS analyses are also performed to characterize compounds on a broader mass range and a molecular information to be obtained by means of the so-called petroleomic approach.

Detailed bio-oil characterization can be seen as a puzzle in which each piece is given by a specific analytical method.



## IX. References

1. Huber, G. W., Iborra, S. & Corma, A. Synthesis of Transportation Fuels from Biomass: Chemistry, Catalysts, and Engineering. *Chem. Rev.* **106**, 4044–4098 (2006).
2. Ma, F. R. & Hanna, M. A. Biodiesel production: a review. *Bioresour. Technol.* **70**, 1–15 (1999).
3. Delrue, F., Li-Beisson, Y., Setier, P.-A., Sahut, C., Roubaud, A., Froment, A.-K. & Peltier, G. Comparison of various microalgae liquid biofuel production pathways based on energetic, economic and environmental criteria. *Bioresour. Technol.* **136**, 205–212 (2013).
4. Devarapalli, M. & Atiyeh, H. K. A review of conversion processes for bioethanol production with a focus on syngas fermentation. *Biofuel Res. J.-Brj* **2**, 268–280 (2015).
5. Alper, K., Tekin, K. & Karagöz, S. Pyrolysis of agricultural residues for bio-oil production. *Clean Technol. Environ. Policy* **17**, 211–223 (2015).
6. Maki-Arvela, P., Simakova, I. L., Salmi, T. & Murzin, D. Y. Production of Lactic Acid/Lactates from Biomass and Their Catalytic Transformations to Commodities. *Chem. Rev.* **114**, 1909–1971 (2014).
7. Chang, C.-C., Green, S. K., Williams, C. L., Dauenhauer, P. J. & Fan, W. Ultra-selective cycloaddition of dimethylfuran for renewable p-xylene with H-BEA. *Green Chem.* **16**, 585–588 (2014).
8. Eerhart, A. J. J. E., Faaij, A. P. C. & Patel, M. K. Replacing fossil based PET with biobased PEF; process analysis, energy and GHG balance. *Energy Environ. Sci.* **5**, 6407–6422 (2012).
9. Sheldon, R. A. Green and sustainable manufacture of chemicals from biomass: state of the art. *Green Chem.* **16**, 950–963 (2014).
10. Johnson, E. Goodbye to carbon neutral: Getting biomass footprints right. *Environ. Impact Assess. Rev.* **29**, 165–168 (2009).
11. Heyne, S. & Harvey, S. Assessment of the energy and economic performance of second generation biofuel production processes using energy market scenarios. *Appl. Energy* **101**, 203–212 (2013).
12. Alonso, D. M., Bond, J. Q. & Dumesic, J. A. Catalytic conversion of biomass to biofuels. *Green Chem.* **12**, 1493–1513 (2010).
13. Demirbas, A. Calculation of higher heating values of biomass fuels. *Fuel* **76**, 431–434 (1997).
14. Klemm, D., Heublein, B., Fink, H.-P. & Bohn, A. Cellulose: fascinating biopolymer and sustainable raw material. *Angew. Chem. Int. Ed Engl.* **44**, 3358–3393 (2005).
15. Hsu, T., Ladisch, M. & Tsao, G. Alcohol from Cellulose. *Chemtech* **10**, 315–319 (1980).
16. H. Isikgor, F. & Remzi Becer, C. Lignocellulosic biomass: a sustainable platform for the production of bio-based chemicals and polymers. *Polym. Chem.* **6**, 4497–4559 (2015).
17. Scheller, H. V. & Ulvskov, P. Hemicelluloses. *Annu. Rev. Plant Biol. Vol 61* **61**, 263–289 (2010).

18. Wettstein, S. G., Alonso, D. M., Guerbuez, E. I. & Dumesic, J. A. A roadmap for conversion of lignocellulosic biomass to chemicals and fuels. *Curr. Opin. Chem. Eng.* **1**, 218–224 (2012).
19. Cherubini, F. The biorefinery concept: Using biomass instead of oil for producing energy and chemicals. *Energy Convers. Manag.* **51**, 1412–1421 (2010).
20. Chakar, F. S. & Ragauskas, A. J. Review of current and future softwood kraft lignin process chemistry. *Ind. Crops Prod.* **20**, 131–141 (2004).
21. Evans, R., Milne, T. & Soltys, M. Direct Mass-Spectrometric Studies of the Pyrolysis of Carbonaceous Fuels .3. Primary Pyrolysis of Lignin. *J. Anal. Appl. Pyrolysis* **9**, 207–236 (1986).
22. Barakat, A., de Vries, H. & Rouau, X. Dry fractionation process as an important step in current and future lignocellulose biorefineries: A review. *Bioresour. Technol.* **134**, 362–373 (2013).
23. Ragauskas, A. J., Beckham, G. T., Bidy, M. J., Chandra, R., Chen, F., Davis, M. F., Davison, B. H., Dixon, R. A., Gilna, P., Keller, M., Langan, P., Naskar, A. K., Saddler, J. N., Tschaplinski, T. J., Tuskan, G. A. & Wyman, C. E. Lignin Valorization: Improving Lignin Processing in the Biorefinery. *Science* **344**, 709–+ (2014).
24. Erickson, D. R. *Practical Handbook of Soybean Processing and Utilization*. (Elsevier, 2015).
25. Santori, G., Di Nicola, G., Moglie, M. & Polonara, F. A review analyzing the industrial biodiesel production practice starting from vegetable oil refining. *Appl. Energy* **92**, 109–132 (2012).
26. Thomas, A., Mueller, S. S. & Frey, H. Beyond Poly(ethylene glycol): Linear Polyglycerol as a Multifunctional Polyether for Biomedical and Pharmaceutical Applications. *Biomacromolecules* **15**, 1935–1954 (2014).
27. Zhu, C., Chiu, S., Nakas, J. P. & Nomura, C. T. Bioplastics from waste glycerol derived from biodiesel industry. *J. Appl. Polym. Sci.* **130**, 1–13 (2013).
28. Pagliaro, M., Ciriminna, R., Kimura, H., Rossi, M. & Della Pina, C. From glycerol to value-added products. *Angew. Chem.-Int. Ed.* **46**, 4434–4440 (2007).
29. Behr, A., Eilting, J., Irawadi, K., Leschinski, J. & Lindner, F. Improved utilisation of renewable resources: New important derivatives of glycerol. *Green Chem.* **10**, 13–30 (2008).
30. Buchanan, R., Cull, I., Otey, F. & Russell, C. Hydrocarbon-Producing and Rubber-Producing Crops - Evaluation of United-States Plant Species. *Econ. Bot.* **32**, 131–145 (1978).
31. Buchanan, R., Cull, I., Otey, F. & Russell, C. Hydrocarbon-Producing and Rubber-Producing Crops - Evaluation of 100 United-States Plant Species. *Econ. Bot.* **32**, 146–153 (1978).
32. Sanders, J., Scott, E., Weusthuis, R. & Mooibroek, H. Bio-refinery as the bio-inspired process to bulk chemicals. *Macromol. Biosci.* **7**, 105–117 (2007).
33. Scott, E., Peter, F. & Sanders, J. Biomass in the manufacture of industrial products - the use of proteins and amino acids. *Appl. Microbiol. Biotechnol.* **75**, 751–762 (2007).
34. Lammens, T. M., Franssen, M. C. R., Scott, E. L. & Sanders, J. P. M. Availability of protein-derived amino acids as feedstock for the production of bio-based chemicals. *Biomass Bioenergy* **44**, 168–181 (2012).

35. Lammens, T. M., Le Notre, J., Franssen, M. C. R., Scott, E. L. & Sanders, J. P. M. Synthesis of Biobased Succinonitrile from Glutamic Acid and Glutamine. *Chemsuschem* **4**, 785–791 (2011).
36. Thy, P., Yu, C., Jenkins, B. M. & Lesher, C. E. Inorganic Composition and Environmental Impact of Biomass Feedstock. *Energy Fuels* **27**, 3969–3987 (2013).
37. Industry Statistics. *Renew. Fuels Assoc.* (2015). at <<http://www.ethanolrfa.org/resources/industry/statistics/>>
38. Sanchez, O. J. & Cardona, C. A. Trends in biotechnological production of fuel ethanol from different feedstocks. *Bioresour. Technol.* **99**, 5270–5295 (2008).
39. Naik, S. N., Goud, V. V., Rout, P. K. & Dalai, A. K. Production of first and second generation biofuels: A comprehensive review. *Renew. Sustain. Energy Rev.* **14**, 578–597 (2010).
40. Waclawovsky, A. J., Sato, P. M., Lembke, C. G., Moore, P. H. & Souza, G. M. Sugarcane for bioenergy production: an assessment of yield and regulation of sucrose content. *Plant Biotechnol. J.* **8**, 263–276 (2010).
41. Panella, L. Sugar Beet as an Energy Crop. *Sugar Tech* **12**, 288–293 (2010).
42. Claassen, P. a. M., van Lier, J. B., Contreras, A. M. L., van Niel, E. W. J., Sijtsma, L., Stams, A. J. M., de Vries, S. S. & Weusthuis, R. A. Utilisation of biomass for the supply of energy carriers. *Appl. Microbiol. Biotechnol.* **52**, 741–755 (1999).
43. Cardona, C. A., Quintero, J. A. & Paz, I. C. Production of bioethanol from sugarcane bagasse: Status and perspectives. *Bioresour. Technol.* **101**, 4754–4766 (2010).
44. Apar, D. K. & Ozbek, B. alpha-amylase inactivation during corn starch hydrolysis process. *Process Biochem.* **39**, 1877–1892 (2004).
45. Robertson, G. H., Wong, D. W. S., Lee, C. C., Wagschal, K., Smith, M. R. & Orts, W. J. Native or raw starch digestion: a key step in energy efficient biorefining of grain. *J. Agric. Food Chem.* **54**, 353–365 (2006).
46. Soni, S. K., Kaur, A. & Gupta, J. K. A solid state fermentation based bacterial  $\alpha$ -amylase and fungal glucoamylase system and its suitability for the hydrolysis of wheat starch. *Process Biochem.* **39**, 185–192 (2003).
47. Pandey, A., Soccol, C. R. & Mitchell, D. New developments in solid state fermentation: I- bioprocesses and products. *Process Biochem.* **35**, 1153–1169 (2000).
48. de Menezes, E. W. & Cataluña, R. Optimization of the ETBE (ethyl tert-butyl ether) production process. *Fuel Process. Technol.* **89**, 1148–1152 (2008).
49. Croezen, H. & Kampman, B. The impact of ethanol and ETBE blending on refinery operations and GHG-emissions. *Energy Policy* **37**, 5226–5238 (2009).
50. Bozbas, K. Biodiesel as an alternative motor fuel: Production and policies in the European Union. *Renew. Sustain. Energy Rev.* **12**, 542–552 (2008).
51. Demirbas, A. Biodiesel production from vegetable oils via catalytic and non-catalytic supercritical methanol transesterification methods. *Prog. Energy Combust. Sci.* **31**, 466–487 (2005).
52. Sonntag, N. Esterification and Interesterification. *J. Am. Oil Chem. Soc.* **56**, A751–A754 (1979).

53. Schwab, A., Bagby, M. & Freedman, B. Preparation and Properties of Diesel Fuels from Vegetable-Oils. *Fuel* **66**, 1372–1378 (1987).
54. Freedman, B., Butterfield, R. & Pryde, E. Transesterification Kinetics of Soybean Oil. *J. Am. Oil Chem. Soc.* **63**, 1375–1380 (1986).
55. Freedman, B., Pryde, E. & Mounts, T. Variables Affecting the Yields of Fatty Esters from Transesterified Vegetable-Oils. *J. Am. Oil Chem. Soc.* **61**, 1638–1643 (1984).
56. Ma, F., Clements, L. D. & Hanna, M. A. The effects of catalyst, free fatty acids, and water on transesterification of beef tallow. *Trans. Asae* **41**, 1261–1264 (1998).
57. Sprules, F. J. & Price, D. Production of fatty esters. US Patent 2. US 2494366 A. (1950). at <<https://www.google.com/patents/US2494366>>
58. Wright, H. J., Segur, J. B., Clark, H. V., Coburn, S. K., Langdon, E. E. & DuPuis, R. N. A report on ester interchange. *Oil Soap* **21**, 145–148 (1944).
59. Bradshaw, G. B. & Meuly, W. C. Preparation of detergents. US Patent 2. US 2360844 A. (1944). at <<https://www.google.com/patents/US2360844>>
60. Smith, M. K. Process of producing esters. US Patent 2. US 2486444 A. (1949). at <<https://www.google.com/patents/US2486444>>
61. Lopez, D. E., Goodwin, J. G., Bruce, D. A. & Lotero, E. Transesterification of triacetin with methanol on solid acid and base catalysts. *Appl. Catal. -Gen.* **295**, 97–105 (2005).
62. Kim, H. J., Kang, B. S., Kim, M. J., Park, Y. M., Kim, D. K., Lee, J. S. & Lee, K. Y. Transesterification of vegetable oil to biodiesel using heterogeneous base catalyst. *Catal. Today* **93–5**, 315–320 (2004).
63. Cantrell, D. G., Gillie, L. J., Lee, A. F. & Wilson, K. Structure-reactivity correlations in MgAl hydrotalcite catalysts for biodiesel synthesis. *Appl. Catal. -Gen.* **287**, 183–190 (2005).
64. Borges, M. E. & Diaz, L. Recent developments on heterogeneous catalysts for biodiesel production by oil esterification and transesterification reactions: A review. *Renew. Sustain. Energy Rev.* **16**, 2839–2849 (2012).
65. Kulkarni, M. G., Gopinath, R., Meher, L. C. & Dalai, A. K. Solid acid catalyzed biodiesel production by simultaneous esterification and transesterification. *Green Chem.* **8**, 1056–1062 (2006).
66. Mohr, A. & Raman, S. Lessons from first generation biofuels and implications for the sustainability appraisal of second generation biofuels. *Energy Policy* **63**, 114–122 (2013).
67. Dutta, K., Daverey, A. & Lin, J.-G. Evolution retrospective for alternative fuels: First to fourth generation. *Renew. Energy* **69**, 114–122 (2014).
68. Chen, W.-H., Lin, B.-J., Huang, M.-Y. & Chang, J.-S. Thermochemical conversion of microalgal biomass into biofuels: A review. *Bioresour. Technol.* **184**, 314–327 (2015).
69. Brown, L. & Zeiler, K. Aquatic Biomass and Carbon-Dioxide Trapping. *Energy Convers. Manag.* **34**, 1005–1013 (1993).
70. Chen, W.-H., Wu, Z.-Y. & Chang, J.-S. Isothermal and non-isothermal torrefaction characteristics and kinetics of microalga *Scenedesmus obliquus* CNW-N. *Bioresour. Technol.* **155**, 245–251 (2014).

71. Mata, T. M., Martins, A. A. & Caetano, N. S. Microalgae for biodiesel production and other applications: A review. *Renew. Sustain. Energy Rev.* **14**, 217–232 (2010).
72. Jambo, S. A., Abdulla, R., Mohd Azhar, S. H., Marbawi, H., Gansau, J. A. & Ravindra, P. A review on third generation bioethanol feedstock. *Renew. Sustain. Energy Rev.* **65**, 756–769 (2016).
73. Vera, J., Castro, J., Gonzalez, A. & Moenne, A. Seaweed Polysaccharides and Derived Oligosaccharides Stimulate Defense Responses and Protection Against Pathogens in Plants. *Mar. Drugs* **9**, 2514–2525 (2011).
74. Meinita, M. D. N., Kang, J.-Y., Jeong, G.-T., Koo, H. M., Park, S. M. & Hong, Y.-K. Bioethanol production from the acid hydrolysate of the carrageenophyte *Kappaphycus alvarezii* (cottonii). *J. Appl. Phycol.* **24**, 857–862 (2012).
75. Abd-Rahim, F., Wasoh, H., Zakaria, M. R., Ariff, A., Kapri, R., Ramli, N. & Siew-Ling, L. Production of high yield sugars from *Kappaphycus alvarezii* using combined methods of chemical and enzymatic hydrolysis. *Food Hydrocoll.* **42**, 309–315 (2014).
76. Demain, A. L., Newcomb, M. & Wu, J. H. D. Cellulase, clostridia, and ethanol. *Microbiol. Mol. Biol. Rev.* **69**, 124–+ (2005).
77. Wei, N., Quarterman, J. & Jin, Y.-S. Marine macroalgae: an untapped resource for producing fuels and chemicals. *Trends Biotechnol.* **31**, 70–77 (2013).
78. Karaosmanoglu, F., Tetik, E. & Gollu, E. Biofuel production using slow pyrolysis of the straw and stalk of the rapeseed plant. *Fuel Process. Technol.* **59**, 1–12 (1999).
79. Chandra, R., Takeuchi, H. & Hasegawa, T. Methane production from lignocellulosic agricultural crop wastes: A review in context to second generation of biofuel production. *Renew. Sustain. Energy Rev.* **16**, 1462–1476 (2012).
80. Glithero, N. J., Wilson, P. & Ramsden, S. J. Straw use and availability for second generation biofuels in England. *Biomass Bioenergy* **55**, 311–321 (2013).
81. Pankin, K. E. Estimated Heats of Combustion of Biofuels Based on Wood and Wood-Waste Pyrolysis Products. *Chem. Technol. Fuels Oils* **52**, 396–401 (2016).
82. Cambero, C., Sowlati, T., Marinescu, M. & Roeser, D. Strategic optimization of forest residues to bioenergy and biofuel supply chain. *Int. J. Energy Res.* **39**, 439–452 (2015).
83. Sannigrahi, P., Ragauskas, A. J. & Tuskan, G. A. Poplar as a feedstock for biofuels: A review of compositional characteristics. *Biofuels Bioprod. Biorefining-Biofpr* **4**, 209–226 (2010).
84. Brosse, N., Dufour, A., Meng, X., Sun, Q. & Ragauskas, A. Miscanthus: a fast-growing crop for biofuels and chemicals production. *Biofuels Bioprod. Biorefining-Biofpr* **6**, 580–598 (2012).
85. Xu, J., Wang, Z. & Cheng, J. J. Bermuda grass as feedstock for biofuel production: A review. *Bioresour. Technol.* **102**, 7613–7620 (2011).
86. van der Horst, D. & Vermeulen, S. Spatial scale and social impacts of biofuel production. *Biomass Bioenergy* **35**, 2435–2443 (2011).
87. Iqbal, M., Bermond, A. & Lamy, I. Impact of miscanthus cultivation on trace metal availability in contaminated agricultural soils: Complementary insights from kinetic extraction and physical fractionation. *Chemosphere* **91**, 287–294 (2013).

88. Techer, D., Martinez-Chois, C., Laval-Gilly, P., Henry, S., Bennasroune, A., D’Innocenzo, M. & Falla, J. Assessment of *Miscanthus x giganteus* for rhizoremediation of long term PAH contaminated soils. *Appl. Soil Ecol.* **62**, 42–49 (2012).
89. Serrano-Ruiz, J. C. & Dumesic, J. A. Catalytic routes for the conversion of biomass into liquid hydrocarbon transportation fuels. *Energy Environ. Sci.* **4**, 83–99 (2010).
90. Hamelinck, C. N., van Hooijdonk, G. & Faaij, A. P. C. Ethanol from lignocellulosic biomass: techno-economic performance in short-, middle- and long-term. *Biomass Bioenergy* **28**, 384–410 (2005).
91. Kabel, M. A., Bos, G., Zeevalking, J., Voragen, A. G. J. & Schols, H. A. Effect of pretreatment severity on xylan solubility and enzymatic breakdown of the remaining cellulose from wheat straw. *Bioresour. Technol.* **98**, 2034–2042 (2007).
92. Zhu, J. Y. & Pan, X. J. Woody biomass pretreatment for cellulosic ethanol production: Technology and energy consumption evaluation. *Bioresour. Technol.* **101**, 4992–5002 (2010).
93. Leibbrandt, N. H., Aboyade, A. O., Knoetze, J. H. & Görgens, J. F. Process efficiency of biofuel production via gasification and Fischer–Tropsch synthesis. *Fuel* **109**, 484–492 (2013).
94. Luque, R., Osa, A. R. de la, Campelo, J. M., Romero, A. A., Valverde, J. L. & Sanchez, P. Design and development of catalysts for Biomass-To-Liquid-Fischer–Tropsch (BTL-FT) processes for biofuels production. *Energy Environ. Sci.* **5**, 5186–5202 (2012).
95. Balat, M. Mechanisms of thermochemical biomass conversion processes. Part 2: Reactions of gasification. *Energy Sources Part -Recovery Util. Environ. Eff.* **30**, 636–648 (2008).
96. Torres, W., Pansare, S. S. & Goodwin, J. G. Hot gas removal of tars, ammonia, and hydrogen sulfide from Biomass gasification gas. *Catal. Rev.-Sci. Eng.* **49**, 407–456 (2007).
97. Mohan, D., Pittman, Charles U. & Steele, P. H. Pyrolysis of Wood/Biomass for Bio-oil: A Critical Review. *Energy Fuels* **20**, 848–889 (2006).
98. Shafizadeh, F. Introduction to Pyrolysis of Biomass. *J. Anal. Appl. Pyrolysis* **3**, 283–305 (1982).
99. Demirbas, A. Pyrolysis of ground beech wood in irregular heating rate conditions. *J. Anal. Appl. Pyrolysis* **73**, 39–43 (2005).
100. Bridgwater, A. V. & Peacocke, G. V. C. Fast pyrolysis processes for biomass. *Renew. Sustain. Energy Rev.* **4**, 1–73 (2000).
101. Russell, S. H., Turrion-Gomez, J. L., Meredith, W., Langston, P. & Snape, C. E. Increased charcoal yield and production of lighter oils from the slow pyrolysis of biomass. *J. Anal. Appl. Pyrolysis* **124**, 536–541 (2017).
102. Horne, P. A. & Williams, P. T. Influence of temperature on the products from the flash pyrolysis of biomass. *Fuel* **75**, 1051–1059 (1996).
103. Demirbas, A. Effect of temperature on pyrolysis products from four nut shells. *J. Anal. Appl. Pyrolysis* **76**, 285–289 (2006).
104. Balat, M. Mechanisms of thermochemical biomass conversion processes. Part 1: Reactions of pyrolysis. *Energy Sources Part -Recovery Util. Environ. Eff.* **30**, 620–635 (2008).

105. Di Blasi, C. Modeling chemical and physical processes of wood and biomass pyrolysis. *Prog. Energy Combust. Sci.* **34**, 47–90 (2008).
106. Caballero, J. A., Conesa, J. A., Font, R. & Marcilla, A. Pyrolysis kinetics of almond shells and olive stones considering their organic fractions. *J. Anal. Appl. Pyrolysis* **42**, 159–175 (1997).
107. Tröger, N., Richter, D. & Stahl, R. Effect of feedstock composition on product yields and energy recovery rates of fast pyrolysis products from different straw types. *J. Anal. Appl. Pyrolysis* **100**, 158–165 (2013).
108. Hassan, E. B., Abou-Yousef, H., Steele, P. & El-Giar, E. Characterization of bio-oils from the fast pyrolysis of white oak and sweetgum. *Energy Sources Part -Recovery Util. Environ. Eff.* **38**, 43–50 (2016).
109. Chiodo, V., Zafarana, G., Maisano, S., Freni, S. & Urbani, F. Pyrolysis of different biomass: Direct comparison among Posidonia Oceanica, Lacustrine Alga and White-Pine. *Fuel* **164**, 220–227 (2016).
110. Lu, W., Ma, M., Zhang, X., Zhang, B., Guo, Y. & Wang, C. Comparison of high calorific fuels obtained from fresh and dried Hydrilla verticillata: Effects of temperature, residence time, catalyst content and material state. *J. Anal. Appl. Pyrolysis* **111**, 76–87 (2015).
111. Salehi, E., Abedi, J. & Harding, T. Bio-oil from Sawdust: Effect of Operating Parameters on the Yield and Quality of Pyrolysis Products. *Energy Fuels* **25**, 4145–4154 (2011).
112. Shen, J., Wang, X.-S., Garcia-Perez, M., Mourant, D., Rhodes, M. J. & Li, C.-Z. Effects of particle size on the fast pyrolysis of oil mallee woody biomass. *Fuel* **88**, 1810–1817 (2009).
113. Heo, H. S., Park, H. J., Yim, J.-H., Sohn, J. M., Park, J., Kim, S.-S., Ryu, C., Jeon, J.-K. & Park, Y.-K. Influence of operation variables on fast pyrolysis of Miscanthus sinensis var. purpurascens. *Bioresour. Technol.* **101**, 3672–3677 (2010).
114. Brammer, J. G. & Bridgwater, A. V. Drying technologies for an integrated gasification bio-energy plant. *Renew. Sustain. Energy Rev.* **3**, 243–289 (1999).
115. Vamvuka, D. Bio-oil, solid and gaseous biofuels from biomass pyrolysis processes—An overview. *Int. J. Energy Res.* **35**, 835–862 (2011).
116. Bridgwater, A. V. Renewable fuels and chemicals by thermal processing of biomass. *Chem. Eng. J.* **91**, 87–102 (2003).
117. Crombie, K. & Masek, O. Pyrolysis biochar systems, balance between bioenergy and carbon sequestration. *Glob. Change Biol. Bioenergy* **7**, 349–361 (2015).
118. Stas, M., Kubicka, D., Chudoba, J. & Pospisil, M. Overview of Analytical Methods Used for Chemical Characterization of Pyrolysis Bio-oil. *Energy Fuels* **28**, 385–402 (2014).
119. Xue, Y., Chen, H., Zhao, W., Yang, C., Ma, P. & Han, S. A review on the operating conditions of producing bio-oil from hydrothermal liquefaction of biomass. *Int. J. Energy Res.* **40**, 865–877 (2016).
120. Chan, Y. H., Yusup, S., Quitain, A. T., Tan, R. R., Sasaki, M., Lam, H. L. & Uemura, Y. Effect of process parameters on hydrothermal liquefaction of oil palm. biomass for bio-oil production and its life cycle assessment. *Energy Convers. Manag.* **104**, 180–188 (2015).

121. Dayton, D. C., Hlebak, J., Carpenter, J. R., Wang, K., Mante, O. D. & Peters, J. E. Biomass Hydrolysis in a Fluidized Bed Reactor. *Energy Fuels* **30**, 4879–4887 (2016).
122. Dimitriadis, A. & Bezergianni, S. Hydrothermal liquefaction of various biomass and waste feedstocks for biocrude production: A state of the art review. *Renew. Sustain. Energy Rev.* **68**, 113–125 (2017).
123. Rachel-Tang, D. Y., Islam, A. & Taufiq-Yap, Y. H. Bio-oil production via catalytic solvolysis of biomass. *RSC Adv.* **7**, 7820–7830 (2017).
124. Liu, Z. & Zhang, F.-S. Effects of various solvents on the liquefaction of biomass to produce fuels and chemical feedstocks. *Energy Convers. Manag.* **49**, 3498–3504 (2008).
125. Peterson, A. A., Vogel, F., Lachance, R. P., Froeling, M., Antal, M. J. & Tester, J. W. Thermochemical biofuel production in hydrothermal media: A review of sub- and supercritical water technologies. *Energy Environ. Sci.* **1**, 32–65 (2008).
126. Balat, M. Mechanisms of thermochemical biomass conversion processes. Part 3: Reactions of liquefaction. *Energy Sources Part -Recovery Util. Environ. Eff.* **30**, 649–659 (2008).
127. Jindal, M. K. & Jha, M. K. Hydrothermal liquefaction of wood: a critical review. *Rev. Chem. Eng.* **32**, 459–488 (2016).
128. Barrow, C. J. Biochar: Potential for countering land degradation and for improving agriculture. *Appl. Geogr.* **34**, 21–28 (2012).
129. Zhang, B., von Keitz, M. & Valentas, K. Thermochemical liquefaction of high-diversity grassland perennials. *J. Anal. Appl. Pyrolysis* **84**, 18–24 (2009).
130. Akhtar, J. & Amin, N. A. S. A review on process conditions for optimum bio-oil yield in hydrothermal liquefaction of biomass. *Renew. Sustain. Energy Rev.* **15**, 1615–1624 (2011).
131. Yin, S., Dolan, R., Harris, M. & Tan, Z. Subcritical hydrothermal liquefaction of cattle manure to bio-oil: Effects of conversion parameters on bio-oil yield and characterization of bio-oil. *Bioresour. Technol.* **101**, 3657–3664 (2010).
132. Tekin, K. & Karagoz, S. Non-catalytic and catalytic hydrothermal liquefaction of biomass. *Res. Chem. Intermed.* **39**, 485–498 (2013).
133. Nigam, P. S. & Singh, A. Production of liquid biofuels from renewable resources. *Prog. Energy Combust. Sci.* **37**, 52–68 (2011).
134. Anex, R. P., Aden, A., Kazi, F. K., Fortman, J., Swanson, R. M., Wright, M. M., Satrio, J. A., Brown, R. C., Daugaard, D. E., Platon, A., Kothandaraman, G., Hsu, D. D. & Dutta, A. Techno-economic comparison of biomass-to-transportation fuels via pyrolysis, gasification, and biochemical pathways. *Fuel* **89**, S29–S35 (2010).
135. Underwood, G. & Graham, R. G. Method of using fast pyrolysis liquids as liquid smoke. US Patent 4. US 4876108 A. (1989). at <<https://www.google.ch/patents/US4876108>>
136. Chum, H. L. & Kreibich, R. E. Process for preparing phenolic formaldehyde resole resin products derived from fractionated fast-pyrolysis oils. US Patent 5. US 5091499 A. (1992). at <<https://www.google.com/patents/US5091499>>



137. Hu, X., Mourant, D., Gunawan, R., Wu, L., Wang, Y., Lievens, C. & Li, C.-Z. Production of value-added chemicals from bio-oil via acid catalysis coupled with liquid-liquid extraction. *Rsc Adv.* **2**, 9366–9370 (2012).
138. Elliott, D. C. & Schiefelbein, G. F. Liquid hydrocarbon fuels from biomass. *Am. Chem. Soc. Div. Fuel Chem. Annu. Meet. Prepr.* 1160–1166 (1989).
139. Czernik, S. & Bridgwater, A. V. Overview of Applications of Biomass Fast Pyrolysis Oil. *Energy Fuels* **18**, 590–598 (2004).
140. Oasmaa, A., Elliott, D. C. & Korhonen, J. Acidity of Biomass Fast Pyrolysis Bio-oils. *Energy Fuels* **24**, 6548–6554 (2010).
141. Oasmaa, A., Korhonen, J. & Kuoppala, E. An Approach for Stability Measurement of Wood-Based Fast Pyrolysis Bio-Oils. *Energy Fuels* **25**, 3307–3313 (2011).
142. Diebold, J. P. *A review of the chemical and physical mechanisms of the storage stability of fast pyrolysis bio-oils.* (2000).
143. Czernik, S., Johnson, D. & Black, S. Stability of Wood Fast Pyrolysis Oil. *Biomass Bioenergy* **7**, 187–192 (1994).
144. Zhou, D., Zhang, L., Zhang, S., Fu, H. & Chen, J. Hydrothermal Liquefaction of Macroalgae *Enteromorpha prolifera* to Bio-oil. *Energy Fuels* **24**, 4054–4061 (2010).
145. Zhu, Z., Rosendahl, L., Toor, S. S., Yu, D. & Chen, G. Hydrothermal liquefaction of barley straw to bio-crude oil: Effects of reaction temperature and aqueous phase recirculation. *Appl. Energy* **137**, 183–192 (2015).
146. Adjaye, J., Sharma, R. & Bakhshi, N. Characterization and Stability Analysis of Wood-Derived Bio-Oil. *Fuel Process. Technol.* **31**, 241–256 (1992).
147. Kosinkova, J., Ramirez, J. A., Ristovski, Z. D., Brown, R. & Rainey, T. J. Physical and Chemical Stability of Bagasse Biocrude from Liquefaction Stored in Real Conditions. *Energy Fuels* **30**, 10499–10504 (2016).
148. Murnieks, R., Kampars, V., Malins, K. & Apseniece, L. Hydrotreating of wheat straw in toluene and ethanol. *Bioresour. Technol.* **163**, 106–111 (2014).
149. Rutten, C., Ramirez, A. & Duque, J. P. Hydrotreating and hydrothermal treatment of alkaline lignin as technological valorization options for future biorefinery concepts: a review. *J. Chem. Technol. Biotechnol.* **92**, 257–270 (2017).
150. Elliott, D. C. Historical developments in hydroprocessing bio-oils. *Energy Fuels* **21**, 1792–1815 (2007).
151. Wang, H., Male, J. & Wang, Y. Recent Advances in Hydrotreating of Pyrolysis Bio-Oil and Its Oxygen-Containing Model Compounds. *ACS Catal.* **3**, 1047–1070 (2013).
152. Marker, T. L., Felix, L. G., Linck, M. B. & Roberts, M. J. Integrated Hydrolysis and Hydroconversion (IH2) for the Direct Production of Gasoline and Diesel Fuels or Blending Components from Biomass, Part 1: Proof of Principle Testing. *Environ. Prog. Sustain. Energy* **31**, 191–199 (2012).
153. Melligan, F., Hayes, M. H. B., Kwapinski, W. & Leahy, J. J. Hydro-Pyrolysis of Biomass and Online Catalytic Vapor Upgrading with Ni-ZSM-5 and Ni-MCM-41. *Energy Fuels* **26**, 6080–6090 (2012).

154. Chen, M., Wang, J., Zhang, M., Chen, M., Zhu, X., Min, F. & Tan, Z. Catalytic effects of eight inorganic additives on pyrolysis of pine wood sawdust by microwave heating. *J. Anal. Appl. Pyrolysis* **82**, 145–150 (2008).
155. Lu, Q., Xiong, W.-M., Li, W.-Z., Guo, Q.-X. & Zhu, X.-F. Catalytic pyrolysis of cellulose with sulfated metal oxides: A promising method for obtaining high yield of light furan compounds. *Bioresour. Technol.* **100**, 4871–4876 (2009).
156. Wildschut, J., Mahfud, F. H., Venderbosch, R. H. & Heeres, H. J. Hydrotreatment of Fast Pyrolysis Oil Using Heterogeneous Noble-Metal Catalysts. *Ind. Eng. Chem. Res.* **48**, 10324–10334 (2009).
157. Olazar, M., Aguado, R., Bilbao, J. & Barona, A. Pyrolysis of sawdust in a conical spouted-bed reactor with a HZSM-5 catalyst. *Aiche J.* **46**, 1025–1033 (2000).
158. Veses, A., Puertolas, B., Manuel Lopez, J., Soledad Callen, M., Solsona, B. & Garcia, T. Promoting Deoxygenation of Bio-Oil by Metal-Loaded Hierarchical ZSM-5 Zeolites. *ACS Sustain. Chem. Eng.* **4**, 1653–1660 (2016).
159. Mullen, C. A., Boateng, A. A., Mihalcik, D. J. & Goldberg, N. M. Catalytic Fast Pyrolysis of White Oak Wood in a Bubbling Fluidized Bed. *Energy Fuels* **25**, 5444–5451 (2011).
160. Corma, A. State of the art and future challenges of zeolites as catalysts. *J. Catal.* **216**, 298–312 (2003).
161. Katikaneni, S., Adjaye, J. & Bakhshi, N. Catalytic Conversion of Canola Oil to Fuels and Chemicals Over Various Cracking Catalysts. *Can. J. Chem. Eng.* **73**, 484–497 (1995).
162. Adjaye, J. D., Katikaneni, S. P. R. & Bakhshi, N. N. Catalytic conversion of a biofuel to hydrocarbons: Effect of mixtures of HZSM-5 and silica-alumina catalysts on product distribution. *Fuel Process. Technol.* **48**, 115–143 (1996).
163. Huang, J., Long, W., Agrawal, P. K. & Jones, C. W. Effects of Acidity on the Conversion of the Model Bio-oil Ketone Cyclopentanone on H-Y Zeolites. *J. Phys. Chem. C* **113**, 16702–16710 (2009).
164. Jacobson, K., Maheria, K. C. & Kumar Dalai, A. Bio-oil valorization: A review. *Renew. Sustain. Energy Rev.* **23**, 91–106 (2013).
165. Al-Sabawi, M., Chen, J. & Ng, S. Fluid Catalytic Cracking of Biomass-Derived Oils and Their Blends with Petroleum Feedstocks: A Review. *Energy Fuels* **26**, 5355–5372 (2012).
166. Ibarra, A., Rodriguez, E., Sedran, U., Arandes, J. M. & Bilbao, J. Synergy in the Cracking of a Blend of Bio-oil and Vacuum Gasoil under Fluid Catalytic Cracking Conditions. *Ind. Eng. Chem. Res.* **55**, 1872–1880 (2016).
167. Graca, I., Lopes, J. M., Cerqueira, H. S. & Ribeiro, M. F. Bio-oils Upgrading for Second Generation Biofuels. *Ind. Eng. Chem. Res.* **52**, 275–287 (2013).
168. Adjaye, J. & Bakhshi, N. Upgrading of a Wood-Derived Oil Over Various Catalysts. *Biomass Bioenergy* **7**, 201–211 (1994).
169. Sharma, R. & Bakhshi, N. Catalytic Upgrading of Pyrolysis Oil. *Energy Fuels* **7**, 306–314 (1993).

170. Adjaye, J. & Bakhshi, N. Production of Hydrocarbons by Catalytic Upgrading of a Fast Pyrolysis Bio-Oil .2. Comparative Catalyst Performance and Reaction Pathways. *Fuel Process. Technol.* **45**, 185–202 (1995).
171. Adjaye, J. & Bakhshi, N. Catalytic Conversion of a Biomass-Derived Oil to Fuels and Chemicals .1. Model-Compound Studies and Reaction Pathways. *Biomass Bioenergy* **8**, 131–149 (1995).
172. Vitolo, S., Seggiani, M., Frediani, P., Ambrosini, G. & Politi, L. Catalytic upgrading of pyrolytic oils to fuel over different zeolites. *Fuel* **78**, 1147–1159 (1999).
173. Gayubo, A. G., Aguayo, A. T., Atutxa, A., Aguado, R. & Bilbao, J. Transformation of oxygenate components of biomass pyrolysis oil on a HZSM-5 zeolite. I. Alcohols and phenols. *Ind. Eng. Chem. Res.* **43**, 2610–2618 (2004).
174. Gayubo, A. G., Aguayo, A. T., Atutxa, A., Aguado, R., Olazar, M. & Bilbao, J. Transformation of oxygenate components of biomass pyrolysis oil on a HZSM-5 zeolite. H. Aldehydes, ketones, and acids. *Ind. Eng. Chem. Res.* **43**, 2619–2626 (2004).
175. Corma, A., Huber, G. W., Sauvanaud, L. & O'Connor, P. Processing biomass-derived oxygenates in the oil refinery: Catalytic cracking (FCC) reaction pathways and role of catalyst. *J. Catal.* **247**, 307–327 (2007).
176. Mortensen, P. M., Grunwaldt, J.-D., Jensen, P. A., Knudsen, K. G. & Jensen, A. D. A review of catalytic upgrading of bio-oil to engine fuels. *Appl. Catal. Gen.* **407**, 1–19 (2011).
177. Furimsky, E. Catalytic hydrodeoxygenation. *Appl. Catal. -Gen.* **199**, 147–190 (2000).
178. Stakheev, A. Y. & Kustov, L. M. Effects of the support on the morphology and electronic properties of supported metal clusters: modern concepts and progress in 1990s. *Appl. Catal. -Gen.* **188**, 3–35 (1999).
179. Moens, L., Black, S. K., Myers, M. D. & Czernik, S. Study of the Neutralization and Stabilization of a Mixed Hardwood Bio-Oil. *Energy Fuels* **23**, 2695–2699 (2009).
180. Junming, X., Jianchun, J., Yunjuan, S. & Yanju, L. Bio-oil upgrading by means of ethyl ester production in reactive distillation to remove water and to improve storage and fuel characteristics. *Biomass Bioenergy* **32**, 1056–1061 (2008).
181. Huber, G. W. & Dumesic, J. A. An overview of aqueous-phase catalytic processes for production of hydrogen and alkanes in a biorefinery. *Catal. Today* **111**, 119–132 (2006).
182. Shabaker, J. W., Davda, R. R., Huber, G. W., Cortright, R. D. & Dumesic, J. A. Aqueous-phase reforming of methanol and ethylene glycol over alumina-supported platinum catalysts. *J. Catal.* **215**, 344–352 (2003).
183. Garcia, L., French, R., Czernik, S. & Chornet, E. Catalytic steam reforming of bio-oils for the production of hydrogen: effects of catalyst composition. *Appl. Catal. -Gen.* **201**, 225–239 (2000).
184. Czernik, S., French, R., Feik, C. & Chornet, E. Hydrogen by catalytic steam reforming of liquid byproducts from biomass thermoconversion processes. *Ind. Eng. Chem. Res.* **41**, 4209–4215 (2002).
185. Huber, G. W. & Corma, A. Synergies between bio- and oil refineries for the production of fuels from biomass. *Angew. Chem.-Int. Ed.* **46**, 7184–7201 (2007).

186. Gayubo, A. G., Valle, B., Aguayo, A. T., Olazar, M. & Bilbao, J. Attenuation of Catalyst Deactivation by Cofeeding Methanol for Enhancing the Valorisation of Crude Bio-oil. *Energy Fuels* **23**, 4129–4136 (2009).
187. Guisnet, M. & Magnoux, P. Organic chemistry of coke formation. *Appl. Catal. -Gen.* **212**, 83–96 (2001).
188. Rezaei, P. S., Shafaghat, H. & Daud, W. M. A. W. Production of green aromatics and olefins by catalytic cracking of oxygenate compounds derived from biomass pyrolysis: A review. *Appl. Catal. Gen.* **469**, 490–511 (2014).
189. Gayubo, A. G., Aguayo, A. T., Atutxa, A., Prieto, R. & Bilbao, J. Deactivation of a HZSM-5 zeolite catalyst in the transformation of the aqueous fraction of biomass pyrolysis oil into hydrocarbons. *Energy Fuels* **18**, 1640–1647 (2004).
190. Furimsky, E. & Massoth, F. E. Deactivation of hydroprocessing catalysts. *Catal. Today* **52**, 381–495 (1999).
191. Bermudez, J. M., Fidalgo, B., Arenillas, A. & Menendez, J. A. CO<sub>2</sub> reforming of coke oven gas over a Ni/gamma Al<sub>2</sub>O<sub>3</sub> catalyst to produce syngas for methanol synthesis. *Fuel* **94**, 197–203 (2012).
192. Wang, S. in *Biomass - Sustain. Growth Use* (ed. Matovic, M. D.) (InTech, 2013). at <<http://www.intechopen.com/books/biomass-now-sustainable-growth-and-use/high-efficiency-separation-of-bio-oil>>
193. Putun, A. E., Ozcan, A. & Putun, E. Pyrolysis of hazelnut shells in a fixed-bed tubular reactor: yields and structural analysis of bio-oil. *J. Anal. Appl. Pyrolysis* **52**, 33–49 (1999).
194. Ozcimen, D. & Karaosmanoglu, F. Production and characterization of bio-oil and biochar from rapeseed cake. *Renew. Energy* **29**, 779–787 (2004).
195. Ozbay, N., Uzun, B. B., Varol, E. A. & Putun, A. E. Comparative analysis of pyrolysis oils and its subfractions under different atmospheric conditions. *Fuel Process. Technol.* **87**, 1013–1019 (2006).
196. Das, P., Sreelatha, T. & Ganesh, A. Bio oil from pyrolysis of cashew nut shell-characterisation and related properties. *Biomass Bioenergy* **27**, 265–275 (2004).
197. Sipila, K., Kuoppala, E., Fagernas, L. & Oasmaa, A. Characterization of biomass-based flash pyrolysis oils. *Biomass Bioenergy* **14**, 103–113 (1998).
198. Oasmaa, A., Kuoppala, E. & Solantausta, Y. Fast pyrolysis of forestry residue. 2. Physico-chemical composition of product liquid. *Energy Fuels* **17**, 433–443 (2003).
199. Oasmaa, A. & Kuoppala, E. Solvent Fractionation Method with Brix for Rapid Characterization of Wood Fast Pyrolysis Liquids. *Energy Fuels* **22**, 4245–4248 (2008).
200. Garcia-Perez, M., Chaala, A., Pakdel, H., Kretschmer, D. & Roy, C. Characterization of bio-oils in chemical families. *Biomass Bioenergy* **31**, 222–242 (2007).
201. Wang, S., Wang, Y., Cai, Q., Wang, X., Jin, H. & Luo, Z. Multi-step separation of monophenols and pyrolytic lignins from the water-insoluble phase of bio-oil. *Sep. Purif. Technol.* **122**, 248–255 (2014).
202. Wang, J., Cui, H., Wei, S., Zhuo, S., Wang, L., Li, Z. & Yi, W. in *2010 Asia-Pac. Power Energy Eng. Conf. Appeec* (Ieee, 2010).

203. Rout, P. K., Naik, M. K., Naik, S. N., Goud, V. V., Das, L. M. & Dalai, A. K. Supercritical CO<sub>2</sub> Fractionation of Bio-oil Produced from Mixed Biomass of Wheat and Wood Sawdust. *Energy Fuels* **23**, 6181–6188 (2009).
204. Bayerbach, R., Nguyen, V. D., Schurr, U. & Meier, D. Characterization of the water-insoluble fraction from fast pyrolysis liquids (pyrolytic lignin): Part III. Molar mass characteristics by SEC, MALDI-TOF-MS, LDI-TOF-MS, and Py-FIMS. *J. Anal. Appl. Pyrolysis* **77**, 95–101 (2006).
205. Andersson, T., Hyotylainen, T. & Riekkola, M. L. Analysis of phenols in pyrolysis oils by gel permeation chromatography and multidimensional liquid chromatography. *J. Chromatogr. A* **896**, 343–349 (2000).
206. Poole, C. F. Derivatization reactions for use with the electron-capture detector. *J. Chromatogr. A* **1296**, 15–24 (2013).
207. Qi, B.-L., Liu, P., Wang, Q.-Y., Cai, W.-J., Yuan, B.-F. & Feng, Y.-Q. Derivatization for liquid chromatography-mass spectrometry. *Trac-Trends Anal. Chem.* **59**, 121–132 (2014).
208. Murwanashyaka, J. N., Pakdel, H. & Roy, C. Step-wise and one-step vacuum pyrolysis of birch-derived biomass to monitor the evolution of phenols. *J. Anal. Appl. Pyrolysis* **60**, 219–231 (2001).
209. Charon, N., Ponthus, J., Espinat, D., Broust, F., Volle, G., Valette, J. & Meier, D. Multi-technique characterization of fast pyrolysis oils. *J. Anal. Appl. Pyrolysis* **116**, 18–26 (2015).
210. Gellerstedt, G., Li, J., Eide, I., Kleinert, M. & Barth, T. Chemical Structures Present in Bio-fuel Obtained from Lignin. *Energy Fuels* **22**, 4240–4244 (2008).
211. Fabbri, D., Torri, C. & Baravelli, V. Effect of zeolites and nanopowder metal oxides on the distribution of chiral anhydrosugars evolved from pyrolysis of cellulose: An analytical study. *J. Anal. Appl. Pyrolysis* **80**, 24–29 (2007).
212. Tessini, C., Müller, N., Mardones, C., Meier, D., Berg, A. & von Baer, D. Chromatographic approaches for determination of low-molecular mass aldehydes in bio-oil. *J. Chromatogr. A* **1219**, 154–160 (2012).
213. Christensen, E. D., Chupka, G. M., Luecke, J., Smurthwaite, T., Alleman, T. L., Lisa, K., Franz, J. A., Elliott, D. C. & McCormick, R. L. Analysis of Oxygenated Compounds in Hydrotreated Biomass Fast Pyrolysis Oil Distillate Fractions. *Energy Fuels* **25**, 5462–5471 (2011).
214. Tessini, C., Vega, M., Mueller, N., Bustamante, L., von Baer, D., Berg, A. & Mardones, C. High performance thin layer chromatography determination of cellobiosan and levoglucosan in bio-oil obtained by fast pyrolysis of sawdust. *J. Chromatogr. A* **1218**, 3811–3815 (2011).
215. Mahinpey, N., Murugan, P., Mani, T. & Raina, R. Analysis of Bio-Oil, Biogas, and Biochar from Pressurized Pyrolysis of Wheat Straw Using a Tubular Reactor. *Energy Fuels* **23**, 2736–2742 (2009).
216. Torri, C. & Fabbri, D. Application of off-line pyrolysis with dynamic solid-phase microextraction to the GC-MS analysis of biomass pyrolysis products. *Microchem. J.* **93**, 133–139 (2009).

217. Busetto, L., Fabbri, D., Mazzoni, R., Salmi, M., Torri, C. & Zanotti, V. Application of the Shvo catalyst in homogeneous hydrogenation of bio-oil obtained from pyrolysis of white poplar: New mild upgrading conditions. *Fuel* **90**, 1197–1207 (2011).
218. Wang, S., Go, Y., Liu, Q., Yao, Y., Guo, Z., Luo, Z. & Cen, K. Separation of bio-oil by molecular distillation. *Fuel Process. Technol.* **90**, 738–745 (2009).
219. Guo, Z., Wang, S., Gu, Y., Xu, G., Li, X. & Luo, Z. Separation characteristics of biomass pyrolysis oil in molecular distillation. *Sep. Purif. Technol.* **76**, 52–57 (2010).
220. Guo, X., Wang, S., Guo, Z., Liu, Q., Luo, Z. & Cen, K. Pyrolysis characteristics of bio-oil fractions separated by molecular distillation. *Appl. Energy* **87**, 2892–2898 (2010).
221. Qiang, L., Xu-lai, Y. & Xi-feng, Z. Analysis on chemical and physical properties of bio-oil pyrolyzed from rice husk. *J. Anal. Appl. Pyrolysis* **82**, 191–198 (2008).
222. Lievens, C., Mourant, D., He, M., Gunawan, R., Li, X. & Li, C.-Z. An FT-IR spectroscopic study of carbonyl functionalities in bio-oils. *Fuel* **90**, 3417–3423 (2011).
223. Scholze, B. & Meier, D. Characterization of the water-insoluble fraction from pyrolysis oil (pyrolytic lignin). Part I. PY–GC/MS, FTIR, and functional groups. *J. Anal. Appl. Pyrolysis* **60**, 41–54 (2001).
224. Hiltner, R. N. & Das, K. C. Comparison of three accelerated aging procedures to assess bio-oil stability. *Fuel* **89**, 2741–2749 (2010).
225. Xu, F., Xu, Y., Lu, R., Sheng, G.-P. & Yu, H.-Q. Elucidation of the Thermal Deterioration Mechanism of Bio-oil Pyrolyzed from Rice Husk Using Fourier Transform Infrared Spectroscopy. *J. Agric. Food Chem.* **59**, 9243–9249 (2011).
226. Tripathi, M. M., Hassan, E. B. M., Yueh, F.-Y., Singh, J. P., Steele, P. H. & Ingram, L. L. Reflection-absorption-based near infrared spectroscopy for predicting water content in bio-oil. *Sens. Actuators B-Chem.* **136**, 20–25 (2009).
227. Cheng, T., Han, Y., Zhang, Y. & Xu, C. Molecular composition of oxygenated compounds in fast pyrolysis bio-oil and its supercritical fluid extracts. *Fuel* **172**, 49–57 (2016).
228. Stankovikj, F., McDonald, A. G., Helms, G. L. & Garcia-Perez, M. Quantification of Bio-Oil Functional Groups and Evidences of the Presence of Pyrolytic Humins. *Energy Fuels* **30**, 6505–6524 (2016).
229. Hao, N., Ben, H., Yoo, C. G., Adhikari, S. & Ragauskas, A. J. Review of NMR Characterization of Pyrolysis Oils. *Energy Fuels* **30**, 6863–6880 (2016).
230. Joseph, J., Baker, C., Mukkamala, S., Beis, S. H., Wheeler, M. C., DeSisto, W. J., Jensen, B. L. & Frederick, B. G. Chemical Shifts and Lifetimes for Nuclear Magnetic Resonance (NMR) Analysis of Biofuels. *Energy Fuels* **24**, 5153–5162 (2010).
231. Doassans-Carrere, N., Ferrasse, J.-H., Boutin, O., Mauviel, G. & Lede, J. Comparative Study of Biomass Fast Pyrolysis and Direct Liquefaction for Bio-Oils Production: Products Yield and Characterizations. *Energy Fuels* **28**, 5103–5111 (2014).
232. Fortin, M., Beromi, M. M., Lai, A., Tarves, P. C., Mullen, C. A., Boateng, A. A. & West, N. M. Structural Analysis of Pyrolytic Lignins Isolated from Switchgrass Fast-Pyrolysis Oil. *Energy Fuels* **29**, 8017–8026 (2015).

233. Yu, Y., Chua, Y. W. & Wu, H. Characterization of Pyrolytic Sugars in Bio-Oil Produced from Biomass Fast Pyrolysis. *Energy Fuels* **30**, 4145–4149 (2016).
234. Ben, H. & Ragauskas, A. J. In Situ NMR Characterization of Pyrolysis Oil during Accelerated Aging. *Chemsuschem* **5**, 1687–1693 (2012).
235. Sudasinghe, N., Cort, J. R., Hallen, R., Olarte, M., Schmidt, A. & Schaub, T. Hydrothermal liquefaction oil and hydrotreated product from pine feedstock characterized by hetero-nuclear two-dimensional NMR spectroscopy and FT-ICR mass spectrometry. *Fuel* **137**, 60–69 (2014).
236. Mullen, C. A., Strahan, G. D. & Boateng, A. A. Characterization of Various Fast-Pyrolysis Bio-Oils by NMR Spectroscopy†. *Energy Fuels* **23**, 2707–2718 (2009).
237. Strahan, G. D., Mullen, C. A. & Boateng, A. A. Characterizing Biomass Fast Pyrolysis Oils by C-13 NMR and Chemometric Analysis. *Energy Fuels* **25**, 5452–5461 (2011).
238. Bi, Y., Wang, G., Shi, Q., Xu, C. & Gao, J. Compositional Changes during Hydrodeoxygenation of Biomass Pyrolysis Oil. *Energy Fuels* **28**, 2571–2580 (2014).
239. Naik, D. V., Kumar, V., Prasad, B., Poddar, M. K., Behera, B., Bal, R., Khatri, O. P., Adhikari, D. K. & Garg, M. O. Catalytic cracking of jatropha-derived fast pyrolysis oils with VGO and their NMR characterization. *Rsc Adv.* **5**, 398–409 (2015).
240. Ben, H. & Ferrell, J. R. In-depth investigation on quantitative characterization of pyrolysis oil by P-31 NMR. *Rsc Adv.* **6**, 17567–17573 (2016).
241. Balakshin, M. & Capanema, E. On the Quantification of Lignin Hydroxyl Groups with P-31 and C-13 Nmr Spectroscopy. *J. Wood Chem. Technol.* **35**, 220–237 (2015).
242. Pu, Y., Cao, S. & Ragauskas, A. J. Application of quantitative 31P NMR in biomass lignin and biofuel precursors characterization. *Energy Environ. Sci.* **4**, 3154–3166 (2011).
243. Stankovikj, F., McDonald, A. G., Helms, G. L., Olarte, M. V. & Garcia-Perez, M. Characterization of the Water-Soluble Fraction of Woody Biomass Pyrolysis Oils. *Energy Fuels* **31**, 1650–1664 (2017).
244. Ben, H. & Ragauskas, A. J. NMR Characterization of Pyrolysis Oils from Kraft Lignin. *Energy Fuels* **25**, 2322–2332 (2011).
245. Huang, F., Pan, S., Pu, Y., Ben, H. & Ragauskas, A. J. F-19 NMR spectroscopy for the quantitative analysis of carbonyl groups in bio-oils. *Rsc Adv.* **4**, 17743–17747 (2014).
246. Kanaujia, P. K., Sharma, Y. K., Agrawal, U. C. & Garg, M. O. Analytical approaches to characterizing pyrolysis oil from biomass. *TrAC Trends Anal. Chem.* **42**, 125–136 (2013).
247. Ferrell, J. R., Olarte, M. V., Christensen, E. D., Padmaperuma, A. B., Connatser, R. M., Stankovikj, F., Meier, D. & Paasikallio, V. Standardization of chemical analytical techniques for pyrolysis bio-oil: history, challenges, and current status of methods. *Biofuels Bioprod. Biorefining* **10**, 496–507 (2016).
248. Choi, Y. S., Johnston, P. A., Brown, R. C., Shanks, B. H. & Lee, K.-H. Detailed characterization of red oak-derived pyrolysis oil: Integrated use of GC, HPLC, IC, GPC and Karl-Fischer. *J. Anal. Appl. Pyrolysis* **110**, 147–154 (2014).
249. Mullen, C. A. & Boateng, A. A. Chemical Composition of Bio-oils Produced by Fast Pyrolysis of Two Energy Crops†. *Energy Fuels* **22**, 2104–2109 (2008).

250. Sobeih, K. L., Baron, M. & Gonzalez-Rodriguez, J. Recent trends and developments in pyrolysis-gas chromatography. *J. Chromatogr. A* **1186**, 51–66 (2008).
251. Qiang, L., Wen-zhi, L., Dong, Z. & Xi-feng, Z. Analytical pyrolysis-gas chromatography/mass spectrometry (Py-GC/MS) of sawdust with Al/SBA-15 catalysts. *J. Anal. Appl. Pyrolysis* **84**, 131–138 (2009).
252. Pattiya, A., Titiloye, J. O. & Bridgwater, A. V. Fast pyrolysis of cassava rhizome in the presence of catalysts. *J. Anal. Appl. Pyrolysis* **81**, 72–79 (2008).
253. Fullana, A., Contreras, J. A., Striebich, R. C. & Sidhu, S. S. Multidimensional GC/MS analysis of pyrolytic oils. *J. Anal. Appl. Pyrolysis* **74**, 315–326 (2005).
254. Marsman, J. H., Wildschut, J., Mahfud, F. & Heeres, H. J. Identification of components in fast pyrolysis oil and upgraded products by comprehensive two-dimensional gas chromatography and flame ionisation detection. *J. Chromatogr. A* **1150**, 21–27 (2007).
255. Marsman, J. H., Wildschut, J., Evers, P., de Koning, S. & Heeres, H. J. Identification and classification of components in flash pyrolysis oil and hydrodeoxygenated oils by two-dimensional gas chromatography and time-of-flight mass spectrometry. *J. Chromatogr. A* **1188**, 17–25 (2008).
256. Sfetsas, T., Michailof, C., Lappas, A., Li, Q. & Kneale, B. Qualitative and quantitative analysis of pyrolysis oil by gas chromatography with flame ionization detection and comprehensive two-dimensional gas chromatography with time-of-flight mass spectrometry. *J. Chromatogr. A* **1218**, 3317–3325 (2011).
257. Michailof, C., Sfetsas, T., Stefanidis, S., Kalogiannis, K., Theodoridis, G. & Lappas, A. Quantitative and qualitative analysis of hemicellulose, cellulose and lignin bio-oils by comprehensive two-dimensional gas chromatography with time-of-flight mass spectrometry. *J. Chromatogr. A* **1369**, 147–160 (2014).
258. Olcese, R., Carré, V., Aubriet, F. & Dufour, A. Selectivity of Bio-oils Catalytic Hydrotreatment Assessed by Petroleomic and GC\*GC/MS-FID Analysis. *Energy Fuels* **27**, 2135–2145 (2013).
259. Olcese, R. N., Lardier, G., Bettahar, M., Ghanbaja, J., Fontana, S., Carre, V., Aubriet, F., Petitjean, D. & Dufour, A. Aromatic Chemicals by Iron-Catalyzed Hydrotreatment of Lignin Pyrolysis Vapor. *Chemsuschem* **6**, 1490–1499 (2013).
260. Xu, F., Xu, Y., Yin, H., Zhu, X. & Guo, Q. Analysis of Bio-oil Obtained by Biomass Fast Pyrolysis Using Low-Energy Electron-Impact Mass Spectrometry. *Energy Fuels* **23**, 1775–1777 (2009).
261. Tessarolo, N. S., Silva, R. C., Vanini, G., Pinho, A., Romão, W., de Castro, E. V. R. & Azevedo, D. A. Assessing the chemical composition of bio-oils using FT-ICR mass spectrometry and comprehensive two-dimensional gas chromatography with time-of-flight mass spectrometry. *Microchem. J.* **117**, 68–76 (2014).
262. Croce, A., Battistel, E., Chiaberge, S., Spera, S., Reale, S. & De Angelis, F. Mass Spectrometry and Nuclear Magnetic Resonance Spectroscopy Study of Carbohydrate Decomposition by Hydrothermal Liquefaction Treatment: A Modeling Approach on Bio-oil Production from Organic Wastes. *Energy Fuels* **29**, 5847–5856 (2015).



263. Liu, Y., Shi, Q., Zhang, Y., He, Y., Chung, K. H., Zhao, S. & Xu, C. Characterization of Red Pine Pyrolysis Bio-oil by Gas Chromatography–Mass Spectrometry and Negative-Ion Electrospray Ionization Fourier Transform Ion Cyclotron Resonance Mass Spectrometry. *Energy Fuels* **26**, 4532–4539 (2012).
264. Koike, N., Hosokai, S., Takagaki, A., Nishimura, S., Kikuchi, R., Ebitani, K., Suzuki, Y. & Oyama, S. T. Upgrading of pyrolysis bio-oil using nickel phosphide catalysts. *J. Catal.* **333**, 115–126 (2016).
265. Scholze, B., Hanser, C. & Meier, D. Characterization of the water-insoluble fraction from fast pyrolysis liquids (pyrolytic lignin) Part II. GPC, carbonyl groups, and C-13-NMR. *J. Anal. Appl. Pyrolysis* **58**, 387–400 (2001).
266. Le Masle, A., Angot, D., Gouin, C., D’Attoma, A., Ponthus, J., Quignard, A. & Heinisch, S. Development of on-line comprehensive two-dimensional liquid chromatography method for the separation of biomass compounds. *J. Chromatogr. A* **1340**, 90–98 (2014).
267. Tomasini, D., Cacciola, F., Rigano, F., Sciarrone, D., Donato, P., Beccaria, M., Caramao, E. B., Dugo, P. & Mondello, L. Complementary Analytical Liquid Chromatography Methods for the Characterization of Aqueous Phase from Pyrolysis of Lignocellulosic Biomasses. *Anal. Chem.* **86**, 11255–11262 (2014).
268. Michailof, C. M., Kalogiannis, K. G., Sfetsas, T., Patiaka, D. T. & Lappas, A. A. Advanced analytical techniques for bio-oil characterization. *Wiley Interdiscip. Rev.-Energy Environ.* **5**, 614–639 (2016).
269. Brown, A. L., Dayton, D. C., Nimlos, M. R. & Daily, J. W. Characterization of biomass pyrolysis vapors with molecular beam, single photon ionization time-of-flight mass spectrometry. *Chemosphere* **42**, 663–669 (2001).
270. Jia, L., Le-Brech, Y., Shrestha, B., Bente-von Frowein, M., Ehlert, S., Mauviel, G., Zimmermann, R. & Dufour, A. Fast Pyrolysis in a Microfluidized Bed Reactor: Effect of Biomass Properties and Operating Conditions on Volatiles Composition as Analyzed by Online Single Photoionization Mass Spectrometry. *Energy Fuels* **29**, 7364–7374 (2015).
271. Marshall, A. G. & Rodgers, R. P. Petroleomics: The Next Grand Challenge for Chemical Analysis. *Acc. Chem. Res.* **37**, 53–59 (2004).
272. Bae, E., Na, J.-G., Chung, S. H., Kim, H. S. & Kim, S. Identification of about 30 000 Chemical Components in Shale Oils by Electrospray Ionization (ESI) and Atmospheric Pressure Photoionization (APPI) Coupled with 15 T Fourier Transform Ion Cyclotron Resonance Mass Spectrometry (FT-ICR MS) and a Comparison to Conventional Oil. *Energy Fuels* **24**, 2563–2569 (2010).
273. Lababidi, S., Panda, S. K., Andersson, J. T. & Schrader, W. Direct Coupling of Normal-Phase High-Performance Liquid Chromatography to Atmospheric Pressure Laser Ionization Fourier Transform Ion Cyclotron Resonance Mass Spectrometry for the Characterization of Crude Oil. *Anal. Chem.* **85**, 9478–9485 (2013).
274. Cao, D., Huang, H., Hu, M., Cui, L., Geng, F., Rao, Z., Niu, H., Cai, Y. & Kang, Y. Comprehensive characterization of natural organic matter by MALDI- and ESI-Fourier transform ion cyclotron resonance mass spectrometry. *Anal. Chim. Acta* **866**, 48–58 (2015).

275. Hawkes, J. A., Dittmar, T., Patriarca, C., Tranvik, L. & Bergquist, J. Evaluation of the Orbitrap Mass Spectrometer for the Molecular Fingerprinting Analysis of Natural Dissolved Organic Matter. *Anal. Chem.* **88**, 7698–7704 (2016).
276. Purcell, J. M., Merdrignac, I., Rodgers, R. P., Marshall, A. G., Gauthier, T. & Guibard, I. Stepwise Structural Characterization of Asphaltenes during Deep Hydroconversion Processes Determined by Atmospheric Pressure Photoionization (APPI) Fourier Transform Ion Cyclotron Resonance (FT-ICR) Mass Spectrometry. *Energy Fuels* **24**, 2257–2265 (2010).
277. Kim, S., Kramer, R. W. & Hatcher, P. G. Graphical Method for Analysis of Ultrahigh-Resolution Broadband Mass Spectra of Natural Organic Matter, the Van Krevelen Diagram. *Anal. Chem.* **75**, 5336–5344 (2003).
278. Smith, E. A., Park, S., Klein, A. T. & Lee, Y. J. Bio-oil Analysis Using Negative Electrospray Ionization: Comparative Study of High-Resolution Mass Spectrometers and Phenolic versus Sugarcane Components. *Energy Fuels* **26**, 3796–3802 (2012).
279. Jarvis, J. M., Page-Dumroese, D. S., Anderson, N. M., Corilo, Y. & Rodgers, R. P. Characterization of Fast Pyrolysis Products Generated from Several Western USA Woody Species. *Energy Fuels* **28**, 6438–6446 (2014).
280. Abdelnur, P. V., Vaz, B. G., Rocha, J. D., de Almeida, M. B. B., Teixeira, M. A. G. & Pereira, R. C. L. Characterization of Bio-oils from Different Pyrolysis Process Steps and Biomass Using High-Resolution Mass Spectrometry. *Energy Fuels* **27**, 6646–6654 (2013).
281. Santos, J. M., dos Santos, L. O., Silva, F. F., Eberlin, M. N. & Wisniewski, A. Comprehensive Characterization of Second-Generation Biofuel from Invasive Freshwater Plants by FT-ICR MS. *Bioenergy Res.* **8**, 1938–1945 (2015).
282. Hartman, B. E. & Hatcher, P. G. Hydrothermal liquefaction of isolated cuticle of *Agave americana* and *Capsicum annuum*: Chemical characterization of petroleum-like products. *Fuel* **156**, 225–233 (2015).
283. Miettinen, I., Makinen, M., Vilppo, T. & Janis, J. Compositional Characterization of Phase-Separated Pine Wood Slow Pyrolysis Oil by Negative-Ion Electrospray Ionization Fourier Transform Ion Cyclotron Resonance Mass Spectrometry. *Energy Fuels* **29**, 1758–1765 (2015).
284. Jarvis, J. M., McKenna, A. M., Hilten, R. N., Das, K. C., Rodgers, R. P. & Marshall, A. G. Characterization of Pine Pellet and Peanut Hull Pyrolysis Bio-oils by Negative-Ion Electrospray Ionization Fourier Transform Ion Cyclotron Resonance Mass Spectrometry. *Energy Fuels* **26**, 3810–3815 (2012).
285. Sudasinghe, N., Dungan, B., Lammers, P., Albrecht, K., Elliott, D., Hallen, R. & Schaub, T. High resolution FT-ICR mass spectral analysis of bio-oil and residual water soluble organics produced by hydrothermal liquefaction of the marine microalga *Nannochloropsis salina*. *Fuel* **119**, 47–56 (2014).
286. Yan, H.-L., Zong, Z.-M., Li, Z.-K. & Wei, X.-Y. Characterization of bio-oils from the alkalolyses of sweet sorghum stalk by electrospray ionization Fourier transform ion cyclotron resonance mass spectrometry. *Fuel* **160**, 596–604 (2015).

287. Yan, H.-L., Zong, Z.-M., Li, Z.-K., Kong, J., Zheng, Q.-X., Zhao, M.-X., Li, Y. & Wei, X.-Y. Insight into the Chemical Complexity of Soluble Portions from Cornstalk Methanolysis. *Energy Fuels* **30**, 3020–3029 (2016).
288. Kekalainen, T., Venalainen, T. & Janis, J. Characterization of Birch Wood Pyrolysis Oils by Ultrahigh-Resolution Fourier Transform Ion Cyclotron Resonance Mass Spectrometry: Insights into Thermochemical Conversion. *Energy Fuels* **28**, 4596–4602 (2014).
289. Tessarolo, N. S., Silva, R. V. S., Vanini, G., Casilli, A., Ximenes, V. L., Mendes, F. L., de Rezende Pinho, A., Romão, W., de Castro, E. V. R., Kaiser, C. R. & Azevedo, D. A. Characterization of thermal and catalytic pyrolysis bio-oils by high-resolution techniques: 1H NMR, GC × GC-TOFMS and FT-ICR MS. *J. Anal. Appl. Pyrolysis* **117**, 257–267 (2016).
290. Alsbou, E. & Helleur, B. Direct Infusion Mass Spectrometric Analysis of Bio-oil Using ESI-Ion-Trap MS. *Energy Fuels* **28**, 578–590 (2014).
291. Benderdour, M., Bui-Van, T., Dicko, A. & Belleville, F. In vivo and in vitro effects of boron and boronated compounds. *J. Trace Elem. Med. Biol.* **12**, 2–7 (1998).
292. Jarvis, J. M., Billing, J. M., Hallen, R. T., Schmidt, A. J. & Schaub, T. M. Hydrothermal Liquefaction Biocrude Compositions Compared to Petroleum Crude and Shale Oil. *Energy Fuels* **31**, 2896–2906 (2017).
293. Cole, D. P., Smith, E. A., Dalluge, D., Wilson, D. M., Heaton, E. A., Brown, R. C. & Lee, Y. J. Molecular characterization of nitrogen-containing species in switchgrass bio-oils at various harvest times. *Fuel* **111**, 718–726 (2013).
294. Leonardis, I., Chiaberge, S., Fiorani, T., Spera, S., Battistel, E., Bosetti, A., Cesti, P., Reale, S. & De Angelis, F. Characterization of Bio-oil from Hydrothermal Liquefaction of Organic Waste by NMR Spectroscopy and FTICR Mass Spectrometry. *Chemsuschem* **6**, 160–167 (2013).
295. Croce, A., Battistel, E., Chiaberge, S., Spera, S., De Angelis, F. & Reale, S. A Model Study to Unravel the Complexity of Bio-Oil from Organic Wastes. *Chemsuschem* **10**, 171–181 (2017).
296. Chiaberge, S., Leonardis, I., Fiorani, T., Cesti, P., Reale, S. & De Angelis, F. Bio-Oil from Waste: A Comprehensive Analytical Study by Soft-Ionization FTICR Mass Spectrometry. *Energy Fuels* **28**, 2019–2026 (2014).
297. Staš, M., Chudoba, J., Kubička, D. & Pospíšil, M. Chemical Characterization of Pyrolysis Bio-oil: Application of Orbitrap Mass Spectrometry. *Energy Fuels* **29**, 3233–3240 (2015).
298. Sanguineti, M. M., Hourani, N., Witt, M., Sarathy, S. M., Thomsen, L. & Kuhnert, N. Analysis of impact of temperature and saltwater on *Nannochloropsis salina* bio-oil production by ultra high resolution APCI FT-ICR MS. *Algal Res.-Biomass Biofuels Bioprod.* **9**, 227–235 (2015).
299. Smith, E. A. & Lee, Y. J. Petroleomic Analysis of Bio-oils from the Fast Pyrolysis of Biomass: Laser Desorption Ionization–Linear Ion Trap–Orbitrap Mass Spectrometry Approach. *Energy Fuels* **24**, 5190–5198 (2010).



---

## *Chapter II*

---

# *Materials & methods*

## Table of Contents

I.	Introduction.....	97
II.	Production of the pyrolysis bio-oils.....	98
II.A.	Fast pyrolysis experiments .....	98
II.A.1.	Pyrolysis parameters and reactor.....	98
II.A.2.	Raw material.....	98
II.A.3.	Raw bio-oil production by pyrolysis .....	99
II.B.	Catalytic deoxygenation .....	100
II.B.1.	Upgraded bio-oil production .....	100
III.	Characterization of the pyrolysis bio-oils by petroleomic approach .....	101
III.A.	Introduction.....	101
III.B.	Ionization sources.....	102
III.B.1.	Electrospray ionization .....	102
III.B.2.	Laser desorption ionization .....	108
III.B.3.	Atmospheric pressure photoionization.....	116
III.C.	Fourier Transform Ion Cyclotron Resonance Mass Spectrometry .....	119
III.C.1.	Introduction.....	119
III.C.2.	Cyclotron motion.....	119
III.C.3.	Trapping potential and magnetron motion.....	122
III.C.4.	Ion excitation in the ICR cell .....	124
III.C.5.	Detection, treatment, and conversion of the ICR signal .....	128
III.C.6.	Data acquisition with a 9.4 T Ion Spec mass spectrometer.....	130
III.C.7.	Data assignment .....	134
III.C.8.	Data graphical representations .....	136
IV.	Other studies in mass spectrometry .....	139
IV.A.	Introduction.....	139
IV.B.	ESI-Linear ion trap (LTQ Velos Pro-Thermo Scientific) .....	139
V.	Conclusion .....	141
VI.	References.....	142

## I. Introduction

This chapter is dedicated to the description of the materials and methods used in this study.

In the first part, the production of the raw and upgraded bio-oils, which will be characterized in the next chapters, is detailed. The different studied bio-oils were produced by the GREENER research group at the *Laboratoire Réactions et Génie des Procédés* (UMR CNRS 7274) in Nancy. More precisely, this group has designed different pyrolysis reactors and has a strong knowledge in biomass pyrolysis processes. This team also adopts a multi-technic approach to characterize the biomass and the pyrolysis products for which we bring the description of the heavy fraction of the bio-oil. In the field of bio-oil production, catalysts are also research area for its upgrading. For this study, the catalysts used for the bio-oil upgrading were produced at the *Institut de Chimie des Milieux et Matériaux of Poitiers* (UMR CNRS 7285) and will be briefly described.

The main objective of this study is focused on the extended molecular characterization of the raw or upgraded bio-oils. For this purpose, Fourier transform ion cyclotron mass spectrometer was used to reach a high mass measurement accuracy and a high mass resolving power to resolve such a complex organic material. Additionally, in a second part, different ionization sources coupled to the mass spectrometer will be presented. Thus, the electrospray ionization (ESI), the laser desorption-ionization (LDI), the matrix assisted LDI (MALDI), and the atmospheric pressure photoionisation (APPI) principles will be detailed. The principle of the Fourier transform-ion cyclotron resonance mass spectrometry (FT-ICR MS) will also be described.

A typical bio-oil FT-ICR mass spectrum is very complex, with thousands of peaks. Therefore, it has to be well-calibrated before assignment. The calibration and the signal assignment are achieved by means of different and specific software (Omega and Composer). The huge amount of data has also to be presented by using various graphical representations to facilitate both the interpretation and the comparison of different experiments. The obtention of these graphical representations will be described.

The last part of this chapter will be briefly dedicated to the principle of the linear ion trap mass spectrometer, which has been used as complementary analytical methods.

## II. Production of the pyrolysis bio-oils

### II.A. Fast pyrolysis experiments

#### II.A.1. Pyrolysis parameters and reactor

The used lab-scale reactor (**Figure II-1**) is a quartz microfluidized bed reactor whose inner diameter and height are about 20 mm and 15 cm, respectively.<sup>1</sup> The bed is made of 150-300  $\mu\text{m}$  particles of silica sand which is placed above a sintered plate of 5 mm thickness made of 150  $\mu\text{m}$  silica sand particles. All these components are carefully chosen to enable a good fluidization. This latter feature is achieved by means of fluidizing gas of pure nitrogen arriving simultaneously in the reactor from bottom and from above. The first one has a constant flow rate of 500  $\text{mL}\cdot\text{min}^{-1}$  and the second one is fixed at 200  $\text{mL}\cdot\text{min}^{-1}$ . It is used as sweep gas. The reactor is placed in a homemade electric furnace with a quartz window which ensures the observation of the fluidization during pyrolysis. The temperatures of the furnace and the microfluidized bed are measured by temperature controllers connected to two distinct thermocouples.

The microfluidized bed has been used in two different modes: continuous or stepwise injection of biomass. For the study of the raw bio-oil (no catalyst), the biomass is introduced by a home-made microfeeder with a 10  $\text{g}\cdot\text{h}^{-1}$  flow rate of biomass particles. To avoid the sand to go up through the injection rod,  $\text{N}_2$  is injected with a 200  $\text{mL}\cdot\text{min}^{-1}$  flow rate. The different flow rates are controlled by mass flowmeters.

For the catalytic pyrolysis of biomass, stepwise injections of wood cylinders were performed within the fluidized bed, only with sand (raw bio-oil) or with zeolites (catalyst).

#### II.A.2. Raw material

Two different raw materials are investigated: Miscanthus (*Miscanthus Giganteus*), from Lorraine (France), and oak, from the Rhône department (France).<sup>2</sup> The raw material was grinded to powder with particle size between 40 and 100  $\mu\text{m}$ . Typically 2 grams are introduced into the microfluidized bed by experiment (in continuous feeding mode).

Oak cylinders of 0.6 g (6 mm x 20 mm) were injected in stepwise mode to study the effect of catalyst on bio-oil composition.<sup>3</sup>



### II.A.3. Raw bio-oil production by pyrolysis

The temperature of the microfluidized bed is kept at 500 °C. The gas-phase residence time in these conditions is about 1.2 s. The produced bio-oil vapors are transported to 3 cold traps via a heated line set at 350 °C to prevent condensation. The first cooler is placed in an ice-water bath at 0 °C which is aimed to trap water and heavy species. The second and third coolers both contain a mixture of propanol and liquid nitrogen, which allows keeping the temperature at -60 °C. A bubbler containing methanol is placed on the line after the three cryogenic traps. At the end of the pyrolysis, all the coolers and the pipes of the line are rinsed with 20 mL of methanol to collect the condensables. A resulting 20 mL bio-oil solution is thus obtained.

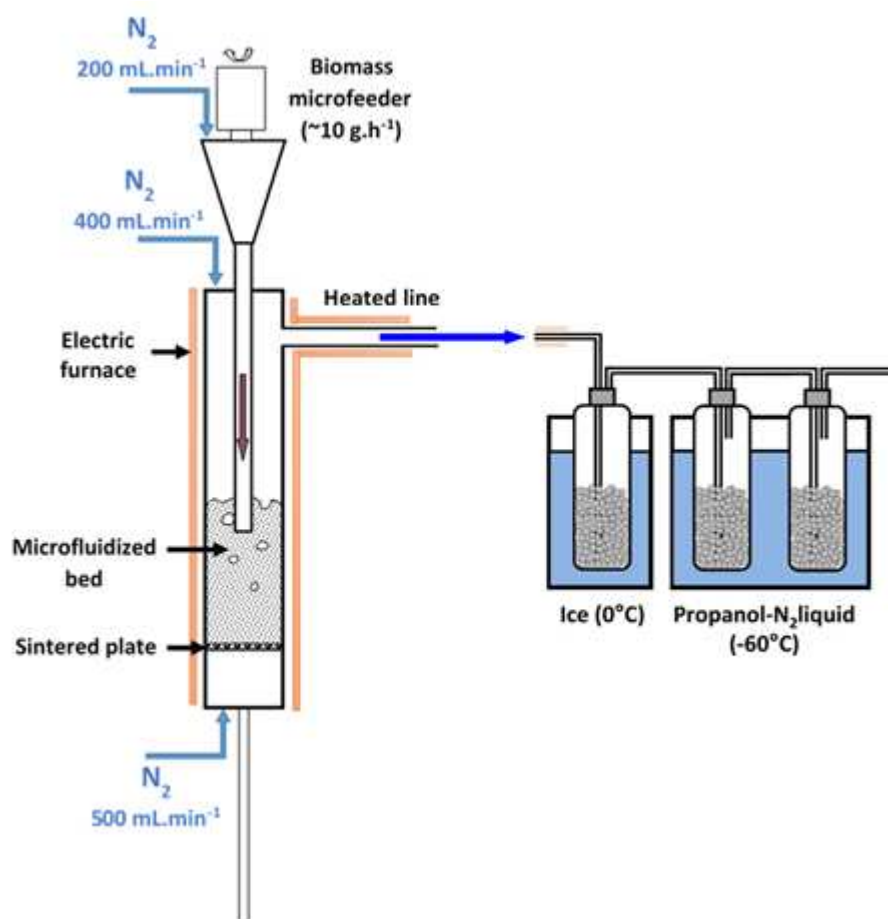


Figure II-1. Scheme of the microfluidized bed reactor and setup used to collect bio-oils<sup>1</sup>

## II.B. Catalytic deoxygenation

### II.B.1. Upgraded bio-oil production

Two different catalysts are used to reduce the oxygen amount of the different bio-oil components. The first one is a HZSM-5 parent zeolite and the second one is a hierarchical HZSM-5 zeolite. They only differ by their structure, as observed on the scanning electron and transmission electron microscopy images (**Figure II-2**).

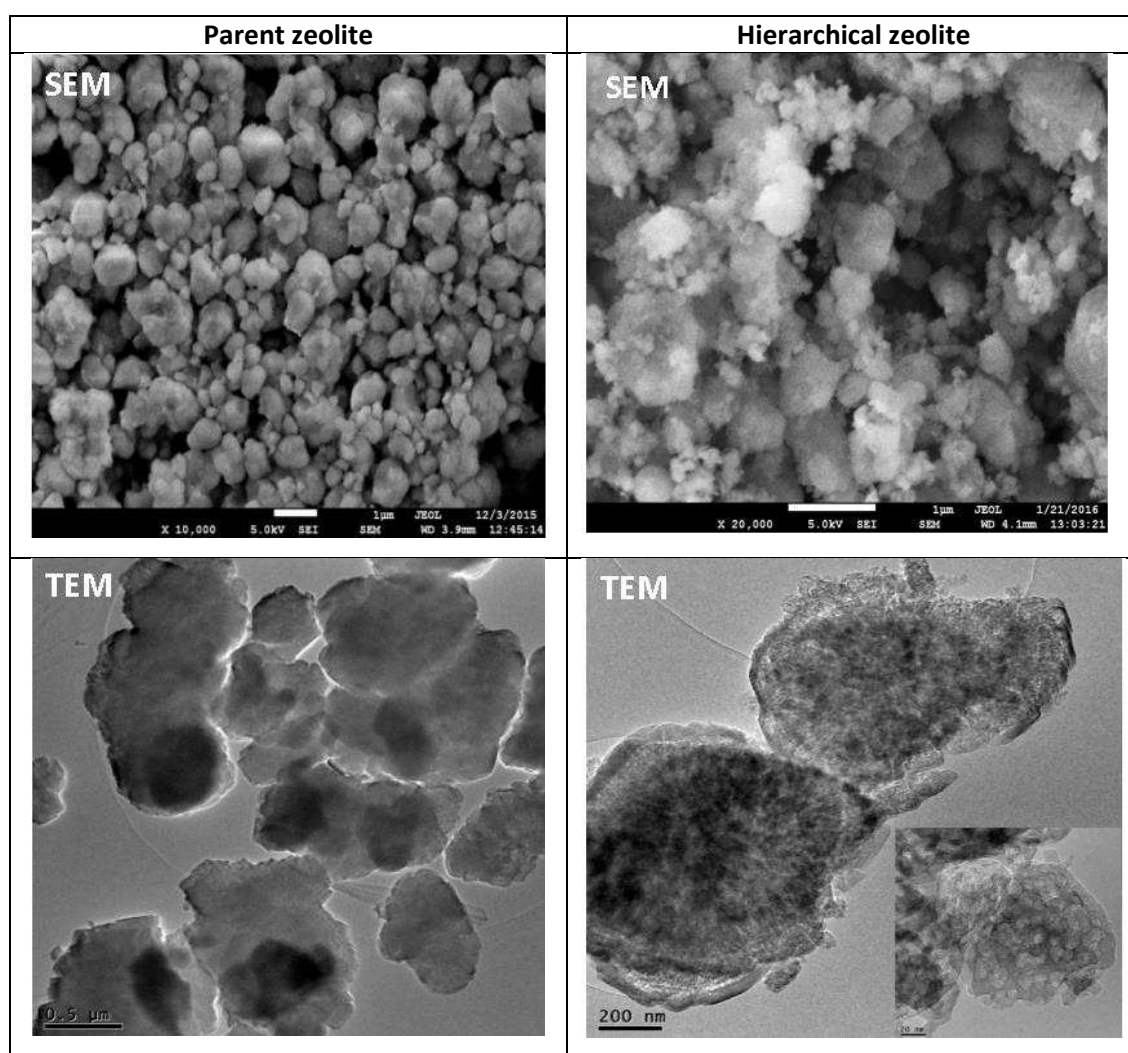


Figure II-2. Scanning electron (top) and transmission electron (bottom) microscopy images of parent (left) and hierarchical (right) zeolites before pyrolysis experiments (From the publication "Catalytic fast pyrolysis of biomass: superior selectivity of hierarchical zeolite to aromatics" of Jia et al., *Green Chemistry*, accepted)

The parent zeolite contains micropores and mesopores whose volumes represent 0.17 and 0.07 cm<sup>3</sup> for 1 g of zeolite, respectively. The hierarchical one, obtained by desilication with NaOH of the parent zeolite, is also composed of micropores (0.15 cm<sup>3</sup>.g<sup>-1</sup>) but is mainly characterized by the higher volume of the mesopores (0.38 cm<sup>3</sup>.g<sup>-1</sup>). Five grams of zeolite

(parent or hierarchical HZSM-5) are initially introduced in the fluidized bed which is firstly heated at 110 °C for 2 hours and secondly at 500 °C for 2 additional hours. The oak cylinders were injected by means of a pulsed mode in the microfluidized bed. One-cylinder injection represents a biomass-to-catalyst ratio of  $\approx 0.12$  (0.6 g /5 g). The pyrolysis parameters as well as the recovering of upgraded bio-oils are identical to what it was described in the previous section.

### III.Characterization of the pyrolysis bio-oils by petroleomic approach

#### III.A. Introduction

In this study the non-targeted petroleomic approach is employed to characterize raw and upgraded pyrolysis bio-oils. This method was introduced by Marshall for the characterization of petroleum crude oil by high resolution Fourier transform ion cyclotron resonance mass spectrometry.<sup>4,5</sup> In this method, the investigated sample is directly analyzed without prior separation. Typically, the different sample components are ionized by field desorption (FD), ESI, APPI, LDI or atmospheric pressure chemical ionization (APCI). Due to the huge number of crude oil compounds, very high resolution mass spectrometer has to be used to distinguish the different features in one mass spectrum. FT-ICR and FT-Orbitrap mass spectrometry are well suited in the petroleomic field.<sup>6</sup> Thus, this non-targeted approach enables to assign more than 30 000 different elemental formulae for a given sample.<sup>7</sup> For very complex mixtures, such as bio-oils from biomass pyrolysis, this approach may be used. The ability of this technique enables to observe a broader range of compounds at the same time, in terms of chemical functions and weight, compared to what it may be obtained by liquid or gas chromatography methods.

As mentioned in Chapter I, no universal ionization source is able to simultaneously ionize different components of a bio-oil. Each ionization source possesses specificity in terms of ionization efficiency for different classes of compounds. In this study, ESI, LDI, MALDI, and APPI are used in order to achieve a bio-oil composition description as extensive as possible. The principle of each of these methods will be described in the following sections. This will allow to easily assess their complementarity.

The principle of the Fourier transform ion cyclotron resonance will be also given which will allow to understand to what extent this technique is a method of choice for the bio-oil characterization and more generally to study complex systems.

### III.B. Ionization sources

#### III.B.1. Electrospray ionization

##### III.B.1.a. Introduction

The first publication dealing with *electrospray ionization* (ESI) was published by Zeleny *et al.* in 1917.<sup>8</sup> They demonstrated that a spray composed of small droplets can be obtained by applying an electric field between a counter electrode and a capillary in which a solution is infused. Some decades later, the research works of Dole *et al.*<sup>9</sup> and Fenn *et al.*<sup>10</sup> assessed that the coupling of ESI with mass spectrometer enabled the determination of the mass of large molecules. Actually, ESI offers the advantage to ward the analytes off dissociation phenomenon during the ionization and ensures to produce, in some cases, multi-charged ions. Therefore, high-molecular mass compounds such as peptides or proteins can be analyzed. For these reasons, ESI can be considered as a soft ionization technique. ESI can also ionize small polar compounds.

##### III.B.1.b. Principles of ESI

In ESI, the analytes are initially in liquid phase and are transferred to the gas phase according to a desolvation/ionization phenomenon. First, analytes are injected through a steel capillary tube with a small flow rate (1-20  $\mu\text{L}\cdot\text{min}^{-1}$ ) under atmospheric pressure. In the absence of electric field, the solution forms a meniscus at the outlet of the capillary (**Figure II-3**). The application of an electric field below a given value named “onset voltage”, between the capillary and the counter-electrode, is responsible of a small deformation of the meniscus. For voltage in the 1 to 6 kV range, the charge accumulation is high enough to ensure that the electrostatic force becomes more important than the surface tension force. Then, the produced electric field ( $10^{-6} \text{ V}\cdot\text{m}^{-1}$ ) leads to the formation of a Taylor cone.<sup>11</sup> The polarity of the electric field defines the nature of the ions at the surface of the meniscus. Cations are formed by applying a negative electric field and *vice-versa*. Moreover, an ESI source has to be

regarded as an electrochemical cell, as it is described in the **Figure II-4**. In positive ion mode, an oxidation process may occur at the outer part of the capillary while reduction takes place on the counter-electrode.

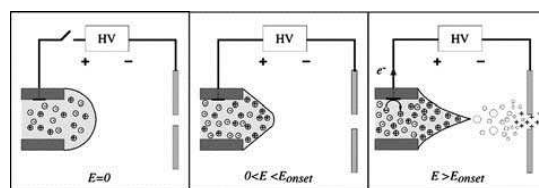


Figure II-3. Shape of the solvent at the outlet capillary according to the value of the applied voltage<sup>12</sup>

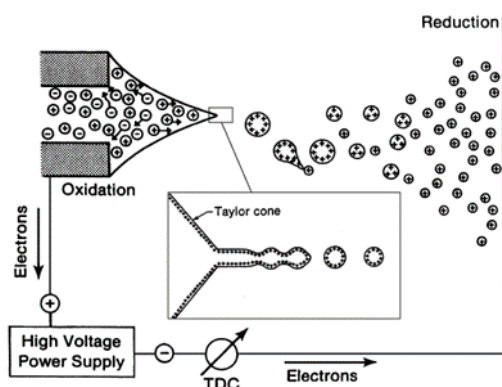


Figure II-4. Gas-phase ion formation in the ESI source, in positive detection mode<sup>13,14</sup>

At the Taylor cone apex, the Coulomb repulsive forces lead to the ejection of highly charged droplets. The resulting jet is directed to the counter electrode. The polarity of the charges accumulated at the surface of the micrometric droplets is depending on the polarity of the electric field (**Figure II-4**). Between the apex cone and the counter-electrode, the radius of the droplet volume decreases because of the solvent evaporation. This process is due to the ion source temperature, the use of desolvation gas ( $N_2$  in our case), and the difference of pressure between the source and the mass spectrometer. Consequently, the charge density continuously increases. When the electrostatic force resulting from the repulsion of charges of the same polarity overcomes the conservative force of the droplet, the Rayleigh limit of charge is reached (**Equation II-1**). At this limit, the droplet explodes, which leads to the formation of smaller droplets. This phenomenon, also called Coulomb explosion, repeats up to the formation of ions in the gas phase. This ultimate stage is not yet fully understood and explained. Two models have been proposed to explain the formation of the ions (**Figure II-5**).

(Eq. II-1)  $Z_{\text{Rayleigh}} \cdot e = 8\pi r_{\text{max}}^{3/2} \sqrt{\gamma \epsilon_0}$  with  $Z$  the charge number,  $e$  the elementary charge,  $r$  the droplet radius,  $\gamma$  the surface tension, and  $\epsilon_0$  the electric permittivity of the surrounding medium.

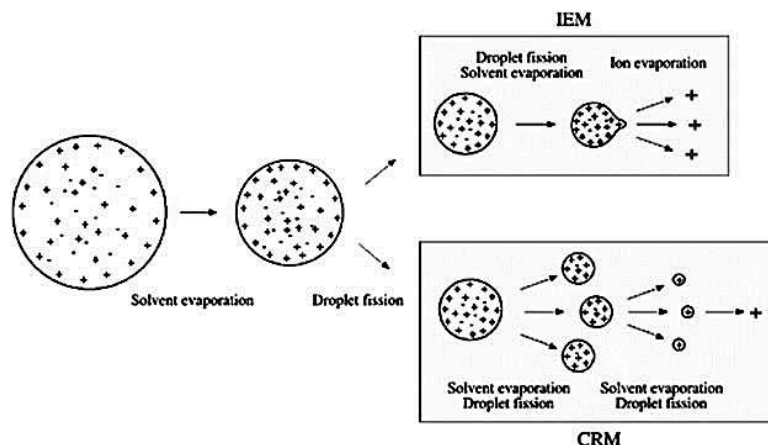


Figure II-5. Ion evaporation (IEM) and charge-residue (CRM) models for the formation of ions in (+) ESI<sup>12</sup>

The first model is called the charged-residue model (CRM) and was proposed by Dole *et al.*<sup>9</sup> The repetition of the Coulomb explosions leads to the formation of droplets made of a single solvated ion. The evaporation of the solvent leads to the production of the gaseous ions.

The second model, the so-called ion evaporation model (IEM), was developed by Iribarne and Thomson.<sup>15</sup> In high electric field, the density of the charges, at the surface of the droplet, induces its deformation and the appearance of a small “Taylor cone” which may act as an emitter of individual gas phase ion. According to these authors, this is thermodynamically more favorable than successive Coulomb explosions.

The debate of the comprehension of ESI process is still ongoing but both phenomena may simultaneously occur. The predominance of one of them is highly analyte/ion dependent. The IEM theory is more suitable for explaining the formation of small single charge ions whereas CRM is more appropriate to explain the formation of multicharged species by ESI for large molecules, such as proteins.<sup>16</sup>

The ion may be formed in solution by electrochemical processes or by ion attachment occurring during ESI event. In solution, the acid-base (Brönsted and Lewis) equilibrium between the analyte and the solvent or another electrolyte governs the ionization (protonation, for example). Thus, protic solvent with a high polarity will better ionize the analytes and increase the ESI sensitivity. The addition of dopant such as ammonium acetate or trifluoroacetic acid (TFA) may also ensure the displacement of the acid/base equilibrium of the analyte. In the gas phase, desolvated molecule can also be ionized. In that case, the process is dependent of the gas phase proton affinity or the gas phase basicity. Moreover cation or anion attachment may be involved to produce pseudomolecular adduct.

### III.B.1.c. Parameters influencing the electrospray ionization

Electrospray ionization is sensitive to various features, only the most critical will be presented.

The onset voltage ensures the formation of the Taylor cone and the generation of the droplet jet. Typically, a low voltage enables to observe high and broader distribution of charges states. Low charge states are generally observed with a strong electric field. The use of a high electric field can also lead to a dissociation of the covalent and non-covalent bounds.<sup>17,18</sup>

The pH of the solution is an important parameter. At low pH, protonation is generally promoted, which ensures the formation of  $[M+nH]^{n+}$  cations. Conversely, at high pH, some functional groups are deprotonated which leads to the detection of  $[M-nH]^{n-}$  anions. Therefore, addition of acid or alkaline solution can be interesting to increase the sensitivity of the ESI source.

Similarly, cationization and anionization agents can be added to the solution to increase the ionization yield. Hence, sodium acetate or ammonium chloride can form  $[M+nNa]^{n+}$  or  $[M+nCl]^{n-}$  adducts, for example. The oxygen atoms through acid/base Lewis interactions have the ability to form strong ionic bounds with cations such as sodium or potassium ion. The use of salts such as ammonium or sodium acetate, can also be responsible of issues by promoting the formation of ionic cluster ions. Consequently, their concentrations in the solution have to be low to avoid the formation of crystallite in the source and/or cluster ions. Indeed, the addition of high quantities of salts generally leads to signal suppression events.<sup>19</sup>

The ions generally observed in ESI mass spectrometry are even-electron species such as  $[M+H]^+$  or  $[M-H]^-$ . In specific cases, molecular radical ions  $M^{\bullet+/\bullet-}$  may be obtained such as what it is observed with polyaromatic hydrocarbons.<sup>20</sup>

The nature of the solvent is also important in respect with its polarity and the ability for protic ones to favor the proton transfer. The molecule conformation may also be affected by the nature of the solvent.<sup>21</sup> The experimental conditions that favor the unfolded conformation of proteins lead to a broad distribution of charges and high charge states by an important accessibility of ionization (protonation) sites. The nature of the spray solvent has also a significant influence on the formation of the Taylor cone and the droplets. The viscosity

of the solvent affects the flow of the solution and the analyte solvation. Moreover, for polar solvents, hydrogen bonds increase the cohesion of the droplet and consequently, the ion formation process may be disfavored.

The efficiency of the ionization by electrospray is also dependent on the used flow rate. The solution containing the analyte may be introduced in the source with flow rates ranging from  $\text{nL}\cdot\text{min}^{-1}$  (nanoESI) to  $\text{mL}\cdot\text{min}^{-1}$ . At high flow rates, the generated droplets are larger and the charge density is lower, which reduces the sensitivity. By reducing the flow, the sensitivity increases. The common flow rates are in the  $\mu\text{L}\cdot\text{min}^{-1}$  range. In these conditions, the ESI is regarded as a “concentration-sensitive” technique. Small changes in the flow rate generally do not affect the signal-to-noise ratio.<sup>22</sup>

#### *III.B.1.d. ESI source design*

Different ESI source designs have been developed in order to improve parameters such as ion transmission or robustness of operation. Nevertheless, they all present a counter-electrode connected, by a HV supply, to a metallic capillary in which the sample is infused. Moreover, they operate at atmospheric pressure, in a heated source with a (heated) desolvation gas. The spray passes through a sampling cone or a capillary and expands into the first pumping stage. Finally, a last skimmer or lens is crossed and the ions are guided to the analyzer under reduced pressure.

In this study, the interface used in the main part of the experiments to investigate bio-oils by FT-ICR MS is a Z-spray configuration (**Figure II-6**). The two consecutive  $90^\circ$  angles formed by the spray ensure the elimination of the neutrals and large droplets. It also limits the pollution of the first hexapole of the mass spectrometer. It was also demonstrated that this source geometry leads to weaker signal suppressions by the additives than other source designs (orthogonal and on-axis geometries).<sup>23</sup> However, the signal obtained with this kind of source is dramatically dependent on the spacing between the capillary and the cone.<sup>24</sup> Indeed, it was evidenced that a larger capillary-cone distance requires a higher capillary voltage to maintain a stable spray and favors the high mass species detection.



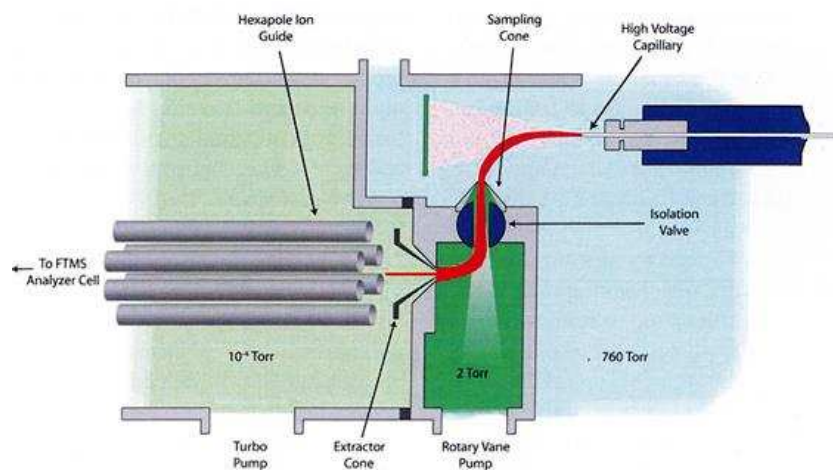


Figure II-6. Micromass ESI source with Z-spray configuration (Ion Spec)

### III.B.1.e. Conclusion

Electrospray ionization source is known to be a soft ionization technique that limits the fragmentation phenomenon. Its combination with mass spectrometers makes ESI a versatile interface for different applications. Different parameters have to be considered to optimize electrospray ionization. It was previously detailed that the ESI principle is notably based on the ability of the analytes to become ionized in liquid or gas phase. This technique is consequently dedicated to medium polar to ionic compounds whose mass varies from a few tens of amu to MDa.

As part of bio-oil characterization, ESI FT-ICR MS analytical methods have been developed in both positive and negative ion detection modes. The effects of the dopant addition on the chemical compositions were investigated with a raw bio-oil from *Miscanthus pyrolysis*.<sup>25</sup> Furthermore, influence of the solvent composition and probe temperature was studied.

However, for a complex mixture such as bio-oils, part of the components may be poorly ionized by ESI. Therefore, alternative ionization sources have to be employed to achieve an extensive description of bio-oil composition. More specifically, laser desorption ionization (LDI) and atmospheric pressure photoionization (APPI) are known to be less sensitive to the polarity of the analyte and more suited for the large aromatic compound analysis.

### III.B.2. Laser desorption ionization

#### III.B.2.a. Introduction

The first works dealing with the use of laser desorption ionization (LDI) coupled to mass spectrometry were published in the 60' by Fenner<sup>26</sup> and Vastola<sup>27</sup>. This method ensures to produce gaseous ions from a solid sample under laser-matter interaction. It is mainly used for the low mass range organic and inorganic compounds that can absorb significantly at the laser wavelength. Typically, UV and Vacuum UV (VUV) laser wavelengths are used. Depending on the laser fluence, two regimes have to be distinguished.<sup>28</sup> For laser fluence lower than a given threshold, desorption process is observed. If the laser fluence is above this threshold, ablation phenomenon takes place. This latter regime deals with a massive removal of material from the sample and often induces important fragmentation and recombination. For these two regimes, ionic species from the laser irradiated samples are expelled and their  $m/z$  can be measured by mass spectrometer. While the main part of ions generated by ablation are due to intense fragmentation, laser desorption may lead to the formation of molecular radical and pseudomolecular ions.

#### III.B.2.b. Principles of LDI

A laser beam is focused on a small surface ( $10^{-4}$ - $10^{-3}$  cm<sup>2</sup>) of a solid sample, which ensures its vaporization. Haglund described the desorption phenomenon into four steps.<sup>29</sup> The first one is the laser energy absorption of the sample by single or multi-photon processes. The energy transfer is governed by the Beer's Law (**Equation II-2**). The photons of the laser beam possess an energy  $h\nu$  that is absorbed by the sample according to its absorption coefficient  $\alpha$  (**Figure II-7**). This energy is then converted by radiative and non-radiative relaxation processes. An excited state is reached, which causes ejection of species in the gas phase. Thus, a more or less dense plume or microplasma, according to the used laser energy, is formed which is mainly composed of atoms, neutrals, and ions, as illustrated on **Figure II-8**. Besides, ionization can also happen in the gas phase by different processes such as proton capture according to proton affinity (PA).

In the desorption regime, internal energy of these species is low and fragmentation event is avoided or at least limited.

(Eq. II-2) 
$$H = H_0 * e^{-\alpha z}$$
 with laser fluence  $H$  into the sample at  $z$  depth; the laser fluence at the sample surface  $H_0$ , and  $\alpha$  the linear absorption coefficient of chromophores

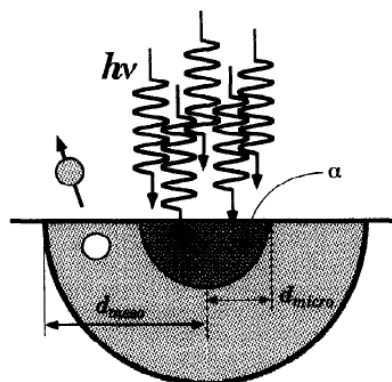


Figure II-7. Characteristic length scales for a laser-excited surface region in the vicinity of an absorbing chromophore.  $\alpha$ : linear absorption coefficient of chromophore;  $d_{\text{meso}}$ : characteristic mesoscopic length scale observed in laser ablation;  $d_{\text{micro}}$ : characteristic microscopic length scale observed in laser desorption.<sup>29</sup>

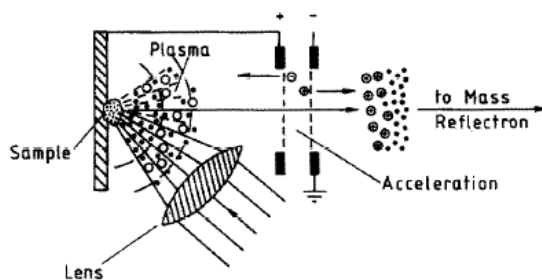


Figure II-8. Plasma formation by laser desorption on a solid surface<sup>30</sup>

The ejection of matter from the surface is stepwise. The photon of the laser pulse, whose duration is of nanosecond order (3-10 ns for UV lasers and 6-200 ns for IR lasers), may also interact with the expelled molecules in the gas phase. Different laser wavelengths may be used in the IR or UV range. Consequently, the molecule or the atom in gas phase can be vibrationally or electronically excited after the absorption of one photon.<sup>31</sup> If the quantum energy  $E=h\nu$  of the absorbed photon is greater than the ionization energy ( $E_i$ ) of one specie, an electron is emitted and a cation is formed. If  $h\nu$  is superior to the sum of  $E_i$  and bond energy, photodissociation may occur. Finally, if  $h\nu$  is not sufficient enough to induce one of the previous processes, two events may occur depending on the lifetime  $\tau$  of the excited species. For low value of  $\tau$ , the excited species undergo radiative process or non-radiative process by collisions and are quickly de-excited. If  $\tau$  is long enough, the absorption of a second photon may occur and ionization and/or fragmentation processes can happen.

Typically, only singly-charged ions of a molecule or fragment are produced by LDI in the form of radical ions  $[M]^{•+/-}$  and cations such as  $[M+H]^+$ ,  $[M+Na]^+$ , or anions  $[M-H]^-$ ,  $[M-Cl]^-$ .

### III.B.2.c. Parameters influencing the LDI ionization

As it was mentioned, in respect with the laser fluence ( $F$ ), the laser-matter interaction may lead to desorption or ablation phenomenon. Another laser parameter is the laser irradiance ( $I$ ) that includes the time duration of the laser pulse (**Equations II-3.a.** and **b.**).<sup>32</sup>

$$\text{(Eq. II-3)} \quad \mathbf{a.} \quad F = \frac{E}{S} \quad \mathbf{b.} \quad I = \frac{F}{\tau} \quad \text{with the laser fluence } F, \text{ the laser energy } E, \text{ the targeted surface } S, \text{ the laser irradiance } I, \text{ and the laser pulse duration } \tau.$$

At very low laser irradiance, the laser-matter interaction leads only to radiative (emission of photon) or non-radiative (emission of heat) process. At higher fluence, a first threshold is reached and desorption occurs. If the irradiance is still increased, desorption-ionization occurs and simultaneous vaporization and ionization of the compounds are carried out during laser irradiation. Finally, for the highest laser irradiance, ablation is observed with the eruption of the material and the formation of a deep crater at the surface of the sample.

Thus, the time duration of the laser pulse is an important parameter. Typically, it is about few ns, but shorter pulses in the ps time scale range may be used. Short laser pulses are known to limit fragmentation processes but they disfavor photoionization in the gas phase.

### III.B.2.d. Principles of matrix-assisted laser desorption/ionization

The main drawback of LDI is the occurrence of fragmentation events upon the laser-matter interaction. To limit the extensive activation of the analytes upon laser illumination, Karas and Hillenkamp, in the late 1980, proposed to mix the analytes with small molecules, the so-called matrix.<sup>33,34</sup> The matrix-assisted laser desorption ionization (MALDI) is known to be a softer method than LDI. This technique is useful for the analysis of a wide range of compounds. Indeed, it is widely used for the characterization of small molecules as well as macromolecules or polymers.<sup>35</sup> The matrix is a small organic molecule with a stronger absorption coefficient  $\alpha$  than the analyte, at the used laser wavelength. Different sample preparations are used to finally obtain a co-crystal of the matrix with the analyte. Typically, the matrix and the analyte are solubilized in a solvent that ensures evaporation to obtain a

solid deposit at the surface of the MALDI target. The matrix and analyte solutions may be mixed prior deposit. Alternatively, matrix solution may be spotted at the surface of the target, dried, and covered by a droplet of analyte solution. After drying, a second deposit of the matrix solution may be applied to obtain a thin layer of the matrix at the surface of the deposit. Another co-crystallization preparation is to grind matrix and analyte in solid phase. To increase the ionization, some dopants can be used such as TFA, to improve protonation, or alkaline or silver salt for oxygenated or pure hydrocarbon polymers.

At the same time, Tanaka also demonstrated the possibility to mix organic compounds with the analyte to limit fragmentation during LDI. Even if this latter preparation is no longer used, these works were awarded by a Nobel Prize in 2002.

MALDI experiments may be conducted with UV or IR laser, which specifically ensures the activation of the electronic and/or vibrational levels of the matrix. When MALDI is performed in UV range (the most developed method), photons are absorbed by the condensed phase, which causes the excitation of the matrix molecules and leads to a rapid heating of the crystals. This induces the localized sublimation of the portion of the crystals and the formation of a plume mainly formed of matrix molecules, which ensures the co-desorption of intact analytes. The Beer's law may be applied. The  $\alpha$  coefficient, given by the **Equation II-4**, is mainly relative to the matrix because of, on the one hand, the high absorption of the matrix and, on the other hand, the concentration ratio  $c_a/c_m$  that is between  $10^{-2}$  and  $10^{-4}$ .

(Eq. II-4) 
$$\alpha = \alpha_a \times c_a + \alpha_m \times c_m \approx \alpha_m \times c_m$$
 with  $\alpha_a$  and  $\alpha_m$ , the molar absorption coefficient and  $c_a$  and  $c_m$ , the concentration of the analyte and the matrix, respectively.

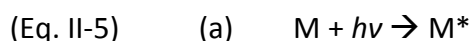
The matrixes used in UV-MALDI have to strongly absorb at the 266, 337 or 355 nm which are the commonly used laser wavelengths. Depending on the nature of the analyte, different matrixes may be used (**Table II-1**).

Analytes	Matrix	Abbreviation
Peptides/proteins	$\alpha$ -Cyano-4-hydroxycinnamic acid	CHCA
	2,5-Dihydrobenzoic acid (gentisic)	DHB
	3,5-Dimethoxy-4-hydroxycinnamic acid (sinapic)	SA
Oligonucleotides	Trihydroxyacetophenone	THAP
	3-Hydroxypicolinic acid	HPA
Carbohydrates	2,5-Dihydrobenzoic acid	DHB
	$\alpha$ -Cyano-4-hydroxycinnamic acid	CHCA
Synthetic polymers	Trihydroxyacetophenone	THAP
	Trans-3-indoleacrylic acid	IAA
	Dithranol	DIT
Organic molecules	2,5-Dihydrobenzoic acid	DHB
Inorganic molecules	2,5-Dihydrobenzoic acid	DHB
Lipids	Trans-2-(3-(4-ter-Butylphenyl)-2methyl-2-propenyliedine)malononitrile	DCTB
	Dithranol	DIT

Table II-1. Common UV-MALDI matrixes and their applications<sup>36</sup>

The first step of the MALDI process, which is the energy absorption, is well-known while the ionization phenomenon is still under intense discussion.<sup>37</sup> Several pathways have been suggested the last 30 years. It is now well accepted that the main part of the ionization takes place in the case where some “pre-ionized molecules” may be present in the deposit.

In the so-called “excited state proton transfer” model, the absorption of one photon by the matrix molecule  $M$  conducts to its excited state which may react with the analyte  $A$  or with another matrix molecule (**Equations II-5**). Thus, a neutral activated matrix molecule is able to capture a proton from the analyte and the  $[A-H]^-$  deprotonated molecule may be detected in negative ion mode.<sup>35</sup> Conversely, an activated protonated molecule of the matrix may transfer its proton to a neutral analyte that will be observed in positive ion mode.



*Excitation of the matrix molecule by photon absorption.*



*Proton transfer between the matrix molecule and the analyte.*



*Proton transfer between two matrix molecules.*

Such processes are governed by the gas phase basicity and the gas phase proton affinity of the matrix and the analyte. If the analyte presents significant absorption at the laser wavelength, photoionization events may also occur.

In 2000, Karas *et al.*<sup>38</sup> proposed the so-called “lucky survivor model” in which different pathways are suggested to explain the detection of singly-charged molecules. In solid phase, the analytes are charged due to pH of the matrix crystal which is often acidic. The electric neutrality of the deposit is maintained by the presence of counter-ions, initially present in the different solutions. Due to high matrix/analyte ratio, from  $10^2$  to  $10^4$ , the analytes are solvated by matrix molecules. The laser desorption of the sample produces small clusters and some of them contain one single analyte ion (**Figure II-9**). Some of these clusters carry an excess or a deficit of positive or negative charge. These singly charged components tend to get neutral by proton transfer between the analyte and the base or acid presents in the cluster. However, among the different combinations of analyte, counter-ion, acid or base that could exist, some analytes pass through the neutralization processes and are in the form of singly charged ion. These species are called “lucky survivors”. The ions typically formed by MALDI, but also by LDI, are given in the **Table II-2**.

Analytes	Positive ions	Negative ions
Non polar	$M^{+}$	$M^{-}$
Medium polarity	$M^{+}$ and/or $[M+H]^{+}$ , $[M+\text{alkali}]^{+}$ , {clusters $[2M]^{+}$ and/or $[2M+H]^{+}$ , $[2M+\text{alkali}]^{+}$ , adducts $[M+Ma+H]^{+}$ , $[M+Ma+\text{alkali}]^{+}$ } <sup>b</sup>	$M^{-}$ and/or $[M-H]^{-}$ , {clusters $[2M]^{-}$ and/or $[2M-H]^{-}$ , adducts $[M+Ma]^{-}$ , $[M+Ma-H]^{-}$ }
Polar	$[M+H]^{+}$ , $[M+\text{alkali}]^{+}$ , exchange $[M-H_n+\text{alkali}_{n+1}]^{+}$ high-mass anal. $[M+2H]^{2+}$ , $[M+2\text{alkali}]^{2+}$ {clusters $[nM+H]^{+}$ , $[nM+\text{alkali}]^{+}$ , adducts $[M+Ma+H]^{+}$ , $[M+Ma+\text{alkali}]^{+}$ }	$[M-H]^{-}$ exchange $[M-H_n+\text{alkali}_{n-1}]^{-}$ {clusters $[nM-H]^{-}$ , adducts $[M+Ma-H]^{-}$ }
Ionic <sup>a</sup>	$C^{+}$ , $[C_n+A_{n-1}]^{+}$ , $\{[CA]^{+}\}$	$A^{-}$ , $[C_{n-1}+A_n]^{-}$ , $\{[CA]^{-}\}$

Ma=matrix molecules

<sup>a</sup> comprising of cation  $C^{+}$  and anion  $A^{-}$

<sup>b</sup> enclosure in parentheses denotes rarely observed species

Table II-2. Ions formed by MALDI and LDI<sup>14</sup>

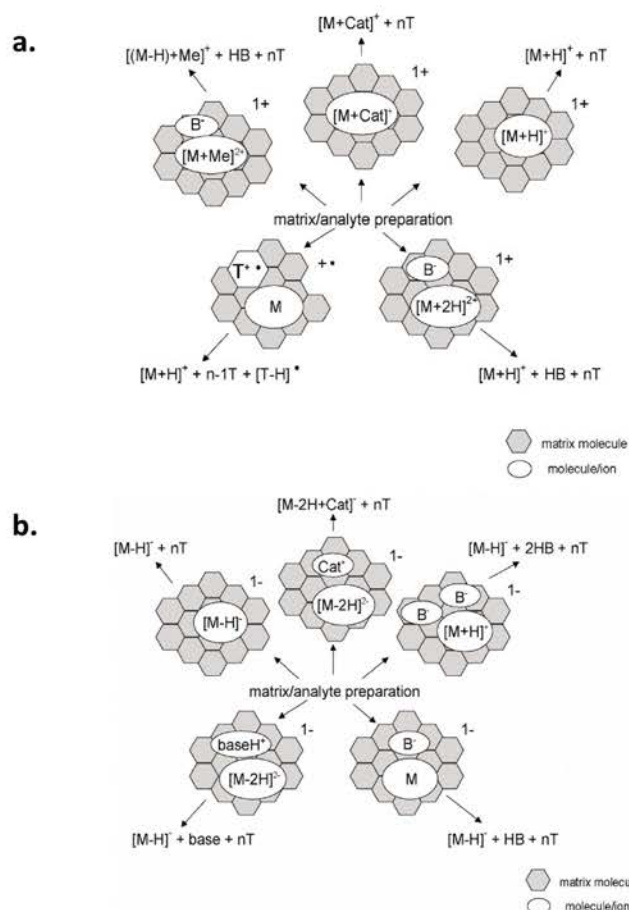


Figure II-9. Pathways proposed for the formation of singly charged ions from clusters. **a.** Positive ions, **b.** Negative ion. **M:** analyte molecule, **T:** matrix molecule, **Cat:** small cation, **Me:** Metal<sup>2+</sup>, **B:** base<sup>38</sup>

### III.B.2.e. Application of LDI and MALDI for bio-oil analyses in this study

In UV-MALDI, the 2,5-Dihydroxybenzoic acid (2,5-DHB) can be used in several applications (see **Table II-1**). For bio-oil analyses, two matrixes have been used: the 2,5-Dihydroxybenzoic acid and the 1,8-Bis(dimethyl-amino)naphthalene (DMAN) (**Figure II-10**). The first one is commonly used in MALDI experiments and absorbs at the 337 and 353 nm laser wavelengths. The second one, also known as proton sponge due to its high acidity constant ( $pK_a$  12.1), enables to perform MALDI analysis in negative detection mode.

The dried droplet method was used. The matrix solutions were prepared as follow. DMAN was dissolved in 1:1 water:methanol to a final concentration of 1 mg.mL<sup>-1</sup>. For the 2,5-DHB, a saturated solution was made by dissolving the matrix molecules in 1:1 water:acetonitrile. For the MALDI experiments, 1  $\mu$ L of bio-oil and 1  $\mu$ L of matrix solutions were thoroughly mixed and 1  $\mu$ L of the achieved solution deposited on the MALDI target plate. The droplet was let dry at atmospheric pressure before acquisition. For the LDI experiments,



the bio-oil was diluted in water to obtain a 7:3 bio-oil:water solution for 1  $\mu\text{L}$  deposits. A stainless steel target plate with 192 sample spots is used for LDI and MALDI measurements (**Figure II-11**).

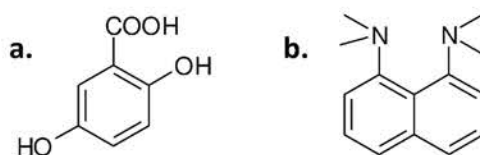


Figure II-10. Chemical representations of 2,5-Dihydroxybenzoic acid (a) and 1,8-Bis(dimethylamino)naphthalene (b)

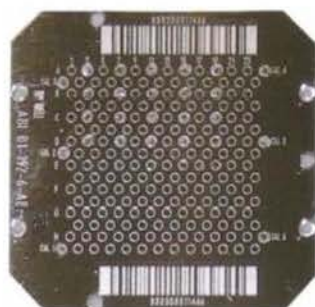


Figure II-11. Photograph of the target plate with 12x16 pattern of spots

### III.B.2.f. LDI source design

The plate, on which the sample is deposited, is placed on a support and put in the introduction chamber which is initially at atmospheric pressure. After connection with the pumping system, the pressure is reduced up to be equal to the source pressure. The separation gate is opened and the target plate moved to the source chamber. This is achieved by means of a cane to a stage which is equipped with motorized displacement steps. The motion of the stage is externally controlled to select the position of the laser impact.

A Nd:YAG Orion air-cooled laser system (New Wave Research Inc., Fremont, CA) and working at 355 nm (frequency-tripled) is used for the experiments. The photon energy at this wavelength is about 3.5 eV. The laser beam whose output power is about 0.7  $\text{J}\cdot\text{cm}^{-2}$  passes through a focusing lens before hitting the surface of the plate, as it is typically illustrated on the **Figure II-8** (angle of 40° from the normal).

### III.B.3. Atmospheric pressure photoionization

#### III.B.3.a. Introduction

The atmospheric pressure photoionization (APPI) is one of the youngest ionization technic, introduced, in 2000.<sup>39</sup> VUV photons are used to ensure the ionization of the analyte in the gas phase. Consequently, the VUV light source has to be associated with a nebulizing probe.

#### III.B.3.b. Principles of APPI and influencing parameters

The VUV photons are typically generated by a discharge lamp fitted with Argon, Krypton or Xenon. The most common one is the Krypton lamp. This light source has the advantage to emit 10.0 and 10.6 eV photons whose energy is lower than the ionization energy of the main components of the air (N<sub>2</sub>, O<sub>2</sub>, and H<sub>2</sub>O) and some of the most widely used solvents, as detailed in the **Figure II-12**. Inversely, the energy of the Krypton lamp is high enough to ensure the direct photoionization of a large part of organic compounds.<sup>40</sup> As an alternative to discharge lamp, VUV photons from a synchrotron light source may be also used.<sup>41</sup>

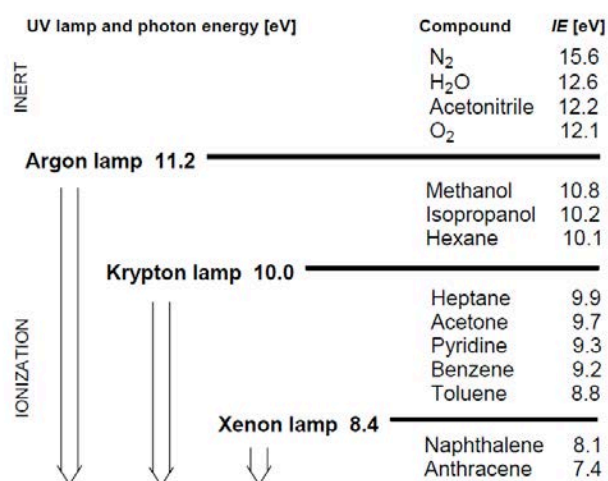


Figure II-12. Ionization energies of typical compounds and photon energies of UV lamps used in APPI<sup>14,42</sup>

The mechanism of photoionization with APPI source implies molecules to be in the gas phase by nebulization step. In the gas phase, a molecule that may be the analyte (AB) or the solvent (S) with a UV chromophore can absorb a photon, which induces different processes.<sup>40</sup>

- **Photoexcitation:**  $AB + h\nu \rightarrow AB^*$

*Due to the low lifetime of the activated  $AB^*$ , it deexcites by different processes.*

- **Photodissociation:**  $AB^* \rightarrow A + B$

*If the dissociation energy of the AB bond is lower than the photon energy.*

- **Radiative decay:**  $AB^* \rightarrow AB + h\nu$
- **Collisional quenching:**  $AB^* + N \rightarrow AB + N^*$  (*N is a molecule of analyte, solvent or air*)
- **Ionization:**  $AB^* \rightarrow AB^{*+} + e^-$

*If the vertical ionization energy of AB is lower than the photon energy.*

When a radical ion is produced, it may be neutralized by various processes.

- **Recombination:**  $AB^{*+} + e^- \rightarrow AB$
- **Moderated recombination:**  $AB^{*+} + e^- + N \rightarrow AB + N$  (*N corresponds to a buffer specie eliminating the excess of energy of this exothermic process.*)

The direct photoionization of the analyte AB is poorly efficient due to its low concentration and/or low photoionization cross section and low photon density. To increase the ionization yield, a substance, called dopant (D), is added to the solution. A suitable dopant has to be good absorbent at the used wavelength and presents an ionization energy lower than the energy of the used photon. Moreover, the associated radical cation  $D^{*+}$  has to present high recombination energy and low proton affinity. The main involved processes are the following ones:

- **Photoionization:**  $D + h\nu \rightarrow D^{*+}$
- **Charge transfer:**  $D^{*+} + AB \rightarrow D + AB^{*+}$

The dopant can also react with a solvent molecule or cluster of solvent molecules to ensure the formation of protonated analyte.

- **Reactant ion formation:**  $D^{*+} + S \rightarrow [D-H]^* + [S+H]^+$  or  $D^{*+} + S_n \rightarrow [D-H]^* + [S_n+H]^+$
- **Proton transfer:**  $[S+H]^+ + AB \rightarrow S + [AB+H]^+$  or  $[S_n+H]^+ + AB \rightarrow S_n + [AB+H]^+$

The most commonly used dopants are toluene, acetone, and aniline.<sup>39,43</sup> As indicated in the **Figure II-13**, one photon from the Krypton lamp ionizes toluene to produce the  $C_7H_8^{*+}$  molecular ion. This radical cation may transfer a proton to a cluster of solvent molecules. By considering the proton affinity of some species involved in the APPI process (**Table II-3**), both

methanol and water cannot undergo proton transfer as their proton affinities are lower than the  $C_7H_7^{\bullet}$  benzyl radical one. But clusters formed from solvent molecules have higher proton affinity, which enables the different reactions previously described. This phenomenon has been evidenced by Kauppila *et al.* who investigated the ionization mechanism for 13 different solvents.<sup>44</sup>

Compound	PA (kJ.mol <sup>-1</sup> )
Benzyl radical	831.4
Acetone	812.0
Toluene	784.0
Acetonitrile	779.2
Methanol	754.3
Water	691.0

Table II-3. Proton affinities (PA) of typical solvents and species used in APPI<sup>45</sup>

According to the reactions involved in the APPI processes, both molecular  $M^{\bullet+}$  and protonated  $[M+H]^+$  ions may be observed for a given analyte. The basic species may be preferentially detected as  $[M+H]^+$  cations whereas protonated event is favored for acidic compounds. The radical cations and anions are typically observed with the less polar compounds presenting small vertical ionization energy and with species having high electron affinity, respectively.

### III.B.3.c. APPI source design

To conduct the study of bio-oil by APPI, the measurements were carried out on a 12 T Solarix Bruker FT-ICR MS. The Bruker Daltonics source is heated at 180 °C and allows the analyte vaporization by means of nebulization system using also drying gas ( $N_2$ ). The photons of the Krypton lamp used for the photoionization interact with the analyte molecules. The light source is placed after analyte vaporization system and before analyte extraction into the mass spectrometer (**Figure II-13**).

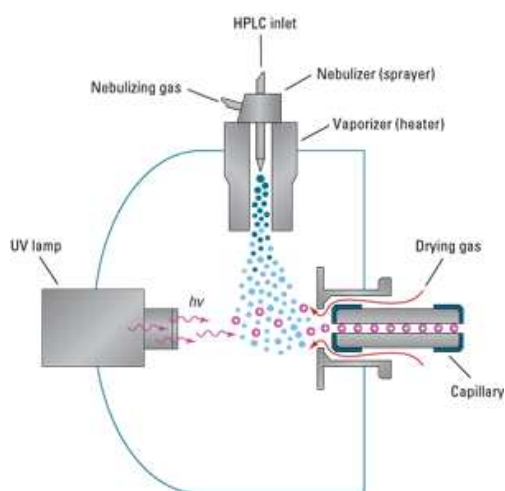


Figure II-13. Diagram of the APPI source with the UV lamp (Agilent)

### III.C. Fourier Transform Ion Cyclotron Resonance Mass Spectrometry

#### III.C.1. Introduction

Ernest O. Lawrence received the Physic Nobel Prize for the discovery of ion cyclotron resonance in 1932.<sup>46</sup> The application of a transverse oscillating electric field into an orthogonal and uniform magnetic field ensures the ions to adopt a circular motion, called cyclotron motion, of different radii depending on their mass. By this way, protons with 1.22 MeV energy were accelerated to reach high velocity. This principle was applied to mass spectrometry and ICR mass spectrometers were built.<sup>47</sup> In the middle of 70's, Marshall and Comisarow implemented Fourier transform for the signal treatment.<sup>48</sup> The FT-ICR MS technique was born. Today, this technique is amongst the most powerful in terms of resolving power ( $10^7$ ) and mass accuracy (0.1 ppm).<sup>49</sup>

#### III.C.2. Cyclotron motion

A charged particle  $q$  (with a  $z$  number of charge) placed in an uniform magnetic field  $B_0$  is subjected to both centrifugal and magnetic forces, as illustrated on the **Figure II-14**.<sup>50</sup> The second law of Newton (**Equation II-6.1**) may be applied to an ion submitted to the centrifugal and magnetic forces (**Equation II-6.2**). It ensures to find a relationship between its mass  $m$ , its speed  $v$ , its radius  $r$ , its charge  $q$ , and the strength of the magnetic field  $B_0$  (**Equation II-6.3**).

$$(Eq. II-6.1) \quad m * \vec{a} = \sum \vec{F}$$

$$(Eq. II-6.2) \quad m * \vec{a} = \vec{F}_{centrifugal} + \vec{F}_{magnetic}$$

$$(Eq. II-6.3) \quad m * \vec{a} = \frac{m}{r} * |\vec{v}_j \cdot \vec{v}_j| + q\vec{v} \wedge \vec{B}_0$$

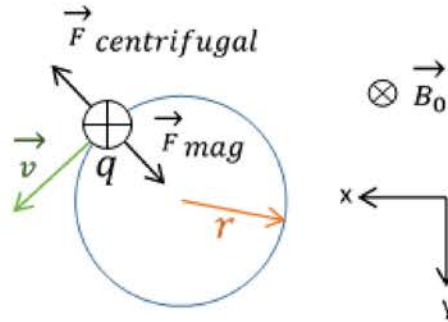


Figure II-14. Cyclotron motion of an ion with a charge  $+q$  in a magnetic field  $B_0$  subjected to both centrifugal and magnetic forces.  $v$  is the ion velocity and  $r$  the radius of the ion orbit.

The ion motion is circular and uniform, consequently, the acceleration is equal to 0, and the equation can be written, in the (xy) plan with  $B_0$  defining the Z axis.

$$(Eq. II-6.4) \quad \frac{m}{r} (v_{xy})^2 = qv_{xy}B_0$$

$$(Eq. II-6.5) \quad \frac{v_{xy}}{r} = \frac{q}{m} B_0$$

$$(Eq. II-6.6) \quad \boxed{\omega_c = \frac{q}{m} B_0}$$

$$(Eq. II-6.7) \quad v_c = \frac{q}{2\pi m} B_0 = \frac{z \cdot e}{2\pi m} B_0$$

The **Equation II-6.6** is the so-called cyclotron equation in which  $\omega_c$  is the ion cyclotron frequency that is inversely proportional to the  $m/z$  mass-to-charge ratio of the ion. Moreover, the cyclotron frequency is independent of the initial ion velocity but proportional to the magnetic field.

From the **Equation II-6.5**, the expression of the ion cyclotron orbital radius may be obtained.

$$(Eq. II-6.8) \quad r = \frac{v_{xy}m}{qB_0}$$

Hence, the magnetic field has an influence on the radius of the ion orbital as illustrated on the **Figure II-15**.<sup>51</sup> For high magnetic fields, small radii are achieved whatever the nature of the ion.

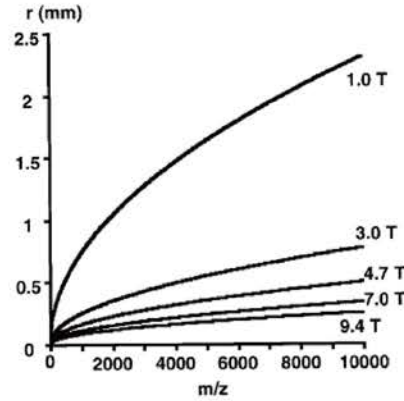


Figure II-15. Correlation of the ion orbital radius  $r$  with the mass-to-charge ratio  $m/z$  for different values of magnetic field  $B_0$ .<sup>46</sup>

The derivation of the **Equation II-6.6** in respect with  $m$  ensures to obtain the following **Equation II-6.9**.

$$\text{(Eq. II-6.9)} \quad \frac{\omega_c}{d\omega_c} = -\frac{m}{dm}$$

It demonstrates that the ion cyclotron frequency and the mass resolution are scalarly identical.

The kinetic energy  $E_k$  of the ion may be deduced from **Equation II-6.5** and is dependent on the  $m/z$  ratio.

$$\text{(Eq. II-6.10)} \quad E_k = \frac{m(v_{xy})^2}{2} = \frac{(qB_0r)^2}{2m}$$

For a given singly charged ion of 500 amu, in a magnetic field of 9.4 T, with an arbitrary orbital radius of 1 cm, its velocity is  $1.77 \cdot 10^4 \text{ m}\cdot\text{s}^{-1}$  and its kinetic energy is 832 eV. Such an energy, also called translational energy, can be responsible of fragmentation of the ion by collision with gas, which ensures the transfer of a part of the  $E_k$  into internal energy. The correlation between the kinetic energy and the ion orbital radius is shown on the **Figure II-16**.

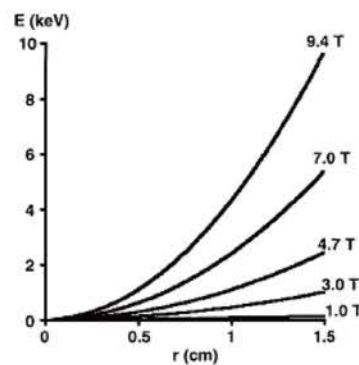


Figure II-16. Translational energy  $E$  versus ion orbital radius  $r$  at different magnetic field strengths for an ion of  $m/z=100$

In strong magnetic fields, the ions can be accelerated to reach significant values of translational energies. This is useful for the implementation of collision-induced dissociation (CID) experiments, which ensures their structural analyses. However it has to be avoided for obtaining a mass spectrum free of ion dissociation. With the velocity previously given, an ion travels a distance of close to 20 km in 1 second. The longest is the travelled distance, the most important is the time measurement and the highest are the mass accuracy and the resolution. That is the reason why  $m/z$  measurements have to be conducted in very high vacuum conditions, typically  $10^{-10}$ - $10^{-11}$  Torr pressure range.

### III.C.3. Trapping potential and magnetron motion

#### III.C.3.a. Trapping potential

As previously detailed, the cyclotron motion ensures the ions to be confined in the (xy) plan by the static magnetic field in the Z direction. To avoid the ion escape in the Z direction during their frequency measurement, the ions must be trapped by applying a small potential  $V_{\text{trap}} (\approx \pm 1 \text{ V})$  on two trapping plates placed perpendicularly to the Z axis (**Figure II-17**).

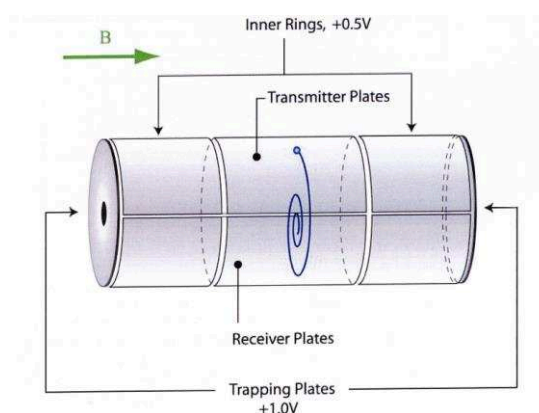


Figure II-17. Ion Spec ICR analyzer cell with the trapping plates and potential (here for storing positive ions)

Under the influence of the trapping electric field, the trapped ions acquire small back and forth motions along the z-axis. The motion of this so-called trapping oscillations may be compared to a harmonic oscillator whose force  $F_{\text{trap}}$  is given by the **Equation II-7.2**.

$$\text{(Eq. II-7.1)} \quad F_{\text{trap}}(z) = E(z) \cdot q \quad E: \text{electric field}; E(z) = -k'z$$

$$\text{(Eq. II-7.2)} \quad F_{\text{trap}}(z) = -qk'Z \quad \text{with } k' \text{ a constant, } q \text{ the ionic charge, and } Z \text{ the position of the ion along the Z-axis.}$$



From this equation, it is possible to deduce the ion trapping oscillating frequency  $\omega_{\text{trap}}$  along the z-axis (**Equation II-7.3**).

$$(Eq. II-7.3) \quad \omega_{\text{trap}} = \sqrt{\frac{k'q}{m}}$$

At one  $V_{\text{trap}}$  potential, the  $k'$  parameter is correlated to the ICR cell design (shape of the trapping electrodes).<sup>51</sup> It has been evidenced that the trapping oscillating frequency  $\omega_{\text{trap}}$  can be expressed as below:

$$(Eq. II-7.4) \quad \omega_{\text{trap}} = \frac{1}{d} \sqrt{\frac{2qV_{\text{trap}}\alpha}{m}} \quad \alpha = \text{trapping scale factor}$$

For a cylindrical ICR cell, the feature  $\alpha$  is equal to 3.86798.<sup>51</sup>

### III.C.3.b. Magnetron motion

The trapping potential  $V_{\text{trap}}$  applied on the ions produces an outward-bound radial force,  $F_R$ .

$$(Eq. II-8.1) \quad F_R = qE(r)$$

$$F_R = q \frac{V_{\text{trap}}\alpha}{d^2} r$$

This force is opposed to the Lorentz magnetic force. Therefore, it is possible to write and modify the **Equation II-6.4** to obtain the following equations.

$$(Eq. II-8.2) \quad \frac{m}{r} (v)^2 = qvB_o - F_R$$

$$mr(\omega)^2 = q\omega r B_o - q \frac{V_{\text{trap}}\alpha}{d^2} r$$

$$\omega^2 - \frac{qB_o}{m} \omega + \frac{q}{m} \frac{V_{\text{trap}}\alpha}{d^2} = 0$$

$$\omega^2 - \omega_c \omega + \frac{(\omega_{\text{trap}})^2}{2} = 0$$

This quadratic equation has two solutions:

$$(Eq. II-8.3) \quad \omega_+ = \frac{\omega_c}{2} + \sqrt{\left(\frac{\omega_c}{2}\right)^2 - \frac{\omega_{\text{trap}}^2}{2}} \quad \text{and}$$

$$(Eq. II-8.4) \quad \omega_- = \frac{\omega_c}{2} - \sqrt{\left(\frac{\omega_c}{2}\right)^2 - \frac{\omega_{\text{trap}}^2}{2}}$$

For an ion with  $m/z = 500$  in a magnetic field  $B_o = 9.4$  T, with  $V_{\text{trap}} = 1$  V,  $d = 2$  cm, and  $\alpha = 3.87$ ,  $\omega_c = 1\,769\,412$  rad.s<sup>-1</sup> which is very close to  $\omega_+ = 1\,768\,382$  rad.s<sup>-1</sup> whereas  $\omega_- = 1030$  rad.s<sup>-1</sup>.

The **Equation II-8.3** gives the reduced cyclotron frequency  $\omega_+$  which is measured and ensures the obtention of the mass spectrum. The **Equation II-8.4** gives the magnetron frequency  $\omega_-$ . The magnetron motion is the precession of an ion along the electrostatic field. It is not of significant importance in most of the applications. However, it may be responsible of small and vicinal peaks on both sides  $\omega_+ \pm k \omega_-$  of the main peak at  $\omega_+$ .<sup>51</sup>

Thus, the ion global motion in an ICR cell is more complex than the only cyclotron mode. Actually, as described in the **Figure II-18**, three natural motional modes and frequencies are involved, the reduced cyclotron rotation ( $\omega_+$ ), the magnetron rotation ( $\omega_-$ ), and the trapping oscillation motion ( $\omega_{trap}$ ).

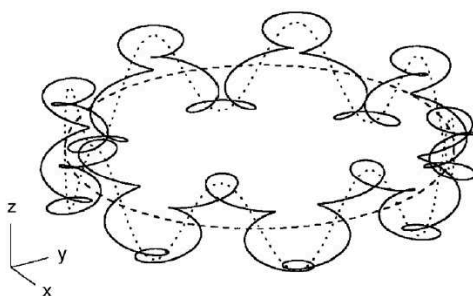


Figure II-18. Ion motion in a ICR cell. Magnetron motion (dashed), magnetron + trapping motion (dotted), and the resulting global motion (solid)<sup>52</sup>

#### III.C.4. Ion excitation in the ICR cell

Initially, the ions in the gas phase form a small cloud with a rotational motion at the center of the ICR cell, centered on the z-axis. In order to obtain a signal that could be detected by the receiver plates (**Figure II-17** and **Figure II-19**), the orbital of the ion packet has to be increased to reach the vicinity of these plates. This is achieved by applying a transverse oscillating electric field at the reduced cyclotron frequency  $\omega_+$ . This electric field, perpendicular to the magnetic field, makes the ions going into resonance, which induces their excitation and their acceleration (**Figure II-19**). This radiofrequency *RF* electric field  $E(t)$  is delivered by the transmitter plates (**Figure II-17**).

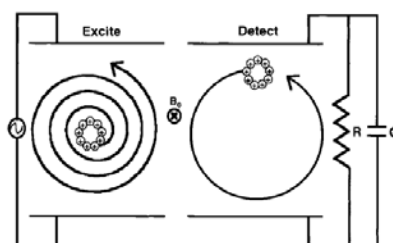


Figure II-19. Excitation of the ion cloud in the ICR cell (on the left) and image current detection (on the right). On the left, the ion package has an incoherent cyclotron orbital motion. On the right, after application of an *RF* electric field, a coherent and detectable motion is obtained.

The electric field excitation is expressed as following (**Equation II-9.1**).

$$(Eq. II-9.1) \quad E(t) = E_0 \cos(\omega_c t) \mathbf{j} \quad \mathbf{j} \text{ is a unit vector along the } y\text{-axis} \\ \text{toward the detection plates.}$$

The electric field  $E_0$  is obtained by the application of  $+V_0$  and  $-V_0$  volts from the two opposite transmitter plates separated by a  $d$  distance. Hence,  $E_0$  can be expressed as followed.

$$(Eq. II-9.2) \quad E_0 = \frac{2V_0}{d} = \frac{2V_{p-p}}{d}$$

The parameter  $V_{p-p}$  is the peak-to-peak voltage difference between the 2 plates.

As it is a linearly-polarized function, the two counter-rotating components  $E_L(t)$  and  $E_R(t)$  can be highlighted.

$$(Eq. II-9.3) \quad E(t) = E_L(t) + E_R(t)$$

$$(Eq. II-9.4) \quad E_L(t) = \frac{E_0}{2} \cos \omega_c t \mathbf{j} + \frac{E_0}{2} \sin \omega_c t \mathbf{i} \quad \mathbf{i} \text{ is a unit vector along the } x\text{-axis.}$$

$$(Eq. II-9.5) \quad E_R(t) = \frac{E_0}{2} \cos \omega_c t \mathbf{j} - \frac{E_0}{2} \sin \omega_c t \mathbf{i}$$

The range of frequencies that has to be applied to excite the ions in a given  $m/z$  range can be deduced from the **Equation II-6.7**. Indeed, it depends to the  $m/z$  range and the magnetic field. For a 9.4 T FT-ICR MS, the frequency bandwidth to cover, in order to excite ions in the 50 to 5000  $m/z$  range, is calculated as follow.

$$\begin{aligned} - \text{ For the } m/z \text{ 50 ion: } \nu_c &= (1.60 \times 10^{-19} \times 9.40) / (2 \times \pi \times 50.00 \times 1.66 \times 10^{-27}) \\ \nu_c &= 2.88 \text{ MHz} \end{aligned}$$

$$\begin{aligned} - \text{ For the } m/z \text{ 5000 ion: } \nu_c &= (1.60 \times 10^{-19} \times 9.40) / (2 \times \pi \times 5000.00 \times 1.66 \times 10^{-27}) \\ \nu_c &= 28.84 \text{ kHz} \end{aligned}$$

Such a large excitation bandwidth has to be applied as homogeneously as possible. This will be described in a following section.

Regarding the previous equations, the increase of the magnetic field strength is advantageous for several reasons. By increasing the value of  $B_0$ , the resolving power also linearly increases (**Equation II-6.9**). The ion cyclotron orbital radius is inversely proportional to  $B_0$  (**Equation II-6.8**), which enables to detect ions with higher  $m/z$ . The kinetic energy also increases with  $B_0^2$  (**Equation II-6.10**), which leads to a better mass resolution and accuracy.

During the excitation, the ion is accelerated and its orbital radius increases and it absorbs power  $A(t)$  whose expression demonstrated by Beauchamp *et al.*<sup>53</sup> is given by the **Equation II-9.6**.

$$(Eq. II-9.6) \quad A(t) = qE(t) \cdot v_{xy} \quad v_{xy} \text{ is the initial velocity of the ion}$$

For an excitation period  $T_{excite}$ , an ion submitted to RF excitation has a power of absorption that can be expressed by this way (**Equation II-9.7**).<sup>51,53</sup>

$$(Eq. II-9.7) \quad A(T_{excite}) = \frac{E_0^2 q^2 T_{excite}}{4m}$$

The integration of the **Equation II-9.6** from 0 to  $T_{excite}$  allows to obtain the energy absorbed during the excitation event. This energy is converted into kinetic energy  $E_k$ .

$$(Eq. II-9.8) \quad E_k = \int_0^{T_{excite}} A(t) dt$$

$$(Eq. II-9.9) \quad \frac{mr^2 \omega_c^2}{2} = \frac{E_0^2 q^2 T_{excite}^2}{8m}$$

By replacing  $\omega_c$  by  $\frac{q}{m} B_o$ , (**Equation II.6.6**) in the **Equation II-9.9**, it is possible to simplify and obtain the expression of the ion orbital radius of the excited ion.

$$(Eq. II-9.10) \quad r = \frac{E_0 T_{excite}}{2B_o} = \frac{V_{p-p} T_{excite}}{2dB_o}$$

From this equation, it is clearly observable that the radius does not depend on the  $m/z$  but increases with the excitation time. If all ions are excited during the same time ( $T_{excite}$ ), all ions reach the same orbital radius. But due to the different cyclotronic frequencies, the heaviest ions rotate less rapidly than the others.

### III.C.4.a. Excitation modes in FT-ICR MS

From the **Equations II-9.8 to II-9.10**, it is obvious that the period of excitation is a crucial feature. A too long excitation time means a high kinetic energy and a high ion orbital radius that could lead to the ion ejection from the ICR cell. It is possible to estimate the magnitude for a given  $T_{excite}$  time. For example, in a 9.4 T FT-ICR MS, the excitation time required to excite a ion and to put it into a 0.5 cm radius orbit, by the two transmitter plates separated by 2 cm with a  $V_{p-p}=1$  V, is estimated at 1.88 ms.

Different excitation modes were developed for ICR measurements. The first and simplest one consists in a single frequency pulse that only excites the ion having the same resonance frequency (**Figure II-20.a**).<sup>48</sup> Recoding a mass spectrum by applying a rectangular pulse to each ion is unrealistic. Moreover, reducing the time-domain excitation affects the

mass resolution (**Figure II-20.b**). Therefore, other methods have been developed that simultaneously excite all the ions in the cell by the application of a large RF bandwidth.

The first excitation method in broadband mode is called “chirp” or “sweep” excitation.<sup>54</sup> One excitation pulse sweeps the frequencies related to the  $m/z$  range of interest. The used voltage is quite low and the magnitude of the achieved frequency-domain is relatively flat (**Figure II-20.c**). However, this excitation mode is not perfectly homogeneous. As a matter of fact, as illustrated on the **Figure II-20.c**, there are some distortions close to the borders of the range, which limits the mass selectivity at the start and at the end of the RF band. The heterogeneity of the excitation amplitude may introduce a bias concerning the apparent relative abundances.

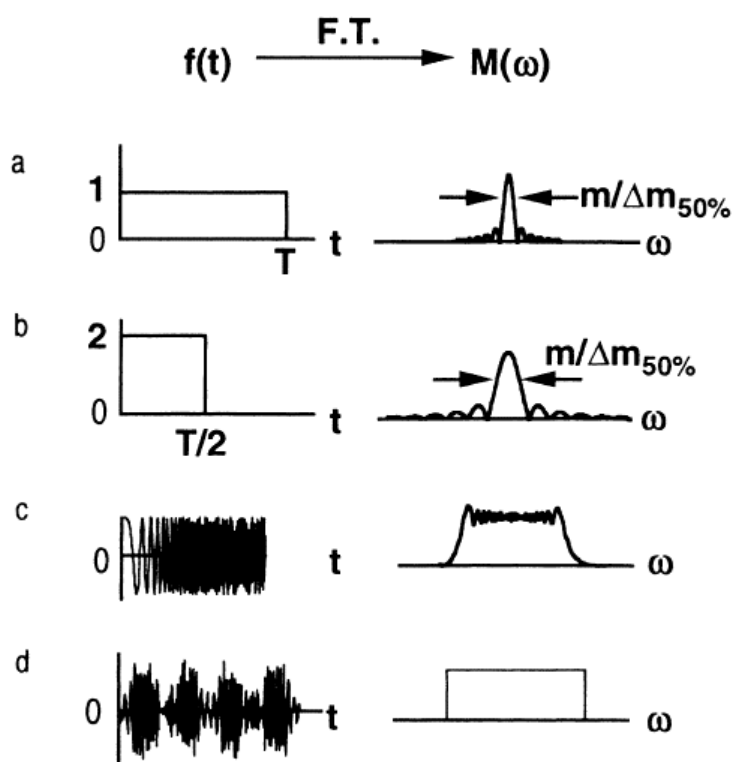


Figure II-20. Time-domain (left) and frequency-domain (right) waveforms with (a) and (b) rectangular pulses, (c) chirp excitation, and (d) SWIFT excitation.

For that reason, another broadband excitation mode was developed. First, the desired mass-domain to excite has to be defined. This one is then converted into frequency domain by applying the relation given by the **Equation II.6.6**. Then, the frequency-domain excitation is translated by the inverse Fourier transform into time-domain excitation. This method is called the “stored waveform inverse Fourier transform” (SWIFT).<sup>55</sup> This general excitation

mode yields a highly linear response, as observed on the frequency-domain waveform, on the **Figure II-20.d**.

### III.C.5. Detection, treatment, and conversion of the ICR signal

#### III.C.5.a. Detection

As previously detailed, the excited ions have a greater ion orbital radius, which makes them detectable by the opposite receiver plates (**Figure II-19**). When an ion packet of same  $m/z$ , with its own cyclotron frequency  $\omega_c$ , repeatedly passes in front of the detector plates, an image current is induced. This current  $\Delta Q$  is given by the **Equation II.10.1** for which  $q$  is the charge,  $v_y$  is the ion velocity and,  $d$  is the distance between the detection plates. It is independent to the ion frequency.

$$\text{(Eq. II-10.1)} \quad \Delta Q = -\frac{2qv_y}{d}$$

The ICR signal is proportional to the induced current and linearly increases with the ion cyclotron post-excitation radius.

The duration of the signal acquisition is limited by collisions between the ions and neutrals in the ICR cell, which reduces the homogeneity of the ion packet. Therefore, it is essential to work at very low pressure. Indeed the collisions disturb the homogeneity of the ion packages and induce opposite-phased currents. Finally, the induced current decreases until reaching zero. This signal declines according to an exponential law and is recorded by the detection plates to generate a transient free induction decay (FID). The transient may have a time duration  $T$  of several seconds when all experimental parameters are optimized, which ensures a very high resolution mass spectrum to be achieved. Indeed resolving power is directly proportional to the acquisition time measurement (**Equation II-11**).<sup>56</sup>

$$\text{(Eq. II-11)} \quad R = \frac{\omega}{\Delta\omega} = \frac{\omega T}{2\pi}$$

#### III.C.5.b. Apodization

Before applying the Fourier transform  $FT$  to convert the time-domain waveform into its frequency-domain equivalent, as described on the **Figure II-20**, a first treatment has to be applied. Actually, the abrupt truncation, at the beginning and at the end of the time-domain

signal which extends on a finite period  $T$ , is responsible after FT of auxiliary wiggles on both sides of the main peaks, as illustrated on the **Figure II-21**. These peaks are troublesome as they can hide small real peaks present in the vicinity of the large ones. To reduce these wiggles, a weight function is thus applied to the transient for windowing the time-domain waveform. Finally, the peaks obtained on the frequency-domain after FT are tailored. Such a function is called apodization and different functions have been developed which force the beginning and the end of the signal to monotonically decrease towards zero (smoothing).<sup>50</sup>

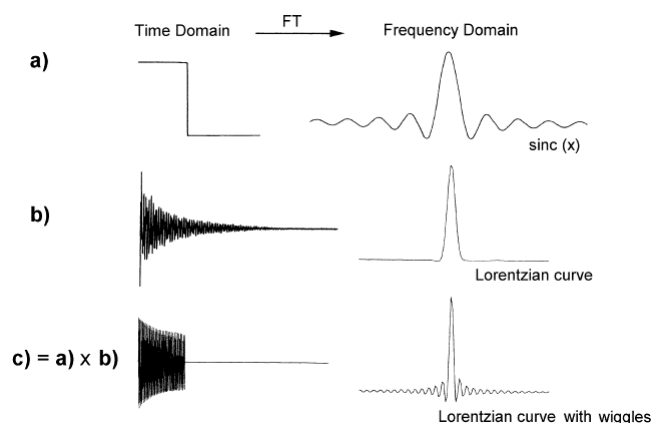


Figure II-21. Fourier transform on different time-domain waveforms. (a) Step (rectangular) function converted to  $\text{sinc}(x)$ , (b) entire FID transient obtained with one RF excitation gives a Lorentzian curve, and (c) the truncated transient product of (a)  $\times$  (b) that yields Lorentzian curve with sidelobes "wiggles".

As part of these research works, it is the Blackman-Harris (3-term) function (**Equation II-12**) that it used for apodization. This function is often used in FT-ICR analyses because it has the ability to significantly decrease the wiggles (**Figure II-22**).

$$\text{(Eq. II-12)} \quad A(t) = 0.424 + 0.497 \cos\left(\frac{\pi t}{T}\right) + 0.079 \cos\left(\frac{2\pi t}{T}\right)$$

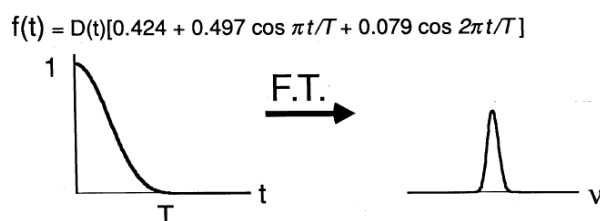


Figure II-22. Blackman-Harris apodization function applied to the time-domain waveform for one excitation RF and the corresponding frequency-domain peak yielded after Fourier transform.<sup>50</sup>

Generally speaking, the windowing by apodization has two effects on the mass spectrum peaks. If it significantly reduces the amplitudes of the sidelobes, it also decreases the mass resolution of the peaks.

Another treatment to yield better defined mass spectrum is called “zero-filling”. It corresponds to the addition of one or more zero-filled interval at the end of the transient, which increases the number of data point per  $m/z$  interval. This treatment results in an improved peak shape, which decreases the error in peak abundance determination.<sup>57,58</sup>

### III.C.5.c. Fourier transform and mass spectrum generation

The sinusoidal signal obtained on the FID time-domain transient is converted (after or without apodization) to frequency-domain waveform by using Fourier transform (**Equations II-13.1** and **II-13.2**). This step is performed by applying the fast Fourier transform (FFT) treatment on the time-domain transient.

$$\text{(Eq. II.13.1)} \quad F(\nu) = \int_0^T f(t) \exp(-i2\pi t) dt$$

$$\text{(Eq. II.13.2)} \quad F(\omega) = \int_0^T f(t) \exp(-i\omega t) dt$$

Then, the frequency-domain is converted to mass spectrum by applying  $\nu=qB_0/2\pi m$  or  $\omega=qB_0/m$ . This step deals with the mass spectrum calibration which will be detailed in a next section (**III.C.6.c**).

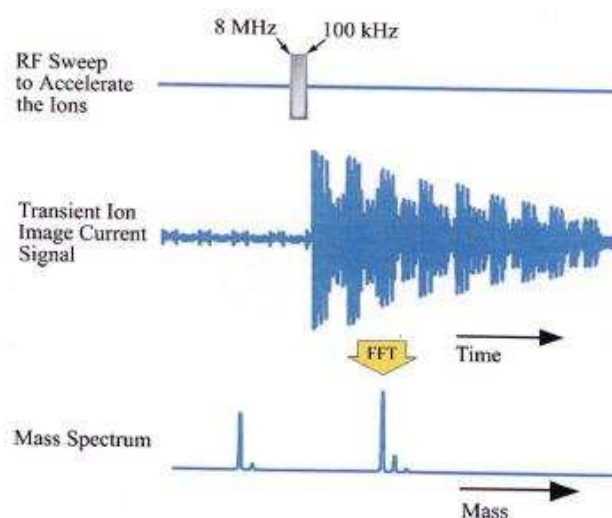


Figure II-23. Main steps for generation of a FT-ICR mass spectrum (from Ion Spec)

### III.C.6. Data acquisition with a 9.4 T Ion Spec mass spectrometer

As part of these research works, two different FT-ICR mass spectrometers were used: a 9.4 T Ion Spec at the LCP-A2MC in Metz and a 12 T Solarix Bruker at the University of Edinburgh. The main part of this study was performed on the 9.4 T mass spectrometer whose configuration and related software are described below. For the 12 T Solarix, the different



ionization methods and operating parameters were optimized *via* the FTMS Control V2.10, build 98 (Bruker Daltonics). The achieved mass spectra were analyzed and calibrated using Data Analysis V4.4, build 102.47.2299 (Bruker Daltonics). For the peak assignment, PetroOrg software (Florida State University) was used.

### III.C.6.a. Mass spectrometer and ionization sources

The HiRes Ion Spec (Lake Forest, CA) FT-ICR mass spectrometer is fitted with a 9.4 T shielded superconducting magnet (Cryomagnetics, Oak Ridge, TN). As shown on the **Figure II-24**, two different and independent devices can be used (not at the same time). They are both fitted with an external ion source, a pumping system, an ion transfer line, and an ICR cell. The device on the right is equipped with a Micromass Z-spray electrospray source to perform ESI FT-ICR MS analyses. The direct infusion of the sample is achieved with a 100  $\mu$ L Hamilton syringe. Nitrogen gas was used to help nebulization processes. On the left, LDI FT-ICR MS measurements can be carried out with the ProMaldi card source. Desorption ablation processes are performed with a Nd:YAG 355 nm laser (Orion, 5 ns time duration, spot area close to 0.056 mm<sup>2</sup>, 250 mJ/cm<sup>2</sup>) but other wavelengths can also be used (266 nm and 213 nm).



Figure II-24. Ion Spec FT-ICR mass spectrometer equipped with two external sources. LDI (on the left) and ESI (on the right).

### III.C.6.b. Acquisition parameters

The FT-ICR MS ionization and acquisition parameters are controlled by the OMEGA software (Varian). The different steps of the acquisition (production, transfer, and analysis of the ions) can be optimized via an interactive scheme of the FT-ICR MS (**Figure II-25**) or by

building an experiment setup (**Figure II-26**). The optimal setup is detailed below for ESI FT-ICR MS experiment.

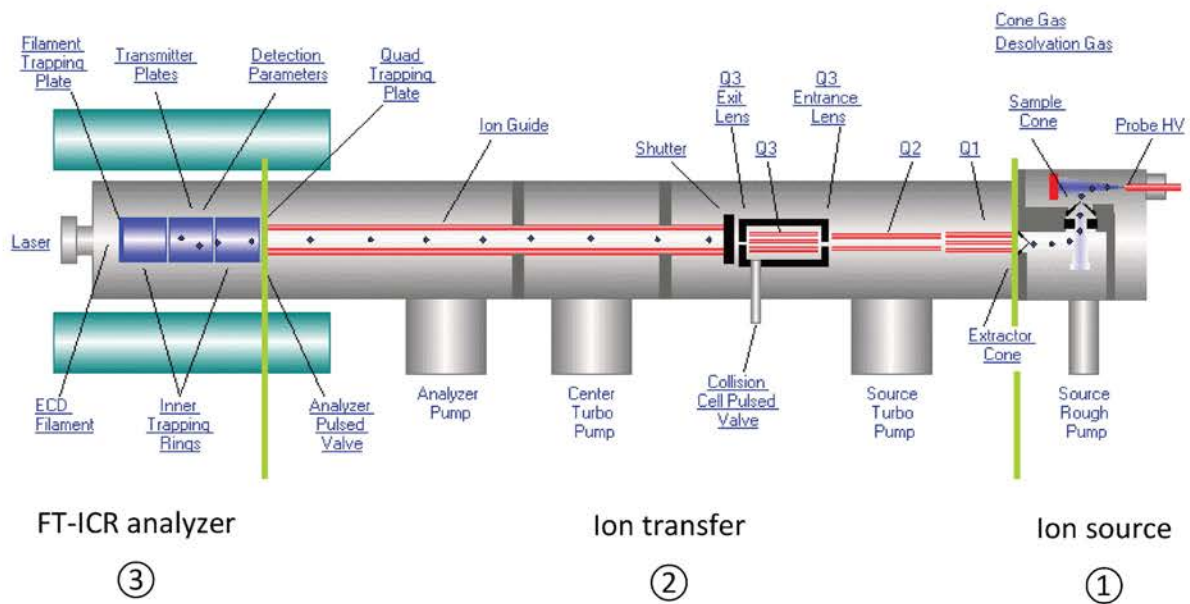


Figure II-25. Schematic interface of the FT-ICR MS (here with the ESI source)

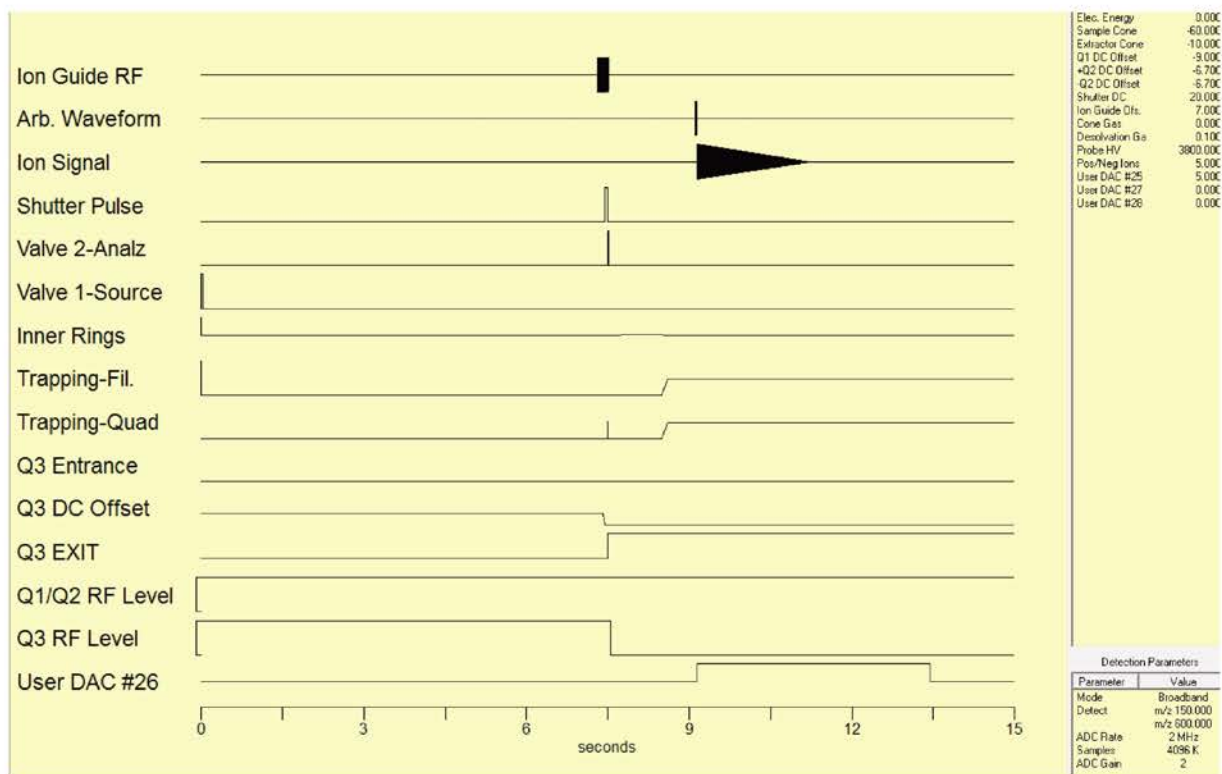


Figure II-26. Experiment setup with overview of the different voltages and timing events occurring during FT-ICR MS experiment – Omega Software

The ion spray is formed by the application of high voltage on a capillary whose value is given in the  $\pm 3\text{-}4$  kV range. The ions enter a chamber through a sample cone at a typical voltage of  $\pm 40$  V (**Figure II-6**). A pumping system enables the decrease of the pressure from 760 to 2 Torr. Then, voltages are deflecting the ions that pass through an extractor cone ( $\pm 10$  V) into the first part of the mass spectrometer, the  $Q_1$  hexapole. The pressure is then reduced to  $10^{-4}$  Torr by a turbomolecular pump.

The first  $Q_1$  hexapole acts as an ion guide with application of RF voltages on the opposite pair rods. The generated potentials enable the ions to be transmitted for a given  $m/z$  range. A second  $Q_2$  quadrupole can be used either as a mass filter or as an ion guide. The ions are then trapped and accumulated in a second hexapole  $Q_3$  working in RF-only mode. It means that all the ions which are stable under the hexapole potentials are stored. The ion fine storage is optimized for each analytical condition and is between 0.5 to 6 s, in this study. An offset voltage is also applied on the transfer setup of all the ions. Moreover, optimization of the ion transfer can be operated at two different RF: Coil 1 at 905 000 Hz and Coil 2 at 1 965 000 Hz.

At the end of the storage time, the exit lens potential is decreased and ions are directed to the RF-only ion guide hexapole. A metallic shutter physically separates the storage hexapole and the ion guide to maintain very low pressure in the FT-ICR cell ( $10^{-10}$  Torr). This shutter has to be opened to allow the transfer of the ions. The Ion Guide hexapole is one meter long and the amplitude of the applied RF-potential must be optimized to ensure ions, in a given  $m/z$  range, to be introduced in the cell.

Then, the ions are trapped in the ICR cell by applying a voltage on the trapping plates ( $\pm 0.5$  V) and they are thermalized by the use of a nitrogen pulse.

The ion excitation is performed by the application of a SWIFT arbitrary waveform function. The conversion of the resulting image current signal into a digital form is processed by a computer with an analog-to-digital converter (ADC). This ADC samples the voltage of the input signal and generates the corresponding digital binary output. The sample rate must be, at least, twice the frequency of the highest frequency from the waveform that could be digitized, according to the Nyquist sampling criterion.<sup>14</sup> Thus, for a singly-charged  $m/z$  150 compound, in a 9.4 T magnetic field, its frequency is about 900 kHz which means that the ADC rate should be at least 1.8 MHz. Here, it is set at 2 MHz.<sup>59</sup>

The obtained FID transient is apotized with a Blackman-Harris function before Fourier transform. From 30 to 100 individual mass spectrum are summed in order to obtain a final mass spectrum with a good signal-to-noise ratio.

For LDI, the source chamber that contains the plate is at reduced pressure. Turbo pump system, throughout the distance travelled by the ions, enables to maintain a low pressure (**Figure II-27**). This feature is needed to obtain a high mass resolving power. Eight laser shoots are performed on a sample. Generated ions are collected in a first hexapole. The following ion transfer to the ICR cell is conducted by an ion guide similar to the ESI-card.

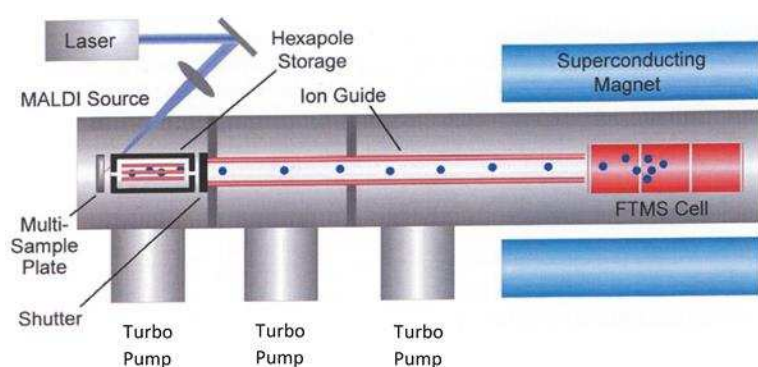


Figure II-27. Scheme of the IonSpec ProMALDI FTMS

### III.C.6.c. Calibration

Prior acquisition, the mass spectrometer is externally calibrated. In ESI, well-known  $C_xH_yO_z$  compounds or calibration mixtures (Thermo calmix positive or negative) are used. These  $C_xH_yO_z$  species correspond to proton or sodium adducts and deprotonated species, in positive and negative ion detection modes, respectively. In LDI, hybrid gold cluster ions are used.

The final calibration of a mass spectrum is performed by an internal calibration with unambiguously identified peaks.

### III.C.7. Data assignment

After calibration, a peak list of signals, whose signal-to-noise ratio is greater than 3, is generated. The assignment of each peak by a unique elemental formula is performed by the Composer software (Sierra Analytics Modesto, CA) with the following criteria:  $C_{1-100}H_{1-100}N_{0-5}O_{0-30}Na_{0-1}^+$  (positive ion) or  $C_{1-100}H_{1-100}N_{0-2}O_{0-30}S_{0-1}^-$  (negative ion) general formula. The

generating formula has to respect a limit of 3 ppm of mass tolerance error and a double bond equivalent (DBE) ranged from - 0.5 to 40 (a DBE = -0.5 corresponds to a saturated compound cationized by  $\text{NH}_4^+$ ). The DBE is given by the **Equation II-14** and reflects the unsaturation degree of a molecule based on its elemental formula  $\text{C}_c\text{H}_h\text{N}_n\text{O}_o^{+/-}$ .

$$\text{(Eq. II-14)} \quad \text{DBE} = c + \frac{n-h}{2} + 1$$

The expected elemental formula can vary according to the sample preparation. Some studies were performed using lithium or potassium acetate or 3-chloroaniline. Therefore, the assignment parameters have been adjusted to include either  $\text{Li}^+$ ,  $\text{K}^+$  or  $\text{Cl}^-$ .

Composer generates a file that contains all the assigned peaks. Each signal is characterized by its experimental, theoretical, nominal, and Kendrick masses (see section **III.C.8.c**) but also by its mass error, elemental formula, and DBE value. These data are exported on Excel where all the assignments, with an error lower than 1 ppm, are used for recalibration according to **Equation II-15**.<sup>60</sup>

$$\text{(Eq. II-15)} \quad \frac{m}{z} = \frac{a}{f} + \frac{b}{f^2} \quad \mathbf{a} \text{ and } \mathbf{b} \text{ constants, } \mathbf{f} \text{ the measured frequency of the ion with a mass } \mathbf{m} \text{ and a charge } \mathbf{z}.$$

The signals whose error is greater than 1 ppm are manually re-assigned using Omega 8 Elemental Composition software (Varian Ion Spec Inc.) with the previously described search criteria. Finally, the quality of the calibration is checked by the graphical representation of the mass error *versus*  $m/z$  (**Figure II-28**) and by calculating the root mean square (RMS) and the algebraic sum of all mass errors that must be lower than 1 ppm.

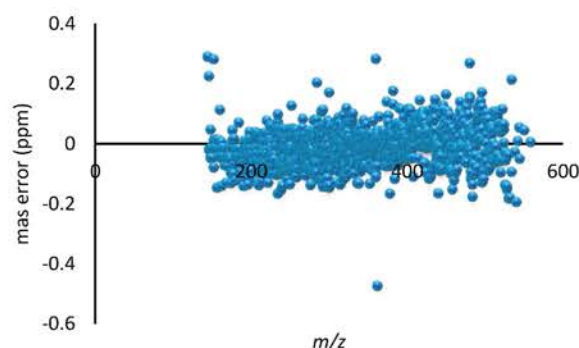


Figure II-28 Mass error (in ppm) vs.  $m/z$  for  $\text{C}_x\text{H}_y\text{O}_z$  compounds of a Oak pyrolysis bio-oil analyzed in (-) ESI FT-ICR MS.

After assignment, some compound families are highlighted. In bio-oils, the most common are  $C_xH_yO_z$ ,  $C_xH_yN_nO_z$ , and  $C_xH_ySO_z$  (in decreasing order of relative abundance). Depending on the ionization source, the detection mode, and the ionization conditions, these compounds are detected in various forms. In (+) ESI, the species are  $[M+H]^+$  or  $[M+Na]^+$  adduct ions whereas in (-) ESI, they are mainly  $[M-H]^-$  deprotonated anions. In LDI and APPI, compounds can be simultaneously detected as  $M^{*+}$  and  $[M+H]^+$ , on the one hand, and  $M^{*-}$  and  $[M-H]^-$ , on the other hand, in negative and positive ion modes, respectively. On the **Figure II-29**, an inset at  $m/z$  373 is done on a (-) ESI FT-ICR mass spectrum of a pyrolysis bio-oil, on which five signals are assigned with errors lower than 1 ppm. That demonstrates the high resolving power of the FT-ICR MS and the quality of the calibration of the mass spectrum. Moreover, it also proves the significant amount of generated data.

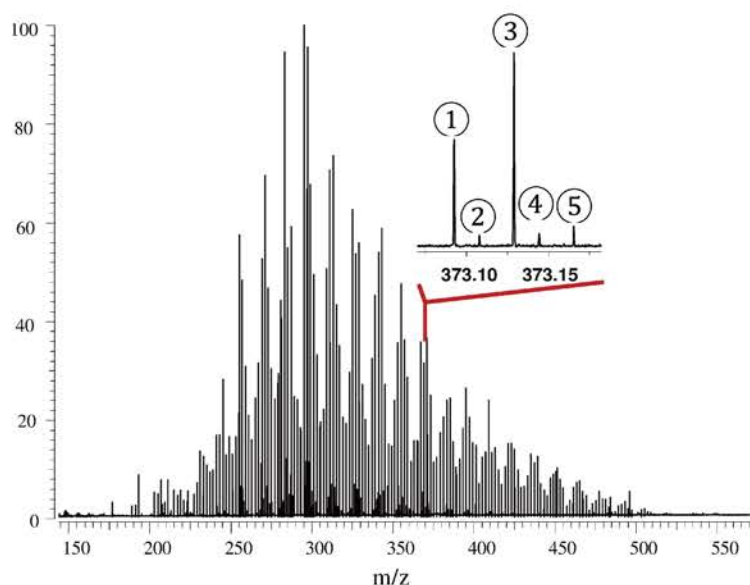


Figure II-29. (-) ESI FT-ICR mass spectrum of *Miscanthus pyrolysis* bio-oil. Five signal are attributed on the inset corresponding to the nominal mass 373. ①  $C_{19}H_{17}O_8^-$  ( $m/z$  373.0918 ; error 0.30 ppm) ; ②  $C_{23}H_{17}O_5^-$  ( $m/z$  373.1081 ; error 0.07 ppm) ; ③  $C_{20}H_{21}O_7^-$  ( $m/z$  373.1288 ; error 0.44 ppm) ; ④  $C_{24}H_{21}O_4^-$  ( $m/z$  373.1444 ; error 0.25 ppm) ; ⑤  $C_{21}H_{25}O_6^-$  ( $m/z$  373.1655 ; error 0.26 ppm)

### III.C.8. Data graphical representations

The FT-ICR mass spectra of mixtures of thousands different species are very complex. Due to the significant amount of information, the interpretation and the comparison are very difficult to be performed. Therefore, different graphical representations are helpful.

### III.C.8.a. Heteroatom class distribution

After assignment, the global bio-oil composition, for a given analytical condition, is described by the relative abundances of the different highlighted compound families (**Figure II-30. Pie chart**). A further insight into a given family enables to obtain the heteroatom class distribution (**Figure II-30. Top bar chart**) and by extension, the DBE distribution (**Figure II-30. Bottom bar chart**). Nevertheless, these graphical representations are not informative enough. Therefore, other representations have been developed that are more efficient for the sample interpretation and the comparison of different mass spectra.

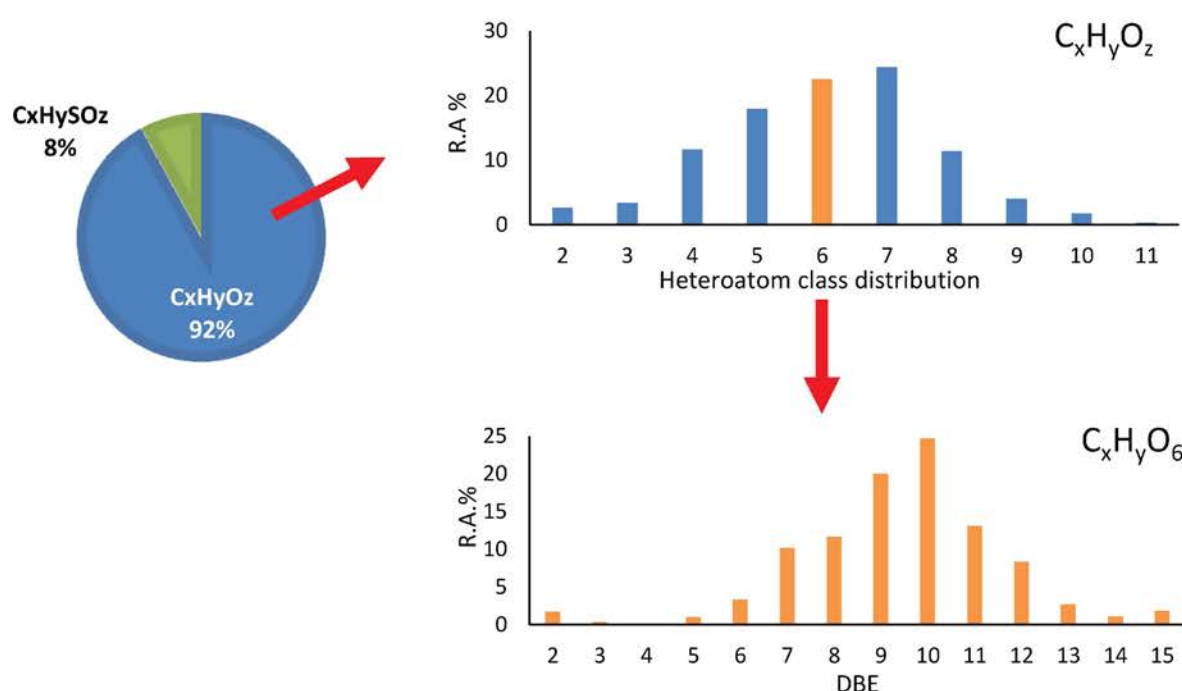


Figure II-30. Global composition description of an Oak bio-oil by (-) ESI FT-ICR MS analysis (Pie chart). Oxygenated compound distribution in respect with the oxygen atom count (top histogram) and DBE distribution for  $C_xH_yO_6$  compounds (bottom histogram).

### III.C.8.b. Van Krevelen diagrams

Van Krevelen diagrams have been initially used for the study of coal<sup>61</sup> and then extended to other complex organic samples.<sup>62,63</sup> They are constructed using the hydrogen to carbon (H/C) and oxygen to carbon (O/C) atom ratios. Other ratios including nitrogen can be used. Thus, a component with its own elemental formula can be represented by a dot whose x and y coordinates are O/C and H/C ratios, respectively. This can be easily applied to thousands of oxygenated compounds whose elemental formulae are  $C_xH_yO_z$ . The achieved van Krevelen diagram enables to evidence the major biochemical classes of compounds

characterized by their own H/C and O/C ratios. Thus, lipids, protein, lignin, carbohydrates, and cellulose can be evidenced in different regions of the van Krevelen diagram (**Figure II-31**). In bio-oil characterization, van Krevelen diagram enables to highlight some of these components that belong to the biomass pyrolysis. It is also useful in order to assess the response of the different ionization sources and detection modes. Moreover, it also allows to evaluate the efficiency of a catalytic treatment for the bio-oil upgrading.

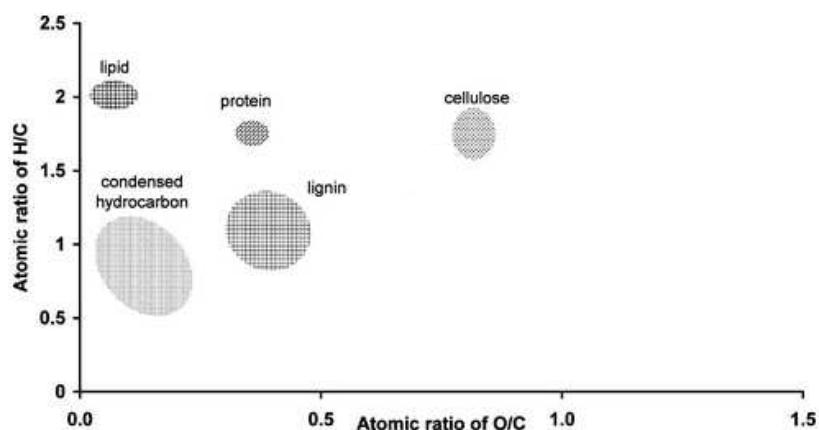


Figure II-31. Van Krevelen diagram with some major biomolecular components grouped in the different areas<sup>62</sup>

### III.C.8.c. Kendrick's maps

Another approach used to simplify the interpretation of complex organic mixtures is the Kendrick mass defect (KMD) analysis.<sup>64</sup> It consists in changing the mass scale by taking CH<sub>2</sub> as the new mass scale reference. Each signal, referred to this new Kendrick mass (KM (CH<sub>2</sub>)), is plotted according to its Kendrick mass defect against its nominal mass. Thus, compounds differing by one or more CH<sub>2</sub> units have the same Kendrick mass defect (**Figure II-32**). Different calculations have to be performed to obtain the KMD (**Equations II-16**).

$$\text{(Eq. II-16.1)} \quad \text{KM (CH}_2\text{)} = \text{IUPAC mass}_{\text{measured}} \times \left[ \frac{\text{Nominal mass CH}_2}{\text{IUPAC mass CH}_2} \right]$$

$$\text{KM (CH}_2\text{)} = \text{IUPAC mass}_{\text{measured}} \times \left[ \frac{14.00000}{14.01565} \right]$$

Where KM is the (exact) Kendrick mass of a peak according to the number of (CH<sub>2</sub>)<sub>n</sub> moiety.

$$\text{(Eq. II-16.2)} \quad \text{KMD (CH}_2\text{)} = \text{nominal mass}_{\text{measured}} - \text{nominal KM (CH}_2\text{)}$$

As illustrated on the **Figure II-32**, it is possible to distinguish, for a given class of compounds, the radical (yellow dots) and deprotonated (blue dots) species as well as the <sup>13</sup>C



isotope contributions (red triangles). Some trend lines are evidenced. The plots aligned on the horizontal line (*a*) are relative to compounds whose elemental formulae only differ by the number of CH<sub>2</sub> units. The species aligned with the oblique line (*b*) have the same carbon number but different unsaturation degree. Thus, it is possible to attribute a molecular formula to each dot by just knowing one. It also possible to change the reference of the mass scale with other structural units such as H<sub>2</sub>O, H<sub>2</sub> or O.<sup>62</sup>

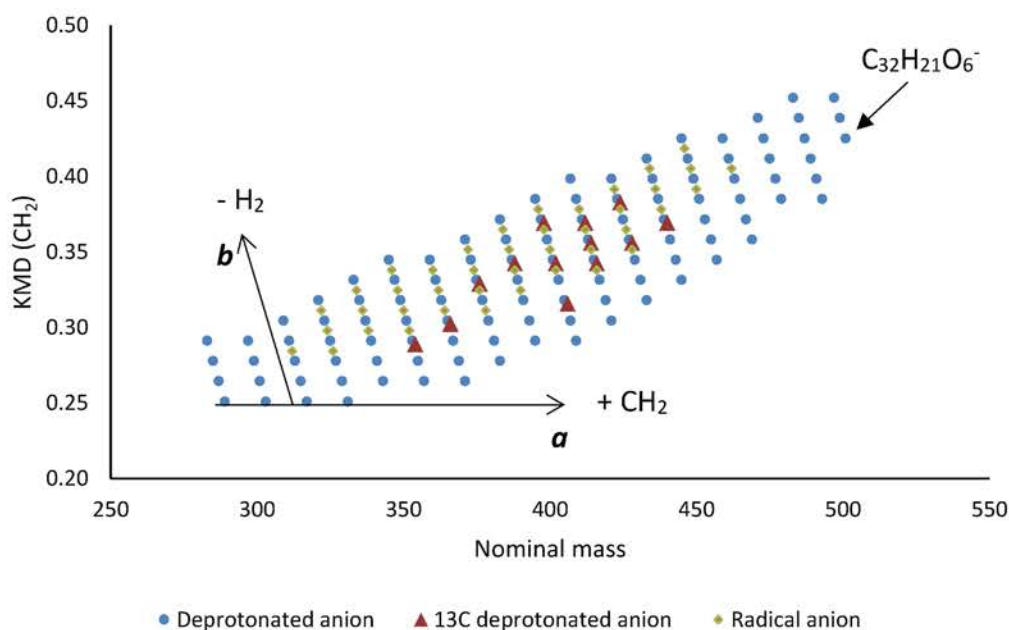


Figure II-32. Kendrick's map of C<sub>x</sub>H<sub>y</sub>O<sub>6</sub> compound family from Oak pyrolysis bio-oil analyzed in (-) LDI FT-ICR MS

## IV. Other studies in mass spectrometry

### IV.A. Introduction

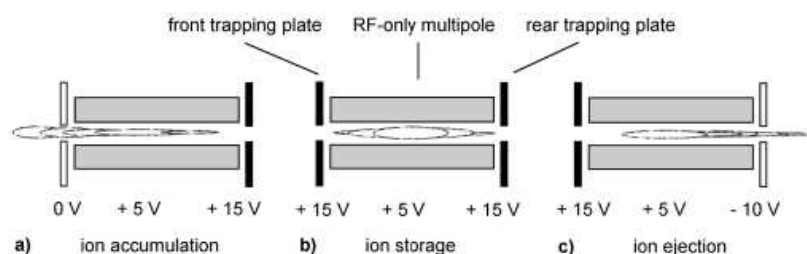
Other experiments have been performed with other instruments that represent a small part of this study. Among them, linear ion trap was used whose principle will be detailed in the next paragraph.

### IV.B. ESI-Linear ion trap (LTQ Velos Pro-Thermo Scientific)

The sample is directly infused in the mass spectrometer via an ESI source in which ions are produced (HESI source from Thermo Scientific). Then, the linear ion trap (LIT) can accumulate,

confine, and eject ions by applying different trapping potentials on axial electrodes (**Figure II-33**). The ions are maintained in the middle of the LIT with a radial RF field.

This instrument was used according to its ability to easily achieve  $MS^n$  experiments for structural characterization. In common ion trap, the selection of the parent ion is performed by the ejection of the other features from linear trap. This is performed by the application of a RF-sweep, corresponding to the different resonance frequencies of the unwanted ions.<sup>65</sup> Thus, the ions are ejected along the radial axis. Another excitation mode is possible with the application of an auxiliary alternative-current field.<sup>66</sup> This excitation leads to an increase of the kinetic energy of the ions which are ejected from the LIT.



*Figure II-33. Illustration of the different operations of a linear RF ion trap at constant DC offset (+5 V) for positive ions. (a) Ion accumulation with application of a voltage at the rear trapping plate. (b) Ion storage with both trapping potentials up. (c) Ion axial ejection after application of an exit potential at the rear trapping plate.*

The configuration of the Thermo Scientific LTQ Velos instrument is a little bit different.<sup>67</sup> A dual-LIT is used (**Figure II-34**). In the first one, the pressure, caused by injection of helium (He) gas, is higher than in the second one. Therefore, in the higher pressure chamber, the ions can be trapped and fragmented. Whereas in the second one, the  $m/z$  measurement of the fragments can be performed with higher scan rate (up to 33 000  $\text{amu}\cdot\text{s}^{-1}$ ) and resolving power (up to 25 000).

Fragmentation is operated by collision induced dissociation *CID* with He gas. A precursor ion  $AB^+$  is excited by a RF and undergoes gas collision, which leads to an increase of its internal energy. If this internal energy is high enough (greater than dissociation energy of some bounds of the molecule), fragmentation occurs. This type of experiment can be reproduced several times to obtain  $MS^n$  spectrum.

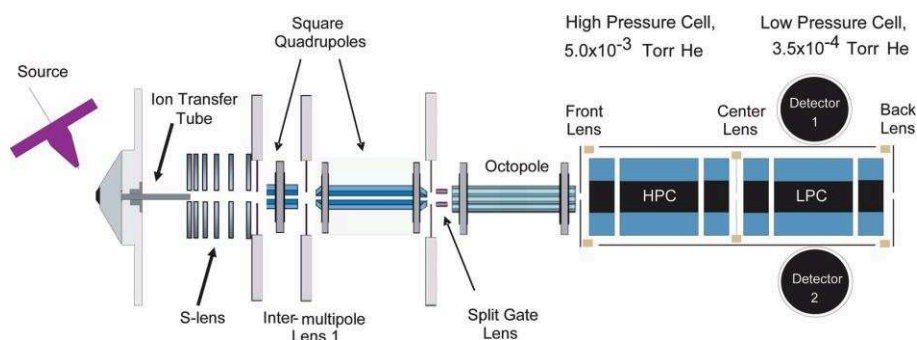


Figure II-34. Schematic representation of the Thermo Scientific LTQ Velos mass spectrometer with the dual-pressure linear ion trap

## V. Conclusion

Characterization of raw and upgraded bio-oils by petroleomic approach requires high resolution mass spectrometers. In this study, the Fourier transform ion cyclotron mass spectrometry was used and its principle was detailed in this chapter. Actually, this powerful instrument enables to identify and assign thousands of different species. Moreover, the use of different ionization sources can be a benefit to extensively explore the “bio-oilomic”. Here, ESI, LDI and, APPI sources were used due to their capabilities to ionize different kinds of compounds in respect with their chemical properties (polarity, unsaturation degree...). The ionization processes involved for each ionization source were also described in this chapter.

The significant amount of a data are graphically represented to facilitate both their interpretation and their comparison. Thanks to these graphical representations, it is easier to highlight which component families are detected. But, these graphs also assess the complementarity of each ionization source and the efficiency of a catalytic treatment. In the next chapters, the different analytical methodologies that have been developed to characterize bio-oils by FT-ICR MS will be detailed. Firstly, the ESI FT-ICR MS method will be discussed, followed by LDI and APPI analyses. The complementarity of these methods will be assessed and different applications such as the catalytic upgrading of bio-oil will be studied.

## VI. References

1. Jia, L., Le-Brech, Y., Shrestha, B., Bente-von Frowein, M., Ehlert, S., Mauviel, G., Zimmermann, R. & Dufour, A. Fast Pyrolysis in a Microfluidized Bed Reactor: Effect of Biomass Properties and Operating Conditions on Volatiles Composition as Analyzed by Online Single Photoionization Mass Spectrometry. *Energy Fuels* **29**, 7364–7374 (2015).
2. Le Brech, Y., Jia, L., Cissé, S., Mauviel, G., Brosse, N. & Dufour, A. Mechanisms of biomass pyrolysis studied by combining a fixed bed reactor with advanced gas analysis. *J. Anal. Appl. Pyrolysis* **117**, 334–346 (2016).
3. Jia, L., Buendia-Kandia, F., Dumarcay, S., Poirot, H., Mauviel, G., Gerardin, P. & Dufour, A. Fast Pyrolysis of Heartwood, Sapwood, and Bark: A Complementary Application of Online Photoionization Mass Spectrometry and Conventional Pyrolysis Gas Chromatography/Mass Spectrometry. *Energy Fuels* **31**, 4078–4089 (2017).
4. Guan, S. H., Marshall, A. G. & Scheppele, S. E. Resolution and chemical formula identification of aromatic hydrocarbons and aromatic compounds containing sulfur, nitrogen, or oxygen in petroleum distillates and refinery streams. *Anal. Chem.* **68**, 46–71 (1996).
5. Marshall, A. G. & Rodgers, R. P. Petroleomics: The Next Grand Challenge for Chemical Analysis. *Acc. Chem. Res.* **37**, 53–59 (2004).
6. Rodgers, R. P. & McKenna, A. M. Petroleum Analysis. *Anal. Chem.* **83**, 4665–4687 (2011).
7. Bae, E., Na, J.-G., Chung, S. H., Kim, H. S. & Kim, S. Identification of about 30 000 Chemical Components in Shale Oils by Electrospray Ionization (ESI) and Atmospheric Pressure Photoionization (APPI) Coupled with 15 T Fourier Transform Ion Cyclotron Resonance Mass Spectrometry (FT-ICR MS) and a Comparison to Conventional Oil. *Energy Fuels* **24**, 2563–2569 (2010).
8. Zeleny, J. Industry application of electrospray technology. *Phys Rev* **10**, 1 (1917).
9. Dole, M., Mack, L. L., Hines, R. L., Mobley, R. C., Ferguson, L. D. & Alice, M. B. Molecular Beams of Macroions. *J. Chem. Phys.* **49**, 2240–2249 (1968).
10. Fenn, J., Mann, M., Meng, C., Wong, S. & Whitehouse, C. Electrospray Ionization for Mass-Spectrometry of Large Biomolecules. *Science* **246**, 64–71 (1989).
11. Taylor, G. Disintegration of Water Drops in an Electric Field. *Proc. R. Soc. Lond. Math. Phys. Eng. Sci.* **280**, 383–397 (1964).
12. Rohner, T. C., Lion, N. & Girault, H. H. Electrochemical and theoretical aspects of electrospray ionisation. *Phys. Chem. Chem. Phys.* **6**, 3056–3068 (2004).
13. Kebarle, P. & Tang, L. From Ions in Solution to Ions in the Gas-Phase - the Mechanism of Electrospray Mass-Spectrometry. *Anal. Chem.* **65**, A972–A986 (1993).
14. Gross, J. H. *Mass Spectrometry: A Textbook*. (Springer Science & Business Media, 2011).
15. Iribarne, J. & Thomson, B. Evaporation of Small Ions from Charged Droplets. *J. Chem. Phys.* **64**, 2287–2294 (1976).
16. Cole, R. B. Some tenets pertaining to electrospray ionization mass spectrometry. *J. Mass Spectrom.* **35**, 763–772 (2000).

17. Banerjee, S. & Mazumdar, S. Electrospray Ionization Mass Spectrometry: A Technique to Access the Information beyond the Molecular Weight of the Analyte. *Int. J. Anal. Chem.* **282574** (2012). doi:10.1155/2012/282574
18. Gabelica, V. & De Pauw, E. Internal energy and fragmentation of ions produced in electrospray sources. *Mass Spectrom. Rev.* **24**, 566–587 (2005).
19. Wilm, M. Principles of Electrospray Ionization. *Mol. Cell. Proteomics* **10**, (2011).
20. Guricza, L. M. & Schrader, W. Electrospray ionization for determination of non-polar polyaromatic hydrocarbons and polyaromatic heterocycles in heavy crude oil asphaltenes. *J. Mass Spectrom.* **50**, 549–557 (2015).
21. Loo, J., Loo, R., Udseth, H., Edmonds, C. & Smith, R. Solvent-Induced Conformational-Changes of Polypeptides Probed by Electrospray-Ionization Mass-Spectrometry. *Rapid Commun. Mass Spectrom.* **5**, 101–105 (1991).
22. Schmidt, A., Karas, M. & Dulcks, T. Effect of different solution flow rates on analyte ion signals in nano-ESI MS, or: When does ESI turn into nano-ESI? *J. Am. Soc. Mass Spectrom.* **14**, 492–500 (2003).
23. Holcapek, M., Volna, K., Jandera, P., Kolarova, L., Lemr, K., Exner, M. & Cirkva, A. Effects of ion-pairing reagents on the electrospray signal suppression of sulphonated dyes and intermediates. *J. Mass Spectrom.* **39**, 43–50 (2004).
24. Gabelica, V., Vreuls, C., Filee, P., Duval, V., Joris, B. & De Pauw, E. Advantages and drawbacks of nanospray for studying noncovalent protein-DNA complexes by mass spectrometry. *Rapid Commun. Mass Spectrom.* **16**, 1723–1728 (2002).
25. Hertzog, J., Carré, V., Le Brech, Y., Dufour, A. & Aubriet, F. Toward Controlled Ionization Conditions for ESI-FT-ICR-MS Analysis of Bio-Oils from Lignocellulosic Material. *Energy Fuels* **30**, 5729–5739 (2016).
26. Fenner, N. & Daly, N. Laser Used for Mass Analysis. *Rev. Sci. Instrum.* **37**, 1068- (1966).
27. Vastola, F., Pirone, A. & Mumma, R. Analysis of Biologically Related Organic Salts by Laser Ionization. *Org. Mass Spectrom.* **1**, 499- (1968).
28. Zhigilei, L. V. & Garrison, B. J. Molecular dynamics simulation study of the fluence dependence of particle yield and plume composition in laser desorption and ablation of organic solids. *Appl. Phys. Lett.* **74**, 1341–1343 (1999).
29. Haglund, R. F. Microscopic and mesoscopic aspects of laser-induced desorption and ablation. *Appl. Surf. Sci.* **96–8**, 1–13 (1996).
30. Mamyryn, B. Laser-Assisted Reflectron Time-of-Flight Mass-Spectrometry. *Int. J. Mass Spectrom. Ion Process.* **131**, 1–19 (1994).
31. Cotter, R. Lasers and Mass-Spectrometry. *Anal. Chem.* **56**, A485- (1984).
32. Aubriet, F. Laser-induced Fourier transform ion cyclotron resonance mass spectrometry of organic and inorganic compounds: methodologies and applications. *Anal. Bioanal. Chem.* **389**, 1381–1396 (2007).
33. Karas, M., Bachmann, D. & Hillenkamp, F. Influence of the Wavelength in High-Irradiance Ultraviolet-Laser Desorption Mass-Spectrometry of Organic-Molecules. *Anal. Chem.* **57**, 2935–2939 (1985).

34. Karas, M. & Hillenkamp, F. Laser Desorption Ionization of Proteins with Molecular Masses Exceeding 10000 Daltons. *Anal. Chem.* **60**, 2299–2301 (1988).
35. Karas, M., Bachmann, D., Bahr, U. & Hillenkamp, F. Matrix-assisted ultraviolet laser desorption of non-volatile compounds. *Int. J. Mass Spectrom. Ion Process.* **78**, 53–68 (1987).
36. Hoffmann, E. D. *Mass Spectrometry: Principles and Applications*. (Wiley-Blackwell, 2007).
37. Knochenmuss, R. Ion formation mechanisms in UV-MALDI. *Analyst* **131**, 966–986 (2006).
38. Karas, M., Gluckmann, M. & Schafer, J. Ionization in matrix-assisted laser desorption/ionization: singly charged molecular ions are the lucky survivors. *J. Mass Spectrom.* **35**, 1–12 (2000).
39. Robb, D. B., Covey, T. R. & Bruins, A. P. Atmospheric Pressure Photoionization: An Ionization Method for Liquid Chromatography–Mass Spectrometry. *Anal. Chem.* **72**, 3653–3659 (2000).
40. Raffaelli, A. & Saba, A. Atmospheric pressure photoionization mass spectrometry. *Mass Spectrom. Rev.* **22**, 318–331 (2003).
41. Ng, C. Y. Vacuum ultraviolet spectroscopy and chemistry by photoionization and photoelectron methods. *Annu. Rev. Phys. Chem.* **53**, 101–140 (2002).
42. Lias, S. G. in *NIST Chem. WebBook NIST Stand. Ref. Database Number 69 Natl. Inst. Stand. Technol. Gaithersburg MD 20899* (2017). at <<http://webbook.nist.gov>>
43. Song, L., Dykstra, A. B., Yao, H. & Bartmess, J. E. Ionization Mechanism of Negative Ion-Direct Analysis in Real Time: A Comparative Study with Negative Ion-Atmospheric Pressure Photoionization. *J. Am. Soc. Mass Spectrom.* **20**, 42–50 (2009).
44. Kauppila, T. J., Kuuranne, T., Meurer, E. C., Eberlin, M. N., Kotiaho, T. & Kostianen, R. Atmospheric pressure photoionization mass spectrometry. Ionization mechanism and the effect of solvent on the ionization of naphthalenes. *Anal. Chem.* **74**, 5470–5479 (2002).
45. Hunter, E. P. & Lias, S. G. in *NIST Chem. WebBook NIST Stand. Ref. Database Number 69 Natl. Inst. Stand. Technol. Gaithersburg MD 20899* (2017). at <<http://webbook.nist.gov>>
46. Lawrence, E. O. & Livingston, M. S. The Production of High Speed Light Ions Without the Use of High Voltages. *Phys. Rev.* **40**, 19–35 (1932).
47. Baldeschwieler, J. D. Ion Cyclotron Resonance Spectroscopy. *Science* **159**, 263–273 (1968).
48. Comisarow, M. & Marshall, A. Fourier-Transform Ion-Cyclotron Resonance Spectroscopy. *Chem. Phys. Lett.* **25**, 282–283 (1974).
49. G. Marshall, A., T. Blakney, G., Chen, T., K. Kaiser, N., M. McKenna, A., P. Rodgers, R., M. Ruddy, B. & Xian, F. Mass Resolution and Mass Accuracy: How Much Is Enough? *Mass Spectrom.* **2**, (2013).
50. Marshall, A. G. & Verdun, F. R. *Fourier Transforms in Nmr, Optical, and Mass Spectrometry: A Users Handbook*. (Elsevier Science Ltd, 1990).
51. Marshall, A. G., Hendrickson, C. L. & Jackson, G. S. Fourier transform ion cyclotron resonance mass spectrometry: A primer. *Mass Spectrom. Rev.* **17**, 1–35 (1998).

52. Schweikhard, L., Ziegler, J., Bopp, H. & Lutzenkirchen, K. The Trapping Condition and a New Instability of the Ion Motion in the Ion-Cyclotron Resonance Trap. *Int. J. Mass Spectrom. Ion Process.* **141**, 77–90 (1995).
53. Beauchamp, J. Theory of Collision-Broadened Ion Cyclotron Resonance Spectra. *J. Chem. Phys.* **46**, 1231–+ (1967).
54. Marshall, A. & Roe, D. Theory of Fourier-Transform Ion-Cyclotron Resonance Mass-Spectroscopy .5. Response to Frequency-Sweep Excitation. *J. Chem. Phys.* **73**, 1581–1590 (1980).
55. Guan, S. H. & Marshall, A. G. Stored waveform inverse Fourier transform (SWIFT) ion excitation in trapped-ion mass spectrometry: Theory and applications. *Int. J. Mass Spectrom.* **157**, 5–37 (1996).
56. Nikolaev, E. N., Kostyukevich, Y. I. & Vladimirov, G. N. Fourier transform ion cyclotron resonance (FT ICR) mass spectrometry: Theory and simulations. *Mass Spectrom. Rev.* **35**, 219–258 (2016).
57. Comisarow, M. & Melka, J. Error Estimates for Finite Zero-Filling in Fourier-Transform Spectrometry. *Anal. Chem.* **51**, 2198–2203 (1979).
58. Goodner, K. L., Milgram, K. E., Williams, K. R., Watson, C. H. & Eyler, J. R. Quantitation of ion abundances in Fourier transform ion cyclotron resonance mass spectrometry. *J. Am. Soc. Mass Spectrom.* **9**, 1204–1212 (1998).
59. Walden, R. H. Analog-to-digital converter survey and analysis. *Ieee J. Sel. Areas Commun.* **17**, 539–550 (1999).
60. Ledford, E., Rempel, D. & Gross, M. Space-Charge Effects in Fourier-Transform Mass-Spectrometry - Mass Calibration. *Anal. Chem.* **56**, 2744–2748 (1984).
61. Hatcher, P., Lerch, H., Bates, A. & Verheyen, T. Solid-State C-13 Nuclear Magnetic-Resonance Studies of Coalified Gymnosperm Xylem Tissue from Australian Brown Coals. *Org. Geochem.* **14**, 145–155 (1989).
62. Kim, S., Kramer, R. W. & Hatcher, P. G. Graphical Method for Analysis of Ultrahigh-Resolution Broadband Mass Spectra of Natural Organic Matter, the Van Krevelen Diagram. *Anal. Chem.* **75**, 5336–5344 (2003).
63. Reinhardt, A., Emmenegger, C., Gerrits, B., Panse, C., Dommen, J., Baltensperger, U., Zenobi, R. & Kalberer, M. Ultrahigh Mass Resolution and Accurate Mass Measurements as a Tool To Characterize Oligomers in Secondary Organic Aerosols. *Anal. Chem.* **79**, 4074–4082 (2007).
64. Kendrick, E. A Mass Scale Based on  $Ch_2=14.0000$  for High Resolution Mass Spectrometry. *Anal. Chem.* **35**, 2146- (1963).
65. Welling, M., Schuessler, H. A., Thompson, R. I. & Walther, H. Ion/molecule reactions, mass spectrometry and optical spectroscopy in a linear ion trap. *Int. J. Mass Spectrom.* **172**, 95–114 (1998).
66. Hager, J. W. A new linear ion trap mass spectrometer. *Rapid Commun. Mass Spectrom.* **16**, 512–526 (2002).

67. Pekar Second, T., Blethrow, J. D., Schwartz, J. C., Merrihew, G. E., MacCoss, M. J., Swaney, D. L., Russell, J. D., Coon, J. J. & Zabrouskov, V. Dual-Pressure Linear Ion Trap Mass Spectrometer Improving the Analysis of Complex Protein Mixtures. *Anal. Chem.* **81**, 7757–7765 (2009).



---

## *Chapter III*

---

*Development of a methodology  
by ESI FT-ICR MS for the charac-  
terization of bio-oils*

## Table of Contents

I.	Introduction.....	147
II.	Influence of the temperature and the solvent on the bio-oil ESI FT-ICR MS signature .....	147
II.A.	Introduction.....	147
II.B.	Experimental procedure.....	148
II.C.	Global description of obtained features in respect with the used ESI parameters .....	148
II.D.	Effect of the capillary temperature on the obtained distributions of C <sub>x</sub> H <sub>y</sub> O <sub>z</sub> compounds ... .....	150
II.E.	Influence of the solvent.....	152
III.	Influence of dopants on the bio-oil composition description .....	155
III.A.	Introduction.....	155
III.B.	Experimental procedure.....	155
III.C.	Bio-oil composition descriptions achieved by ESI FT-ICR MS analysis .....	156
III.C.1.	Analyses in negative ion mode .....	156
III.C.2.	Analyses in positive ion mode .....	161
III.D.	Complementarity of the detection modes .....	171
III.E.	Conclusion .....	172
IV.	Evidence of carbonyl compounds in complex mixtures with primary amines by petroleomic approach.....	173
IV.A.	Introduction.....	173
IV.B.	Materials and methods .....	174
IV.B.1.	Sample preparation.....	174
IV.B.2.	Mass spectrometry measurements.....	176
IV.C.	Study of standard carbonyl compounds by ESI LIT MS .....	177
IV.C.1.	Vanillin .....	177
IV.C.2.	Cinnamaldehyde.....	185
IV.C.3.	Butyrophenone.....	189
IV.C.4.	Trihydroxyacetophenone .....	194
IV.D.	Complementary NMR analyses .....	200
IV.D.1.	Introduction.....	200
IV.D.2.	Materials and methods .....	200
IV.D.3.	<sup>13</sup> C NMR measurements .....	201
IV.D.4.	Conclusion .....	205
IV.E.	Conclusion .....	205
IV.F.	(+) ESI-FT-ICR-MS analysis of bio-oil doped with 3-chloroaniline .....	205
IV.G.	Conclusion .....	211
V.	Conclusion .....	211
VI.	References.....	213

## I. Introduction

The characterization of the biomass derived bio-oils can be performed by means of different and complementary methods which have been widely described in the Chapter I. Among them, the petroleomic approach ensures to obtain the chemical signature of bio-oils and the elemental formula of its components. Generally, the studies dealing with the bio-oil characterization are conducted by (-) ESI-HRMS. Nevertheless, the previous published works never really dealt with the optimization of the ESI-HRMS for the bio-oil characterization. Therefore, this chapter will be focused on the development of a sensitive and robust ESI FT-ICR MS methodology, in both positive and negative detection modes. Different parameters influencing the ESI process will be examined and their effects on the bio-oil signature will be studied. The influence of the used solvent as well as the importance of the temperature of the probe used to infuse the sample in the ESI source will be investigated. The effect of different dopants commonly used to promote cationization/protonation or anionization/deprotonation processes will be evaluated. The influence of the dopants will be discussed in respect with (i) the increase of sensitivity, (ii) the increase of repeatability, and (iii) its ability to yield a bio-oil signature consistent with its CHNOS analysis. This part of this chapter corresponds to a paper published in *Energy & Fuels* in 2016.<sup>1</sup> Finally, the possibility that the most commonly used dopant in (-) ESI petroleomic analysis, i.e. NH<sub>4</sub>OH, may induce misinterpretation and analytical bias will be discussed in the last section of this chapter.

## II. Influence of the temperature and the solvent on the bio-oil ESI FT-ICR MS signature

### II.A. Introduction

The physicochemical properties of the solution infused in an ESI source significantly influence the electrospray ionization process. Indeed, a solvent with a high dielectric constant will promote the formation of droplets with a high charge density. Such solvent will better separate the ions and stabilize the multiply charged species. Additionally, it is known that protic solvents favor proton transfer phenomenon.<sup>2</sup> The temperature is another important param-

ter which affects the efficiency of the solvent evaporation and, consequently, the ion formation.<sup>3</sup> In this study, methanol, water, and mixture of both of them, were used. The main physicochemical properties of water and methanol are reported in the **Table III-1**.

	Proton affinity (kJ.mol <sup>-1</sup> )	Boiling point at 1 atm ( °C)	Dielectric constant at 25 °C (F.m <sup>-1</sup> )
Methanol	754	64.7	32.7
Water	691	100	78.5

Table III-1. Physicochemical properties of methanol and water<sup>4,5</sup>

The purpose of this part of the study is to define the influence of the global variation of the solvent polarity, as well as the temperature at which the bio-oil solutions are infused in the ESI source, on the obtained features.

### II.B. Experimental procedure

The oak pyrolysis bio-oil was used. It was diluted by 10 in 1:0, 4:1, 1:1, 1:4, and 0:1 H<sub>2</sub>O:MeOH solutions. Sodium acetate was added to the bio-oil solutions to a final concentration of 0.1 mg.mL<sup>-1</sup> to favor cationization process in positive ion ESI FT-ICR MS. The used solvents and chemicals are analytical grade. The achieved samples were infused at a 2  $\mu$ L.min<sup>-1</sup> flow rate in the ESI source heated at 70 °C and with a probe kept at 75 °C or 110 °C. The measurements were performed with a 9.4 T FT-ICR mass spectrometer in positive detection mode. Nitrogen was used as a desolvation gas and 80 individual mass spectra were summed to generate a final mass spectrum with a high signal-to-noise ratio.

The comparison of the results is first conducted by considering different simple criteria: the total ion current (TIC), the number of identified peaks, and the relative abundance of the different classes of compound.

### II.C. Global description of obtained features in respect with the used ESI parameters

Whatever the experimental conditions, signals are observed in the 200 to 550  $m/z$  range. The obtained global bio-oil composition for the different ESI conditions is reported in the **Table III-2**. The obtained distributions for the different experimental conditions are very similar. The C<sub>x</sub>H<sub>y</sub>O<sub>z</sub> compounds detected as [M+Na]<sup>+</sup> adducts represent close to 99 % of the signal. A tiny part of the TIC is assigned to both protonated C<sub>x</sub>H<sub>y</sub>O<sub>z</sub> and C<sub>x</sub>H<sub>y</sub>NO<sub>z</sub> compounds. This bio-oil

description is in agreement with the elemental composition of wood pyrolysis bio-oil that evidences a significant amount of oxygen (56 wt. %) and a poor content of nitrogen (< 2 wt. %).<sup>6</sup> Both the value of the TIC and the number of assigned signals vary in respect with the probe temperature or the H<sub>2</sub>O:MeOH ratio. The TIC increases with the temperature whereas the number of assigned peaks decreases or remains constant. These behaviors are not antagonist when the particularities of the ICR mass spectrometry are known. Indeed, the ICR cell is an ion trap in which all the ions are simultaneously present whatever their *m/z* ratio. The increase of the TIC is relative to an increase of the number of ions in a restricted area of the space. The increase of the charge density, the so-called space charge effects, induces the deterioration of the coherence of the ion cyclotron motion. This affects the S/N ratio which may decrease due to the growth of the noise. Nevertheless, the most pronounced effect is the disappearance or, at least, the decrease of the signal relative to the poor abundant ions. Indeed, they are more affected by space charge effects than the more abundant ions. As a consequence, the detected species, when a high TIC value is obtained, are associated to the main components of the bio-oil. This also explains why the distribution of the different classes of compounds is poorly affected by the modification of the experimental parameters.

H <sub>2</sub> O:MeOH	Number of assigned peaks		TIC		C <sub>x</sub> H <sub>y</sub> NaO <sub>z</sub>		C <sub>x</sub> H <sub>y</sub> O <sub>z</sub>		C <sub>x</sub> H <sub>y</sub> NO <sub>z</sub>	
	75 °C	110 °C	75 °C	110 °C	75 °C	110 °C	75 °C	110 °C	75 °C	110 °C
<b>0:1</b>	607	370	7284	31196	99.1 %	100 %	-	-	0.9 %	-
<b>1:4</b>	502	385	4587	23542	97.7 %	99.5 %	1.2 %	-	1.1 %	0.5 %
<b>1:1</b>	353	393	9860	29544	99.0 %	99.5 %	0.1 %	-	0.9 %	0.5 %
<b>4:1</b>	361	369	19061	27381	99.7 %	99.4 %	0.1 %	-	0.2 %	0.6 %
<b>1:0</b>	360	344	18705	41886	99.8 %	99.9 %	-	-	0.2 %	0.1 %

Table III-2. Number of assigned peaks, total ion current, and relative abundance of the different compound families obtained in the study of oak bio-oil by (+) ESI FT-ICR MS in respect with the H<sub>2</sub>O:MeOH ratio and the probe temperature

## II.D. Effect of the capillary temperature on the obtained distributions of $C_xH_yO_z$ compounds

The **Figure III-1** represents the distribution of  $C_xH_yNaO_z$  compounds in respect with the oxygen atom count, the probe temperature, and the nature of the solvent. The  $O_3$ - $O_{14}$  compounds are systematically observed and present a bimodal distribution. The first massif is centered on the  $O_6$  species and the second, on the  $O_{11}$ - $O_{12}$  ones. The first massif involves lignin derivatives and the second, the cellulose and hemicellulose derived species. More details and explanations will be given in the following part (section **III.C.2.d**).

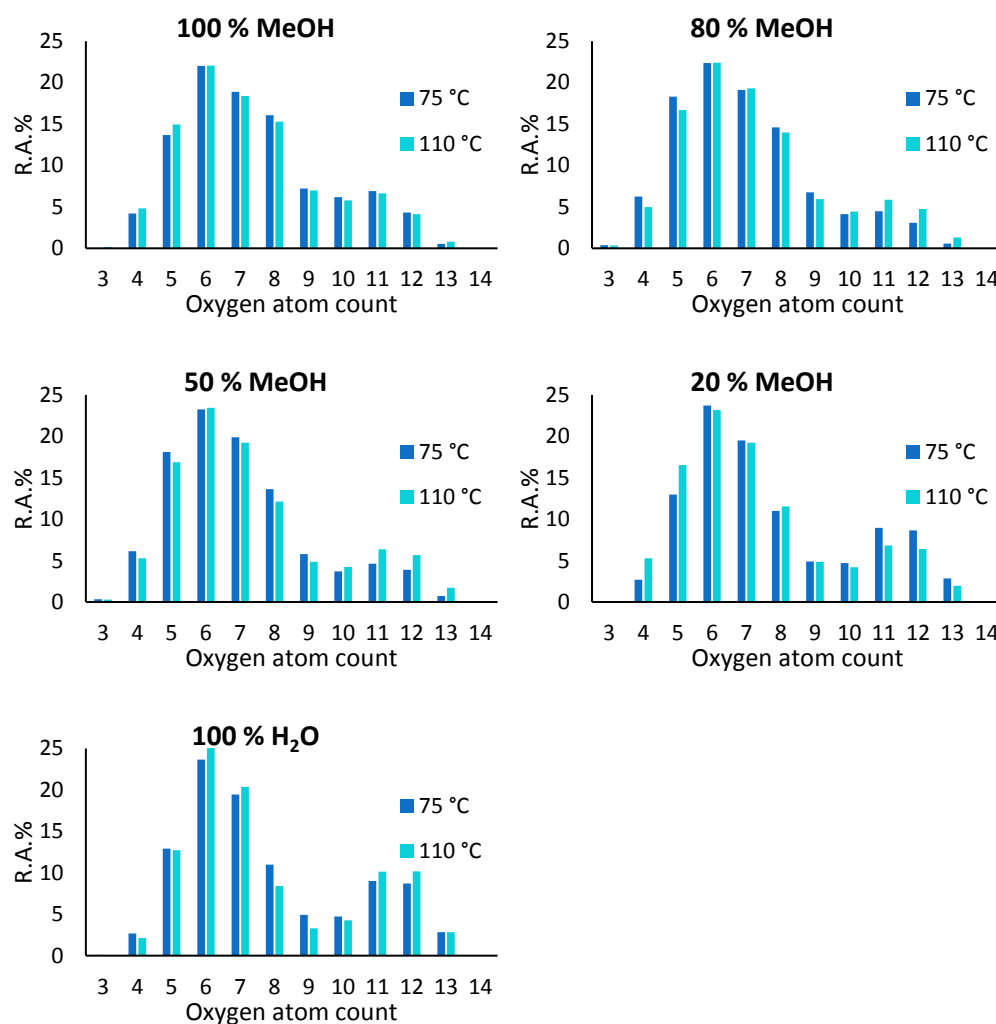


Figure III-1. Comparison of the  $C_xH_yNaO_z$  distribution in respect with the oxygen atom count obtained for identical water:methanol ratios for capillary temperatures at 75 and 110 °C.

Nevertheless, pyrolytic lignin components are characterized by a low oxygen content ( $O_3$ - $O_9$ ) and a high unsaturation degree which have to be correlated with the phenolic subunits of this biomass constituent. The sugarc derivatives are more oxygenated ( $O_8$ - $O_{14}$ ) and less unsaturated. Consequently, they are expected to be more polar than the lignin derivatives.

The  $C_xH_yO_z$  distributions obtained with pure methanolic solution at 75 and 110 °C do not reflect significant differences. The addition of water modifies this behavior. At the exception of the 4:1 water:methanol solutions, the relative abundance of the sugarc species ( $O_9$ - $O_{14}$ ) increases with the probe temperature. For pyrolytic lignin species, no specific trend can be evidenced.

However, the examination of the cumulative S/N ratio of lignin derivatives, on the one hand, and of sugarc derivatives, on the other hand, ensures to consider that sugarc species are better observed at 110 °C than at 75 °C, at least, when the amount of methanol is lower than 50 % (**Figure III-2**).

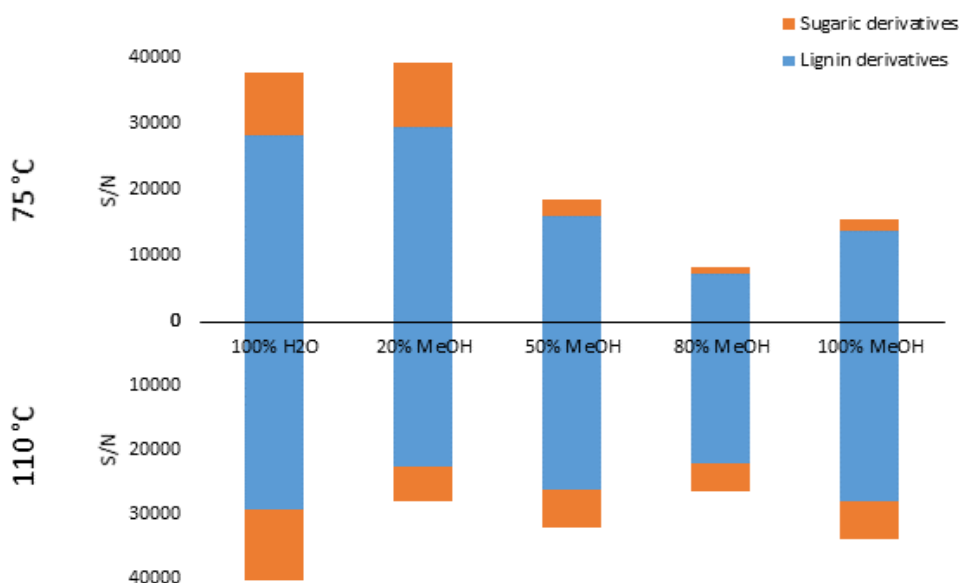


Figure III-2. Cumulative S/N ratios of lignin and sugarc derivatives obtained for different methanol:water ratios at 75 and 110 °C.

The sugarc derivatives are more polar and tend to be better solvated by the most polar solvent molecules (water). According to the binary MeOH:water phase diagram (see **Annex I**), for MeOH:water ratio greater than 1, at 75 °C, the methanol is essentially in the gas state and stepwise water enrichment of the droplet, during the ESI process, is expected. The high affinity of polar sugarc compounds to water limits their ionization. Indeed, it has to be kept in mind that ions are detected as  $[M+Na]^+$  adduct species. The sodium cations are also solvated by the

water molecules. The direct interaction of sugarc compound and  $\text{Na}^+$  is, consequently, limited by their own solvation shell. In contrast, the phenolic compounds are more accessible to  $\text{Na}^+$  due to a less pronounced interaction with the water molecule.

At 110 °C, water and methanol evaporation rates are comparable and no water enrichment is expected. This explains why the contribution of sugarc compounds significantly increases in that case. For pure water or 1:4 methanol:water solutions, the evaporation of both solvents is comparable. The boiling point of 1:4 methanol:water is equal to 82 °C, which is higher than the probe temperature when experiments are conducted at 75 °C.

Similar behavior has also been observed by Page *et al.* in the study of reserpine in a 1:1 water:methanol (1 % acetic acid) solution.<sup>7</sup> They demonstrated an increase of the reserpine signal when the probe temperature increased from 60 to 140 °C. Gabelica *et al.*, who demonstrated that low probe temperatures are responsible of incomplete desolvation, confirm these meanings.<sup>8</sup>

Thus, the probe temperature influences the obtained bio-oil fingerprint when water or water-methanol solutions are used. At 110 °C, an intense signal and a high sensitivity for the sugarc derivatives are observed. Nevertheless, the bio-oils are not thermodynamically stable and high temperature favors chemical reactions involved in its aging process.<sup>9,10</sup> Haverly *et al.* demonstrated that compositional changes occurred quickly in fractionated pyrolysis bio-oil at temperature higher than 100 °C.<sup>11</sup> These processes affect the TAN, the average molecular weight, and the moisture content which globally increase with the time and the temperature. Therefore, it was chosen to use the lowest temperature to limit the aging of the bio-oil components during the analysis. The probe temperature was systematically set at 75 °C in the following experiments.

### *II.E. Influence of the solvent*

The compound class distribution is only poorly affected by the modification of the water:methanol ratio (**Table III-2**). Nevertheless, bimodal  $\text{C}_x\text{H}_y\text{O}_z$  distribution in respect with the oxygen atom count displays some interesting behavior.

Higher is the water amount and more sensitive is the analysis towards sugarc compounds. Indeed, 80 % and 100 % water solutions lead to a significant increase of the relative



abundance of the O<sub>11</sub> to O<sub>13</sub> species whereas the relative abundance of the O<sub>3</sub>-O<sub>5</sub> ones decreases (**Figure III-3**).

It has also to be noticed that very close distributions are observed for these solvent conditions whatever the considered oxygen atom count. This is not the case for pure methanolic solution which demonstrates a monotonic evolution of the relative abundance. Explanations have still been given considering the binary diagram of water:methanol mixture (**Annex I**). For mixture with more than 42 % of methanol, water enrichment of the droplet may occur with a probe temperature at 75 °C and limits the desolvation of the polar sugarc compounds which are preferentially solvated by water.

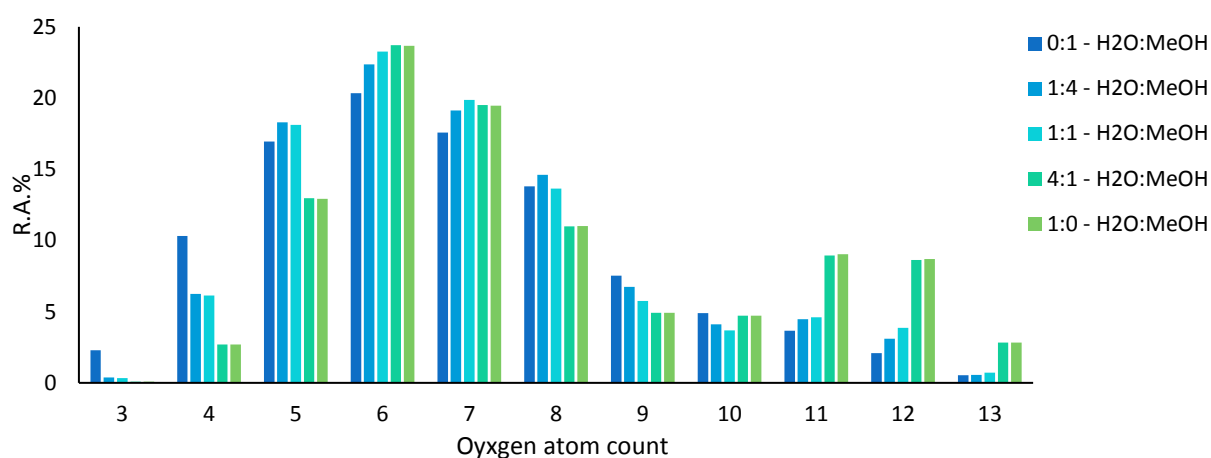


Figure III-3. Distribution of the C<sub>x</sub>H<sub>y</sub>NaO<sub>z</sub> compounds in respect with the oxygen atom count according to the water:methanol ratios, at 75 °C

The van Krevelen diagrams of the C<sub>x</sub>H<sub>y</sub>NaO<sub>z</sub> family demonstrate that lipids, pyrolytic lignin, and sugarc derivatives are detected whatever the used solvent conditions (**Figure III-4**). The relative abundance of each biomass derived components are coherent with those obtained in the **Figure III-3**. The cellulose and hemicellulose linked species are significantly better detected with solutions presenting a high water:methanol ratio. High amount of methanol is more suited for a more sensitive observation of the pyrolytic lignin and, in a lesser extent, the lipids.

The distinction of sugarc and lignin derivatives presented in this work is in agreement with the works of Miettinen *et al.*<sup>12</sup> and Jarvis *et al.*<sup>13</sup> Both of them separated different pyrolysis bio-oils into an aqueous and an oily fraction before (-) ESI FT-ICR MS analysis. The obtained distribution of the C<sub>x</sub>H<sub>y</sub>O<sub>z</sub> compounds from the oily phase in respect with the oxygen atom count was centered on lower values of oxygen atom count than the one obtained with the aqueous phase. The van Krevelen diagrams achieved by Miettinen *et al.* demonstrated that

both lipids and pyrolytic lignin composed the two phases whereas sugarc derivatives were only evidenced in the aqueous fraction.

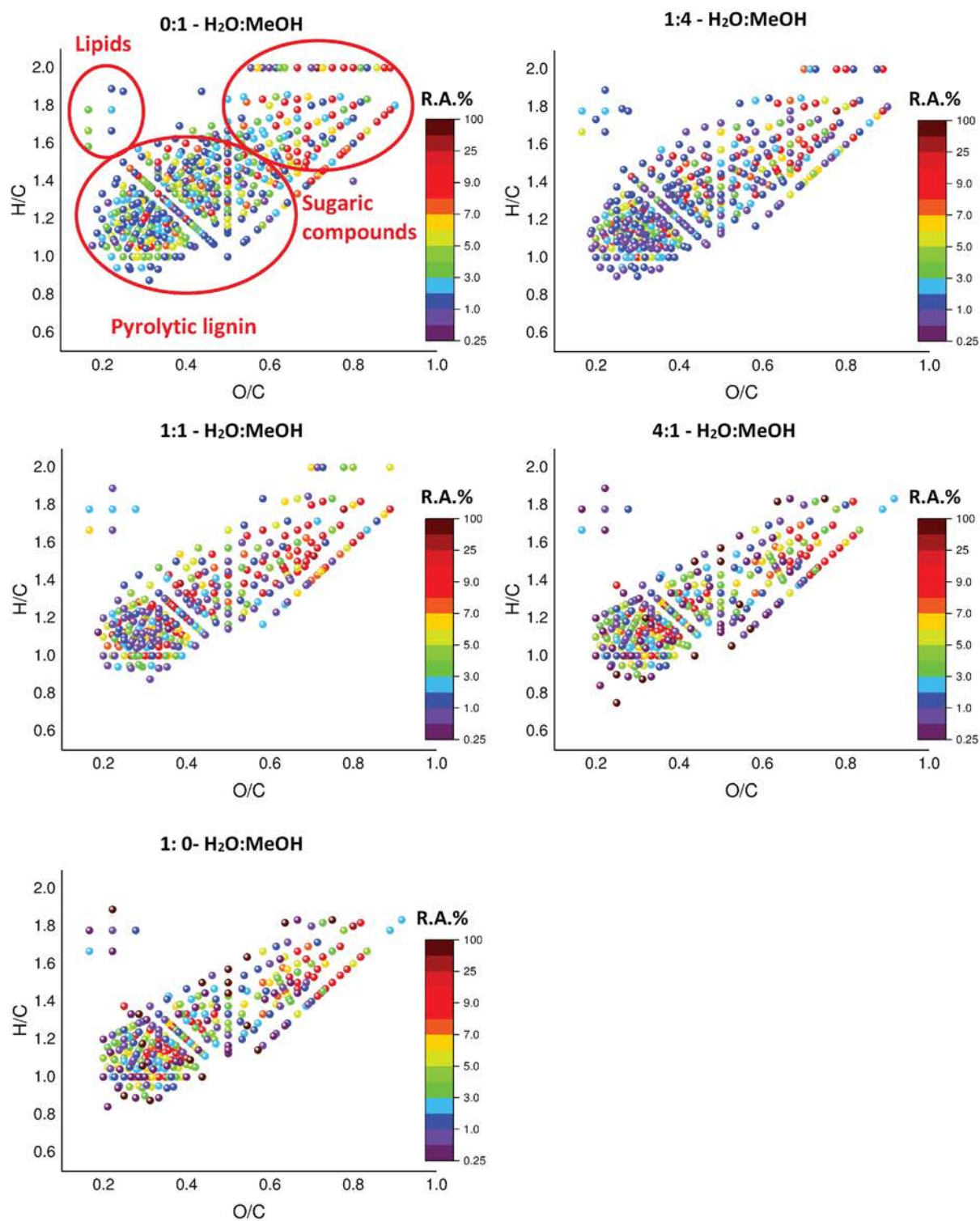


Figure III-4. Van Krevelen diagrams of the  $C_xH_yNaO_z$  species of the oak bio-oil assigned after (+) ESI FT-ICR MS analysis for different water:methanol ratios at 75 °C

### III. Influence of dopants on the bio-oil composition description

The main part of the results presented in this section are included in the publication “To-ward Controlled Ionization Conditions for ESI-FT-ICR-MS Analysis of Bio-Oils from Lignocellulosic Material”, *Energy & Fuels* **30**, 5729–5739, 2016.

#### III.A. Introduction

Cationization and anionization agents are other features influencing the ESI process. As part of the bio-oil characterization, several studies have been performed in which dopants have been used. Typically, ammonium hydroxide and formic acid promote deprotonation and protonation for analyses in negative and positive ion ESI-MS, respectively.<sup>14–16</sup> In these conditions, the detected species are in the form of  $[M+H]^+$  and  $[M-H]^-$ , respectively. Other dopants such as NaCl and NH<sub>4</sub>Cl may be used, which ensures the ions to be detected as  $[M+Na]^+$ ,  $[M+Cl]^-$ , and  $[M+NH_4]^+$  adducts.<sup>17</sup> However no systematic study has been performed to assess the selectivity of the dopant towards bio-oil components. Therefore, in this study, various dopants with different chemical properties will be investigated and the corresponding bio-oil composition description will be assessed in both positive and negative ion ESI FT-ICR MS. Thus, the most commonly used formic acid and ammonium hydroxide will be initially evaluated for experiments performed in positive and negative detection modes, respectively. Alternatively, ammonium hydroxide, ammonium acetate, and alkaline acetate will be used to favor the cationization. For both ion detection modes, the results obtained without dopant will be compared with those yielded with dopant.

#### III.B. Experimental procedure

The different experiments were performed with a pyrolysis bio-oil from Miscanthus. The bio-oil was diluted by ten in methanol. Different dopants were added to the bio-oil solution at different concentrations. Thus, formic acid and ammonium hydroxide were introduced to a final concentration of 1 % (v:v). The concentration of ammonium acetate and alkaline acetate were adjusted and set at 1 mg.mL<sup>-1</sup> and 0.1 mg.mL<sup>-1</sup>, respectively. ESI FT-ICR MS measurements were conducted in both positive and negative ion detection modes with the 9.4 T FT-ICR mass spectrometer. The used high voltage (HV) was  $\pm 3500$  V. Nitrogen was used to assist solvent evaporation. The sample was infused in the ion source at a flow rate of 3 to 6  $\mu\text{L}\cdot\text{min}^{-1}$ .

<sup>1</sup>. The temperature of the source and probe were both kept at 80 °C. From 30 to 140 individual mass spectra were accumulated to obtain a final mass spectrum with a high signal-to-noise ratio.

### III.C. Bio-oil composition descriptions achieved by ESI FT-ICR MS analysis

For each experimental condition, the results obtained are gathered in the **Table III-3**. All the measurements have been performed, at least, twice and similar results have been obtained (see for example the results with sodium acetate in **Table III-3**), except in case of positive ion experiments performed without dopant.

Dopant	Number of assigned peaks	TIC	O <sub>z</sub>	NO <sub>z</sub>	N <sub>2</sub> O <sub>z</sub>	N <sub>3</sub> O <sub>z</sub>	N <sub>4-5</sub> O <sub>z</sub>	SO <sub>z</sub>
<b>Negative ions</b>								
Without	529	4626	98 %	–	–	–	–	2 %
NH <sub>4</sub> OH	920	9756	73 %	24 %	3 %	–	–	–
HCOOH	532	588	66 %	–	–	–	–	34 %
<b>Positive ions</b>								
Without	413	724 <sup>a</sup>	96 %	4 %	–	–	–	–
	425	8373 <sup>b</sup>	32 %	48 %	19 %	<1 %	–	–
HCOOH	1500	2957	15 %	52 %	29 %	3 %	<1 %	–
AcONH <sub>4</sub>	920	8397	3 %	8 %	39 %	38 %	12 %	–
NH <sub>4</sub> OH	1197	3661	11 %	27 %	42 %	17 %	3 %	–
AcONa	858	8038 <sup>a</sup>	98 %	2 %	–	–	–	–
	890	9050 <sup>b</sup>	98 %	2 %	–	–	–	–
AcOLi	735	10623	98 %	2 %	–	–	–	–
AcOK	952	8102	81 %	15 %	4 %	–	–	–

<sup>a</sup> Analysis I, <sup>b</sup> Analysis II.

Table III-3. Number of assigned peaks, total ion current, and assigned compound families observed in positive and negative ESI–FT-ICR-MS experiments for the different investigated ionization conditions with *Miscanthus* bio-oil.

#### III.C.1. Analyses in negative ion mode

A huge number of signals is observed in the 170–550 *m/z* range, on the (-) ESI mass spectrum of the bio-oil (**Figure III-5**). The inset of the **Figure III-5** demonstrates the need to use FT-ICR mass spectrometry to distinguish and unambiguously identify each of the detected signals.

Thus, five individual formulae are assigned in a 0.075  $m/z$  range with a mass measurement error lower than 500 ppb at the  $m/z$  373 nominal mass. Most of them are relative to oxygenated  $C_xH_yO_z$  species. They are thought to result from deprotonation of the neutral molecules during ionization, leading to the formation of  $[M-H]^-$  ions. This is confirmed by the increase of the TIC (from  $\sim 4600$  to  $\sim 9750$ ) and the number of detected peaks (from 529 to 920) when more alkaline conditions are used (addition of ammonium hydroxide) and their decrease (TIC  $\sim 590$  and 530 identified peaks) when formic acid is added (**Table III-3**). More specifically, 98 % and 73 % of the TIC is attributed to  $C_xH_yO_z$  species when experiments are conducted without dopant and with ammonium hydroxide, respectively.

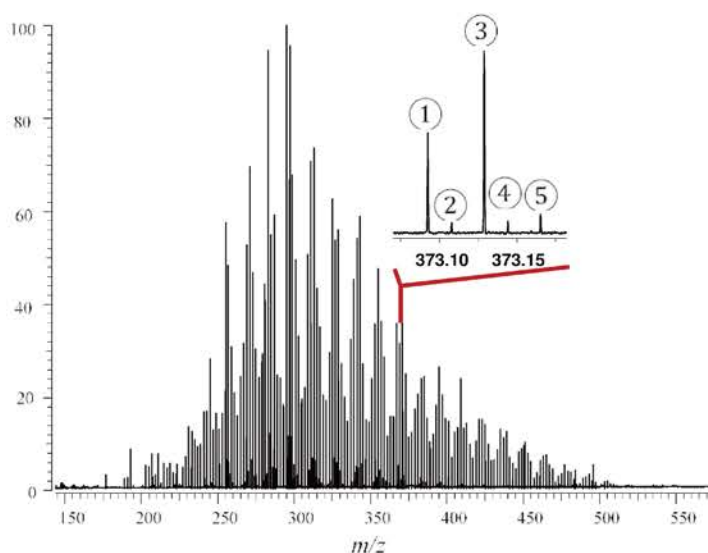


Figure III-5. Mass spectrum of the pyrolysis *Miscanthus* bio-oil obtained in (-) ESI FT-ICR MS. Inset corresponds to the  $m/z$  373 nominal mass : ①  $C_{19}H_{17}O_8^-$  ( $m/z$  373.0918 error 0.30 ppm), ②  $C_{23}H_{17}O_5^-$  ( $m/z$  373.1081 error 0.07 ppm), ③  $C_{20}H_{21}O_7^-$  ( $m/z$  373.1288 error 0.44 ppm), ④  $C_{24}H_{21}O_4^-$  ( $m/z$  373.1444 error 0.25 ppm) and, ⑤  $C_{21}H_{25}O_6^-$  ( $m/z$  373.1655 error 0.26 ppm).

Some general trends may be given whatever the ionization conditions. For oxygenated hydrocarbons, the observed DBE values range from 3 to 17 and the hydrocarbon skeleton involves between 10 and 30 carbon atoms. For a given DBE value, measurements performed with ammonium hydroxide lead to the detection of the compounds with the highest carbon number (**Figure III-6**). The most abundant classes of compounds are always the  $O_4$ - $O_7$  ones. This appears to be a general trend when pyrolyzed bio-oils are investigated by ESI-MS. The same dominant oxygen classes of compounds have been observed by Sudasinghe *et al.*<sup>15</sup> and Abdelnur *et al.*<sup>18</sup> when they characterized pine, eucalyptus, eucalyptus bark, and cellulosic

mud bio-oils by (-) ESI FT-ICR MS after addition of 0.1 to 0.2 % ammonium hydroxide (v:v) or in the study performed by Alsbou *et al.*<sup>17</sup> on forest residue bio-oils doped with NaOH.

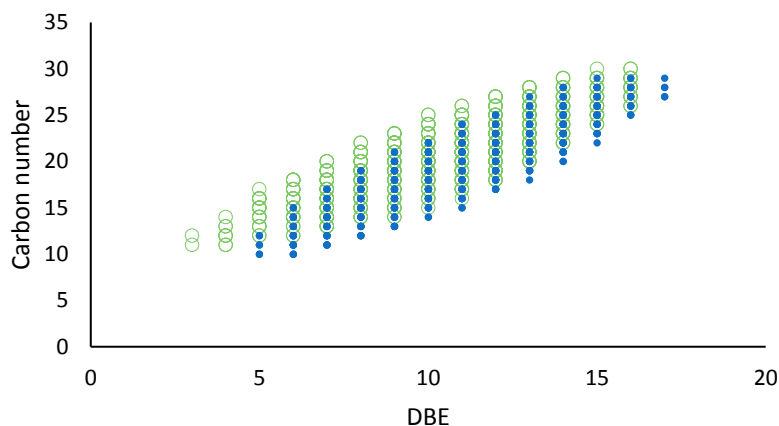


Figure III-6. Carbon number vs. DBE value distribution of  $C_xH_yO_z$  ions observed in (-) ESI without (solid blue circle) and with  $NH_4OH$  (open green circle)

In addition to  $C_xH_yO_z$  species, 2 % of the TIC is assigned to  $C_xH_ySO_z$  ions, when experiments were conducted without dopant. The main part includes at least three oxygen atoms. Such a behavior has been previously observed by Miettinen *et al.*<sup>12</sup> and was assigned to the sulfur present in small quantities in softwood lignin, typically in the form of sulfonic acid. The efficiency of ionization is high enough to ensure the easy detection of such sulfonated species.

Without dopant, the signal relative to nitrogen compounds is very low (< 0.1 %). This may be explained by the low abundance of nitrogen in Miscanthus but also by the chemical properties of  $C_xH_yN_nO_z$ . According to the acidity of bio-oils, nitrogen species are thought to be preferentially protonated or neutral and consequently not detectable in negative detection mode.

The negative mass spectrum of the bio-oil with 1 % of ammonium hydroxide leads to the specific observation of  $C_xH_yNO_{3-9}$  and  $C_xH_yN_2O_{4-8}$  compounds. The signal relative to these N and  $N_2$  species corresponds to 27 % of the TIC. This is surprising according to the low amount of nitrogen in Miscanthus (0.23 wt. %).<sup>19</sup> Some tentative explanations will be given in the discussion section and in the next part of this chapter.

### III.C.1.a. Discussion

The predominance of the  $C_xH_yO_z$  compounds in negative detection mode was previously evidenced in the study of different kinds of bio-oils produced by HTL and pyrolysis.<sup>14,18,20,21</sup> The distribution of this compound family in respect with the number of oxygen atoms is slightly modified by the ionization conditions. Without dopant, the  $O_z$  classes of compounds range from  $O_2$  to  $O_{10}$  whereas a narrower distribution from  $O_3$  to  $O_9$  is observed when

1 % of ammonium hydroxide is added to the bio-oil. Nevertheless, the detailed examination of the  $O_2$  class distributions highlights a small shift to higher oxygen amounts with  $NH_4OH$  (**Figure III-7.a**). Whatever the sprayed solution, the  $O_5$  compounds are the most prominent species and correspond, at least, to 25% of the TIC. When the unsaturation distributions of these  $C_xH_yO_5$  species (value of the DBE) are considered, some differences appear. While the DBE value ranges from 5 to 15, the addition of  $NH_4OH$  clearly favors the detection of more unsaturated compounds (**Figure III-7.b**). The DBE distribution of  $C_xH_yO_5$  ions decreases by one unit when  $NH_4OH$  is used. This behavior is also systematically observed for the other  $O_2$  class of compounds.

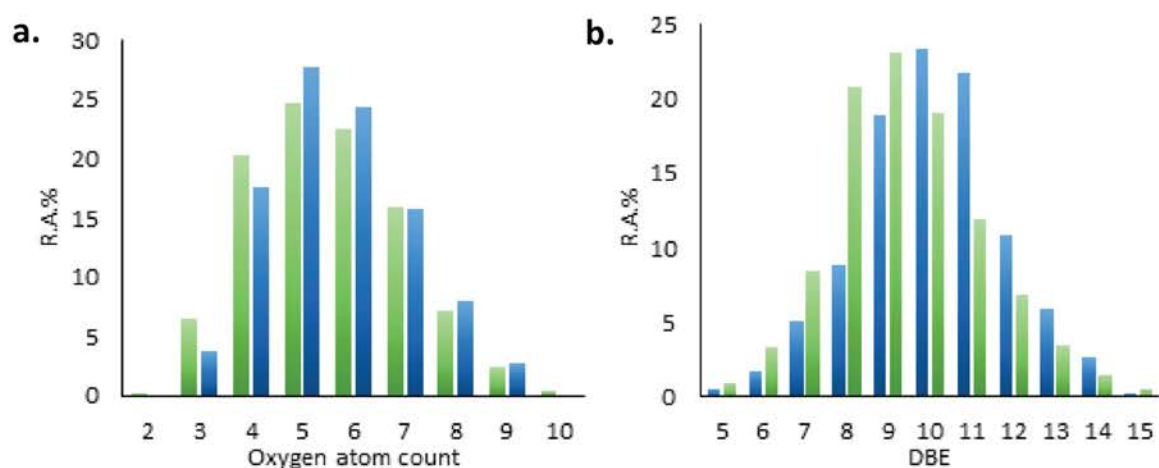
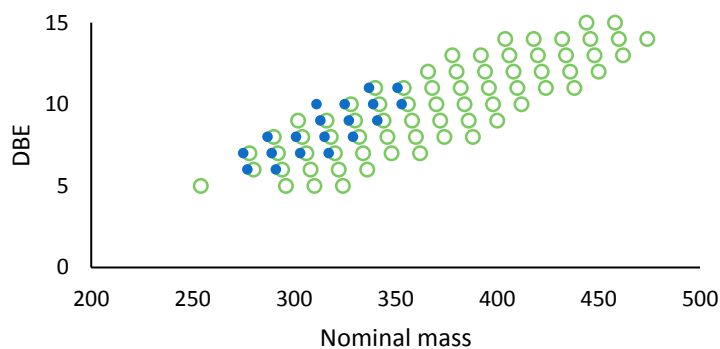


Figure III-7. (a) Distribution of the  $C_xH_yO_2$  species in respect with oxygen atom count and (b) relative abundance vs. DBE value distributions of the  $C_xH_yO_5$  compounds achieved from analyses in (-) ESI FT-ICR MS with the *Miscanthus* bio-oil without dopant (green) and with  $NH_4OH$  (blue)

The most obvious explanation may be relative to the modification of the ionization conditions (variation of the pH) which may influence the relative distribution of the detected species but the addition of 1 %  $NH_4OH$  may also favor some chemical reactions. It is well known that under basic condition, the nucleophile addition of  $OH^-$  may occur to the carbonyl carbon followed by the protonation or, in this specific case, the methylation of the carbonyl oxygen through the reaction with methanol.<sup>22</sup> The efficiency of this reaction may be improved by the temperature of the ionization source. Moreover, the electric field generated by the application of the high voltage as well as the ESI mechanism itself also ensure the increase of the polarity of the molecules.<sup>23</sup> In this case, the polarity of the  $C=O$  bond favors the addition of the hydroxyl anion on the carbon atom. Such behavior may induce an increase of the number of oxygen (addition of  $OH^-$ ) for carbonyl part of the bio-oil components and a decrease of the DBE value by one unit. That is exactly what it is observed when the bio-oil is sprayed with

$\text{NH}_4\text{OH}$  (**Figure III-6** and **Figure III-7**). Moreover, the reaction of methanol with the compound resulting from the nucleophile addition of  $\text{OH}^-$  may lead to an increase of the number of carbon (methyl addition). This is observed when  $\text{O}_5$  and  $\text{O}_6$  compounds with a DBE value between 7 and 11 are considered. Nevertheless, the used alkaline condition limits the methyl addition and ensures that, at least, part of compounds resulting from the hydroxyl addition does not react with methanol. This assertion is confirmed by considering the positive ion result for which such a behavior (shift of the DBE value by one unit) is not observed.

Finally, the significant detection of  $\text{C}_x\text{H}_y\text{NO}_{3-9}$  and  $\text{C}_x\text{H}_y\text{N}_2\text{O}_{4-8}$  compounds by using ammonium hydroxide depicts a better ionization yield of  $\text{NO}_2$  and  $\text{N}_2\text{O}_2$  components of the bio-oil. It is worth noting that nitrogen-containing compounds have, at least, three oxygen atoms. Different phenomena may occur to explain their deprotonation features by adding  $\text{NH}_4\text{OH}$ . Their DBE values (between 5 and 15) mean that these compounds are expected to present an aromatic moiety (**Figure III-8**). It is well-known that the substitution of an aromatic ring by a  $\text{NO}_2$  group significantly modifies the behavior of the other substituents especially the hydroxyl and the carboxylic acid ones. Indeed, the resonance ensures the increase of the lability of the hydrogen atom of the  $-\text{OH}$  and  $-\text{COOH}$  functions which yield more easily “phenolate” or “carboxylate” anion, respectively, in basic medium. Moreover, the formation of a strong interaction between the ammonium ion and some chemical functions of bio-oil compounds may occur. Due to (i) the high amount of oxygen atoms in a large part of bio-oil constituents, (ii) their acid properties (pH is generally down to 2.5), and (iii) the total acid number (TAN) in the 80 – 100  $\text{mg KOH.g}^{-1}$  range, a significant part of the  $\text{C}_x\text{H}_y\text{O}_z$  compounds are expected to be polycarboxylic acid.<sup>12,24</sup> The addition of  $\text{NH}_4\text{OH}$  may ensure the formation of a carboxylated ammonium salt by reaction with a carboxylic acid group. The deprotonation of another carboxylic acid group may ensure the formation of the  $[\text{M}-\text{H}]^-$  species detected by mass spectrometry.



*Figure III-8. DBE vs. nominal mass distribution of  $\text{C}_x\text{H}_y\text{NO}_z$  (open green circle) and  $\text{C}_x\text{H}_y\text{N}_2\text{O}_z$  (solid blue circle) species of the *Miscanthus* bio-oil observed in (-) ESI FT-ICR MS with  $\text{NH}_4\text{OH}$*



According to the distribution of the molecular species detected in negative detection mode, it appears that ESI without any dopant is more representative of the real composition of the investigated bio-oil. In spite of the increase of the TIC and the number of identified peaks, the addition of  $\text{NH}_4\text{OH}$  conducts to artefacts, which enhances the signal of nitrogen species.

### III.C.2. Analyses in positive ion mode

#### III.C.2.a. Without dopant

Two (+) ESI FT-ICR MS experiments were conducted with the same acquisition method, the same day, on the same bio-oil prepared without any dopant. Approximately, the same number of compounds has been identified (**Table III-3**). Unexpectedly, a poor mass spectrum repeatability is observed as it can be seen in **Table III-3** and **Figure III-9**.

Both the TIC and the ion distributions in respect with the compound class are significantly different. In the first MS analysis (noted Analysis I), a small TIC ( $\sim 700$ ) is obtained but the main part of the 406 identified peaks (96 % of the TIC) corresponds to oxygenated hydrocarbons, whose class compound ranges from  $\text{O}_2$  to  $\text{O}_{14}$ . The second experiment (noted Analysis II) described in this section leads to very different results. An intense TIC ( $\sim 8400$ ) is obtained which corresponds to an increase by, at least, one order of magnitude in comparison with the Analysis I, but the number of detected and assigned ions remains constant (425 assignments). Only one third of the TIC is relative to  $\text{C}_x\text{H}_y\text{O}_z$  ions. The most important class of compounds is the  $\text{NO}_z$  one, whose relative abundance is close to the half of the TIC. In addition, the  $\text{N}_2\text{O}_z$  and  $\text{N}_3\text{O}_z$  compounds have a significant abundance which is close to 20 % of the TIC. Due to the acidity of the pyrolysis bio-oils, it is expected that the ions observed on the (+) ESI FT-ICR mass spectra are protonated  $[\text{M}+\text{H}]^+$ .

Consequently, (+) ESI results from the same bio-oil samples clearly evidence the dramatic competition which takes place during the ionization event. Small variations of the ESI conditions (temperature, moisture...) are sufficient enough to induce a significant modification on the bio-oil mass spectrum. The fixation of a proton on a bio-oil compound to finally generate a  $[\text{M}+\text{H}]^+$  ion is controlled by equilibria which take place in condensed and/or gas phase relative to  $\text{pK}_a$  and proton affinity, respectively.<sup>25,26</sup> The huge number of bio-oil constit-

uents, which possess acid–base properties, and the extreme sensitivity of the involved equilibria during the nebulization/ionization event in the ion source are responsible of the extraordinary variability of the resulting mass spectrum. As a consequence, well and perfectly controlled ionization parameters are required to analyze bio-oils in positive ion mode with a high level of confidence and a high robustness. The use of dopant that is described in the following sections is an interesting way to achieve this requirement.

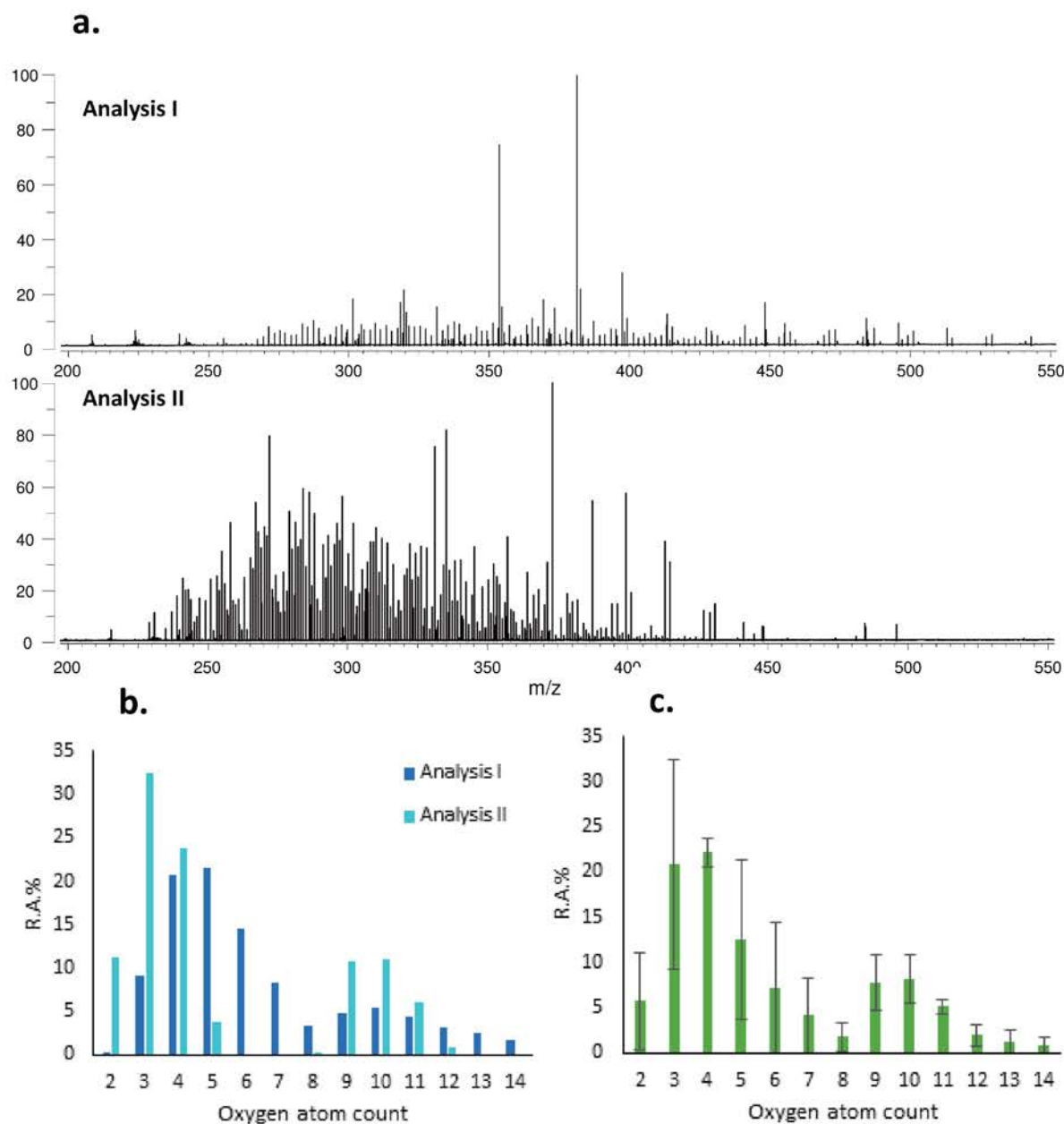


Figure III-9. (a) Mass spectra obtained by (+) ESI FT-ICR-MS analysis of a pyrolysis *Miscanthus* bio-oil. (b) Relative distribution of  $C_xH_yO_z$  compounds detected in positive ion mode for Analysis I and II. (c) Average relative distribution of  $C_xH_yO_z$  compounds detected in positive ion mode for Analysis I and II without dopant. Error bar is relative to the standard deviation for the two considered measurements.

### III.C.2.b. With formic acid (1 %)

The addition of formic acid in the bio-oil sprayed solution leads to an intense, stable, and repeatable signal. The TIC is about 3000 and 1465 mass peaks are assigned. The main part of the detected ions are in the form of  $[M+H]^+$ . In a lesser extent, sodiated species are also observed. Close to 85 % of the TIC is relative to compounds involving nitrogen atoms. Thus, the fractions of the TIC associated with  $NO_{2-10}$ ,  $N_2O_{1-8}$ , and  $N_3O_{1-5}$  are equal to 52 %, 29 %, and 3 %, respectively. Such compounds have also been observed in pyrolysis bio-oils by Tessarolo *et al.*<sup>21</sup> and Jarvis *et al.*<sup>13</sup> in negative detection mode but with relative abundances lower than few percent of the TIC. The use of acidic condition (protonation of amines) ensures an efficient ionization of the basic nitrogen compounds, which induces an overestimation of their relative abundance in positive detection mode. Thus, under these ionization conditions, the  $C_xH_yO_z$  bio-oil compounds represent less than 10 % of the TIC.

### III.C.2.c. With ammonium acetate (1 %) and ammonium hydroxide (1 %)

Ammonium acetate and ammonium hydroxide are also used as dopants to increase the efficiency and the repeatability of the ionization processes. It is expected that ionization efficiency increases according to two ways, the attachment of on ammonium cation (formation of  $[M+NH_4]^+$  adducts) and/or the transfer of one proton. The use of ammonium acetate and ammonium hydroxide ensures to obtain insights of such ionization process on a pH variation viewpoint (ammonium acetate is a well-known buffer and the addition of  $NH_4OH$  to an acid bio-oil solution may also buffer the spray solution). As expected, the ionization yield increased compared to what was previously observed. A repeatable TIC equal to 8400 and 3650 is obtained with ammonium acetate and ammonium hydroxide, respectively. A significant fraction of the TIC is found to be related to the  $NO_2$  ions, whose, at least, a part of them is expected to be associated with  $[M+NH_4]^+$ . Nevertheless, some differences appear when the compound class distributions are compared. For  $AcONH_4$ , 97 % of the signal and 920 attributions are relative to the oxygen-nitrogen  $N_{1-4}O_z$  species whereas they are responsible of 89 % of the TIC, which corresponds to 1197 features, when  $NH_4OH$  is used. The  $C_xH_yO_z$  ions represent 3 % and 11 % of the signal for each of these ionization conditions (**Table III-3**).

In spite of an increase of the TIC and an excellent repeatability of the measurement, ammonium hydroxide or ammonium acetate in (+) ESI mass spectrometry analysis of bio-oils

is not advised. The obtained description does not reflect the real composition of the investigated sample and may also generate some artefacts such as the overestimation of nitrogen compounds.

#### III.C.2.d. Sodium acetate (0.01 %)

The addition of small amount of sodium acetate leads to a significant increase of both the TIC and the repeatability of the mass spectrum. Indeed, the obtained TIC, close to 8000, is one of the highest obtained in this study. The large part of the 858 identified peaks, corresponding to 98 % of the signal, is due to the  $C_xH_yO_z$  species, which are mainly observed as  $[M+Na]^+$  and only a few percent of them is relative to protonated molecules. These latter generally present a high DBE value and a small number of oxygen atoms. Finally, the  $NO_2$  species only represent 2 % of the TIC. As a consequence, the relative distribution of the ions, on the obtained mass spectrum, is more representative to the real composition of the bio-oil. The analysis of pyrolysis bio-oil of *Miscanthus* by (+) ESI with sodium acetate is repeatable and yields a bio-oil description in agreement with the elemental analysis (**Table III-3** and **Figure III-10**).

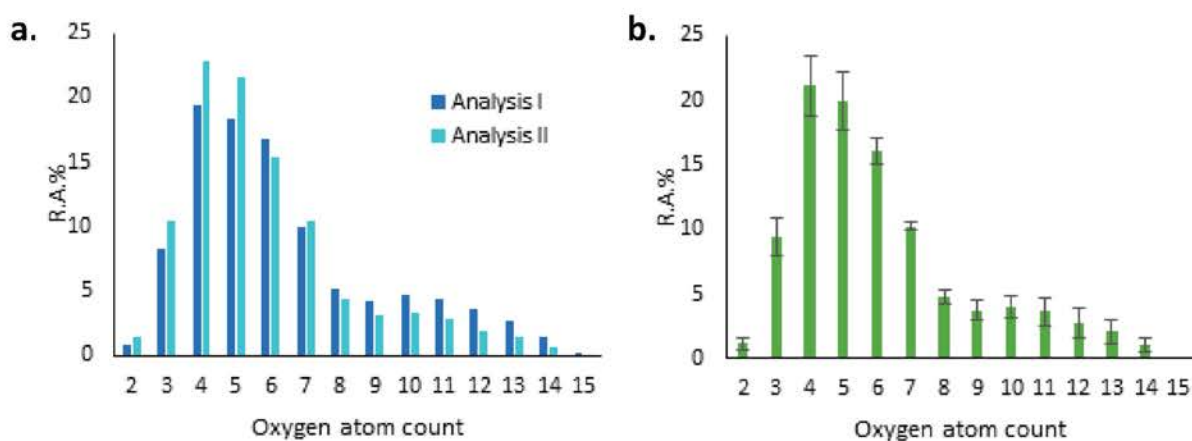


Figure III-10. (a) Distribution of the  $C_xH_yNaO_z$  species in respect with the oxygen atom count by (+) ESI FT-ICR MS analysis of *Miscanthus* bio-oil with sodium acetate. (b) Average relative distribution of the  $C_xH_yNaO_z$  compounds from Analysis I and Analysis II. Error bar is relative to the standard deviation for the two considered measurements.

Other alkaline dopants (lithium and potassium acetate) are evaluated in this study. The experimental conditions are similar to those previously described with sodium acetate. The **Table III-3** reports the number of assignments, TIC values, and global bio-oil composition achieved whereby the used alkaline dopant. The  $C_xH_yO_z$  compounds highlighted in the bio-oil

analyses performed with AcOLi and AcOK are mainly in the form of  $[C_xH_yO_z+Li]^+$  and  $[C_xH_yO_z+K]^+$  adducts, respectively.

Regarding both the number of assignments and TIC values, the nature of the dopant has not a significant influence. Nevertheless, the distributions of the classes of compounds indicate some differences. The analyses performed with lithium and sodium acetate yield similar global description with 98 % and 2 % of the TIC relative to the  $C_xH_yO_z$  and  $C_xH_yNO_z$  compounds, respectively. With potassium acetate, the  $C_xH_yO_z$  and  $C_xH_yN_{1-2}O_z$  compounds represent 81 % and 19 % of the signal, respectively.

The distribution of the oxygen-containing class in regards with the oxygen atom count (**Figure III-11**) is coherent and is ranging from  $O_2$  to  $O_{15}$ , whatever the alkaline cation. As previously observed, a bimodal distribution is obtained whatever the alkali dopant. The first massif is centered on the  $O_5$  species whereas, the second one, on the  $O_{10}$  compounds.

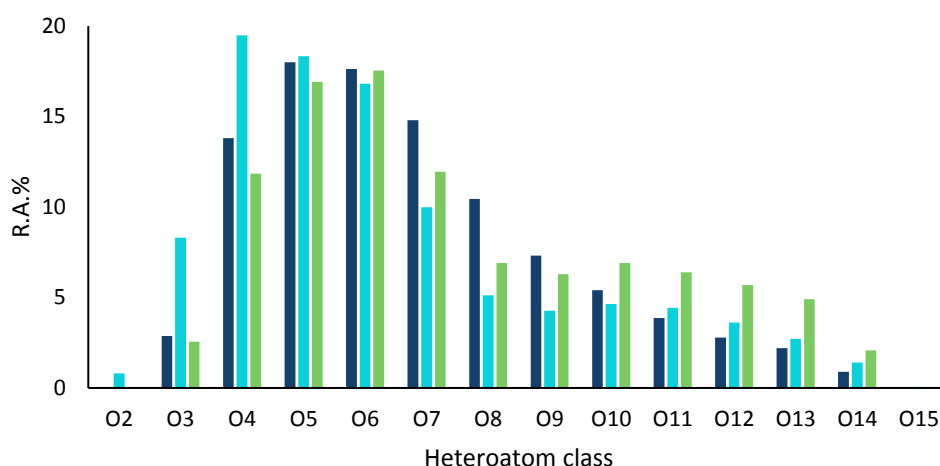


Figure III-11. Distribution of the  $C_xH_yO_z$  compounds in respect with the oxygen atom count obtained by (+) ESI FT-ICR MS analysis of a *Miscanthus* bio-oil with lithium (dark blue), sodium (light blue), and potassium (green) acetate.

Nevertheless, the relative abundances linked to the sugarc species (2<sup>nd</sup> massif) increase with the radius of the alkali cation  $K^+ > Na^+ > Li^+$ . The needed energy for the molecules to fold and chelate  $K^+$  is lower than with  $Li^+$  and  $Na^+$ , due to its larger radius. Therefore, the second massif is more pronounced. Reciprocally, the lignin derivatives that are less oxygenated and more unsaturated, have less Lewis basic sites and are less flexible to chelate potassium, which explains their lower relative abundance. The sodium acetate has an intermediate behavior to the potassium and lithium acetates due to its intermediate ionic size.

Such a trend has been observed in several studies dealing with the interactions between polyethylene glycols and alkali metal ions in mass spectrometry.<sup>27–30</sup> It was demonstrated that the selectivity towards a high-radius cation increases with the polymerization index and reciprocally. Thus, more oxygen atoms and molecule folding are suitable for the coordination of larger alkali cations.

The poor affinity of the potassium cation for the lignin derivatives can be responsible of the lower contribution of the  $C_xH_yO_z$  species to the TIC and similarly, the increase of the  $C_xH_yN_{1-2}O_z$  ones. Consequently, sodium acetate appears to be the most suitable dopant for the bio-oil characterization in (+) ESI-MS. It enables to cationize more equally the different biomass components.

### III.C.2.e. Discussion

Whatever the used ionization parameters, two kinds of compound classes were detected by (+) ESI-MS. Their relative distribution is highly dependent on the nature of the dopant. The first ones are the  $C_xH_yO_z$  compounds that are directly connected with the bio-oil composition and the second ones are  $C_xH_yN_{1-5}O_z$  species. The abundance of these latter ions, which may represent more than 95 % of the TIC, does not always reflect the real importance of nitrogen compounds in the lignocellulosic based bio-oils, which only represent a few percent.<sup>13,21</sup>

It is also of significant importance to note, the nature of detected  $C_xH_yN_{1-5}O_z$  species varies in respect with the used dopant. This is clearly evidenced, when the  $C_xH_yN_1O_z$  and  $C_xH_yN_2O_z$  van Krevelen diagrams are considered (**Figure III-12**) in respect with the used experimental conditions. Without dopant (Analysis II), the O/C and H/C ratios of the compounds range from 0.05 to 0.42 and from 0.7 to 1.5, respectively, whereas more oxygenated (O/C up to 0.53) and less unsaturated (H/C up to 1.93) are observed when formic acid is added.

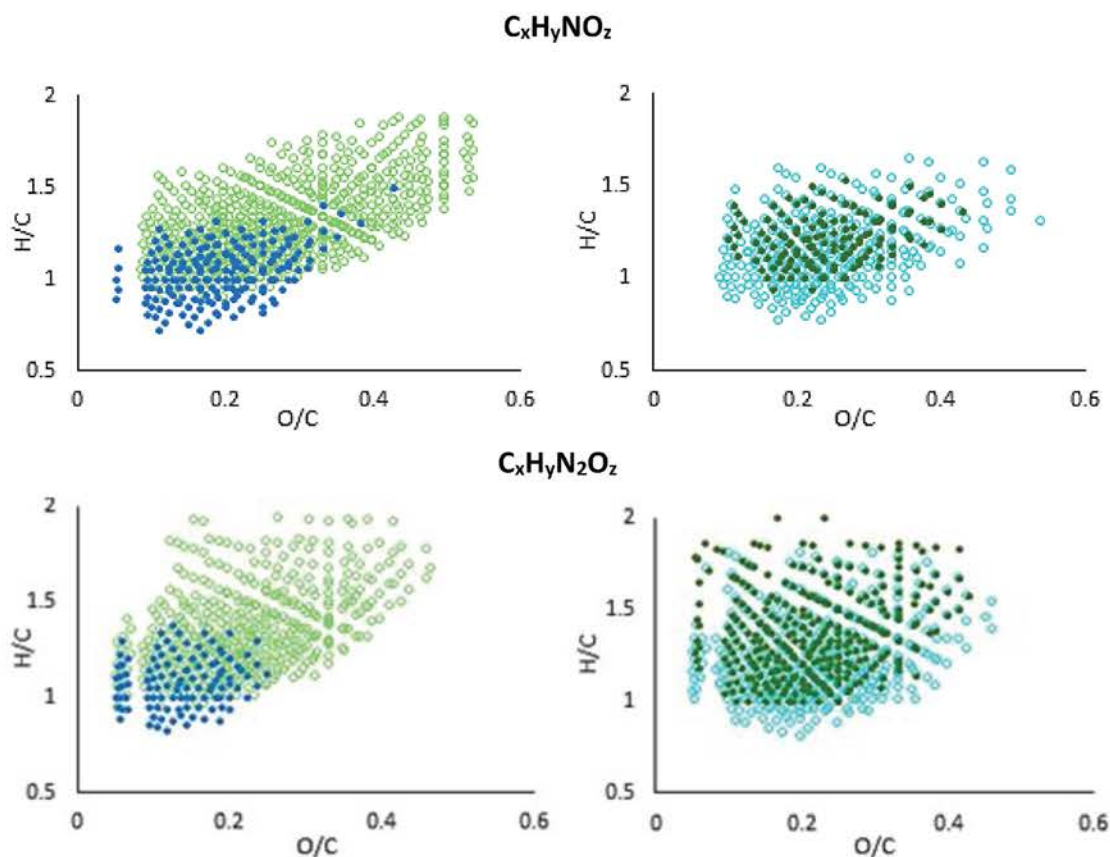
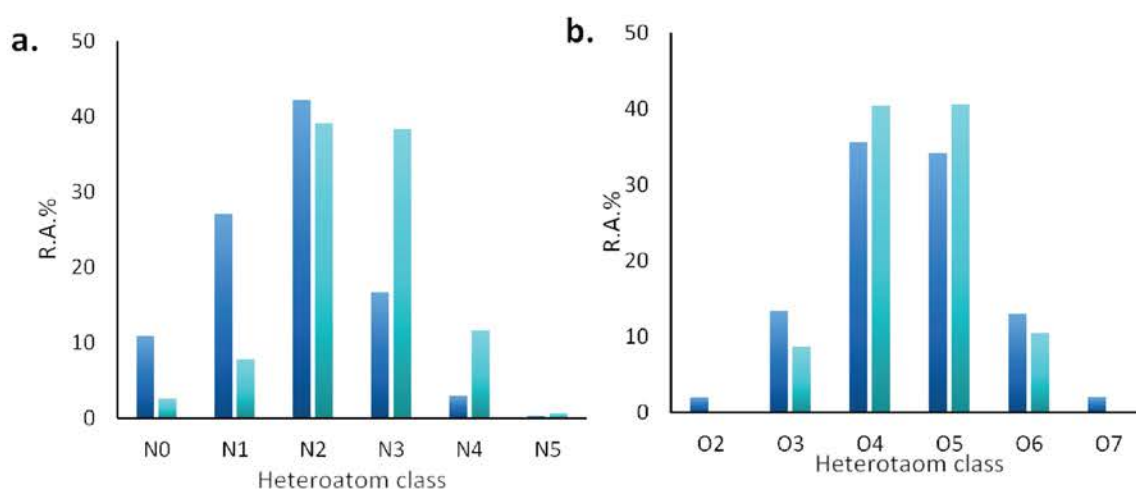


Figure III-12. Van Krevelen diagrams of  $[C_xH_yNO_z + H]^+$  and  $[C_xH_yN_2O_z + H]^+$  ions detected in (+) ESI FT-ICR MS without dopant for the Analysis II (solid blue circle), with formic acid (open green circle), ammonium acetate (solid green circle), and ammonium hydroxide (open blue circle)

Consequently, it is reasonable to consider that, when formic acid is used, a large part of the detected  $C_xH_yN_{1-5}O_z$  species are relative to polar compounds (mainly amine ones) which easily form quaternary ammonium cation under acidic conditions. The addition of ammonium acetate leads also to a significant detection of compounds with a higher H/C ratio compared to the results obtained without dopant. This is more pronounced for the  $C_xH_yN_2O_z$  species. For some of them, the H/C ratio is close to 2, which corresponds to poorly unsaturated compounds. These ions are thought to mainly result from  $NH_4^+$  cationization, which is generally observed for polar and poorly unsaturated compounds.<sup>17,31,32</sup> This behavior is also very different to what it was observed with ammonium hydroxide (**Figure III-13**). With  $AcONH_4$ , the observed ions involve more nitrogen atoms and, in a lesser extent, more oxygen atoms than with  $NH_4OH$ . More precisely, the ion distribution obtained using  $AcONH_4$  appears to be shifted to one more nitrogen atom, which confirms that cationization by  $NH_4^+$  is clearly involved as an ionization mechanism in these experimental conditions. According to the huge number of  $N_{1-4}O_z$  species and their significant contributions to the TIC, the formation of  $[M+H]^+$  or  $[M+NH_4]^+$  adducts is not the unique explanation of the obtained results. This is particularly true when

ammonium hydroxide is used and for which neither the protonation nor the  $\text{NH}_4^+$  cationization may be reasonably considered to significantly contribute to the ionization mechanism. The large abundance of multi-nitrogen compounds, on the one hand, and the differences observed in **Figure III-13**, on the other, may be indicative of other processes which take place in the solution or during the ionization event. These processes ensure the enhancement of  $\text{N}_{1-4}\text{O}_z$  signals not only by alteration or modification of the ionization event but also through the reaction of some bio-oil constituents with ammonium cation. This aspect will be detailed in the section **IV**.



*Figure III-13. Relative distribution of the heteroatom classes detected in (+) ESI FT-ICR MS with addition of ammonium hydroxide (dark blue) and ammonium acetate (light blue) in respect with (a) the number of nitrogen atoms for the  $\text{C}_x\text{H}_y\text{N}_n\text{O}_z$  compounds and (b) the number of oxygen atoms for the  $\text{C}_x\text{H}_y\text{O}_z$  compounds*

The  $\text{C}_x\text{H}_y\text{O}_z$  species observed without any dopant (Analysis I) are detected as protonated or  $\text{Na}^+$  adducts. However, these compounds have different properties depending on the considered  $[\text{M}+\text{H}]^+$  or  $[\text{M}+\text{Na}]^+$  adduct (**Figure III-9.b**). The protonated ions are relative to highly unsaturated compounds with a H/C ratio lower than 1 and correspond to  $\text{O}_2$ ,  $\text{O}_3$ ,  $\text{O}_4$ , and  $\text{O}_5$  classes of compounds. In contrast, the attachment of  $\text{Na}^+$  is observed for the  $\text{C}_x\text{H}_y\text{O}_{8-12}$  species, whose H/C ratio ranges from 1.3 to 1.7. According to the specific compound regions defined in a van Krevelen diagram,<sup>33</sup> the  $[\text{M}+\text{H}]^+$  ions have to be associated<sup>33</sup> with phenolic compounds resulting from the pyrolysis of the lignin, whereas  $[\text{M}+\text{Na}]^+$  cations are only relative to sugary compounds coming from the cellulose and the hemicellulose pyrolysis. Similar trends are observed when formic acid is added. The **Figure III-14** displays the nature (protonated or sodiated) of the detected  $\text{O}_z$  ions in respect with the number of oxygen atom and the DBE. More specifically, the  $\text{O}_5$  class of compounds is reported in the **Figure III-14.c**. The protonation



is clearly favored with oxygen-poor compounds ( $O_2$  to  $O_7$ ) and high DBE values (phenolic compounds). The most saturated and the most oxygen-rich compounds (sugar derivatives) lead preferentially to the attachment of  $Na^+$  cation.

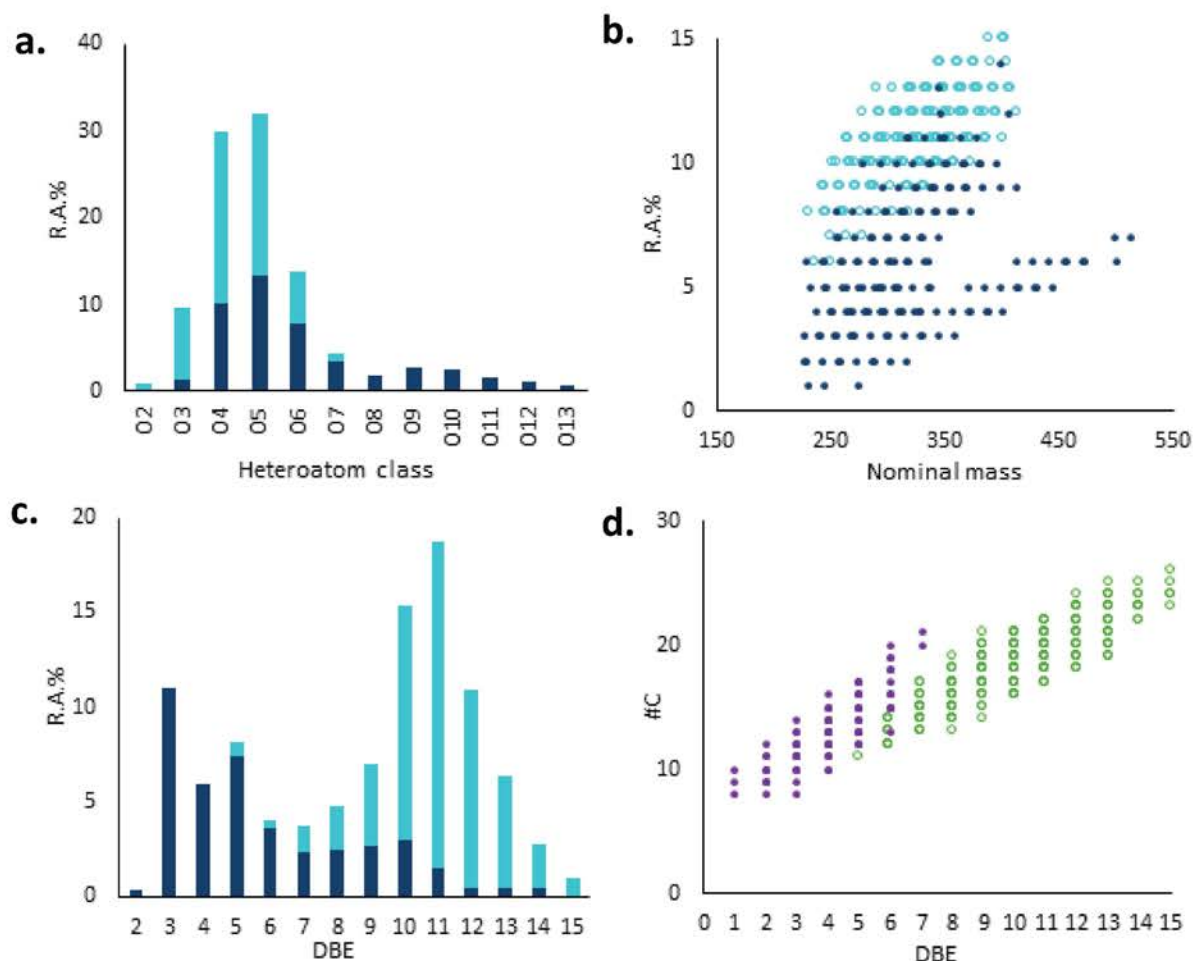


Figure III-14. (a) Relative distributions in respect with the oxygen atom count and (b) DBE vs. nominal mass plot of the  $[C_xH_yO_z + H]^+$  (light blue) and  $[C_xH_yO_z + Na]^+$  (dark blue) ions. (c) Relative distributions of the  $[C_xH_yO_z + H]^+$  (light blue) and  $[C_xH_yO_z + Na]^+$  (dark blue) ions according to the DBE value. (d) DBE vs. carbon number of  $C_xH_yO_z$  compounds for phenolic-like (solid purple circle) and sugarc-like (green circle) compounds. These results are obtained from the analysis Miscanthus bio-oil by (+) ESI FT-ICR MS doped with formic acid.

This ionization behavior described for  $C_xH_yO_z$  compounds in these experiments may be rationalized. The cationization by  $Na^+$  results from Lewis acid/base interaction between the Lewis  $Na^+$  acid cation and the lone pairs of oxygen atoms. The chelation of one sodium ion is consequently favored by highly oxygenated ( $O_7$  to  $O_{13}$ ) and/or flexible (poorly unsaturated) molecules. The distributions of the  $[M+Na]^+$  ions in respect with their oxygen atom number and their unsaturation number (DBE) given in **Figure III-14.a** and **Figure III-14.c**, exhibit an intriguing bimodal behavior. The first one is centered on  $O_5$  compounds and the second one is relative to the most oxygenated compounds (the center of the distribution is  $O_9$ - $O_{10}$ ) (**Figure**

**III-14.a**). While this observation suggests the detection of dimers cationized by sodium ion, their DBE distributions do not support this hypothesis. Indeed, in **Figure III-14.b**, the main cloud of points at lower masses and on a huge DBE range corresponds to low oxygenated compounds and the secondary cloud which spreads in a higher mass range are the most oxygenated species and have a low value of DBE. Consequently, the most oxygenated compounds ( $O_7$  to  $O_{13}$ ) are not dimers of  $O_2$  to  $O_7$  molecules but are related to pyrolysis products of the different lignocellulosic biomass components. The behavior observed when ammonium hydroxide is used may be surprising if it is compared to what it was reported with formic acid or ammonium acetate. Indeed, the use of more alkaline ionization conditions leads to a more significant detection of protonated ions such as  $[C_xH_yO_z+H]^+$ . The number of oxygen never exceeds 7, this corresponds to phenolic compounds. Such compounds are less oxygenated but more unsaturated than cellulosic ones and can be identified by considering their O/C (lower than 0.6) and H/C ratio (lower than 1.4). Complex and still unclear mechanisms take place during ESI process (especially at the surface of the droplets), which may favor the transfer of a proton to highly unsaturated species from the easily deprotonated cellulosic compounds (highly oxygenated and poorly unsaturated). Complex equilibria in condensed and gas phase are involved, but difference in terms of acidity constant (liquid phase) and/or proton affinity and gas phase basicity (gas phase) between phenolic compounds and cellulosic ones may be considered. The explanation of such phenomenon is still under progress.

The addition, of sodium acetate leads to a more reproducible and sensitive analysis. The bimodal distribution of the  $C_xH_yO_{2-14}$  ions is clearly evidenced (**Figure III-15.a**). Moreover, their unsaturation degree in regards with their masses (**Figure III-15.b**) also adopts a double distribution which looks like a “mitten” corresponding to the overlap of the main cloud with a secondary distribution ( $m/z$  up to 580 and DBE value ranging from 2 to 8). Both bimodal distributions are linked: the detected ions of the thumb of the mitten involves the  $O_{10}$  to  $O_{14}$  compounds (sugarc fraction of the bio-oil), whereas the bulk unsaturation distribution is associated with the phenolic compounds (O/C lower than 0.6 and H/C ratio lower than 1.4) resulting from the pyrolysis of the lignin, according to their DBE value and their amounts of oxygen atoms (from 2 to 9).

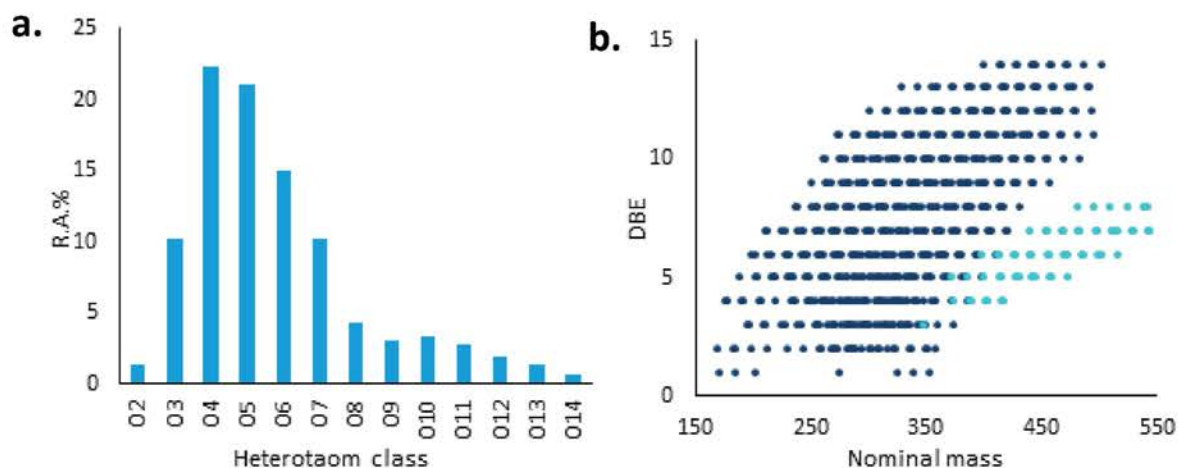


Figure III-15.(a) Relative distribution of the  $[C_xH_yO_z + Na]^+$  ions according to the oxygen atom count and (b) their DBE vs. nominal mass plot with the O<sub>2</sub>–O<sub>9</sub> (dark blue) and O<sub>10</sub>–O<sub>14</sub> (light blue) compounds. These results are obtained from the *Miscanthus* bio-oil analysis by (+) ESI FT-ICR MS doped with sodium acetate (Analysis II).

The different experiments conducted in (+) ESI involved the use of small amounts of dopants known for their ability to improve the protonation or cationization during the ionization process: formic acid, ammonium acetate, ammonium hydroxide or sodium acetate. Thus, it was demonstrated that the nature of the ionization process may be helpful to identify the bio-oil constituents (cellulose, hemicellulose, and lignin) and it can be tailored by selecting the specific dopant.

### III.D. Complementarity of the detection modes

Both positive and negative ion signals are dealing with the real composition of the investigated bio-oil. Indeed, the van Krevelen diagram and the Kendrick map of the combined negative and positive  $C_xH_yO_z$  features reported in the **Figure III-16**. They have to be seen as a comprehensive molecular signature of the investigated pyrolysis bio-oil. The different components of lignocellulosic based bio-oil (lipids, sugaric and lignin derivatives) are simultaneously evidenced in positive detection mode by cationisation with sodium ion. The negative measurement ensures to complete the description of bio-oil by a more sensitive detection of the acidic compounds.

The results obtained on bio-oil in this work may be compared with those previously published, in particular, those of Jarvis *et al.*<sup>13</sup> and Miettinen *et al.*<sup>12</sup> Both authors introduced a fractionation of the sample prior the ESI FT-ICR MS analysis. Indeed, they distinguished two

phases: the oily and the aqueous ones. Each of these fractions may be associated to the compounds resulting from the pyrolysis of the different constituents of the lignocellulosic biomass. Indeed, the phenolic compounds of the bio-oil come mainly from the pyrolysis of the lignin and are the main contributor of the oily phase, whereas the pyrolysis of the cellulose and the hemicellulose leads to the formation of sugarc species which are soluble in water. In this study, no fractionation is needed to obtain a full description of the bio-oil components. Indeed, in (+) ESI, the use of sodium acetate allows to efficiently and to simultaneously ionize the compounds relative to the oily and aqueous phases. This methodology has consequently the great advantage to assess the relative importance of each of these fractions in the investigated bio-oil, in contrast to other methods, without any tedious fractionation steps.

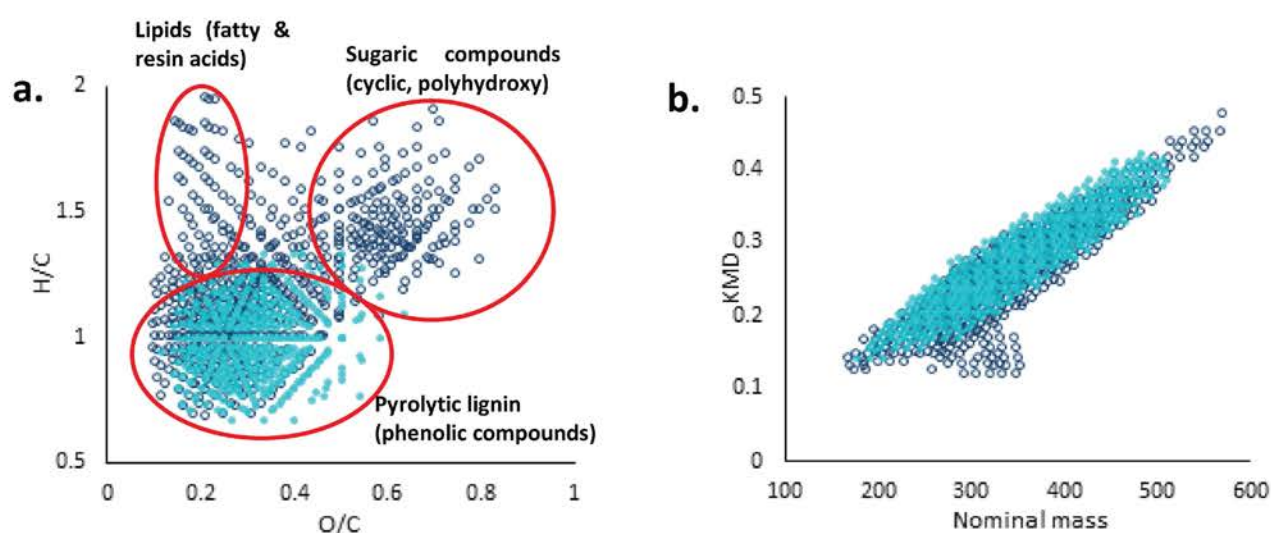


Figure III-16. (a) van Krevelen diagrams and (b) Kendrick's map of the  $[C_xH_yO_z + Na]^+$  (dark blue) and  $[C_xH_yO_z - H]^+$  (light blue) ions assigned from the analysis of the *Miscanthus* bio-oil in (+) ESI with AcONa and (-) ESI without dopant, respectively.

### III.E. Conclusion

An exhaustive characterization of a bio-oil produced by the lignocellulosic biomass pyrolysis may be achieved by a petroleomic approach combining the features obtained in (-) ESI and (+) ESI FT-ICR MS analyses. The very high mass resolution and mass accuracy are required to unambiguously distinguish and identify the huge number of bio-oil constituents. The importance of the well-controlled composition of the sample solution, which ensures the good sensitivity and repeatability, was demonstrated as well as the dramatic effect of common ESI dopants on the whole bio-oil description. This clearly demonstrates the ionization competition when non-targeted analysis of complex mixture is conducted by direct infusion ESI FT-ICR MS

analysis. Another illustration of this behavior is the non-detection of nitrogen compounds in negative ion detection mode when the experiment is conducted without dopant due to an easier ionization of the  $C_xH_yO_z$  species. Significant detection of nitrogen compounds is achieved when ammonium hydroxide (positive and negative ion modes), ammonium acetate (positive ion mode) or formic acid (positive ion mode) is used as dopant. Moreover, the measurements in (+) ESI FT-ICR MS analysis without dopant are poorly repeatable. Thus, these methods are not appropriate for bio-oil characterization. In contrast, a robust analytical method is defined by the combination of the mass features obtained in negative ion mode without dopant and in positive ion mode when sodium acetate is added. In both cases, a sensitive and repeatable analysis is achieved.

## IV. Evidence of carbonyl compounds in complex mixtures with primary amines by petroleomic approach

*The main part of the results presented in this section are included in the paper entitled “Semi-targeted analysis of complex matrices or how an experimental bias may be used as an analytical tool” which has been submitted to Journal of the American Society for Mass Spectrometry in October 2017.*

### IV.A. Introduction

The experiments performed on the Miscanthus bio-oil by ESI FT-ICR MS in both positive and negative detection modes, after addition of  $NH_4OH$ , demonstrated a significant contribution of the nitrogen-containing species. Such a bio-oil description is not in agreement with the CHNOS analysis which evidences a nitrogen amount of  $\sim 0.2$  wt. %.<sup>19</sup>

In (+) ESI, one simple explanation may be the formation of ammonium adducts but this cannot account of either the detection of polynitrogenated species or the difference of behavior when ammonium hydroxide and ammonium salts are used as dopant. Moreover, the increase of the pH may lead to the protonation of the basic nitrogen compounds<sup>15,34,35</sup> and the displacement of acidic-base equilibrium to the neutral form of the carboxylic acid. This leads to an enhancement of the signal related to the nitrogen species, which does not reflect the real bio-oil composition. These explanations do not fully make sense in negative ion. Other

processes have to be considered and explained to really know if these nitrogen species are or not relevant of the bio-oil components.

It has been demonstrated that bio-oils are not thermodynamically stable due to the large amounts of highly oxygenated compounds.<sup>10,36,37</sup> Part of these compounds may be highly reactive and explain the bio-oil aging (increase of the viscosity and water amount). Among the different functional groups involving oxygen atom, the carbonyl one, represented by aldehydes and ketones, is of major concern because of its significant reactivity which ensures polymerization or condensation phenomenon.<sup>10</sup> The carbonyl compounds are known to react with amine to form imines, which may also be responsible of the biased composition description of ESI FT-ICR MS measurements when NH<sub>4</sub>OH dopant is used. To evaluate this hypothesis, different solutions of standard carbonyl compounds have been investigated in positive ESI – MS with and without ammonium hydroxide to evidence the formation of imines. To confirm these results, measurements were also conducted on these same compounds with aniline and 3-chloroaniline. Tandem mass spectrometry was used to confirm the structure of the different yielded ions. Finally, an oak bio-oil was investigated by (+) ESI FT-ICR MS after addition of 3-chloroaniline.

In this section, it will be also demonstrated how the drawback of imine formation, due to addition of amine as dopant, may be used as a tool for semi-directed analysis of complex mixtures such as bio-oils by non-targeted approach.

## *IV.B. Materials and methods*

### *IV.B.1. Sample preparation*

#### *IV.B.1.a. Bio-oil*

The bio-oil from pyrolysis of oak powder was used. It was diluted to a final concentration of 10 % in methanol with 3-chloroaniline (0.1 % v/v).

#### *IV.B.1.b. Standard compounds*

The vanillin, cinnamaldehyde, butyrophenone, and 2,4,6-trihydroxyacetophenone monohydrate (**Table III-4**) were chosen in respect with the involved chemical function (aldehyde or ketone) and due to their proven presence in bio-oil or because of their very close structure

to bio-oil components.<sup>38-42</sup> They were solubilized in methanol to a final concentration of  $5 \times 10^{-3}$  mol.L<sup>-1</sup>. In addition, standard carbonyl compound samples were also prepared by dissolving, at the same concentration, the studied aldehyde or ketone in methanol/NH<sub>4</sub>OH (1 % v/v), methanol/aniline (1 % v/v), and methanol/3-chloroaniline (1 % v/v).

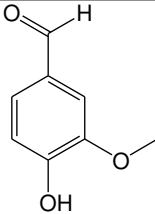
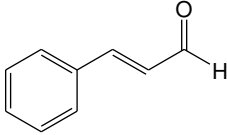
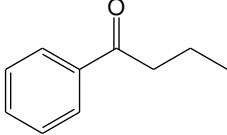
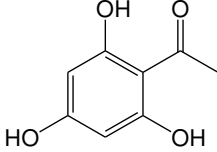
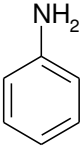
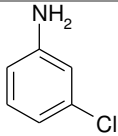
Name	Formula	Structure	MW (g.mol <sup>-1</sup> )
Vanillin	C <sub>8</sub> H <sub>8</sub> O <sub>3</sub>		152.15
Trans-Cinnamaldehyde	C <sub>9</sub> H <sub>8</sub> O		132.16
Butyrophenone	C <sub>10</sub> H <sub>12</sub> O		148.20
Trihydroxyacetophenone	C <sub>8</sub> H <sub>8</sub> O <sub>4</sub>		168.15
Aniline	C <sub>6</sub> H <sub>5</sub> NH <sub>2</sub>		93.13
3-chloroaniline	C <sub>6</sub> H <sub>4</sub> NH <sub>2</sub> Cl		127.57

Table III-4. Structure and molecular weight (MW) of the four selected standard carbonyl compounds and of the aniline and 3-chloroaniline.

## IV.B.2. Mass spectrometry measurements

### IV.B.2.a. HESI LTQ MS

The study of vanillin, trans-cinnamaldehyde, butyrophenone, and 2,4,6-trihydroxyacetophenone with and without ammonium hydroxide, aniline, and 3-chloroaniline was carried out with a linear ion trap mass spectrometer (LTQ Velos Pro – Thermo Scientific). A heated-electrospray ionization (HESI) probe was used and the different solutions were infused at a  $3 \mu\text{L}\cdot\text{min}^{-1}$  flow rate. The temperature of the ion source was set at  $40 \text{ }^\circ\text{C}$ , the sheath gas flow rate at 5 psi, the spray voltage at 3 kV, and the ion transfer tube was maintained at  $250 \text{ }^\circ\text{C}$ . Helium was used as collision gas. The used activation energy at the center of the mass  $E_{\text{COM}}$  was ranging from 0.5 to 0.9 eV.

### IV.B.2.b. ESI FT-ICR MS

The bio-oil solution was analyzed in positive ion detection mode with an IonSpec HiRes FT-ICR MS (IonSpec, Lake Forest, CA) fitted with a 9.4 T shielded superconducting magnet and a Micromass Z-spray electrospray source. The probe was set at + 3500 V and its temperature was kept at  $85 \text{ }^\circ\text{C}$  while the source was set at  $70 \text{ }^\circ\text{C}$ . An infusion flow rate of  $3 \mu\text{L}\cdot\text{min}^{-1}$  was used. The sample and extraction cone voltages were kept constant to 40 V and 10 V respectively. Ions were accumulated during 2 s in a RF-only hexapole before to be transferred in the FT-ICR-MS cell. The ions were trapped with a + 0.7 V potential and then excited by an arbitrary excitation wave function applied on the excitation plates. The signal was detected, amplified, digitized, apotized (Blackman), and Fourier transform applied to yield the mass spectrum. The signal was sampled during 2.1 s with 4096 K data points. The mass resolution at  $m/z$  315 is close to  $\sim 350\,000$  and the mass measurement accuracy was generally lower than 1 ppm. To increase signal-to-noise ratio, 40 individual mass spectra were summed to obtain a final mass spectrum ranging from  $m/z$  150 to 600.

Calibration and data-post treatment of FT-ICR MS features are similar to those previously used. Apart from the assignment criteria on the Composer software that were  $\text{C}_{1-100}\text{H}_{1-100}\text{N}_{0-4}\text{O}_{0-20}\text{S}_{0-1}\text{Cl}_{0-3}^+$ .



#### IV.C. Study of standard carbonyl compounds by ESI LIT MS

The different solutions of standard carbonyl compounds have been analyzed by positive electrospray ionization coupled with a linear ion trap mass spectrometer (ESI LIT-MS). They were first analyzed in methanol without dopant and then, after dopant addition. The used dopants are ammonium hydroxide, which is typically used for the non-targeted analysis in the field of petroleomic, aniline, and 3-chloroaniline. These two aryl amines were used to confirm the reaction between the amine and the studied aldehyde or ketone. The 3-chloroaniline was preferred to the other chloroaniline isomers to avoid activation phenomenon relative to ortho- and para-chloroaniline. It is well known that carbonyl compounds may react with amines according to the following reaction scheme to form imine (**Figure III-17**).

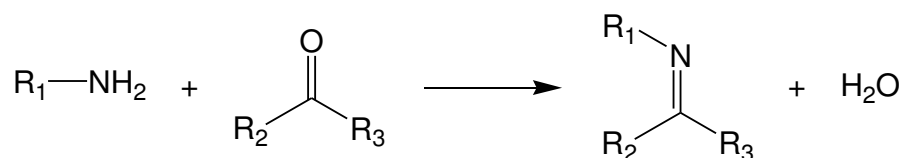


Figure III-17. Reaction of imine formation.

Thus, the resulting imine compound is obtained by condensation of an aldehyde or a ketone on an amine and the elimination of water. When R<sub>1</sub> is an aryl or alkyl group, the yielded compound is a so-called Schiff base. The imine compounds easily form, by protonation, iminium ion that may be observed by (+) ESI LIT MS.

For all used experimental conditions (with or without ammonium hydroxide or amine), MS<sup>n</sup> experiments were conducted to confirm the structure of the investigated carbonyl compounds and of their imine derivate.

##### IV.C.1. Vanillin

The (+) ESI LIT mass spectra of the vanillin obtained without dopant, with NH<sub>4</sub>OH, aniline, and 3-chloroaniline are reported in **Figure III-18**. Without dopant, an intense signal is observed at *m/z* 153, which corresponds to the [M+H]<sup>+</sup> protonated vanillin (**Figure III-18.a**). With 1 % (v/v) of ammonium hydroxide, a signal is observed at *m/z* 152 corresponding to the iminium cation obtained by reaction of the vanillin with ammonium hydroxide (**Figure III-18.b**). The ability of vanillin to form imine with a primary amine, in solution or during the ESI process, is confirmed on the **Figure III-18.c** and **Figure III-18.d**. Indeed, the protonated N-vanillylidene aniline and N-vanillylidene 3-chloroaniline Schiff bases are detected at *m/z* 228 and 262/264

(isotopic distribution of chlorine), respectively. When the experiment is conducted with a methanol/3-chloroaniline (1% v/v) vanillin solution, both  $[M+H]^+$  ions of vanillin and 3-chloroaniline are observed at  $m/z$  153 and 128/130 respectively, which indicates that the reaction is not complete.

To confirm the structure of the vanillin and its corresponding imine derivatives, tandem mass spectrometry experiments are carried out. The nature of the daughter ions and the mechanisms of fragmentation are reported in the **Table III-5** and **Figure III-19-22** and are detailed in the following subsection.

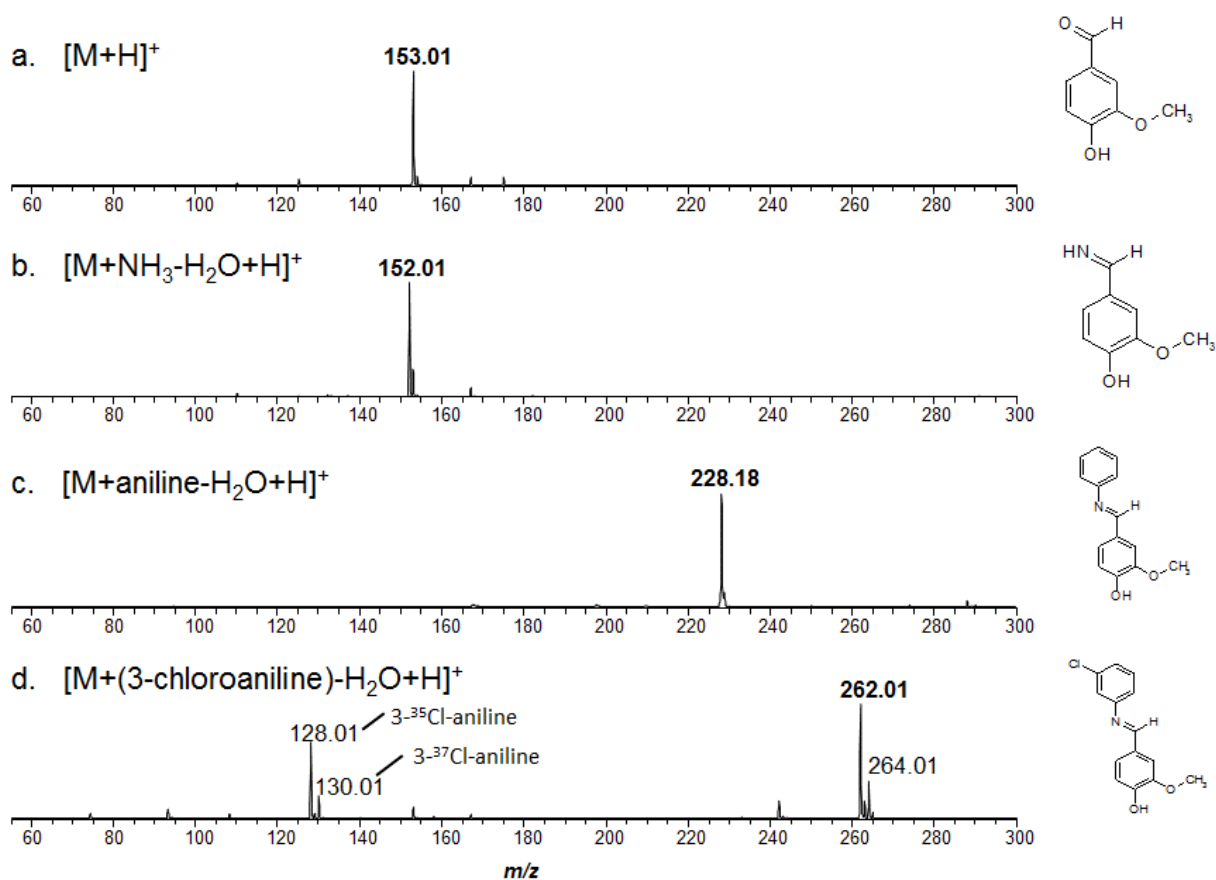


Figure III-18. (+) ESI LIT MS of vanillin in (a) methanol, (b) methanol/ $NH_4OH$  (1% v/v), (c) methanol/aniline (1% v/v), and (d) methanol/3-chloroaniline (1% v/v).

	MS <sup>1</sup> [M+H] <sup>+</sup>	MS <sup>2</sup>		MS <sup>3</sup>		MS <sup>4</sup>	
		E <sub>COM</sub> (eV)	m/z (abundance) – loss	E <sub>COM</sub> (eV)	m/z (abundance) – loss	E <sub>COM</sub> (eV)	m/z (abundance) – loss
<b>Vanillin</b>	C <sub>8</sub> H <sub>9</sub> O <sub>3</sub> <sup>+</sup> m/z 153	0.51	125 (100) – CO	0.62	110 (4) – CH <sub>3</sub> <sup>•</sup> 93 (100) – CH <sub>3</sub> OH	0.84	82 (100) – CO
			93 (5) – CO – CH <sub>3</sub> OH	0.82	65 (100) – CO		
<b>Vanillin – NH<sub>4</sub>OH imine</b>	C <sub>8</sub> H <sub>10</sub> NO <sub>2</sub> <sup>+</sup> m/z 152	0.67	137 (3) – CH <sub>3</sub> <sup>•</sup> 125 (100) – CNH	0.62	110 (100) – CH <sub>3</sub> <sup>•</sup> 107 (29) – H <sub>2</sub> O 93 (74) – CH <sub>3</sub> OH		
			110 (9) – CNH – CH <sub>3</sub> <sup>•</sup>	0.88	93 (8) – <sup>•</sup> OH 82 (100) – CO		
			107 (3) – CNH – H <sub>2</sub> O 93 (4) – CNH – CH <sub>3</sub> OH	0.72 0.74	79 (100) – CO 65 (100) – CO		
			213 (7) – CH <sub>3</sub> <sup>•</sup>	0.37	212 (100) – H <sup>•</sup> 196 (55) – OH <sup>•</sup>		
<b>Vanillin – Aniline Schiff base</b>	C <sub>14</sub> H <sub>14</sub> NO <sub>2</sub> <sup>+</sup> m/z 228	0.57	212 (4) – CH <sub>4</sub> 196 (3) – CH <sub>3</sub> OH	0.60	168 (100) – CO 93 (1) – C <sub>6</sub> H <sub>5</sub> NC		
			125 (2) – C <sub>6</sub> H <sub>5</sub> NC	0.62	110 (8) – CH <sub>3</sub> <sup>•</sup> 107 (3) – H <sub>2</sub> O		
			104 (100) – C <sub>7</sub> H <sub>8</sub> O <sub>2</sub> 77 (6) – C <sub>7</sub> H <sub>8</sub> O <sub>2</sub> – HCN	0.85	93 (100) – CH <sub>3</sub> OH 77 (100) – HCN	0.66	65 (100) – CO
			247 (3) – CH <sub>3</sub> <sup>•</sup>	0.62	219 (100) – CO 211 (35) – H <sup>35</sup> Cl		
<b>Vanillin – 3-chloroaniline Schiff base</b>	C <sub>14</sub> H <sub>13</sub> N <sup>35</sup> ClO <sub>2</sub> <sup>+</sup> m/z 262	0.53	246 (2) – CH <sub>4</sub> 230 (2) – CH <sub>3</sub> OH 138 (100) – C <sub>7</sub> H <sub>8</sub> O <sub>2</sub> 125 (5) – C <sub>7</sub> H <sub>4</sub> N <sup>35</sup> Cl 111 (5) – C <sub>7</sub> H <sub>8</sub> O <sub>2</sub> – CNH				
			93 (1) – CH <sub>3</sub> OH – C <sub>6</sub> H <sub>4</sub> <sup>35</sup> CIN <sup>•</sup> CH				
			249 (3) – CH <sub>3</sub> <sup>•</sup>	0.61	221 (100) – CO 211 (34) – H <sup>37</sup> Cl		
	C <sub>14</sub> H <sub>13</sub> N <sup>37</sup> ClO <sub>2</sub> <sup>+</sup> m/z 264	0.51	248 (2) – CH <sub>4</sub> 232 (2) – CH <sub>3</sub> OH 140 (100) – C <sub>7</sub> H <sub>8</sub> O <sub>2</sub> 125 (5) – C <sub>7</sub> H <sub>4</sub> N <sup>35</sup> Cl 113 (4) – C <sub>7</sub> H <sub>8</sub> O <sub>2</sub> – CNH				
			93 (1) – CH <sub>3</sub> OH – C <sub>6</sub> H <sub>4</sub> <sup>37</sup> CIN <sup>•</sup> CH				

Table III-5. Tandem mass spectrometry analysis of protonated [M+H]<sup>+</sup> ion of vanillin and its corresponding imine compounds.

#### IV.C.1.a. Tandem mass spectrometry of vanillin protonated ion

Two fragments are observed after activation of [M+H]<sup>+</sup>. The former at *m/z* 125 is the most intense and corresponds to the elimination of CO and the second one at *m/z* 93 (**Figure III-19**). The protonation is expected to occur on the oxygen of the methoxy group. A rH<sub>15</sub> exchange ensures the tautomerization and the displacement of the equilibrium to the quinone form, which is favorable to the elimination of one CO molecule. The dissociation of the *m/z* 125 daughter ion confirms that a consecutive fragmentation process allowing the elimination of a methanol molecule produces the *m/z* 93 ion. Thus, an inductive fragmentation process

allows the migration of the charge on the cyclopentadiene ring and the elimination of  $\text{CH}_3\text{OH}$ . The activation of the resulting ion after a  $\text{rH}_{14}$  transfer ensures the loss of a second  $\text{CO}$  molecule to produce the cyclopentadienyl ion at  $m/z$  65. One competitive process of the methanol elimination corresponds to the homolytic cleavage of the  $\text{O}-\text{CH}_3$  bond, which yields the  $\text{C}_6\text{H}_6\text{O}_2^{+\bullet}$  radical cation. A  $\text{rH}_{13}$  process, followed by a homolytic cleavage, leads to the loss of a carbon monoxide. A poor stable cyclobutadiene ring is obtained, which is thought to open and to yield the substituted butadiene cation at  $m/z$  82.

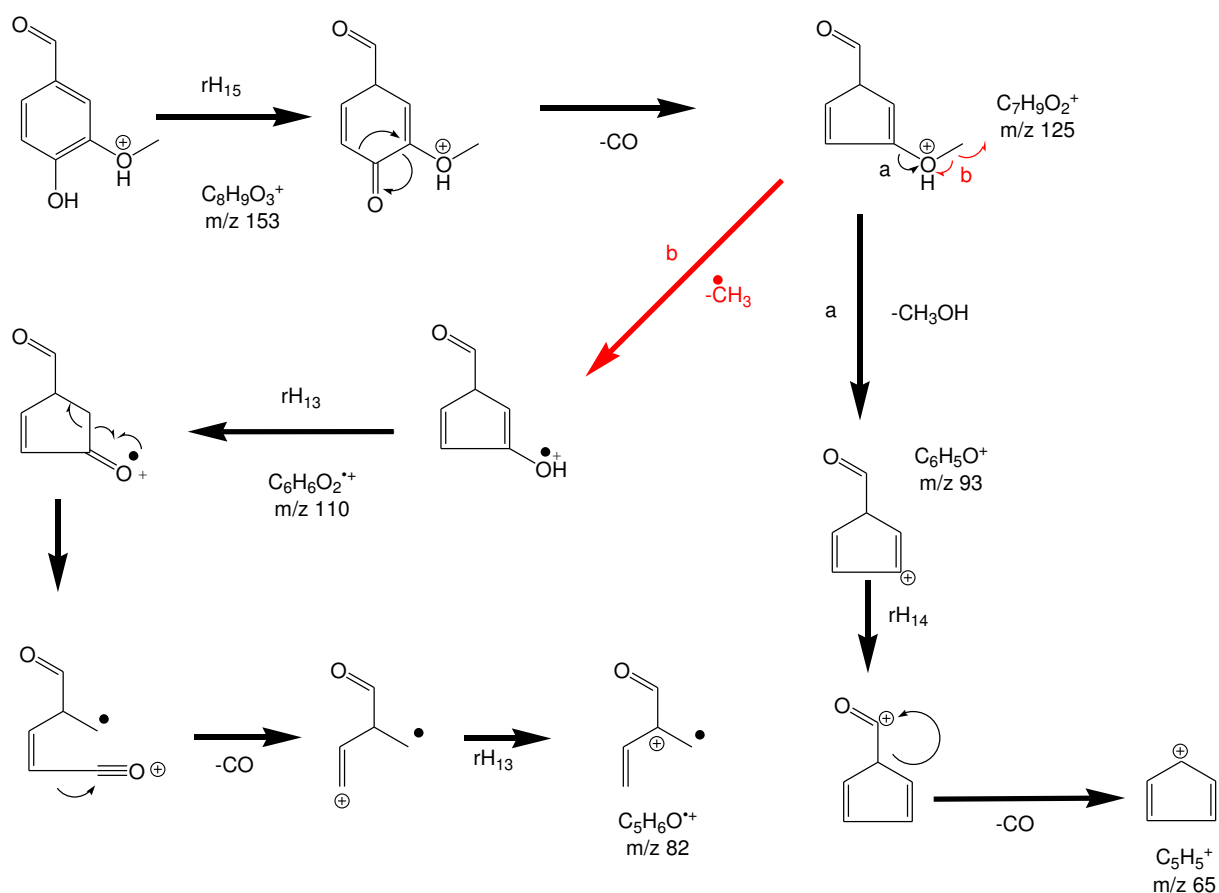


Figure III-19. Proposed mechanisms of  $[\text{M}+\text{H}]^+$  vanillin  $\text{MS}^n$  fragmentation.

#### IV.C.1.b. Tandem mass spectrometry of the vanillin protonated imine ion

The protonation of the vanillin imine is expected to occur on the phenyl ring. Indeed, the  $\text{MS}/\text{MS}$  of the parent ion does not lead to either the elimination of water (expected in the case of the hydroxyl protonation) or the elimination of methanol (expected in the case of the protonation of the methoxy group) (**Figure III-20**). Moreover, the protonation of the imine is thought to be poorly efficient. Indeed, after a hydrogen transfer process, this protomer permits the  $\text{NH}_3$  elimination, which is not observed. Five daughter ions are observed at  $m/z$  137,

125, 110, 107, and 93. Only the two former ones are expected to result from fragmentation of the parent ion. The other fragment ions, whose intensity is low, are also observed on MS<sup>3</sup>. The less preferred fragmentation pathway (formation of the C<sub>7</sub>H<sub>7</sub>NO<sub>2</sub><sup>+</sup> radical cation *m/z* 137) is the elimination of the methyl radical from the homolytic cleavage of the O–CH<sub>3</sub> bond, which requires, earlier, a poor efficient rH<sub>14</sub> transfer. After activation, the main fragmentation mechanism necessitates the rH<sub>13</sub> transfer of the hydrogen, in α–position of the imine on the C6 ring, followed by an inductive dissociation, which leads to the elimination of CNH and the formation of the *m/z* 125 ion. A MS<sup>3</sup> behavior, dissimilar to what it was observed in the previous section, clearly confirms a different structure to what it was proposed for the daughter ion of the protonated vanillin at *m/z* 125. The MS<sup>3</sup> spectrum demonstrates the elimination of a methanol molecule or a methyl radical after rH<sub>13</sub> transfer to yield *m/z* 93 and 110 ions, respectively. The implied mechanisms are similar to what it was proposed in the previous section. After activation, the tautomerization equilibrium of the phenol like ion at *m/z* 93 ensures the easy elimination of CO. The benzenediol radical cation resulting from the elimination of a methyl radical at *m/z* 110, after activation and tautomerization, leads to the formation of the hydroxypentadienyl radical cation at *m/z* 82 by the CO elimination. A third fragmentation pathway of the C<sub>7</sub>H<sub>9</sub>O<sub>2</sub><sup>+</sup> ion at *m/z* 125 is the elimination of water molecule to yield the *m/z* 107. This process requires that activation induces the transfer of a hydrogen atom of the cycle on the oxygen atom of the phenol. The activation of this latter ion leads to the elimination of a CO molecule. According to the structure proposed on **Figure III-20**, the mechanism is not trivial. Nevertheless, it was investigated few years ago by Russell *et al.*<sup>43</sup> The activation of *m/z* 107 ion leads to the transfer of one hydrogen from the methyl to the C6 ring to form the methylaryloxy C<sub>6</sub>H<sub>5</sub>–O–CH<sub>2</sub><sup>+</sup> ion. These authors suggested that a facile rearrangement due to ‘ortho’ effect may happen, which leads to an equilibrium between the methylaryloxy and the 2-hydroxybenzyl ions. This latter obeys to an equilibrium with the hydroxytropylium, which leads to the keto-form by tautomerization and finally the loss of CO and the formation of the *m/z* 79 ion.

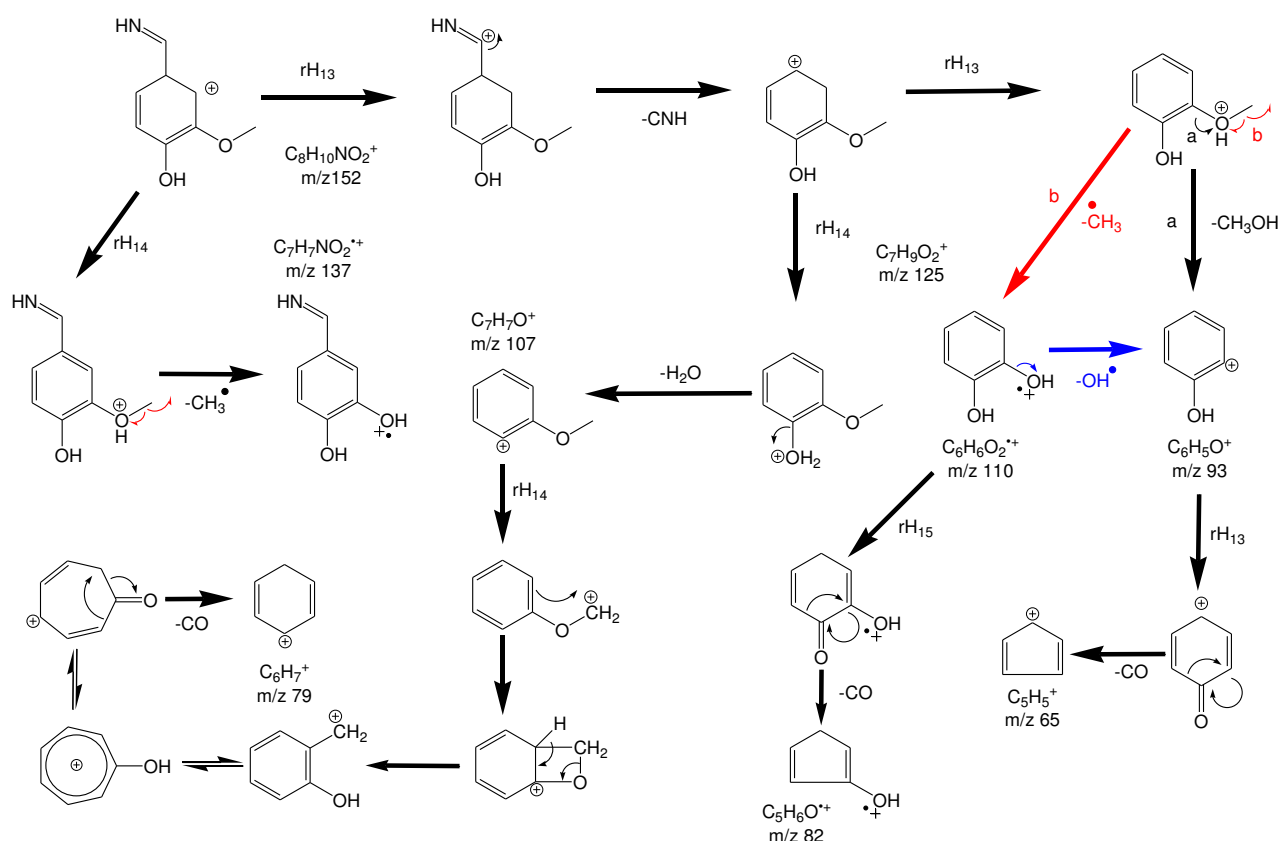


Figure III-20. Proposed mechanisms of  $[M+H]^+$  vanillin+ $NH_4OH$  imine  $MS^n$  fragmentation.

#### IV.C.1.c. Tandem mass spectrometry of the vanillin protonated Schiff bases

The protonated N-vanillylidene aniline and N-vanillylidene 3-chloroaniline Schiff bases are detected at  $m/z$  228 and 262/264, respectively. Some MS/MS measurements have been undertaken on these ions (**Figure III-21** and **Figure III-22**). For the 3-chloroaniline Schiff bases, the tandem mass spectrometry experiments are conducted on both  $^{35}Cl$  and  $^{37}Cl$  parent ion contributions to confirm assignment and mechanism. Whatever the nature of the parent ion, the same fragmentation patterns are observed. Part of the dissociation mechanisms have been observed with the vanillin imine. Thus, the formation of the  $m/z$  213 (with aniline) and 247/249 (with 3-chloroaniline) daughter ions corresponds to the loss of methyl radical. The  $m/z$  125 daughter ion is associated with the elimination of the imine moiety (not shown in **Figure III-21**). The  $MS^3$  behavior of the  $C_7H_9O_2^+$  ion is similar to what it was observed for vanillin imine.

The main fragment ion is observed at  $m/z$  104 (138/140 for 3-chloroaniline Schiff base). It is relative to an inductive process whose result is the elimination of the 3-methoxy 4-hydroxyphenyl. The consecutive elimination of HCN, which is confirmed by MS<sup>3</sup>, leads to the formation of the phenyl ( $m/z$  77) or chlorophenyl ( $m/z$  111/113) cation. Alternatively, these ions may be directly formed by MS<sup>2</sup> through the inductive dissociation of the carbon–nitrogen bond of the aniline or chloroaniline. The hydrogen transfer, from the aromatic ring to the methoxy oxygen atom, is the driving force that ensures to understand the formation of the last three daughter ions at  $m/z$  213 (247/249), 212 (246/248), and 196 (230/232). As previously mentioned, the **a** process leads to the elimination of methyl radical by homolytic bond cleavage and the formation of the C<sub>13</sub>H<sub>11</sub>NO<sub>2</sub><sup>+•</sup> dihydroxyl radical ion. The **b** process, still observed in the MS<sup>3</sup> of vanillin imine, corresponds to the loss of a methanol molecule by inductive cleavage. Alternatively, this C<sub>13</sub>H<sub>10</sub>NO<sup>+</sup> specie may be formed by the hydroxyl elimination from the C<sub>13</sub>H<sub>11</sub>NO<sub>2</sub><sup>+•</sup> ion (process **a'**) in the specific case of the aniline Schiff base. Finally, the loss of CH<sub>4</sub>, by a recombination process (**c** mechanism), yields the 1,2 benzoquinone like ion detected at  $m/z$  212 (246/248). For the aniline Schiff base, the MS<sup>3</sup> experiment demonstrates the ability of C<sub>13</sub>H<sub>11</sub>NO<sub>2</sub><sup>+•</sup> ion (process **b'**) to lose a hydrogen radical to form the  $m/z$  212 ion. Interestingly, the C<sub>13</sub>H<sub>10</sub>ClNO<sub>2</sub><sup>+•</sup> does not lead to the **a'** and **b'** MS<sup>3</sup> processes. The MS<sup>3</sup> daughter ions correspond in that case to the elimination of CO ( $m/z$  219/221) or HCl ( $m/z$  211) (**Figure III-22**). The important interaction (hydrogen bond) between the chlorine atom and one hydroxyl group of the second aryl may explain this difference of MS<sup>3</sup> behavior. Such interaction promotes the pyridine formation by cyclization and the loss of HCl, which ensures the formation of a high-condensed four fused ring radical cation. Alternatively, the tautomerization of the keto-form permits the easy loss of CO and the formation of the  $m/z$  219/221 ions. Finally, the MS<sup>3</sup> experiment performed on the C<sub>13</sub>H<sub>10</sub>NO<sup>+</sup> cation leads, after the tautomerization to the keto-form, to the elimination of carbon monoxide (ion at  $m/z$  168) and the formation of the ketonic C<sub>6</sub>H<sub>5</sub>O<sup>+</sup> cation.

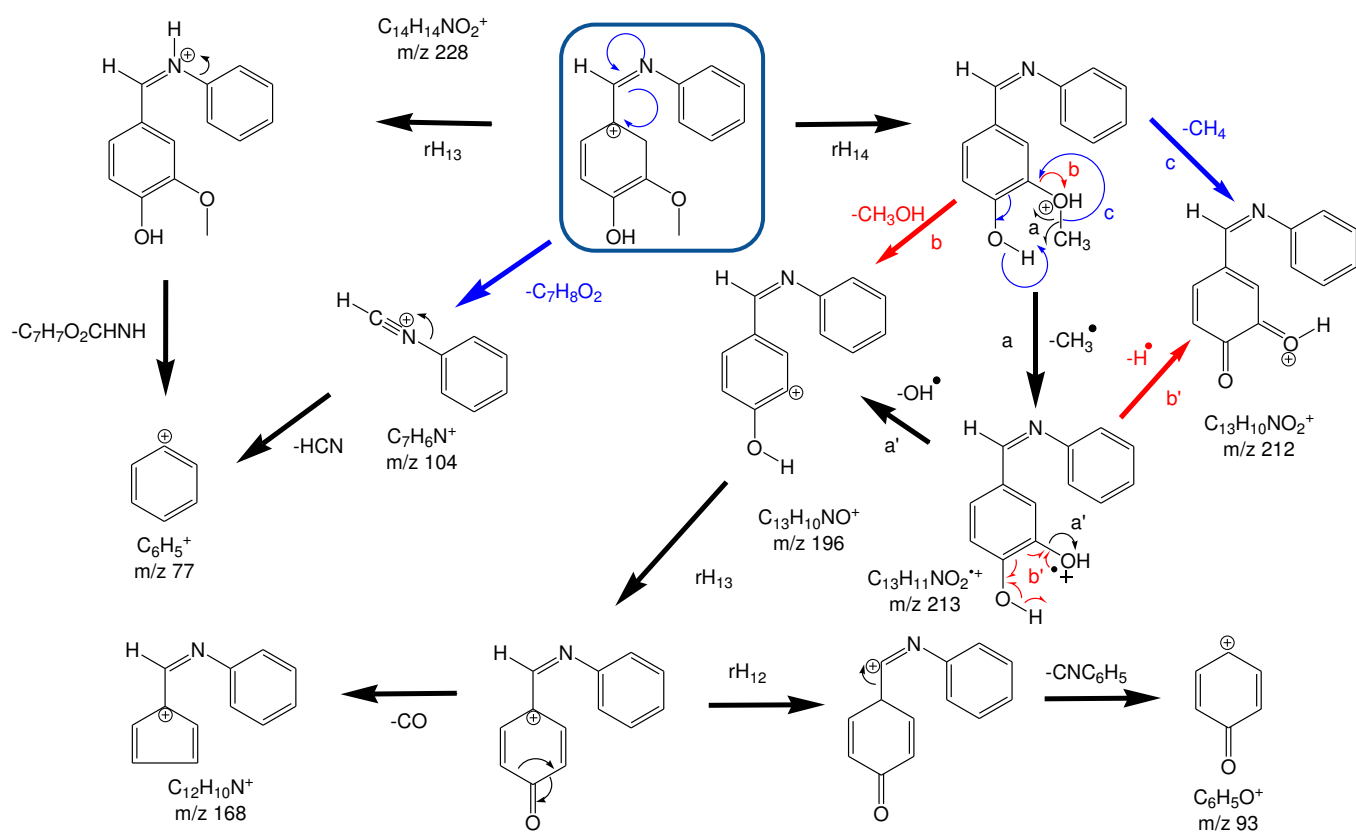


Figure III-21. Proposed mechanisms of  $[M+H]^+$  vanillin+aniline Schiff base  $MS^n$  fragmentation.

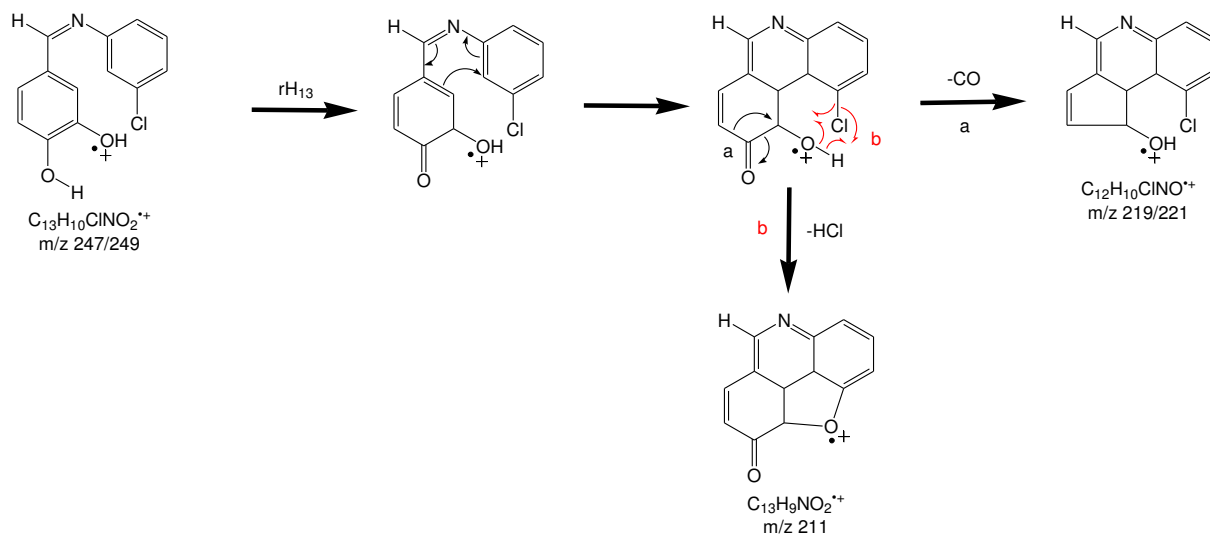


Figure III-22. Proposed mechanisms of  $[M+H]^+$  vanillin+3-chloroaniline Schiff base  $MS^n$  fragmentation.



In conclusion, the tandem mass measurements clearly demonstrate the formation of imine and Schiff base by reaction of primary amine (ammonium hydroxide, aniline, and 3-chloroaniline) with the vanillin, in solution or during the ESI process. The behavior of the vanillin will be compared to what it was observed with the three other standard carbonyl compounds.

#### IV.C.2. Cinnamaldehyde

The cinnamaldehyde was analyzed in the same experimental conditions. Without amine, the cinnamaldehyde is detected as  $[M+H]^+$  ion at  $m/z$  133 (**Figure III-23.a**). The addition of ammonia leads to the observation of an intense signal at  $m/z$  132 (**Figure III-23.b**). When aniline and 3-chloroaniline are used, ions are evidenced at  $m/z$  208 and 242/244, respectively (**Figure III-23.c and d**). The tandem mass spectrometry measurements performed on the different protonated parent ions are reported in **Table III-6**.

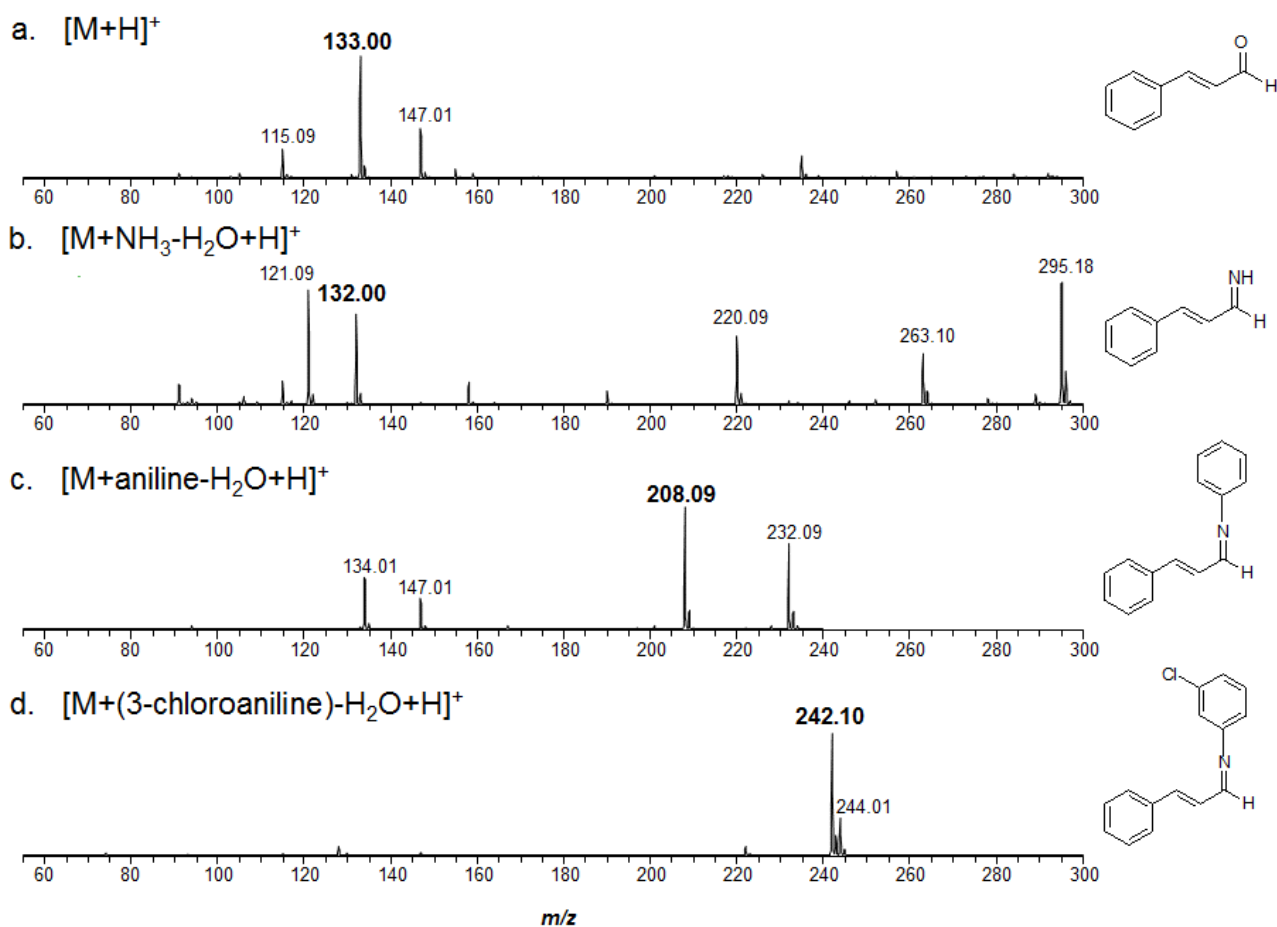


Figure III-23. (+) ESI LIT MS of cinnamaldehyde in (a) methanol, (b) methanol/ $NH_4OH$  (1% v/v), (c) methanol/aniline (1% v/v) and, (d) methanol/3-chloroaniline (1% v/v).

	MS <sup>1</sup>	MS <sup>2</sup>		MS <sup>3</sup>	
	[M+H] <sup>+</sup>	E <sub>COM</sub> (eV)	m/z (abundance) – loss	E <sub>COM</sub> (eV)	m/z (abundance) – loss
<b>Cinnamaldehyde</b>	C <sub>9</sub> H <sub>9</sub> O <sup>+</sup> m/z 133	0.70	115 (100) – H <sub>2</sub> O	0.91	No fragment
			105 (18) – CO		
			91 (11) – CO – CH <sub>2</sub> CO		
<b>Cinnamaldehyde imine</b>	C <sub>9</sub> H <sub>10</sub> N <sup>+</sup> m/z 132	0.71	115 (100) – NH <sub>3</sub>	0.91	No fragment
			105 (1) – CNH		
<b>Cinnamaldehyde – Aniline Schiff Base</b>	C <sub>15</sub> H <sub>14</sub> N <sup>+</sup> m/z 208	0.55	130 (100) – C <sub>6</sub> H <sub>6</sub>	0.87	103 (100) – HCN
			115 (75) – C <sub>6</sub> H <sub>5</sub> NH <sub>2</sub>		
			91 (60) – C <sub>6</sub> H <sub>5</sub> NHCCH		
<b>Cinnamaldehyde – 3-chloroaniline Schiff Base</b>	C <sub>15</sub> H <sub>13</sub> N <sup>35</sup> Cl <sup>+</sup> m/z 242	0.49	207 (34) – <sup>35</sup> Cl•		
			206 (16) – H <sup>35</sup> Cl		
			164 (100) – C <sub>6</sub> H <sub>6</sub>		
			115 (95) – C <sub>6</sub> H <sub>4</sub> <sup>35</sup> ClNH <sub>2</sub>		
			91 (52) – C <sub>6</sub> H <sub>4</sub> <sup>35</sup> Cl NHCCH		
<b>Cinnamaldehyde – 3-chloroaniline Schiff Base</b>	C <sub>15</sub> H <sub>13</sub> N <sup>37</sup> Cl <sup>+</sup> m/z 244	0.49	207 (34) – <sup>37</sup> Cl•		
			206 (15) – H <sup>37</sup> Cl		
			166 (100) – C <sub>6</sub> H <sub>6</sub>		
			115 (94) – C <sub>6</sub> H <sub>4</sub> <sup>37</sup> ClNH <sub>2</sub>		
			91 (50) – C <sub>6</sub> H <sub>4</sub> <sup>37</sup> Cl NHCCH		

Table III-6. Tandem mass spectrometry analysis of protonated [M+H]<sup>+</sup> ion of cinnamaldehyde and its corresponding imine compounds.

#### IV.C.2.a. Tandem mass spectrometry of cinnamaldehyde protonated ion

Three daughter ions are observed after the collisional activation of protonated cinnamaldehyde at  $m/z$  115, 105, and 91, which corresponds to the loss of a water, a carbon monoxide, and a cetene molecule, respectively (**Figure III-24**). The MS<sup>3</sup> of these ions does not lead to an additional fragmentation, even at high collision energy, except for  $m/z$  105 ion that leads to the formation of the phenyl ion ( $m/z$  77). Consequently, the  $m/z$  115 and 91 ions are particularly stable and charge delocalization on their structure is expected. The attachment of the proton is expected to take place on the side-chain. The activation of the [M+H]<sup>+</sup> ensures the rH<sub>13</sub> hydrogen transfer on the oxygen atom. A rearrangement, engaging both the resulting hydroxyl and a hydrogen atom, leads to the elimination of water and the formation of the very stable indene cation observed at  $m/z$  115. Another rH<sub>13</sub> transfer involving the labile hydrogen of the aldehyde ensures the formation of a pendant CO group, which is eliminated (process **a**) to yield the C<sub>8</sub>H<sub>9</sub><sup>+</sup> ion at  $m/z$  105. The elimination of an ethene molecule by inductive fragment allows the charge to migrate on the phenyl ring and the observation of the C<sub>6</sub>H<sub>5</sub><sup>+</sup> cation. An alternative fragmentation pathway of this process is the elimination of the ketene by β-elimination and the production of the very stable tropylium ion at  $m/z$  91 (process **b**).

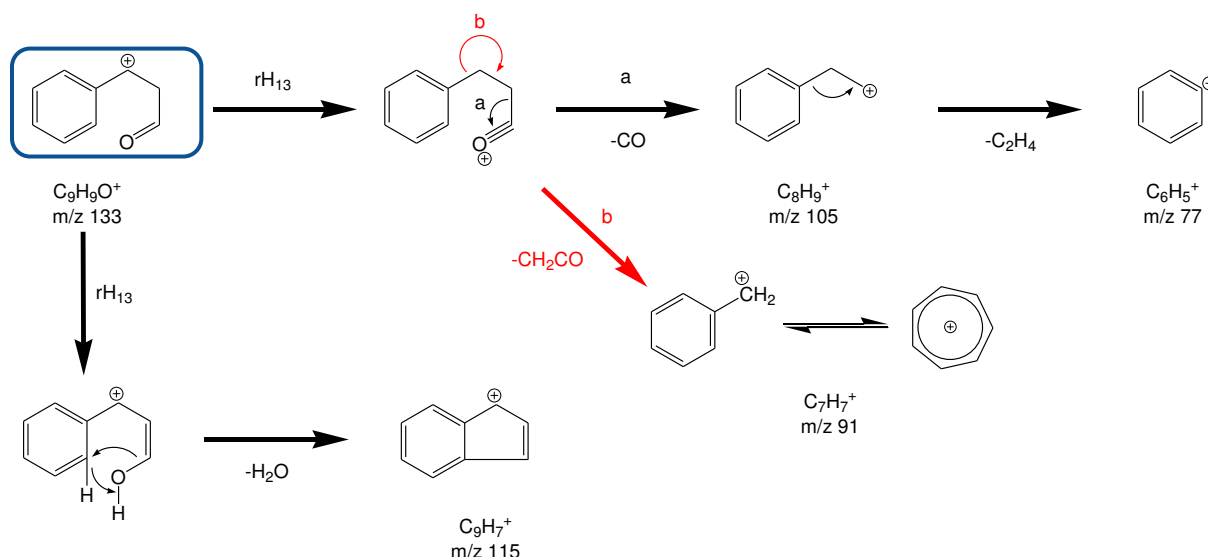


Figure III-24. Proposed mechanisms of  $[M+H]^+$  cinnamaldehyde  $MS^n$  fragmentation.

#### IV.C.2.b. Tandem mass spectrometry of cinnamaldehyde protonated imine

The fragmentation of the  $C_9H_{10}N^+$  ion is quite similar to what it was observed with the protonated cinnamaldehyde (**Figure III-25**). The transfer of one hydrogen on the nitrogen atom ensures the easy elimination of  $NH_3$  and results in the formation of the indene cation. The  $rH_{13}$  hydrogen transfer from the iminium carbon to the tertiary carbon of the side chain is expected to yield the  $m/z$  105 by elimination of  $CNH$ . This process is more favorable than the elimination of an acetonitrile molecule, which would yield the tropylium ion.

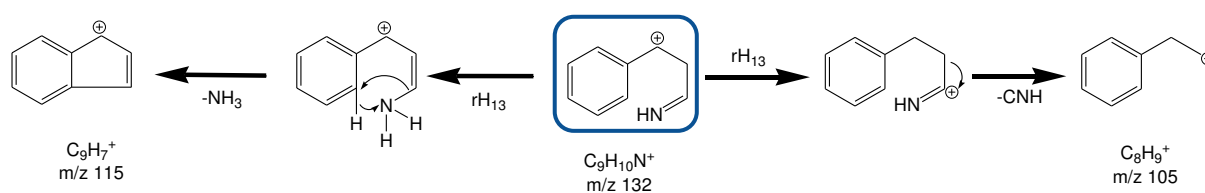


Figure III-25. Proposed mechanisms of  $[M+H]^+$  cinnamaldehyde+ $NH_4OH$  imine  $MS^n$  fragmentation.

#### IV.C.2.c. Tandem mass spectrometry of cinnamaldehyde protonated Schiff bases

Parts of the mechanisms observed for the imine derivative of the cinnamaldehyde are also evidenced for the different Schiff bases (**Figure III-26**). Indeed, the systematic formation of  $m/z$  115 ion obeys to the mechanism previously described and implies the loss of the aniline or the chloroaniline. The  $rH_{13}$  transfer of the hydrogen of the iminium carbon ensures the migration of the charge and finally the formation of the tropylium ion by the elimination of R–

$\text{NH}-\text{C}\equiv\text{CH}$  ( $\text{R} = \text{C}_6\text{H}_5$  or  $\text{C}_6\text{H}_4\text{Cl}$ ). A rearrangement similar to what it is observed for the elimination of aniline and chloroaniline may explain the loss of a benzene molecule. First, the mesomeric form of the parent ion, engaging the nitrogen lone pair, gives a highly conjugated structure. The pyridine cyclization allows the rearrangement to occur. The hydrogen on the ortho-position is transferred to the phenyl ring and ensures the simultaneous elimination of benzene and the formation of the protonated quinoline at  $m/z$  130 or its chlorinated analogues at  $m/z$  164/166.

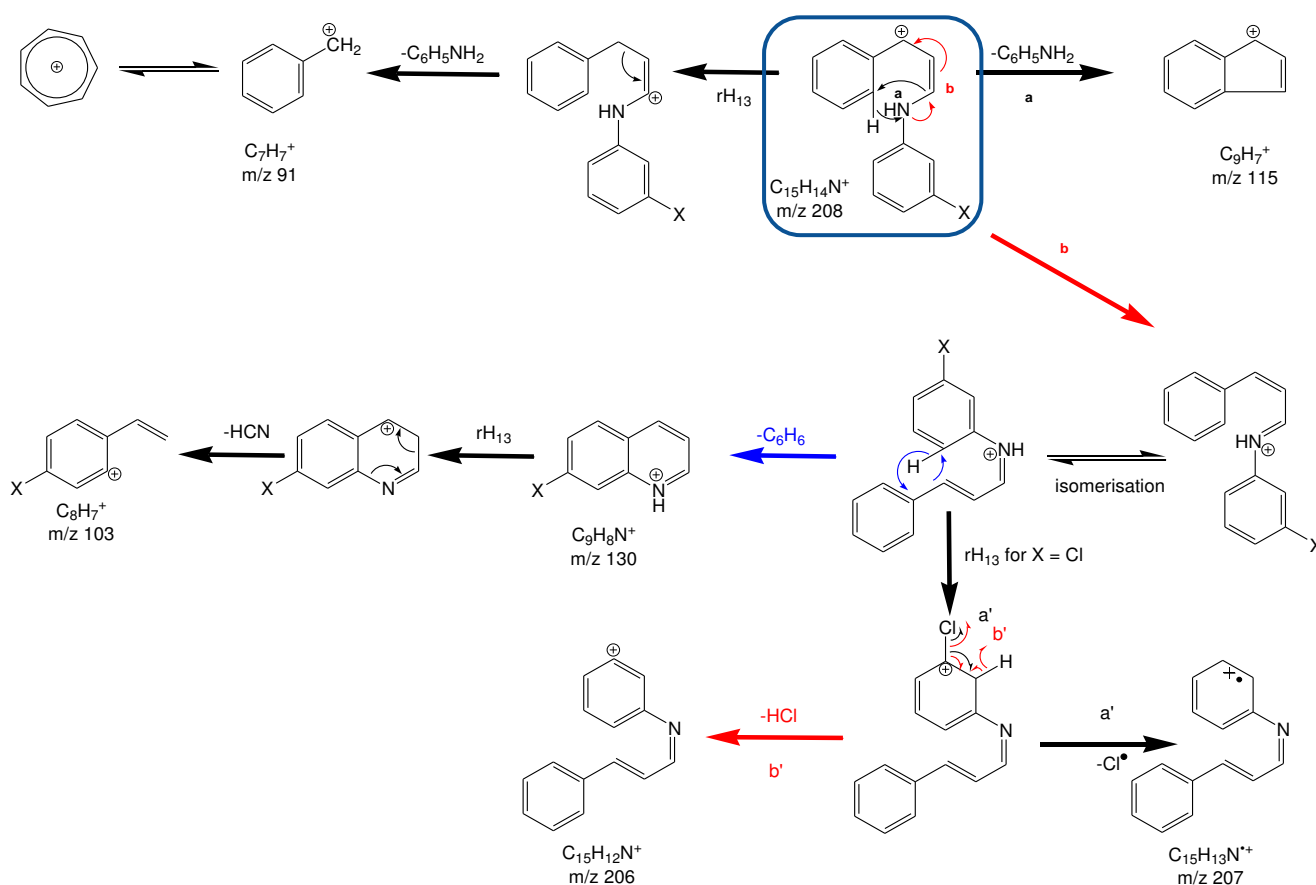


Figure III-26. Proposed mechanisms of  $[M+H]^+$  cinnamaldehyde+ aniline Schiff base  $\text{MS}^n$  fragmentation.

The substitution of the aniline by a chlorine ensures to observe two other specific dissociation pathways. The starting point is the highly conjugated structure of the parent ion. A  $\text{rH}_{13}$  transfer from the nitrogen to the aromatic ring may lead to the elimination of chlorine by two processes. The former one is the homolytic cleavage of the carbon–chlorine bond (process **a'**) which leads to the  $\text{C}_{13}\text{H}_{11}\text{NO}_2^{+\bullet}$  radical cation at  $m/z$  207. The second one is associated with the concerted elimination of the chlorine and a hydrogen atom bonded to an adjacent carbon to ensure the loss of HCl and the formation of the  $m/z$  206 ion (process **b'**). For each of these

ions ( $m/z$  206 and 207), cyclization may occur to stabilize the obtained structure by resonance effects as phenyl quinoline structure.

#### IV.C.3. Butyrophenone

The analysis of butyrophenone by ESI-MS leads to the observation of the  $[M+H]^+$  ion at  $m/z$  149 (**Figure III-27.a**). The  $m/z$  148 ion, which is expected to be relative to the butyrophenone imine, is detected when  $NH_4OH$  is added to the solution infused in the ESI source (**Figure III-27.b**). The use of aniline or chloroaniline as dopant leads to the detection of  $m/z$  224 or 258/260 ions (**Figure III-27.c and d**), respectively. These species are associated with the expected Schiff bases. The tandem mass spectrometry investigations ensure to confirm the formation of the butyrophenone imine and Schiff bases. The results are gathered in **Table III-7**.

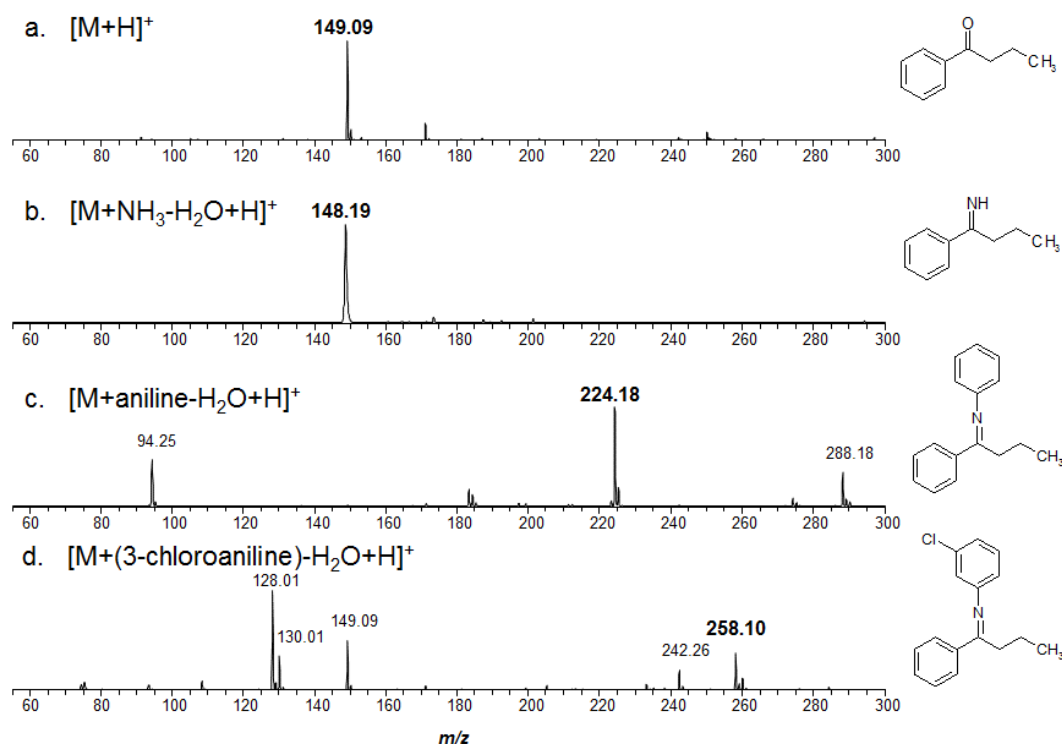


Figure III-27. (+) ESI LIT MS of butyrophenone in (a) methanol, (b) methanol/ $NH_4OH$  (1% v/v), (c) methanol/aniline (1% v/v) and, (d) methanol/3-chloroaniline (1% v/v).

	MS <sup>1</sup> [M+H] <sup>+</sup>	MS <sup>2</sup>		MS <sup>3</sup>	
		E <sub>COM</sub> (eV)	m/z (abundance) – loss	E <sub>COM</sub> (eV)	m/z (abundance) – loss
Butyrophenone	C <sub>10</sub> H <sub>13</sub> O <sup>+</sup> m/z 149	0.58	131 (14) – H <sub>2</sub> O	0.80	116 (10) – CH <sub>3</sub> <sup>•</sup>
			107 (37) – C <sub>3</sub> H <sub>6</sub>	0.72	115 (5) – CH <sub>4</sub>
			105 (8) – C <sub>3</sub> H <sub>8</sub>		91 (100) – C <sub>3</sub> H <sub>4</sub>
			91 (11) – H <sub>2</sub> O – C <sub>3</sub> H <sub>4</sub>		79 (100) – CO
			71 (100) – C <sub>6</sub> H <sub>6</sub>		
Butyrophenone imine	C <sub>10</sub> H <sub>14</sub> N <sup>+</sup> m/z 148	0.74	131 (72) – NH <sub>3</sub>	0.71	91 (100) – C <sub>3</sub> H <sub>4</sub>
			106 (100) – C <sub>3</sub> H <sub>6</sub>	0.87	79 (100) – CNH
			91 (15) – NH <sub>3</sub> – C <sub>3</sub> H <sub>4</sub>		
			71 (12) – C <sub>6</sub> H <sub>5</sub> <sup>•</sup>		
Butyrophenone – Aniline Schiff Base	C <sub>16</sub> H <sub>18</sub> N <sup>+</sup> m/z 224	0.63	195 (44) – C <sub>2</sub> H <sub>5</sub> <sup>•</sup>	0.77	91 (100) – C <sub>3</sub> H <sub>4</sub>
			182 (95) – C <sub>3</sub> H <sub>6</sub>		
			146(83) – C <sub>6</sub> H <sub>6</sub>		
			131 (100) – C <sub>6</sub> H <sub>5</sub> NH <sub>2</sub>		
			94 (22) – C <sub>6</sub> H <sub>5</sub> CCC <sub>2</sub> H <sub>5</sub>		
Butyrophenone – 3- chloroaniline Schiff Base	C <sub>16</sub> H <sub>17</sub> N <sup>35</sup> Cl <sup>+</sup> m/z 258	0.59	229 (29) – C <sub>2</sub> H <sub>5</sub> <sup>•</sup>		
			216 (98) – C <sub>3</sub> H <sub>6</sub>		
			180 (100) – C <sub>6</sub> H <sub>6</sub>		
			131 (79) – C <sub>6</sub> H <sub>4</sub> <sup>35</sup> CINH <sub>2</sub>		
			91 (16) – C <sub>6</sub> H <sub>4</sub> <sup>35</sup> CINH <sub>2</sub> – C <sub>3</sub> H <sub>4</sub>		
	C <sub>16</sub> H <sub>17</sub> N <sup>37</sup> Cl <sup>+</sup> m/z 260	0.59	231 (29) – C <sub>2</sub> H <sub>5</sub> <sup>•</sup>		
218 (98) – C <sub>3</sub> H <sub>6</sub>					
			182 (100) – C <sub>6</sub> H <sub>6</sub>		
			131 (78) – C <sub>6</sub> H <sub>4</sub> <sup>37</sup> CINH <sub>2</sub>		
			91 (17) – C <sub>6</sub> H <sub>4</sub> <sup>37</sup> CINH <sub>2</sub> – C <sub>3</sub> H <sub>4</sub>		

Table III-7. Tandem mass spectrometry analysis of protonated [M+H]<sup>+</sup> ion of butyrophenone and its corresponding imine compounds.

#### IV.C.3.a. Tandem mass spectrometry of butyrophenone protonated ion

The protonation of the butyrophenone is expected to occur by fixation of the proton on the aromatic ring or on the carbonyl function (**Figure III-28**). A rH<sub>13</sub> hydrogen transfer allows to switch from one protomer to another one. The protonation of the phenyl ensures to easily explain the formation of the m/z 71 by inductive cleavage of the carbon–carbon bond between the carbonyl and the C<sub>6</sub>H<sub>6</sub> ring, which results in the loss of a benzene molecule. A rH<sub>15</sub> hydrogen transfer for this same protomer, followed by the cleavage of the bond of the other side of the molecule, leads to the elimination of propene and the formation of the C<sub>6</sub>H<sub>7</sub>CO<sup>+</sup> ion at m/z 107. A MS<sup>3</sup> experiment performed on this latter highlights the loss of CO and the formation of C<sub>6</sub>H<sub>7</sub><sup>+</sup> ion, which confirms the structure proposed for the C<sub>7</sub>H<sub>7</sub>O<sup>+</sup> cation. The second protomer is the starting point of the other fragmentation processes. The recombination phenomenon allows the loss of a propane molecule and the formation of the Ph–CO<sup>+</sup> ion at m/z 105. The rH<sub>13</sub> transfer has also to be linked to the tautomerization equilibrium displacement to the protonated enol. This latter easily loss a water molecule to form the C<sub>10</sub>H<sub>11</sub><sup>+</sup> ion. The activation of this ion leads to a rH<sub>13</sub> hydrogen transfer on the side chain of the phenyl

and to two fragmentation pathways. The first one implies the loss of a propyne molecule (process **a**) by a heterolytic bond cleavage and the formation of the tropylium ion at  $m/z$  91. The second one (process **b**) produces the protonated indene by the elimination of methane through a concerted mechanism. The MS<sup>3</sup> of the  $C_{10}H_{11}^+$  ion also yields a third daughter ion by the release of a methyl radical. The process begins with the  $rH_{13}$  hydrogen transfer from the phenyl to its side chain to form a substituted phenyl cation. A concerted mechanism allows the homolytic elimination of  $\cdot CH_3$  and the cyclization of a C5 ring to occur. This process leads to the formation of the indene radical ion.

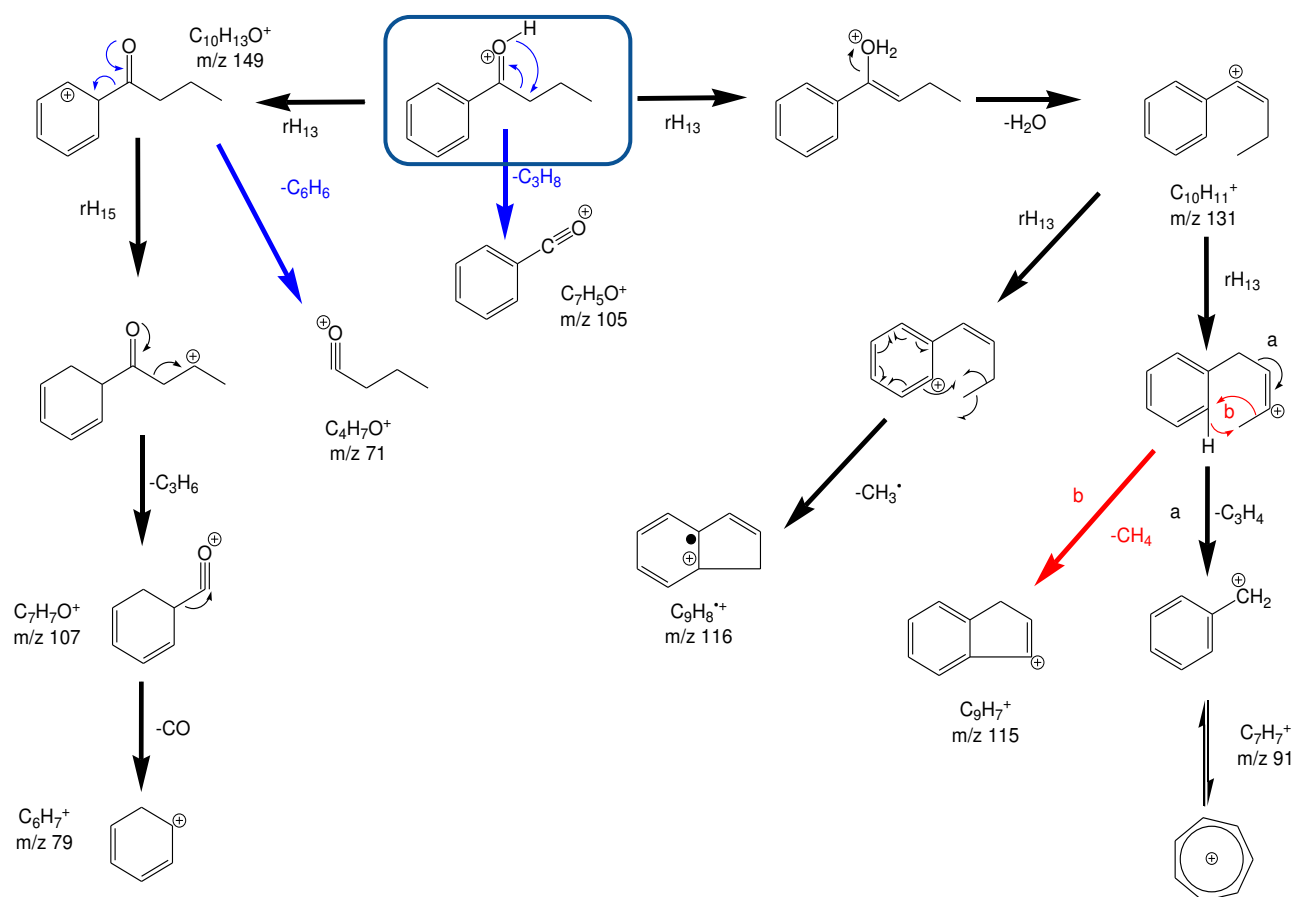


Figure III-28. Proposed mechanisms of  $[M+H]^+$  butyrophenone MS<sup>n</sup> fragmentation.

#### IV.C.3.b. Tandem mass spectrometry of butyrophenone protonated imine ion

The mechanisms involved in the formation of the daughter ion of butyrophenone imine ion are very similar to what it was described in the previous section (**Figure III-29**). The protomer, which corresponds to the protonation of the phenyl, undertakes a  $\beta$  inductive cleavage and the loss of propene, after a  $rH_{15}$  hydrogen transfer. The resulting ion detected at  $m/z$  106

exclusively lost CNH to form the  $C_6H_7^+$  protonated benzene ion by  $MS^3$ . The tautomer equilibrium between the second protomer (protonation on the nitrogen atom) ensures the easy elimination of ammonia and the observation of the  $m/z$  131 ion, whose  $MS^3$  behavior is close to what it was reported in the previous section. The poor signal of the  $C_{10}H_{11}^+$  and the lower  $E_{COM}$  do not allow observing either the loss of methane or the elimination of the methyl radical. At the difference of the protonated butyrophenone, the elimination of benzene by inductive cleavage is not observed. The imine leads to the homolytic dissociation of the bond between the phenyl and the imine function, which is evidenced by the detection of the  $C_4H_9N^{+\bullet}$  radical cation. A lower electronegativity of the nitrogen atom compared to the oxygen one may be a reasonable explanation of this behavior.

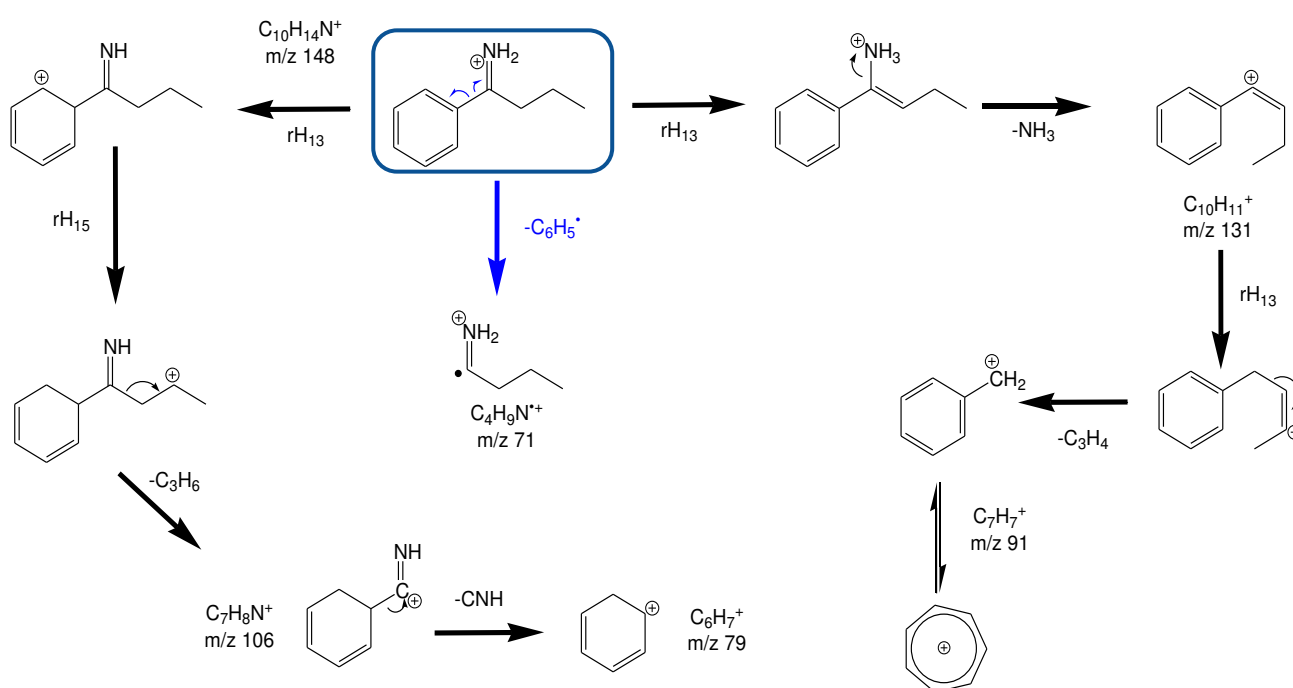


Figure III-29. Proposed mechanisms of  $[M+H]^+$  butyrophenone+ $NH_4OH$  imine  $MS^n$  fragmentation.

#### IV.C.3.c. Tandem mass spectrometry of butyrophenone protonated Schiff bases

The  $MS^2$  behavior of the two protonated Schiff bases obtained by reaction of butyrophenone with aniline or 3-chloroaniline is very close to what it was described for the protonated butyrophenone and/or butyrophenone imine (**Figure III-30**). The  $m/z$  131 daughter ion results from the loss of aniline (or 3-chloroaniline). The involved process is identical to those involved in the elimination of water for protonated butyrophenone or the elimination of ammonia from



the butyrophenone imine. The MS<sup>3</sup> of this first daughter ion leads also to the specific formation of the tropylium cation. It is interesting to note that in spite of a low  $E_{\text{COM}}$  used to activate the 3-chloroaniline Schiff base, this consecutive process is evidenced on the MS<sup>2</sup> spectrum. This is the reason why the  $\text{C}_{10}\text{H}_{11}^+$  ion is not the base peak in that case. Both the elimination of benzene and propene molecule, as it was described in the two previous sections, are observed for both Schiff bases. The last fragmentation pathway is specific to the butyrophenone Schiff bases, it corresponds to the elimination of an ethyl radical and the formation the  $\text{C}_{14}\text{H}_{13}\text{N}^{+\bullet}$  and  $\text{C}_{14}\text{H}_{12}\text{ClN}^{+\bullet}$  daughter ions at  $m/z$  195 and 229/231, respectively. The  $\beta$ -homolytic elimination of the side hydrocarbon chain seems to be favored by the attractive properties of the aniline or 3-chloroaniline substituent.

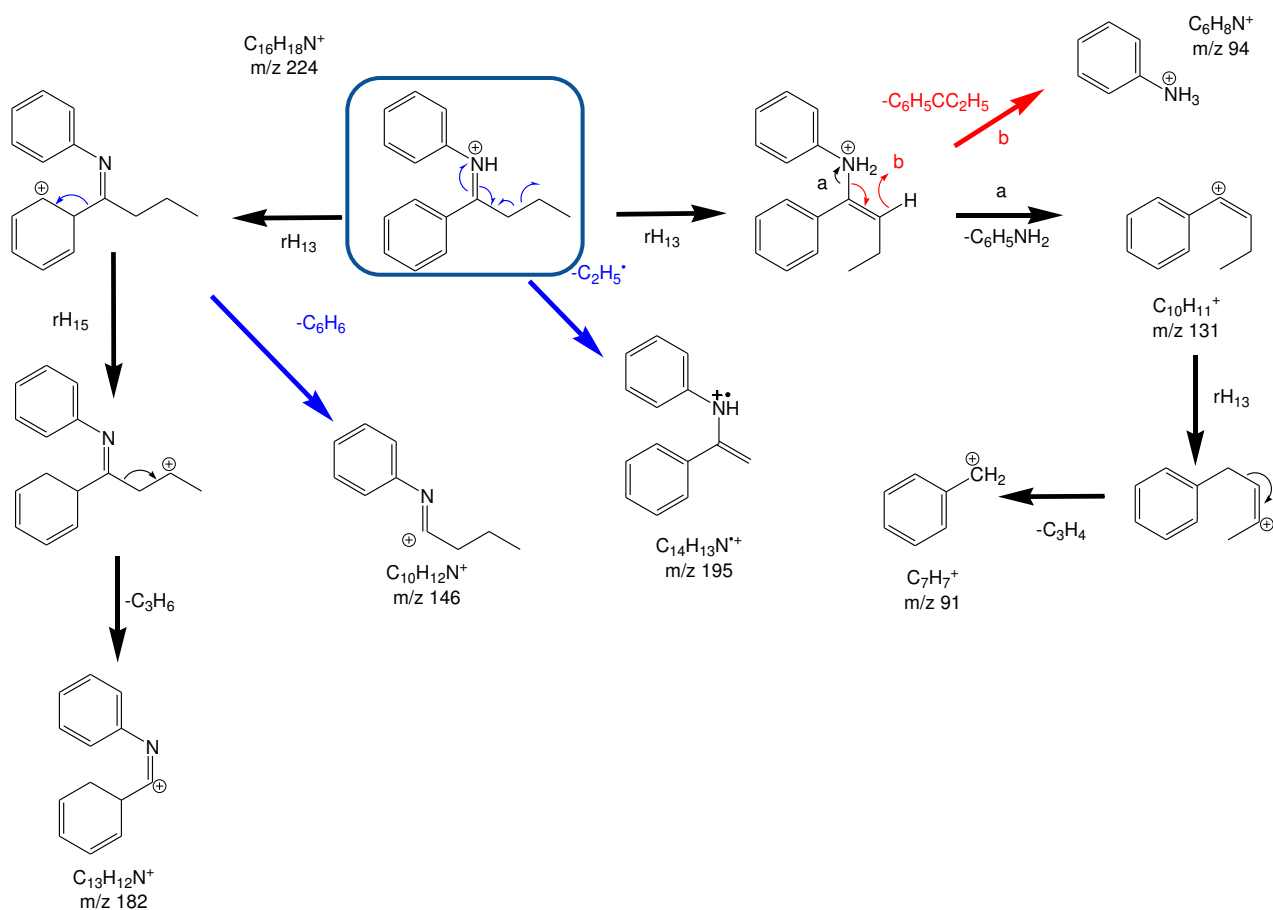


Figure III-30. Proposed mechanisms of  $[\text{M}+\text{H}]^+$  butyrophenone+aniline Schiff base MS<sup>n</sup> fragmentation.

## IV.C.4. Trihydroxyacetophenone

The protonated trihydroxyacetophenone is observed at  $m/z$  169, whereas the  $[M+H]^+$  of the trihydroxyacetophenone imine and the Schiff bases obtained with aniline and 3-chloroaniline are detected at  $m/z$  168, 244, and 278/280, respectively (**Figure III-31**). The structural analysis by tandem mass spectrometry, which confirms the different assignments, is gathered in **Table III-8**.

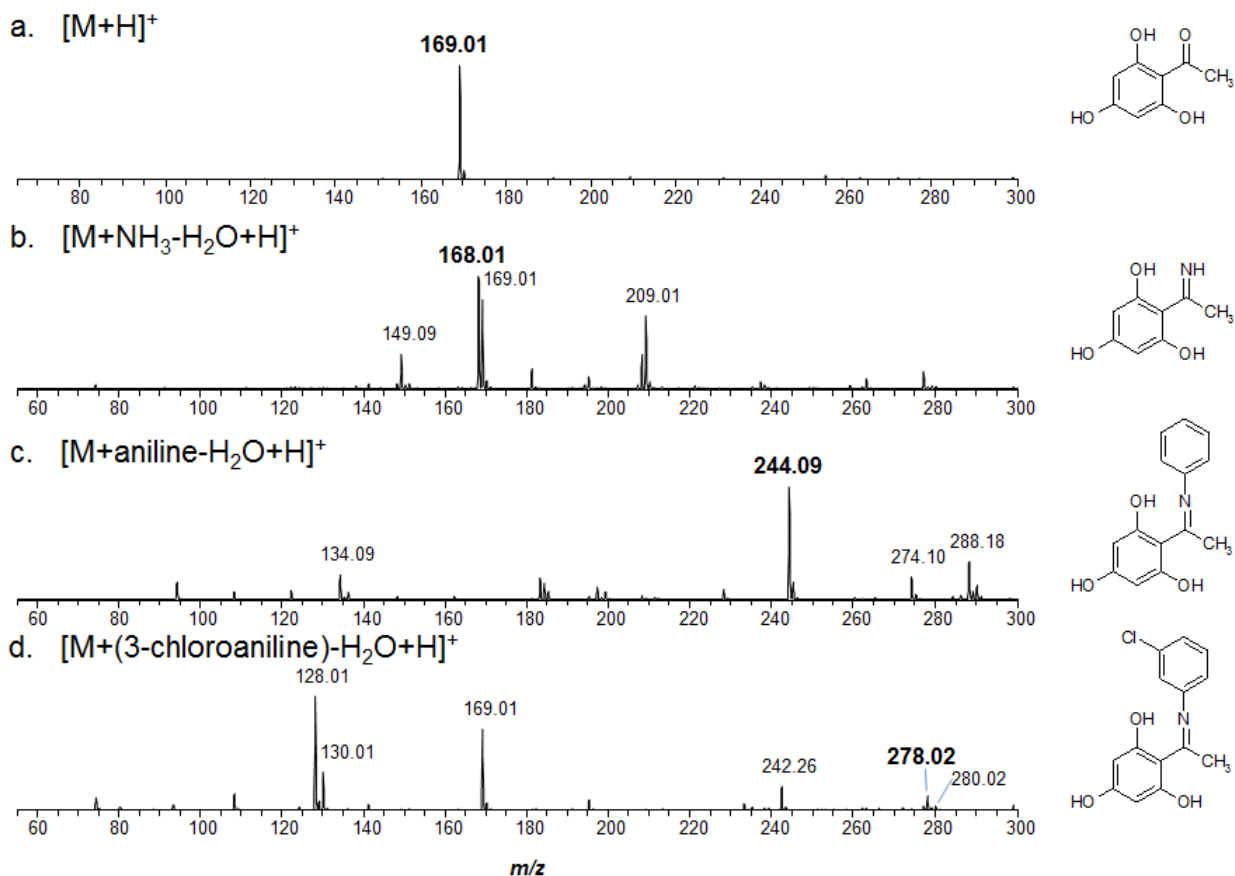


Figure III-31. (+) ESI LIT MS of trihydroxyacetophenone in (a) methanol, (b) methanol/ $NH_4OH$  (1% v/v), (c) methanol/aniline (1% v/v) and, (d) methanol/3-chloroaniline (1% v/v).

	MS <sup>1</sup> [M+H] <sup>+</sup>	MS <sup>2</sup>		MS <sup>3</sup>		MS <sup>4</sup>	
		E <sub>COM</sub> (eV)	m/z (abundance) – loss	E <sub>COM</sub> (eV)	m/z (abundance) – loss	E <sub>COM</sub> (eV)	m/z (abundance) – loss
Trihydroxyaceto phenone	C <sub>8</sub> H <sub>9</sub> O <sub>4</sub> <sup>+</sup> m/z 169	0.55	151 (100) – H <sub>2</sub> O	0.57	123 (100) – CO	0.79	95 (100) – CO
			127 (56) – CH <sub>2</sub> CO	0.76	95 (1) – CO – CO 109 (100) – H <sub>2</sub> O 99 (39) – CO 85 (96) – CH <sub>2</sub> CO 81 (12) – H <sub>2</sub> O – CO	0.71	81 (100) – CO
Trihydroxyaceto phenone imine	C <sub>8</sub> H <sub>10</sub> NO <sub>3</sub> <sup>+</sup> m/z 168	0.53	151 (100) – •OH	0.54	123 (100) – CO 95 (2) – CO – CO	0.69	95 (100) – CO
			127 (5) – C <sub>2</sub> H <sub>3</sub> N 126 (4) – •C <sub>2</sub> H <sub>4</sub> N 84 (2) – C <sub>4</sub> H <sub>4</sub> O <sub>2</sub>				
Trihydroxyaceto phenone – Aniline Schiff Base	C <sub>14</sub> H <sub>14</sub> NO <sub>3</sub> <sup>+</sup> m/z 244	0.48	227 (10) – •OH	0.54	212 (10) – CH <sub>3</sub> • 209 (5) – H <sub>2</sub> O 199 (100) – CO 185 (45) – CH <sub>2</sub> CO 159 (7) – C <sub>4</sub> H <sub>4</sub> O		
			160 (4) – C <sub>4</sub> H <sub>4</sub> O <sub>2</sub> 151(4) – C <sub>6</sub> H <sub>5</sub> NH <sub>2</sub> 118 (100) – C <sub>6</sub> H <sub>6</sub> O <sub>3</sub> 77 (2) – C <sub>6</sub> H <sub>6</sub> O <sub>3</sub> – CH <sub>3</sub> CN	0.82	77 (100) – CH <sub>3</sub> CN		
Trihydroxyaceto phenone – 3- chloroaniline Schiff Base	C <sub>14</sub> H <sub>13</sub> N <sup>35</sup> ClO <sub>3</sub> <sup>+</sup> m/z 278	0.43	261 (2) – •OH 260 (7) – H <sub>2</sub> O 194 (3) – C <sub>4</sub> H <sub>4</sub> O <sub>2</sub> 152 (100) – C <sub>6</sub> H <sub>6</sub> O <sub>3</sub>				
			C <sub>14</sub> H <sub>13</sub> N <sup>37</sup> ClO <sub>3</sub> <sup>+</sup> m/z 280	0.42	263 (2) – •OH 262 (5) – H <sub>2</sub> O 196 (3) – C <sub>4</sub> H <sub>4</sub> O <sub>2</sub> 154 (100) – C <sub>6</sub> H <sub>6</sub> O <sub>3</sub>		

Table III-8. Tandem mass spectrometry analysis of protonated [M+H]<sup>+</sup> ion of trihydroxyacetophenone and its corresponding imine compounds.

#### IV.C.4.a. Tandem mass spectrometry of trihydroxyacetophenone protonated ion

Two fragments are observed by MS<sup>2</sup> of the protonated trihydroxyacetophenone (**Figure III-32**). The main one is relative to the loss of water and the second one corresponds to the elimination of CH<sub>2</sub>CO. At the low activation energy used, it is expected that no significant structural modification occurs before the fragmentation process. It is consequently reasonable to consider that the ionization of this molecule by ESI is mainly associated with the attachment of a proton on a hydroxyl substituent, which permits the easy dehydration of the parent ion and the formation of the C<sub>8</sub>H<sub>7</sub>O<sub>3</sub><sup>+</sup> cation detected at *m/z* 151. Finally, fragmentation of the C<sub>8</sub>H<sub>7</sub>O<sub>3</sub><sup>+</sup> cation induces two consecutive CO losses after displacement of tautomeric equilibrium to keto form. These processes lead to the successive formation of *m/z* 123 and 95 ions, which is confirmed by the MS<sup>4</sup> experiment performed on the C<sub>7</sub>H<sub>7</sub>O<sub>2</sub><sup>+</sup> ion.

For the second fragmentation pathway from the protonated trihydroxyacetophenone, a first rH<sub>13</sub> hydrogen transfer is considered to shift the charge on the aromatic ring. The acetyl moiety is subjected to a tautomer equilibrium, which may be displaced to the enol form by

collisional activation. A concerted rearrangement mechanism allows to achieve the elimination of  $\text{CH}_2\text{CO}$  and the displacement of the enolic hydrogen to one hydroxyl substituent of the aromatic ring to yield the  $m/z$  127 ion corresponding to the protonated trihydroxybenzene. The additional activation of this ion ensures the elimination of water and the formation of the  $\text{C}_6\text{H}_5\text{O}_2^+$  at  $m/z$  109. It is followed by the CO loss after the displacement of the tautomeric equilibrium to the ketone form. The resulting ion at  $m/z$  81 corresponds to the protonated form of the hydroxycyclopentadiene. The activation of the protonated trihydroxybenzene leads to the  $\text{rH}_{13}$  hydrogen transfer from one hydroxyl to the aromatic ring and the displacement of the tautomeric equilibrium to the ketone form, which allows two fragmentation pathways to be opened. The first one is the loss of carbon monoxide (process **b**), which ensures the formation of the protonated dihydroxycyclopentadiene at  $m/z$  99 and the second one (process **a**) induces the opening of the ring and the loss of the  $\text{CH}_2\text{CO}$  (ketene) to yield the  $\text{C}_4\text{H}_5\text{O}_2^+$  cation at  $m/z$  85.

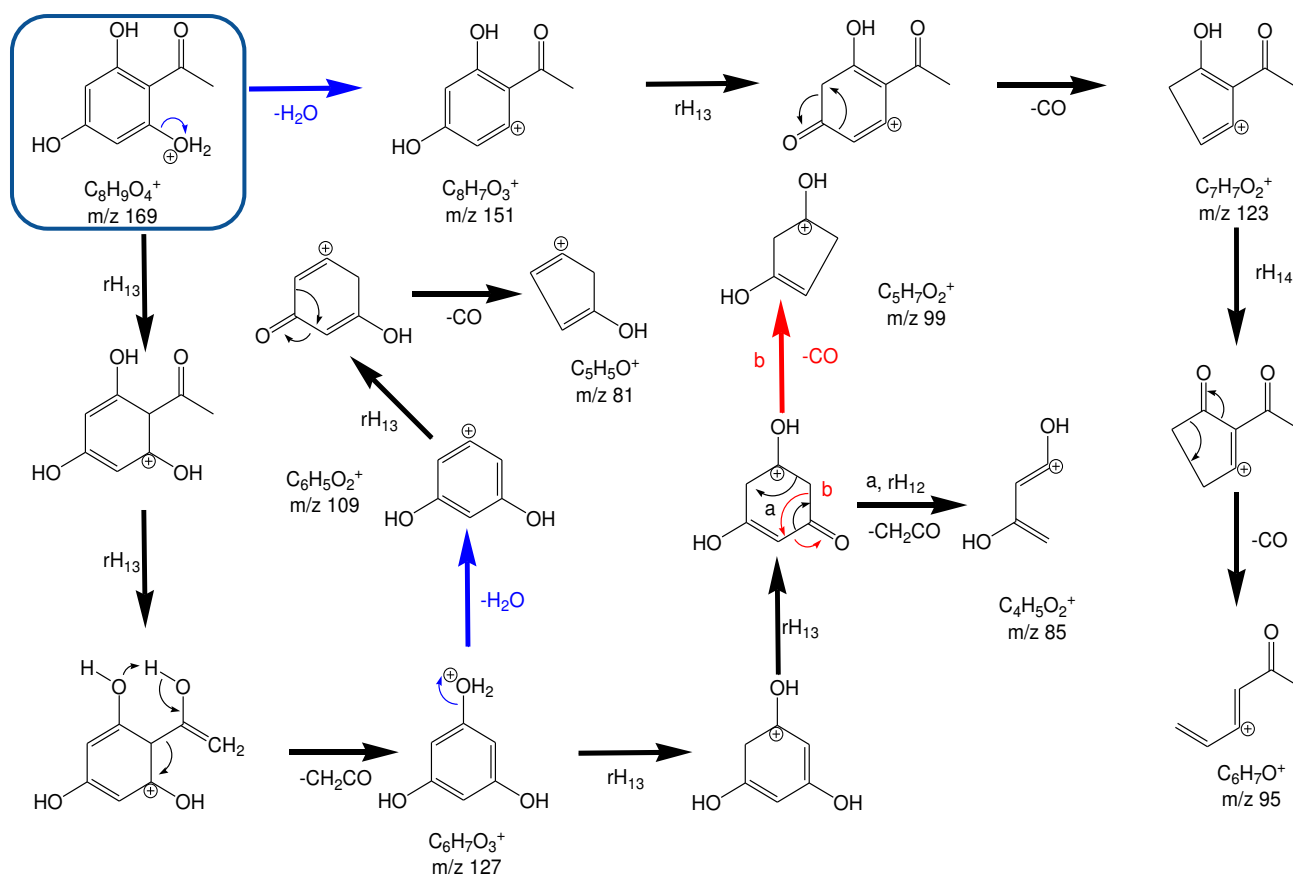


Figure III-32. Proposed mechanisms of  $[M+H]^+$  trihydroxyacetophenone  $\text{MS}^n$  fragmentation.

IV.C.4.b. Tandem mass spectrometry of trihydroxyacetophenone protonated imine ion

Two protomers may be considered for the  $m/z$  168 trihydroxyacetophenone protonated imine ion (**Figure III-33**). The first one is obtained by protonation of the nitrogen and the second one by attachment of a proton to the aromatic ring. The  $rH_{13}$  hydrogen transfer allows both protomers to be interconnected. Nevertheless, the four different dissociation pathways systematically involve the second protomer. Both homolytic and heterolytic bond cleavages occur. The displacement of the imine–amine tautomeric equilibrium to the amine form ensures three fragmentation pathways to be achieved.

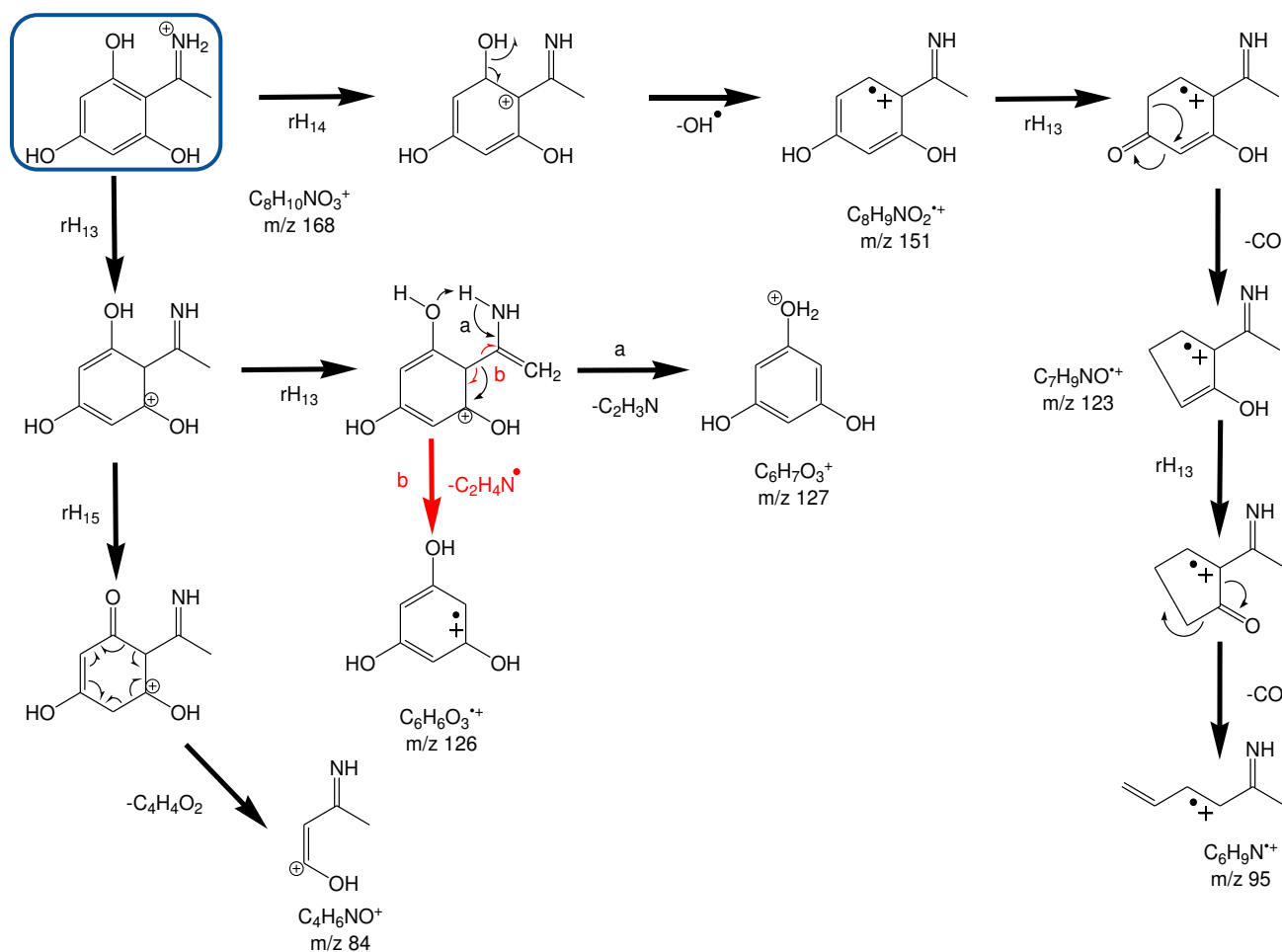


Figure III-33. Proposed mechanisms of  $[M+H]^+$  trihydroxyacetophenone+ $NH_4OH$  imine  $MS^n$  fragmentation.

The first one (process **a**) engages the migration of one hydrogen of the amine to an adjacent hydroxyl and the elimination of the pendant  $C_2H_3N$ , to form the protonated trihydroxybenzene at  $m/z$  127. Alternatively, the elimination of the trihydroxyphenyl side chain

may involve a homolytic bond cleavage (process **b**), which leads to the formation of the radical trihydroxybenzene daughter ion at  $m/z$  126. The last fragmentation corresponds to a retro Diels-Alder (RDA) mechanism, after the displacement of tautomerization equilibrium to the keto form by a  $rH_{15}$  hydrogen migration. It ultimately leads to the formation of the  $C_4H_6NO^+$  ion. The fourth fragmentation phenomenon is the elimination of the one hydroxyl radical to form the dihydroxyacetophenone radical ion at  $m/z$  151. The successive displacement of the two tautomeric equilibria to the keto-form ensures the loss of two carbon oxide molecules and the formation of  $m/z$  123 and 95 ions as described in the previous section.

#### IV.C.4.c. Tandem mass spectrometry of trihydroxyacetophenone protonated Schiff bases

Part of the fragmentation observed in the study of the protonated trihydroxyacetophenone imine are also evidenced after the activation of the trihydroxyacetophenone protonated Schiff bases whatever the used primary amine (**Figure III-34**). Thus, the elimination of one hydroxyl radical leads to the detection of the  $m/z$  227 and 261/263 ions for the aniline and 3-chloroaniline Schiff bases, respectively. For Schiff bases, the RDA mechanism, which has been described in the previous section, also ensures the elimination of  $C_4H_4O_2$  and the formation of the  $m/z$  160 and 194/196 daughter ions in respect with the nature of the used primary amine. Alternatively, the inductive dissociation of the bond between the trihydroxyphenyl and the iminium carbon ensures the migration of the charge on this carbon atom and the elimination of the trihydroxybenzene. It leads to the formation of the  $C_8H_8N^+$  ( $C_8H_7ClN^+$ ) daughter ion at  $m/z$  118 (152/154). The consecutive elimination of an acetonitrile molecule, which is confirmed by  $MS^3$ , produces the phenyl cation. For the protonated N-phenyl imine derivate of the trihydroxyacetophenone, a specific dissociation is observed and corresponds to the elimination of the aniline by inductive cleavage involving the ammonium protomer. The non-observation of this dissociation pathway for the 3-chloroaniline seems to indicate that the induction effect associated with the chlorine substituent disfavors the ammonium protomer. In contrast, this effect increases the lability of the hydrogen of the imine, which may be transferred to an adjacent hydroxyl group and leads to the loss of a water molecule to yield the  $m/z$  260/262 ions (insert **Figure III-34**).

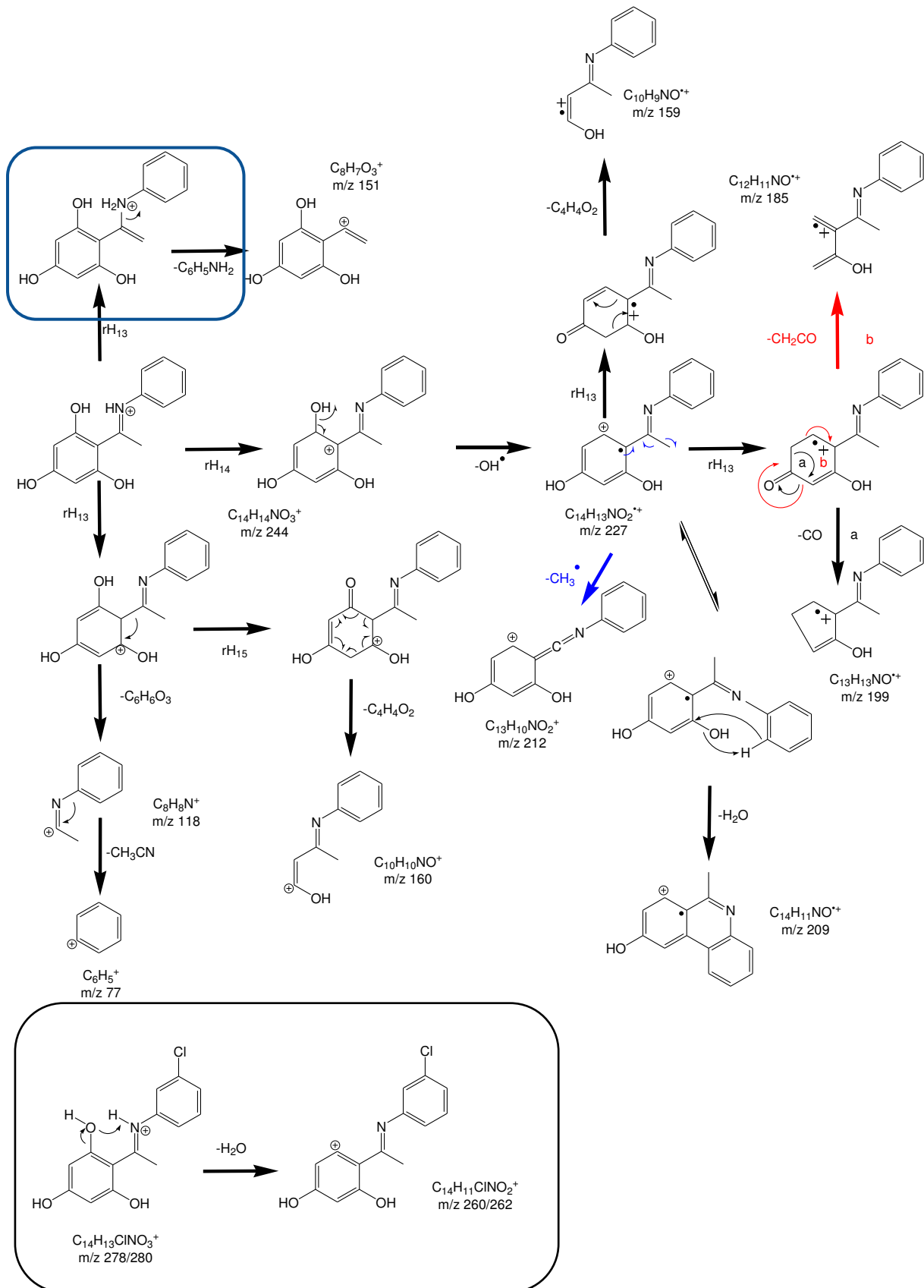


Figure III-34. Proposed mechanisms of  $[M+H]^+$  trihydroxyacetophenone+aniline Schiff base  $MS^n$  fragmentation.

The MS<sup>3</sup> experiments conducted on the radical dihydroxyacetophenone Schiff base at  $m/z$  227 leads, as it was described for the imine, to the elimination of CO (process **a**) and the formation of the  $m/z$  199 ion. This process is in competition with the ketene elimination and the production of the C<sub>12</sub>H<sub>11</sub>NO<sup>+•</sup> radical cation at  $m/z$  185 (process **b**). The tautomerization equilibrium yields a structure close to what is was previously proposed, which attests that a pseudo RDA mechanism is favored. The final daughter ion is observed at  $m/z$  159. The different resonance forms of the radical cation ensure to rationalize the loss of water and methyl radical. The resonance form on the dihydroxyphenyl group has to be considered to explain the recombination process, which ultimately leads to its dehydration. The elimination of the pendant methyl requires the radical charge to be on the nitrogen. In that case, the homolytic dissociation of the carbon-carbon bond ensures the formation of a carbon–nitrogen triple bond.

#### IV.D. Complementary NMR analyses

##### IV.D.1. Introduction

Complementary measurements were performed by <sup>13</sup>C NMR on the solutions infused in the ESI source in order to confirm the formation of imine and Schiff bases.

The reference data tables reporting the chemical shifts of the ion of interest according to the chemical functions are given in **Annex II** and were used for assignment. The chemical shifts for primary imines and Schiff bases are  $\delta \approx 164$  ppm and from  $\sim 140$  to 170 ppm, respectively.<sup>44,45</sup>

##### IV.D.2. Materials and methods

###### IV.D.2.a. NMR instrument

The <sup>13</sup>C NMR measurements were performed on a 400 MHz spectrometer (Bruker) at the NMR platform of the CRM<sup>2</sup> in Metz.

###### IV.D.2.b. Sample preparation for <sup>13</sup>C NMR analyses

For the <sup>13</sup>C NMR analyses,  $\sim 60$  mg of each carbonyl standard was dissolved in 600  $\mu$ L deuterated methanol in vials (99.8 % D, Euriso-top). The vanillin and the butyrophenone solutions



are light yellow and the trihydroxyacetophenone and cinnamaldehyde solutions are colorless. The solutions were then transferred into NMR tubes.

For the analyses with  $\text{NH}_4\text{OH}$ , the same procedure was applied and 25  $\mu\text{L}$  of  $\text{NH}_4\text{OH}$  (25 %) were added in NMR tubes which were heated for 1 hour in water bath at 70 °C (the temperature of the ESI source and probe). A color change was observed for all solutions, apart from the butyrophenone solution (**Figure III-35**). This highlights that chemical reactions occur when ammonium hydroxide is added.



*Figure III-35. Vanillin, trihydroxyacetophenone, cinnamaldehyde, and butyrophenone (from left to right) solutions after addition of  $\text{NH}_4\text{OH}$  and heating for 1 hour at 70 °C.*

Alternatively, the four carbonyl standards were dissolved in 100  $\mu\text{L}$  of aniline and heated as previously described. The formation of a precipitate was observed for vanillin, tri-hydroxyacetophenone, and cinnamaldehyde. For butyrophenone, a bi-phasic solution was obtained. The precipitates were dissolved in deuterated methanol before the  $^{13}\text{C}$  NMR measurements. The bi-phasic solution of butyrophenone was directly transferred into the NMR tubes before acquisition.

#### IV.D.3. $^{13}\text{C}$ NMR measurements

The contribution of the methanol solvent signal is observed as a multiplet centred on  $\delta=49.00$  ppm.

The  $^{13}\text{C}$  NMR spectrum of the vanillin solution with ammonium hydroxide (**Figure III-37**) significantly differs from the  $^{13}\text{C}$  NMR spectrum of the vanillin (**Figure III-36**). This evidences the formation of the corresponding imine. More specifically, the signals observed in this NMR spectrum correspond to the keto form of the imine. Indeed, the signal at  $\delta=169$  ppm is understood as the carbon of the imine function and the one at  $\delta=191$  ppm is the carbon of the

ketone function. The formation of the Schiff base from the condensation of the vanillin and the aniline is confirmed by the spectrum reported in the **Figure III-38**. The signal corresponding to the carbon of the imine function is detected at  $\delta=163$  ppm.

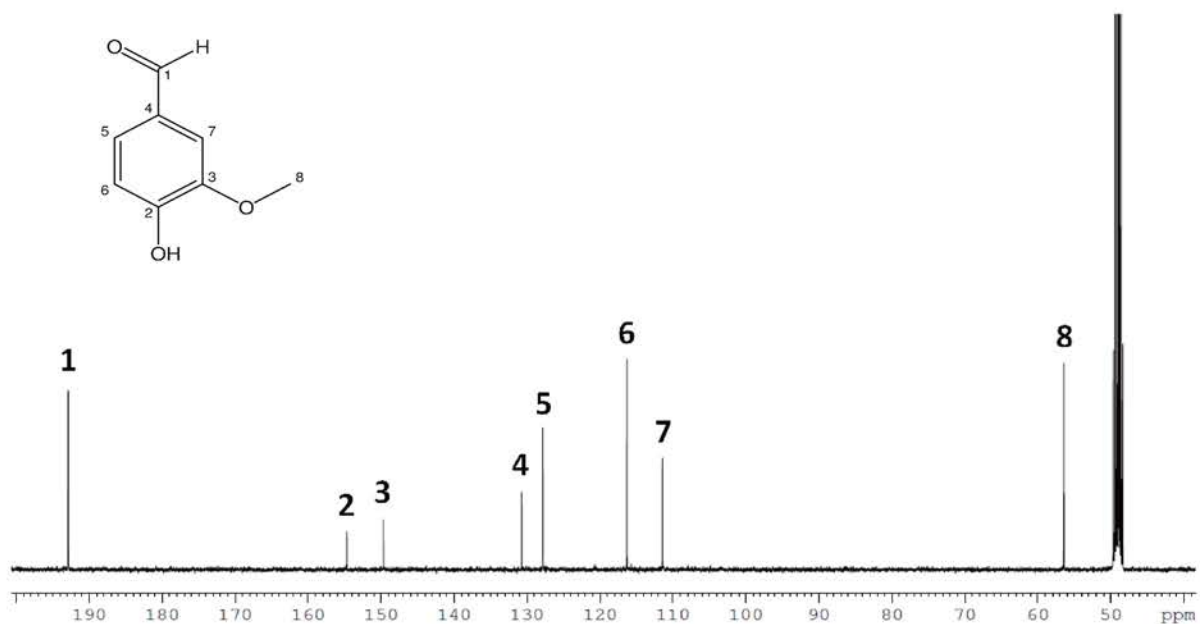


Figure III-36.  $^{13}\text{C}$  NMR spectrum of the vanillin in MeOD

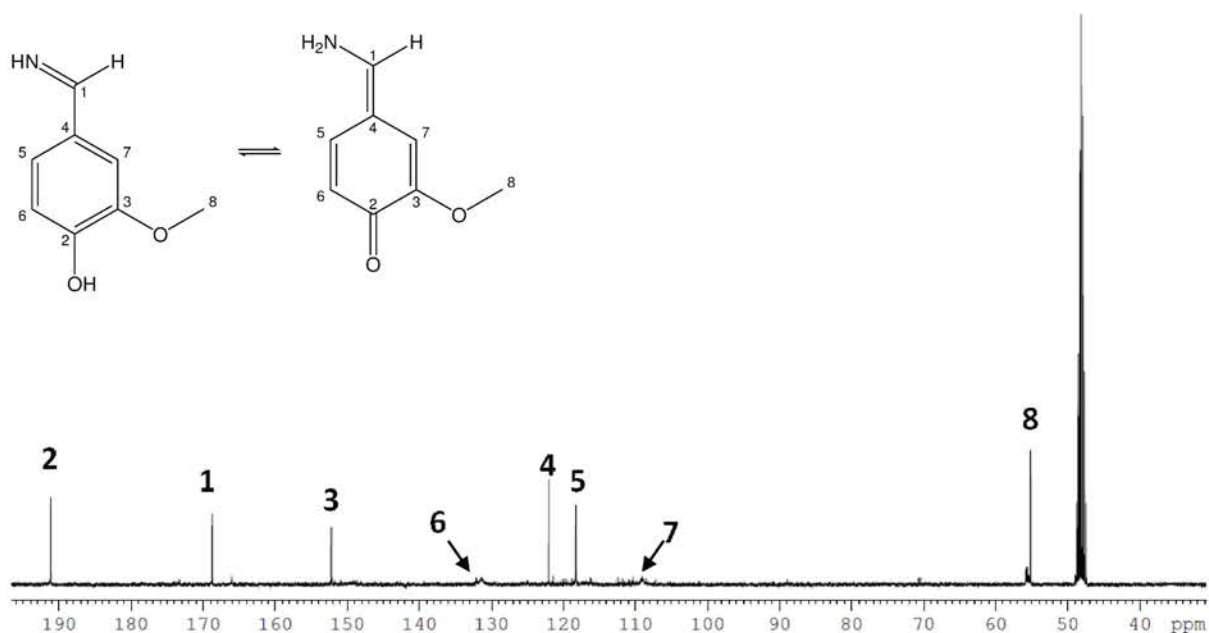


Figure III-37.  $^{13}\text{C}$  NMR spectrum of the vanillin+ $\text{NH}_4\text{OH}$  imine in MeOD

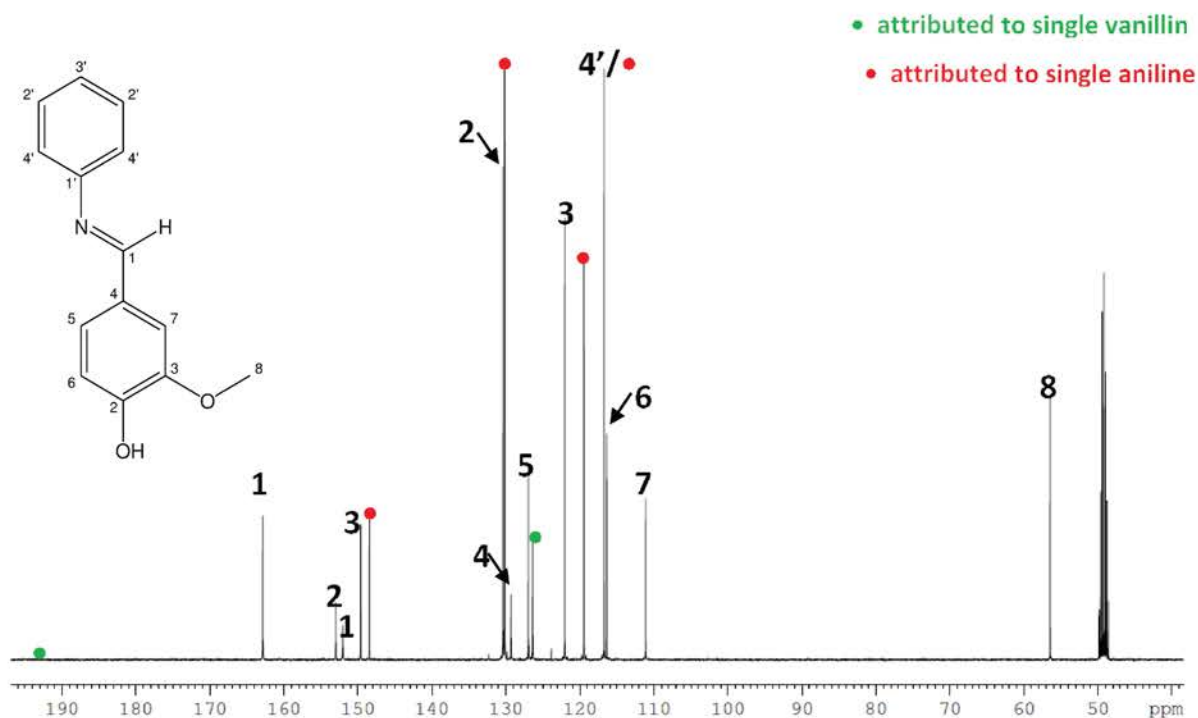


Figure III-38.  $^{13}\text{C}$  NMR spectrum of the vanillin+aniline Schiff base in MeOD.

The  $^{13}\text{C}$  NMR spectrum recorded with cinnamaldehyde are not exploitable as additional peaks are observed which do not correspond to the investigated compounds (**Figure III-39**) but are pollutant of the cinnamaldehyde. These compounds were still evidenced by mass spectrometry (**Figure III-23**). Moreover, after addition of  $\text{NH}_4\text{OH}$  or aniline, the observed  $^{13}\text{C}$  signals cannot clearly be assigned to the imine compound.

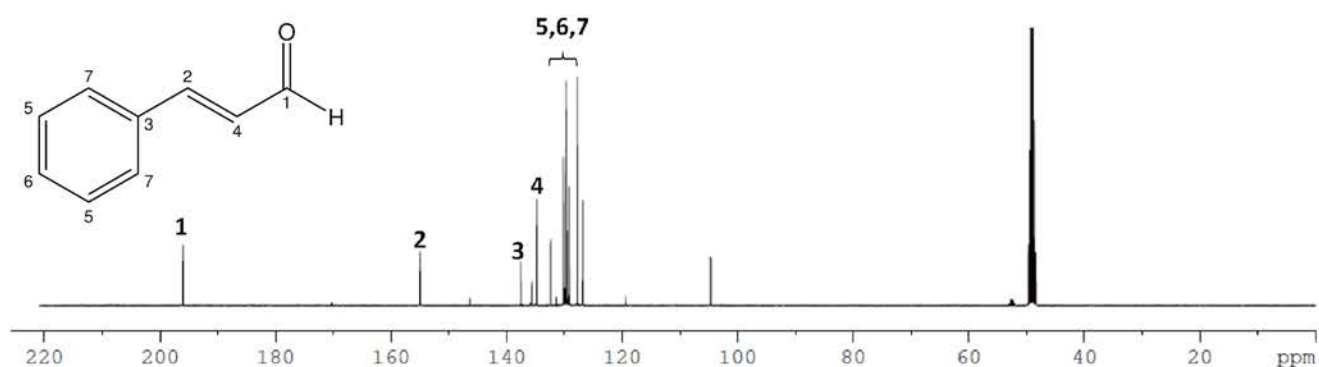


Figure III-39.  $^{13}\text{C}$  NMR spectrum of the cinnamaldehyde in MeOD.

With the butyrophenone, the  $^{13}\text{C}$  NMR spectra obtained whatever the conditions are similar to those achieved with the molecule without primary amine (**Figure III-40**). Indeed, no

signal is observed in the imine area. That could be explained by a lower reactivity of the ketone carbon towards the primary amine due to the steric hindrance.

The  $^{13}\text{C}$  NMR spectrum obtained with the 2,4,6-trihydroxyacetophenone demonstrates that an imine is formed with ammonium hydroxide (**Figure III-42**). The observed signals are relative to the keto configuration of the molecule (carbonyl carbon of the observed at  $\delta=177$  ppm and carbon of the imine at  $\delta=160$  ppm). The NMR spectrum of the solution with the 2,4,6-trihydroxyacetophenone and the aniline is close to what it was separately obtained with aniline and 2,4,6-trihydroxyacetophenone. This assesses that the corresponding imine was not efficiently formed. This may be due to the low reactivity of the ketone and, more particularly, the high steric hindrance associated with the aniline molecule.

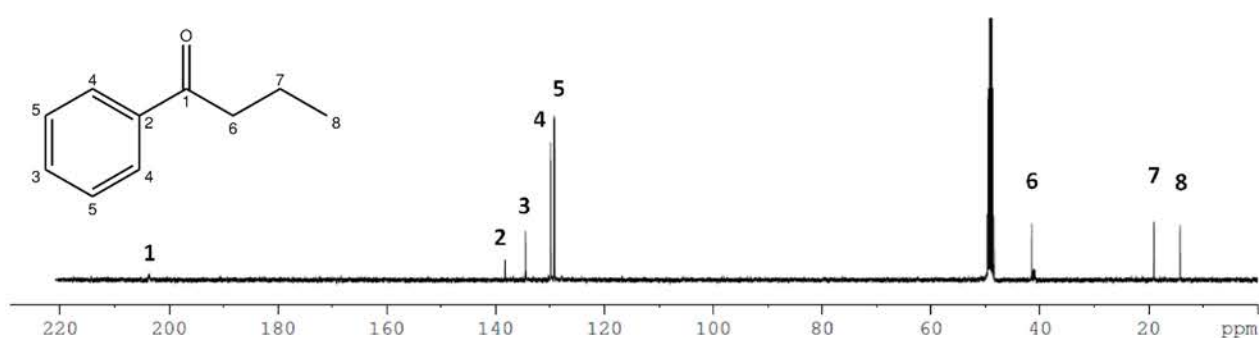


Figure III-40.  $^{13}\text{C}$  NMR spectrum of the butyrophenone in MeOD.

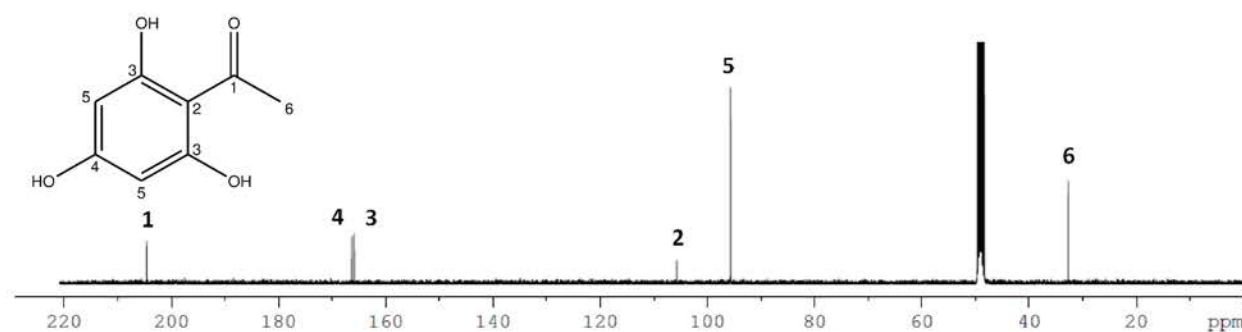


Figure III-41.  $^{13}\text{C}$  NMR spectrum of the 2,4,6-trihydroxyacetophenone in MeOD.

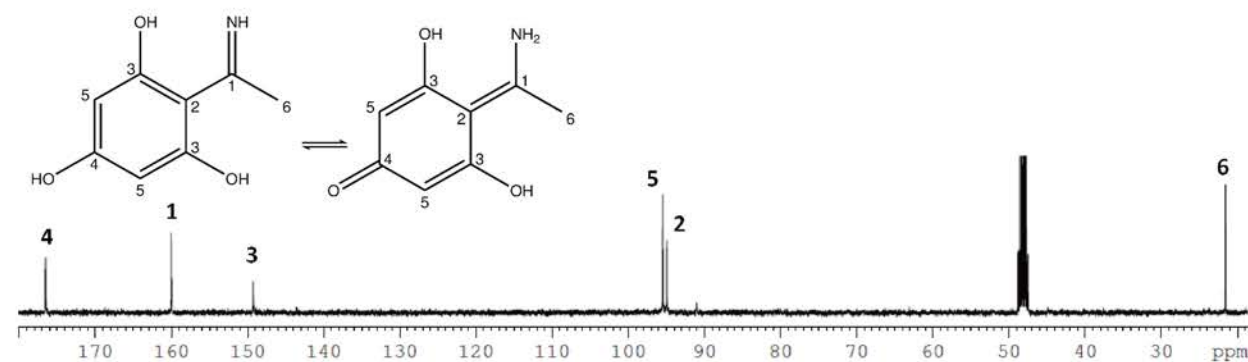


Figure III-42.  $^{13}\text{C}$  NMR spectrum of the 2,4,6-trihydroxyacetophenone+ $\text{NH}_4\text{OH}$  imine in MeOD.

#### IV.D.4. Conclusion

The complementary measurements performed in  $^{13}\text{C}$  NMR evidenced the formation, for at least part of the carbonyl compounds, of imine and Schiff bases. Nevertheless, the observation of signal relative to the imine and Schiff bases by  $^{13}\text{C}$  NMR required to heat the solution for 1 hour at 70 °C. This clearly indicates that such process is not spontaneous and only poorly efficient at room temperature. Consequently, the formation of imine and Schiff bases are thought to mainly take place during the ESI process and consequently constitutes an experimental bias for the analysis of complex mixtures containing carbonyl compounds.

#### IV.E. Conclusion

The infusion of standard carbonyl compounds with primary amine (ammonia, aniline or 3-chloroaniline) in an ESI source clearly demonstrates the formation of imine and Schiff bases. This may be a significant drawback for the analysis of complex mixtures conducted in negative ion detection mode with  $\text{NH}_4\text{OH}$ . Indeed, part of the detected nitrogen compounds may be formed by the reaction with ammonium hydroxide, typically used to favor deprotonation. This behavior explains the results obtained in one of our previously published work, which evidenced a significant number of nitrogen species when a bio-oil doped with  $\text{NH}_4\text{OH}$  was investigated by ESI.<sup>1</sup> Nevertheless, this experimental bias may be used to specifically evidence bio-oil components, which easily form imine or Schiff bases. To unambiguously evidence such compounds, the primary amine has to be carefully chosen. Indeed, the nitrogen amount, in the 0 to 2 % weight range, implies that some bio-oil components still contain nitrogen. The use of 3-chloroaniline appears to be well suited. Indeed, the simultaneous presence of chlorine and nitrogen atoms is specifically linked to the formation of a Schiff base. As a consequence, (+) ESI FT-ICR MS experiments have been conducted with an Oak pyrolysis bio-oil doped with 0.1 % of 3-chloroaniline. The results are described in the following section.

#### IV.F. (+) ESI-FT-ICR-MS analysis of bio-oil doped with 3-chloroaniline

The (+) ESI FT-ICR mass spectrum obtained by infusion of the Oak bio-oil solution doped with 0.1 % of 3-chloroaniline is reported in **Figure III-43**. Close to 860 peaks are assigned and their accurate examination leads to clearly assign chlorine-containing compounds (some are

indicated by green dots on the mass spectrum). On a general point of view, the total ion current is relative to five classes of ions:  $C_xH_yO_zNCl$  (205 assigned formulae, 43 % of the TIC),  $C_xH_yNO_z$  (322, 31 %),  $C_xH_yO_z$  (177, 13 %),  $C_xH_yO_zN_2Cl_2$  (62, 7 %), and  $C_xH_yO_zNa$  (41, 3 %). The chlorine families are unambiguously associated with carbonyl components of bio-oil derivatized by the 3-chloroaniline. It is interesting to note that  $C_xH_yO_zN_2Cl_2$  species originally correspond to oxygenated compounds, which enables the formation of two imines. For  $C_xH_yO_zNCl$  compounds, the putative elemental formula of the original  $C_xH_yO_z$  compound (noted  $C_xH_yO_z^*$ ) is obtained by the subtraction of  $C_6H_4ClNH_2$  and addition of  $H_2O$ . For  $C_xH_yO_zN_2Cl_2$ ,  $C_6H_4ClNH_2$  and  $H_2O$  are respectively deduced and added twice to obtain the  $C_xH_yO_z^{**}$  putative formula. A similar procedure is used to define the nature of the  $C_xH_yO_z$  compounds that are detected as proton or sodium adduct.

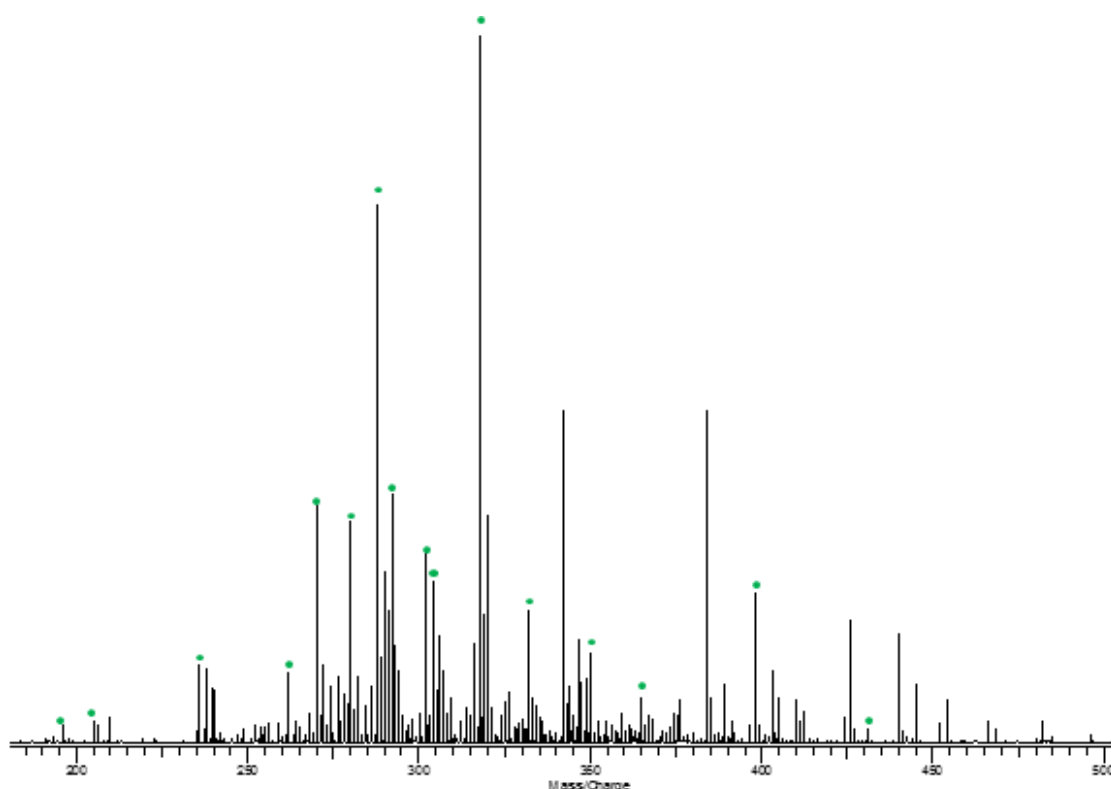


Figure III-43. (+) ESI FT-ICR mass spectrum of oak pyrolysis bio-oil doped with 0.1 % of 3-chloroaniline.

This data treatment allows to obtain the van Krevelen diagram (i.e. the representation of the H/C ratio in respect to the O/C ratio) and the relative distribution of the  $C_xH_yO_z$  in respect with the oxygen atom count. Both graphical representations are displayed in the **Figure III-44**. As it was previously observed by (+) ESI FT-ICR analysis without 3-chloroaniline, the  $C_xH_yO_z$  species are ranging from  $O_3$  to  $O_{12}$ .<sup>46</sup> The  $C_xH_yO_{3-7}$  species are mainly observed as protonated and are relative to lignin derivatives ( $0.5 < H/C < 1.5$  and  $0.1 < O/C < 0.6$ ), whereas the

$C_xH_yO_{7-12}$  sugarc compounds ( $1.5 < H/C < 2$  and  $O/C < 0.5$ ) specifically form sodium adducts. Both  $C_xH_yO_{3-7}^*$  lignin derived species and  $C_xH_yO_{7-8}^*$  sugarc compounds are observed after derivation by one 3-chloroaniline molecule. The  $C_xH_yO_{2-5}^{**}$  twice-derivatized compounds are only associated with the pyrolysis products of the lignin.

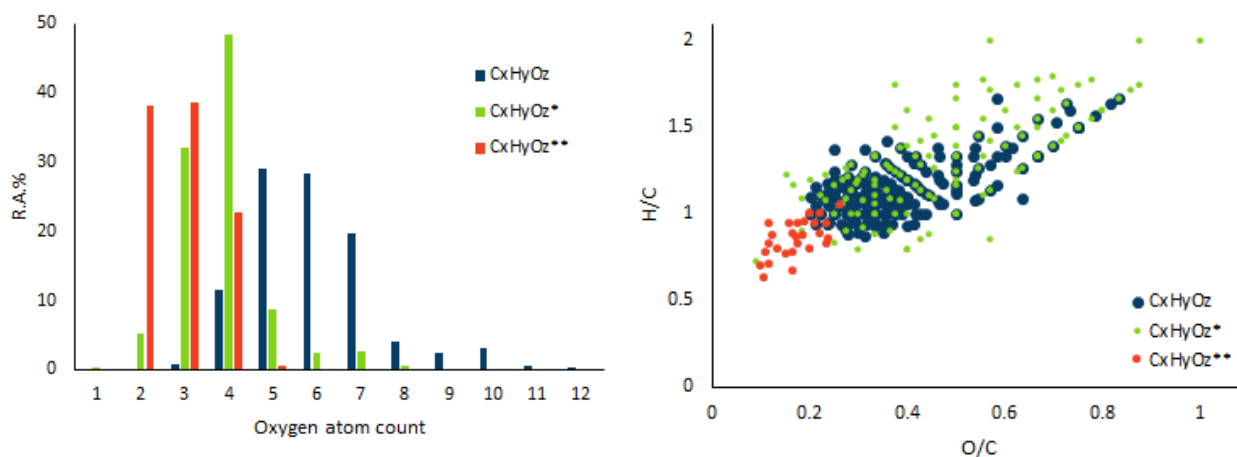


Figure III-44. (Left) Relative distribution in respect with their oxygen atom count and (Right) van Krevelen diagrams of the  $C_xH_yO_z$ ,  $C_xH_yO_z^*$ , and  $C_xH_yO_z^{**}$  compound classes assigned in the analysis of oak pyrolysis bio-oil by (+) ESI FT-ICR MS.

For these latter compounds, the representation of their DBE in respect with their nominal mass, reported in **Figure III-45**, demonstrates that they are mainly low mass species. Without their twice imine derivatization, they should not be detected by our FT ICR-MS instrument because of its low mass cut-off at  $m/z$  150. This is also partially the case for the  $C_xH_yO^*$  compounds.

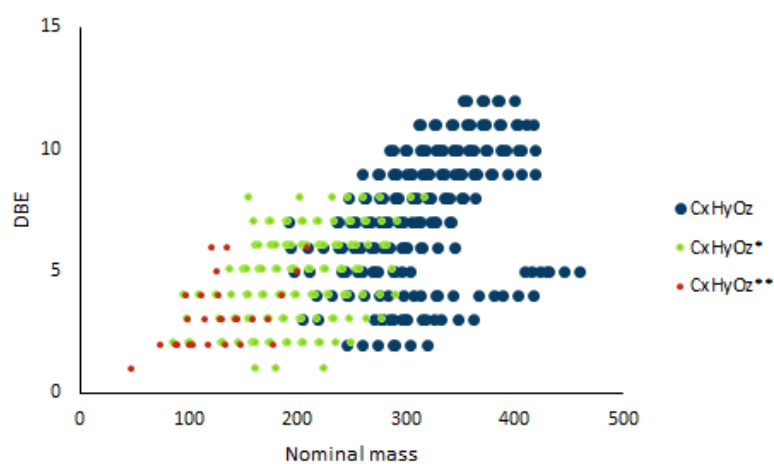


Figure III-45. DBE vs. Nominal mass of the  $C_xH_yO_z$ ,  $C_xH_yO_z^*$ , and  $C_xH_yO_z^{**}$  compound classes.

The capability of this approach to highlight carbonyl compounds in an extended mass range is an additional advantage. The Venn diagram displayed in the **Figure III-46** evidences that close to 45 % of the chemical formulae are relative to carbonyl compounds of the bio-oil. Among them, about one quarter has also non-carbonyl isomers in the bio-oil (such as phenolic compounds). This demonstrates the ability of this approach to increase the discrimination of the bio-oil components depending on their chemical structure.

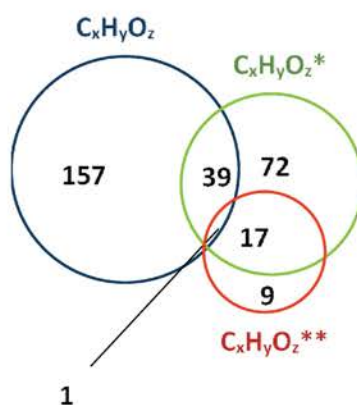


Figure III-46. Venn diagram of the  $C_xH_yO_z$ ,  $C_xH_yO_z^*$ , and  $C_xH_yO_z^{**}$  compound formulae assigned by (+) ESI FT-ICR MS analysis of oak bio-oil.

To deepen knowledge of these carbonyl compounds, some tentative assignments are gathered in **Table III-9** and are supported by previously published works. The focus is put on the low mass  $C_xH_yO_{2-5}^{**}$  compounds, which have been twice derivatized by 3-chloroaniline, and more particularly on the nine bio-oil components which have been specifically detected by this way. The main part of these compounds involved two carbonyl functions which may be ketone or aldehyde (succinaldehyde, methylglyoxal, sinapaldehyde,...).



<i>m/z</i>	<i>Assigned formula</i>	<i>Putative formula</i>	<i>Proposed assignment</i>	<i>References</i>
<b>265.029381</b>	C <sub>13</sub> H <sub>10</sub> N <sub>2</sub> Cl <sub>2</sub>	CH <sub>2</sub> O <sub>2</sub>	Formic acid	20,38,40,42,47
<b>291.045031</b>	C <sub>15</sub> H <sub>12</sub> N <sub>2</sub> Cl <sub>2</sub>	C <sub>3</sub> H <sub>4</sub> O <sub>2</sub>	Methylglyoxal	48,49
<b>305.060681</b>	C <sub>16</sub> H <sub>14</sub> N <sub>2</sub> Cl <sub>2</sub>	C <sub>4</sub> H <sub>6</sub> O <sub>2</sub>	Succinaldehyde	42,48–51
<b>307.039946</b>	C <sub>15</sub> H <sub>12</sub> N <sub>2</sub> O <sub>1</sub> Cl <sub>2</sub>	C <sub>3</sub> H <sub>4</sub> O <sub>3</sub>	Pyruvic acid	52,53
			Hydroxymalonaldehyde	54
<b>319.076331</b>	C <sub>17</sub> H <sub>16</sub> N <sub>2</sub> Cl <sub>2</sub>	C <sub>5</sub> H <sub>8</sub> O <sub>2</sub>	Glutaral	50,55
<b>333.055596</b>	C <sub>17</sub> H <sub>14</sub> N <sub>2</sub> O <sub>1</sub> Cl <sub>2</sub>	C <sub>5</sub> H <sub>6</sub> O <sub>3</sub>	2,5-Hexanedione	42
<b>335.071246</b>	C <sub>17</sub> H <sub>16</sub> N <sub>2</sub> O <sub>1</sub> Cl <sub>2</sub>	C <sub>5</sub> H <sub>8</sub> O <sub>3</sub>	Levulinic acid	41
			Acetoxyacetone	20,40–42,49,55,56
<b>339.045031</b>	C <sub>19</sub> H <sub>12</sub> N <sub>2</sub> Cl <sub>2</sub>	C <sub>7</sub> H <sub>4</sub> O <sub>2</sub>	Benzoic acid*(-H <sub>2</sub> )	40
<b>343.039946</b>	C <sub>18</sub> H <sub>12</sub> N <sub>2</sub> O <sub>1</sub> Cl <sub>2</sub>	C <sub>6</sub> H <sub>4</sub> O <sub>3</sub>	2,5-Furandicarbaldehyde	57
<b>349.050510</b>	C <sub>17</sub> H <sub>14</sub> N <sub>2</sub> O <sub>2</sub> Cl <sub>2</sub>	C <sub>5</sub> H <sub>6</sub> O <sub>4</sub>	1-(Acetyloxy)-2-butanone	38,41,55
<b>353.060681</b>	C <sub>20</sub> H <sub>14</sub> N <sub>2</sub> Cl <sub>2</sub>	C <sub>8</sub> H <sub>6</sub> O <sub>2</sub>	Phenylglyoxal	58
<b>365.081810</b>	C <sub>18</sub> H <sub>18</sub> N <sub>2</sub> O <sub>2</sub> Cl <sub>2</sub>	C <sub>6</sub> H <sub>10</sub> O <sub>4</sub>	Adipic acid	59,60
<b>417.076725</b>	C <sub>21</sub> H <sub>18</sub> N <sub>2</sub> O <sub>3</sub> Cl <sub>2</sub>	C <sub>9</sub> H <sub>10</sub> O <sub>5</sub>	Syringic acid	38
<b>427.097460</b>	C <sub>23</sub> H <sub>20</sub> N <sub>2</sub> O <sub>2</sub> Cl <sub>2</sub>	C <sub>11</sub> H <sub>12</sub> O <sub>4</sub>	Sinapaldehyde	40,56,61

Table III-9. Putative C<sub>x</sub>H<sub>y</sub>O<sub>z</sub> formulae and proposed assignments for some C<sub>x</sub>H<sub>y</sub>N<sub>2</sub>Cl<sub>2</sub>O<sub>z</sub> compounds evidenced in the oak bio-oil by (+) ESI FT-ICR MS.

Nevertheless, part of them are carboxylic acid such as formic acid. In that case, a specific process is involved. It is reported in **Figure III-47**. Such process may be followed by a side reaction, which complicates the interpretation. As a first step, the amine reacts with the carbonyl of the carboxylic acid function to yield an imine. The tautomerization of the achieved compound leads to the amide form. This ensures a second addition of an amine to occur on the carbonyl group of the amide, which leads to the formation of an imine. The direct formation of the amide by reaction of the carboxylic acid with the amine is thought to be poor favorable due to the acidic medium of the bio-oil.

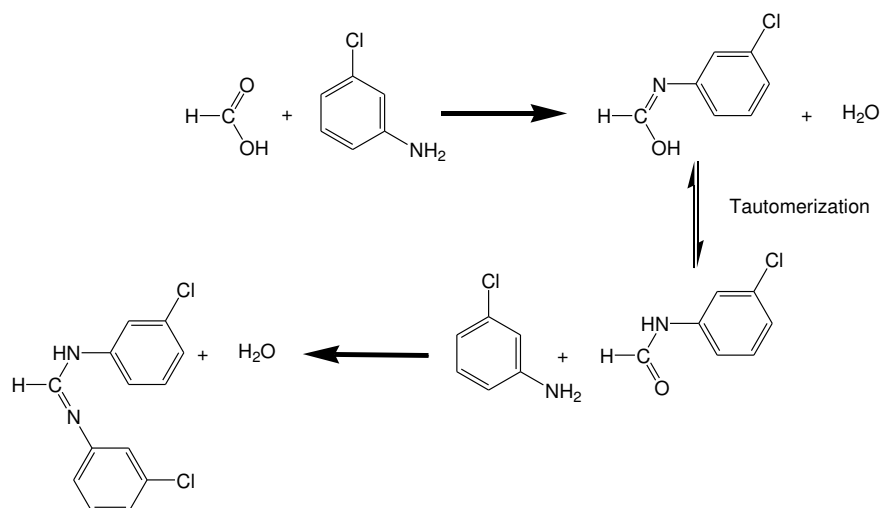


Figure III-47. Reaction mechanisms proposed for the successive addition of two molecules of 3-chloroaniline on formic acid to form a twice derivatized formic acid.

Finally, the  $m/z$  339.045031 ion cannot be directly associated with a twice-derivatized oxygenated compound. Nevertheless, it is thought to come from the twice derivatization of the benzoic acid (one significant component of pyrolysis bio-oil) followed by an additional dehydrogenation reaction, which allows the stability of the product compound to be increased by the extension its aromaticity domain (**Figure III-48**). The experiments performed by (+) ESI-LIT-MS demonstrated that such twice derivatized compound was not formed.

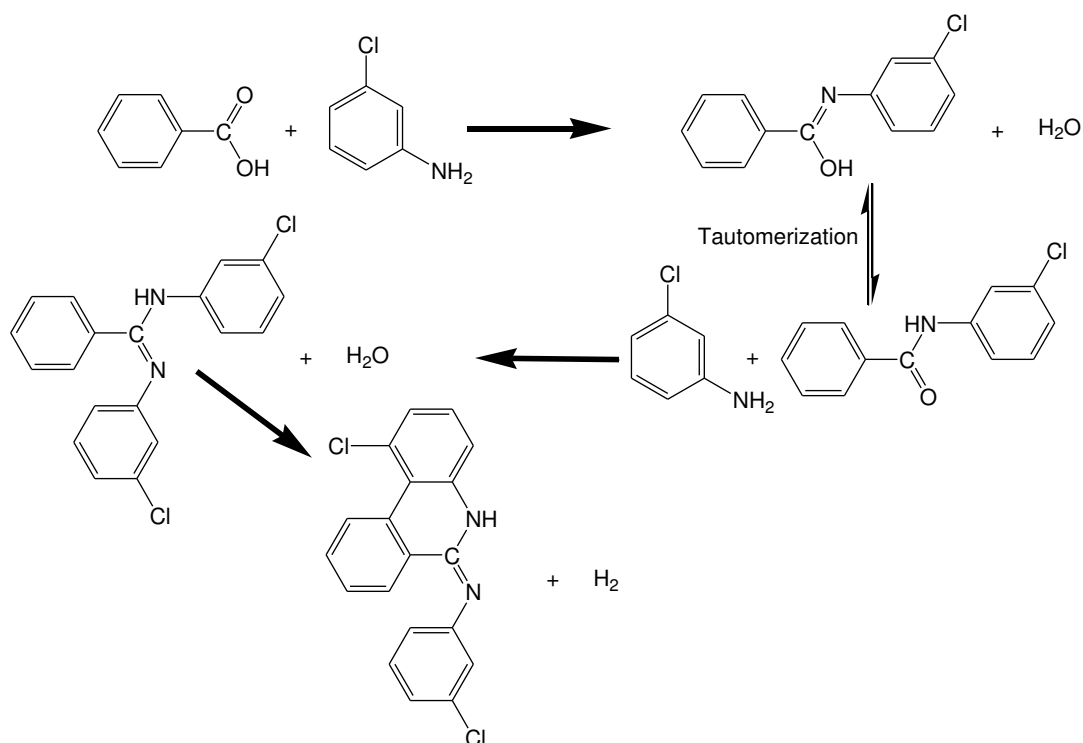


Figure III-48. Reaction mechanisms proposed for the successive addition of two molecules of 3-chloroaniline on benzoic acid to form a twice derivatized benzoic acid.

#### IV.G. Conclusion

The ammonium hydroxide dopant, which is commonly used to favor the deprotonation phenomenon and increase the sensitivity, may spontaneously react with highly reactive carbonyl compounds in the ESI source during the infusion. Indeed, imine compounds may be formed, which consequently biases the sample composition description. Such phenomenon has to be carefully checked when a non-targeted analytical approach is used and a significant number of still published results have to be re-examined to be sure that no misinterpretation has been done. Nevertheless, this drawback may be used to try to deepen the classical non-targeted approach and more particularly the petroleomic analysis. The capability to attach a chemical moiety involving an atom with a specific isotopic pattern, as chlorine or bromine, may be helpful to perform semi-directed non-targeted analysis. In the particular case described in this work, carbonyl compounds (aldehydes, ketones, and carboxylic acids) have been pointed out.

### V. Conclusion

The aim of this study was to develop robust, sensitive, and repeatable methods by ESI FT-ICR MS in both detection modes. The focus was put on the different parameters involved in the ionization process of ESI such as the solvent, the probe temperature, and the addition of ionization agents.

Thus, it has been evidenced that depending on the water/methanol ratio, the relative abundance of the sugaric and lignin derivatives changed. Moreover, the different measurements performed with probe temperatures at 75 °C and 110 °C did not evidence significant changes on the bio-oil composition. The greatest number of assigned peaks was obtained at 75 °C with 100 % methanol. These optimal conditions were kept to investigate the effect of some dopants on chemical composition of the bio-oil.

The influence of different dopants, on the bio-oil composition obtained by ESI FT-ICR MS in both detection modes, have been tested. It was found that sodium acetate is the most suited to perform (+) ESI analysis of bio-oils. For (-) ESI, the analyses are preferred to be performed without dopant. Both developed methods ensure to reach a bio-oil composition in agreement with its elemental analysis.

In a second part, the formation of imines yielded by the reaction between the ammonium hydroxide and the carbonyl compounds (aldehydes and ketones) of the bio-oil was evidenced. This dopant is commonly used by researchers for the bio-oil characterization in (-) ESI as it promotes deprotonation of bio-oil components. The analyses performed by ESI Ion-Trap and NMR spectroscopy, with standard aldehydes and ketones and different primary amines, confirmed the formation of imine. Such approach was applied with the (+) ESI FT-ICR MS analysis of bio-oil with 3-chloroaniline. The  $C_xH_yNO_zCl$  and  $C_xH_yN_2O_zCl_2$  compounds classes observed confirmed the formation of imine and, by extent, the presence of carbonyl compounds. To our knowledge, this is the first time that primary amine was used to evidence functional groups in a complex mixture, such as bio-oil, by petroleomic approach. Furthermore, addition of  $NH_4OH$  introduces a bias in the bio-oil composition, which tends to reconsider the results of the previously published studies in which  $NH_4OH$  is used as dopant for the bio-oil analysis.

ESI analyses ensures the detection of mid-polar to polar compounds which are not representative of the entire bio-oil components. Therefore, other analytical methods have to be carried out to ionize less polar compounds in order to obtain, by mass spectrometry, an as extensive as possible description of the bio-oils.

## VI. References

1. Hertzog, J., Carré, V., Le Brech, Y., Dufour, A. & Aubriet, F. Toward Controlled Ionization Conditions for ESI-FT-ICR-MS Analysis of Bio-Oils from Lignocellulosic Material. *Energy Fuels* **30**, 5729–5739 (2016).
2. Banerjee, S. & Mazumdar, S. Electrospray Ionization Mass Spectrometry: A Technique to Access the Information beyond the Molecular Weight of the Analyte. *Int. J. Anal. Chem.* 282574 (2012). doi:10.1155/2012/282574
3. Van Stipdonk, M. J., Ince, M. P., Perera, B. A. & Martin, J. A. Cluster ions derived from sodium and potassium tetrafluoroborate and their collision induced dissociation in an ion trap mass spectrometer. *Rapid Commun. Mass Spectrom.* **16**, 355–363 (2002).
4. Hunter, E. P. L. & Lias, S. G. Evaluated gas phase basicities and proton affinities of molecules: An update. *J. Phys. Chem. Ref. Data* **27**, 413–656 (1998).
5. Albright, P. S. & Gosting, L. J. Dielectric Constants of the Methanol-Water System from 5 to 55°1. *J. Am. Chem. Soc.* **68**, 1061–1063 (1946).
6. Czernik, S. & Bridgwater, A. V. Overview of Applications of Biomass Fast Pyrolysis Oil. *Energy Fuels* **18**, 590–598 (2004).
7. Page, J. S., Kelly, R. T., Tang, K. & Smith, R. D. Ionization and Transmission Efficiency in an Electrospray Ionization–Mass Spectrometry Interface. *J. Am. Soc. Mass Spectrom.* **18**, 1582–1590 (2007).
8. Gabelica, V., De Pauw, E. & Karas, M. Influence of the capillary temperature and the source pressure on the internal energy distribution of electrosprayed ions. *Int. J. Mass Spectrom.* **231**, 189–195 (2004).
9. Czernik, S., Johnson, D. & Black, S. Stability of Wood Fast Pyrolysis Oil. *Biomass Bioenergy* **7**, 187–192 (1994).
10. Diebold, J. P. *A review of the chemical and physical mechanisms of the storage stability of fast pyrolysis bio-oils.* (2000).
11. Haverly, M. R., Okoren, K. V. & Brown, R. C. Thermal Stability of Fractionated Bio-Oil from Fast Pyrolysis. *Energy Fuels* **30**, 9419–9426 (2016).
12. Miettinen, I., Makinen, M., Vilppo, T. & Janis, J. Compositional Characterization of Phase-Separated Pine Wood Slow Pyrolysis Oil by Negative-Ion Electrospray Ionization Fourier Transform Ion Cyclotron Resonance Mass Spectrometry. *Energy Fuels* **29**, 1758–1765 (2015).
13. Jarvis, J. M., McKenna, A. M., Hilten, R. N., Das, K. C., Rodgers, R. P. & Marshall, A. G. Characterization of Pine Pellet and Peanut Hull Pyrolysis Bio-oils by Negative-Ion Electrospray Ionization Fourier Transform Ion Cyclotron Resonance Mass Spectrometry. *Energy Fuels* **26**, 3810–3815 (2012).
14. Sudasinghe, N., Cort, J. R., Hallen, R., Olarte, M., Schmidt, A. & Schaub, T. Hydrothermal liquefaction oil and hydrotreated product from pine feedstock characterized by heteronuclear two-dimensional NMR spectroscopy and FT-ICR mass spectrometry. *Fuel* **137**, 60–69 (2014).

15. Sudasinghe, N., Dungan, B., Lammers, P., Albrecht, K., Elliott, D., Hallen, R. & Schaub, T. High resolution FT-ICR mass spectral analysis of bio-oil and residual water soluble organics produced by hydrothermal liquefaction of the marine microalga *Nannochloropsis salina*. *Fuel* **119**, 47–56 (2014).
16. Santos, J. M., dos Santos, L. O., Silva, F. F., Eberlin, M. N. & Wisniewski, A. Comprehensive Characterization of Second-Generation Biofuel from Invasive Freshwater Plants by FT-ICR MS. *Bioenergy Res.* **8**, 1938–1945 (2015).
17. Alsbou, E. & Helleur, B. Direct Infusion Mass Spectrometric Analysis of Bio-oil Using ESI-Ion-Trap MS. *Energy Fuels* **28**, 578–590 (2014).
18. Abdelnur, P. V., Vaz, B. G., Rocha, J. D., de Almeida, M. B. B., Teixeira, M. A. G. & Pereira, R. C. L. Characterization of Bio-oils from Different Pyrolysis Process Steps and Biomass Using High-Resolution Mass Spectrometry. *Energy Fuels* **27**, 6646–6654 (2013).
19. Le Brech, Y., Delmotte, L., Raya, J., Brosse, N., Gadiou, R. & Dufour, A. High Resolution Solid State 2D NMR Analysis of Biomass and Biochar. *Anal. Chem.* **87**, 843–847 (2015).
20. Liu, Y., Shi, Q., Zhang, Y., He, Y., Chung, K. H., Zhao, S. & Xu, C. Characterization of Red Pine Pyrolysis Bio-oil by Gas Chromatography–Mass Spectrometry and Negative-Ion Electrospray Ionization Fourier Transform Ion Cyclotron Resonance Mass Spectrometry. *Energy Fuels* **26**, 4532–4539 (2012).
21. Tessarolo, N. S., Silva, R. C., Vanini, G., Pinho, A., Romão, W., de Castro, E. V. R. & Azevedo, D. A. Assessing the chemical composition of bio-oils using FT-ICR mass spectrometry and comprehensive two-dimensional gas chromatography with time-of-flight mass spectrometry. *Microchem. J.* **117**, 68–76 (2014).
22. Berry, K. A. Z. & Murphy, R. C. Characterization of acrolein-glycerophosphoethanolamine lipid adducts using electrospray mass spectrometry. *Chem. Res. Toxicol.* **20**, 1342–1351 (2007).
23. Wang, R. & Zenobi, R. Evolution of the Solvent Polarity in an Electrospray Plume. *J. Am. Soc. Mass Spectrom.* **21**, 378–385 (2010).
24. Moens, L., Black, S. K., Myers, M. D. & Czernik, S. Study of the Neutralization and Stabilization of a Mixed Hardwood Bio-Oil. *Energy Fuels* **23**, 2695–2699 (2009).
25. Cole, R. B. *Electrospray and MALDI Mass Spectrometry: Fundamentals, Instrumentation, Practicalities, and Biological Applications*. (John Wiley & Sons, 2011).
26. Pramanik, B. N., Ganguly, A. K. & Gross, M. L. *Applied Electrospray Mass Spectrometry: Practical Spectroscopy Series*. (CRC Press, 2002).
27. Keki, S., Szilagy, L. S., Deak, G. & Zsuga, M. Effects of different alkali metal ions on the cationization of poly(ethylene glycol)s in matrix-assisted laser desorption/ionization mass spectrometry: a new selectivity parameter. *J. Mass Spectrom.* **37**, 1074–1080 (2002).
28. Shimada, K., Matsuyama, S., Saito, T., Kinugasa, S., Nagahata, R. & Kawabata, S. Conformational effects on cationization of poly(ethylene glycol) by alkali metal ions in matrix-assisted laser desorption/ionization time-of-flight mass spectrometry. *Int. J. Mass Spectrom.* **247**, 85–92 (2005).

29. Wang, Y. Q., Rashidzadeh, H. & Guo, B. C. Structural effects on polyether cationization by alkali metal ions in matrix-assisted laser desorption/ionization. *J. Am. Soc. Mass Spectrom.* **11**, 639–643 (2000).
30. Chan, K. & Cook, K. Mass-Spectrometric Study of Interactions Between Poly(ethylene Glycols) and Alkali-Metals in Solution. *Macromolecules* **16**, 1736–1740 (1983).
31. Keki, S., Nagy, L., Deak, G. & Zsuga, M. Multiple charging of poly(propylene glycol) by binary mixtures of cations in electrospray. *J. Am. Soc. Mass Spectrom.* **16**, 152–157 (2005).
32. Grossert, J. S., Herrera, L. C., Ramaley, L. & Melanson, J. E. Studying the Chemistry of Cationized Triacylglycerols Using Electrospray Ionization Mass Spectrometry and Density Functional Theory Computations. *J. Am. Soc. Mass Spectrom.* **25**, 1421–1440 (2014).
33. Roullier-Gall, C., Witting, M., Gougeon, R. D. & Schmitt-Kopplin, P. High precision mass measurements for wine metabolomics. *Front. Chem.* **2**, 102 (2014).
34. Yan, H.-L., Zong, Z.-M., Li, Z.-K. & Wei, X.-Y. Characterization of bio-oils from the alkalolyses of sweet sorghum stalk by electrospray ionization Fourier transform ion cyclotron resonance mass spectrometry. *Fuel* **160**, 596–604 (2015).
35. Cole, D. P., Smith, E. A., Dalluge, D., Wilson, D. M., Heaton, E. A., Brown, R. C. & Lee, Y. J. Molecular characterization of nitrogen-containing species in switchgrass bio-oils at various harvest times. *Fuel* **111**, 718–726 (2013).
36. Hilten, R. N. & Das, K. C. Comparison of three accelerated aging procedures to assess bio-oil stability. *Fuel* **89**, 2741–2749 (2010).
37. Stas, M., Kubicka, D., Chudoba, J. & Pospisil, M. Overview of Analytical Methods Used for Chemical Characterization of Pyrolysis Bio-oil. *Energy Fuels* **28**, 385–402 (2014).
38. Bertero, M., de la Puente, G. & Sedran, U. Fuels from bio-oils: Bio-oil production from different residual sources, characterization and thermal conditioning. *Fuel* **95**, 263–271 (2012).
39. Murwanashyaka, J. N., Pakdel, H. & Roy, C. Step-wise and one-step vacuum pyrolysis of birch-derived biomass to monitor the evolution of phenols. *J. Anal. Appl. Pyrolysis* **60**, 219–231 (2001).
40. Evans, R. J. & Milne, T. A. Molecular characterization of the pyrolysis of biomass. *Energy Fuels* **1**, 123–137 (1987).
41. Kantarelis, E., Yang, W. & Blasiak, W. Production of Liquid Feedstock from Biomass via Steam Pyrolysis in a Fluidized Bed Reactor. *Energy Fuels* **27**, 4748–4759 (2013).
42. Branca, C., Giudicianni, P. & Di Blasi, C. GC/MS Characterization of Liquids Generated from Low-Temperature Pyrolysis of Wood. *Ind. Eng. Chem. Res.* **42**, 3190–3202 (2003).
43. Russell, D., Freiser, B., Mcbay, E. & Canada, D. The Structure of Decomposing [c7h7o]<sup>+</sup> Ions - Benzyl Versus Tropylium Ion Structures. *Org. Mass Spectrom.* **18**, 474–485 (1983).
44. Lacombe, S., Pellerin, B., Guillemin, J. C., Denis, J. M. & Pfister-Guillouzo, G. Application of photoelectron spectroscopy to molecular properties. Part 40. Synthesis of P-chlorophosphaethene and N-chloromethanimine: estimation of chlorine substitution on the electronic structure of heteroatomic double bonds. *J. Org. Chem.* **54**, 5958–5963 (1989).

45. Neuvonen, K., Fülöp, F., Neuvonen, H., Koch, A., Kleinpeter, E. & Pihlaja, K. Comparison of the Electronic Structures of Imine and Hydrazone Side-Chain Functionalities with the Aid of <sup>13</sup>C and <sup>15</sup>N NMR Chemical Shifts and PM3 Calculations. The Influence of CN-Substitution on the Sensitivity to Aromatic Substitution. *J. Org. Chem.* **68**, 2151–2160 (2003).
46. Hertzog, J., Carré, V., Le Brech, Y., Mackay, C. L., Dufour, A., Mašek, O. & Aubriet, F. Combination of electrospray ionization, atmospheric pressure photoionization and laser desorption ionization Fourier transform ion cyclotron resonance mass spectrometry for the investigation of complex mixtures - Application to the petroleomic analysis of bio-oils. *Anal. Chim. Acta* **969**, 26–34 (2017).
47. Qiang, L., Xu-lai, Y. & Xi-feng, Z. Analysis on chemical and physical properties of bio-oil pyrolyzed from rice husk. *J. Anal. Appl. Pyrolysis* **82**, 191–198 (2008).
48. Torri, C. & Fabbri, D. Application of off-line pyrolysis with dynamic solid-phase microextraction to the GC-MS analysis of biomass pyrolysis products. *Microchem. J.* **93**, 133–139 (2009).
49. Faix, O., Fortmann, I., Bremer, J. & Meier, D. Thermal-Degradation Products of Wood - Gas-Chromatographic Separation and Mass-Spectrometric Characterization of Polysaccharide Derived Products. *Holz Als Roh- Werkst.* **49**, 213–219 (1991).
50. Qiang, L., Wen-zhi, L., Dong, Z. & Xi-feng, Z. Analytical pyrolysis-gas chromatography/mass spectrometry (Py-GC/MS) of sawdust with Al/SBA-15 catalysts. *J. Anal. Appl. Pyrolysis* **84**, 131–138 (2009).
51. Marsman, J. H., Wildschut, J., Evers, P., de Koning, S. & Heeres, H. J. Identification and classification of components in flash pyrolysis oil and hydrodeoxygenated oils by two-dimensional gas chromatography and time-of-flight mass spectrometry. *J. Chromatogr. A* **1188**, 17–25 (2008).
52. Lange, J.-P. Lignocellulose conversion: an introduction to chemistry, process and economics. *Biofuels Bioprod. Biorefining-Biofpr* **1**, 39–48 (2007).
53. Gayubo, A. G., Valle, B., Aguayo, A. T., Olazar, M. & Bilbao, J. Pyrolytic lignin removal for the valorization of biomass pyrolysis crude bio-oil by catalytic transformation. *J. Chem. Technol. Biotechnol.* **85**, 132–144 (2010).
54. Huang, J., He, C., Wu, L. & Tong, H. Theoretical studies on thermal decomposition mechanism of arabinofuranose. *J. Energy Inst.* **90**, 372–381 (2017).
55. Djokic, M. R., Dijkmans, T., Yildiz, G., Prins, W. & Van Geem, K. M. Quantitative analysis of crude and stabilized bio-oils by comprehensive two-dimensional gas-chromatography. *J. Chromatogr. A* **1257**, 131–140 (2012).
56. Sipila, K., Kuoppala, E., Fagernas, L. & Oasmaa, A. Characterization of biomass-based flash pyrolysis oils. *Biomass Bioenergy* **14**, 103–113 (1998).
57. Lv, X.-N., Li, G., Yang, F., Gao, P., Liu, Z., Meng, L. & Yu, X.-Q. Homogeneous Degradation of Cotton Cellulose into Furan Derivatives in ZnCl<sub>2</sub> Solution by Integration Technology of Reaction and Extraction. *Ind. Eng. Chem. Res.* **52**, 297–302 (2013).



58. Vardon, D. R., Sharma, B. K., Scott, J., Yu, G., Wang, Z., Schideman, L., Zhang, Y. & Strathmann, T. J. Chemical properties of biocrude oil from the hydrothermal liquefaction of *Spirulina* algae, swine manure, and digested anaerobic sludge. *Bioresour. Technol.* **102**, 8295–8303 (2011).
59. Beardslee, T. & Picataggio, S. Bio-based adipic acid from renewable oils. *Lipid Technol.* **24**, 223–225 (2012).
60. Han, J. A bio-based ‘green’ process for catalytic adipic acid production from lignocellulosic biomass using cellulose and hemicellulose derived  $\gamma$ -valerolactone. *Energy Convers. Manag.* **129**, 75–80 (2016).
61. Faix, O., Meier, D. & Fortmann, I. Thermal-Degradation Products of Wood - Gas-Chromatographic Separation and Mass-Spectrometric Characterization of Monomeric Lignin Derived Products. *Holz Als Roh- Werkst.* **48**, 281–285 (1990).



---

## *Chapter IV*

---

*Development of complementary  
methodologies by LDI and APPI  
FT-ICR MS for the characteriza-  
tion of bio-oils*

## Table of content

I.	Introduction.....	219
II.	Development of a LDI FT-ICR MS method to characterize bio-oils in positive and negative detection modes.....	219
II.A.	Introduction.....	219
II.B.	Experimental procedure.....	220
II.C.	Global bio-oil composition descriptions obtained by LDI and MALDI FT-ICR MS .....	220
II.D.	Influence of the laser fluence on the bio-oil composition description .....	222
II.E.	Comparison of MALDI and LDI for the investigation of bio-oils.....	225
II.E.1.	Negative ion mode .....	225
II.E.2.	Positive ion mode .....	228
II.E.3.	Conclusion .....	230
II.F.	Comparison of the data obtained by LDI FT-ICR MS in positive and negative ion detection modes .....	230
II.G.	Conclusion .....	231
III.	Development of a APPI FT-ICR MS method to characterize bio-oils in positive and negative detection modes.....	231
III.A.	Introduction.....	231
III.B.	Experimental procedure.....	231
III.C.	Effect of the dopant on the APPI mass spectrum of bio-oil.....	232
III.C.1.	Positive ion mode .....	232
III.C.2.	Negative ion mode .....	235
III.D.	Bio-oil composition descriptions obtained by APPI FT-ICR MS.....	236
III.D.1.	Bio-oil composition descriptions obtained in positive and negative ion APPI FT-ICR MS .....	236
III.D.2.	Ionization pathways involved in APPI analysis of bio-oil.....	238
III.E.	Conclusion .....	240
IV.	Complementarity of the ESI, APPI, and LDI FT-ICR MS for the extensive characterization of bio-oils .....	240
IV.A.	Introduction.....	240
IV.B.	Experimental procedure.....	240
IV.B.1.	ESI FT-ICR MS.....	241
IV.B.2.	LDI FT-ICR MS.....	241
IV.B.3.	APPI FT-ICR MS .....	241
IV.C.	Global composition descriptions of the bio-oil in respect with the analytical conditions .....	242
IV.C.1.	Bio-oil descriptions obtained by ESI with the 12 T FT-ICR mass spectrometer... ..	242
IV.C.2.	Bio-oil composition descriptions obtained by LDI with the 12 T FT-ICR mass spectrometer.....	247
IV.D.	Complementarity of the different ionization sources.....	248
IV.D.1.	Positive ion mode analyses .....	249
IV.D.2.	Negative ion mode analyses.....	250
IV.E.	Conclusion .....	252
V.	Conclusion .....	252
VI.	References.....	254

## I. Introduction

In this chapter the focus is put on techniques which ensure the ionization of bio-oil components which are not or poorly ionized by ESI. More specifically, LDI and APPI sources were used. LDI is known to be less sensitive to the polarity of the analytes compared to ESI or APPI. APPI is well suited to investigate less polar and/or apolar bio-oil components.

First of all, the development of positive and negative ion LDI FT-ICR MS methodologies for bio-oil characterization will be described. In that case, the influence of the sample preparation (use or not of a MALDI matrix) and of the laser fluence will be discussed.

The investigations carried out in APPI FT-ICR MS in both detection modes, to optimize the bio-oil characterization, will be presented in a second section. The influence of dopants for the investigation of bio-oils will be detailed.

The last part of this chapter will be dedicated to the presentation of the complementarity of ESI, LDI, and APPI sources for an intensive bio-oil description. A large part (mainly the last sub-section) of this chapter is the adaptation of the article “*Combination of electrospray ionization, atmospheric pressure photoionization and laser desorption ionization Fourier transform ion cyclotron resonance mass spectrometry for the investigation of complex mixtures - Application to the petroleomic analysis of bio-oils*”, *Analytica Chimica Acta* **969**, 26–34, 2017.<sup>1</sup>

## II. Development of a LDI FT-ICR MS method to characterize bio-oils in positive and negative detection modes

### II.A. Introduction

The principle and the parameters influencing the laser desorption ionization (LDI) as well as the matrix-assisted laser desorption ionization (MALDI) efficiency have been described in the second chapter of this dissertation. Among them, the laser fluence plays a key role. At a given value, desorption/ionization of the analytes takes place whereas at higher fluences, the laser ablation phenomenon dominates. In that latter case, intense fragmentation and/or recombination events occur and the observed ions are only poorly connected to the nature of the analyte. A softer methodology, the so-called MALDI, has been developed using a matrix which absorbs the laser energy and transfers it to the analyte molecules, the matrix also assists

the ionization of the analyte. Nevertheless, well controlled LDI experiments may be as efficient as MALDI ones to investigate complex mixtures. The influence of the laser fluence will be firstly investigated by LDI and MALDI experiments. For MALDI ones, two matrixes will be considered. One is able to induce protonation and the other enables deprotonation

### II.B. Experimental procedure

The bio-oil obtained from the pyrolysis of oak powder was used for this part of the study and analyzed by a 9.4 T Ion Spec mass spectrometer equipped with a 355 nm Nd:YAG laser. The ion guide was tuned to optimize the efficient transfer of ions in the 150-500  $m/z$  range. A 2.097 s transient length was acquired with 8192 K data points which resulted in mass resolution of  $\sim 300\,000$  at  $m/z$  400.

The 2,5-Dihydroxybenzoic acid (2,5-DHB) and the 1,8-Bis(dimethyl-amino)naphthalene (DMAN) matrixes were used (**Figure IV-1**). Both of them absorb at the 355 nm laser wavelength. DMAN was dissolved in 1:1 water:methanol to a final concentration of  $1\text{ mg}\cdot\text{mL}^{-1}$ . For the 2,5-DHB, a saturated solution was prepared in a 1:1 water:acetonitrile solution. For the MALDI experiments,  $1\ \mu\text{L}$  of the bio-oil solution and  $1\ \mu\text{L}$  of one of the matrix solution were mixed and  $1\ \mu\text{L}$  of the achieved solution was deposited on a stainless steel target plate. The solvent was evaporated at atmospheric pressure before introduction in the source of the FT-ICR instrument. For the LDI experiments, the bio-oil was diluted in water to obtain a 7:3 bio-oil:water solution. One  $\mu\text{L}$  of this solution was deposited on a stainless steel plate.

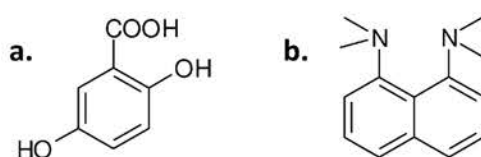


Figure IV-1. Structures of the 2,5-Dihydroxybenzoic acid (a) and 1,8-Bis(dimethylamino)naphthalene (b).

### II.C. Global bio-oil composition descriptions obtained by LDI and MALDI FT-ICR MS

The LDI measurements were conducted in positive and negative ion detection mode, whereas MALDI experiments were specifically performed, in one or the other polarity, in respect with the expected phenomenon (protonation/deprotonation). With the DMAN, also

named “proton sponge” measurements were only carried out in negative detection mode whereas positive ions were studied when the 2,5-DHB matrix was used.

The positive ions range from  $m/z$  200 to 500 and the negative ones, from  $m/z$  200 to 600, whatever the used sample preparation method. In all cases, the main part of the signal is relative to  $C_xH_yO_z$  species, as reported in the **Table IV-1**.

Matrix	Laser fluence (J.cm <sup>-2</sup> )	Number of assigned monoisotopic peaks	C <sub>x</sub> H <sub>y</sub>	C <sub>x</sub> H <sub>y</sub> O <sub>z</sub>	C <sub>x</sub> H <sub>y</sub> NO <sub>z</sub>	C <sub>x</sub> H <sub>y</sub> SO <sub>z</sub>	Other*
<b>Negative ion mode</b>							
-	0.6	1222 <sup>a</sup>	-	81 %	3 %	< 1 %	16 %
-	0.6	940 <sup>b</sup>	-	81 %	1 %	-	18 %
-	0.6	669 <sup>c</sup>	-	77 %	1 %	7 %	16 %
-	0.9	1301	5 %	70 %	10 %		15 %
<b>DMAN</b>	0.6	1004	-	87 %	3 %	< 1 %	10 %
<b>Positive ion mode</b>							
-	0.6	415	-	83 %	17 %	-	-
<b>2,5-DHB</b>	0.6	389	4 %	72 %	24 %	-	-

\*concerns complexes formed with the iron of the target plate with acidic C<sub>x</sub>H<sub>y</sub>O<sub>z</sub> bio-oil compounds

<sup>a</sup>Analysis I, <sup>b</sup>Analysis II, <sup>c</sup>Analysis III

Table IV-1. Number of assigned peaks and relative abundance of the compound families obtained by LDI and MALDI analyses at different laser fluences.

Significant amount of C<sub>x</sub>H<sub>y</sub>NO<sub>z</sub> ions is systematically obtained by LDI and MALDI with 2,5-DHB. They are from basic nitrogen bio-oil components which easily protonate, as observed by (+) ESI when dopants promoting protonation phenomenon were added.

In negative ion mode, a significant part of the signal is relative to combination of C<sub>x</sub>H<sub>y</sub>O<sub>z</sub> species with iron and, in a lesser extent, with chromium. Both of these compounds come from the stainless steel plate which interacts with some of the components of the bio-oils. Indeed, the bio-oils produced by pyrolysis of the biomass are known to be acidic which may react with the stainless steel passivation layer at the surface of the plate. Moreover, the highly oxygenated compounds may interact with iron and chromium species to form stable complexes. It was reported that iron leads to the formation of complexes with polycarboxylate species.<sup>2</sup> It is reasonable to consider that the main part of C<sub>x</sub>H<sub>y</sub>FeO<sub>z</sub><sup>+</sup> species are polycarboxylate complexes of iron cation. The distribution of these ions in respect with the number of oxygen at-

oms (6 to 10) and their van Krevelen diagram (O/C ranging from 0.2 to 0.6 and H/C from 0.5 to 1) seem to confirm that lignin derived compounds, in their carboxylate form, interact with the iron cation (**Figure IV-2**). It was also previously demonstrated that iron cation forms stable complexes with polyphenols which have a structure close to part of the lignin derivatives.<sup>3</sup> Nevertheless, the stoichiometry of the complex may not be known by only considering the  $m/z$  ratio. The absence of  $C_xH_yFeO_z$  with  $z < 6$  seems to indicate that part of these complexes involves one iron cation and, at least, two ligands (formation of octahedral complexes with three  $O_2$  compounds or with two  $O_3$  species). Consequently, it is difficult to finally interpret the results for this class of ions. To avoid any misinterpretation, these iron species will not be considered in the data interpretation. The different parameters of LDI and MALDI experiments will be now described and discussed.

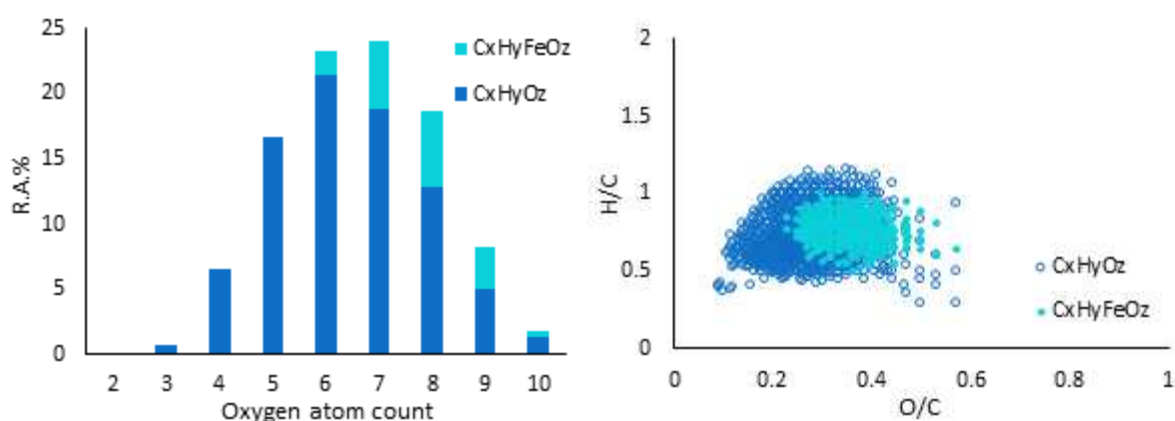


Figure IV-2. (Left) Distribution in respect with the oxygen atom count and (right) van Krevelen diagram of the  $C_xH_yO_z$  and  $C_xH_yFeO_z$  compounds of the oak bio-oil analysis by (-) LDI at  $0.6 \text{ J.cm}^{-2}$  laser fluence.

#### II.D. Influence of the laser fluence on the bio-oil composition description

The negative ion LDI FT-ICR MS experiments were carried out at a laser fluence of 0.6 and  $0.9 \text{ J.cm}^{-2}$ . The lowest value corresponds to the laser fluence for which a repeatable mass spectrum is obtained with a good signal-to-noise ratio. It is just above the laser desorption/ionization threshold.

More than 1000 signals are assigned for both experimental conditions (Analysis I at  $0.6 \text{ J.cm}^{-2}$ ). At the highest laser fluence, pure hydrocarbons are evidenced. They obey to the general  $C_xH_y^-$  formula and are typically observed when high fluence is used in LDI-MS of organic compounds (**Table IV-1**).<sup>4</sup>



The distribution of the  $C_xH_yO_z$  and  $C_xH_y$  compounds in respect with the oxygen atom count is given for both laser fluences in **Figure IV-3**. At  $0.6 \text{ J.cm}^{-2}$ ,  $O_3$  to  $O_{10}$  compounds are observed whereas at the  $0.9 \text{ J.cm}^{-2}$  fluence, the observed species never contain more than 8 oxygen atoms. Moreover, the maximum distribution is shifted from  $O_6$  to  $O_4$ - $O_5$ . This demonstrates that significant fragmentations occur with the loss of  $H_2O$ ,  $CO$ , and  $CO_2$ .

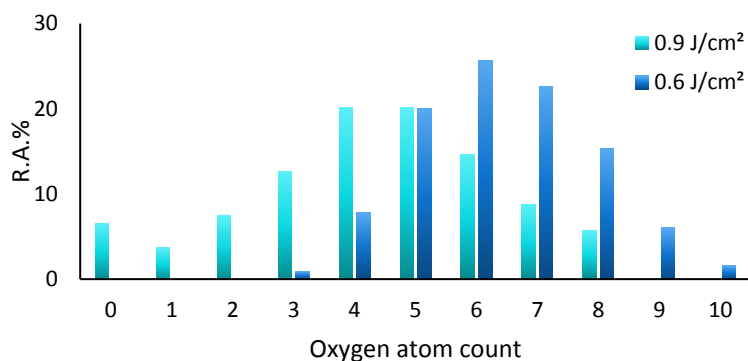


Figure IV-3. Distribution of the assigned  $C_xH_yO_z/C_xH_y$  compounds in respect with the oxygen atom count in the analysis of oak bio-oil by (-) LDI FT-ICR MS at  $0.6$  and  $0.9 \text{ J.cm}^{-2}$  laser fluence.

This is confirmed by the van Krevelen diagrams obtained in both fluence conditions (**Figure IV-4.a**). Compounds with a  $O/C < 0.1$  ratio, as well as  $C_xH_y$  species, are observed at a laser fluence of  $0.9 \text{ J.cm}^{-2}$ . Moreover, these less oxygenated compounds are more unsaturated (decrease of the  $H/C$  ratio) than the species identified in the experiments performed at  $0.6 \text{ J.cm}^{-2}$ , which confirms that dehydration events occur. The very significant decrease of the average percentage of  $O/C$  ratio indicates decarboxylation phenomenon. Whatever the operating conditions, the evidenced  $C_xH_yO_z$  compounds are mainly related to lignin derivatives. The **Figure IV-4.b** represents the DBE vs. nominal mass of the  $C_xH_yO_z$  and  $C_xH_y$  bio-oil components. The evidence of low-mass ions and the increase of the DBE value clearly support the occurrence of fragmentation phenomenon. Moreover, the high-mass ions observed at the highest fluence present very important DBE values, up to 35, which corresponds to a shift of 10, compared with  $0.6 \text{ J.cm}^{-2}$  experiment, whereas the  $m/z$  of the largest species is not significantly modified. The recombination phenomenon at the  $0.9 \text{ J.cm}^{-2}$  fluence ascertains this behavior rather than fragmentation which may also involve a shift to lower  $m/z$  values.

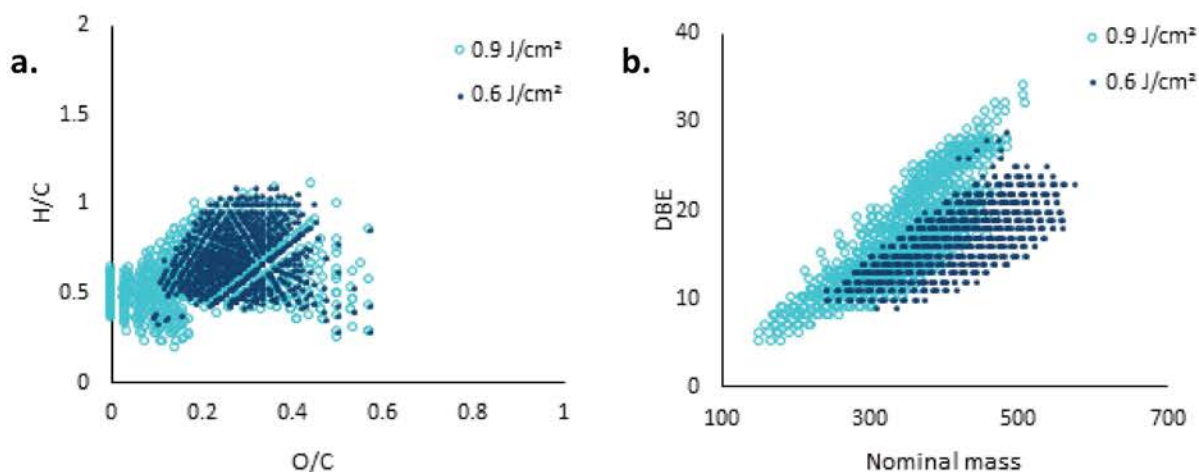


Figure IV-4. (a) van Krevelen diagram and (b) DBE vs. nominal mass representation of the  $C_xH_y$  and  $C_xH_yO_z$  compounds of the oak bio-oil by (-) LDI FT-ICR MS with laser fluence at 0.6 and 0.9  $J.cm^{-2}$ .

Similar results were obtained by Rathsack *et al.* who carried out LDI and MALDI FT-ICR MS analyses on liquids from pyrolysis of scrap tires.<sup>5</sup> They observed that an increase of the laser power from 16 % to 24 % was responsible of an increase of the relative abundance of the  $C_xH_y$  compounds. The relative abundance of  $C_xH_yO_z$ ,  $C_xH_yNO_z$ , and  $C_xH_yS$  compound families reached a maximum at the laser power of 20 % and decreased for higher values. Moreover, they evidenced that the DBE range of the  $C_xH_yO_1$  compounds was shifted to higher values for higher laser powers. This is in a perfect agreement with the results reported in this section.

Consequently, the laser fluence has a critical influence on the mass spectrum of a bio-oil. LDI experiments must be performed at the lowest laser fluence to avoid intense fragmentation and recombination processes, which does not allow to obtain a realistic fingerprint of the investigated bio-oils. Same behaviors have been observed when experiments were conducted in positive ion mode.

In these conditions, the experiments have been performed in triplicate. The number of assigned signals varies from  $\sim 670$  (Analysis III) to  $\sim 1220$  (Analysis I). Nevertheless, the additional features observed in the analysis I are poorly intense. A large part of them is also observed in analyses II and III but with a S/N lower than the 3 threshold. Whatever the analysis, the obtained chemical composition descriptions are very similar. Close to 80 % of the TIC is related to  $C_xH_yO_z$  compounds. Some  $[Fe(C_xH_yO_z)]$  iron complexes,  $C_xH_yNO_z$  nitrogen, and  $C_xH_ySO_z$  sulfur species are also observed. They contribute to  $\sim 17$  %,  $\sim 2$  %, and  $\sim 5$  % of the signal, respectively. The distribution of the oxygenated compounds according to the oxygen atom

count is reported in the **Figure IV-5**. The obtained standard deviations never exceed few per cent, which demonstrates the repeatability of the measurement.

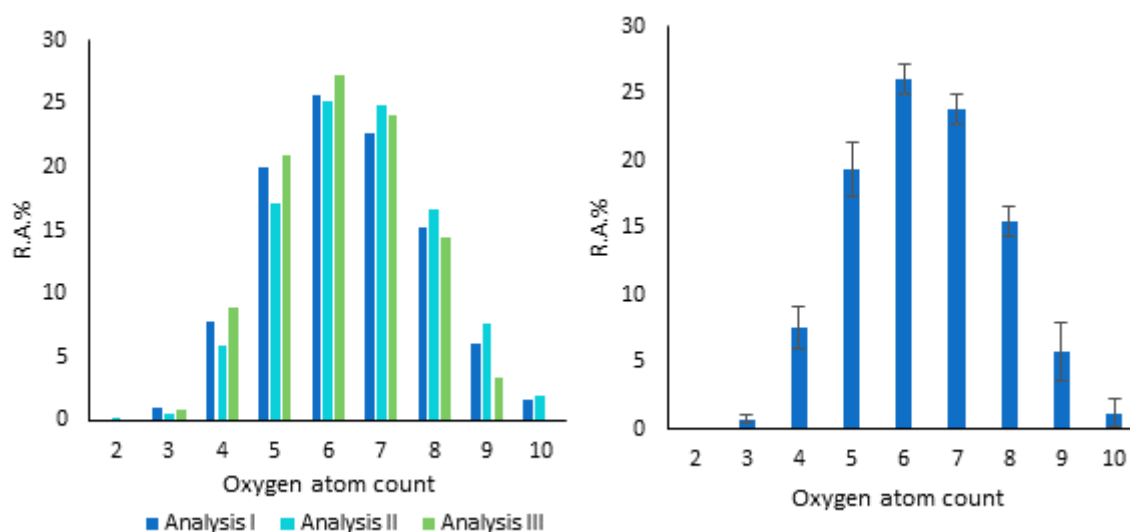


Figure IV-5. (Left) Distributions of the  $C_xH_yO_z$  species from oak bio-oil in respect with oxygen atom count achieved from three analyses performed in (-) LDI FT-ICR MS with a laser fluence of  $0.6 \text{ J.cm}^{-2}$ . (Right) Average relative distribution of the  $C_xH_yO_z$  compounds detected in (-) LDI. Error bar is relative to the standard deviation for the three considered measurements.

## II.E. Comparison of MALDI and LDI for the investigation of bio-oils

All the experiments were conducted at a  $0.6 \text{ J.cm}^{-2}$  laser fluence with a 355 nm laser wavelength.

### II.E.1. Negative ion mode

The mass spectra obtained by LDI and MALDI with the DMAN matrix are reported in the **Figure IV-6**. The DMAN, also called proton-sponge<sup>®</sup>, was used in order to promote deprotonation of the bio-oil components.<sup>6</sup> The shape of the obtained mass spectra for both ionization conditions is very similar.

The distribution of the different features in respect with the class compounds looks like very similar (**Table IV-1**). More than 94 % of the signal is assigned to  $C_xH_yO_z$  alone or coordinates with iron or chromium. This is coherent with the elemental analysis. It has to be noticed that  $C_xH_yO_z$  total signal is greater with DMAN.

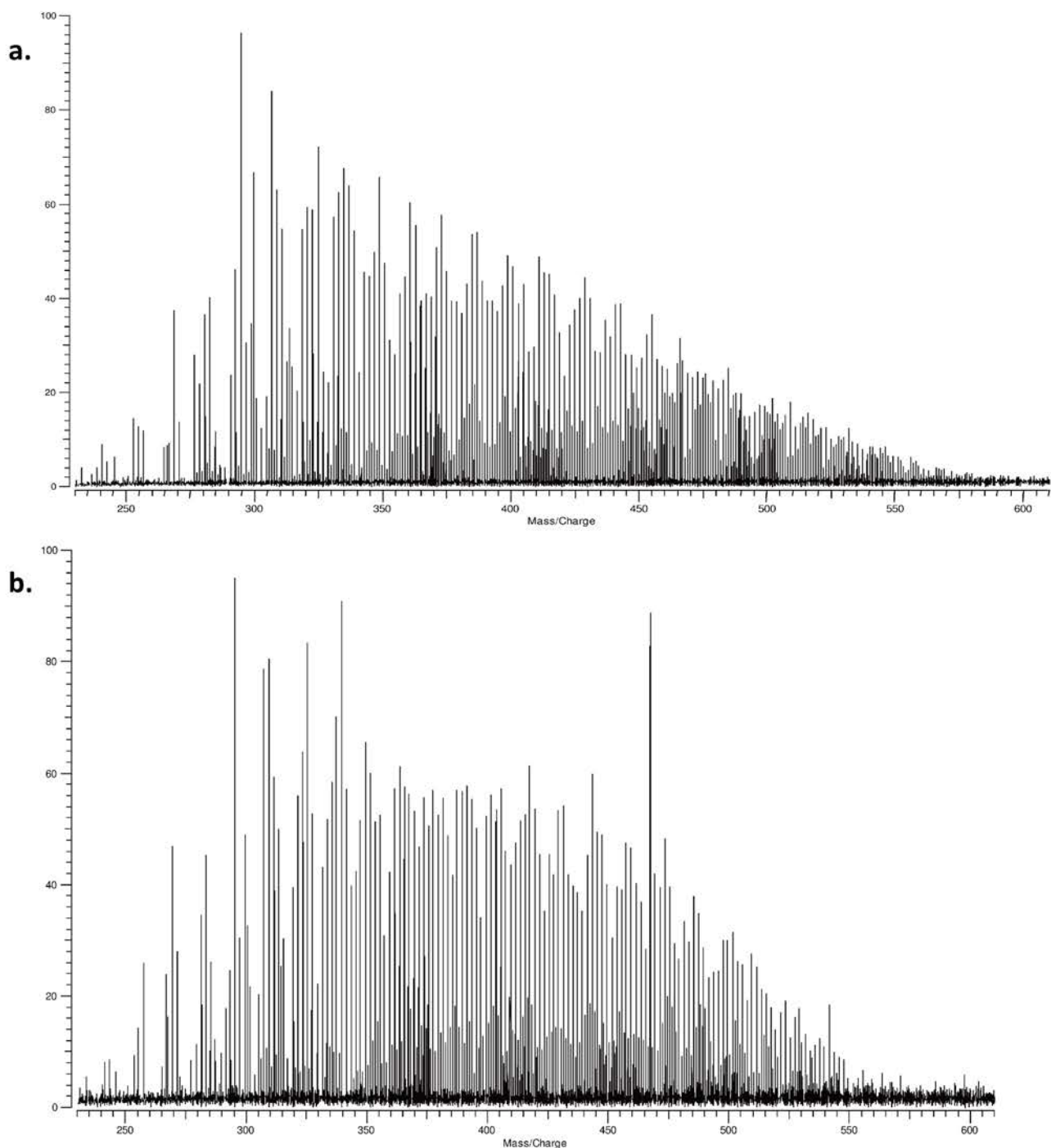


Figure IV-6. Mass spectra of oak bio-oil obtained by (a) LDI FT-ICR MS and (b) MALDI FT-ICR MS with DMAN in negative ion detection mode.

The distribution of this class of compounds in respect with the oxygen atom count presents tiny differences with those obtained without matrix at  $0.6 \text{ J}\cdot\text{cm}^{-2}$  (**Figure IV-7**). Indeed,  $\text{O}_1$  to  $\text{O}_{10}$  compounds are detected by LDI whereas  $\text{O}_4$  to  $\text{O}_{11}$  ones are evidenced by MALDI with DMAN. Moreover, a shift of one unit to higher oxygen amounts is observed. This is also well illustrated on van Krevelen diagrams (**Figure IV-8**) on which the cloud of points for MALDI features is slightly shifted to higher O/C ratios.

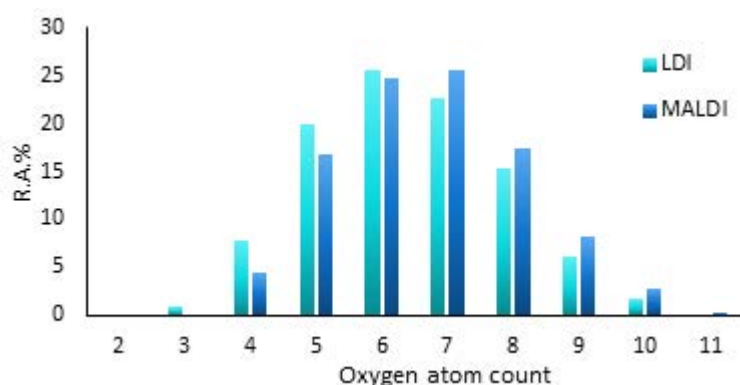


Figure IV-7.  $C_xH_yO_z$  compound distribution in respect with oxygen atom count in analysis of the oak bio-oil by LDI and MALDI with DMAN in negative ion detection mode.

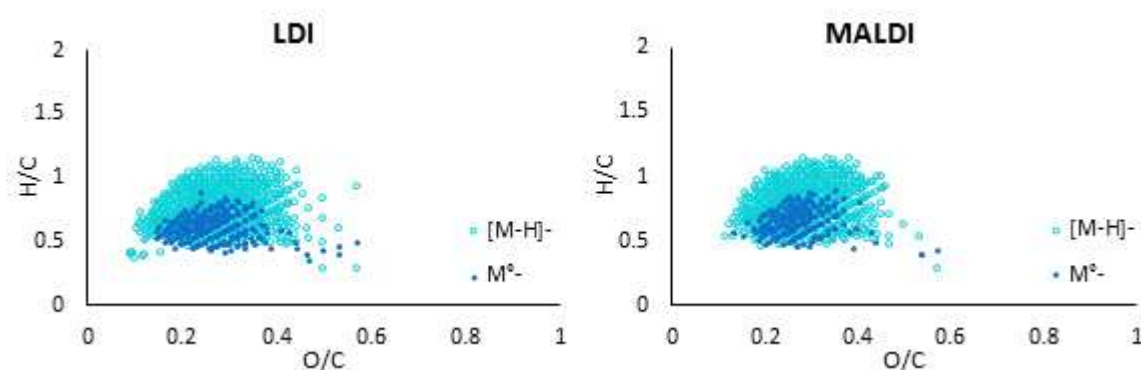


Figure IV-8. van Krevelen diagrams of the  $C_xH_yO_z$  compounds of the analysis of the oak bio-oil by LDI (left) and MALDI (right) with DMAN in negative ion detection mode for  $M^{\bullet-}$  and  $[M-H]^-$  anions.

This behavior may be due to the ability of the DMAN to easily deprotonate carboxylic acids rather than other oxygenated chemical functions as hydroxyl, for example. In that case, the use of DMAN introduces an analytical bias which has to be avoided. This behavior may also be relative to a better ionization of high-mass bio-oil components (in comparison with the relative intensity of the signal in 350-500  $m/z$  range with DMAN). The  $[M-H]^-$  anions, detected by LDI and MALDI, represent 85 and 87 % of the  $C_xH_yO_z$  compound signals, respectively. They are understood to be lignin derivatives, and more specifically, lesser unsaturated ones ( $0.8 < H/C < 1.2$ ). The  $M^{\bullet-}$  species correspond to 15 and 13 % of the  $C_xH_yO_z$  signals, respectively, and concern more unsaturated lignin derived species ( $0.5 < H/C < 0.8$ ). Some polyphenols, which can be involved in iron complex, may typically form radical anion.

In summary, no important differences are observed when the data collected by LDI and MALDI with DMAN on the oak bio-oil are compared. A similar conclusion was reported by Smith *et al.* who characterized fast pyrolysis bio-oil by LDI-Orbitrap-MS in negative ion mode.<sup>7</sup>

They used different matrixes and did not observe significant changes to what they obtained by LDI. Similar conclusion was obtained by Blackburn *et al.* in the study of natural organic matter for which the structure of the compounds is close to part of the bio-oil ones by (-) LDI and MALDI FT-ICR MS.<sup>8</sup>

### II.E.2. Positive ion mode

Both LDI FT-ICR MS and MALDI FT-ICR MS with 2,5-DHB lead to the detection of ~400 features when oak bio-oil is investigated in positive ion mode. Two classes of compounds are evidenced, the  $C_xH_yO_z$  and the  $C_xH_yNO_z$  ones. The former ones represent between 75 % (MALDI) and 80 % (LDI) of the detected signals. More nitrogen compounds are observed in positive ion mode because of protonation of their basic sites. The protons come from the matrix (MALDI) and from the compounds which easily deprotonate under laser-matter interaction. Such behavior has been highlighted in the previous chapter and in different studies in ESI and APPI.<sup>9-11</sup> A restricted number of features is associated with  $C_xH_y^{+•}$  species in MALDI.

The oxygen compound class distribution obtained by (+) LDI is ranging from  $O_2$  to  $O_{14}$  with a bimodal behavior (**Figure IV-9**). The first maximum is observed for  $O_4$ - $O_5$  species and the second one for  $O_{11}$ - $O_{12}$ . The compounds with 2 to 9 oxygen atoms are observed as  $[M+H]^+$  (70 %) or  $M^{*+}$  (21 %) ions whereas the  $O_{11}$ - $O_{14}$  are detected as sodium adducts (9 %) when experiments are conducted by LDI.  $Na^+$ , which is an impurity of the solvent, easily coordinates with poorly unsaturated compounds containing a significant amount of oxygen atoms. When MALDI experiments are considered same behavior is observed (**Figure IV-10**).

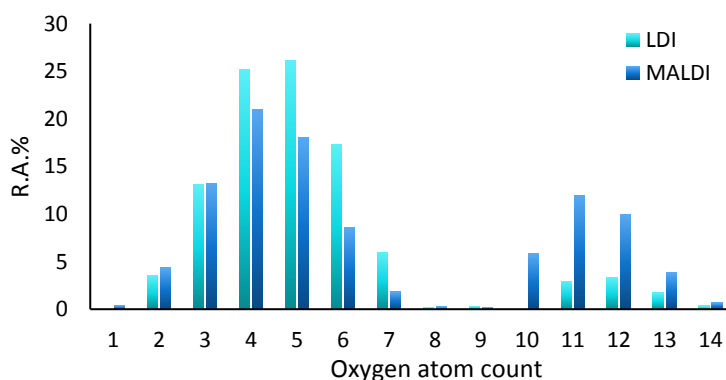


Figure IV-9. Distribution of the  $C_xH_yO_z$  class of oak bio-oil assigned by LDI and MALDI FT-ICR MS in positive ion mode.

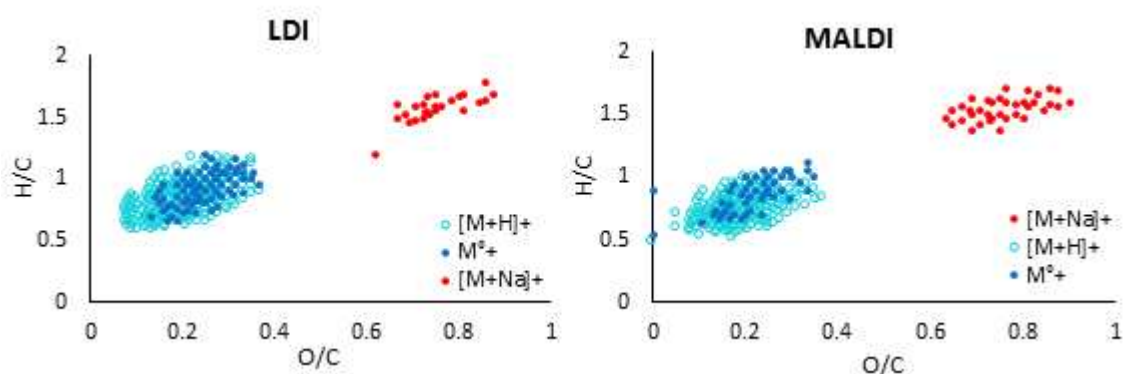


Figure IV-10. van Krevelen diagrams of the  $C_xH_y/C_xH_yO_z$  compounds of the analysis of the oak bio-oil by LDI (left) and MALDI (right) with 2,5-DHB in positive ion detection mode in respect with the nature of the detected cations.

Indeed, 15 % of the  $C_xH_yO_z$  signal correspond to radical cations and 55 % to protonated ones. Both of these species are from lignin derivatives. According to the absorption properties of part of them, whose structure is close to commonly used matrixes, it is not surprising to observe radical cations. Sugarc derivatives (31 % of the TIC) are specifically observed as sodium adducts. Their poor unsaturation degree (H/C ratio between 1.5 and 2) enables compounds derived from the cellulose and the hemicellulose to easily coordinate sodium cation according to the significant flexibility of their structure and the high number of oxygen (O/C ratio in the 0.6 to 1 range).

The comparison of the van Krevelen diagrams, obtained with LDI and MALDI features, indicates that both lignin and sugarc derivatives are evidenced whatever the experimental conditions. Nevertheless, the distribution of the  $C_xH_yO_z$  compounds in respect with the oxygen atom count reveals some significant differences. MALDI ensures a more sensitive detection of sugarc components of the bio-oils. The contribution of lignin ones is less important. This may be due to the addition of the 2,5-DHB matrix which absorbs a significant part of the photons. Consequently, the direct absorption by the lignin derivatives is restricted, which decreases the efficiency of their desorption/ionization. MALDI experiments also lead to the detection of  $C_xH_y^{+\bullet}$  features which may be related to recombination phenomena. Note that a decrease of the laser fluence leads to an inefficiency of laser desorption/ionization phenomenon. In addition, some features of the mass spectrum is associated with the 2,5-DHB molecule itself. Part of the bio-oil components has structure close to 2,5-DHB and it is impossible to distinguish species produced by the laser interaction with the matrix or with the bio-oil constituents. This may lead to an analytical bias which has to be avoided.

### II.E.3. Conclusion

According to the different reported MALDI results, the use of a matrix did not evidence significant differences with the LDI experiments. Moreover, part of the matrix ions may interfere with those relative to the bio-oil components. This can lead to a misinterpretation of the bio-oil mass spectra. For these reasons, LDI experiments have to be preferred to MALDI ones for a confident characterization of bio-oils.

### II.F. Comparison of the data obtained by LDI FT-ICR MS in positive and negative ion detection modes

In both cases, the  $C_xH_yO_z$  compounds contribute to close to 80 % of the signal. A broader range of oxygenated compounds is obtained for (+) LDI ( $O_2-O_{14}$ ) than for (-) LDI ( $O_2-O_{10}$ ). The convolution of the obtained results is given on the van Krevelen diagrams reported in the **Figure IV-11**. The cellulose and hemicellulose derivatives are specifically detected in positive ion detection mode whereas lignin linked species are observed in both detection modes. These sugarc components are characterized by high H/C and O/C ratios, which explains the broader range of the oxygenated class distribution ( $O_2-O_{14}$ ) in positive detection mode. The (-) LDI analysis ensures to detect a broader variety of pyrolytic lignin, which is more unsaturated and oxygenated than what it is obtained in (+) LDI. This is also responsible of the greater number of assigned peaks in (-) LDI. The significant acidity of the pyrolytic bio-oil means that a large part of its components present a carboxylic function which easier deprotonates than protonates. This also explains why a large part of species are detected in (+) LDI as protonated ions. The proton released upon laser irradiation by part of lignin derivatives ensures the protonation of other lignin derived compounds and their detection in (+) LDI.

Finally, (+) and (-) LDI analyses can be regarded as complementary. They ensure to assess either sugarc derivatives or different kinds of lignin derived species.



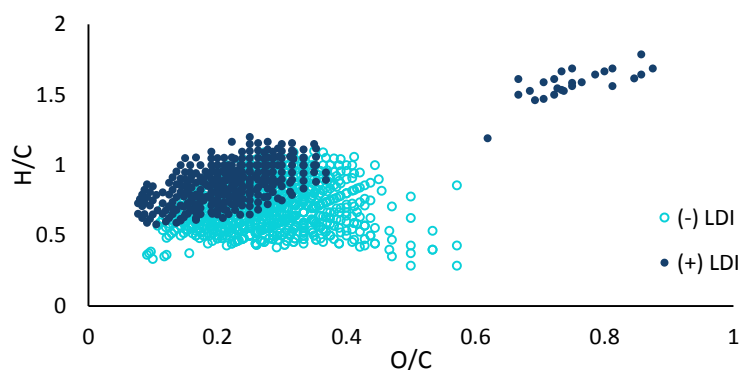


Figure IV-11. Van Krevelen diagrams of the  $C_xH_yO_z$  compounds of oak bio-oil obtained by LDI in positive and negative ion modes.

### II.G. Conclusion

Different parameters influencing the laser desorption/ionization process have been investigated for the development of a robust LDI FT-ICR MS bio-oil analysis, in both ion detection modes. The optimal laser fluence was defined which avoids recombination and fragmentation phenomena. The two investigated matrixes did not evidence a significant improvement for the bio-oil characterization. Consequently, the most suited conditions to characterize bio-oil were established to be pure LDI at a  $0.6 \text{ J}\cdot\text{cm}^{-2}$  laser fluence.

## III. Development of a APPI FT-ICR MS method to characterize bio-oils in positive and negative detection modes

### III.A. Introduction

The APPI method was used to try to ionize the bio-oil components which are poorly polar or apolar. Dopants (toluene, acetone) are typically employed to increase the ionization efficiency. Consequently, the influence of different experimental parameters has been investigated (without dopant, with acetone or with toluene) to establish a robust and efficient method.

### III.B. Experimental procedure

The different APPI FT-ICR MS analyses were performed with a 12 T mass spectrometer (Solarix Bruker) equipped with a Krypton lamp which delivers photons with 10.0 and 10.6 eV

energy. The experiments were carried out in positive and negative ion modes. The voltages of the capillary and the end plate were set at  $\pm 1000$  V and  $-500$  V, respectively. The source was heated at  $180$  °C and the nebulizer and dry gas were tuned at  $1.8$  bar and  $6$  L.min<sup>-1</sup>, respectively. The sample was infused at a flow rate of  $1$  mL.h<sup>-1</sup> and  $2$  mL.h<sup>-1</sup> for analyses in positive and negative detection modes, respectively. The ions were accumulated for  $0.05$  s and the mass spectrum acquired in the  $129$ - $1000$   $m/z$  range was the sum of  $100$  analyses. The transient length was  $1.5$  s and the mass resolution was  $\approx 340\,000$  at  $m/z$   $400$ .

The bio-oil from oak powder pyrolysis was used and diluted to a final concentration of  $4$  %. Different solvent conditions were used. The first one is with methanol and without dopant. The second ones are with toluene and acetone dopants. In that cases, methanol:toluene or methanol:acetone solution, either at v:v  $50:50$  or  $90:10$ , was used. Sodium acetate in methanol ( $0.1$  mg.mL<sup>-1</sup>) was also used to investigate its influence on the bio-oil analysis in (+) APPI.

### *III.C. Effect of the dopant on the APPI mass spectrum of bio-oil*

#### *III.C.1. Positive ion mode*

The different mass spectra acquired with or without dopant were ranging from  $m/z$   $123$  to  $m/z$   $800$ . The obtained results are displayed in **Figure IV-12**. Some differences can be highlighted in respect with the used analytical conditions. As reported on the **Figure IV-12**, the addition of dopant (toluene or acetone) is responsible of a decrease of the signal. Some focuses for low and high mass  $m/z$  ranges demonstrate a loss of sensitivity in these conditions (**Figure IV-13**). The effect of the addition of sodium acetate is more contrasted. For low-mass compounds ( $m/z < 350$ ), the sensitivity appears to be greater than with only methanol, which is not the case for the high-mass bio-oil components.

The modification of the ionization efficiency for low-mass species with sodium acetate may not be associated with a dopant effect. Indeed, this compound is not usually employed in APPI. It is thought to be responsible of a displacement of acid/base equilibrium. Sodium acetate is a buffer which may favor the carboxylate form of the species with the lowest pKa. Consequently, these species are more difficult to be ionized (it seems to be the case for high-mass bio-oil components). On the contrary, species that are in their neutral form are more efficiently ionized due to a decrease of the ionization competition event. This seems to be the

case for part of the low-mass components. Therefore, it appears that APPI with only methanol is the best compromise to ensure the sensitive detection of a broader range of compounds.

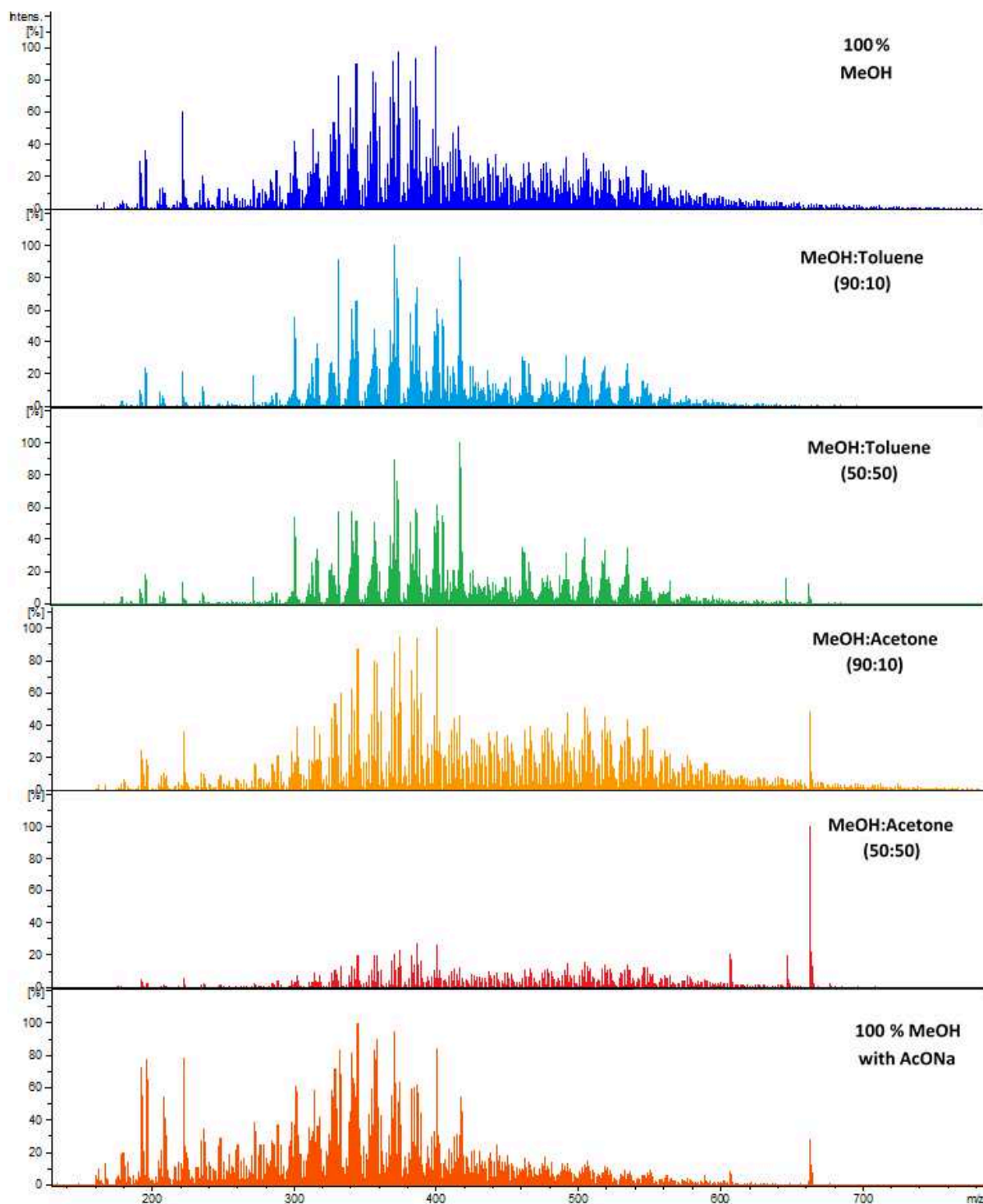
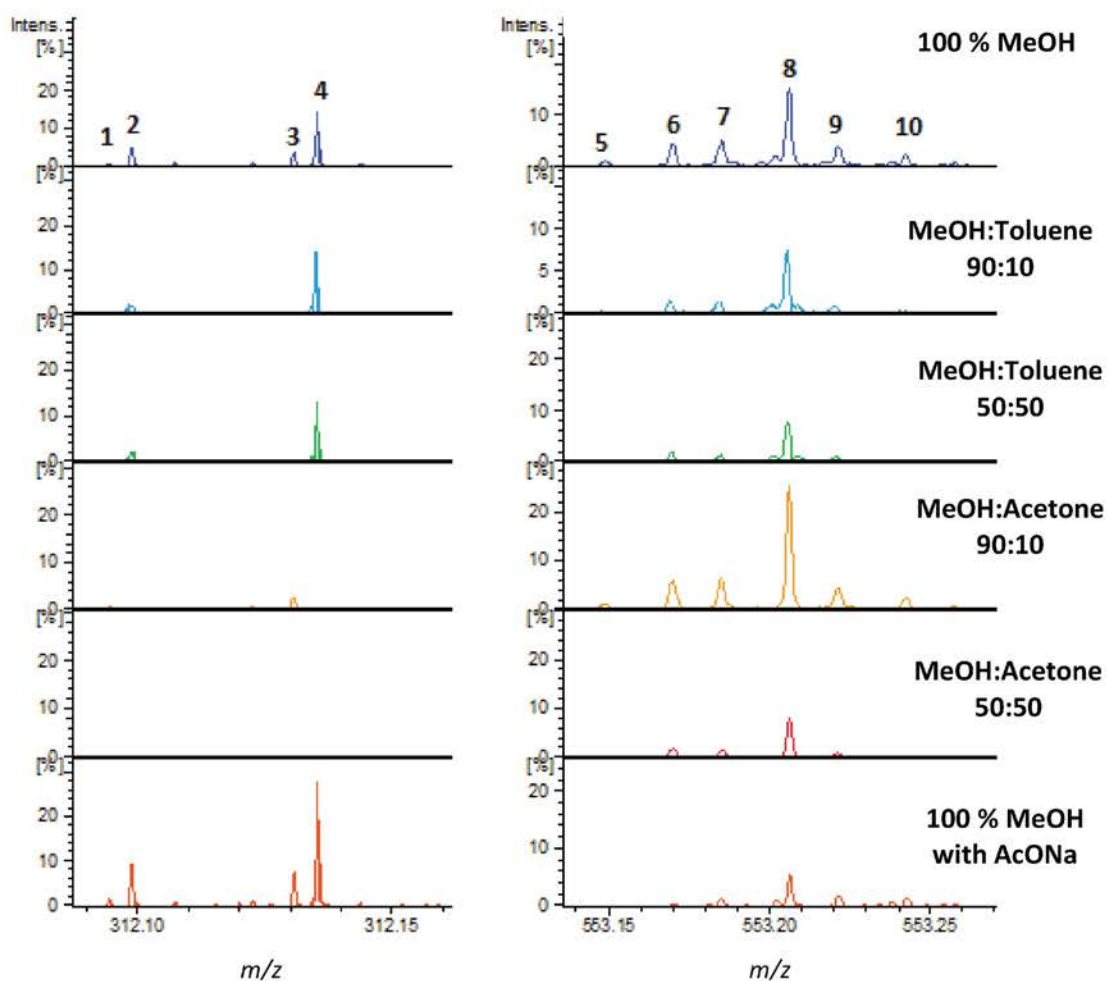


Figure IV-12.(+) APPI mass spectra of oak bio-oil acquired without, with dopant (toluene or acetone), and with sodium acetate.



Peak	<i>m/z</i>	Assigned formula	Mass error
1	312.09476	C <sub>17</sub> H <sub>15</sub> <sup>13</sup> CO <sub>5</sub> <sup>+</sup>	0.01 ppm
2	312.09923	C <sub>18</sub> H <sub>16</sub> O <sub>5</sub> <sup>+</sup>	0.01 ppm
3	312.13113	C <sub>18</sub> H <sub>19</sub> <sup>13</sup> CO <sub>4</sub> <sup>+</sup>	-0.04 ppm
4	312.13560	C <sub>19</sub> H <sub>20</sub> O <sub>4</sub> <sup>+</sup>	-0.04 ppm
5	553.14932	C <sub>32</sub> H <sub>25</sub> O <sub>9</sub> <sup>+</sup>	0.02 ppm
6	553.17036	C <sub>29</sub> H <sub>29</sub> O <sub>11</sub> <sup>+</sup>	-0.15 ppm
7	553.18565	C <sub>33</sub> H <sub>29</sub> O <sub>8</sub> <sup>+</sup>	0.08 ppm
8	553.20662	C <sub>30</sub> H <sub>33</sub> O <sub>10</sub> <sup>+</sup>	-0.37 ppm
9	553.22185	C <sub>34</sub> H <sub>33</sub> O <sub>7</sub> <sup>+</sup>	-0.42 ppm
10	553.24291	C <sub>31</sub> H <sub>37</sub> O <sub>9</sub> <sup>+</sup>	-0.54 ppm

Figure IV-13. Focus at *m/z* 314.12 and *m/z* 553.2 of the (+) APPI mass spectra of oak bio-oil acquired without, with dopant (toluene or acetone), and with sodium acetate. The assignments of the most intensely detected peaks with the pure methanolic solution are reported in the above chart.

## III.C.2. Negative ion mode

In negative ion APPI, mass spectra were acquired in the 129 to 800  $m/z$  range with only methanol, with methanol:toluene or methanol:acetone (v:v 50:50 and 90:10) solution. The behavior observed in (+) APPI whereby the experimental conditions were also evidenced in (-) APPI. The addition of the commonly used toluene and acetone dopants leads to a decrease of the sensitivity (**Figure IV-14**). Both a reduction of the signal abundance and of the  $m/z$  range were observed.

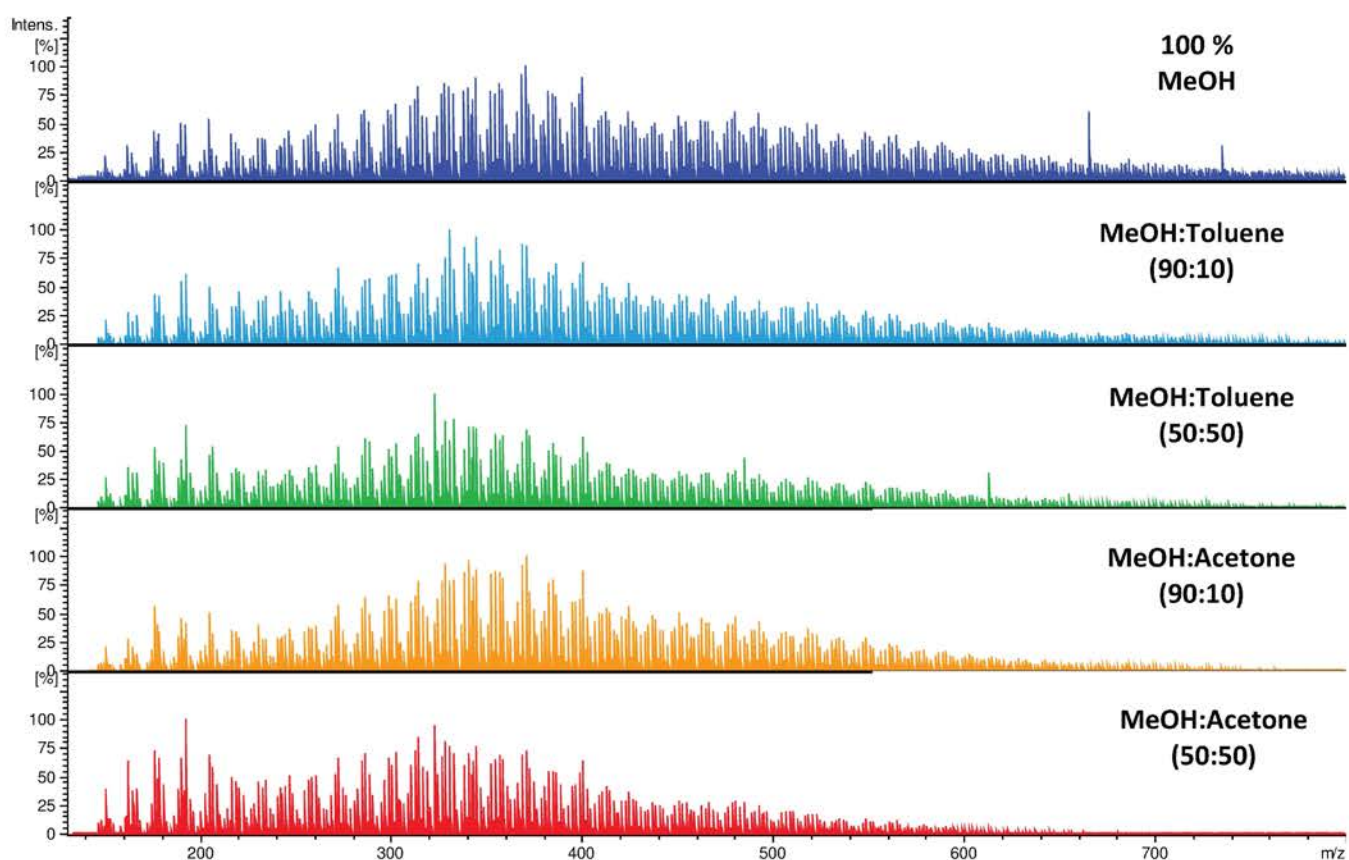


Figure IV-14. (-) APPI mass spectra of oak bio-oil acquired without and with dopant (toluene or acetone).

As a consequence, APPI measurements have to be preferably done without dopant whatever the ion detection mode. Similar conditions were also used by Lababidi *et al.* to characterize crude oil mixtures by APPI FT-ICR MS.<sup>12</sup>

### III.D. Bio-oil composition descriptions obtained by APPI FT-ICR MS

As it was previously demonstrated in ESI and LDI, the comparison and the convolution of the APPI results in both detection modes has been performed to achieve the as extensive as possible description of the bio-oil components.

#### III.D.1. Bio-oil composition descriptions obtained in positive and negative ion APPI FT-ICR MS

The global bio-oil description achieved in (+) and (-) APPI demonstrates that 90 % and 10 % of the TIC is related to the  $C_xH_yO_z$  and  $C_xH_yN_nO_z$  compounds, respectively (**Table IV-2**). No differences are highlighted in respect with the used ion detection mode.

Polarity	Number of assigned peaks	$C_xH_yO_z$	$C_xH_yN_nO_z$
(+)	3537	90 %	10 %
(-)	2683	90 %	10 %

Table IV-2. Number of assigned peaks and compound families evidenced by APPI FT-ICR MS analyses of the oak bio-oil in positive and negative ion modes.

The distributions of the oxygenated compound class extent from  $O_1$  to  $O_{13}$  with maxima around  $O_6$ - $O_7$  for (+) APPI (**Figure IV-15**). A broader distribution, from  $O_2$  to  $O_{17}$ , is obtained in (-) APPI with a small shift to high oxygen atom count.

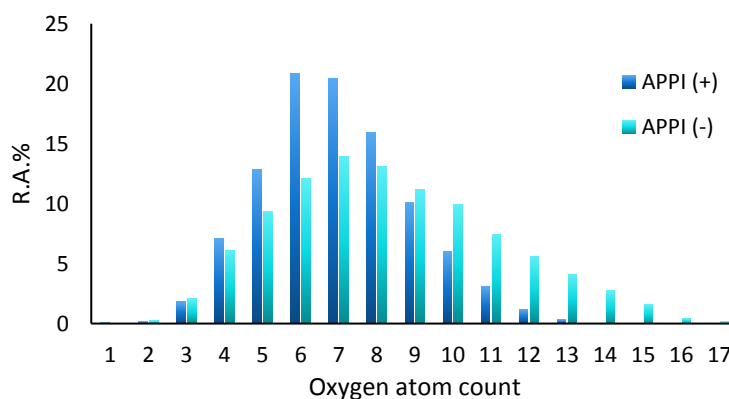


Figure IV-15. Distribution in respect with the oxygen atom count of the  $C_xH_yO_z$  compounds of the oak bio-oil assigned by APPI FT-ICR MS in both detection modes.

The corresponding van Krevelen diagrams (**Figure IV-16**) indicate that detected features are mainly from lignin derivatives whatever the ion detection mode. Less numerous lipid

compounds are observed in (-) APPI. Only lignin derived compounds and lipids, but not cellulose linked species, were detected. APPI should be considered as inefficient for the ionization of sugarc derivatives.

The comparison of the two van Krevelen diagrams of the  $C_xH_yO_z$  species indicates that (+) APPI is more sensitive to compounds with lower O/C and higher H/C ratios than (-) APPI.

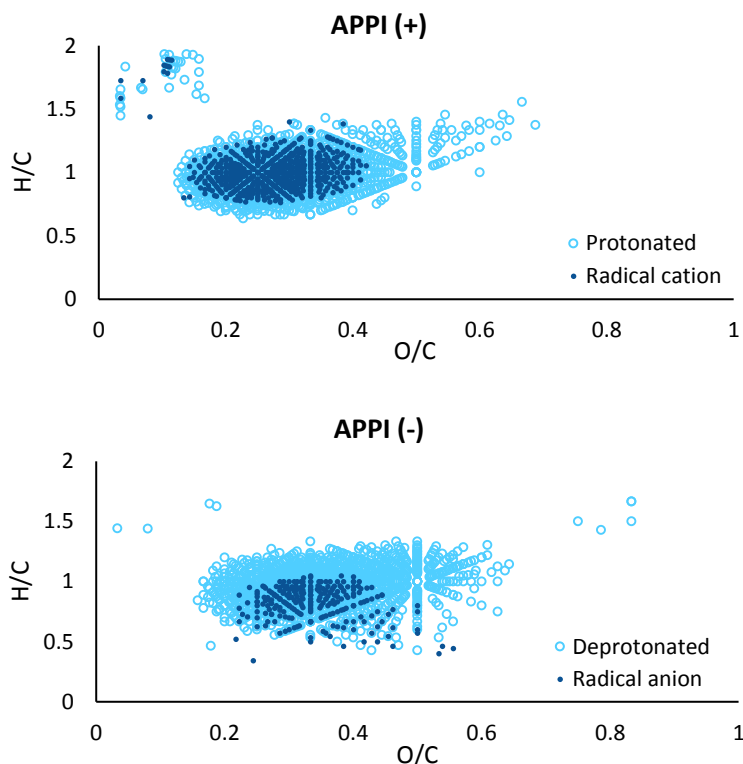


Figure IV-16. van Krevelen diagrams of the  $C_xH_yO_z$  compounds, in respect with their ion parity, assigned in positive (top) and negative (bottom) APPI FT-ICR MS.

Interestingly, the fine examination of the positive and negative APPI mass spectra, reveals that 75 % and 92 % of the TIC for oxygen-containing bio-oil components is associated with protonated and deprotonated species, respectively. Molecular radical ions are consequently more numerous and intense in (+) APPI. For both detection modes, these radical ions are lignin derivatives. They have systematically a O/C ratio in the 0.2 to 0.4 range but different H/C ratio in respect with the polarity of the ions. Cations are less unsaturated ( $0.6 < H/C < 1.5$ ) than anions ( $0.4 < H/C < 1.2$ ). The fixation of an electron is consequently favored if it has the capability to be delocalized on a large area of the molecule. This is not an absolute requirement for cation for which radical cation and protonated cation superimposed on the van Krevelen diagram. This also explains the broader variety of radical ions in (+) APPI. They are

easier to be formed and more stable than anionic ones. The different pathways of APPI mechanism deserve to be more deeply considered. They will be discussed in the following section.

### III.D.2. Ionization pathways involved in APPI analysis of bio-oil

#### III.D.2.a. In positive ion mode

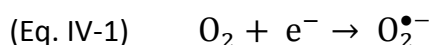
For positive ion mode, different ionization pathways may explain the formation of the observed cations, considering that no dopant was added in (+) APPI experiments. Due to the ionization energy of methanol (10.84 eV), the solvent cannot be directly photoionized by Kr photons (10.6 eV), but the dimer of methanol, corresponding to 2 % of the methanol in solution, has a lower ionization energy (9.74 eV) and is efficiently ionized.<sup>13</sup> The radical cation dimer may yield a protonated methanol ion by elimination of a  $\text{CH}_3\text{O}^\bullet$  (or  $^\bullet\text{CH}_2\text{OH}$ ) radical. Additionally, the generation of large protonated methanol clusters is facilitated by the large binding energy of neutral  $\text{CH}_3\text{OH}$  to protonate solvent clusters, e.g.,  $\text{CH}_3\text{OH}$  binding energy with  $[\text{CH}_3\text{OH}]_n\text{H}^+$  is  $-33 \text{ kcal.mol}^{-1}$  for  $n = 1$ ;  $-22 \text{ kcal.mol}^{-1}$  for  $n = 2$ ; and  $-16 \text{ kcal.mol}^{-1}$  for  $n = 3$ .<sup>14</sup>

The interaction of these protonated methanol clusters with oxygen-containing bio-oil components induces the transfer of the proton, and eventually the fission of the methanol cluster, to the most acidic bio-oil compounds. Wood pyrolysis bio-oils have typically a low pH value and significant amount of acidic compounds.<sup>15</sup> More specifically, this happens for  $\text{O/C} > 0.4$  compounds, which have odd  $m/z$  values (**Figure IV-16 (top)**). The formation of even  $m/z$  ions may be the result of the direct photoionization, according to the low ionization energy of highly unsaturated and conjugated species or charge transfer from the  $[\text{CH}_3\text{OH}]_2^{\bullet+}$  ion. Alternatively, part of the large number of the bio-oil components may act as a self-dopant.

#### III.D.2.b. In negative ion mode

In negative ion mode, some reaction pathways have been reported which explain anion formation.<sup>16</sup> The main ionization processes are the proton transfer, the electron capture, and the charge transfer.

For the former one, it has been evidenced that  $\text{O}_2$  plays a key role in the formation of  $[\text{M-H}]^-$  ions. Because of its ubiquity in the API sources and its high electron affinity ( $\text{EA}(\text{O}_2^\bullet) = 0.451 \text{ eV}$ ), it easily captures photoelectrons to yield the superoxide ion,  $\text{O}_2^{\bullet-}$  (**Equation IV-1**).<sup>17,18</sup>

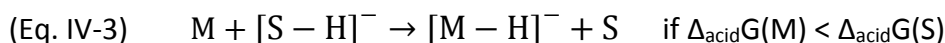




The  $O_2^{\bullet-}$  ion is a strong base in gas phase and serves as deprotonation reagent, with the acidic analytes and solvents, by proton transfer (**Equation IV-2**).<sup>19,20</sup>



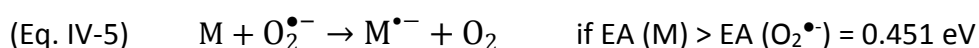
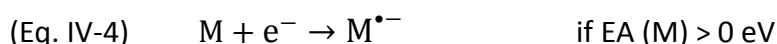
This reaction is possible if the gas-phase acidity of the analyte is higher than the  $HO_2^{\bullet}$  one ( $\Delta_{\text{acid}}G(M) < \Delta_{\text{acid}}G(HO_2^{\bullet})$ ). Instead of an analyte, this reaction may also occur with solvent molecule or cluster (S), if  $\Delta_{\text{acid}}G(S) < \Delta_{\text{acid}}G(HO_2^{\bullet})$ . Then, the deprotonated  $[S-H]^-$  ion may interact with the analytes according to the **Equation IV-3**.



This pathway can also explain the deprotonation of the bio-oil compounds and their detection as  $[M-H]^-$ . Indeed,  $\Delta_{\text{acid}}G(\text{methanol})=1565 \text{ kJ.mol}^{-1}$  whereas  $\Delta_{\text{acid}}G(\text{phenol})$  and  $\Delta_{\text{acid}}G(\text{benzoic acid})$ , which are both compounds structurally close to lignin-derivatives, are equal to 1432 and 1393  $\text{kJ.mol}^{-1}$ , respectively.<sup>21</sup>

Deprotonation was evidenced to be more efficient in neutral (hexane, water, methanol, acetonitrile) and basic (0.1 % ammonium acetate or hydroxide) solvents. Indeed, these solvents produce reactant ions with low gas-phase acidities such as  $HO^-$ , deprotonated molecules or clusters of methanol.<sup>21</sup>

The molecules can also be detected as radical anions  $M^{\bullet-}$  due to electron capture. This ionization pathway may occur directly (**Equation IV-4**) or by charge exchange *via*  $O_2^{\bullet-}$  (**Equation IV-5**).<sup>16</sup> Electrons come from the direct photoionization of methanol clusters.



As previously seen with proton transfer, neutral and basic solvents also promote the formation of the negative radical molecular ion.<sup>21</sup>

Regarding the high percentage of the TIC related to deprotonated  $C_xH_yO_z$  compounds in the bio-oil (92 %), it appears that deprotonation preferentially occurs. This process is ensured by  $O_2^{\bullet-}$ . Therefore, the assigned bio-oil species are understood to be mainly proton-donors. This is in agreement with the higher unsaturation degree and the broader oxygen range observed in these conditions. Such compounds may more easily give a proton as they are stabilized by mesomeric effect.

Similar results were obtained by Purcell *et al.* who characterized complex mixtures (bitumen and crude-oils) by APPI FT-ICR MS in positive and negative ion modes.<sup>22,23</sup> They observed that more than 99 % of the assigned peaks from the (-) APPI mass spectra are [M-H]<sup>-</sup> anions.

### III.E. Conclusion

APPI FT-ICR MS analysis ensures to observe low polar compounds. Lignin derived compounds were observed in both detection modes whereas lipids were detected in positive ion mode. Moreover, it has been evidenced that some pyrolytic lignin species were exclusively detected whereby the ion detection mode. Therefore, positive and negative ion APPI analyses are complementary for the exhaustive bio-oil description.

## IV. Complementarity of the ESI, APPI, and LDI FT-ICR MS for the extensive characterization of bio-oils

### IV.A. Introduction

In this study, FT-ICR MS coupled to ESI, APPI, and LDI is used to obtain the as extensive as possible bio-oil description in order to assess and improve the pyrolysis and catalysis processes. The last part of this chapter is dedicated to evidence the complementarity of the established methodologies to obtain complementary information on the bio-oil composition. Thus, some of the results previously obtained in positive and negative ion LDI and in positive ion APPI will be used for comparison. The ESI analyses were achieved with a Bruker 12 T FT-ICR MS (University of Edinburgh).

### IV.B. Experimental procedure

The same oak bio-oil was used to perform the different experiments. The latter were conducted with the 12 T SolariX FT-ICR mass spectrometer equipped with ESI, APPI, and LDI sources. Alternatively, some LDI FT-ICR MS measurements were performed on the 9.4 T Ion-Spec mass spectrometer.

#### *IV.B.1. ESI FT-ICR MS*

The bio-oil was diluted to a final concentration of 2 % in methanol. Sodium acetate (0.1 mg.mL<sup>-1</sup>) was added to favor cationization.

ESI FT-ICR MS analyses were performed in both positive and negative ion modes. The capillary voltage was set at  $\pm 4000$  V and the end plate offset at -500 V. The source gas was tuned with nebulizer gas (1-1.8 bar), dry gas (4-6 L.min<sup>-1</sup>), and heated at 180 °C. The sample was infused at a flow rate of 200 mL.h<sup>-1</sup> into the ion source. The ions were accumulated for 0.3 s per scan and 200 analyses were summed to obtain the final mass spectrum in the 129-1000  $m/z$  range. The length of the transient was 3 s and the mass resolution was  $\approx 680\,000$  at  $m/z$  400.

#### *IV.B.2. LDI FT-ICR MS*

For the LDI experiments, 1 mL of 70:30 bio-oil:water solution was deposited on a stainless steel target and dried at room temperature.

With the 12 T mass spectrometer, the measurements were only performed in negative ion mode. Fifty analyses were accumulated to obtain the final mass spectrum in the 147-1000  $m/z$  range. Measurements were conducted at the 355 nm wavelength with a diameter of the laser spot of 300  $\mu$ m. Six hundred laser shots per analysis were accumulated at a 1000 Hz laser frequency. A 1.7 s transient length was acquired, which resulted in mass resolution of  $\approx 390\,000$  at  $m/z$  400. The power of the laser was optimized to avoid fragmentation and recombination phenomenon.

With the 9.4 T mass spectrometer, the acquisitions were performed in both positive and negative ion modes. It concerns the Analysis I obtained in (-) LDI FT-ICR MS and the analysis achieved by (+) LDI FT-ICR MS.

#### *IV.B.3. APPI FT-ICR MS*

For the APPI experiments, the sample was diluted in methanol (4% v/v) without addition of dopant.

#### IV.C. Global composition descriptions of the bio-oil in respect with the analytical conditions

The **Table IV-3** demonstrates that close to 90 % of the signal is related to  $C_xH_yO_z$  compounds whatever the analytical conditions, which is consistent with the elemental analysis of oak bio-oil.<sup>24</sup> The (+) APPI bio-oil composition was previously detailed in the section III. The LDI measurements performed with the 9.4 T mass spectrometer, in both positive and negative detection modes, are fully described in the section II. The bio-oil descriptions achieved by ESI and LDI FT-ICR MS with the 12 T mass spectrometer will be discussed in the next paragraphs.

Source	Number of assigned monoisotopic peaks	$C_xH_yO_z$	$C_xH_yN_nO_z$	$C_xH_ySO_z$	Other <sup>b</sup>
(+) ESI	1521	95 %	5 %	-	-
(-) ESI	1382	95 %	2 %	3 %	-
(+) APPI	2778	90 %	10 %	-	-
(-) LDI	936	92 %	3 %	5 %	-
(+) LDI <sup>a</sup>	415	83 %	17 %	-	-
(-) LDI <sup>a</sup>	1222	81 %	3 %	< 1 %	16 %

<sup>a</sup> 9.4 T FT-ICR MS; <sup>b</sup> concern complexes formed with the iron of the target plate with acidic  $C_xH_yO_z$  bio-oil compounds

Table IV-3. Relative distribution of compound families identified in bio-oil in positive and negative detection modes in ESI, APPI, and LDI FT-ICR MS.

##### IV.C.1. Bio-oil descriptions obtained by ESI with the 12 T FT-ICR mass spectrometer

Whatever the ion detection mode, 95 % of the signal is attributed to  $C_xH_yO_z$  compounds (**Table IV-3**). In (+) ESI, the remaining signal is attributed to  $C_xH_yN_nO_z$  compounds whereas in (-) ESI, both  $C_xH_yN_nO_z$  and  $C_xH_ySO_z$  species are identified and correspond to 2 % and 3 % of the total ion signal, respectively. In (+) ESI,  $NO_z$  ions are detected as  $[M+H]^+$ , which corresponds to protonation of the basic sites of the molecules, such as amine group or pyridine ring.<sup>10</sup> This is in agreement with the dramatic increase of the signals attributed to nitrogen containing species when formic acid is added to the sample.<sup>25</sup>  $NO_z$  anions are thought to be related to neutral or acidic compounds, which may include, for example, an indole moiety. It is proposed

that the  $\text{SO}_2$  species are associated with aromatic sulfonated compounds which easily deprotonate. Alternatively, they may also correspond to  $\text{HSO}_4^-$  attachment to  $\text{C}_x\text{H}_y\text{O}_z$  bio-oil components during the ESI process.<sup>26</sup>

The  $[\text{M}-\text{H}]^-$  anion and the  $[\text{M}+\text{Na}]^+$  cation distributions of the  $\text{C}_x\text{H}_y\text{O}_z$  bio-oil components present similarities in terms of DBE and number of oxygen atoms. Nevertheless, differences are highlighted when the relative intensity of these compounds is considered (**Figure IV-17**). In (-) ESI, the  $[\text{M}-\text{H}]^-$  ions illustrate a wide variation in the number of oxygen atoms ( $\text{O}_2$  to  $\text{O}_{16}$ ). The most important signal is observed for  $\text{O}_4$  to  $\text{O}_6$  compounds. In (+) ESI, sodiated cations  $[\text{M}+\text{Na}]^+$  are detected for  $\text{O}_1$  to  $\text{O}_{14}$  bio-oil components, the most abundant signal is obtained for  $\text{O}_5$  and  $\text{O}_6$  species and a bimodal distribution is observed. The second massif is centered on  $\text{O}_{11}$  compounds. Furthermore, the van Krevelen diagrams of  $\text{C}_x\text{H}_y\text{O}_z$  compounds detected in (-) ESI and (+) ESI are reported in **Figure IV-18**. Lipids are predominantly observed in (-) ESI but are also observed in (+) ESI. In both ion detection modes, the pyrolytic lignin derivatives constitute the majority of the signal. Nevertheless, (-) ESI analysis reveals a more extended distribution of compounds in terms of unsaturation number and oxygen amount. The sugarc compounds are more numerous and abundant in (+) ESI. The ability of highly oxygenated compounds to easily polycoordinate the sodium cation explains this behavior.

It has to be noted that these results display significant similarities with the works of Miettinen *et al.*<sup>27</sup> and Jarvis *et al.*<sup>28</sup> who investigated the oily and aqueous phases from different pyrolysis bio-oils, after fractionation, by (-) ESI FT-ICR MS. Lipids and pyrolytic lignin derivatives were common to both fractions whereas “sugarc species” which correspond to the most oxygenated compounds were only highlighted in the aqueous phase. These latter compounds are relative to the second distribution (centered on  $\text{O}_{11}$ ) observed in this study for  $[\text{M}+\text{Na}]^+$  ions. The first massif of the oxygen-containing bio-oil components, common to both ion detection modes, is indicative of the pyrolytic lignin derivatives. In spite of a lower sensitivity of (+) ESI for pyrolytic lignin derivatives and lipids, it is the only experimental condition able to give semi-quantitative information regarding the sugarc and lignin pyrolysis compounds. As a conclusion, both detection modes are useful for the thorough characterization of bio-oil.

The comparison of the obtained results with previously published works<sup>29–31</sup> can be made to tentatively assign some signals, obtained by (+) or (-) ESI FT-ICR MS, to well-known pyrolysis compounds derived from the wood constituents. Thus, the ions observed at  $m/z$

185.04213, 203.05270, and 347.09467 may be attributed to  $[M+Na]^+$  adducts of levoglucosan, glucose, and cellobiosan, which are cellulose and hemicellulose pyrolysis products, respectively. The specific compounds which derivate from the lignin pyrolysis may also be observed in the form of  $[M+Na]^+$  and/or  $[M-H]^-$ . Cinnamic acid and coniferyl aldehyde, two of the lignin *p*-coumaryl unit derivatives, are detected as  $[M-H]^-$  ion at *m/z* 147.04512 and 177.05571, respectively. Pyrolysis compounds of guaiacyl (vanillin, eugenol, acetoguaiacon) and syringyl (syringol, methylsyringol, syringaldehyde) units were also evidenced.

The bio-oil composition descriptions achieved by ESI with the 12 T FT-ICR instrument were coherent with those obtained with the same bio-oil with the 9.4 T mass spectrometer (Chapter III). This demonstrates the reproducibility of the developed analytical methods with the addition of sodium acetate to perform (+) ESI analyses and without dopant to carry out (-) ESI measurements.

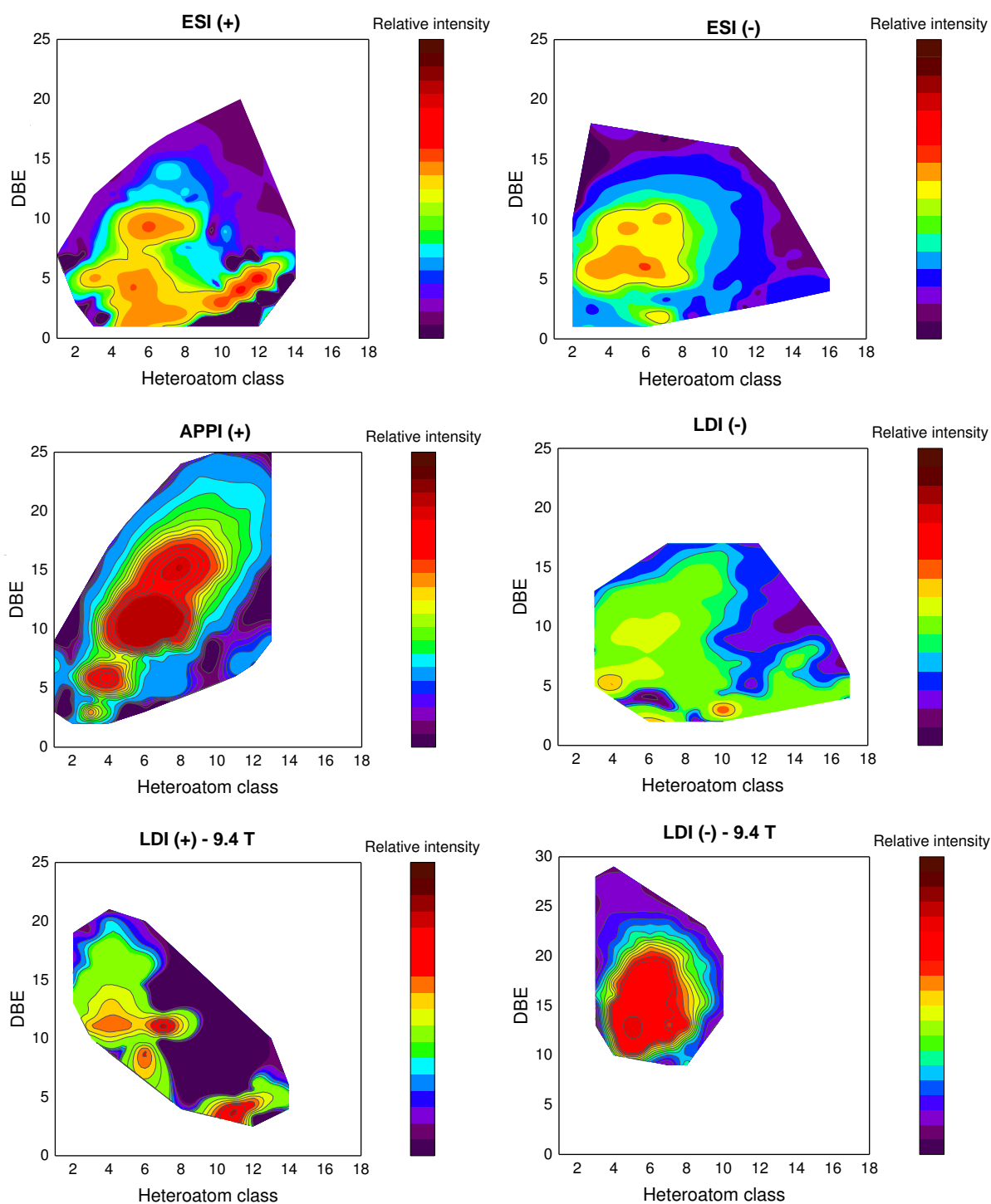


Figure IV-17. Relative intensities of the  $C_xH_yO_z$  compounds in (+) and (-) ESI, APPI, and LDI FT-ICR MS spectra of oak pyrolysis bio-oil according to the DBE and oxygen atom distribution.

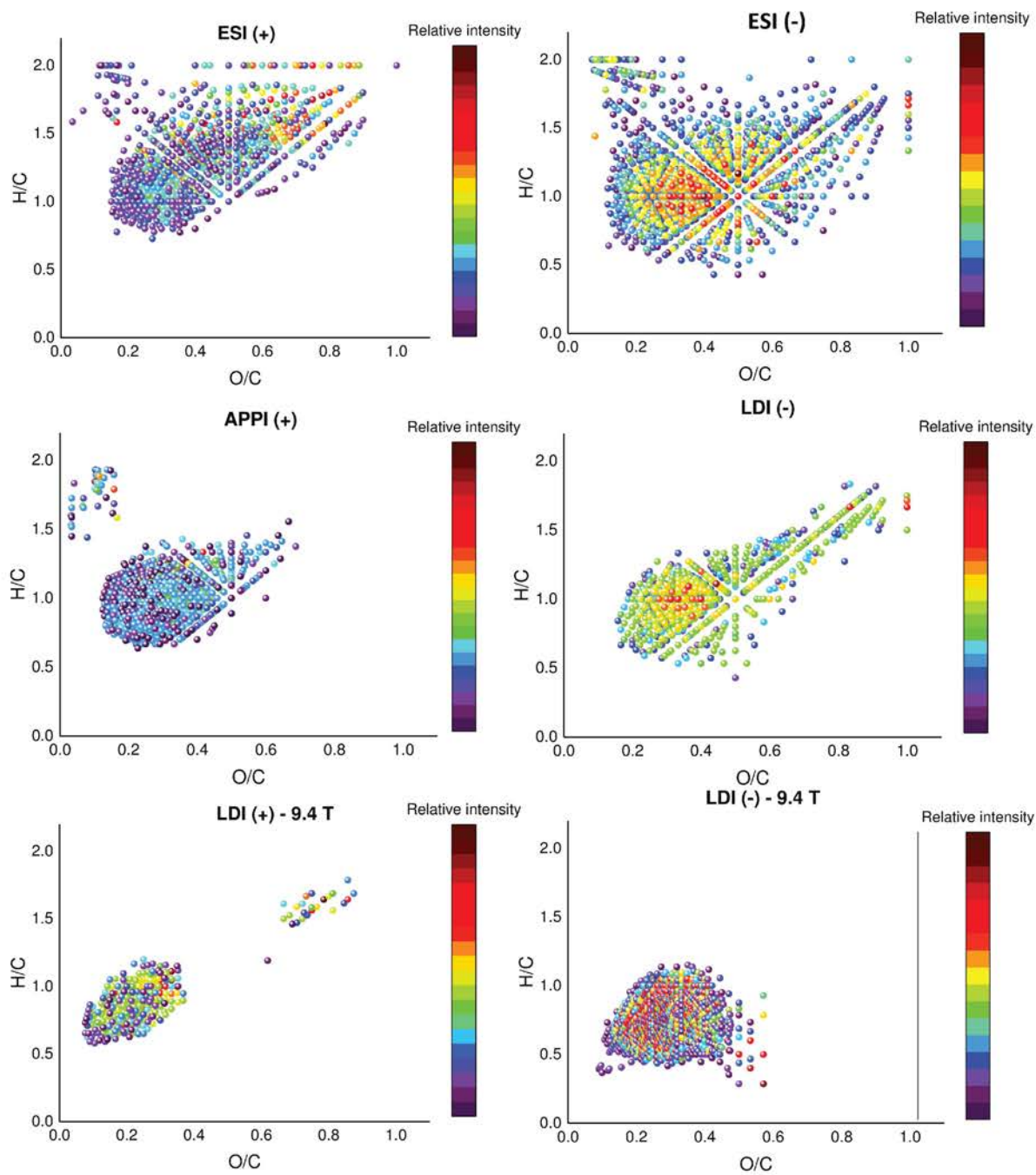


Figure IV-18. Relative intensities of the  $C_xH_yO_z$  compounds represented on the van Krevelen diagrams according to their H/C and O/C ratios as obtained in (+) and (-) ESI, APPI, and LDI FT-ICR MS.



#### IV.C.2. Bio-oil composition descriptions obtained by LDI with the 12 T FT-ICR mass spectrometer

In negative LDI FT-ICR MS, the obtained distribution with the 12 T instrument is  $C_xH_yO_z$  (92 %),  $C_xH_yN_nO_z$  (3 %) and  $C_xH_ySO_z$  (5 %) (**Table IV-3**). The distribution of oxygen-containing species is ranging from  $O_3$  to  $O_{17}$  and presents a maximum at  $O_6$ .

According to the O/C and H/C ratios, both pyrolytic lignin derivatives and sugarc compounds (but not lipids) are detected on the 12 T (-) LDI mass spectrum (**Figure IV-18**). The 9.4 T (-) LDI, leads to the specific observation of the pyrolytic lignin compounds. Lignin linked compounds are observed in the LDI experiments due to their significant absorption properties at the used laser wavelength. This is confirmed by previous work carried out by Olcese *et al.*<sup>32</sup> who investigated bio-oils produced by pyrolysis of lignin in which  $O_2$  to  $O_8$  compounds with DBE values ranging from 7 to 25 were observed. Smith *et al.*<sup>7</sup> also observed that  $O_4$ ,  $O_5$ , and  $O_6$  were the main oxygen-containing bio-oil components observed by LDI-Orbitrap MS. Differences in (-) LDI results obtained with the 12 T and 9.4 T instruments can be explained with the different 355 nm laser profiles of both setups. The energy surface distribution of the smartbeam™ laser coupled with the 12 T FT-ICR MS instrument is less homogeneous than the Orion. Indeed, the “average homogeneity” of the smartbeam™ is obtained by the repetition on the same area of a large number of different laser shots.<sup>33</sup> For the Orion laser, each laser shot is more homogeneous. As a consequence, the smartbeam laser leads to the formation of hot (and cold) spots, for which the laser energy may be higher (and lower) than the laser energy deposited at the surface of the sample by the Orion laser. Typically, the compounds which have low absorption properties (in this case sugarc compounds) need high laser energy to be desorbed and ionized. Such conditions occur in the hot spots of the smartbeam™ laser but not with the homogeneous Orion laser.

In LDI, compounds are detected as radical or protonated/deprotonated ions. The radicals are highly unsaturated compounds ( $H/C < 1$ ) with  $O/C < 0.4$ , as shown in **Figure IV-19**. Among the oxygen-containing species, only 4 % of the signal is attributed to  $M^{\bullet-}$  ions using the 12 T mass spectrometer, whereas, when using the 9.4 T equipped with the Orion laser, they represent 22 % ( $M^{\bullet+}$ ) and 15 % ( $M^{\bullet-}$ ). It is proposed that these differences are linked to the laser-sample interaction which is strongly dependent on the laser beam, as previously mentioned.

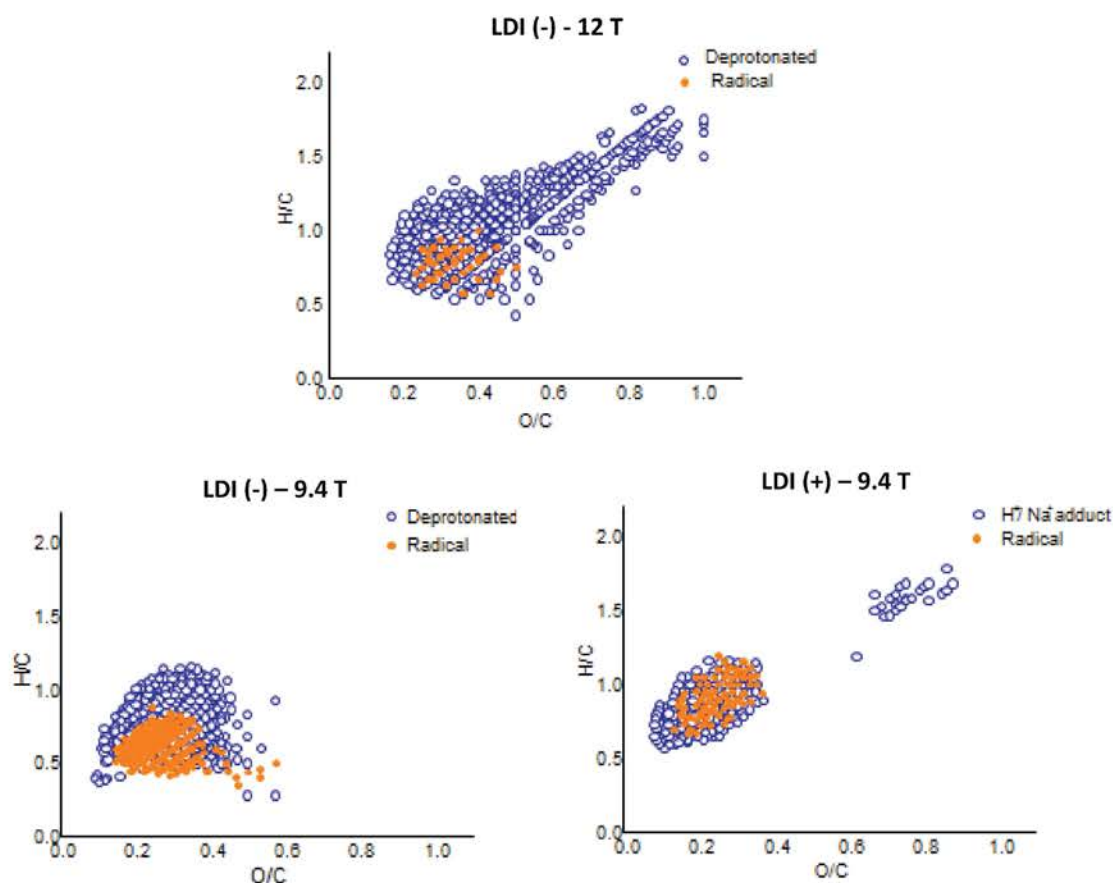


Figure IV-19. Van Krevelen diagrams for  $C_xH_yO_z$  compounds with radical and protonated/deprotonated ions identified in (+) and (-) LDI FT-ICR MS.

#### IV.D. Complementarity of the different ionization sources

Irrespective of the used ionization method and ion detection mode, the obtained compound class distribution is mainly associated with oxygen-containing compounds, which is consistent with CHNOS elemental analysis, at least 90 % of the TIC is related to  $C_xH_yO_z$  compounds (**Table IV-3**). Nitrogen species are always detected while  $SO_2$  compounds are only detected in negative ion detection mode. **Figure IV-18** and **Figure IV-20** well illustrate the complexity of the bio-oil samples and the complementarity of ESI, APPI, and LDI sources for their ionization and analysis.

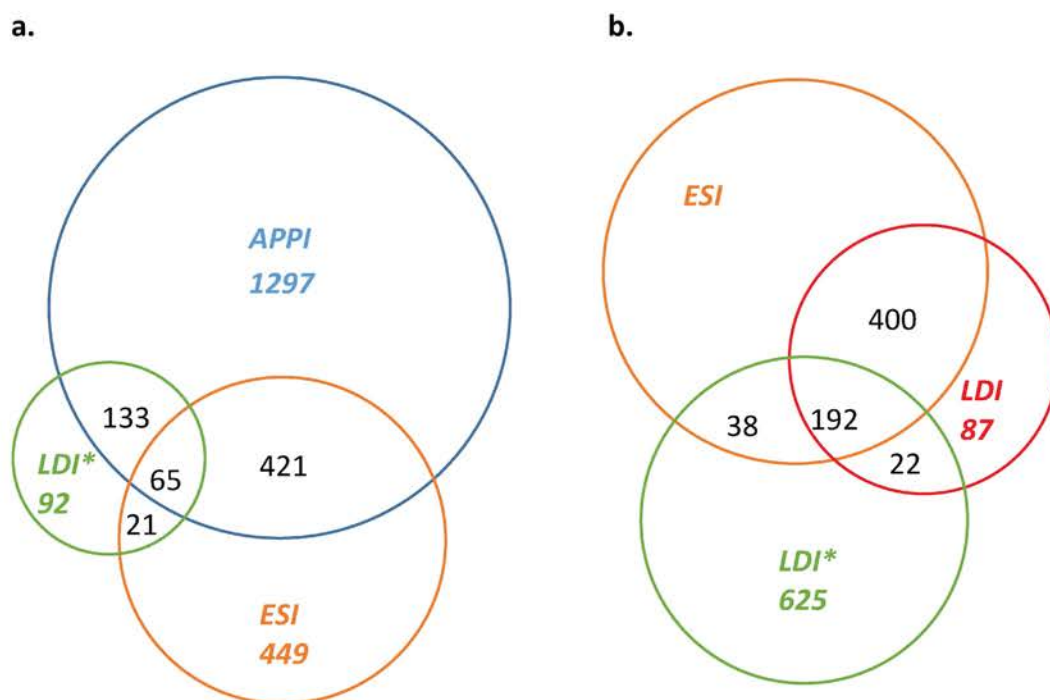


Figure IV-20. Venn diagrams of  $C_xH_yO_z$  compounds obtained by APPI, LDI, and ESI analyses of the oak bio-oil in (a) positive and (b) negative ion detection modes.

#### IV.D.1. Positive ion mode analyses

The distributions of the oxygenated species achieved in (+) ESI and (+) APPI appear very similar based on the importance of  $O_2$  bio-oil components (**Table IV-3**), which extend over a similar range, from  $O_1$  to  $O_{14}$  and from  $O_1$  to  $O_{13}$ , respectively. However, further insights can be gained by assessing the intensity of the DBE distribution for each heteroatom class (**Figure IV-17**). In ESI, the most intensely detected compounds contain 10 and 11 oxygen atoms and have  $DBE < 5$ . The other prominent species are composed of 5-7 oxygen atoms and their DBE values range from 0 to 5. The most oxygenated species have the properties of pyrolytic sugarc derivatives whereas the less oxygenated ones are pyrolytic lignin derivatives and lipids. These components were also evidenced on a *Miscanthus* bio-oil in (+) ESI.<sup>25</sup> On the other hand, in case of APPI, compounds having 10 or more oxygen atoms are not significant, which means that sugarc compounds are not ionized in APPI. However, species containing 4 to 8 oxygen atoms are intensely detected, which is also seen in ESI. But their unsaturation degree is much more important, with DBE ranging between 5 and 20. These molecular properties can be at-

tributed to pyrolytic lignin derivatives and lipids. Moreover, compounds identified in ESI contain up to 30 carbon atoms on a mass range of  $m/z$  150 to 600 whereas in APPI, they have up to 40 carbon atoms and a mass range from  $m/z$  200 to 800.

Thus, APPI is useful to observe the highest mass-to-charge-ratio compounds with high DBE values and low polarity (not observed on (+) ESI mass spectrum). Nevertheless, these heteropolyaromatic compounds are not totally apolar due to their capability to be ionized in APPI by protonation rather than charge transfer. ESI is a suitable method to observe polar to middle polar compounds which are characterized by a low unsaturation degree and a significant amount of heteroatoms such as oxygen in the case of bio-oils.<sup>12,34,35</sup> The (+) LDI analysis yields results very similar to those obtained by (+) ESI and (+) APPI. It leads to an intermediate behavior and allows both middle polar to low polar bio-oil components to be observed at the exception of the high mass species. The combination of the different used ionization methods is consequently well suited to exhaustively describe pyrolytic bio-oil. The examination of the obtained signals in respect to the DBE value and the number of oxygen atoms for the three different ionization techniques (**Figure IV-17**) highlights that positive ESI is more sensitive to ionization competition. More specifically, highly saturated compounds with high levels of oxygen are well suited to form stable sodium adducts, which leads to the increase of the associated signal. The same kind of discrimination is observed with components presenting a high proton affinity when bio-oil is directly infused in the ESI source. In contrast, positive APPI and, in a lesser extent, positive LDI lead to a less compound-dependent ionization and ensure a more precise description of the bio-oil component distribution but only on pyrolytic lignin species.

#### *IV.D.2. Negative ion mode analyses*

The  $C_xH_yO_z$  compound distributions obtained in (-) ESI and (-) LDI are very similar in respect with the oxygen atom amount (**Figure IV-17**). In both ionization modes, a broad oxygen class of compounds are detected with  $O_2$ - $O_{16}$  components in (-) ESI and  $O_3$ - $O_{17}$  in (-) LDI using the 12 T FT-ICR MS. The O-species range obtained with the 9.4 T FT-ICR MS is narrower ( $O_3$  to  $O_{10}$  oxygen atoms). However, when using either instrument, the  $O_4$  to  $O_6$  species are the most predominant. These observed trends are very similar to those obtained in positive detection mode with ESI, LDI, and APPI. As shown in **Figure IV-17**, degree of unsaturation is more important for compounds detected in LDI than those in ESI. These results are consistent

with published literature. For example, the LDI and ESI analyses of extracts from fast pyrolysis char, obtained by Cole *et al.*<sup>36</sup>, present similar distribution of compounds in respect to their heteroatom classes, with a DBE distribution centered on higher values in LDI. Consequently, this behavior has to be considered as a generalization for woody bio-oils as it was previously reported for lignin pyrolysis products.<sup>32</sup> Thus, negative LDI exhibits the capability to efficiently ionize low to medium polar compounds presenting different amounts of oxygen atoms and a high number of unsaturation. This is due to the absorption properties at the wavelength of the ionization laser. Whereas negative ESI is more suited to more polar species such as lipids.

The comparison of positive and negative mode van Krevelen diagrams for lignin derivative compounds is also of significant interest. The O/C ratio is very similar and generally ranges from 0.1 to 0.7. In contrast, the H/C ratio varies significantly. For LDI and APPI, this ratio, for the  $C_xH_yO_z$  compounds, is centered on 1. In contrast, it is significantly higher in positive ESI and lower in negative ESI. ESI ensures the efficient ionization of polar compounds, positive ESI is sensitive to basic compounds whereas negative ESI is well suited to neutral or acidic species. APPI and LDI are less sensitive to these differences of chemical properties and, as a consequence, the acidic and neutral fraction of bio-oil is predominantly made of highly unsaturated species. These latter easily deprotonate to produce anions which are stabilized by significant mesomeric effects.

The complementarity of the ionization sources is also assessed by the Venn diagrams giving the repartition of the different 4500 compound formulae depending on the ionization source and the ion polarity (**Figure IV-20**). In positive ion mode (**Figure IV-20.a**), APPI enabled to assign 1297 exclusive formulae whereas ESI and LDI allowed to attribute 449 and 92 own formulae, respectively. As a result, only 65 compounds were common to the 3 ionization sources. Besides, the same representation was done in negative ion mode (**Figure IV-20.b**), with ESI and LDI. It appeared that 617 formulae were specific to ESI, and 625 to LDI in the best conditions. Finally, as (-) ESI has been the only ionization method in most bio-oil analyses<sup>37</sup>, it is clearly demonstrated here that this strategy nearly highlights 1250/4500 elemental formulae corresponding to less than 28 % of the total bio-oil components.

#### IV.E. Conclusion

Comprehensive petroleomic analysis of bio-oil by ESI, APPI, and LDI FT-ICR MS, showed that the heteroatom distributions, as obtained by these three different methods, were very similar. In fact, for any given ion detection mode, the  $C_xH_yO_z$  species are the most abundant compound family and their distributions extend across comparable ranges of oxygen atom numbers. However, when focuses on the DBE distributions are done for each of the ionization modes, some differences appeared. In ESI, the compounds were more highly saturated, with  $2 < \text{DBE} < 10$ , whereas in APPI, they were more unsaturated with  $5 < \text{DBE} < 20$ . In LDI, the range of unsaturation was between those obtained by ESI and APPI but it was also affected by the FT-ICR MS laser configuration. With a nonhomogeneous laser beam, identified components were less unsaturated.

This approach successfully demonstrated that the characterization of complex mixtures by non-targeted analysis required the use of different but complementary ionization sources in order to have the as exhaustive as possible description. Indeed, at the maximum, the common used negative ESI only allowed the MS detection of less than 28 % of the combined features obtained by ESI, APPI, and LDI FT-ICR MS.

## V. Conclusion

LDI and APPI analyses were developed as they are less sensitive to the ion polarity than ESI. The optimum analytical methodologies were established by assessing specific parameters of each of these ionization techniques.

Thus, positive and negative ion laser/desorption ionization experiments demonstrated that the most suitable way to perform bio-oil characterization is without matrix and with the lowest laser fluence.

For APPI, in both detection modes, the experiments, carried out to investigate the influence of the dopant on the obtained features, evidenced that no dopant is required to reach APPI mass spectrum with a high sensitivity and on a broad  $m/z$  range.

The bio-oil composition descriptions obtained with these optimized analytical methods were then compared with those achieved by ESI FT-ICR MS. It was evidenced that exclusive compound formulae were observed for each ionization method. Consequently, the analyses in positive and negative ion ESI, LDI, and APPI are complementary and ensure to reach an

extensive bio-oil description. ESI ensures to specifically ionize sugarc derivatives while APPI and LDI allow to ionize pyrolytic lignin species.

The development of analytical methods dedicated to ionize the low polar to apolar compounds is also interesting to assess the efficiency of upgrading treatment on bio-oils. Indeed, such treatments are aimed to increase the energy density of the bio-oils by oxygen removal and/or increase of the unsaturation degree of the bio-oil molecules. The capability of this approach will be described in the last chapter for the investigation of the efficiency of catalytic deoxygenation treatments.

## VI. References

1. Hertzog, J., Carré, V., Le Brech, Y., Mackay, C. L., Dufour, A., Mašek, O. & Aubriet, F. Combination of electrospray ionization, atmospheric pressure photoionization and laser desorption ionization Fourier transform ion cyclotron resonance mass spectrometry for the investigation of complex mixtures - Application to the petroleomic analysis of bio-oils. *Anal. Chim. Acta* **969**, 26–34 (2017).
2. Chen, Z., Megharaj, M. & Naidu, R. Confirmation of iron complex formation using electrospray ionization mass spectrometry (ESI-MS) and sample stacking for analysis of iron polycarboxylate speciation by capillary electrophoresis. *Microchem. J.* **86**, 94–101 (2007).
3. Fernandez, M. T., Mira, M. L., Florencio, M. H. & Jennings, K. R. Iron and copper chelation by flavonoids: an electrospray mass spectrometry study. *J. Inorg. Biochem.* **92**, 105–111 (2002).
4. Creasy, W. & Brenna, J. Large Carbon Cluster Ion Formation by Laser Ablation of Polyimide and Graphite. *Chem. Phys.* **126**, 453–468 (1988).
5. Rathsack, P., Kroll, M., Rieger, A., Haseneder, R., Gerlach, D., Repke, J.-U. & Otto, M. Analysis of high molecular weight compounds in pyrolysis liquids from scrap tires using Fourier transform ion cyclotron resonance mass spectrometry. *J. Anal. Appl. Pyrolysis* **107**, 142–149 (2014).
6. Shroff, R. & Svatos, A. Proton sponge: a novel and versatile MALDI matrix for the analysis of metabolites using mass spectrometry. *Anal. Chem.* **81**, 7954–7959 (2009).
7. Smith, E. A. & Lee, Y. J. Petroleomic Analysis of Bio-oils from the Fast Pyrolysis of Biomass: Laser Desorption Ionization–Linear Ion Trap–Orbitrap Mass Spectrometry Approach. *Energy Fuels* **24**, 5190–5198 (2010).
8. Blackburn, J. W. T., Kew, W., Graham, M. C. & Uhrin, D. Laser Desorption/Ionization Coupled to FTICR Mass Spectrometry for Studies of Natural Organic Matter. *Anal. Chem.* **89**, 4382–4386 (2017).
9. Santos, J. M., dos Santos, L. O., Silva, F. F., Eberlin, M. N. & Wisniewski, A. Comprehensive Characterization of Second-Generation Biofuel from Invasive Freshwater Plants by FT-ICR MS. *Bioenergy Res.* **8**, 1938–1945 (2015).
10. Cole, D. P., Smith, E. A., Dalluge, D., Wilson, D. M., Heaton, E. A., Brown, R. C. & Lee, Y. J. Molecular characterization of nitrogen-containing species in switchgrass bio-oils at various harvest times. *Fuel* **111**, 718–726 (2013).
11. Sudasinghe, N., Dungan, B., Lammers, P., Albrecht, K., Elliott, D., Hallen, R. & Schaub, T. High resolution FT-ICR mass spectral analysis of bio-oil and residual water soluble organics produced by hydrothermal liquefaction of the marine microalga *Nannochloropsis salina*. *Fuel* **119**, 47–56 (2014).
12. Lababidi, S. & Schrader, W. Online normal-phase high-performance liquid chromatography/Fourier transform ion cyclotron resonance mass spectrometry: Effects of different ionization methods on the characterization of highly complex crude oil mixtures. *Rapid Commun. Mass Spectrom.* **28**, 1345–1352 (2014).



13. Short, L. C., Cai, S.-S. & Syage, J. A. APPI-MS: Effects of Mobile Phases and VUV Lamps on the Detection of PAH Compounds. *J. Am. Soc. Mass Spectrom.* **18**, 589–599 (2007).
14. Grimsrud, E. & Kebarle, P. Gas-Phase Ion Equilibria Studies of Solvation of Hydrogen-Ion by Methanol, Dimethyl Ether, and Water - Effect of Hydrogen-Bonding. *J. Am. Chem. Soc.* **95**, 7939–7943 (1973).
15. Vamvuka, D. Bio-oil, solid and gaseous biofuels from biomass pyrolysis processes—An overview. *Int. J. Energy Res.* **35**, 835–862 (2011).
16. Robb, D. B. & Blades, M. W. State-of-the-art in atmospheric pressure photoionization for LC/MS. *Anal. Chim. Acta* **627**, 34–49 (2008).
17. Horning, E., Carroll, D., Dzidic, I., Lin, S., Stillwell, R. & Thenot, J. Atmospheric-Pressure Ionization Mass-Spectrometry - Studies of Negative-Ion Formation for Detection and Quantification Purposes. *J. Chromatogr.* **142**, 481–495 (1977).
18. Song, L., Wellman, A. D., Yao, H. & Bartmess, J. E. Negative Ion-Atmospheric Pressure Photoionization: Electron Capture, Dissociative Electron Capture, Proton Transfer, and Anion Attachment. *J. Am. Soc. Mass Spectrom.* **18**, 1789–1798 (2007).
19. Sawyer, D. T., Gibian, M. J., Morrison, M. M. & Seo, E. T. On the chemical reactivity of superoxide ion. *J. Am. Chem. Soc.* **100**, 627–628 (1978).
20. Dzidic, I., Carroll, D., Stillwell, R. & Horning, E. Gas-Phase Reactions - Ionization by Proton-Transfer to Superoxide Anions. *J. Am. Chem. Soc.* **96**, 5258–5259 (1974).
21. Kauppila, T. J., Kotiaho, T., Kostianen, R. & Bruins, A. P. Negative ion-atmospheric pressure photoionization-mass spectrometry. *J. Am. Soc. Mass Spectrom.* **15**, 203–211 (2004).
22. Purcell, J. M., Hendrickson, C. L., Rodgers, R. P. & Marshall, A. G. Atmospheric Pressure Photoionization Fourier Transform Ion Cyclotron Resonance Mass Spectrometry for Complex Mixture Analysis. *Anal. Chem.* **78**, 5906–5912 (2006).
23. Purcell, J. M., Hendrickson, C. L., Rodgers, R. P. & Marshall, A. G. Atmospheric Pressure Photoionization Proton Transfer for Complex Organic Mixtures Investigated by Fourier Transform Ion Cyclotron Resonance Mass Spectrometry. *J. Am. Soc. Mass Spectrom.* **18**, 1682–1689 (2007).
24. Le Brech, Y., Jia, L., Cissé, S., Mauviel, G., Brosse, N. & Dufour, A. Mechanisms of biomass pyrolysis studied by combining a fixed bed reactor with advanced gas analysis. *J. Anal. Appl. Pyrolysis* **117**, 334–346 (2016).
25. Hertzog, J., Carré, V., Le Brech, Y., Dufour, A. & Aubriet, F. Toward Controlled Ionization Conditions for ESI-FT-ICR-MS Analysis of Bio-Oils from Lignocellulosic Material. *Energy Fuels* **30**, 5729–5739 (2016).
26. Jiang, Y. & Cole, R. B. Oligosaccharide analysis using anion attachment in negative mode electrospray mass spectrometry. *J. Am. Soc. Mass Spectrom.* **16**, 60–70 (2005).
27. Miettinen, I., Makinen, M., Vilppo, T. & Janis, J. Compositional Characterization of Phase-Separated Pine Wood Slow Pyrolysis Oil by Negative-Ion Electrospray Ionization Fourier Transform Ion Cyclotron Resonance Mass Spectrometry. *Energy Fuels* **29**, 1758–1765 (2015).

28. Jarvis, J. M., McKenna, A. M., Hilten, R. N., Das, K. C., Rodgers, R. P. & Marshall, A. G. Characterization of Pine Pellet and Peanut Hull Pyrolysis Bio-oils by Negative-Ion Electrospray Ionization Fourier Transform Ion Cyclotron Resonance Mass Spectrometry. *Energy Fuels* **26**, 3810–3815 (2012).
29. Alsbou, E. & Helleur, B. Direct Infusion Mass Spectrometric Analysis of Bio-oil Using ESI-Ion-Trap MS. *Energy Fuels* **28**, 578–590 (2014).
30. Le Masle, A., Angot, D., Gouin, C., D’Attoma, A., Ponthus, J., Quignard, A. & Heinisch, S. Development of on-line comprehensive two-dimensional liquid chromatography method for the separation of biomass compounds. *J. Chromatogr. A* **1340**, 90–98 (2014).
31. Staš, M., Chudoba, J., Auersvald, M., Kubička, D., Conrad, S., Schulzke, T. & Pospíšil, M. Application of orbitrap mass spectrometry for analysis of model bio-oil compounds and fast pyrolysis bio-oils from different biomass sources. *J. Anal. Appl. Pyrolysis* doi:10.1016/j.jaap.2017.02.002
32. Olcese, R., Carré, V., Aubriet, F. & Dufour, A. Selectivity of Bio-oils Catalytic Hydrotreatment Assessed by Petroleomic and GC\*GC/MS-FID Analysis. *Energy Fuels* **27**, 2135–2145 (2013).
33. Holle, A., Haase, A., Kayser, M. & Hoehndorf, J. Optimizing UV laser focus profiles for improved MALDI performance. *J. Mass Spectrom.* **41**, 705–716 (2006).
34. Chiaberge, S., Leonardis, I., Fiorani, T., Cesti, P., Reale, S. & De Angelis, F. Bio-Oil from Waste: A Comprehensive Analytical Study by Soft-Ionization FTICR Mass Spectrometry. *Energy Fuels* **28**, 2019–2026 (2014).
35. Staš, M., Chudoba, J., Kubička, D. & Pospíšil, M. Chemical Characterization of Pyrolysis Bio-oil: Application of Orbitrap Mass Spectrometry. *Energy Fuels* **29**, 3233–3240 (2015).
36. Cole, D. P., Smith, E. A. & Lee, Y. J. High-Resolution Mass Spectrometric Characterization of Molecules on Biochar from Pyrolysis and Gasification of Switchgrass. *Energy Fuels* **26**, 3803–3809 (2012).
37. Michailof, C. M., Kalogiannis, K. G., Sfetsas, T., Patiaka, D. T. & Lappas, A. A. Advanced analytical techniques for bio-oil characterization. *Wiley Interdiscip. Rev.-Energy Environ.* **5**, 614–639 (2016).

---

## *Chapter V*

---

*Application of the developed  
approach to assess the  
efficiency of the  
deoxygenation/cracking  
treatment by zeolites*

## Table of Contents

I.	Introduction.....	257
II.	Experimental procedure.....	257
III.	Results and discussion.....	258
III.A.	Effect of the nature of the catalyst on the bio-oil composition description ...	258
III.A.1.	Composition description of the raw bio-oil .....	258
III.A.2.	Effect of the zeolites on the bio-oil composition description .....	262
III.B.	Monitoring of the catalyst lifetime .....	273
III.B.1.	Upgraded bio-oil with catalysts – 8 to14 Oak cylinders .....	273
IV.	Conclusion .....	280
V.	References.....	281

## I. Introduction

In this chapter, the previous methodology, combining ESI, APPI, and LDI FT-ICR MS, was applied for the extensive description of bio-oils that have undergone a catalytic deoxygenation treatment on two different zeolite catalysts. The purpose is to observe the deep-compositional changes when pyrolysis was conducted with two different zeolite based catalysts, in order to assess the influence of their nature. The evolution of the catalytic treatment in respect with the catalyst aging will also be evaluated. More specifically, the effects of parent HZSM-5 catalyst will be compared to the HZSM-5 hierarchical one which presents a more pronounced mesoporous structure and a lower Si/Al ratio than the parent one.

The results presented in this chapter have been subjected to an article *“Evidence of the hierarchical zeolite efficiency during catalytic fast pyrolysis of lignocellulosic biomass”*, submitted to *ACS Sustainable Chemistry & Engineering* in October 2017.

## II. Experimental procedure

The raw and upgraded bio-oils investigated in this study have been produced by pyrolysis of oak cylinders as described in the Chapter II.

For the raw bio-oil, seven oak cylinders were injected in stepwise mode (corresponding to a biomass-to-catalyst ratio of 0.85) and the vapors were condensed by three different cold traps.

Upgraded bio-oils were produced by catalyst fast pyrolysis (CFP) with parent (A) or hierarchical (B) HZSM-5 zeolites. The structure of both catalysts was detailed in the Chapter II. First, 5 g of zeolite were introduced in the bed to be fluidized and heated. Then, 14 oak cylinders were stepwise injected, which corresponds to a final biomass-to-catalyst ratio of 1.7. The liquid bio-oil obtained from the pyrolysis of the first seven cylinders was collected. Then, the 8 to 14 cylinders were stepwise injected and a second bio-oil solution was collected.

Finally, five different samples were obtained in respect with the experimental conditions: the raw and upgraded A 1-7, A 8-14, B 1-7, and B 8-14 bio-oils.

The samples were prepared for the MS analyses, as described in the Chapter IV, with the raw bio-oil. The (+) APPI and (+) and (-) ESI experiments were performed on a 12 T FT-ICR mass spectrometer while the (-) LDI ones were carried out with the 9.4 T instrument. The acquisition parameters according to the instrument and the data treatment were the same as those given in the previous chapter.

### III. Results and discussion

First of all, whatever the analyzed bio-oil sample, the compounds detected by ESI are sodium adducts  $[M+Na]^+$ , in positive ion mode, and deprotonated ions  $[M-H]^-$ , in negative ion mode. By (+) APPI, both radical and protonated ions are detected, and by (-) LDI, deprotonated ions and, in a lesser extent, radical ions are detected. Using different ionization conditions for the analysis of bio-oils ensures to take advantage of the petroleomic approach.<sup>1-3</sup> The formula of each detected ion is considered for the comparison of chemical composition description of raw and upgraded bio-oils.

In a first part, the effect of the nature of the catalyst on the heavy bio-oil fraction from CFP of oak is achieved by comparing the results obtained with the catalysts noted A (parent zeolite) and B (hierarchical zeolite), and with silica sand (noted “Raw BO”). Thus, the comparison was conducted with the upgraded bio-oils from the fast-pyrolysis of the first seven oak cylinders as representative of the catalyst effect (samples A 1-7 and B 1-7).

In a second part, the upgraded bio-oils, from the last 7 injections (8-14) of oak cylinders, were considered to investigate the catalyst lifetime on the composition of the generated bio-oils (samples A 8-14 and B 8-14).

#### *III.A. Effect of the nature of the catalyst on the bio-oil composition description*

##### *III.A.1. Composition description of the raw bio-oil*

As previously demonstrated<sup>1</sup>, a raw bio-oil (without catalyst), from pyrolysis of lignocellulosic material, may be extensively described by using compositional data obtained by (+/-) ESI, (+) APPI, and (-) LDI FT-ICR MS. This combining approach applied to this raw bio-oil from oak pyrolysis, gives the same description. The achieved bio-oil composition gives close to 90 % of the total ion current (TIC) attributed to  $C_xH_yO_z$  compounds (**Table V-1**) and the remaining part of the signal is attributed to  $C_xH_yNO_z$  and  $C_xH_ySO_z$  species. Sulphur containing species are only observed in negative ion mode analyses (8 % of the TIC by ESI and 9 % by LDI) whereas nitrogen compounds are observed in ESI (8 %) and APPI (1 %), in positive ion mode. The distributions of the  $C_xH_yO_z$  compounds in respect with their oxygen atom count are ranging from 0 to 13 with maximum for  $O_4$  to  $O_6$  species (**Figure V-1**). In (+) ESI, a bimodal distribution is obtained with the first massif centered on  $O_5$  and the second one, on  $O_{10}$ . This

shape was described in a previous work.<sup>4</sup> The first massif, which corresponds to lignin derivatives as well as lipids, is also described by (-) ESI, (+) APPI, and (-) LDI analyses. The second one is less intense, more specifically detected by (+) ESI, and is attributed to pyrolytic sugarc derivatives. The representations of the  $C_xH_yO_z$  formulae on van Krevelen diagrams enable to highlight these different biomass derivatives (**Figure V-2**).

	Samples	# <sup>12</sup> C signals	$C_xH_y$	$C_xH_yO_z$	$C_xH_yN_xO_z$	$C_xH_ySO_z$
<b>(+) ESI</b>	Raw BO	1577	-	92 %	8 %	-
	BO A 1-7	629	-	90 %	10 %	-
	BO A 8-14	1298	-	89 %	11 %	-
	BO B 1-7	496	-	96 %	4 %	-
	BO B 8-14	487	-	96 %	4 %	-
<b>(-) ESI</b>	Raw BO	1290	-	92 %	1 %	7 %
	BO A 1-7	1890	-	91 %	2 %	7 %
	BO A 8-14	1516	-	91 %	2 %	7 %
	BO B 1-7	1944	-	88 %	3 %	9 %
	BO B 8-14	1778	-	91 %	2 %	7 %
<b>(+) APPI</b>	Raw BO	1662	1 %	98 %	1 %	-
	BO A 1-7	2141	2 %	98 %	-	-
	BO A 8-14	2185	1 %	99 %	< 1 %	-
	BO B 1-7	1361	14 %	85 %	< 1 %	-
	BO B 8-14	1276	3 %	97 %	-	-
<b>(-) LDI</b>	Raw BO	510	< 1 %	91 %	-	9 %
	BO A 1-7	436	5 %	91 %	-	4 %
	BO A 8-14	1203	-	99 %	-	1 %
	BO B 1-7	944	6 %	93 %	-	1 %
	BO B 8-14	1142	-	91 %	-	9 %

Table V-1. Relative distribution of compound families identified in positive and negative ion ESI, LDI, and APPI FT-ICR MS in raw bio-oil and upgraded A and B bio-oils from the pyrolysis of the 1-7 and 8-14 oak cylinders.

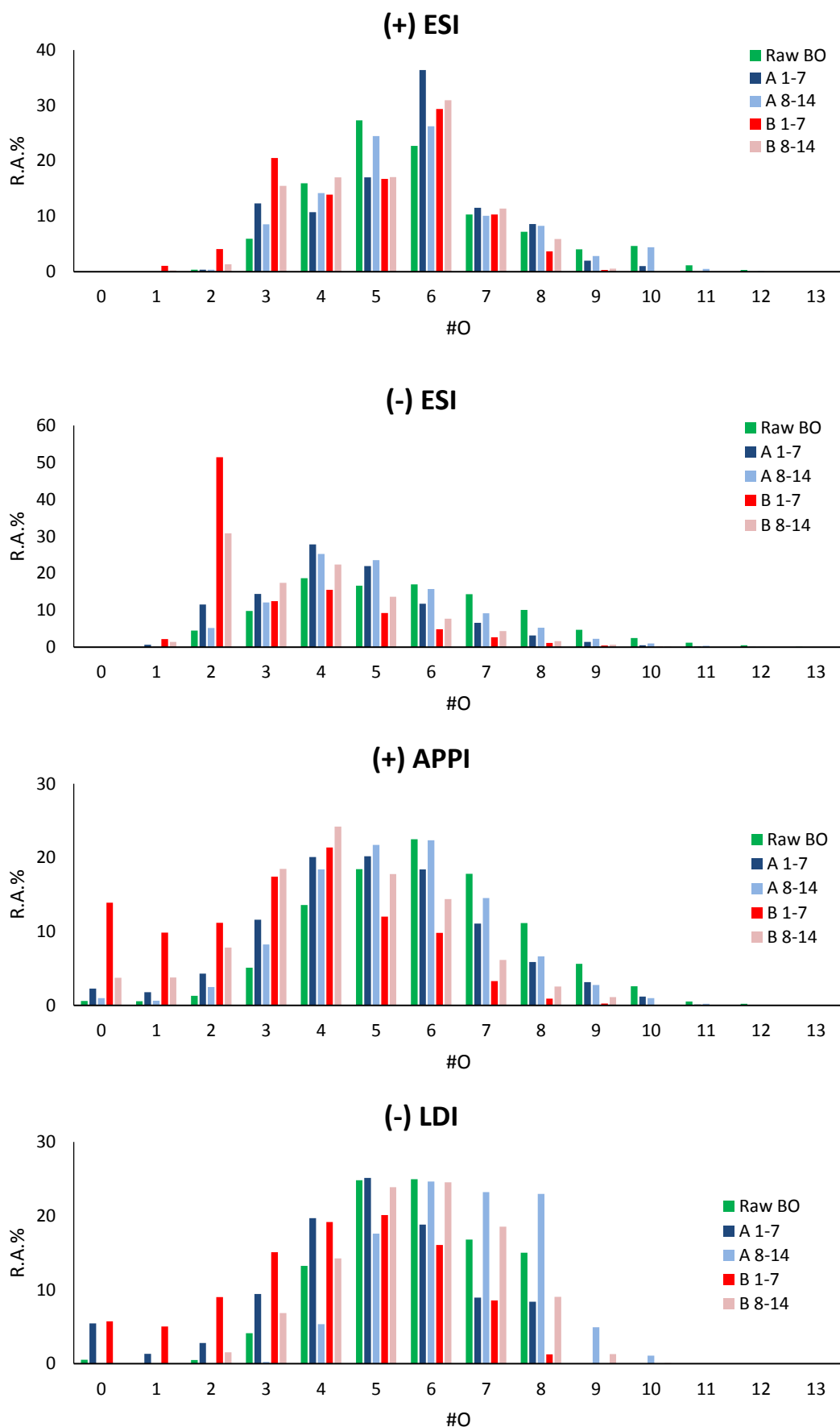


Figure V-1. Relative distribution of  $C_xH_y$  and  $C_xH_yO_z$  compounds in respect with the number of oxygen atoms in positive and negative ion ESI, LDI, and APPI FT-ICR MS for raw bio-oil and upgraded A and B bio-oils from the pyrolysis of the 1-7 and 8-14 oak cylinders.



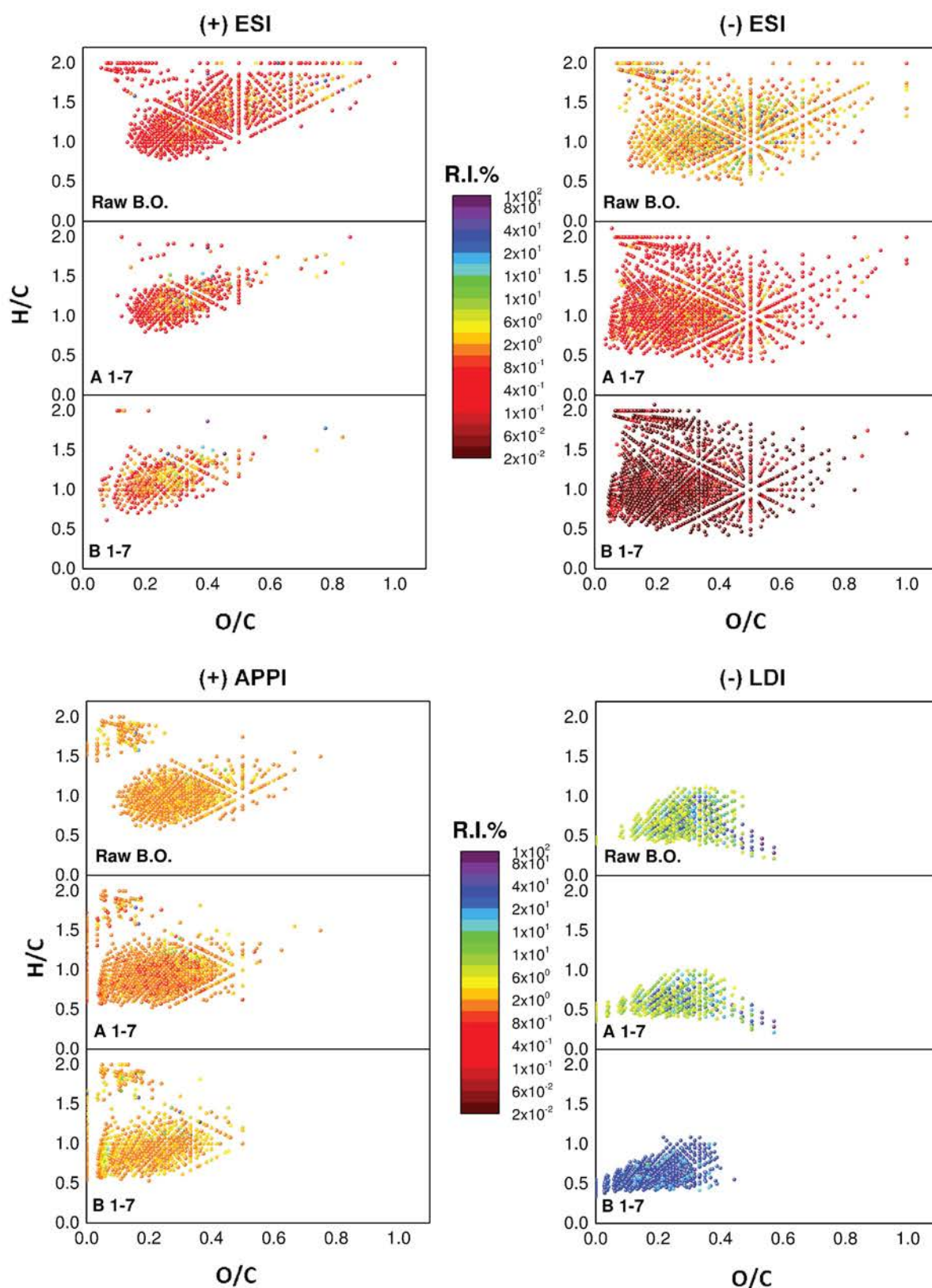


Figure V-2. Relative intensities of the  $C_xH_y$  and  $C_xH_yO_z$  compounds in raw bio-oil and upgraded A and B bio-oils from the pyrolysis of the 1-7 oak cylinders represented on the van Krevelen diagrams according to their H/C and O/C ratios as obtained by (+) and (-) ESI, APPI, and LDI FT-ICR MS.

Finally, as expected, a large panel of components of the raw bio-oil heavy fraction are extensively described by this analytical method. This is a prerequisite to investigate the selectivity of the catalysts used for CFP of oak.

### III.A.2. Effect of the zeolites on the bio-oil composition description

In addition to raw bio-oil data, the **Table V-1** displays the relative abundance of the  $C_xH_y$ ,  $C_xH_yO_z$ ,  $C_xH_yNO_z$ , and  $C_xH_ySO_z$  compound families identified in (+/-) ESI, (-) LDI, and (+) APPI FT-ICR MS for upgraded bio-oils. Overall, close to 90 % of the TIC is due to  $C_xH_yO_z$  compounds. The other contributions are nitrogen and sulphur species which are mainly observed in positive and negative ion modes, respectively. However, some different trends, depending on the analytical conditions, can be shown. In addition to  $C_xH_yO_z$  compounds, pure hydrocarbons,  $C_xH_y$ , are specifically detected by (-) LDI and (+) APPI. Moreover, the number of identified formulae in bio-oils can be similar or higher than in the raw bio-oil, this is the case for (-) ESI, (-) LDI, and (+) APPI analyses whereas in (+) ESI, they are three times less numerous.

The distributions of the  $C_xH_yO_z$  and  $C_xH_y$  compounds in respect with the oxygen atom content is displayed in the **Figure V-1**. The ranges obtained for the upgraded bio-oils are slightly narrower and shifted to lower values of oxygen atoms. **Figure V-1** also indicates that the distribution of the chemical families is greatly dependent on the used ionization condition. APPI and LDI seem to show similar trends in regard to the detected chemical families of upgraded bio-oils whereas (+) and (-) ESI reveal different features. Therefore, for all these reasons, it is necessary to have a deeper insight into the differences observed between the raw and the upgrading bio-oil compositions for each analytical condition before giving a real view of the selectivity of the catalysts.

In (+) ESI, the abundances of the oxygen-poor compounds ( $O_1$ ,  $O_2$ , and  $O_3$ ) are greater in the upgraded bio-oils, more especially in the B one, than in the raw bio-oil. The upgraded bio-oils contain species with up to 10 oxygen atoms and the second massif previously observed in the raw bio-oil distribution is no longer present in the upgraded bio-oil samples. This change relative to the catalytic treatment is attested on the van Krevelen diagrams. Indeed, the area corresponding to the sugarc derivatives species is almost empty for the bio-oils A 1-7 and B 1-7 (**Figure V-2**). It means that these compounds are well converted by the two catalysts. Concerning the pyrolytic lignin derivatives, they are detected in the 3 samples but their O/C and H/C ratios are shifted to lower values when a catalyst was used, especially in the sample B 1-7. In the **Figure V-1**, the relative abundances of the  $O_6$  species are still significant, even in

the catalytic bio-oils. Nevertheless, their distribution regarding the DBE value are quite different depending on the sample (**Figure V-3**). Low unsaturated compounds (with DBE=2 prominent) are specifically detected in the raw bio-oil whereas more unsaturated ones are detected in upgraded samples. This difference is even pronounced when the number of oxygen atom per molecules increases until O<sub>11</sub>-O<sub>12</sub>, which are only detected in the raw bio-oil. Looking at the DBE distribution of the low oxygenated compounds, (O<sub>1</sub>, O<sub>2</sub>, and O<sub>3</sub>, **Figure V-3**) new aromatic compounds are formed due to catalytic treatment, especially with the catalyst B, and are characterized by #C 10 - 22.

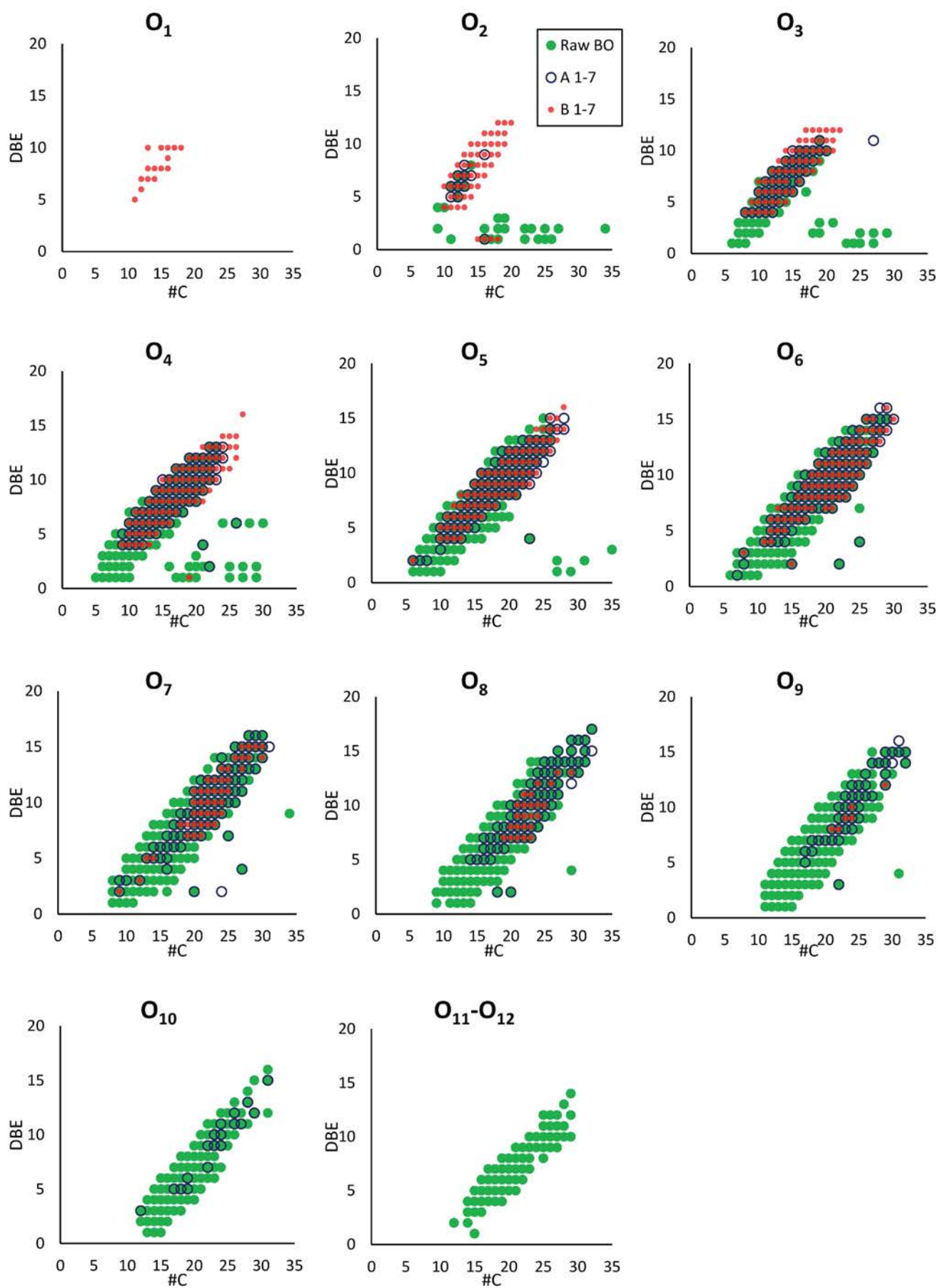


Figure V-3. Carbon number vs. DBE distribution of  $C_xH_yO_z$  compounds observed in (+) ESI for raw bio-oil and upgraded A and B bio-oils from the pyrolysis of the 1-7 oak cylinders

The results achieved in (-) ESI show, for the  $C_xH_yO_z$  and  $C_xH_y$  compounds classes, a nearly similar range of the oxygen atom count between the bio-oil samples (**Figure V-1**) even if the number of assignments is half more important in upgraded bio-oils (**Table V-1**). However, if the  $O_4$  compounds are prominent in the 3 samples, the species having 2 to 5 oxygen atoms are more abundant in the bio-oil A 1-7 and, to a lesser extent in the B 1-7, than in the raw bio-oil. Inversely, the  $O_6$  to  $O_{13}$  compounds are more abundant in the raw sample. A unique behavior is observed for the upgraded bio-oil B 1-7 for which the  $O_2$  species are dramatically detected. A deep insight into this compound family demonstrates that they correspond to pyrolytic lignin derivatives. Among them, the most abundant species have DBE=6 and contain between 10 and 15 carbon atoms. These features are close to those of phenolic species. Nevertheless, whatever the used catalyst, these compounds are the main peaks detected in negative ion mode by ESI and will be discussed later. The van Krevelen diagrams obtained for the upgraded bio-oils look similar to the raw one (**Figure V-2**). However, new compounds at very low O/C values appear, which indicates a partial deoxygenated effect of both catalysts. Splitting these data and looking at the DBE distribution according to the number of carbon atoms for each  $O_z$  family allows to confirm this trend (**Figure V-4**). Both catalysts show the same effect on bio-oil. Apart from the most oxygenated species which are only detected in the raw bio-oil ( $O_{11}$  -  $O_{12}$ ), the compounds identified in the raw bio-oil are also detected when a catalyst was used during pyrolysis. Nonetheless, for catalytic bio-oils, their distribution is extended to higher unsaturation range and higher number of carbon atoms. This is specifically the case for  $O_2$ - $O_5$  classes. This demonstrates the appearance of new heavy oligomeric compounds which are aromatic and less oxygenated. Furthermore, increasing aromaticity of acidic compounds may drastically increase their ability to be deprotonated and detected in negative ESI.<sup>5</sup> New light  $O_1$  compounds are also specifically detected in the CFP bio-oils.

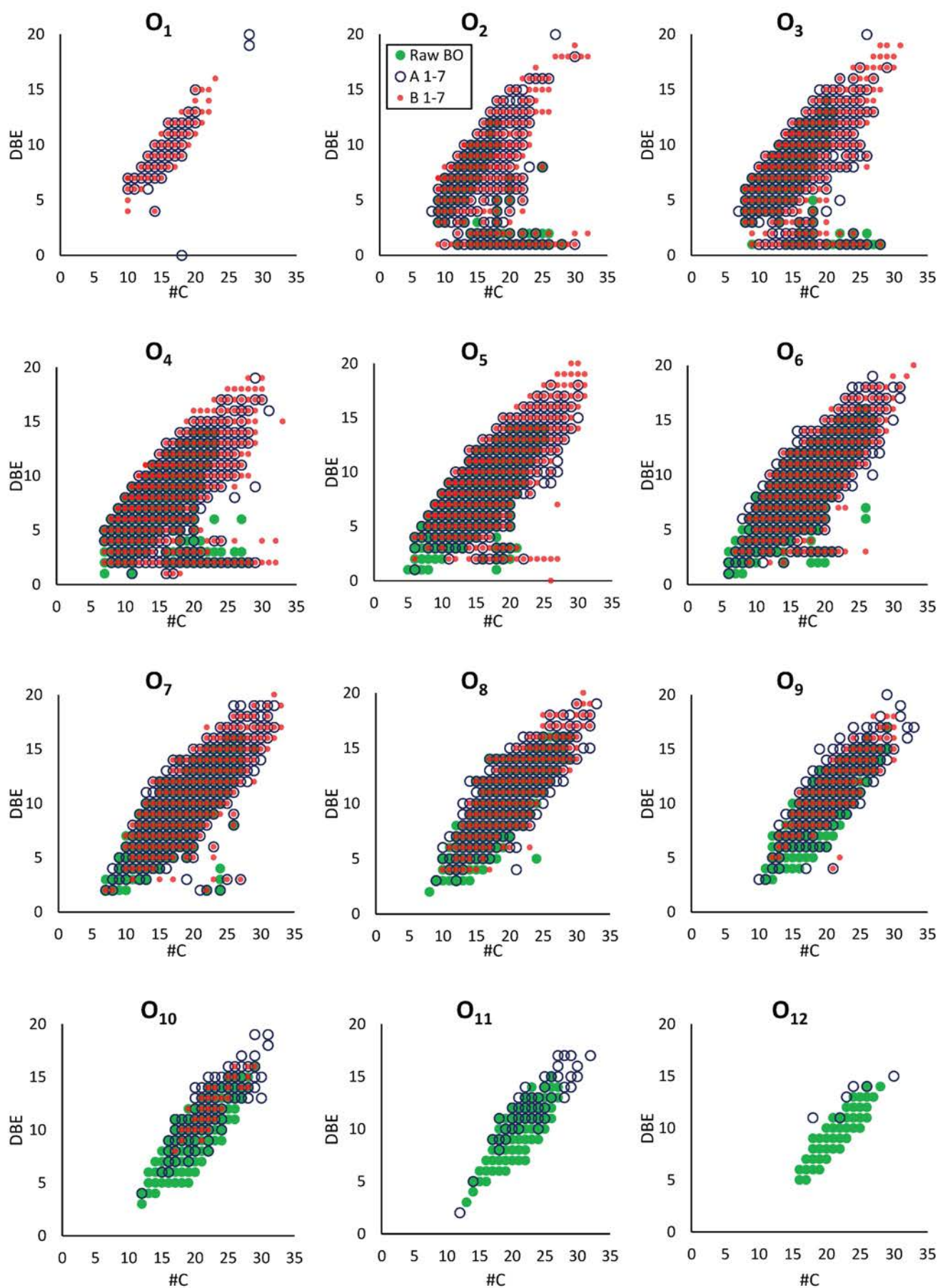


Figure V-4. Carbon number vs. DBE distribution of  $C_xH_yO_z$  compounds observed in (-) ESI for raw bio-oil and upgraded A and B bio-oils from the pyrolysis of the 1-7 oak cylinders.

In APPI (+), the number of detected mass peaks is higher for A 1-7 sample than for the raw one and the B 1-7 sample (**Table V-1**). The range of the distribution of the  $C_xH_yO_z$  compounds, in respect with the oxygen atom number, is clearly shifted to lower values when a catalyst was used, especially with the hierarchical zeolite (**Figure V-1**). Thus, while the contribution of the most oxygenated compounds dropped in the catalytic bio-oils (**Table V-1**), the  $C_xH_y$  and  $O_1-O_4$  components are prominent in the sample B 1-7, and, to a lesser extent, in the bio-oil A 1-7. This trend is also observable in the **Figure V-2** where only pyrolytic lignin and lipids are detected. Regarding the point cloud of the lignin derivatives, it is more intense in the lower O/C values when a catalyst is used, more especially with the hierarchical one. Moreover, this effect is balanced by the emergence of some new  $C_xH_y$  compounds. These compounds have a DBE ranging from 6 to 21 and a #C from 11 to 29 which indicates their aromatic feature (**Figure V-5**).

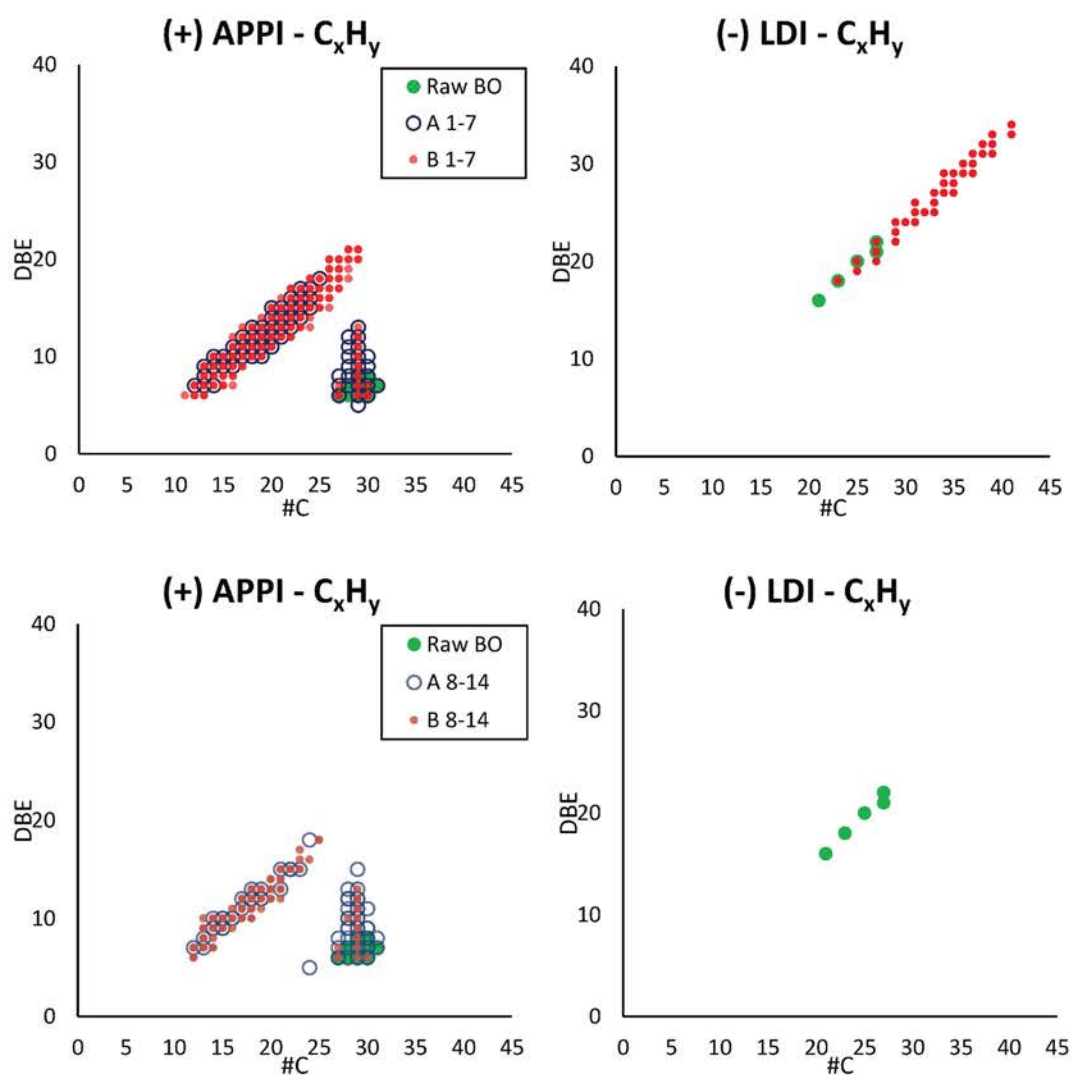


Figure V-5. Carbon number vs. DBE distribution of  $C_xH_y$  compounds observed in (+) APPI and (-) LDI for raw bio-oil and upgraded A and B bio-oils from the pyrolysis of the 1-7 (top) and 8-14 (bottom) oak cylinders.

A similar distribution of  $O_1$  compounds are also specifically detected on upgraded bio-oils (**Figure V-6**). Saturated or poor unsaturated lipids ( $O_1$ - $O_4$  and DBE = 0-5) are also detected and seem to be not impacted by the catalytic treatment. The **Figure V-3** shows that raw bio-oil and bio-oil A 1-7 are quite similar in terms of number of carbon atoms and DBE range for  $O_4$  -  $O_{10}$  species. For each #C, additional compounds of the sample A 1-7 are detected at a DBE+1 value at the top of the distribution of the raw bio-oil compounds. In the sample B 1-7, the high mass and high unsaturated compounds have been removed from  $O_7$  to  $O_{11}$  families. Thus, these specific compounds are clearly more reactive towards the hierarchical zeolite than to the parent one.

The differences between raw and upgraded bio-oil compositions observed in (-) LDI FT-ICR MS are comparable to those achieved in (+) APPI but at higher and complementary DBE values. The  $C_xH_yO_z$  compounds contained less oxygen atoms in the upgraded bio-oils than in the raw one (**Figure V-1**). The detected species of the three bio-oil samples have from 0 to 8 oxygen atoms. However, the relative abundances attributed to  $C_xH_y$  and  $C_xH_yO_z$  ( $z=1-3$ ) compounds are higher in the catalyzed samples than in the raw one, especially for  $O_1$ ,  $O_2$ , and  $O_3$  in the sample B 1-7. The most oxygenated species (with  $z > 5$ ) are more intensely detected in the raw bio-oil. These results are coherent with the van Krevelen diagrams of these compound families (**Figure V-2**). Pyrolytic lignin is commonly identified in all experiments. Nevertheless, some changes can be highlighted. In fact, after catalytic treatment, these components are less oxygenated, which is illustrated by a shift of the point cloud to lower O/C ratio values. This observation is slightly more pronounced for the bio-oil B 1-7. By displaying the DBE values of detected compounds according to the number of carbon atoms, the (-) LDI analyses give details on the aromatic range of hydrocarbons (**Figure V-5**). Specifically in the sample B 1-7, a significant distribution is highlighted which is extended to high value of DBE and high number of carbon atoms (high masses). This suggests a specific capacity of the B catalyst to produce and release such heavy polycyclic aromatic hydrocarbons (PAH) in the gas phase. For all the O-classes, catalyst B generates more unsaturated species than the raw and the A 1-7 bio-oils (**Figure V-7**).



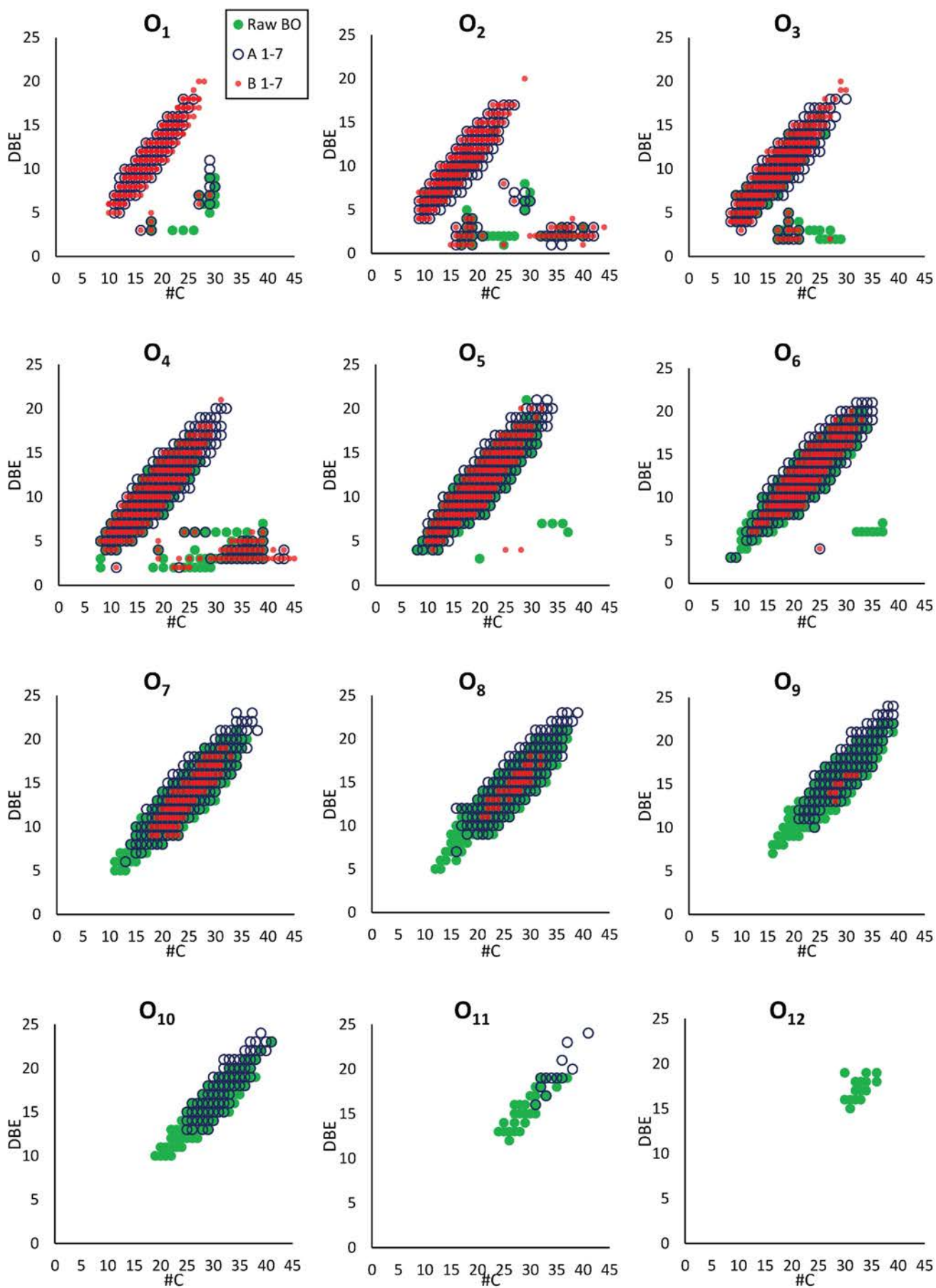


Figure V-6. Carbon number vs. DBE distribution of C<sub>x</sub>H<sub>y</sub>O<sub>z</sub> compounds observed in (+) APPI for raw bio-oil and upgraded A and B bio-oils from the pyrolysis of the 1-7 oak cylinders.

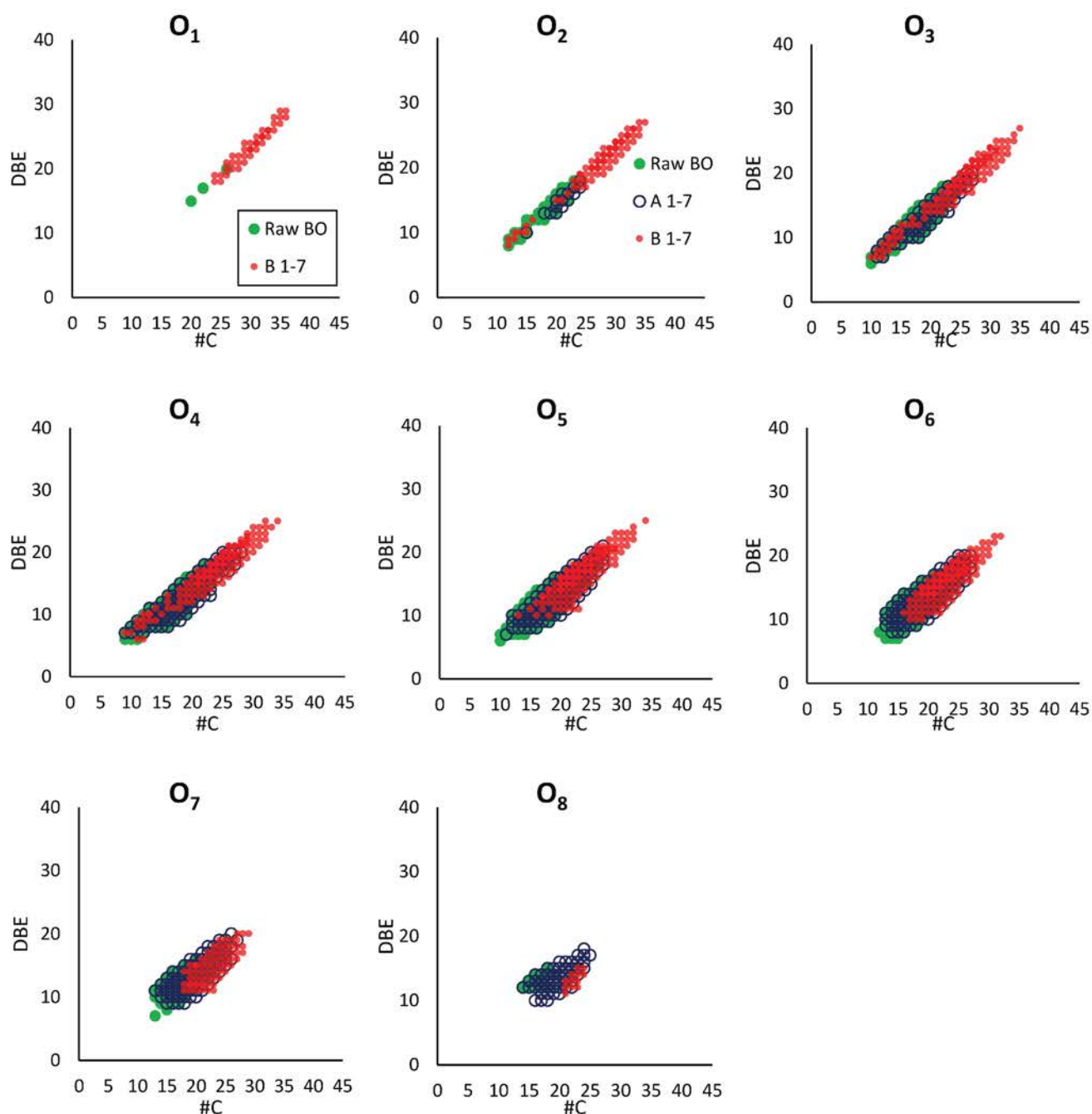


Figure V-7. Carbon number vs. DBE distribution of  $C_xH_yO_z$  compounds observed in (-) LDI raw bio-oil and upgraded A and B bio-oils from the pyrolysis of the 1-7 oak cylinders.

Finally, integrating the results obtained by petroleomic approach using different ion sources leads to reveal several effects of the zeolite catalysts on the heavy fraction of the bio-oil. A high deoxygenation effect is firstly marked by the removal of the sugarc species derived from cellulose and hemicellulose which are no more detected (notably by (+) ESI). This effect, observed for parent and hierarchical HZSM-5, is balanced by an increase of the number of compounds relative to lignin derivatives (**Figure V-2**). For these latter bio-oil components, their oxygen proportion (O/C) drops and O<sub>1</sub>-O<sub>5</sub> compounds arise, as it is particularly

highlighted by (+) APPI, (-) ESI, and (-) LDI. This demonstrates that these bio-oil components are from lignin oligomers.

The most oxygenated species ( $O_{10}$  to  $O_{13}$ ) which are in the highest mass range of the lignin derivatives disappear when a catalyst is used. Nevertheless, some of them, at high DBE value (DBE=10-25) and with a high carbon atom count ( $\#C > 15$ ), are still detected when parent zeolite is used but are no longer detected in the bio-oil upgraded with the hierarchical zeolite (**Figure V-6**).

Concerning the moderate oxygenated compounds of the lignin derivatives ( $O_6$  to  $O_9$ ), their distribution in mass and DBE are very close to those detected in the non-catalyzed pyrolysis bio-oil and differ mainly by their abundances. It has to be noted that with the hierarchical zeolite, the most unsaturated oxygen-containing compounds are less detected than with the parent zeolite (by (+) APPI). A specific behavior of the parent zeolite, and to a lesser extent of the hierarchical one, is observed for these compounds. Systematically, for a same O-class and a given #C series, the detected compounds have higher DBE values, at least, by 1 unit compared to raw bio-oil. Cyclization reaction is therefore suspected to induce this additional unsaturation.

For  $O_2$  to  $O_5$  compounds, apart from the most saturated compounds which are still detected (associated to “lipids”), the CFP bio-oils contain not only the same compounds than in the raw bio-oil but also new compounds at higher number of carbon atoms and DBE values. This is more pronounced with the hierarchical zeolite. These polyaromatic compounds containing 2, 3, 4, and 5 oxygen atoms appear to be correlated with the loss of higher mass compounds which contain more oxygen and carbon atoms and have similar or lower DBE value. It suggests that the decomposition of lignin products is promoted by the catalyst by a concomitant removing of oxygen groups and an increase of aromaticity. This effect is more noticeable when the catalyst contains mesopores. Aromatization on hierarchical zeolites is suggested to be the main deoxygenation mechanism of bio-oils. Interesting behavior is observed for  $C_xH_yO_2$  compounds with DBE=6. These  $C_{10}$ - $C_{16}$  molecules are more intensely detected by (-) ESI whatever the used catalyst (**Figure V-8**). Even if their signals in (+) APPI is less significant than in (-) ESI (on the basis that they correspond to the same compounds), they remain predominant with the catalyst B. In (+) ESI, these compounds are the most strongly detected in the bio-oil B 1-7 as  $[M+Na]^+$  ions. This suggests that these species contain either carboxylic group or two vicinal oxygen group, such as an aldol, able to interact with a sodium ion. The  $C_{10}$  ions have been also intensely detected in bio-oils by Bi *et al.*<sup>6</sup> and Tessarolo *et al.*<sup>7</sup>

They were attributed to a phenol fused with a cyclohexanone. This is in accordance with its ability to be ionized by sodium adduct. This group of O<sub>2</sub> compounds may then correspond to intermediate catalytic products involving a phenolic group and a cyclohexanone-type moiety. Nevertheless, even if the zeolite is known to promote decarboxylation, we cannot neglect the contribution of an aromatic carboxylic acid. Indeed, a very interesting study intended to rationalize the ionization efficiency of some model polar compounds with different ion sources.<sup>5</sup> They demonstrated that isomeric carboxylic acids with DBE=6 have a dramatic different ionization efficiency in negative ESI depending on the isomer structure.

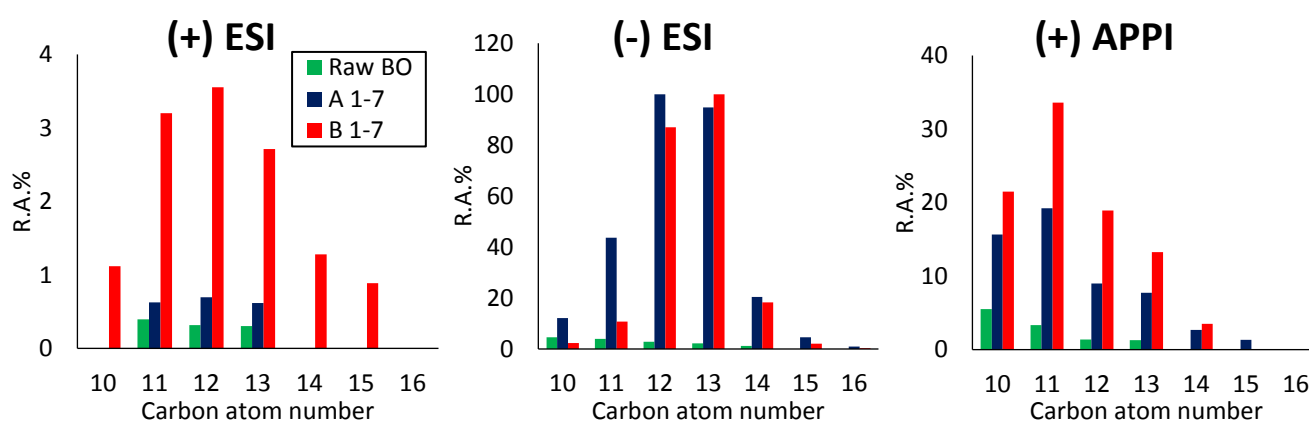


Figure V-8. Relative intensity distribution of the C<sub>x</sub>H<sub>y</sub>O<sub>2</sub> compounds with DBE=6 in positive and negative ion ESI and APPI FT-ICR MS for raw bio-oil and upgraded A and B bio-oils from the pyrolysis of the 1-7 oak cylinders.

Except a group of compounds those formulae may be linked to triterpenols or triterpenoids (area at #C from 27 to 30 and DBE=6-11), O<sub>1</sub> compounds are aromatics and polyaromatics. They are exclusively formed during catalytic pyrolysis and are systematically the lower mass compounds of the total distribution (O<sub>1</sub> by (+) APPI, (+/-) ESI, and (-) LDI in **Figure V-3, 4, 6, and 7**, respectively). This result observed for the poor oxygenated catalytic products is also extended to the pure hydrocarbons.

Apart from compounds associated to triterpene-like hydrocarbons (with one or more unsaturation, area at #C from 27 to 31 and DBE=6-13), new pure hydrocarbon products appear specifically in the composition of these catalyst bio-oils (C<sub>x</sub>H<sub>y</sub> with #C from 10 to 40 with DBE=6-34) (**Figure V-5**). They correspond to aromatic and polyaromatic hydrocarbon compounds (PAH and alkyl-PAH) whose range of degrees of aromaticity depends on the nature of catalyst. The ability of HZSM-5 catalyst to produce heavy aromatics is evidenced. The reaction network leading to their generation involves numerous routes depending on the bio-oil component.<sup>8</sup> Diels Alder reaction between light compounds, such as furans and olefins<sup>9</sup>, may conduct to large aromatics. This is what it is observed, in particularly, with the

hierarchical catalyst which leads to compounds with a broader range of aromaticity (DBE value can be as high as 34). This is one of the major differences between the parent and the hierarchical zeolite. This finding reveals that the mesopores formed by desilication can promote the formation of heavy pure hydrocarbons. The pore network in the hierarchical zeolite may enhance the transport and the release of a broader range of compounds from the zeolite crystallites. These heavy hydrocarbons could be important precursors of coke in zeolite, which is currently a problem in CFP. Indeed, it limits the activity of the catalyst by blocking the accessibility of the active acidic sites. Nevertheless, the presence of mesoporous structures in the hierarchical zeolite may reduce the formation of toxic coke<sup>10,11</sup> by promoting the transport of heavy hydrocarbons to the external surface of zeolite particles. The stability of both zeolites in regards to coke deposit is the purpose of the next section.

### *III.B. Monitoring of the catalyst lifetime*

The evolution of the composition of the bio-oils obtained by the pyrolysis of the 8 to 14 oak cylinders gives insights on the stability of both catalysts.

#### *III.B.1. Upgraded bio-oil with catalysts – 8 to 14 Oak cylinders*

The bio-oils A 8-14 and B 8-14 were analyzed by applying the same methodology used for the characterization of the raw, A 1-7, and B 1-7 bio-oils. As previously observed for the A 1-7 and B 1-7, the signal is mainly assigned to  $C_xH_yO_z$  ( $z=1-12$ ) compound class with relative abundance close to 90 % (**Table V-1**). Minor compounds corresponding to  $C_xH_yNO_z$  and  $C_xH_ySO_z$  families (from 0 to 10 % and from 1 to 9 % of the TIC, respectively) are also assigned. However the signal abundance of the  $C_xH_y$  falls to maximum 3 % (by (+) APPI). The number of signals in B-catalyzed bio-oil are nearly the same from 1-7 to 7-14 samples, an increase is observed in the bio-oil A (see by (+) ESI and (-) LDI).

The  $C_xH_yO_z$  compounds from the bio-oil A 8-14 contain up to 12 oxygen atoms against 11 for the bio-oil A 1-7 (**Figure V-1**). Overall, the intensities of the most oxygenated compounds are more significant in the sample A 8-14 whereas the less oxygenated ones are more abundant in the sample A 1-7. Furthermore, the bimodal distribution is obtained in (+) ESI with the upgraded bio-oil A 8-14 as with the raw bio-oil. This second massif is attributed to sugarc derivatives whose presence is confirmed by the (+) ESI van Krevelen diagram (**Figure V-9**).

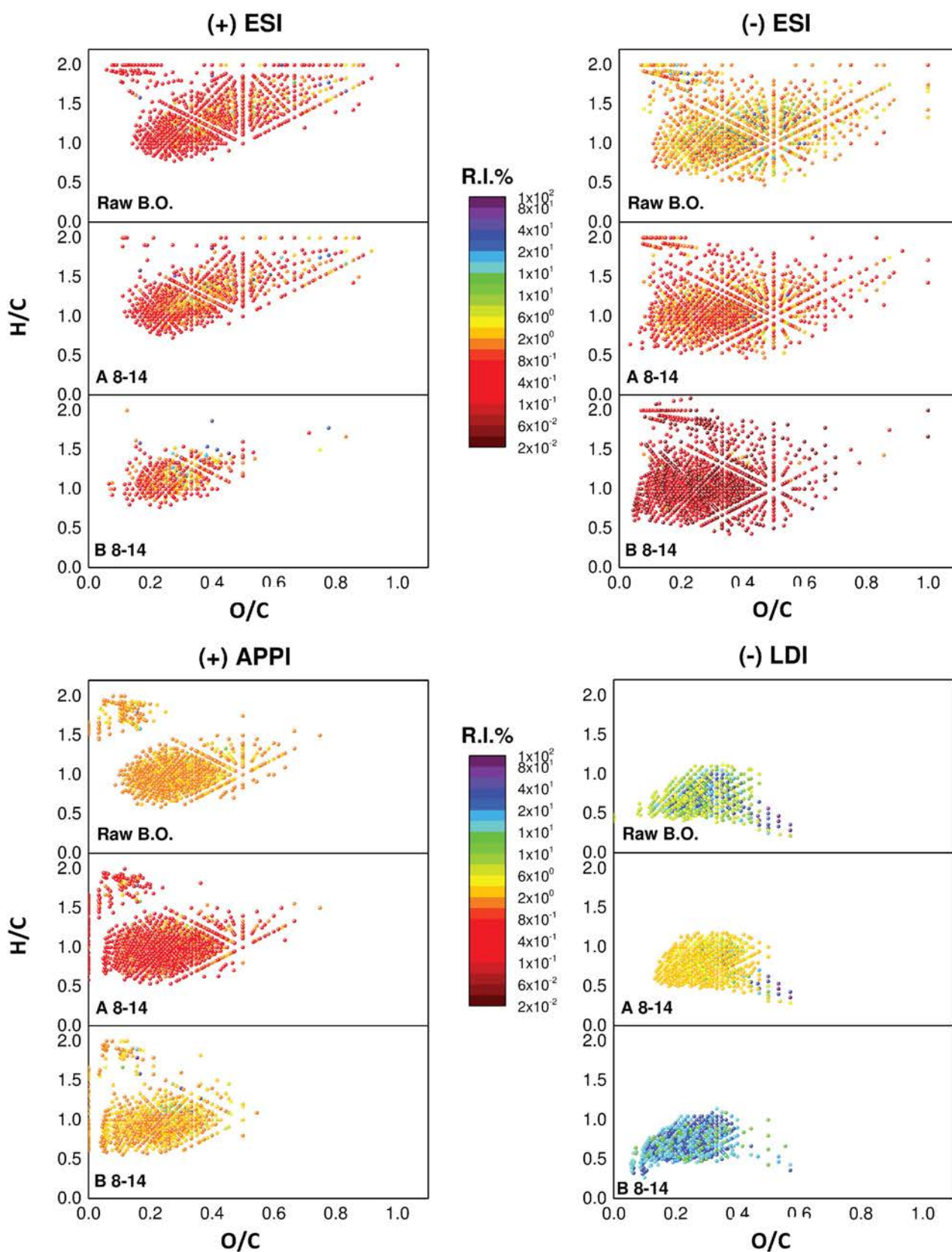


Figure V-9. Relative intensities of the  $C_xH_y$  and  $C_xH_yO_2$  compounds in raw bio-oil and A and B upgraded bio-oils from the pyrolysis of the 8 to 14 oak cylinders represented on the van Krevelen diagrams according to their H/C and O/C ratios as obtained by (+) and (-) ESI, APPI and LDI FT-ICR MS.

These biomass components are significantly more represented in this sample than in the A 1-7 one. Lipids are evidenced on the van Krevelen diagrams obtained by (-) ESI and (+) APPI analyses. Lignin derivatives are highlighted on all diagrams. Nevertheless, in (+) APPI and (-) LDI, some  $C_xH_yO_z$  formulae are plotted with a higher O/C ratio than in the bio-oil A 1-7.

For the sample B 8-14, similar observations can be done. The oxygen-poor species are more abundant in the bio-oil B 1-7 whereas in the bio-oil B 8-14, the relative abundances of the most oxygenated species are higher (**Figure V-1**). However, the range is not different between the two samples which is attested by the van Krevelen diagrams (**Figure V-9**). Indeed, the plotted  $C_xH_yO_z$  compounds do not present a higher O/C ratio. These diagrams are very close to those obtained with the bio-oil B 1-7. Thus, lipids are highlighted in (-) ESI and (+) APPI and lignin derivatives, in all measurements. Sugarc components are still not detected in this sample which demonstrates that the mesoporous zeolite is still active for sugarc compounds conversion even at the high biomass-to-catalyst ratios.

Thorough comparison of the catalytic response, displaying the DBE vs. the number of carbon atoms, clearly evidences the deactivation of parent HZSM-5 and the sustainable efficiency of the hierarchical one (**Figure V-10, 11, 12, and 13**). Bio-oil produced by CFP with HZSM-5 catalyst highlights nearly the same compounds as those observed in the raw bio-oil whatever the ionization and detection mode. Inversely, CFP with hierarchical catalyst still evidences a loss of numerous highly oxygenated compounds as it was observed for the first 1 to 7 wood injections. Nevertheless, pure hydrocarbons are less abundant and their unsaturation degree is less extended (DBE max = 18, **Figure V-5**).

The diminution of the effectiveness after several pyrolysis runs also illustrates the deactivation of the parent zeolite due to coke deposit. The carbon deposition occurring in the micropores may block the access of the bio-oil compounds to acidic sites for deoxygenation reactions.<sup>11,12</sup> Nevertheless, some active sites are still accessible even after coking for hierarchical zeolite whose mesoporous structure balances the limitation of the microporous diffusion.<sup>13</sup> The consequence is a more stable activity of hierarchical catalyst to produce compounds with higher aromaticity even at high biomass-to-catalyst ratio.

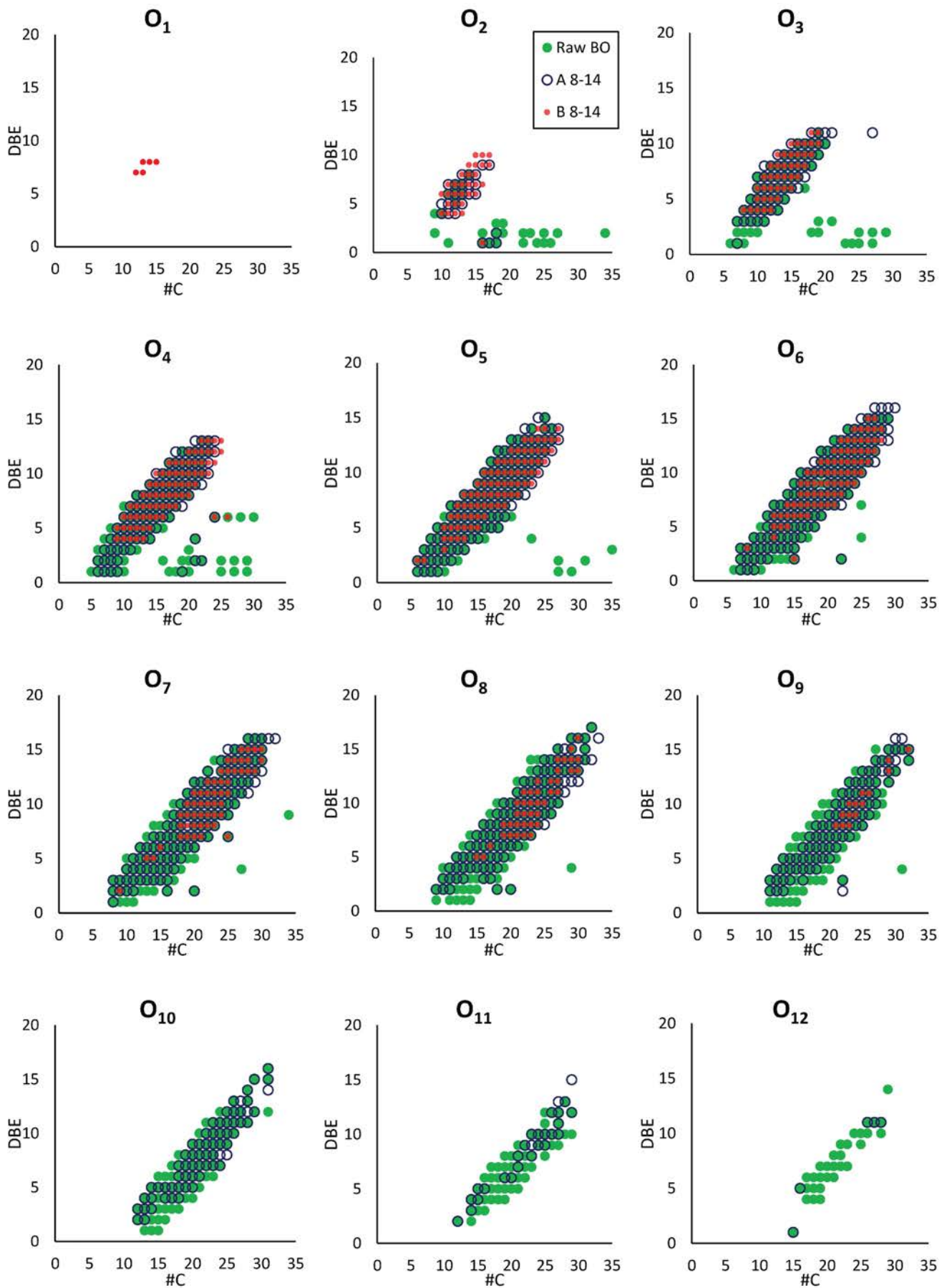


Figure V-10. Carbon number vs. DBE distribution of C<sub>x</sub>H<sub>y</sub>O<sub>z</sub> compounds observed in (+) ESI for raw bio-oil and A and B upgraded bio-oils from the pyrolysis of the 8 to 14 oak cylinders.



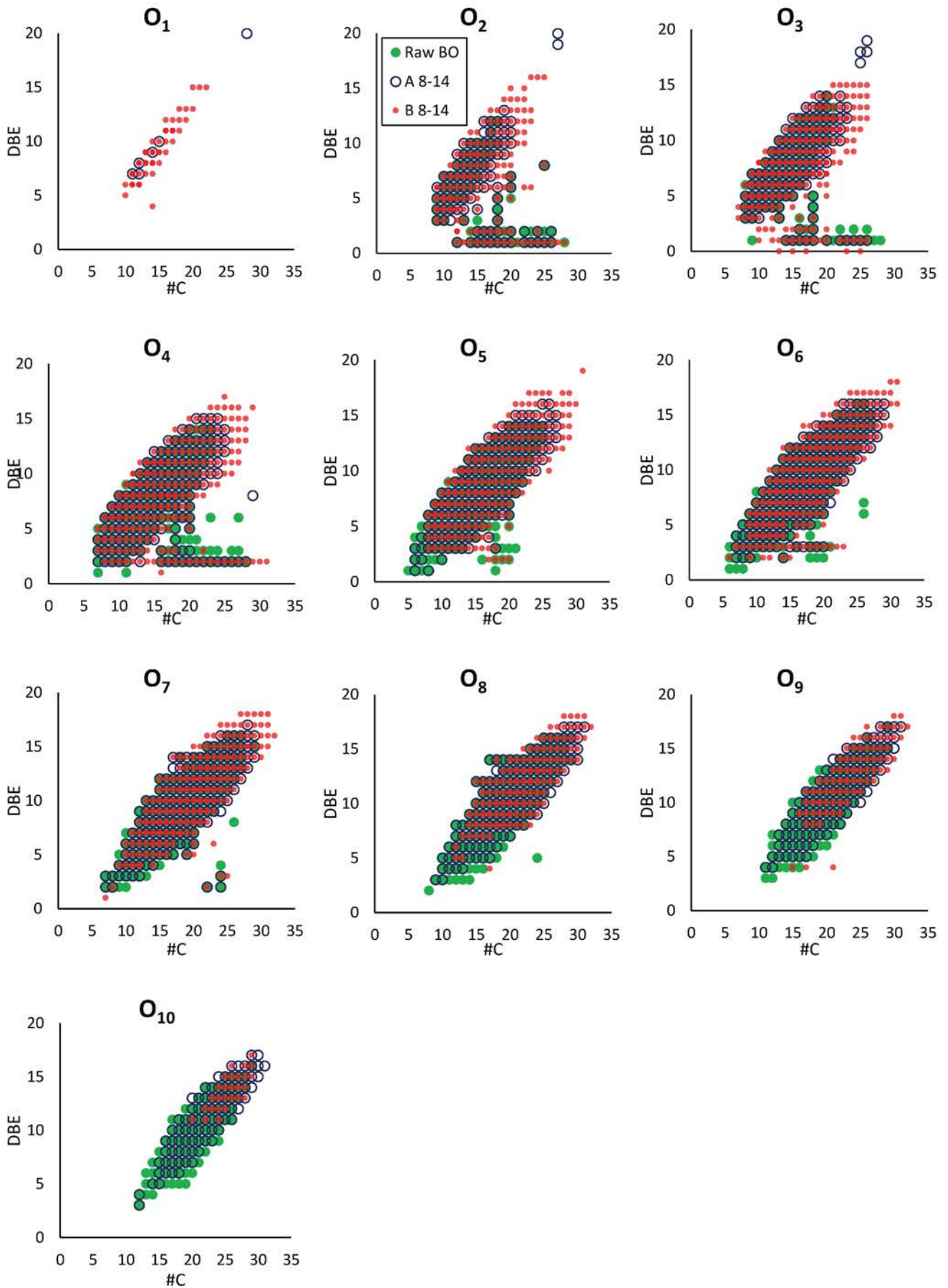


Figure V-11. Carbon number vs. DBE distribution of  $C_xH_yO_z$  compounds observed in (-) ESI for raw bio-oil and A and B upgraded bio-oils from the pyrolysis of the 8 to 14 oak cylinders.

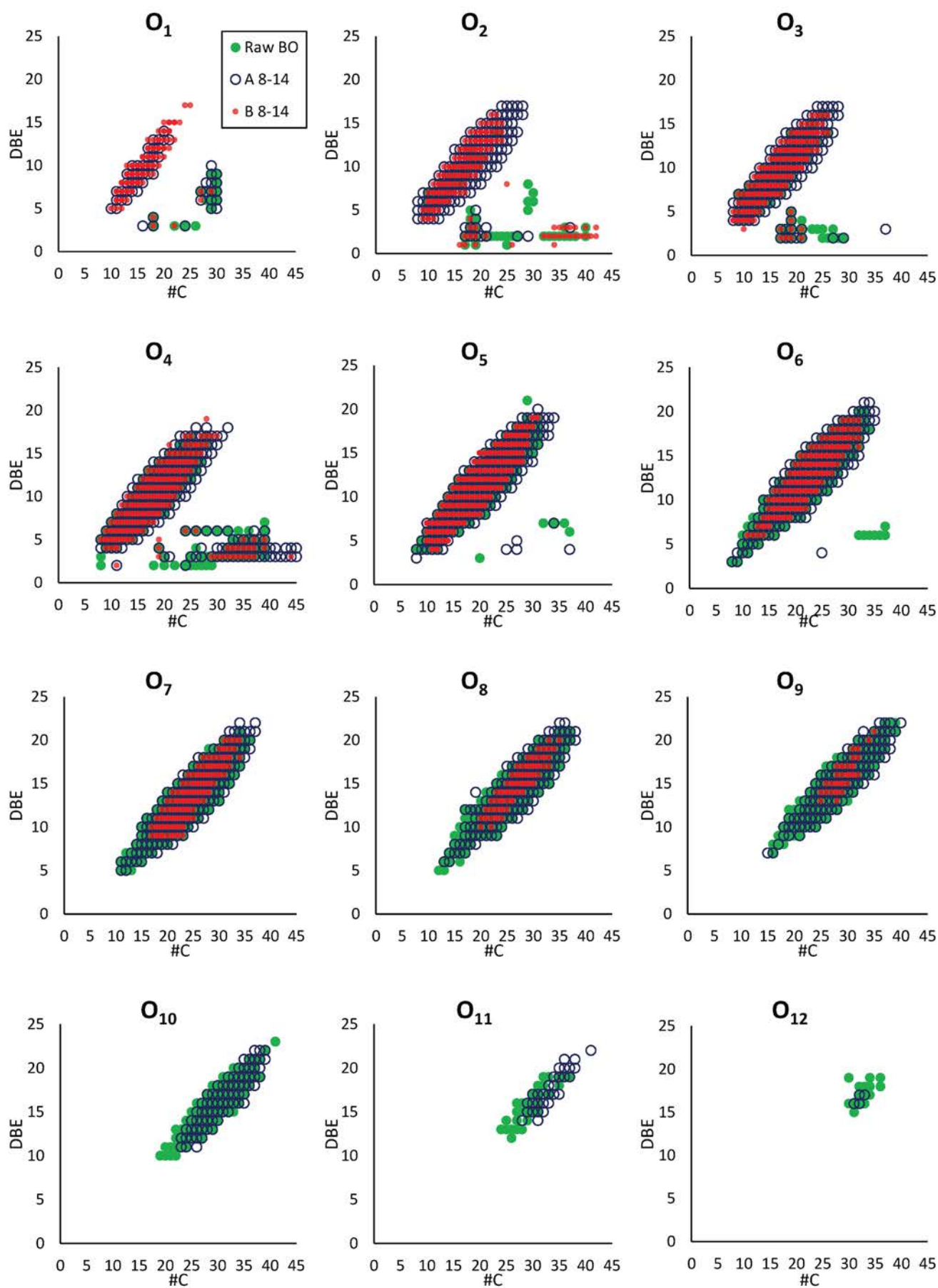


Figure V-12. Carbon number vs. DBE distribution of C<sub>x</sub>H<sub>y</sub>O<sub>z</sub> compounds observed in (+) APPI for raw bio-oil and A and B upgraded bio-oils from the pyrolysis of the 8 to 14 oak cylinders.

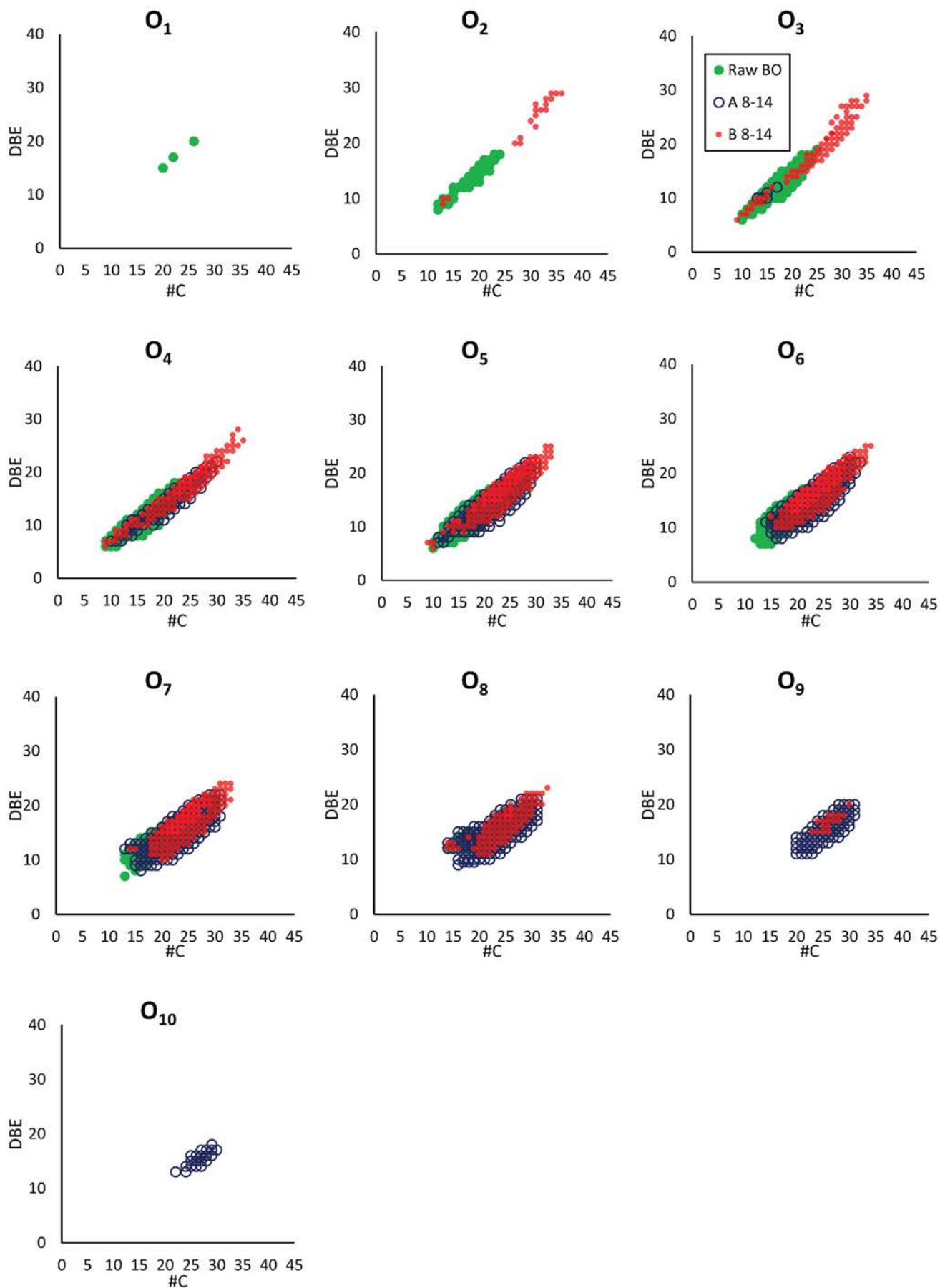


Figure V-13. Carbon number vs. DBE distribution of C<sub>x</sub>H<sub>y</sub>O<sub>z</sub> compounds observed in (-) LDI for raw bio-oil and A and B upgraded bio-oils from the pyrolysis of the 8 to 14 oak cylinders.

## IV. Conclusion

In this chapter, compositional changes between raw and upgraded bio-oil were observed by petroleomic approach with ESI, APPI, and LDI FT-ICR MS. This non-targeted analysis is a quick way to have a global description of the samples. It enabled to observe the deoxygenation efficiency which is particularly evident for sugarcane compounds and some oxygen-rich lignin derivatives during CFP with zeolite. Nevertheless, a major part of the pyrolytic lignin is refractory to deoxygenation. Pure heavy hydrocarbons are generated, especially by the hierarchical zeolite (even after more than 7 pyrolysis experiments). It is clearly demonstrated that the parent zeolite has few effects on the heavy products compared to the hierarchical one. These products exhibit a poor interaction with the parent catalyst because they cannot access to the micropores of the parent zeolite. Furthermore, the parent HZSM-5 zeolite becomes inefficient by deactivation after the first uses. Hierarchical zeolite still demonstrates deoxygenation efficiency even after coke formation. Big oligomers could be important precursor of coke in zeolite but they may also incur depolymerization/cracking to produce lighter compounds. The mesoporosity of the hierarchical zeolite seems to enhance the conversion of these large oligomers.

## V. References

1. Hertzog, J. *et al.* Combination of electrospray ionization, atmospheric pressure photoionization and laser desorption ionization Fourier transform ion cyclotron resonance mass spectrometry for the investigation of complex mixtures - Application to the petroleomic analysis of bio-oils. *Anal. Chim. Acta* **969**, 26–34 (2017).
2. Miettinen, I. *et al.* Characterization of fast pyrolysis oil from short-rotation willow by high-resolution Fourier transform ion cyclotron resonance mass spectrometry. *Fuel* **207**, 189–197 (2017).
3. Staš, M., Chudoba, J., Kubicka, D., Blazek, J. & Pospíšil, M. Petroleomic Characterization of Pyrolysis Bio-oils: A Review. *Energy Fuels* (2017). doi:10.1021/acs.energyfuels.7b00826
4. Hertzog, J., Carré, V., Le Brech, Y., Dufour, A. & Aubriet, F. Toward Controlled Ionization Conditions for ESI-FT-ICR-MS Analysis of Bio-Oils from Lignocellulosic Material. *Energy Fuels* **30**, 5729–5739 (2016).
5. Pudenzi, M. A. & Eberlin, M. N. Assessing Relative Electrospray Ionization, Atmospheric Pressure Photoionization, Atmospheric Pressure Chemical Ionization, and Atmospheric Pressure Photo- and Chemical Ionization Efficiencies in Mass Spectrometry Petroleomic Analysis via Pools and Pairs of Selected Polar Compound Standards. *Energy Fuels* **30**, 7125–7133 (2016).
6. Bi, Z. *et al.* Biocrude from pretreated sorghum bagasse through catalytic hydrothermal liquefaction. *Fuel* **188**, 112–120 (2017).
7. Tessarolo, N. S. *et al.* Characterization of thermal and catalytic pyrolysis bio-oils by high-resolution techniques: <sup>1</sup>H NMR, GC × GC-TOFMS and FT-ICR MS. *J. Anal. Appl. Pyrolysis* **117**, 257–267 (2016).
8. Puertolas, B. *et al.* Porosity-Acidity Interplay in Hierarchical ZSM-5 Zeolites for Pyrolysis Oil Valorization to Aromatics. *Chemsuschem* **8**, 3283–3293 (2015).
9. Cheng, Y.-T. & Huber, G. W. Production of targeted aromatics by using Diels-Alder classes of reactions with furans and olefins over ZSM-5. *Green Chem.* **14**, 3114–3125 (2012).
10. Veses, A. *et al.* Promoting Deoxygenation of Bio-Oil by Metal-Loaded Hierarchical ZSM-5 Zeolites. *Acs Sustain. Chem. Eng.* **4**, 1653–1660 (2016).
11. Jia, L. *et al.* Catalytic fast pyrolysis of biomass: superior selectivity of hierarchical zeolite to aromatics. *Green Chem.* (2017). doi:10.1039/C7GC02309J
12. Gayubo, A. G., Valle, B., Aguayo, A. T., Olazar, M. & Bilbao, J. Attenuation of Catalyst Deactivation by Cofeeding Methanol for Enhancing the Valorisation of Crude Bio-oil. *Energy Fuels* **23**, 4129–4136 (2009).
13. Hoff, T. C. *et al.* Decoupling the Role of External Mass Transfer and Intracrystalline Pore Diffusion on the Selectivity of HZSM-5 for the Catalytic Fast Pyrolysis of Biomass. *ACS Sustain. Chem. Eng.* **5**, 8766–8776 (2017).



---

## *General conclusion*

---





The aim of this PhD thesis was to develop analytical methods to obtain the as detailed as possible description of bio-oils produced by the pyrolysis of lignocellulosic biomass. The extensive characterization of such complex materials is required in order to improve the pyrolysis and the upgrading catalysis processes. The experiments were carried out by FT-ICR mass spectrometry with different ionization sources to evidence the bio-oil components on a broad range of polarity and mass.

First of all, an ESI FT-ICR MS method was established in both negative and positive ion detection modes. The influence of some ionization parameters on the detected features has been investigated. Thus, solvents with different water/methanol ratios were used and the influence of the probe temperature was studied. An increase of the water amount is responsible of an increase of the signal related to the cellulose and hemicellulose derived species and a decrease of the total number of assigned signals, whatever the used probe temperature. For bio-oil solutions with a high methanol content, the number of assignments is lower when high probe temperature is used. Consequently, the more relevant experimental conditions were found to be a probe temperature of 75 °C and the infusion of a pure methanolic bio-oil solution.

The main part of the optimization of the ESI petroleomic approach of bio-oil was the investigation of the effect of dopant on the obtained distribution of compound classes. Experiments were conducted without dopant in (+) and (-) ESI. For (-) ESI, the bio-oil solution was doped with formic acid or ammonium hydroxide. The mass spectra achieved with these conditions demonstrated an ionization enhancement of the minor nitrogen and sulfur bio-oil components. The features obtained by (-) ESI without dopant are more in agreement with the bio-oil elemental analysis and the weight percentages of carbon, hydrogen, and oxygen that constitute close to 98 % of a bio-oil. Indeed, 90 % of the signal is related to  $C_xH_yO_z$  compounds when no dopant is used. According to the van Krevelen diagrams of the  $C_xH_yO_z$  species the detected compounds are related to lipids and lignin derivatives. In (+) ESI, ammonium hydroxide, formic acid, ammonium acetate, and different alkaline acetates were investigated. The analyses performed without dopant evidenced a poor repeatability. In contrast, the addition of a dopant, which allows a better control of the ionization processes, ensures to obtain repeatable measurements. Among the different investigated dopants, the alkaline acetates are the most suited to achieve a bio-oil description which reflects the elemental

composition of the bio-oil. Moreover, the van Krevelen diagram demonstrated that the identified  $C_xH_yO_z$  species (90 % of the signal) are related to the pyrolysis of lignin, sugarc compounds, and lipids.

An additional study evidences the formation of imines. Indeed, the highly reactive carbonyl compounds react with ammonia and, consequently, biases the description achieved by ESI petroleomic analysis. This is, on our knowledge, the first time that the deleterious behavior of ammonium hydroxide, typically added to promote deprotonation, is evidenced. Such behavior is partially responsible of the significant detection of  $C_xH_yN_nO_z$  ions by ESI-MS of bio-oils. It was clearly demonstrated that the carbonyl (aldehyde and ketone) compounds of the bio-oil react with the amine to yield imines. The formation of such imines was confirmed by additional Ion-Trap and  $^{13}C$  NMR measurements with different amines (aniline, 3-chloroaniline, and  $NH_4OH$ ) and model aldehydes and ketones. This drawback was advantageously used to highlight carbonyl compounds in bio-oils.

These methods have been developed with a 9.4 T FT-ICR mass spectrometer. Similar experiments were conducted with a 12 T FT-ICR mass spectrometer on the same bio-oils (with sodium acetate in (+) ESI and without dopant in (-) ESI). Identical bio-oil composition description and oxygen class distributions were obtained, which demonstrates the robustness and the reproducibility of the developed methods. ESI is well-adapted for the detection of the polar to mid-polar compounds, which represents only a fraction of the bio-oil components. More suited ionization sources to poor polar and apolar compounds have also been investigated.

Thus, the second part of this study was relative to the establishment of new methodologies for the petroleomic analysis of bio-oils by LDI and APPI FT-ICR MS. In LDI FT-ICR MS, the laser fluence was optimized to avoid fragmentation and recombination phenomena. MALDI experiments with different matrixes were also conducted. This comparison ensures to establish that pure LDI is the most suited approach. At least, in this study, the MALDI analyses, with these experimental conditions, do not improve the quality of the bio-oil description. On the contrary, MALDI experiments introduce an analytical bias by promoting the ionization of minor nitrogen bio-oil components. The oxygenated species, also detected by LDI, are linked to lignin derivatives. Some sugarc derivatives were observed in (+) LDI as  $[M+Na]^+$  cations.

The optimization of the APPI measurement demonstrated that the commonly used dopants (toluene and acetone) do not ensure an improvement of the sensitivity. The result is, in fact, the opposite of what it is expected. As a consequence, the positive and negative ion APPI analyses were carried without dopant. Whatever the ion detection mode, the APPI measurement leads to the assignment of 90 % of the TIC to  $C_xH_yO_z$  compounds. These species are lignin derivatives and, in a lesser extent, lipids.

The complementarity of the three FT-ICR MS petroleomic approaches has been demonstrated. Indeed, each ionization source ensures the detection of specific compounds. Interestingly, only a restricted fraction of bio-oil components are detectable by the three ionization techniques. The ESI is well-adapted to ionize the cellulose and hemicellulose derived compounds as they are polar species. Both LDI and APPI are less sensitive to the compound polarity. Thus, the most unsaturated lignin derivatives are detectable by each of them. In order to reach the most extensive bio-oil composition, the combination of ESI, LDI, and APPI FT-ICR MS in both ion detection modes is required.

This analytical strategy was applied to investigate upgraded bio-oils which have been obtained by treatment on two different zeolite catalysts. These catalysts are well suited to perform deoxygenation and cracking treatments. It was demonstrated that ESI, LDI, and APPI analyses, yielded complementary information on the efficiency of the catalytic treatment. The compounds produced by deoxygenation and cracking are observed by APPI and LDI, and, in a lesser extent, by ESI. The comparison of the van Krevelen diagrams of the  $C_xH_yO_z$  compounds evidenced by ESI FT-ICR MS, before and after catalytic treatment with both catalysts, demonstrates the elimination of the sugarc derivatives and, consequently, their sensitivity towards the applied catalytic treatment. Pure hydrocarbons, resulting from deoxygenation upgrading, are evidenced by APPI.

The study performed during these PhD works clearly attested the necessity of the non-targeted analyses, with different ionization sources, to achieve the extensive description of the pyrolysis bio-oil products. It is necessary to improve the pyrolysis process and to well adapt the upgrading treatment. Indeed, these complex mixtures, which may lead to second generation biofuels, have to be accurately described. FT-ICR MS petroleomic approaches are, in that way, powerful tools.

Some complementary analyses have to be considered to obtain additional information on the bio-oil composition and to try to overcome some of the drawbacks of the used non-targeted approach. The ion mobility may be used to distinguish the isomeric compounds which appear at the same  $m/z$  in FT-ICR MS. Some experiments are actually in progress in collaboration with the COBRA laboratory of the University of Rouen. Structural information have also to be obtained by tandem mass spectrometry. Different strategies may be considered due to the fact that it is impossible with FT-ICR MS to efficiently isolate a parent ion whose  $m/z$  differ from the neighboring ion by some  $m/z$ . The first one is to separate the bio-oil component by chromatography and to perform  $MS^n$  experiment. In that case, high resolution is not required and low resolution mass spectrometers may be used. The main advantage of this approach is the ability to perform  $MS^n$  with  $n > 2$  and to assess the possible quantitation according to the TIC. Nevertheless, the huge number of features will make this approach difficult and long. An alternative method, but limited to  $MS^2$ , is the so-called 2D FT-ICR MS analysis. In that case, the  $MS/MS$  experiment of all features of 1D FT-ICR mass spectrum may be conducted in few hours. Nevertheless, huge data treatment is required and big data are generated. First preliminary experiments have been performed with the Professor Peter O'Connor at the University of Warwick. Unfortunately, no exploitable results are yet available. Finally, the approach described in the Chapter III to focus non-targeted approach to specific class of components has to be deeper examined for validation, and alternative dopants have to be defined to evidence other classes of compounds.

## Tables of figures

<b>Figure I-1.</b>	Cycle of the CO <sub>2</sub> for the petroleum and biomass based fuels.	8
<b>Figure I-2.</b>	Hierarchical and structural compositions of biomass from the cell membrane to the molecular level. The main components are cellulose, hemicellulose, and lignin.	9
<b>Figure I-3.</b>	Sucrose molecule.	12
<b>Figure I-4.</b>	Principle of the enzymatic hydrolysis of starch	13
<b>Figure I-5.</b>	Overall transesterification reaction from triglyceride and alcohol to produce alkyl-fatty esters (biodiesel) and glycerol.	14
<b>Figure I-6.</b>	Reactional scheme of the simultaneous solid acid catalyzed esterification and transesterification.	15
<b>Figure I-7.</b>	Conversion processes of lignocellulosic biomass into liquid biofuels (green arrows refer to biochemical routes, red arrows to thermochemical routes, and blue arrows to catalytic routes).	18
<b>Figure I-8.</b>	Scheme of a fluidized bed pyrolysis system.	22
<b>Figure I-9.</b>	Yielded products by biomass hydrothermal liquefaction and possible applications.	24
<b>Figure I-10.</b>	Pyrolysis bio-oil applications	25
<b>Figure I-11.</b>	Upgrading pathways for the conversion of the biomass and pyrolysis bio-oil into biofuels and chemicals.	27
<b>Figure I-12.</b>	Representation of the structure of the ZSM-5 catalyst.	28
<b>Figure I-13.</b>	Representative reactions associated with catalytic bio-oil upgrading.	29
<b>Figure I-14.</b>	Upgrading pathways involved in the aqueous phase reforming process.	31
<b>Figure I-15.</b>	Fractionation scheme with water-based LLE of bio-oil.	34
<b>Figure I-16.</b>	Derivatization reactions of various hydroxyl functional groups with TMDP. Chemical shifts and assignments of the products in <sup>31</sup> P NMR.	41
<b>Figure I-17.</b>	Derivatization reaction of carbonyl group with 4-(trifluoromethyl)phenylhydrazine.	41
<b>Figure I-18.</b>	Chromatograms achieved in GC (top) and 2DGC (bottom).	44
<b>Figure I-19.</b>	Scheme of the GCxGC (heart-cutting)/MS-FID-FID device.	45
<b>Figure I-20.</b>	Pie chart representing the typical portions of the bio-oil fractions.	46
<b>Figure I-21.</b>	Van Krevelen diagram with some major biomolecular components areas.	51
<b>Figure I-22.</b>	Oxygen class distribution for each bio-oil analyzed by (-) ESI FT-ICR MS.	59
<b>Figure I-23.</b>	Biomass fast pyrolysis pilot for bio-oil (7) and light fraction bio-oil (9) reservoirs.	60
<b>Figure I-24.</b>	Distribution of C <sub>x</sub> H <sub>y</sub> O <sub>z</sub> compounds in respect with oxygen atom count from the oily and aqueous phases analyzed by (-) ESI FT-ICR MS.	62
<b>Figure I-25.</b>	Color-mapped van Krevelen diagrams of C <sub>x</sub> H <sub>y</sub> O <sub>z</sub> compounds in the oily and aqueous phases analyzed by (-) ESI FT-ICR MS.	62
<b>Figure I-26.</b>	Solvent fractionation process.	64
<b>Figure I-27.</b>	Solvent fractionation procedure for cornstalk bio-oil obtained by methanolysis. PE=Petroleum ether, EOE=ethoxyethane, and CDS=carbon disulphide.	65
<b>Figure I-28.</b>	Van Krevelen diagram of C <sub>x</sub> H <sub>y</sub> O <sub>z</sub> compounds assigned by (-) ESI FT-ICR MS analysis of the raw pyrolysis bio-oil. Red lines represent chemical reactions: methoxylation/demethoxylation (A), hydrogenation/dehydrogenation (B), hydration/dehydration (A/C), hydrodeoxygenation (D), decarboxylation (E), decarbonylation (F), and de-ethoxyl (G).	67
<b>Figure I-29.</b>	Heteroatom class distributions derived from the (+) ESI (top left), (-) ESI (top right), and (+) APPI (bottom) mass spectra in respect with the different samples.	71
<b>Figure I-30.</b>	Relative abundances in respect with the DBE value of the compound classes identified in bio-oil by (+) APPI FT-ICR MS.	72
<b>Figure I-31.</b>	Oxygen (top) and DBE (bottom) distributions for the C <sub>x</sub> H <sub>y</sub> O <sub>z</sub> compounds of the raw lignin pyrolysis bio-oil analyzed in ESI and LDI FT-ICR MS in negative ion mode.	75

<b>Figure II-1.</b>	Scheme of the microfluidized bed reactor and setup used to collect bio-oils.	99
<b>Figure II-2.</b>	Scanning electron (top) and transmission electron (bottom) microscopy images of parent (left) and hierarchical (right) zeolites before pyrolysis experiments (From the publication “Catalytic fast pyrolysis of biomass: superior selectivity of hierarchical zeolite to aromatics” of Jia <i>et al.</i> , Green Chemistry, accepted).	100
<b>Figure II-3.</b>	Shape of the solvent at the outlet capillary according to the value of the applied voltage.	103
<b>Figure II-4.</b>	Gas-phase ion formation in the ESI source, in positive detection mode.	103
<b>Figure II-5.</b>	Ion evaporation (IEM) and charge-residue (CRM) models for the formation of ions in (+) ESI.	104
<b>Figure II-6.</b>	Micromass ESI source with Z-spray configuration (Ion Spec).	107
<b>Figure II-7.</b>	Characteristic length scales for a laser-excited surface region in the vicinity of an absorbing chromophore. $\alpha$ : linear absorption coefficient of chromophore; $d_{\text{més0}}$ : characteristic mesoscopic length scale observed in laser ablation; $d_{\text{micro}}$ : characteristic microscopic length scale observed in laser desorption.	109
<b>Figure II-8.</b>	Plasma formation by laser desorption on a solid surface.	109
<b>Figure II-9.</b>	Pathways proposed for the formation of singly charged ions from clusters. a. Positive ions, b. Negative ion.	114
<b>Figure II-10.</b>	Chemical representations of 2,5-Dihydroxybenzoic acid (a) and 1,8-Bis(dimethylamino)naphthalene (b).	115
<b>Figure II-11.</b>	Photograph of the target plate with 12x16 pattern of spots.	115
<b>Figure II-12.</b>	Ionization energies of typical compounds and photon energies of UV lamps used in APPI.	116
<b>Figure II-13.</b>	Diagram of the APPI source with the UV lamp (Agilent).	119
<b>Figure II-14.</b>	Cyclotron motion of an ion with a charge +q in a magnetic field $B_0$ subjected to both centrifugal and magnetic forces. v is the ion velocity and r the radius of the ion orbit.	118
<b>Figure II-15.</b>	Correlation of the ion orbital radius r with the mass-to-charge ratio $m/z$ for different values of magnetic field $B_0$ .	121
<b>Figure II-16.</b>	Translational energy E versus ion orbital radius r at different magnetic field strengths for an ion of $m/z=100$ .	121
<b>Figure II-17.</b>	Ion Spec ICR analyzer cell with the trapping plates and potential (here for storing positive ions).	122
<b>Figure II-18.</b>	Ion motion in a ICR cell. Magnetron motion (dashed), magnetron + trapping motion (dotted), and the resulting global motion (solid).	124
<b>Figure II-19.</b>	Excitation of the ion cloud in the ICR cell (on the left) and image current detection (on the right). On the left, the ion package has an incoherent cyclotron orbital motion. On the right, after application of an RF electric field, a coherent and detectable motion is obtained.	124
<b>Figure II-20.</b>	Time-domain (left) and frequency-domain (right) waveforms with (a) and (b) rectangular pulses, (c) chirp excitation, and (d) SWIFT excitation.	127
<b>Figure II-21.</b>	Fourier transform on different time-domain waveforms. (a) Step (rectangular) function converted to $\text{sinc}(x)$ , (b) entire FID transient obtained with one RF excitation gives a Lorentzian curve, and (c) the truncated transient product of a) x b) that yields Lorentzian curve with sidelobes “wiggles”.	129
<b>Figure II-22.</b>	Blackman-Harris apodization function applied to the time-domain waveform for one excitation RF and the corresponding frequency-domain peak yielded after Fourier transform.	129
<b>Figure II-23.</b>	Main steps for generation of a FT-ICR mass spectrum (from Ion Spec).	130
<b>Figure II-24.</b>	Ion Spec FT-ICR mass spectrometer equipped with two external sources. LDI (on the left) and ESI (on the right).	131
<b>Figure II-25.</b>	Schematic interface of the FT-ICR MS (here with the ESI source).	132
<b>Figure II-26.</b>	Experiment setup with overview of the different voltages and timing events occurring during FT-ICR MS experiment – Omega Software.	132
<b>Figure II-27.</b>	Scheme of the IonSpec ProMALDI FTMS.	134

<b>Figure II-28.</b>	Mass error (in ppm) vs. $m/z$ for $C_xH_yO_z$ compounds of a Oak pyrolysis bio-oil analyzed in (-) ESI FT-ICR MS.	135
<b>Figure II-29.</b>	(-) ESI FT-ICR mass spectrum of Miscanthus pyrolysis bio-oil. Five signal are attributed on the inset corresponding to the nominal mass 373. ① $C_{19}H_{17}O_8^-$ ( $m/z$ 373.0918; error 0.30 ppm); ② $C_{23}H_{17}O_5^-$ ( $m/z$ 373.1081; error 0.07 ppm); ③ $C_{20}H_{21}O_7^-$ ( $m/z$ 373.1288; error 0.44 ppm); ④ $C_{24}H_{21}O_4^-$ ( $m/z$ 373.1444; error 0.25 ppm); ⑤ $C_{21}H_{25}O_6^-$ ( $m/z$ 373.1655; error 0.26 ppm)	136
<b>Figure II-30.</b>	Global composition description of an Oak bio-oil by (-) ESI FT-ICR MS analysis (Pie chart). Oxygenated compound distribution in respect with the oxygen atom count (top histogram) and DBE distribution for $C_xH_yO_6$ compounds (bottom histogram).	137
<b>Figure II-31.</b>	Van Krevelen diagram with some major biomolecular components grouped in the different areas.	138
<b>Figure II-32.</b>	Kendrick's map of $C_xH_yO_6$ compound family from Oak pyrolysis bio-oil analyzed in (-) LDI FT-ICR MS.	139
<b>Figure II-33.</b>	Illustration of the different operations of a linear RF ion trap at constant DC offset (+ 5 V) for positive ions. (a) Ion accumulation with application of a voltage at the rear trapping plate. (b) Ion storage with both trapping potentials up. (c) Ion axial ejection after application of an exit potential at the rear trapping plate.	140
<b>Figure II-34.</b>	Schematic representation of the Thermo Scientific LTQ Velos mass spectrometer with the dual-pressure linear ion trap.	141
<b>Figure III-1.</b>	Comparison of the $C_xH_yNaO_z$ distribution in respect with the oxygen atom count obtained for identical water:methanol ratios for capillary temperatures at 75 and 110 °C.	150
<b>Figure III-2.</b>	Cumulative S/N ratios of lignin and sugarc derivatives obtained for different methanol:water ratios at 75 and 110 °C.	151
<b>Figure III-3.</b>	Distribution of the $C_xH_yNaO_z$ compounds in respect with the oxygen atom count according to the water:methanol ratios, at 75 °C	153
<b>Figure III-4.</b>	Van Krevelen diagrams of the $C_xH_yNaO_z$ species of the oak bio-oil assigned after (+) ESI FT-ICR MS analysis for different water:methanol ratios at 75 °C	154
<b>Figure III-5.</b>	Mass spectrum of the pyrolysis Miscanthus bio-oil obtained in (-) ESI FT-ICR MS.	157
<b>Figure III-6.</b>	Carbon number vs. DBE value distribution of $C_xH_yO_z$ ions observed in (-) ESI without (solid blue circle) and with $NH_4OH$ (open green circle).	158
<b>Figure III-7.</b>	(a) Distribution of the $C_xH_yO_z$ species in respect with oxygen atom count and (b) relative abundance vs. DBE value distributions of the $C_xH_yO_5$ compounds achieved from analyses in (-) ESI FT-ICR MS with the Miscanthus bio-oil without dopant (green) and with $NH_4OH$ (blue).	159
<b>Figure III-8.</b>	DBE vs. nominal mass distribution of $C_xH_yNO_z$ (open green circle) and $C_xH_yN_2O_z$ (solid blue circle) species of the Miscanthus bio-oil observed in (-) ESI FT-ICR MS with $NH_4OH$ .	160
<b>Figure III-9.</b>	(a) Mass spectra obtained by (+) ESI FT-ICR-MS analysis of a pyrolysis Miscanthus bio-oil. (b) Relative distribution of $C_xH_yO_z$ compounds detected in positive ion mode for Analysis I and II. (c) Average relative distribution of $C_xH_yO_z$ compounds detected in positive ion mode for Analysis I and II without dopant. Error bar is relative to the standard deviation for the two considered measurements.	162
<b>Figure III-10.</b>	(a) Distribution of the $C_xH_yNaO_z$ species in respect with the oxygen atom count by (+) ESI FT-ICR MS analysis of Miscanthus bio-oil with sodium acetate. (b) Average relative distribution of the $C_xH_yNaO_z$ compounds from Analysis I and Analysis II. Error bar is relative to the standard deviation for the two considered measurements.	164
<b>Figure III-11.</b>	Distribution of the $C_xH_yO_z$ compounds in respect with the oxygen atom count obtained by (+) ESI FT-ICR MS analysis of a Miscanthus bio-oil with lithium (dark blue), sodium (light blue), and potassium (green) acetate.	165

<b>Figure III-12.</b>	Van Krevelen diagrams of $[C_xH_yNO_2 + H]^+$ and $[C_xH_yN_2O_2 + H]^+$ ions detected in (+) ESI FT-ICR MS without dopant for the Analysis II (solid blue circle), with formic acid (open green circle), ammonium acetate (solid green circle), and ammonium hydroxide (open blue circle).	167
<b>Figure III-13.</b>	Relative distribution of the heteroatom classes detected in (+) ESI FT-ICR MS with addition of ammonium hydroxide (dark blue) and ammonium acetate (light blue) in respect with (a) the number of nitrogen atoms for the $C_xH_yN_nO_z$ compounds and (b) the number of oxygen atoms for the and $C_xH_yO_z$ compounds.	168
<b>Figure III-14.</b>	(a) Relative distributions in respect with the oxygen atom count and (b) DBE vs. nominal mass plot of the $[C_xH_yO_z + H]^+$ (light blue) and $[C_xH_yO_z + Na]^+$ (dark blue) ions. (c) Relative distributions of the $[C_xH_yO_5 + H]^+$ (light blue) and $[C_xH_yO_5 + Na]^+$ (dark blue) ions according to the DBE value. (d) DBE vs. carbon number of $C_xH_yO_z$ compounds for phenolic-like (solid purple circle) and sugarc-like (green circle) compounds. These results are obtained from the analysis Miscanthus bio-oil by (+) ESI FT-ICR MS doped with formic acid.	169
<b>Figure III-15.</b>	(a) Relative distribution of the $[C_xH_yO_z + Na]^+$ ions according to the oxygen atom count and (b) their DBE vs. nominal mass plot with the $O_2 - O_9$ (dark blue) and $O_{10} - O_{14}$ (light blue) compounds. These results are obtained from the Miscanthus bio-oil analysis by (+) ESI FT-ICR MS doped with sodium acetate (Analysis II).	171
<b>Figure III-16.</b>	(a) van Krevelen diagrams and (b) Kendrick's map of the $[C_xH_yO_z + Na]^+$ (dark blue) and $[C_xH_yO_z - H]^+$ (light blue) ions assigned from the analysis of the Miscanthus bio-oil in (+) ESI with AcONa and (-) ESI without dopant, respectively.	172
<b>Figure III-17.</b>	Reaction of imine formation.	177
<b>Figure III-18.</b>	(+) ESI LIT MS of vanillin in (a) methanol, (b) methanol/ $NH_4OH$ (1% v/v), (c) methanol/aniline (1% v/v), and (d) methanol/3-chloroaniline (1% v/v).	178
<b>Figure III-19.</b>	Proposed mechanisms of $[M+H]^+$ vanillin $MS^n$ fragmentation.	180
<b>Figure III-20.</b>	Proposed mechanisms of $[M+H]^+$ vanillin+ $NH_4OH$ imine $MS^n$ fragmentation.	182
<b>Figure III-21.</b>	Proposed mechanisms of $[M+H]^+$ vanillin+aniline Schiff base $MS^n$ fragmentation.	184
<b>Figure III-22.</b>	Proposed mechanisms of $[M+H]^+$ vanillin+3-chloroaniline Schiff base $MS^n$ fragmentation.	184
<b>Figure III-23.</b>	(+) ESI LIT MS of cinnamaldehyde in (a) methanol, (b) methanol/ $NH_4OH$ (1% v/v), (c) methanol/aniline (1% v/v) and, (d) methanol/3-chloroaniline (1% v/v).	185
<b>Figure III-24.</b>	Proposed mechanisms of $[M+H]^+$ cinnamaldehyde $MS^n$ fragmentation.	187
<b>Figure III-25.</b>	Proposed mechanisms of $[M+H]^+$ cinnamaldehyde+ $NH_4OH$ imine $MS^n$ fragmentation.	187
<b>Figure III-26.</b>	Proposed mechanisms of $[M+H]^+$ cinnamaldehyde+aniline Schiff base $MS^n$ fragmentation.	188
<b>Figure III-27.</b>	(+) ESI LIT MS of butyrophenone in (a) methanol, (b) methanol/ $NH_4OH$ (1% v/v), (c) methanol/aniline (1% v/v) and, (d) methanol/3-chloroaniline (1% v/v).	189
<b>Figure III-28.</b>	Proposed mechanisms of $[M+H]^+$ butyrophenone $MS^n$ fragmentation.	191
<b>Figure III-29.</b>	Proposed mechanisms of $[M+H]^+$ butyrophenone+ $NH_4OH$ imine $MS^n$ fragmentation.	192
<b>Figure III-30.</b>	Proposed mechanisms of $[M+H]^+$ butyrophenone+aniline Schiff base $MS^n$ fragmentation.	193
<b>Figure III-31.</b>	(+) ESI LIT MS of trihydroxyacetophenone in (a) methanol, (b) methanol/ $NH_4OH$ (1% v/v), (c) methanol/aniline (1% v/v) and, (d) methanol/3-chloroaniline (1% v/v).	194
<b>Figure III-32.</b>	Proposed mechanisms of $[M+H]^+$ trihydroxyacetophenone $MS^n$ fragmentation.	196
<b>Figure III-33.</b>	Proposed mechanisms of $[M+H]^+$ trihydroxyacetophenone+ $NH_4OH$ imine $MS^n$ fragmentation.	197
<b>Figure III-34.</b>	Proposed mechanisms of $[M+H]^+$ trihydroxyacetophenone+aniline Schiff base $MS^n$ fragmentation.	199
<b>Figure III-35.</b>	Vanillin, trihydroxyacetophenone, cinnamaldehyde, and butyrophenone (from left to right) solutions after addition of $NH_4OH$ and heating for 1 hour at 70 °C	201
<b>Figure III-36.</b>	$^{13}C$ NMR spectrum of the vanillin in MeOD.	202
<b>Figure III-37.</b>	$^{13}C$ NMR spectrum of the the vanillin+ $NH_4OH$ imine in MeOD.	202
<b>Figure III-38.</b>	$^{13}C$ NMR spectrum of the vanillin+aniline Schiff base in MeOD.	203
<b>Figure III-39.</b>	$^{13}C$ NMR spectrum of the cinnamaldehyde in MeOD.	203
<b>Figure III-40.</b>	$^{13}C$ NMR spectrum of the butyrophenone in MeOD.	204
<b>Figure III-41.</b>	$^{13}C$ NMR spectrum of the 2,4,6-trihydroxyacetophenone in MeOD.	204



<b>Figure III-42.</b>	$^{13}\text{C}$ NMR spectrum of the 2,4,6-trihydroxyacetophenone+ $\text{NH}_4\text{OH}$ in MeOD.	204
<b>Figure III-43.</b>	(+) ESI FT-ICR mass spectrum of oak pyrolysis bio-oil doped with 0.1 % of 3-chloroaniline.	206
<b>Figure III-44.</b>	(Left) Relative distribution in respect with their oxygen atom count and (Right) van Krevelen diagrams of the $\text{C}_x\text{H}_y\text{O}_z$ , $\text{C}_x\text{H}_y\text{O}_z^*$ , and $\text{C}_x\text{H}_y\text{O}_z^{**}$ compound classes assigned in the analysis of oak pyrolysis bio-oil by (+) ESI FT-ICR MS.	207
<b>Figure III-45.</b>	DBE vs. Nominal mass of the $\text{C}_x\text{H}_y\text{O}_z$ , $\text{C}_x\text{H}_y\text{O}_z^*$ , and $\text{C}_x\text{H}_y\text{O}_z^{**}$ compound classes.	207
<b>Figure III-46.</b>	Venn diagram of the $\text{C}_x\text{H}_y\text{O}_z$ , $\text{C}_x\text{H}_y\text{O}_z^*$ , and $\text{C}_x\text{H}_y\text{O}_z^{**}$ compound formulae assigned by (+) ESI FT-ICR MS analysis of oak bio-oil	208
<b>Figure III-47.</b>	Reaction mechanisms proposed for the successive addition of two molecules of 3-chloroniline on formic acid to form a twice derivatized formic acid.	210
<b>Figure III-48.</b>	Reaction mechanisms proposed for the successive addition of two molecules of 3-chloroniline on benzoic acid to form a twice derivatized benzoic acid.	210
<b>Figure IV-1.</b>	Structures of the 2,5-Dihydroxybenzoic acid (a) and 1,8-Bis(dimethylamino)naphthalene (b).	220
<b>Figure IV-2.</b>	(Left) Distribution in respect with the oxygen atom count and (right) van Krevelen diagram of the $\text{C}_x\text{H}_y\text{O}_z$ and $\text{C}_x\text{H}_y\text{FeO}_z$ compounds of the oak bio-oil analysis by (-) LDI at $0.6 \text{ J.cm}^{-2}$ laser fluence.	222
<b>Figure IV-3.</b>	Distribution of the assigned $\text{C}_x\text{H}_y\text{O}_z/\text{C}_x\text{H}_y$ compounds in respect with the oxygen atom count in the analysis of oak bio-oil by (-) LDI FT-ICR MS at $0.6$ and $0.9 \text{ J.cm}^{-2}$ laser fluence.	223
<b>Figure IV-4.</b>	(a) van Krevelen diagram and (b) DBE vs. nominal mass representation of the $\text{C}_x\text{H}_y$ and $\text{C}_x\text{H}_y\text{O}_z$ compounds of the oak bio-oil by (-) LDI FT-ICR MS with laser fluence at $0.6$ and $0.9 \text{ J.cm}^{-2}$ .	224
<b>Figure IV-5.</b>	(Left) Distributions of the $\text{C}_x\text{H}_y\text{O}_z$ species from oak bio-oil in respect with oxygen atom count achieved from three analyses performed in (-) LDI FT-ICR MS with a laser fluence of $0.6 \text{ J.cm}^{-2}$ . (Right) Average relative distribution of the $\text{C}_x\text{H}_y\text{O}_z$ compounds detected in (-) LDI. Error bar is relative to the standard deviation for the three considered measurements.	225
<b>Figure IV-6.</b>	Mass spectra of oak bio-oil obtained by (a) LDI FT-ICR MS and (b) MALDI FT-ICR MS with DMAN in negative ion detection mode.	226
<b>Figure IV-7.</b>	$\text{C}_x\text{H}_y\text{O}_z$ compound distribution in respect with oxygen atom count in analysis of the oak bio-oil by LDI and MALDI with DMAN in negative ion detection mode.	227
<b>Figure IV-8.</b>	van Krevelen diagrams of the $\text{C}_x\text{H}_y\text{O}_z$ compounds of the analysis of the oak bio-oil by LDI (left) and MALDI (right) with DMAN in negative ion detection mode for $\text{M}^*$ and $[\text{M-H}]^-$ anions.	227
<b>Figure IV-9.</b>	Distribution of the $\text{C}_x\text{H}_y\text{O}_z$ class of oak bio-oil assigned by LDI and MALDI FT-ICR MS in positive ion mode.	228
<b>Figure IV-10.</b>	van Krevelen diagrams of the $\text{C}_x\text{H}_y/\text{C}_x\text{H}_y\text{O}_z$ compounds of the analysis of the oak bio-oil by LDI (left) and MALDI (right) with 2,5-DHB in positive ion detection mode in respect with the nature of the detected cations.	229
<b>Figure IV-11.</b>	Van Krevelen diagrams of the $\text{C}_x\text{H}_y\text{O}_z$ compounds of oak bio-oil obtained by LDI in positive and negative ion modes.	231
<b>Figure IV-12.</b>	(+) APPI mass spectra of oak bio-oil acquired without, with dopant (toluene or acetone), and with sodium acetate.	233
<b>Figure IV-13.</b>	Focus at $m/z$ 314.12 and $m/z$ 553.2 of the (+) APPI mass spectra of oak bio-oil acquired without, with dopant (toluene or acetone), and with sodium acetate. The assignments of the most intensely detected peaks with the pure methanolic solution are reported in the above chart.	234
<b>Figure IV-14.</b>	(-) APPI mass spectra of oak bio-oil acquired without and with dopant (toluene or acetone).	235
<b>Figure IV-15.</b>	Distribution in respect with the oxygen atom count of the $\text{C}_x\text{H}_y\text{O}_z$ compounds of the oak bio-oil assigned by APPI FT-ICR MS in both detection modes.	236
<b>Figure IV-16.</b>	Van Krevelen diagrams of the $\text{C}_x\text{H}_y\text{O}_z$ compounds, in respect with their ion parity, assigned in positive (top) and negative (bottom) APPI FT-ICR MS	237
<b>Figure IV-17.</b>	Relative intensities of the $\text{C}_x\text{H}_y\text{O}_z$ compounds in (+) and (-) ESI, APPI, and LDI FT-ICR MS spectra of oak pyrolysis bio-oil according to the DBE and oxygen atom distribution.	245

<b>Figure IV-18.</b>	Relative intensities of the $C_xH_yO_z$ compounds represented on the van Krevelen diagrams according to their H/C and O/C ratios as obtained in (+) and (-) ESI, APPI, and LDI FT-ICR MS.	246
<b>Figure IV-19.</b>	Van Krevelen diagrams for $C_xH_yO_z$ compounds with radical and protonated/deprotonated ions identified in (+) and (-) LDI FT-ICR MS.	248
<b>Figure IV-20.</b>	Venn diagrams of $C_xH_yO_z$ compounds obtained by APPI, LDI, and ESI analyses of the oak bio-oil in (a) positive and (b) negative ion detection modes.	249
<b>Figure V-1.</b>	Relative distribution of $C_xH_y$ and $C_xH_yO_z$ compounds in respect with the number of oxygen atoms in positive and negative ion ESI, LDI, and APPI FT-ICR MS for raw bio-oil and upgraded A and B bio-oils from the pyrolysis of the 1-7 oak cylinders.	260
<b>Figure V-2.</b>	Relative intensities of the $C_xH_y$ and $C_xH_yO_z$ compounds in raw bio-oil and upgraded A and B bio-oils from the pyrolysis of the 1-7 oak cylinders represented on the van Krevelen diagrams according to their H/C and O/C ratios as obtained by (+) and (-) ESI, APPI, and LDI FT-ICR MS.	261
<b>Figure V-3.</b>	Carbon number vs. DBE distribution of $C_xH_yO_z$ compounds observed in (+) ESI for raw bio-oil and upgraded A and B bio-oils from the pyrolysis of the 1-7 oak cylinders.	264
<b>Figure V-4.</b>	Carbon number vs. DBE distribution of $C_xH_yO_z$ compounds observed in (-) ESI for raw bio-oil and upgraded A and B bio-oils from the pyrolysis of the 1-7 oak cylinders.	266
<b>Figure V-5.</b>	Carbon number vs. DBE distribution of $C_xH_y$ compounds observed in (+) APPI and (-) LDI for raw bio-oil and upgraded A and B bio-oils from the pyrolysis of the 1-7 (top) and 8-14 (bottom) oak cylinders.	267
<b>Figure V-6.</b>	Carbon number vs. DBE distribution of $C_xH_yO_z$ compounds observed in (+) APPI for raw bio-oil and upgraded A and B bio-oils from the pyrolysis of the 1-7 oak cylinders.	269
<b>Figure V-7.</b>	Carbon number vs. DBE distribution of $C_xH_yO_z$ compounds observed in (-) LDI raw bio-oil and upgraded A and B bio-oils from the pyrolysis of the 1-7 and 8-14 oak cylinders.	270
<b>Figure V-8.</b>	Relative intensity distribution of the $C_xH_yO_z$ compounds with DBE=6 in positive and negative ion ESI and APPI FT-ICR MS for raw bio-oil and upgraded A and B bio-oils from the pyrolysis of the 1-7 oak cylinders.	272
<b>Figure V-9.</b>	Relative intensities of the $C_xH_y$ and $C_xH_yO_z$ compounds in raw bio-oil and A and B upgraded bio-oils from the pyrolysis of the 8 to 14 oak cylinders represented on the van Krevelen diagrams according to their H/C and O/C ratios as obtained by (+) and (-) ESI, APPI and LDI FT-ICR MS.	274
<b>Figure V-10.</b>	Carbon number vs. DBE distribution of $C_xH_yO_z$ compounds observed in (+) ESI for raw bio-oil and A and B upgraded bio-oils from the pyrolysis of the 8 to 14 oak cylinders.	276
<b>Figure V-11.</b>	Carbon number vs. DBE distribution of $C_xH_yO_z$ z compounds observed in (-) ESI for raw bio-oil and A and B upgraded bio-oils from the pyrolysis of the 8 to 14 oak cylinders.	277
<b>Figure V-12.</b>	Carbon number vs. DBE distribution of $C_xH_yO_z$ compounds observed in (+) APPI for raw bio-oil and A and B upgraded bio-oils from the pyrolysis of the 8 to 14 oak cylinders.	278
<b>Figure V-13.</b>	Carbon number vs. DBE distribution of $C_xH_yO_z$ compounds observed in (-) LDI for raw bio-oil and A and B upgraded bio-oils from the pyrolysis of the 8 to 14 oak cylinders.	279

## Tables of tables

<b>Table I-1.</b>	Pyrolysis methods and their key features.	19
<b>Table I-2.</b>	Pyrolysis product yields in respect with the used feedstock and temperature.	21
<b>Table I-3.</b>	Characteristics of different pyrolysis units.	22
<b>Table I-4.</b>	Typical physicochemical properties of pyrolysis, liquefaction, and heavy fuel oil.	25
<b>Table I-5.</b>	Typical abundances of major classes of bio-oil components.	26
<b>Table I-6.</b>	Typical functional groups observed by FT-IR in bio-oil.	37
<b>Table I-7.</b>	Major compounds observed in typical bio-oils from biomass pyrolysis.	47
<b>Table I-8.</b>	Experimental conditions and results of the separation by RPLCxRPLC of the aqueous phase of a bio-oil.	49
<b>Table I-9.</b>	Analytical capabilities of the common high resolution mass spectrometers.	50
<b>Table I-10.</b>	Overview of the publications dealing with analysis of bio-oils by ESI-HRMS.	53-57
<b>Table I-11.</b>	Overview of the publications dealing with analysis of bio-oils by APPI, APCI, and LDI-HRMS as complement to ESI-HRMS analyses.	69-70
<b>Table II-1.</b>	Common UV-MALDI matrixes and their applications.	112
<b>Table II-2.</b>	Ions formed by MALDI and LDI.	113
<b>Table II-3.</b>	Proton affinities (PA) of typical solvents and species used in APPI.	118
<b>Table III-1.</b>	Physicochemical properties of methanol and water.	148
<b>Table III-2.</b>	Number of assigned peaks, total ion current, and relative abundance of the different compound families obtained in the study of oak bio-oil by (+) ESI FT-ICR MS in respect with the H <sub>2</sub> O:MeOH ratio and the probe temperature.	149
<b>Table III-3.</b>	Number of assigned peaks, total ion current, and assigned compound families observed in positive and negative ESI-FT-ICR-MS experiments for the different investigated ionization conditions with Miscanthus bio-oil.	156
<b>Table III-4.</b>	Structure and molecular weight (MW) of the four selected standard carbonyl compounds and of the aniline and 3-chloroaniline.	175
<b>Table III-5.</b>	Tandem mass spectrometry analysis of protonated [M+H] <sup>+</sup> ion of vanillin and its corresponding imine compounds.	179
<b>Table III-6.</b>	Tandem mass spectrometry analysis of protonated [M+H] <sup>+</sup> ion of cinnamaldehyde and its corresponding imine compounds.	186
<b>Table III-7.</b>	Tandem mass spectrometry analysis of protonated [M+H] <sup>+</sup> ion of butyrophenone and its corresponding imine compounds.	190
<b>Table III-8.</b>	Tandem mass spectrometry analysis of protonated [M+H] <sup>+</sup> ion of trihydroxyacetophenone and its corresponding imine compounds.	195
<b>Table III-9.</b>	Putative C <sub>x</sub> H <sub>y</sub> O <sub>z</sub> formulae and proposed assignments for some C <sub>x</sub> H <sub>y</sub> N <sub>z</sub> Cl <sub>2</sub> O <sub>z</sub> compounds evidenced in the oak bio-oil by (+) ESI FT-ICR MS.	209
<b>Table IV-1.</b>	Number of assigned peaks and relative abundance of the compound families obtained by LDI and MALDI analyses at different laser fluences.	221
<b>Table IV-2.</b>	Number of assigned peaks and compounds families evidenced by APPI FT-ICR MS analyses of the oak bio-oil in positive and negative ion modes.	236
<b>Table IV-3.</b>	Relative distribution of compound families identified in bio-oil in positive and negative detection modes in ESI, APPI, and LDI FT-ICR MS	242

**Table V-1.** Relative distribution of compound families identified in positive and negative ion ESI, LDI, and APPI FT-ICR MS in raw bio-oil and upgraded A and B bio-oils from the pyrolysis of the 1-7 and 8-14 oak cylinders. 259

---

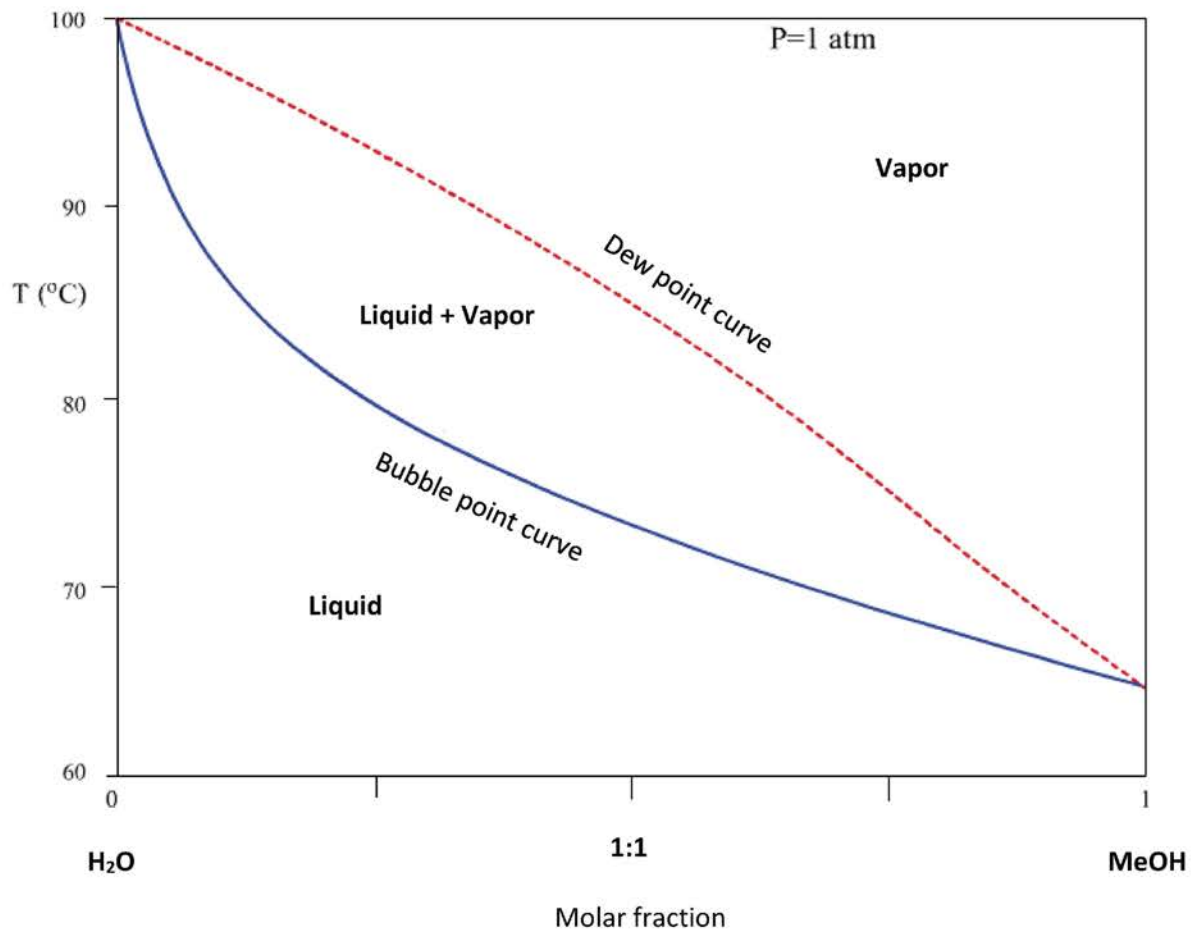
## *Annexes*

---



## Annex I

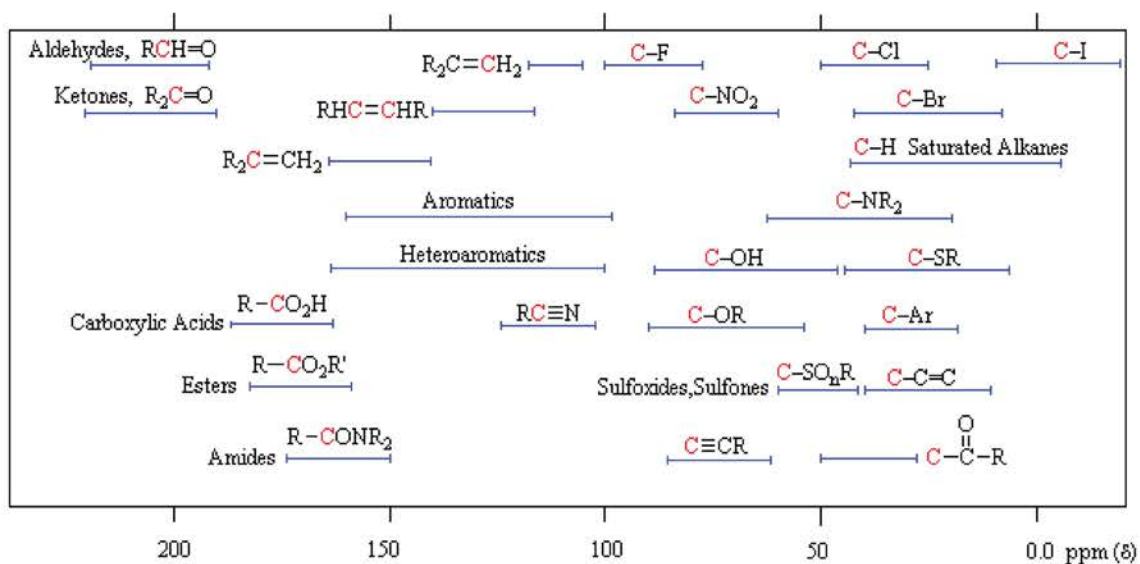
### Water-methanol phase diagram<sup>1</sup>



<sup>1</sup> From the website of the École des Mines d'Albi (France)  
[http://nte.mines-albi.fr/Thermoinstro/fr/co/uc\\_ELIV.html](http://nte.mines-albi.fr/Thermoinstro/fr/co/uc_ELIV.html)

## Annex II

### Tables of characteristic $^{13}\text{C}$ NMR assignments<sup>2</sup>



<sup>2</sup> From the website of the Michigan State University  
<http://www2.chemistry.msu.edu/faculty/reusch/orgpage/nmr.htm>



## Annex III

### Scientific articles and communications

#### Scientific publications

- 1 **Combination of electrospray ionization, atmospheric pressure photoionization and laser desorption ionization Fourier transform ion cyclotron resonance mass spectrometry for the investigation of complex mixtures – Application to the petroleomic analysis of bio-oils** – J. Hertzog, V. Carré, Y. Le Brech, C. L. Mackay, A. Dufour, O. Mašek, F. Aubriet – *Analytica Chimica Acta*, **2017**, 969, 26-34.
  - 2 **Towards controlled ionization conditions for ESI-FT-ICR-MS analysis of bio-oils from lignocellulosic material** - J.Hertzog, V. Carré, Y. Le Brech, A. Dufour, F. Aubriet – *Energy & Fuels*, **2016**, 30 (7), 5729-5739.
    - **Evidence of the hierarchical zeolite efficiency during catalytic fast pyrolysis of lignocellulosic biomass** (submitted to *ACS Sustainable Chemistry & Engineering*)
- In progress
- **Semi-targeted analysis of complex matrices by ESI FT-ICR MS or how an experimental bias may be used as an analytical tool** (submitted to *JASMS*)

#### Oral communications in international scientific meeting

- 1 J. Hertzog, V. Carré, L. Jia, Y. Le Brech, L. Pinard, C. L. Mackay, O. Mašek, A. Dufour, F. Aubriet - **Complementarity of ESI, APPI and LDI FT-ICR MS analyses for the comprehensive description of raw and deoxygenated pyrolysis bio-oils** – 65<sup>th</sup> Conference on Mass Spectrometry and Allied Topics ASMS, Indianapolis (USA), 4-8 June 2017
- 2 J. Hertzog, V. Carré, A. Dufour, F. Aubriet - **Development of a robust methodology for the characterization of biomass pyrolysis bio-oil by electrospray ionization** - 12<sup>th</sup> European Fourier Transform Mass Spectrometry EFTMS Workshop, Matera (Italy), 4-8 April 2016.
- 3 T. Ghislain, V. Carré, J. Hertzog, A. Sonnette, Y. Le Brech, A. Dufour, G. Mauviel, F. Aubriet - **Characterization of biomass and biochar by LDI-FTICRMS: Effect of the laser wavelength and raw biomass material** – 18<sup>th</sup> European Conference on Analytical Chemistry EuroAnalysis, Bordeaux (France), 6-10 September 2015.

#### Oral communications in national scientific meeting

- 1 J. Hertzog, V. Carré, A. Dufour, O. Mašek, F. Aubriet – **Monitoring of catalytic deoxygenation of pyrolysis bio-oil by ESI and APPI FT-ICR MS** – 22<sup>nd</sup> Workshop of the Young Members of the French Society of Mass Spectrometry, Trélon (France), 20-24 March 2017.
- 2 J. Hertzog, V. Carré, A. Dufour, F. Aubriet – **Towards an analytical method of biomass pyrolysis bio-oils by LDI and MALDI-FT ICRMS** – 21<sup>st</sup> Workshop of the Young Members of the French Society of Mass Spectrometry, Moustiers-Sainte-Marie (France), 21-25 March 2016.
- 3 J. Hertzog, V. Carré, A. Dufour, F. Aubriet - **Optimization of an ESI-FT ICRMS method to investigate biomass pyrolysis bio-oils** – French Congress of Mass Spectrometry and Proteomic Analysis SMAP, Ajaccio (France), 15-18 September 2015.

#### Seminars and group meetings

- 1 J. Hertzog - **Petroleomic approach for the characterization of lignocellulosic bio-oils** - Seminary at the Karolinska Institutet (Sweden) – 19 April 2017
- 2 J. Hertzog – **FT-ICR MS applied to pyrolysis bio-oils** – Seminary at the University of Edinburgh (UK) – 10 October 2016
- 3 O. Mašek, M. Ghidotti, J. Feroso, J.Hertzog, L. Mackay, J. Pietrzyk, D. Fabbri - **High-resolution mass spectrometry for characterization of biomass products** – COST Action FP1306 WG1+WG3 meeting, Lisbon (Portugal), 26-27 September 2016.

#### Poster in international scientific meeting

- 1 J. Hertzog, V. Carré, Y. Le Brech, A. Dufour, F. Aubriet - **Towards a better characterization of biomass pyrolysis bio-oil by ESI-FTICRMS** – 21<sup>st</sup> International Symposium on Analytical and Applied Pyrolysis Pyro – Nancy (France), 9-12 May 2016.

#### Poster in national scientific meeting

- 1 J. Hertzog, V. Carré, C.L. Mackay, L.Y. Jia, L. Pinard, O. Mašek, A. Dufour, F. Aubriet - **Determination of the efficiency of two deoxygenation catalysts for the upgrading of pyrolysis bio-oil by petroleomic approach.** - French Congress of Mass Spectrometry and Proteomic Analysis SMMAP, Marne-la-Vallée (France), 2-5 October 2017.
- 2 J. Hertzog, V. Carré, Y. Le Brech, C.L. Mackay, A. Dufour, O. Mašek, F. Aubriet - **Extensive characterization of pyrolysis bio-oils from lignocellulosic biomass by ESI/APPI/LDI FT-ICR MS** – Thematic day “Analytical chemistry for the energy”, French Society of Chemistry, Paris, 11 May 2017.
- 3 A. Sonnette, V. Carré, J. Hertzog, A. Dufour, F. Aubriet - **Comparison of bio-oils from the Douglas and Miscanthus fast and slow pyrolysis by ESI- FTICR MS and LDI – FTICR MS analysis** - French Congress of Mass Spectrometry and Proteomic Analysis SMAP, Ajaccio (France), 15-18 September 2015.

Etude par spectrométrie de masse à haute résolution de bio-huiles  
issues de la pyrolyse de la biomasse lignocellulosique

Résumé en français de la thèse

Présentée par

Jasmine Hertzog

En vue de l'obtention du grade de

DOCTEUR EN CHIMIE DE L'UNIVERSITÉ DE LORRAINE

## I. Introduction

Les ressources fossiles (pétrole, gaz et charbon) sont responsables de nombreux problèmes environnementaux, économiques et géopolitiques. De plus, leurs réserves s'amenuisent alors que la population mondiale et la demande énergétique croissent fortement. C'est pourquoi, il est nécessaire de développer d'autres ressources énergétiques plus écologiques et plus durables. Parmi les solutions existantes, comme le solaire et l'éolien, la valorisation de la biomasse présente une alternative prometteuse pour la production de biocarburants mais également comme source de produits de base pour l'industrie chimique.<sup>1</sup> La biomasse rassemble l'ensemble de la matière organique d'origine végétale ou animale. Seules 3 % des 10<sup>11</sup> tonnes produites annuellement sont utilisées pour l'alimentation humaine et animale, le reste est, par conséquent, disponible et témoigne du fort potentiel de cette ressource.<sup>2</sup> Les plantes utilisent le CO<sub>2</sub> atmosphérique et l'énergie solaire pour croître. L'empreinte carbone des biocarburants issus de cette biomasse est donc bien moins élevée que celles des énergies fossiles. Il existe différents types de biocarburants et la production des premiers d'entre eux date des années 1820.<sup>3</sup>

Les biocarburants de première génération sont actuellement les plus développés et correspondent au bioéthanol<sup>4</sup> et au biodiesel.<sup>5</sup> Le bioéthanol est obtenu par fermentation du sucre extrait de la canne à sucre ou de la betterave sucrière.<sup>6</sup> Pour le biodiesel, ce sont les triglycérides des plantes oléagineuses, comme le colza, le tournesol et le palmier à huile, qui sont employés. Ils sont convertis par transestérification avec un alcool (typiquement le méthanol ou l'éthanol) en ester d'acide gras.<sup>7</sup>

Les procédés de production de ces biocarburants sont relativement simples, mais leur production pose de sérieux problèmes éthiques et écologiques. En effet, l'emploi de denrées alimentaires (humaines et/ou animales) ainsi que des surfaces agricoles dédiées vient concurrencer les circuits d'alimentation humaine ou conduit à des déforestations massives.<sup>8</sup>

Une nouvelle génération de biocarburants, dite de deuxième génération, est en développement. Ils ont pour but de ne plus concurrencer l'industrie alimentaire car ils sont produits à partir de résidus forestiers<sup>9</sup> et agricoles<sup>10</sup> ou encore de cultures dédiées, telles que le *Miscanthus Giganteus*.<sup>11</sup> Cette plante a la faculté de facilement pousser sur des friches agricoles ou industrielles.<sup>12,13</sup> Les ressources engagées dans la production de ces biocarburants sont communément appelées «biomasse lignocellulosique». Elle correspond en

fait à un matériau composite constitué principalement de cellulose, d'hémicellulose et de lignine (Figure 1).<sup>14</sup> La cellulose est l'homopolymère organique (chaîne de glucose) le plus abondant sur Terre et constitue 41 % de la biomasse.<sup>15</sup> L'hémicellulose est un hétéropolysaccharide (sucres en C5 et C6) et représente près de 30 % de la biomasse.<sup>16</sup> La lignine, qui constitue 25 % de la biomasse, est un polymère complexe fait de motifs phénoliques.<sup>17</sup>

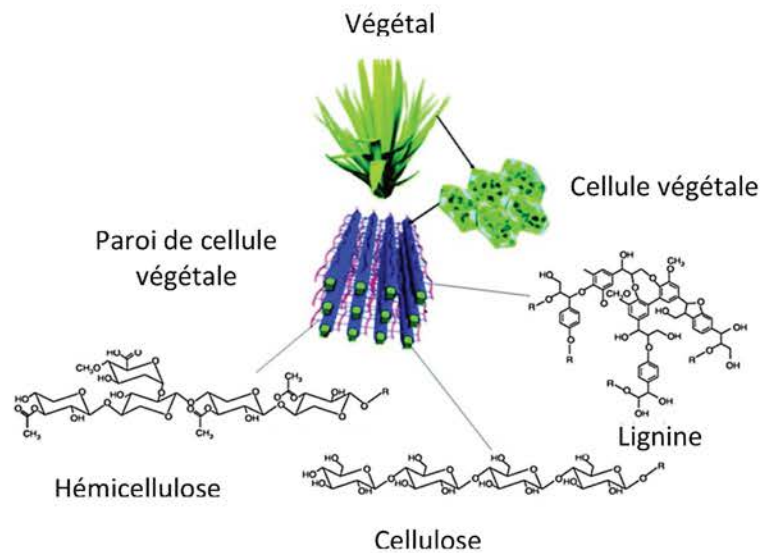


Figure 1. Composition de la biomasse<sup>18</sup>

Il existe plusieurs procédés de conversion de la biomasse lignocellulosique en combustibles liquides.<sup>19</sup> Les plus communément utilisés sont la pyrolyse et la liquéfaction hydrothermale (HTL) et conduisent, tous deux, à la formation d'une bio-huile dont les propriétés n'en permettent pas l'usage direct comme biocarburant.<sup>1</sup> Dans le cadre de la pyrolyse, la composition élémentaire des bio-huiles est de l'ordre de 56 % en carbone, 6 % en hydrogène et 38 % en oxygène. Des traces d'azote et de soufre sont également présentes.<sup>20</sup> Cette forte teneur en oxygène ainsi que l'acidité de ces bio-huiles qui lui est associée sont responsables de problèmes de corrosion et de stockage, mais également d'une densité énergétique limitée.<sup>21</sup> La diminution voire l'élimination de l'oxygène apparaît comme une nécessité pour valoriser ces bio-huiles en «pétrole vert». Plusieurs moyens sont utilisés, notamment des traitements catalytiques semblables à ceux utilisés dans le raffinage pétrolier. Ils permettent l'hydrodésoxygénation et la désoxygénation voire le craquage.<sup>1</sup> Comme le pétrole, une bio-huile est un mélange extrêmement complexe de plusieurs milliers de composés présentant des propriétés physicochimiques différentes et des fonctionnalités chimiques variées.<sup>22</sup>

Afin d'évaluer et d'améliorer les paramètres de pyrolyse et de catalyse, une description, la plus détaillée possible, de la bio-huile est nécessaire. Elle doit être effectuée avant et après traitement pour évaluer, la nature des composés présents mais également l'efficacité du traitement effectué. Aucune technique de caractérisation n'est universelle. La méthodologie classiquement utilisée combine les informations obtenues par plusieurs techniques.<sup>22</sup> On peut les classer en deux grandes catégories: les méthodes ciblées et les méthodes non-ciblées.<sup>23</sup>

Les analyses ciblées permettent de caractériser et de quantifier un nombre donné de composés ou de familles de composés. On peut se limiter à l'identification de fonctions chimiques particulières (spectroscopies infrarouge et par résonance magnétique nucléaire), ou encore rechercher de manière spécifique un composé donné en utilisant une technique séparative (chromatographie liquide ou gazeuse) associée éventuellement à une analyse moléculaire (spectrométrie de masse) ou structurale (spectrométrie de masse en tandem). Dans ce cas, les informations sont multiples (temps de rétention, spectre de masse, spectre de fragmentation).

La seconde catégorie regroupe les méthodes non-ciblées. Dans le cas de la caractérisation de pétrole ou de composés qui lui sont associés, on parle d'approche pétroléomique. C'est elle qui est utilisée dans le cadre de cette étude. Contrairement aux approches ciblées, elle ne permet pas d'obtenir d'informations directes de structure ou encore de réaliser de la quantification. Cependant, elle permet d'accéder simultanément à la formule brute de plusieurs milliers de composés et ce sur une large gamme de masse. Dans ce type d'approche, un spectromètre de masse de haute résolution est nécessaire.

De manière synthétique, l'objectif de cette étude est de développer différentes méthodes d'analyses pétroléomiques robustes afin de caractériser des bio-huiles de pyrolyse et d'en obtenir une description la plus complète possible. Ces développements ont été menés par spectrométrie de masse à résonance cyclotronique des ions à transformée de Fourier (FT-ICR MS). Les sources d'ionisation par électro-nébulisation (ESI), désorption/ionisation laser (LDI) et photoionisation à pression atmosphérique (APPI) ont été utilisées en raison de leur capacité à ioniser des composés de polarités différentes. Cela permet ainsi d'avoir une description de la diversité moléculaire de ces bio-huiles aussi importante que possible. Ces méthodes ont été ensuite appliquées à des bio-huiles ayant subi un traitement de désoxygénation catalytique.

## II. Principe de l'approche pétroléomique

L'approche pétroléomique a été utilisée pour la première fois par Marshall *et al.* pour caractériser des pétroles.<sup>24</sup> Classiquement, l'échantillon est directement introduit dans le spectromètre de masse sans séparation chromatographique préalable. En raison de la complexité de ce type d'échantillon, des spectromètres de masse de haute résolution sont nécessaires. En effet, le grand pouvoir résolutif délivré par ces appareils (> 400 000) permet de distinguer les espèces isobariques. Les spectres de masse obtenus présentent jusqu'à plusieurs dizaines de milliers de pics comme cela est illustré sur la *Figure 2*.<sup>25</sup> La très grande précision de mesure de masse de ces instruments (< 1 ppm) permet d'attribuer à chaque pic une unique formule brute de type  $C_cH_hN_nO_oS_s$  (*Figure 2*). Cette approche permet d'obtenir une analyse «globale» de l'échantillon. Mais la grande quantité de données générées rend l'interprétation difficile et l'absence de séparation en amont peut conduire à des compétitions à l'ionisation. Enfin, cette méthode ne permet pas de distinguer les isomères.

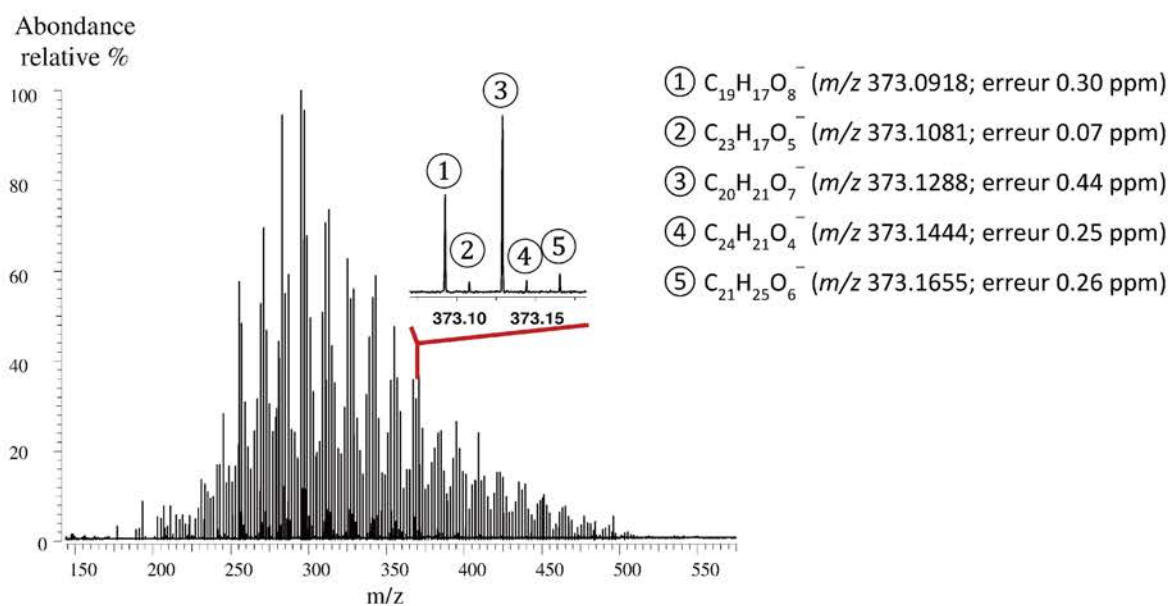


Figure 2. Spectre de masse de bio-huile de pyrolyse de *Miscanthus* obtenu par (-) ESI FT-ICR MS

La très grande quantité d'informations obtenue nécessite des représentations graphiques pour faciliter leur interprétation et leur comparaison. Par exemple, sur les diagrammes de van Krevelen, chaque espèce de type  $C_xH_yO_z$  est représentée par un point dont les coordonnées x et y correspondent aux rapports O/C et H/C, respectivement.<sup>26</sup> Si l'information du rapport  $m/z$  est perdue, dans le cadre de l'analyse des bio-huiles, ces diagrammes permettent de mettre

en évidence des composés relatifs à la lignine, à la cellulose, à l'hémicellulose et aux lipides (Figure 3).

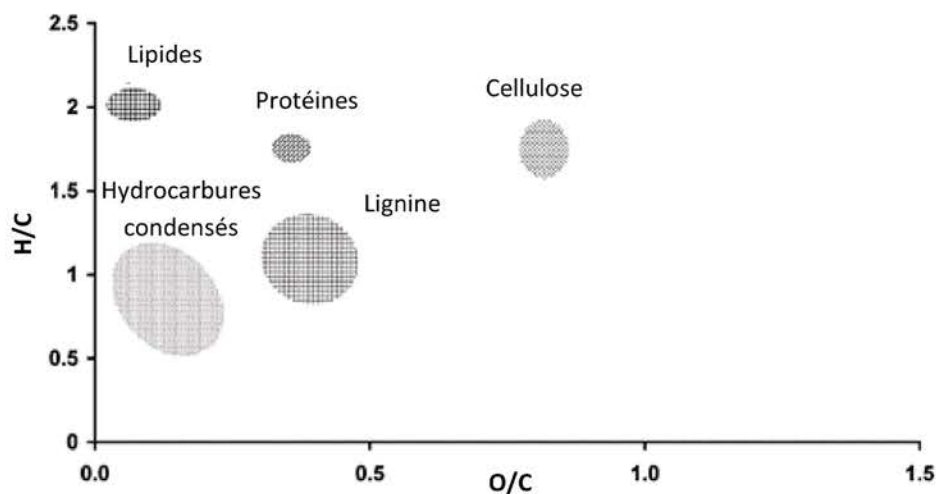


Figure 3. Diagramme de van Krevelen représentant les principaux constituants de la biomasse<sup>26</sup>

Il est également possible de représenter le degré d'insaturation et d'aromaticité d'une molécule en calculant son équivalent en double liaison *DBE* (Double Bound Equivalent). Il est facilement obtenu à l'aide de l'équation suivante:  $DBE = C - \frac{H}{2} + \frac{N}{2} + 1$  et traduit le nombre d'insaturation (liaisons multiples et cycles).

Dans le cadre de l'étude de bio-huiles, l'application de l'approche pétroliomique a déjà permis de mettre en évidence des différences de composition en fonction de la matière première utilisée, du prétraitement appliqué à la bio-huile (fractionnement, extraction par solvants...), du procédé de production (pyrolyse, liquéfaction, traitement catalytique) et des paramètres de production (température, solvant dans le cadre de l'HTL...). Bon nombre de ces études ont été réalisées par spectrométrie de masse de haute résolution, notamment de type FT-ICR MS.<sup>23</sup>

## II.A. La FT-ICR MS

Le principe de fonctionnement de la FT-ICR repose sur la propriété qu'a un ion, placé dans un champ magnétique uniforme  $B_0$ , à adopter une trajectoire circulaire et uniforme, s'il est initialement animé d'une vitesse perpendiculaire à ce champ. Ce mouvement est appelé mouvement cyclotron dont la pulsation est donnée par  $\omega_c = \frac{q}{m} B_0$ .<sup>27</sup> La charge  $q$  de cet ion étant égale à  $z$  fois la charge élémentaire  $e$ , la pulsation est donc inversement proportionnelle



au rapport  $m/z$ :  $\omega_c = \frac{e}{m/z} B_0$ . Afin de piéger les ions dans les trois dimensions, un puits de potentiel est créé en appliquant sur les plaques, dites de piégeage perpendiculaires à  $B_0$ , un potentiel de l'ordre du volt (*Figure 4*). Initialement, les ions de même rapport  $m/z$  présentent un mouvement incohérent au centre de la cellule ICR, appelée piège de Penning. Leurs fréquences de giration, dépendantes de la valeur de  $B_0$ , sont comprises entre quelques dizaines de kHz pour les lourds à quelques dizaines de MHz pour les plus légers.<sup>28</sup>

L'application, sur les plaques d'excitation, d'un champ radiofréquence constitué de la superposition de fréquences comprises entre quelques kHz et quelques MHz conduit à l'augmentation de l'énergie cinétique des ions. Le rayon de leur trajectoire cyclotronique augmente. Cette étape a aussi pour conséquence d'augmenter la cohérence de leur mouvement. Après arrêt de l'excitation par radiofréquence, le mouvement des ions se stabilise sur une orbite haute, proche des plaques qui constituent le piège de Penning. Ils peuvent ainsi passer à proximité des plaques de détection sur lesquelles ils induisent un courant alternatif de fréquence égale à la fréquence de leur mouvement cyclotronique.<sup>28</sup>

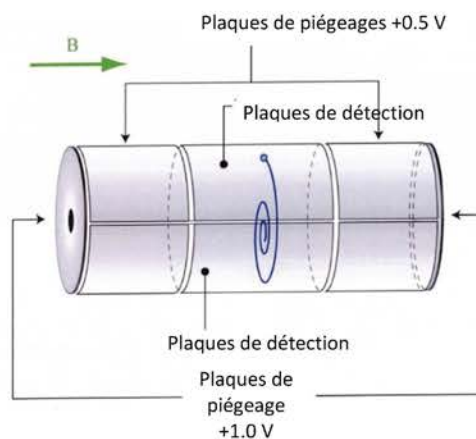


Figure 4. Mouvement cyclotronique d'un d'ion dans un champ magnétique  $B$  dans une cellule d'analyse ICR (IonSpec)

Le signal obtenu est en fait un interférogramme correspondant à la combinaison des fréquences de tous les ions présents dans la cellule (*Figure 5*). Ce signal décroît exponentiellement avec le temps du fait d'une perte de la cohérence du mouvement cyclotronique au travers de processus collisionnels et/ou d'interactions électrostatiques. L'application d'une opération de transformée de Fourier permet le passage du domaine du temps à celui des fréquences, puis à celui des rapports  $m/z$  en appliquant l'équation  $\nu_c = \frac{eB_0}{2\pi m/z}$ . La présence simultanée d'un champ électrique et d'un champ magnétique ne permet

cependant pas d'obtenir de manière aussi simple le rapport  $m/z$ . On pourra se reporter, si on le souhaite, aux équations exactes de mouvement décrites par Verdun *et al.*<sup>29,30</sup>

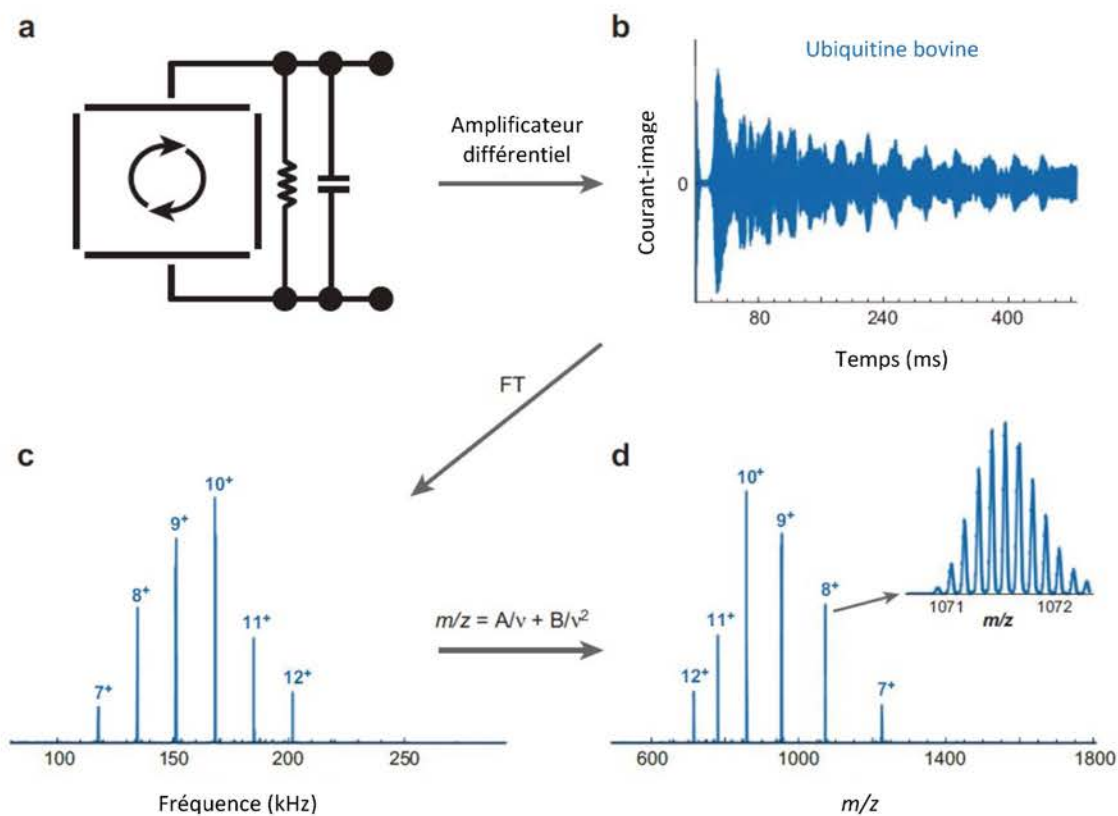


Figure 5. (a) Représentation du mouvement cyclotronique d'un ion excité, (b) interférogramme enregistré par les plaques de détection, (c) spectre fréquentiel obtenu par transformée de Fourier rapide et (d) spectre de masse obtenu après calibration et conversion du domaine fréquentiel en rapport  $m/z$ .

## II.B. Les sources d'ionisation

Les sources d'ionisation utilisées dans le cadre de cette étude sont l'électronébulisation (ESI), la désorption/ionisation laser (LDI) et la photoionisation à pression atmosphérique (APPI).

L'ESI est principalement employée pour ioniser des espèces moyennement à fortement polaires. La solution contenant l'analyte est infusée dans un capillaire sur lequel est appliquée une différence de potentiel. Ceci a pour conséquence de déformer le ménisque en bout de capillaire et de former un cône dit de Taylor. Sous l'effet du champ électrique, des gouttelettes sont produites à l'extrémité du cône. La température de la source, l'utilisation d'un gaz de désolvatation et la différence de pression entre la source et le spectromètre de masse sont responsables de l'évaporation du solvant au sein de ces gouttelettes. Cela conduit à une

augmentation de la densité de charge jusqu'au moment où la force électrostatique, résultant des charges en répulsion, est supérieure aux forces de cohésion de la gouttelette. A cette limite, dite de Rayleigh, les gouttelettes explosent en de plus petites gouttelettes (explosions coulombiennes). Ce processus se répète jusqu'à obtention d'ions en phase gazeuse. Les facteurs influençant le procédé d'ionisation par ESI sont la température de la source et du capillaire, la nature du solvant et la présence d'agents favorisant les processus de cationisation, d'anionisation, de protonation ou de déprotonation.<sup>31</sup>

L'ionisation/désorption laser est moins sensible à la polarité des analytes et permet la mise en évidence de composés sur une plus grande gamme de polarité. La désorption/ionisation laser est induite par l'interaction des photons d'un faisceau laser avec l'échantillon.<sup>32</sup> Elle est extrêmement efficace lorsque les composés analysés absorbent fortement à la longueur d'onde du faisceau laser utilisé, ici 355 nm. Il s'agit en particulier, dans le cadre des bio-huiles, de composés hétéroatomiques présentant des insaturations. Au-delà de ces processus de désorption/ionisation pure, on peut assister à des processus de co-désorption et de co-ionisation. Dans ce cas, l'interaction des espèces absorbant à la longueur d'onde du faisceau laser va permettre la détection d'espèces qui présentent une absorbance faible voire nulle. Ce principe est à la base de la méthode MALDI.<sup>33</sup> Les paramètres critiques en LDI sont la longueur d'onde (plus particulièrement le coefficient d'absorption molaire de l'échantillon), la fluence du laser et l'ajout d'une matrice pour aider à la co-désorption/-ionisation. Le paramètre de fluence est le plus critique. Une fluence trop faible ne permettra pas la formation d'ions alors que si elle est trop élevée, l'excès d'énergie sera converti en énergie interne qui sera à la base de processus de fragmentation et de recombinaisons.<sup>32</sup> La nature des espèces obtenues n'aura alors que peu de lien avec celle des analytes. Il convient donc de choisir une fluence juste supérieure au seuil de désorption/ionisation pour réduire les artefacts tout en produisant des ions de manière sensible.

L'APPI permet l'ionisation de composés faiblement polaires voire apolaires. Des photons d'énergie (10,0 et 10,6 eV) émis par une lampe à décharge (contenant du krypton) permettent la photoionisation en phase gazeuse des composés analysés par différents processus. Soit directement si leur énergie d'ionisation est inférieure à l'énergie des photons, ou par des processus de transfert de proton à partir d'agrégats de molécules de solvant. L'emploi de dopants (toluène, acétone) permet d'accroître, dans certains cas, l'efficacité d'ionisation.<sup>34</sup>

### III. Matériel et méthodes

#### III.A. Spectromètres de masse à résonance cyclotronique de ions à transformée de Fourier

Les analyses ont été effectuées avec un appareil FT-ICR de 9,4 T (HiRes Ion Spec) au *Laboratoire de Chimie et Physique Approche Multi-échelles des Milieux Complexes*, à Metz. Cet instrument est équipé des sources d'ionisation ESI (Micromass Z-spray) et LDI avec un laser Nd:YAG à 355 nm (Orion air-cooled system).

D'autres analyses ont été effectuées à l'Université d'Edimbourg, dans le cadre du COST Lignoal, avec un appareil FT-ICR de 12 T (Bruker Solarix) équipé des sources ESI, LDI et APPI (Bruker Daltonics).

#### III.B. Production des bio-huiles

Les différentes bio-huiles analysées dans le cadre de cette étude ont été produites par le groupe de recherche GREENER au *Laboratoire Réactions et Génie des Procédés* (UMR CNRS 7274) de Nancy. Les zéolithes employées pour effectuer le traitement de désoxygénation ont été synthétisées et caractérisées à l'*Institut de Chimie des Milieux et Matériaux de Poitiers* (UMR CNRS 7285). Il s'agit de zéolithes HZSM-5 parent et hiérarchique.

Les bio-huiles ont été obtenues par pyrolyse de chêne ou de Miscanthus introduit, sous la forme de poudre (2 g) ou de cylindre (0,6 g), dans un réacteur à micro-lit fluidisé chauffé à 500 °C pendant 12 min (*Figure 6*). Le temps de résidence des vapeurs dans le réacteur est de 1,2 s. Un système de pièges cryogéniques, placé à la sortie du réacteur, permet de condenser les vapeurs de bio-huile et de les séparer des gaz incondensables (N<sub>2</sub>, CO<sub>2</sub>...).<sup>35,36</sup>

Des analyses ont été effectuées pour déterminer l'efficacité de désoxygénation des deux zéolithes considérées sur une bio-huile de chêne. Dans ce cas, 5 g de zéolithe sont introduits dans le réacteur et chauffés pendant 4 heures, selon un programme de température défini, avant que les cylindres de chêne ne soient introduits dans le micro-lit fluidisé. Les conditions de pyrolyse sont identiques à celles décrites précédemment. Le chêne a été choisi comme composé modèle car il permet d'obtenir des bio-huiles avec un rendement et une composition répétables.

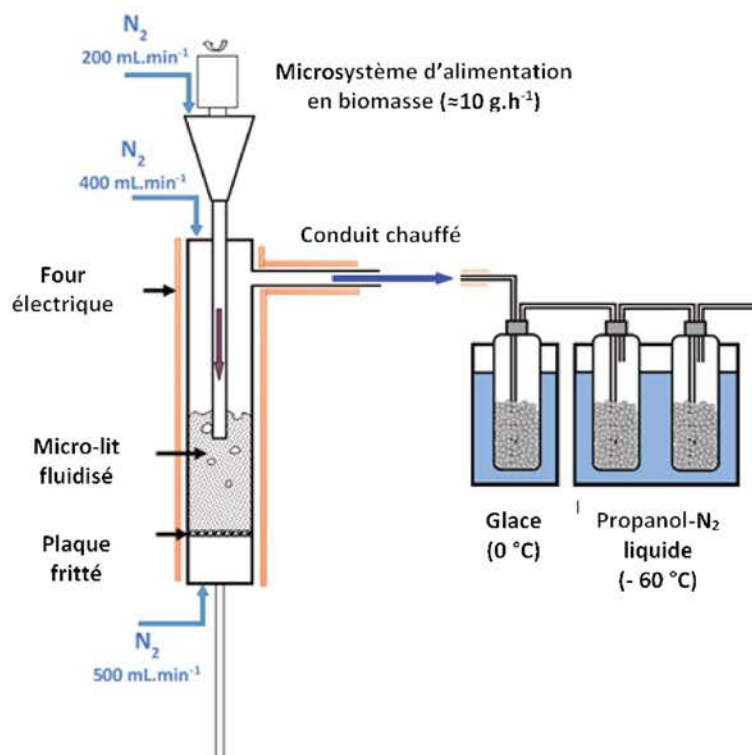


Figure 6. Réacteur à micro-lit fluidisé et pièges cryogéniques utilisés pour la production et la collecte de bio-huiles de pyrolyse

## IV. Méthodologies d'analyse des bio-huiles développées en FT-ICR MS

### IV.A. ESI FT-ICR MS

Pour mettre en place une méthodologie d'analyse optimale de bio-huile par ESI FT-ICR MS, plusieurs facteurs influençant l'ionisation ont été étudiés. Ainsi, l'étude de l'influence d'un agent d'ionisation, de la température du capillaire et de la composition du solvant utilisé a été entreprise. L'ensemble des analyses a été réalisé par ESI FT-ICR MS avec un aimant de 9,4 T.

#### IV.A.1. Influence des agents d'ionisation

Si de nombreux travaux de caractérisation des bio-huiles ont été réalisés par ESI FT-ICR MS en mode de détection négatif, aucun, à notre connaissance, n'a porté sur une analyse systématique et méthodique des paramètres d'ionisation pour asseoir la robustesse de la méthodologie pétroliomique.<sup>23</sup> A cet effet, l'influence de dopants (acétate d'ammonium, de lithium, de sodium et de potassium, acide formique et hydroxyde d'ammonium) a été évaluée tant en mode de détection positif que négatif et comparée à une analyse sans dopant. Dans tous les cas, une bio-huile de *Miscanthus* diluée à 10 % dans le méthanol a été utilisée.

En (-) ESI, l'ajout de 1 % v/v d'hydroxyde d'ammonium, classiquement employé pour favoriser les processus de déprotonation, ou d'acide formique a conduit à la détection de composés oxygénés  $C_xH_yO_z$ . Ils sont les plus intensément détectés et représentent 73 % et 66 % du courant total d'ions, respectivement. Sans dopant, cette proportion est portée à 98 %. Les autres signaux observés sont relatifs à des espèces azotées  $C_xH_yNO_z$  et soufrées  $C_xH_ySO_z$ . Au regard de l'analyse élémentaire<sup>35</sup>, c'est l'analyse sans dopant qui rend mieux compte de la composition de la bio-huile à l'étude. La représentation des composés oxygénés sur un diagramme de van Krevelen permet de mettre en évidence des lipides mais surtout les dérivés de la lignine (Figure 7).

L'influence de la nature du dopant en (+) ESI a été réalisée en examinant des solutions de bio-huile diluée à 10 % dans le méthanol contenant 1 % v/v d'acide formique pour favoriser la protonation, 1 % v/v d'hydroxyde d'ammonium, 1 mg.mL<sup>-1</sup> d'acétate d'ammonium pour favoriser la détection d'espèces  $[M+NH_4]^+$  ou encore 0,1 mg.mL<sup>-1</sup> d'acétate de sodium pour permettre la formation d'adduits  $[M+Na]^+$ .

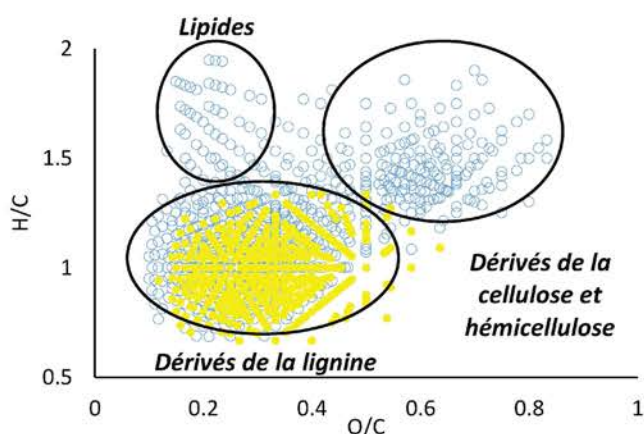


Figure 7. Diagrammes de van Krevelen des composés oxygénés identifiés dans la bio-huile de *Miscanthus* par ESI FT-ICR MS sous la forme  $[M+Na]^+$  en mode de détection positif (bleu) et  $[M-H]$  en mode négatif (jaune)

L'introduction de dopants permet de mieux contrôler les processus d'ionisation qui sont alors parfaitement répétables. Cependant, la distribution des signaux obtenue dans le cadre d'ajout de HCOOH, AcONH<sub>4</sub> et NH<sub>4</sub>OH laisse apparaître une forte proportion d'espèces azotées voire polyazotées alors que ces espèces sont peu présentes dans de telles bio-huiles. Leur analyse élémentaire montre effectivement un pourcentage en azote inférieur à 2 %. A l'inverse, la distribution des familles de composés obtenue après ajout d'AcONa est beaucoup plus fidèle à l'analyse élémentaire. En effet, 98 % du signal est attribuable aux espèces  $C_xH_yO_z$  détectées sous la forme d'adduits sodés. Le diagramme de van Krevelen correspondant à ces

espèces démontre qu'il s'agit de lipides, de dérivés de la lignine et de dérivés de la cellulose et de l'hémicellulose (*Figure 7*).

#### IV.A.2. Influence de la composition du solvant et de la température du capillaire d'injection

Des études ont été menées pour déterminer l'influence de la température du capillaire (la température de la source étant maintenue à 70 °C) et celle de la composition du solvant. L'analyse est réalisée en mode de détection positif en utilisant l'acétate de sodium (0,1 mg.mL<sup>-1</sup>) comme dopant. Ces conditions assurent la détection de tous les composés produits par pyrolyse de la biomasse.

Ainsi, une bio-huile de chêne a été diluée à 10 % dans divers mélanges eau/méthanol (v/v 0/1, 1/4, 1/1, 4/1 et 1/0) et analysée. Les mesures ont été effectuées avec un capillaire d'injection chauffé à 75 ou 110 °C. Dans tous les cas, plus de 98 % du TIC est relié aux espèces oxygénées détectées sous la forme d'adduits sodés. Les diagrammes de van Krevelen de cette famille de composés montrent que tous les composants de la biomasse sont ionisés: les lipides, les dérivés de la lignine, de la cellulose et de de l'hémicellulose.

Cependant, il a été observé, pour les deux températures de capillaire, qu'un rapport croissant en eau était responsable d'une diminution du nombre d'attributions et d'une diversité plus faible de composés dérivés de la lignine. La *Figure 8* représente la somme des valeurs de rapport signal/bruit (S/B) calculée pour les dérivés de la cellulose et de l'hémicellulose, d'une part, et de la lignine, d'autre part. L'évolution des rapports S/B, en fonction de la composition du solvant pour les deux dérivés de la biomasse, suit une même tendance à 75 et 100 °C. On remarque que pour un rapport en eau plus important, le S/B relatif aux espèces cellulosiques est plus grand et ce, peu importe la température du capillaire. Cela est dû au fait que ces espèces, qui sont plus polaires, sont mieux solvatées dans l'eau et donc plus facilement ionisables. De manière générale, le rapport S/B est plus élevé pour des solutions à fort rapport en eau, bien que moins de composés soient identifiés. En effet, si la présence d'eau permet une meilleure ionisation de certains composés, les espèces les plus apolaires, comme les dérivés de la lignine, seront davantage solvatées par un solvant moins polaire comme le méthanol, d'où la plus grande diversité de ces composés obtenue avec 100 % de méthanol. La plus grande sensibilité obtenue avec des rapports en eau importants peut

être également responsable de phénomène de suppression de signal qui conduit à un nombre plus faible de composés identifiés.



Figure 8. Distribution de la somme des rapports signal/bruit relatifs aux composés dérivés de la lignine (en bleu) et de la cellulose/hémicellulose (en orange) en fonction de la composition du solvant pour des températures de capillaire d'infusion de 75 et 110 °C.

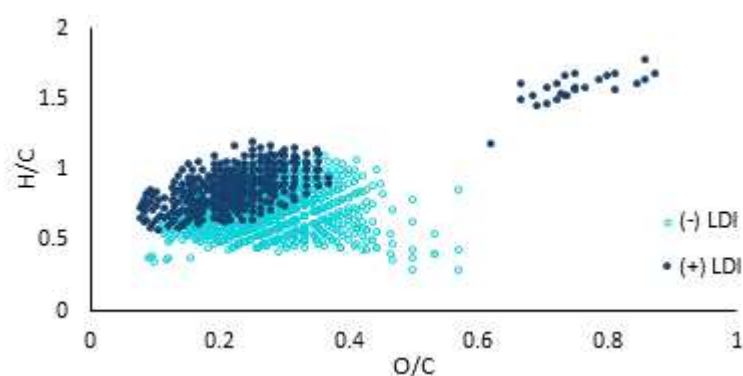
#### IV.B. LDI FT-ICR MS

L'étude des bio-huiles par LDI est menée à 355 nm en présence ou en l'absence de matrice. Deux matrices ont été employées, la 2,5-DHB (acide 2,5-dihydroxybenzoïque) et la DMAN (1,8-bis(diméthylamino)naphthalène), également appelée éponge à proton. Dans un premier temps, la valeur optimale de fluence laser a été déterminée. Elle s'établit à 0.6 J.cm<sup>-2</sup> et correspond à une valeur pour laquelle l'obtention des spectres de masse est répétable sans que ne soient observés des produits de fragmentation (espèces oxygénées de type C<sub>x</sub>H<sub>y</sub>O<sub>1-2</sub>) ni des produits de recombinaison de type C<sub>x</sub>H<sub>y</sub>.

L'exemple de la 2,5-DHB, en mode de détection positif, assure l'observation de composés protonés de type C<sub>x</sub>H<sub>y</sub>O<sub>z</sub> (72 % du courant d'ion total) et C<sub>x</sub>H<sub>y</sub>NO<sub>z</sub> (24 % du TIC). Une propension importante des espèces minoritaires azotées et basiques à se protoner conduit à une forte efficacité d'ionisation comme cela a pu être démontré en ESI avec des agents de protonation. L'utilisation de l'éponge à proton, en mode de détection négatif, limite cet artefact puisque seul 3 % du TIC est relatif aux espèces azotées alors que près de 90 % des ions observés sont des anions de type C<sub>x</sub>H<sub>y</sub>O<sub>z</sub><sup>-</sup> ou C<sub>x</sub>H<sub>y</sub>O<sub>z</sub><sup>•-</sup>. Il est également à noter que 10 %



du TIC, en mode de détection négatif, sont relatifs à des espèces  $C_xH_yFeO_z^-$ . Ces anions viennent de la dissolution, par les bio-huiles acides, de la couche de passivation de la plaque en acier inoxydable sur laquelle les dépôts sont effectués. Ces mêmes espèces sont également observées en LDI. La détection faible en (-) LDI ou limitée en (+) LDI des espèces azotées conduit à considérer que la non utilisation de matrice est la mieux adaptée à l'analyse des bio-huiles. Outre l'absence de préparation, un spectre de masse LDI est dépourvu de signaux relatifs à la molécule de matrice, ce qui en facilite l'interprétation. Dans ce cas, plus de 80 % du signal est associé aux seules espèces  $C_xH_yO_z^{+/-}$  présentant de 4 à 11 atomes d'oxygène. Ils sont principalement relatifs à des espèces dérivées de la lignine comme le montre la *Figure 9*.



*Figure 9. Diagramme de van Krevelen des composés  $C_xH_yO_z$  identifiés dans la bio-huile de chêne par LDI FT-ICR MS en mode de détection positif (bleu foncé) et négatif (bleu clair)*

#### IV.C. APPI FT-ICR MS

L'analyse APPI FT-ICR MS a été réalisée en diluant la bio-huile à 4 % dans différents mélange de solvants: 100 % méthanol, méthanol/toluène et méthanol/acétone (90/10 v/v, 50/50 v/v). Dans les deux derniers cas, le toluène et l'acétone sont introduits car communément utilisés comme dopant en APPI. Les mesures ont été effectuées en APPI positif et négatif. Une solution d'acétate de sodium ( $0,1 \text{ mg.mL}^{-1}$  dans du méthanol) a également été utilisée pour des analyses en mode positif. L'ajout de dopant n'améliore en rien la sensibilité de l'analyse. Les mêmes espèces sont systématiquement observées. Certaines conditions de dopage conduisent même à une diminution du rapport signal/bruit. L'analyse d'une bio-huile en APPI positif et négatif à 4 % dans le méthanol conduit principalement à l'observation d'espèces  $C_xH_yO_z$  majoritairement non radicalaires. Elles représentent 90 % du TIC et sont relatives aux dérivés de la lignine et aux lipides (*Figure 10*).

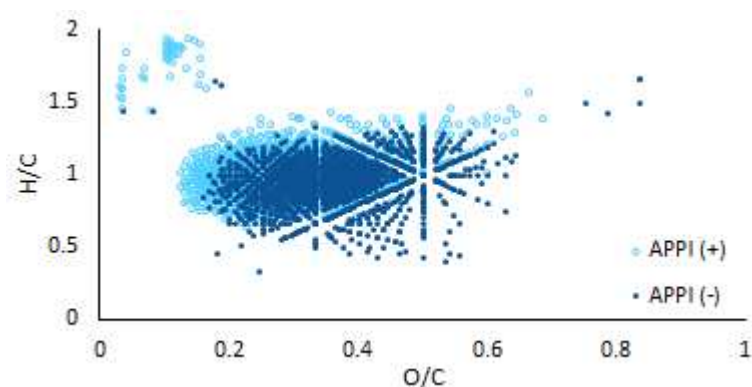


Figure 10. Diagrammes de van Krevelen des composés  $C_xH_yO_z$  identifiés dans la bio-huile de chêne par APPI FT-ICR MS en mode de détection positif (bleu clair) et négatif (bleu foncé)

#### IV.D. Complémentarité des méthodes d'analyses développées

Les distributions de famille de composés obtenues par la combinaison des analyses effectuées sur une bio-huile de chêne, selon les méthodes développées, sont répertoriées dans le *Tableau 1* et sur la *Figure 11*. Dans tous les cas, les espèces  $C_xH_yO_z$  représentent plus de 80 % du signal détecté.

	Nombre de composés attribués	$C_xH_yO_z$	$C_xH_yN_nO_z$	$C_xH_ySO_z$
(+) ESI <sup>a</sup>	1521	95 %	5 %	–
(-) ESI <sup>a</sup>	1382	95 %	2 %	3 %
(+) APPI <sup>a</sup>	2778	90 %	10 %	–
(-) APPI <sup>a</sup>	2181	90 %	10 %	–
(+) LDI <sup>b</sup>	415	83 %	17 %	–
(-) LDI <sup>b</sup>	1222	97 %	3 %	–

<sup>a</sup> 12 T FT-ICR MS    <sup>b</sup> 9.4T FT-ICR MS

Tableau 1. Distribution relative des familles de composés identifiées dans la bio-huile de chêne par ESI, LDI et APPI FT-ICR MS en mode de détection positif et négatif

L'examen précis de ces espèces (*Figure 11*) permet de définir qu'une part significative d'entre elles est spécifique à chaque mode d'ionisation. Par exemple, moins de 3 % des signaux observés en mode de détection positif correspondent à une formule brute identique pour les trois modes d'ionisation. Les diagrammes de Venn regroupent, dans chaque mode de détection, les résultats obtenus et démontrent bien la complémentarité des sources LDI, ESI et APPI (*Figure 11*). Un critère de comparaison supplémentaire consiste à calculer la valeur de DBE moyenne pondérée ( $\overline{DBE}$ ) et la teneur moyenne pondérée en oxygène ( $\overline{O}$ ) pour les espèces spécifiques ou communes aux spectres de masse obtenus dans les trois modes d'ionisation. Ainsi l'analyse ESI FT-ICR MS assure la détection de composés dérivés de la

cellulose et de l'hémicellulose (faible valeur de  $\overline{DBE}$  et valeur importante de  $\overline{O}$ ). Les composés oxygénés ionisés et détectés en APPI sont principalement relatifs aux dérivés de la lignine et donc plus insaturés (valeur de  $\overline{DBE}$  élevée). Ceux obtenus en (+) LDI sont moins nombreux et rassemblent les dérivés de la lignine, de la cellulose et de l'hémicellulose et ont un comportement intermédiaire. Enfin, en (-) LDI, les espèces oxygénées sont essentiellement des dérivés de la lignine et ont une valeur de  $\overline{DBE}$  importante, de l'ordre de 19.

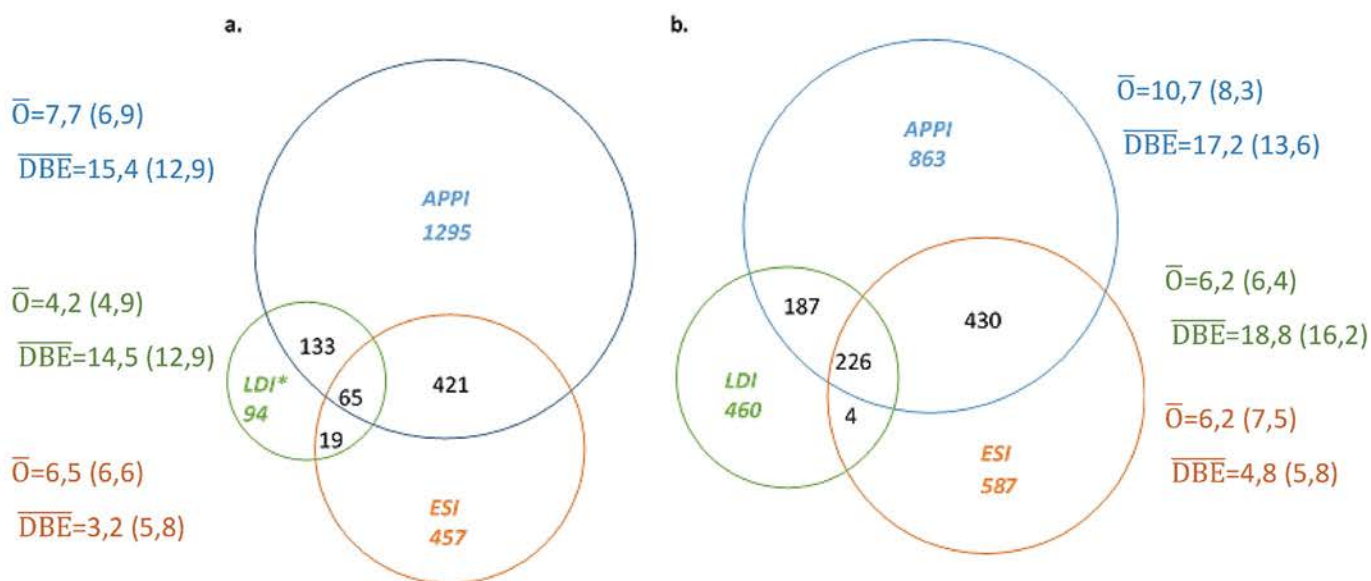


Figure 11. Diagrammes de Venn comportant le nombre de composés  $C_xH_yO_z$  identifiés par analyse de la bio-huile de pyrolyse de chêne par ESI, LDI et APPI FT-ICR MS en mode de détection positif (a) et négatif (b). Les moyennes pondérées du nombre d'atomes d'oxygène et de la DBE ont été calculées pour tous les composés identifiés dans chaque analyse, valeur entre parenthèse, et pour ceux qui sont exclusifs à chaque analyse.

L'emploi des méthodes d'analyse par ESI, LDI et APPI FT-ICR MS est donc souhaitable pour obtenir la composition la plus complète possible de ces mélanges complexes que constituent les bio-huiles. Cette approche a été utilisée comme outil pour mettre en évidence des différences de composition de bio-huiles et de bio-huiles traitées après désoxygénation catalytique.

## V. Application de l'approche pétroléomique pour définir l'efficacité d'un traitement catalytique

Dans la mesure où les analyses ESI et APPI en mode de détection positif ont montré la plus forte complémentarité sur les bio-huiles brutes, cette partie se limitera à ces deux approches.

L'analyse de deux bio-huiles traitées catalytiquement par désoxygénation sur une zéolithe HZSM-5 parent et une zéolithe HZSM-5 hiérarchique a été réalisée. Seuls les résultats obtenus avec la zéolithe la plus efficace (le catalyseur hiérarchique) sont reportés ici. La comparaison des bio-huiles brute et traitée est reportée sur les *Figure 12* et *Figure 13*. L'analyse globale des bio-huiles, quelle que soit sa nature ou la méthode d'ionisation employée, montre une composition semblable avec près de 90 % du TIC relatifs aux composés  $C_xH_yO_z$ . Les diagrammes de van Krevelen permettent d'effectuer un constat autre en indiquant clairement des différences de composition moléculaire (*Figure 12*).

Les résultats ESI montrent une disparition des espèces relatives aux dérivés de la cellulose et de l'hémicellulose dans la bio-huile traitée et témoigne de l'efficacité de ce traitement pour ces composés. Par ailleurs, les composés dérivés de la lignine, observés dans la bio-huile traitée, ont un rapport O/C plus faible. Certains sont donc partiellement désoxygénés, d'autres beaucoup moins puisque le nuage observé ne voit son allure que faiblement modifiée. Bien qu'il y ait une diminution du nombre d'atomes d'oxygène, les dérivés de la lignine sont les plus réfractaires au traitement catalytique.

L'analyse en APPI confirme ces résultats tout en montrant également que les composés lipidiques résistent de manière importante au traitement. Elle permet également de démontrer la formation d'hydrocarbures de formule  $C_xH_y$  et témoigne que l'efficacité du traitement de désoxygénation peut être total.

Par conséquent, en plus d'être complémentaires pour la caractérisation de bio-huiles, ces méthodes d'analyse permettent d'accéder à différentes informations sur les composés répondant ou non au traitement catalytique. Cette complémentarité est illustrée sur les diagrammes de Venn correspondants (*Figure 13*). En ESI et APPI, il y a une diminution de la valeur de la moyenne pondérée en oxygène pour les composés  $C_xH_yO_z$ . L'augmentation de la valeur de  $\overline{DBE}$  en ESI après le traitement traduit la disparition des espèces dérivées de la cellulose et de l'hémicellulose (les plus saturées) et la persistance de certains dérivés de la

lignine (plus insaturés). En APPI, les espèces présentent une valeur de  $\overline{DBE}$  plus faible et révèlent l'efficacité des processus de craquage catalytique opérés par la zéolithe.

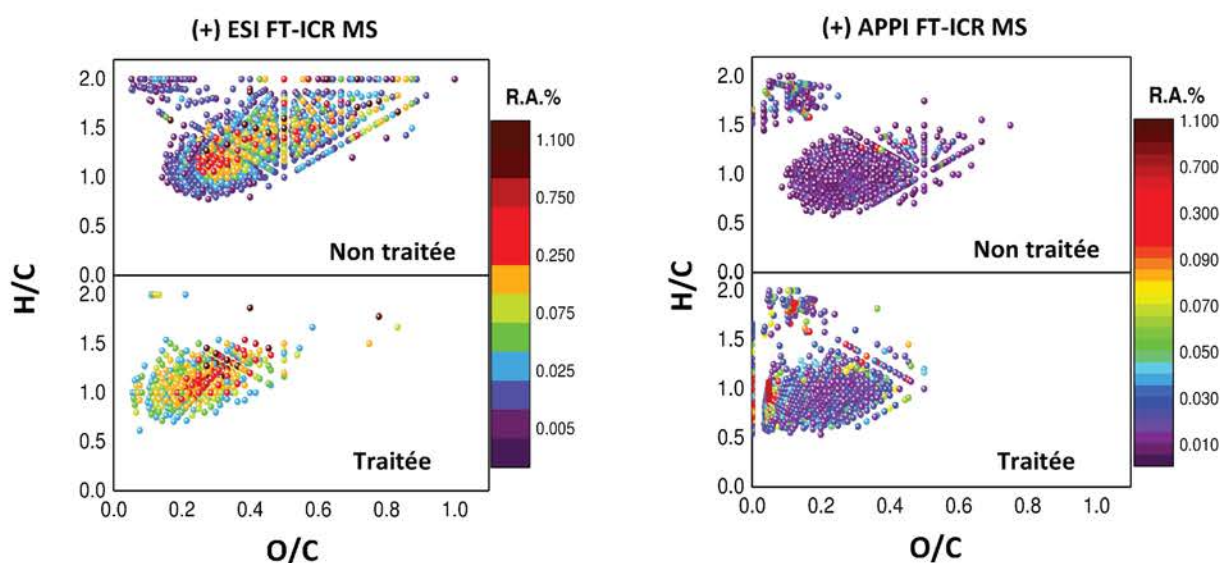


Figure 12. Diagrammes de van Krevelen des composés  $C_xH_y$  et  $C_xH_yO_z$  identifiés par ESI et APPI FT-ICR MS en mode positif dans l'étude des bio-huiles brute et traitée.

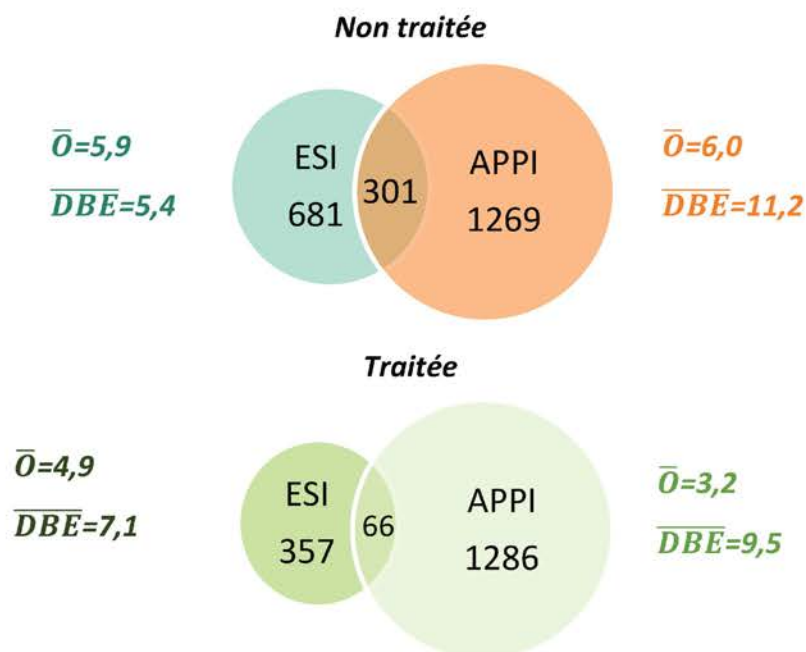


Figure 13. Diagrammes de Venn comportant le nombre de composés  $C_xH_y$  et  $C_xH_yO_z$  identifiés dans l'étude par ESI et APPI FT-ICR MS en mode de détection positif, de la bio-huile de pyrolyse de chêne brute et traitée. Pour chaque analyse, les moyennes pondérées du nombre d'atomes d'oxygène et de DBE ont été calculées.

## VI. Conclusion

Cette étude a permis de mettre en place et d'optimiser des méthodologies d'analyses sensibles, répétables et robustes par ESI, LDI et APPI FT-ICR MS de bio-huiles issues de pyrolyse de biomasse lignocellulosique. La caractérisation la plus détaillée possible de ces mélanges complexes est nécessaire pour mieux comprendre et améliorer les procédés de pyrolyse et ceux de catalyse qui conduisent *in fine* à la production de «pétrole vert» exploitable comme le pétrole actuel.

Dans le cadre de la mise en place de l'analyse par ESI FT-ICR MS, nous avons notamment mis en évidence l'influence des dopants sur la description de la composition des bio-huiles.<sup>37</sup> L'emploi de ces dopants doit cependant être effectué avec précaution puisque des processus chimiques peuvent avoir lieu avant ou pendant l'infusion dans la source ESI, comme nous les avons par ailleurs démontrés, entre les composés carbonylés et l'ammoniaque. Ce dopant est souvent utilisé pour favoriser la déprotonation. Une relecture des travaux déjà publiés s'impose donc. Cependant, cette réactivité des composés carbonylés (aldéhydes, cétones et acides carboxyliques) contenus dans la bio-huile, vis-à-vis des amines primaires, peut également permettre de les mettre en évidence.<sup>38</sup>

Nous avons également déterminé que les analyses ESI FT-ICR MS étaient complémentaires des analyses LDI et APPI pour la caractérisation exhaustive de bio-huiles non traitées.<sup>39</sup>

Cette approche, appliquée à des bio-huiles ayant subi un traitement de désoxygénation par deux zéolithes différentes, permet de mettre en évidence que chacune de ces techniques d'analyse apporte une contribution sur la compréhension de l'acte catalytique. La nature de la zéolithe a une influence sur la composition de la bio-huile produite et sur l'efficacité du traitement.<sup>40</sup>

## VII. Références

1. Huber, G. W., Iborra, S. & Corma, A. Synthesis of Transportation Fuels from Biomass: Chemistry, Catalysts, and Engineering. *Chem. Rev.* **106**, 4044–4098 (2006).
2. Sheldon, R. A. Green and sustainable manufacture of chemicals from biomass: state of the art. *Green Chem.* **16**, 950–963 (2014).
3. Institute, W. *Biofuels for Transport: Global Potential and Implications for Sustainable Energy and Agriculture*. (Earthscan, 2012).
4. Industry Statistics. *Renewable Fuels Association* (2015).
5. Bozbas, K. Biodiesel as an alternative motor fuel: Production and policies in the European Union. *Renew. Sustain. Energy Rev.* **12**, 542–552 (2008).
6. Sanchez, O. J. & Cardona, C. A. Trends in biotechnological production of fuel ethanol from different feedstocks. *Bioresour. Technol.* **99**, 5270–5295 (2008).
7. Demirbas, A. Biodiesel production from vegetable oils via catalytic and non-catalytic supercritical methanol transesterification methods. *Prog. Energy Combust. Sci.* **31**, 466–487 (2005).
8. Mohr, A. & Raman, S. Lessons from first generation biofuels and implications for the sustainability appraisal of second generation biofuels. *Energy Policy* **63**, 114–122 (2013).
9. Cambero, C., Sowlati, T., Marinescu, M. & Roeser, D. Strategic optimization of forest residues to bioenergy and biofuel supply chain. *Int. J. Energy Res.* **39**, 439–452 (2015).
10. Chandra, R., Takeuchi, H. & Hasegawa, T. Methane production from lignocellulosic agricultural crop wastes: A review in context to second generation of biofuel production. *Renew. Sustain. Energy Rev.* **16**, 1462–1476 (2012).
11. Brosse, N., Dufour, A., Meng, X., Sun, Q. & Ragauskas, A. Miscanthus: a fast-growing crop for biofuels and chemicals production. *Biofuels Bioprod. Biorefining-Biofpr* **6**, 580–598 (2012).
12. Iqbal, M., Bermond, A. & Lamy, I. Impact of miscanthus cultivation on trace metal availability in contaminated agricultural soils: Complementary insights from kinetic extraction and physical fractionation. *Chemosphere* **91**, 287–294 (2013).
13. Techer, D., Martinez-Chois, C., Laval-Gilly, P., Henry, S., Bennisroune, A., D’Innocenzo, M. & Falla, J. Assessment of Miscanthus x giganteus for rhizoremediation of long term PAH contaminated soils. *Appl. Soil Ecol.* **62**, 42–49 (2012).
14. Demirbas, A. Calculation of higher heating values of biomass fuels. *Fuel* **76**, 431–434 (1997).
15. Klemm, D., Heublein, B., Fink, H.-P. & Bohn, A. Cellulose: fascinating biopolymer and sustainable raw material. *Angew. Chem. Int. Ed Engl.* **44**, 3358–3393 (2005).
16. Scheller, H. V. & Ulvskov, P. Hemicelluloses. *Annu. Rev. Plant Biol. Vol 61* **61**, 263–289 (2010).
17. Evans, R., Milne, T. & Soltys, M. Direct Mass-Spectrometric Studies of the Pyrolysis of Carbonaceous Fuels .3. Primary Pyrolysis of Lignin. *J. Anal. Appl. Pyrolysis* **9**, 207–236 (1986).

18. Zhang, S., Sun, J., Zhang, X., Xin, J., Miao, Q. & Wang, J. Ionic liquid-based green processes for energy production. *Chem. Soc. Rev.* **43**, 7838–7869 (2014).
19. Serrano-Ruiz, J. C. & Dumesic, J. A. Catalytic routes for the conversion of biomass into liquid hydrocarbon transportation fuels. *Energy Environ. Sci.* **4**, 83–99 (2010).
20. Elliott, D. C. & Schiefelbein, G. F. Liquid hydrocarbon fuels from biomass. *Am. Chem. Soc. Div. Fuel Chem. Annu. Meet. Prepr.* 1160–1166 (1989).
21. Oasmaa, A., Korhonen, J. & Kuoppala, E. An Approach for Stability Measurement of Wood-Based Fast Pyrolysis Bio-Oils. *Energy Fuels* **25**, 3307–3313 (2011).
22. Stas, M., Kubicka, D., Chudoba, J. & Pospisil, M. Overview of Analytical Methods Used for Chemical Characterization of Pyrolysis Bio-oil. *Energy Fuels* **28**, 385–402 (2014).
23. Michailof, C. M., Kalogiannis, K. G., Sfetsas, T., Patiaka, D. T. & Lappas, A. A. Advanced analytical techniques for bio-oil characterization. *Wiley Interdiscip. Rev.-Energy Environ.* **5**, 614–639 (2016).
24. Marshall, A. G. & Rodgers, R. P. Petroleomics: The Next Grand Challenge for Chemical Analysis. *Acc. Chem. Res.* **37**, 53–59 (2004).
25. Bae, E., Na, J.-G., Chung, S. H., Kim, H. S. & Kim, S. Identification of about 30 000 Chemical Components in Shale Oils by Electrospray Ionization (ESI) and Atmospheric Pressure Photoionization (APPI) Coupled with 15 T Fourier Transform Ion Cyclotron Resonance Mass Spectrometry (FT-ICR MS) and a Comparison to Conventional Oil. *Energy Fuels* **24**, 2563–2569 (2010).
26. Kim, S., Kramer, R. W. & Hatcher, P. G. Graphical Method for Analysis of Ultrahigh-Resolution Broadband Mass Spectra of Natural Organic Matter, the Van Krevelen Diagram. *Anal. Chem.* **75**, 5336–5344 (2003).
27. Lawrence, E. O. & Livingston, M. S. The Production of High Speed Light Ions Without the Use of High Voltages. *Phys. Rev.* **40**, 19–35 (1932).
28. Marshall, A. G., Hendrickson, C. L. & Jackson, G. S. Fourier transform ion cyclotron resonance mass spectrometry: A primer. *Mass Spectrom. Rev.* **17**, 1–35 (1998).
29. Marshall, A. G. & Verdun, F. R. *Fourier Transforms in Nmr, Optical, and Mass Spectrometry: A Users Handbook.* (Elsevier Science Ltd, 1990).
30. Marshall, A. G. & Hendrickson, C. L. High-Resolution Mass Spectrometers. *Annu. Rev. Anal. Chem.* **1**, 579–599 (2008).
31. Banerjee, S. & Mazumdar, S. Electrospray Ionization Mass Spectrometry: A Technique to Access the Information beyond the Molecular Weight of the Analyte. *Int. J. Anal. Chem.* 282574 (2012). doi:10.1155/2012/282574
32. Haglund, R. F. Microscopic and mesoscopic aspects of laser-induced desorption and ablation. *Appl. Surf. Sci.* **96–8**, 1–13 (1996).
33. Karas, M., Gluckmann, M. & Schafer, J. Ionization in matrix-assisted laser desorption/ionization: singly charged molecular ions are the lucky survivors. *J. Mass Spectrom.* **35**, 1–12 (2000).
34. Raffaelli, A. & Saba, A. Atmospheric pressure photoionization mass spectrometry. *Mass Spectrom. Rev.* **22**, 318–331 (2003).



35. Jia, L., Le-Brech, Y., Shrestha, B., Bente-von Frowein, M., Ehlert, S., Mauviel, G., Zimmermann, R. & Dufour, A. Fast Pyrolysis in a Microfluidized Bed Reactor: Effect of Biomass Properties and Operating Conditions on Volatiles Composition as Analyzed by Online Single Photoionization Mass Spectrometry. *Energy Fuels* **29**, 7364–7374 (2015).
36. Le Brech, Y., Jia, L., Cissé, S., Mauviel, G., Brosse, N. & Dufour, A. Mechanisms of biomass pyrolysis studied by combining a fixed bed reactor with advanced gas analysis. *J. Anal. Appl. Pyrolysis* **117**, 334–346 (2016).
37. Hertzog, J., Carré, V., Le Brech, Y., Dufour, A. & Aubriet, F. Toward Controlled Ionization Conditions for ESI-FT-ICR-MS Analysis of Bio-Oils from Lignocellulosic Material. *Energy Fuels* **30**, 5729–5739 (2016).
38. Hertzog, J., Carré, V., Dufour, A. & Aubriet, F. Application of a non-targeted approach for the detection of carbonyl compounds in complex mixtures with primary amines. *J. Am. Soc. Mass Spectrom.* (to be submitted).
39. Hertzog, J., Carré, V., Le Brech, Y., Mackay, C. L., Dufour, A., Mašek, O. & Aubriet, F. Combination of electrospray ionization, atmospheric pressure photoionization and laser desorption ionization Fourier transform ion cyclotronic resonance mass spectrometry for the investigation of complex mixtures - Application to the petroleomic analysis of bio-oils. *Anal. Chim. Acta* **969**, 26–34 (2017).
40. Hertzog, J., Carré, V., Jia, L., Pinard, L., Mackay, C. L., Masek, O., Dufour, A. & Aubriet, F. Study of heavy products from zeolite catalytic fast pyrolysis of lignocellulosic biomass by ultra-high resolution mass spectrometry analysis. *Acs Sustain. Chem. Eng.* (to be submitted).





## ABSTRACT

The products of lignocellulosic biomass pyrolysis are potential sources of renewable materials such as bio-fuels, biochars, and chemicals. However, their ready-to-use capacity is limited by their high chemical complexity and their high oxygen content. Therefore, they have to be upgraded by different treatments such as deoxygenation and/or cracking. In order to assess the most suited upgrading process, it is necessary to obtain an extensive composition description of the raw pyrolysis products. The works carried out during this PhD thesis are dealing with the development of though analytical methods to reach the most detailed composition description of bio-oils. This study was performed by Fourier transform ion cyclotron resonance mass spectrometry (FT-ICR MS) using different ionization sources. The electrospray ionization (ESI), in controlled-conditions, ensures to ionize the cellulose and the hemicellulose derived compounds as well as the lipids and the lignin derivatives. The atmospheric pressure photoionisation (APPI) and the laser desorption/ionization (LDI) allow specifically to detect more unsaturated pyrolytic lignin species. The combination of the different results ensures to obtain an extensive bio-oil description. The established methodology was applied to raw and upgraded (catalytic deoxygenation/cracking treatment on different zeolites) bio-oils. The ESI FT-ICR MS measurements evidenced the selectivity of the used catalysts on sugarc compounds whereas the APPI and LDI highlighted the nature of the resulting compounds which are less oxygenated and produced, for a part of them, by catalytic cracking.

*Keywords: bio-oils, pyrolysis, Fourier transform ion resonance mass spectrometry, petroleomic approach, ionization sources*

---

Etude par spectrométrie de masse à haute résolution de bio-huiles issues de la pyrolyse de la biomasse lignocellulosique

## RESUMÉ

Les produits de la pyrolyse de la biomasse lignocellulosique présentent un potentiel important dans le cadre des ressources renouvelables. Cependant, leur utilisation directe est réduite en raison de leur importante complexité et de leur teneur élevée en oxygène. Il est nécessaire de leur faire subir des traitements de désoxygénation et/ou de craquage. Afin de déterminer quels sont les traitements les mieux adaptés, il est indispensable de connaître aussi précisément que possible leur composition. Les travaux menés dans le cadre de cette thèse portent sur la mise en place de méthodologies d'analyse robustes pour obtenir la description la plus exhaustive possible des bio-huiles. Pour cela, la spectrométrie de masse à résonance cyclotronique d'ions à transformée de Fourier (FT-ICR MS) a été employée en couplage avec différentes sources d'ionisation. L'électronébulisation (ESI), dans des conditions contrôlées d'ionisation, permet d'observer plus particulièrement les composés dérivés de la cellulose et de l'hémicellulose ainsi que des lipides et des dérivés de la lignine. La photoionisation à pression atmosphérique (APPI) et la désorption-ionisation par laser (LDI) sont plus spécifiques des espèces relatives à la lignine. Celles qui sont alors observées sont plus insaturées qu'en ESI. La complémentarité des différentes techniques d'analyse a été établie et a permis la description détaillée de bio-huiles. Cette méthodologie a été appliquée à des bio-huiles avant et après traitement de désoxygénation/cracking sur zéolithes. L'analyse par ESI FT-ICR MS a mis en évidence la sélectivité de ces catalyseurs envers les dérivés cellulosiques alors que l'étude par APPI et LDI a permis de déterminer la nature des composés obtenus après traitement catalytique. Ceux-ci présentent une diminution de la teneur en oxygène et résultent, pour une partie d'entre eux, du craquage catalytique sur les composés de la bio-huile originelle.

*Mots-clés : Bio-huiles, pyrolyse, spectrométrie de masse à résonance cyclotronique des ions à transformée de Fourier, approche pétroléomique, sources d'ionisation*